Final Technical Report

Federal Agency and Organization Element to Which Report is Submitted	Office of Fossil Energy U.S. Department of Energy National Energy Technology Laboratory
Federal Grant or Other Identifying Number Assigned by Agency	DE-FE0029900
Project Title	Fundamental Studies on the Recovery of Rare Earth Elements from Coal and Coal Byproducts
PD/PI Name, Title and Contact Information (e-mail address and phone number)	Dr. Roe-Hoan Yoon Center for Advanced Separation Technologies 146 Holden Hall – Virginia Tech Blacksburg, VA 24061 Email: ryoon@vt.edu Phone: 540-231-7056
Name of Submitting Official, Title, and Contact Information (e-mail address and phone number), if other than PD/PI	Dr. Roe-Hoan Yoon Center for Advanced Separation Technologies 146 Holden Hall – Virginia Tech Blacksburg, VA 24061 Email: ryoon@vt.edu Phone: 540-231-7056
Submission Date	August 8, 2022
DUNS Number	003137015
Recipient Organization (Name and Address)	Virginia Polytechnic Institute & State University Office of Sponsored Programs 0170 300 Turner Street NW, Suite 4200 Blacksburg, VA 24061-0001
Project/Grant Period (Start Date, End Date)	8/1/2017-3/31/2022
Reporting Period End Date	March 31, 2022
Report Term or Frequency	Final
Signature of Submitting Official	

FUNDAMENTAL STUDIES ON THE RECOVERY OF RARE EARTH ELEMENTS FROM COAL AND COAL BYPRODUCTS

Project Final Report

Award Information

Prime Sponsor: US Department of Energy
Lead Institution: Virginia Tech
Principle Investigator: Roe-Hoan Yoon
Federal Award Number: DE-FE0029900
Federal Project Manager: Christian Robinson

DISCLAIMER

EXECUTIVE SUMMARY

Project Objectives

The *objective* of this project was to collect fundamental information that can be used to develop disruptive physical and chemical separation methods that may be used to extract the rare earth elements (REEs) from coal-based feedstocks in a highly efficient, cost-effective, and environmentally benign manner. To meet the stated objective, a set of interrelated fundamental studies have been conducted. The project has been subdivided into three broad areas of tasks as follows,

1) Measurement of surface forces in the thin liquid films (TLFs) of water confined between two macroscopic surfaces to establish the optimal conditions for efficiently collecting the ultrafine particles of rare earth minerals (REMs) present in the coal-based feedstocks using the flotation and/or the hydrophobic-hydrophilic separation process(es),
2) Identification of the fundamental mechanisms by which REE ions adsorb and desorb on clay minerals present in coal byproducts, and the characterization of the ion-adsorption clays (IACs) present in U.S. coals, and
3) Developing methods of extracting the REEs from the REMs and IACs present in US coal byproducts in a cost-effective and sustainable manner.

Project Findings

The fundamental studies conducted in the present work led to the findings that much of the REEs in the U.S. coals are associated with kaolin clay as suggested by Bryan *et al*. (2015) and that monazite is the major REM. It has also been found that the particle sizes of the REMs are mostly below 10 μm, which makes it difficult to recover them using a physical separation process, *e.g*., flotation, prior to chemical leaching. Furthermore, the grades of the feedstocks are very low, typically in the range of 300-600 ppm, which makes it difficult to extract the REEs into solution economically. What makes it more challenging is the fact that much of the REEs in the Appalachian coal are present as phosphates that are extremely stable when combined with REEs and hence require aggressive conditions to decompose the compounds as part of the chemical extraction processes. One of the major findings of the project was that the IACs found in the eastern U.S. coal byproducts are passivated by phosphate (PO_4^{2-}) ions, which makes it difficult to extract them using the traditional ion-exchange leaching process using ammonium sulfate ($(NH_4)_2SO_4$) as a lixiviant. Spectroscopic analysis conducted on the synthetic IACs prepared in the present work supported the mechanisms associated with the difficulties in extracting REEs from the clayey materials found in coal byproducts. A series of extraction tests conducted on a Chinese IAC sample showed also that ion-exchange leaching becomes extremely difficult after spiking the clay with phosphate ions.

The results of the fundamental studies summarized above suggest two approaches that may lead to practicable solutions. One is to find ways to cope with the REEs being present mostly as phosphates, and the other is to upgrade the REE-bearing minerals prior to chemical extraction. As part of the first approach, we have developed a novel method of extracting REEs from monazite under mild conditions to minimize wastewater generation. The process entails a pretreatment of monazite concentrate at a relatively low caustic solution at temperatures below 80°C, followed by ion-exchange leaching at pH 4 at an ambient temperature. In addition, we have developed a method of activating the passivated IACs to improve extraction efficiencies. As part of the second approach, we have developed a novel method of preconcentrating a feedstock from 300-500 ppm to the range of 0.3-56% REEs using the hydrophobic hydrophilic separation process (HHS) developed at Virginia Tech. It is hoped that a combination of the two approaches will lead to commercially-viable processes that can be used to extract REEs from coal byproducts to meet domestic needs for years to come. A byproduct of this process will be a salable dry carbon feedstock.

CONTENTS

Disclaimer ..... **i**
Executive Summary ..... **ii**
Project Objectives ii
Project Findings ii
Contents ..... **iii**
Technical Background **1**
Project Achievements **2**
Task 1: Project Management & Planning 2
Task 2: Two-Liquid Flotation 4
Task 3: Control of Surface Hydrophobicity 21
Task 4: Study of Thin Liquid Films 50
Task 5: Chemical Extraction 96
Products **380**
References **381**

TECHNICAL BACKGROUND

Extracting rare earth elements (REEs) from the U.S. coal and coal byproducts is difficult for various reasons. The most significant challenge is the low-contained values due to their low head grades, which limit viable options. Another problem is that they are not in easily-extractable forms. The rare earth elements present in fly ash are usually encapsulated in glassy materials, requiring costly alkali cracking, flowed by acid-leaching processes. For another, the rare earth minerals (REMs) found in refuse are smaller than 10 μm, making it difficult to recover them by flotation - the standard separation method used in the minerals processing industry. Under this situation, recovery by chemical leaching may be the only option. However, chemical extraction processes are inherently costlier than physical extraction processes often by orders of magnitudes.

Recognizing the challenges noted above, we explored the possibility of developing lower-cost extraction methods based on more fundamental studies. Our approach has been to identify the species in coal byproducts first and then to devise appropriate extraction methods for the target species. We thought that the most promising approach was to extract the REEs from clay minerals in coal byproducts. According to Bryan *et. al*. (2015), they are partitioned mostly to clay minerals and only small amounts are fixed to organic matrix by ion-exchange mechanism.

Since the mid-1990s, most of the world's heavy rare earth elements (HREEs), *e.g*., Tb, Dy, and Y, have been produced from the ion-adsorption clays in Southeast China (Yang *et. al*., 2013). Despite its low grades (500-3,000 ppm), the extraction costs are lower than any other methods due to its simplicity. Ion adsorption clay deposits are formed due to the adsorption of the trivalent lanthanide ions (Ln^{3+}) on the mineral surface. Clay minerals acquire negative charges on the surface as part of the lattice Al^{3+} ions have been substituted by divalent cations such as Fe^{2+} while the lattice Si^{4+} ions substituted by Al^{3+} and Fe^{3+} ions. These substitutions occur during formative stages, *i.e.*, weathering of feldspar. The clay minerals formed in this manner are transported to a coal basin along with the REE ions also formed due to weathering of rare earth minerals present in granite.

Since lanthanide (Ln^{3+}) ions are trivalent and small is size, their charge densities are high and hence adsorb readily on the negatively charged clay surfaces. If the adsorption is controlled by the electrical double-layer (EDL) forces, the standard free energies of adsorption (ΔG_f^o) can be calculated to be in the range of a few kcal/mole, while those for rare earth minerals are in hundreds of kcal/mole. Therefore, they can be readily displaced by other cations such NH_4^+, Na^+, and Mg^{2+} ions, provided that the activities of the lixiviants are high. Once the Ln^{3+} ions are extracted into solution, they can be precipitated with bicarbonate (or oxalic acid). Ion-adsorption clays were also found recently in the U.S. on the foothills of Appalachian Mountains in South Carolina (Bern *et al*., 2017) and Virginia. The REE concentrations in these deposits are in the range of 300 to 1,000 ppm.

A question to be raised is whether the ion-adsorption clays also exist in coal byproducts. Rozelle *et al*. (2016) were the first to report that REEs can be extracted from the underclay of the Upper Kittanning coal using ammonium sulfate as lixiviant. In addition, we have detected REE species adsorbed on both the ion-adsorption clays prepared in our laboratory and some of the refuse samples isolated from an operating coal cleaning plants in West Virginia.

There are many advantages of extracting REEs from the clay minerals present in coal refuse. *First*, most of the REEs in coal are associated clay minerals as note above (Bryan *et al*., 2015). *Second*, Ln^{3+} ions are likely adsorbed on clay surfaces by weak EDL forces; therefore, less energy may be required to recover by ion-exchange leaching than by using strong acids to break stronger chemical bonds. *Third*, clay minerals constitute 60-70% of the mineral matter in coal (Renton, 1982). *Fourth*, clay minerals congregate to thickeners in coal cleaning plants, obviating the cost of remining. *Fifth*, the amounts of REEs that can be recovered from operating coal cleaning plants may exceed 50% of the domestic consumption. *Sixth*, the REEs extracted from clay are rich in HREEs and energy critical materials. *Seventh*, the amounts of

radioactive elements, *i.e.*, Th and U, are very low. *Eighth,* the clay minerals are rich sources of yttrium (Y) and scandium (Sc). Ninth, the ion-exchange leaching process does not entail significant dissolution of clay minerals, which will substantially minimize the cost of effluent treatment. *Tenth*, processing thickener underflows will produce salable coal as byproducts. *Finally*, the reject materials will produce high-grade REM concentrates that can be used as feedstocks for producing rare earth metals using the acid- or alkali-cracking and leaching processes.

PROJECT ACHIEVEMENTS

Task 1: Project Management & Planning

Approach and Task Objectives

This task included all work elements needed to develop and maintain a robust project management plan, as well as the efforts needed to manage and report on activities in accordance with the plan.

Results and Discussion

Within 30 days of project initiation, a formal *Project Management Plan* was submitted to the US Department of Energy (DOE) federal project manager for review and approval. Throughout the project, the principle investigator and the project management committee routinely met to discuss project goals, priorities, and objectives. Project risks were identified early, and adequate mitigation plans were developed and continually assessed. All periodic reports as well as supplemental Interim Accomplishment Reports were submitted to DOE as requested. The final project milestone log is included in Table 1.

Table 1. Project Milestone Summary

ID	Milestone Title/Description (Completion of Task/Subtask)	Completion Date		Verification Method	Comments (progress toward achieving milestone, explanation of deviation from plan, etc.)
		Planned	Actual		
5.1	MS1: Sample identification and collection complete	7/31/2020	7/31/2020	All field samples needed for laboratory study are obtained.	Milestone complete
5.2	MS2: Thermodynamic simulations complete	7/31/2020	7/31/2020	Thermodynamic simulations reveal at least three promising lixiviants.	Milestone complete
5.2	MS3: Synthetic sample leaching and surface analysis complete	6/30/2021	6/30/2021	Leaching and XPS analysis of synthetically-prepared clay samples reveals mechanism for passivation.	Milestone complete.
5.3	MS4: Field sample leaching complete	8/31/2021	3/31/2022	Leaching of field samples validates findings from thermodynamic and synthetic clay testing.	Milestone complete.
4.4	MS5: Hydrophobic-hydrophilic separation testing complete	8/31/2021	3/31/2022	Separations tests show optimal operation conditions and equipment configuration that maximizes the enrichment of rare earth minerals	Milestone complete.
5.3	MS6: Techno-economic analysis complete	9/30/2021	3/31/2022	Techno-economic analysis shows primary cost drivers, process sensitivity, and overall economic merit.	Milestone complete

Task 2: Two-Liquid Flotation

Introduction

Most of the metals we use today are produced by flotation – a separation process patented in 1905. The process is inefficient, however, for the recovery of particles finer than ~10 μm. It happens that the grain size of the rare earth minerals (REMs) found in coal and coal byproducts are in this range, making it difficult to recover by using flotation. In the present work, we use the hydrophobic hydrophilic separation (HHS) process, which was patented in 2016 (US Patent 9,5158,241) for the REMs recovery. In this process, small droplets of recyclable oil (e.g., pentane and heptane) droplets rather than air bubbles are used to collect hydrophobic particles. The process is rather similar to the solvent extraction process, which is widely using in industry in Nano-scale. One of the objectives of the present work is to improve and optimize the HHS process, which was designed originally for coal recovery, so that it can also be used for the recovery of micron- and submicron-sized REMs from coal and coal byproducts. The approach taken is to increase our understanding of the basic mechanisms involved. Tasks 2-4 are designed to collect the necessary database and information to increase our fundamental knowledge.

Studies were initiated under Task 2 – Two-Liquid Flotation to study the mechanisms by which mineral fines form Pickering emulsions in a mixture of two immiscible liquids, i.e., water and oil. In effect, hydrophobic particles act as a "solid surfactant" that can stabilize one phase (e.g., oil) in another (e.g., water) or vice versa. The effects of particle hydrophobicity and phase volume on emulsification were studied. In the HHS process, ultrafine particles are recovered in the form of oil-in-water (O/W) emulsions, which are subsequently transformed to water-in-oil (W/O) emulsion by a phenomenon known as phase inversion. The science of phase inversion is not yet fully understood particularly for the emulsions stabilized by fine particles (Pickering emulsions). Therefore, the project team needs to generate a database through a series of systematic experiments and theoretical analyses. The research conducted at Virginia Tech established that control of particle hydrophobicity is most critically important for achieving phase inversion. The phase inversion is essential for producing high-grade REM concentrates. Until this project started, the research team did not know how to transform the O/W emulsions formed with REMs into W/O emulsions. With this limited knowledge, it was not possible to produce REM concentrates assaying 1-2% REEs on a mineral matter basis. With improved understanding of phase inversion, it is possible that the grade may be improved substantially, possibly over 10% REEs.

Emulsion Stability

It is well known that rare earth minerals (REMs) found in coal products are of micron sizes (< 5-6 μm), which are beyond the lower particle size limit of flotation. One way to address this problem may be to use the two-liquid flotation method, which was shown to be able to recover submicronic particles better than flotation (Mellgren and Shergold, 1966; Lai and Fuerstenau, 1968). A more recent study conducted by Macunsky et al. (2009) showed that nanoparticles of magnetite can be recovered by two-liquid flotation, which the authors called liquid-liquid phase transfer. In these methods, organic solvents (e.g., octane) rather than air bubbles are used to recover hydrophobic particles, which is rather similar to solvent extraction. In this regard, the process has no lower particle size limit in principle, which should be good for the recovery of micron- and submicron size REMs from coal sources.

Using an organic solvent can be costlier than using air bubbles, which may be an inherent disadvantage associated with the two-liquid flotation. The hydrophobic-hydrophilic separation (HHS) process developed at Virginia Tech (Yoon, US Patent, 9,519,241, 2016; Yoon et al., 9,789,492, 2017) is designed to reduce the cost by using a recyclable solvent (e.g., C5-C7 alkanes). These reagents are more hydrophobic than the isooctane used by Mellgren and Shergold (1966) and Lai and Fuerstenau (1968) by virtue of their shorter chain lengths and hence can achieve higher recoveries. Furthermore, the HHS process is designed to eliminate the water and gangue minerals entrained during the recovery step, which is accomplished by using a specially designed unit operation known as Morganizer.

The objective of this task is to study the various factors affecting the stability of the emulsions stabilized by particles of different surface properties, otherwise known as Pickering emulsions (Pickering, 1907), that may occur in the Morganizer. The surface properties to be studied include particle hydrophobicity as represented by contact angle (θ), phase volume (ϕ), or organic-to-water ratio, electrolyte concentrations, %solids, particle composition and size, etc. The majority of the work is to be conducted using particles of pure minerals such as silica, monazite, and bastnaesite. Experimental work has been conducted on two different minerals, i.e., silica (SiO_2) and chalcopyrite ($CuFeS_2$). The information will serve as a basis for studying the behavior of rare earth minerals, i.e., monazite and bastnaesite.

Sample Preparation

The glass microspheres (EMB-10) with a mean size of 5 μm were purchased from Potters Industries LLC. They were cleaned in a piranha solution – mixture of sulfuric acid and hydrogen peroxide – to remove organic matter, rinsed with deionized water, and then dried. The glass beads cleaned in this manner were hydrophobized by immersion in an octadecyltrichlorosilane (OTS)-in-toluene solution. The hydrophobicity of the glass beads was controlled by varying the OTS concentration and immersion time. The glass beads were silylated together with a quartz plate in the same OTS solution, so that contact angles could be measured using the sessile drop technique.

Chunky samples of chalcopyrite were purchased from Ward's Science. They were crushed by means of a hammer to less than <0.6 mm and subsequently wet-ground in a motor-driven mortar and pestle to micron sizes. The samples obtained in this manner assayed 32.8 %Cu using the ICP-MS analyzer.

Potassium amyl xanthate (KAX) of >95% purity from TCI America was used to hydrophobize the chalcopyrite sample. The reagent was purified twice before use by dissolving in acetone (HPLC grade, FisherSci.) and re-crystallizing in diethyl ether (99.999%, Sigma-Aldrich). A KAX solution was prepared freshly just before use. An HPLC grade heptane (99%, Fisher) was used in all tests. Other chemicals, which included SMO (sorbitan monooleate), KCl, and NaOH were obtained from Sigma-Aldrich. Deionized water with a resistivity of 18.2 MΩ cm at 25°C was used for the preparation of reagent solutions.

Preparation of Pickering Emulsions

Hydrophobic Silica as Emulsifier

In two-liquid flotation, hydrophobic particles are collected by oil droplets. The oil-particle aggregates may be construed as agglomerates and/or emulsions, in which case hydrophobic particles act as solid surfactants. In the present work, hydrophobic silica was used as a model solid emulsifier. In each test, 0.5 g silica particles were placed in a 50 ml beaker containing desired volumes of water and dispersed using an overhead mixer using an impeller with a 3-twisted blades of 1-inch diameter for 5 min at 800 RPM. The mixture was transferred to a vial with a screw cap and allowed to settle.

Hydrophobic Chalcopyrite as Emulsifier

A series of agglomeration/emulsification tests was also conducted using micronized chalcopyrite particles as a solid emulsifier. In each test, 1 gram of solid was added to a 125 ml cylindrical separatory funnel containing 40 ml of a KAX solution of known concentration and the mixture was hand shaken for 5 min to allow chalcopyrite particle were hydrophobized by xanthate adsorption. The pH was 9.5. After the particle had been hydrophobized, a volume (40 ml) of heptane was added to the separatory funnel and the mixture was agitated by handshaking for another 5 min. During this time, the oil was broken into small droplets, which then collected the hydrophobic chalcopyrite particles and formed agglomerates and/or oil-in-water emulsions droplets. The cylindrical separatory funnel was then allowed to stand to achieve a phase separation, with the aqueous phase at the bottom and oil phase at the top. The weights of the particles in the water and oil phases were measured to calculate the recovery of chalcopyrite particles by the oil drops. The recoveries varied with the contact angles of the particles among other parameters as will be shown below.

Results & Discussion

Hydrophobic Silica Particles as Emulsifier

Effect of Contact Angle: Figure 1 shows the results of the two-liquid flotation tests conducted on the 5-μm silica particles suspended in water using heptane as collector. As shown, the results varied with the contact angles (θ) of the particles. At θ =5°, most of the particles stayed in the water phase at the bottom, resulting in a low recovery. As θ was increased to 54° and 79°, the silica recovery was increased substantially as can be seen visually in the second and third vials.

The particles collected under these conditions, *i.e.*, $\theta < 90^o$, oil-in-water (o/w) emulsions were formed. Thermodynamically, this phenomenon is rather similar to the recovery of hydrophobic particles recovered by air bubbles in flotation. In effect, the bubble-particle aggregates formed during flotation may be considered air/water (a/w) emulsions. In both the two-liquid flotation and in the conventional air bubble flotation, hydrophobic particles stabilize the oil and air bubbles, respectively, so that the two hydrophobic collectors, i.e., oil drops and air bubbles, acquire certain degrees of kinetic stabilities in aqueous phase.

When the θ of the silica spheres was further increased to > 90°, the situation changes drastically. As shown in the fourth vial, the silica particles of θ = 95° formed water-in-oil (w/o) emulsions rather than the o/w emulsions observed at $\theta < 90^o$. This phenomenon is referred to as phase inversion in emulsion science. A conversion of an o/w emulsion to a w/o immersion can be readily induced by using a low-HLB surfactant, *e.g.*, sorbitan monooleate. In the present, we observed the same conversion of phase inversion when the contact angle of silica particles was increased above 90°.

Note here that the w/o emulsions formed with silica spheres of $\theta > 90^o$ are located in aqueous phase below the oil/water phase boundary. The reason for this is that hydrophobic particles can cross the oil/water interface and enter the oil phase if the contact angle is greater than 90° as shown below,

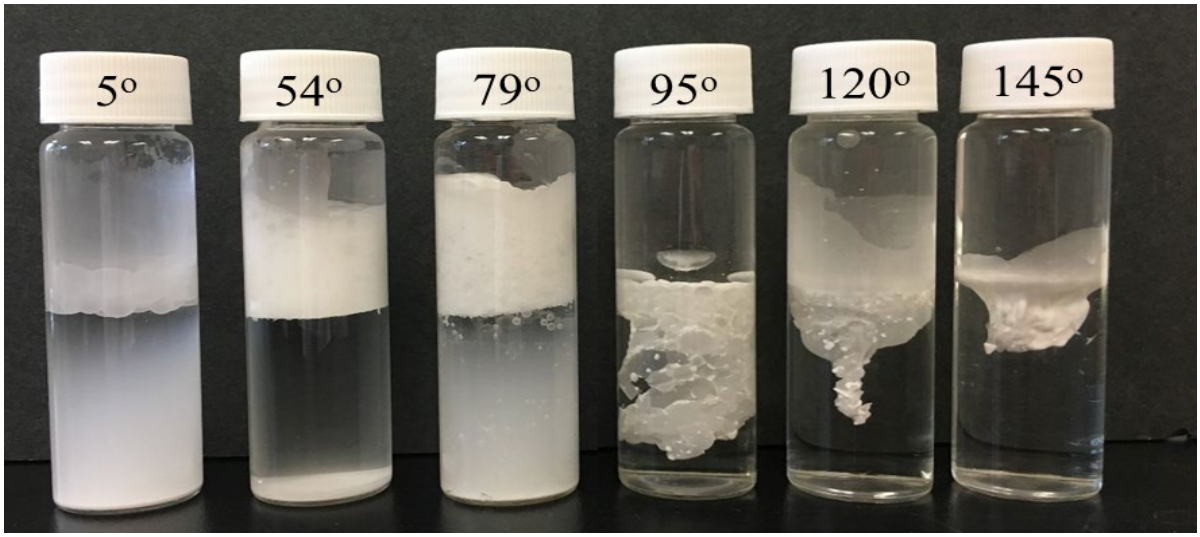

Figure 1. Recovery of silica particles with θ ranging from 5° to 145° using the two-liquid flotation method. At θ < 90°, the particles were recovered in the form of o/w emulsions. At θ > 90°, they were recovered as w/o emulsions. At θ = 95°, a substantial amount of water was entrained in the form of w/o emulsions. The entrained water decreased at higher contact angles.

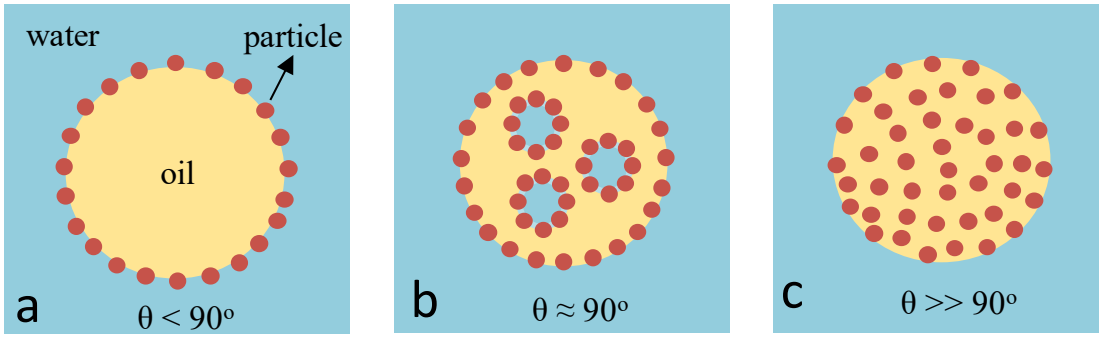

Figure 2. Effect of contact angle on the recovery of fine particles by two-liquid flotation.

$$\Delta G = \gamma_{ow}\cos\theta \qquad [2.1]$$

where ΔG is the free energy of transfer and γ_{ow} is the oil/water interfacial tension. If θ is slightly above 90°, the silica particles may stabilize the entrained micro-water droplets effectively, forming w/o emulsions inside an oil droplet, which may be considered as multiple emulsion. If θ is substantially larger than 90°, no such emulsions will form. The results obtained at θ = 95°, 120°, and 145° support this thermodynamic analysis. As shown, drooping of oil drops diminished with increasing contact angle, indicating that water entrainment becomes less significant at higher contact angles.

Based on the results shown in Figure 1, the effect of contact angles on the two-liquid flotation recovery is illustrated in Figure 2. At θ < 90°, hydrophobic particles are collected on the surface of oil droplets in the same manner as with air bubbles in flotation. At θ slightly above 90°, some particles adsorbed others go inside the oil droplet, forming a w/o/w multiple emulsion. At θ >> 90°, the particles are fully submersed into the oil droplet. In practice, particles will have distributed contact angles, allowing all three cases possible.

Effect of Phase Volume: The results presented in the foregoing paragraph showed that one can readily form w/o emulsions by increasing θ above 90°. It would be of interest to find a different way to induce the phase inversion. According to the phase diagram shown in Figure 3, this could be achieved by controlling the volume fraction of oil (or phase volume, ϕ_o). As shown, an o/w emulsion can be converted to a w/o emulsion by simply increasing ϕ_o above 0.74, which is what we do in the HHS process for the recovery of ultrafine coal. After a coal recovery using a small volume of C5-C7 oil, additional oil is added to induce a phase inversion. The value of ϕ_o=0.74 represents the volume fraction of oil, at which spherical oil drops form a close packed structure. Beyond this point, oil drops will touch each other and coalesce, forming a continuous phase. The water can then be dispersed in the oil phase to form a w/o emulsion.

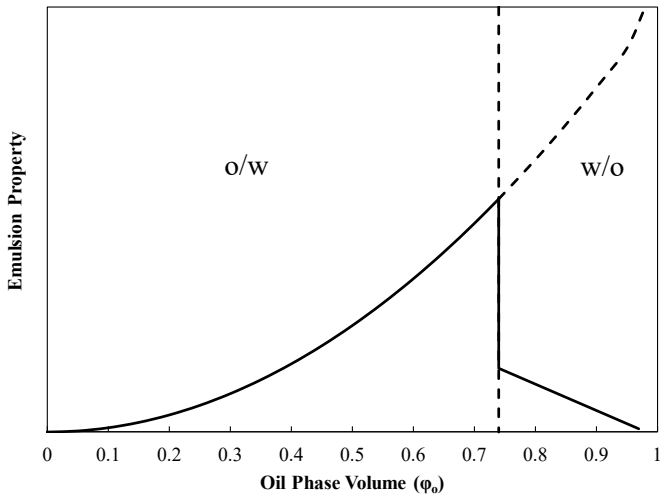

Figure 3. Effect of phase volume on phase inversion.

To explore the possibility of achieving phase inversion at θ < 90°, a series of emulsification tests were conducted by varying ϕ_o in the range of

0.1 to 0.8 in the presence of silica spheres with θ=79°. Initially, a 2 g silica sample was added to a 40 ml water in a 200 ml beaker and agitated for a few minutes to disperse the particles in water. The dispersion was agitated further after adding a desired volume of oil (heptane), during which time small droplets of oil collected the hydrophobic silica particles. The amount of silica particles recovered increased with increasing ϕ_o as shown in Figure 4. As ϕ_o was increased, the recovery of the silica particles increased. At ϕ_o=0.8, they were recovered as w/o emulsions.

Thus, the results presented in Figure 4 show that it is possible to achieve a phase inversion with particles of $\theta < 90^o$. It was necessary, however, to use a high-shear agitation for the phase inversion at $\theta = 79^o$. At $\theta = 54°$, it was not possible to induce phase inversion at any energy level.

Effect of KCl: Figure 5 shows the results obtained with silica particles with θ=79° in the presence of 0.05 M KCl. The emulsions were prepared on the silica particles of an oil contact angle at 79° using KCl in the range of 0 to 0.5 M. The tests were conducted at ϕ_o=0.50. As shown, the silica particles were recovered as o/w emulsions rather than w/o emulsions. Apparently, the contact angles of the hydrophobic particles did not increase significantly in the presence of KCl, contrary to what was suggested by Ashby and Binks (2000) and Zhang (2012).

Figure 6 shows the results obtained with silica particles with θ=120° in varying concentrations of KCl. At such a high contact angle, w/o emulsions can be formed spontaneously as depicted in Figure 2(b). Since the water droplets are stabilized by hydrophobic particles are heavier that the continuous phase (oil), they settle to the bottom. Since the bottom is the deformable oil/water interface, it protrudes out into the aqueous phase due to the excess weight. It is interesting to note here that the volume of the protruding mass becomes smaller at higher KCl concentrations. Although the reasons for this observation is not clear at this point of our research, it seems clear that the size of the water droplets becomes smaller at higher electrolyte concentrations. As is well known, air bubbles can be readily generated in seawater without a frothing agent (surfactant). Likewise, water drops may become smaller in high electrolyte solutions. The results obtained at 0.5 M KCl show the protruding mass is small.

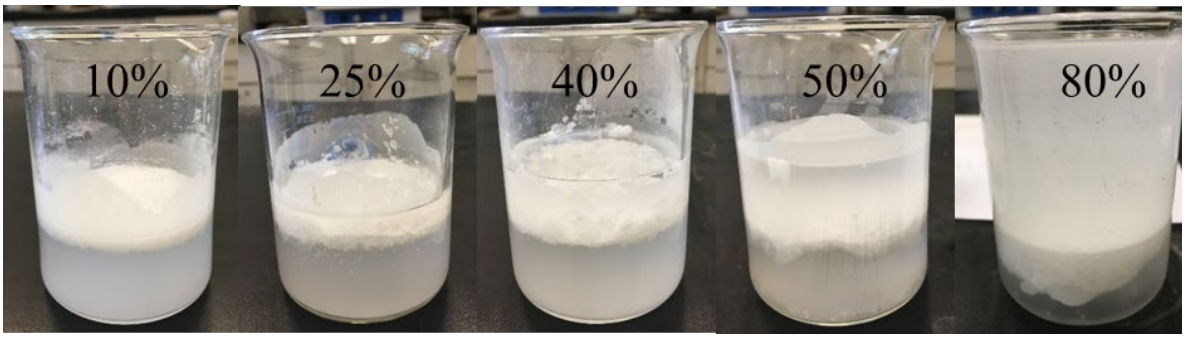

Figure 4. Effect of phase volume (ϕ_o) of oil on the recovery of silica particles with θ = 79°. At ϕ_o = 0.1-0.4, the particles were recovered as agglomerates (or o/w emulsions). At ϕ_o > 0.5, the silica particles were recovered as w/o emulsions. At ϕ_o = 0.8, the phase inversion was complete.

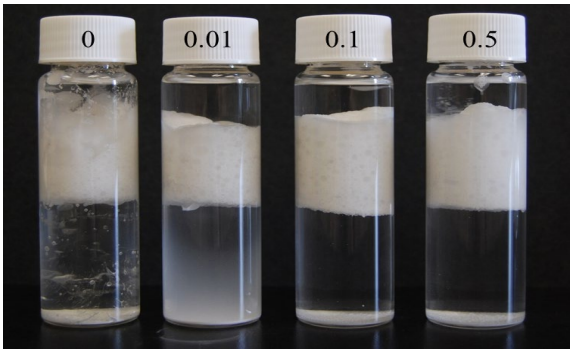

Figure 5. Effect of KCl concentration (M) on emulsification. The contact angle of the silica particles is 79°. The oil/water ratio was 1:1. The emulsions formed under different KCl concentrations were o/w type.

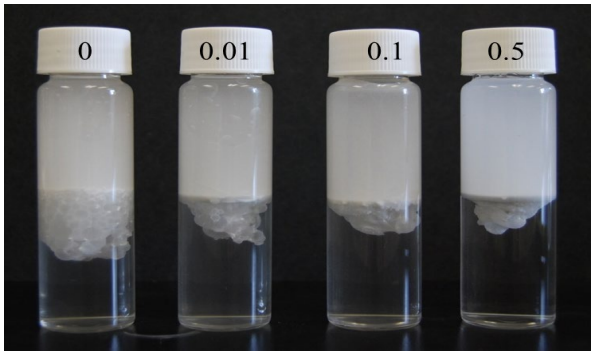

Figure 6. Effect of KCl concentration (M) on emulsification. The contact angle of the silica particles is 120°. The oil/water ratio was 1:1. The emulsions formed under different KCl concentrations were w/o type.

The vials in Figure 6 show that oil phase is murky due to the hydrophobic particles dispersed the oil phase. Some of the more hydrophobic particles in the silica sample are fully dispersed in oil without forming agglomerates (or emulsion drops) as depicted in Figure 2(c).

Effect of SMO: Non-ionic surfactants with HLB numbers in the range of 3.5 and 6.0 are commonly used to produce w/o emulsions. In the present work, sorbitan monooleate (SMO) with HLB = 4.3 were used as emulsifier for silica particles with $\theta = 79°$. The tests were conducted at SMO concentrations in the range of 0 to 10^{-3} M and ϕ_o=0.50. As shown in Figure 7, the recovery of silica increased with increasing SMO concentration. As concentration increased to $5x10^{-4}$ M and 10^{-3}, w/o emulsions were formed. However, the w/o emulsions formed using the chemical emulsifier was too stable to be destabilized by a mechanical means in a Morganizer.

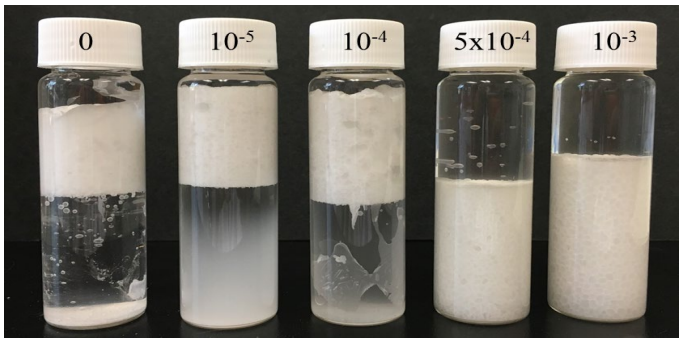

Figure 7. Results obtained with silica particles with $\vartheta = 79°$ using varying concentrations of SMO.

Hydrophobic Chalcopyrite Particles as Emulsifier

A series of two-liquid flotation tests was conducted using pure chalcopyrite samples wet-ground to d_{80}=29 and 15 µm. They were hydrophobized with KAX at different concentrations and subjected to the tests using a cylindrical separatory funnel, with the results presented as images shown in Figure 8. The mineral sample with d_{80} = 29 µm was recovered as o/w emulsions at KAX concentrations above 10^{-5} M KAX, while the same was recovered as w/o emulsions at higher concentrations. The d_{80} = 15 µm sample behaved likewise. The changeover from the o/w to w/o emulsions represented a phase inversion due to contact angle change.

After recording the images shown in Figure 8, the particles were allowed to settle for 5 minutes and removed the water along with the particles left in it. The weight of the particles in the aqueous phase was determined after filtration and drying. The particles left in the separatory funnel were separated from the water and heptane and weighed after appropriate solid-liquid separation and drying. From the weights, the chalcopyrite recoveries were plotted as functions of KAX concentrations (Figure 9).

To better understand the mechanisms of phase inversion shown in Figure 8, contact angle measurements were conducted on polished chalcopyrite surfaces after KAX treatment. The measurements were conducted using two different methods: one using water drops and the other using heptane drops. The results obtained with the former are equivalent to those measured with air bubbles. The results presented in Table 2 and Figure

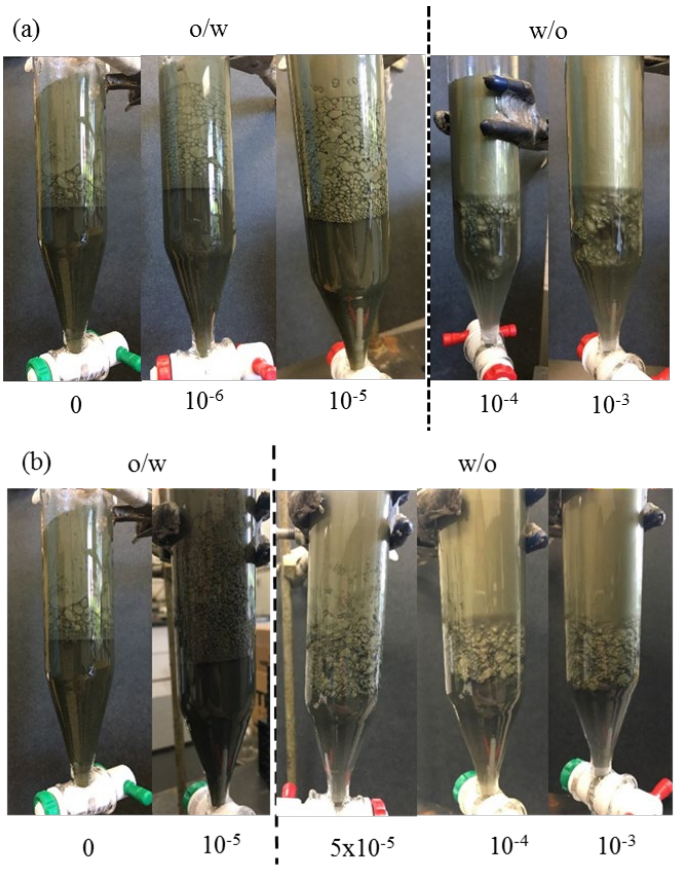

Figure 8. Results of two-liquid flotation tests conducted on the pure chalcopyrite samples with a) d_{80} = 29 µm and b) d_{80} = 15 µm. The samples were hydrophobized at different KAX concentrations, pH 9.5, and ϕ_o = 0.5.

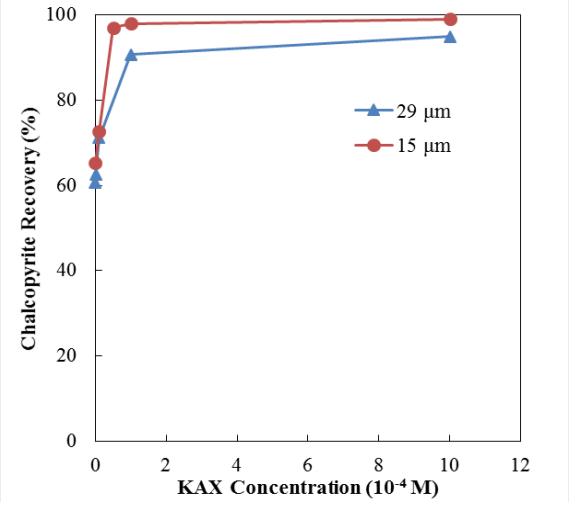

Figure 9. Effect of KAX concentration on the two-liquid flotation recoveries of chalcopyrite particles with d_{80} = 29 and 15 µm.

9 show that the contact angles measured using heptane drops were substantially larger than those measured with air bubbles, which is a thermodynamic rationale to use oil drops rather than air bubbles to recover fine particles. The data show also that θ became larger than 90° at 10^{-5} M KAX, according to which phase inversion should occur at this concentration, while the images of Figure 8 show that it actually occurred at higher concentrations. This discrepancy may be attributed to the likelihood that the KAX concentration decreased considerably during experiments due to adsorption on the surface of fine chalcopyrite particles. Placing a flat mineral surface in a xanthate solution for contact angle measurement would not significantly change the xanthate concentration due to small surface area.

Table 2. Effect of KAX on the air bubble and heptane contact angles of chalcopyrite surfaces.

KAX Conc. (M)	Contact Angle (θ^o)	
	Air	Heptane
10^{-3}	91	145.6
10^{-4}	87.7	136.1
5 x 10^{-5}	71.6	125.6
10^{-5}	64.5	98.9
10^{-6}	44.7	76.7
0	27.7	52.1

TLF vs. HHS

The two liquid flotation (TLF) and hydrophobic-hydrophilic (HHS) processes are essentially the same is a sense that oil rather than air bubble is used to recover fine particles in both. What distinguishes the two from each other is that in the latter the o/w emulsions formed during the recovery step are converted to w/o emulsions so that they can be dispersed in oil in a Morganizer, which removes the entrained impurities and water. To demonstrate the advantages of the HHS process, a set of TLF and HHS tests was conducted on artificial mixtures of pure chalcopyrite and pure silica particles for comparison. In each test, 1 g chalcopyrite was intermixed with varying amounts of silica particles (d_{80}=5 µm) and conditioned in 10^{-4} M KAX solutions before separations tests.

In the HHS tests, the chalcopyrite concentrates recovered in the TLF process as o/w emulsions were subjected to the Morganizing step. The results presented in Table 3 show that the HHS process produced concentrates with substantially higher grades. The product grades were very close to the theoretical maximum grade of 34.6% Cu for the chalcopyrite mineral.

Table 3. Results of the TLF and HHS tests conducted on artificial mixture of chalcopyrite and silica.

Chalcopyrite (d_{80}, µm)	Grade (%Cu)				Cu Recovery (%)
	Feed	Tailings	Concentrate		
			TLF	HHS*	
29	21.72	0.49	30.84	34.43	99.3
	12.38	0.20	22.93	33.91	99.3
	3.89	0.06	22.68	32.92	98.7
15	22.07	0.06	27.80	34.11	99.9
	12.82	0.18	24.30	34.14	99.3
	4.18	0.06	22.27	33.86	98.9

**Feed conditioned in 10^{-4} M KAX solutions at pH 9.5 for 5 min. Particle size of silica was 5 µm.*

Minerals Testing

Sample Preparation

Samples of rare earth minerals are difficult and costly to obtain. Therefore, we conducted the initial laboratory tests using chalcopyrite. For this purpose, chunky samples of chalcopyrite were purchased from Ward's Science. They were crushed by means of a handheld hammer to < 0.6 mm and subsequently wet-ground in a motor-driven mortar and pestle to d_{80} =10 μm. The samples obtained in this manner assayed 32.8 %Cu as determined by using the ICP-MS analyzer.

Once we learned how to achieve phase inversion with the chalcopyrite sample, we purchases monazite specimens originating from the Ambatofotsikely pegmatite, Madagascar, from the Khyber Mineral Company, Westmont, IL. They were crushed by means of a handheld hammer and subsequently dry-ground in a shatter box to d_{80} =16 μm. The samples obtained in this manner assayed 24.3% REEs a determined by using an ICP-MS analyzer.

Samples of chalcopyrite were hydrophobized using potassium amyl xanthate (KAX) of >95% purity, which was obtained from TCI America. The reagent was purified twice before use by dissolving the as-received KAX in acetone (HPLC grade, FisherSci.) and re-crystallizing in diethyl ether (99.999%, Sigma-Aldrich). A KAX solution was prepared freshly just before use.

For the hydrophobization of the monazite sample, we purchased a variety of regents, which included a group of fatty acids (sodium oleate, sodium palmitate, and sodium laurate), hydroxamates (octanohydroxamic acid and benzohydroxamic acid) from Fisher Scientific. In addition, we purchased a group of low HLB surfactants as hydrophobicity-enhancing agents, which included Span 65 (sorbitan tristearate), Span 80 (sorbitan monooleate), Span 83 (sorbitan sequioleate), and Span 85 (sorbitan trioleate) from TCI America and Fisher Scientific. We also acquired a group of hydrophobic polymers as hydrophobizing agents, which included polyethylene-block-poly(ethylene glycol), polymethylhydrosiloxane (PMHS), polybutadiene (dicarboxy terminated), poly(methyl methacrylate), and poly(ethyl vinyl ether).

Preparation of Pickering Emulsions

Recovery of Chalcopyrite as Pickering Emulsion

In two-liquid flotation, hydrophobic particles are recovered by oil droplets rather than by the air bubbles used in flotation. The oil-particle aggregates act as 'solid surfactants' that can stabilize Pickering emulsions by reducing the oil/water interfacial tension. Recognizing that emulsions are formed by surfactant molecules, the two-liquid flotation process should be able to recover Nano-size particles.

Figure 10 shows how the surface activity varies with particle contact angles (θ). Thermodynamically, particles with θ = 90° are the most surface-active as shown in Figure 10, as the volume of each particle is equally partitioned in the oil and water phases. For particles with θ < 90°, the volume of each particle residing in water is larger, and the opposite is true for particles with θ > 90°. As a result, oil-in-water (o/w) emulsions and water-in-oil (w/o) emulsions are formed, provided that the phase volume (ϕ) of the continuous phase is larger than 0.76.

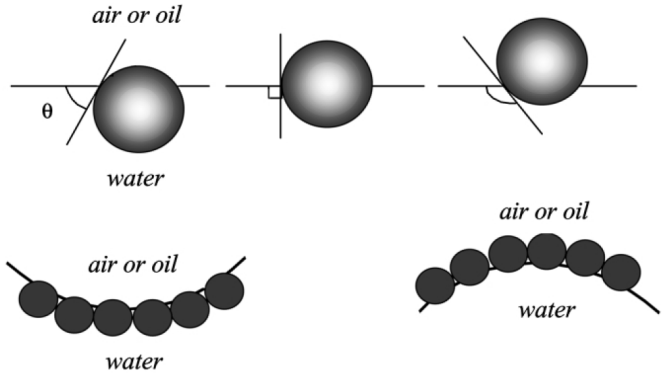

Figure 10. Effect of contact angles on the emulsification (Aveyard et al., 2003)

In the HHS process, a small volume of particles with $\theta > 0$ are collected with recyclable oil with C5-C7 oils to form an o/w emulsion, which is converted to a w/o emulsions by increasing ϕ_o above 0.76. Figure 11 shows the phase inversion. The w/o emulsion is then destabilized by a mechanical means so that the hydrophobic particles with $\theta > 90^o$ are separated from the water droplets. The water droplets fall out of the oil phase along with the hydrophilic particles dispersed in them and sink to the aqueous phase below, leaving only the hydrophobic particles in the oil phase. Separation between of the oil from the hydrophobic particles using an appropriate solid-liquid separation step leaves a high-grade concentrate practically free of gangue minerals and surface moisture (Yoon, US Patent 9,518,241, 2016).

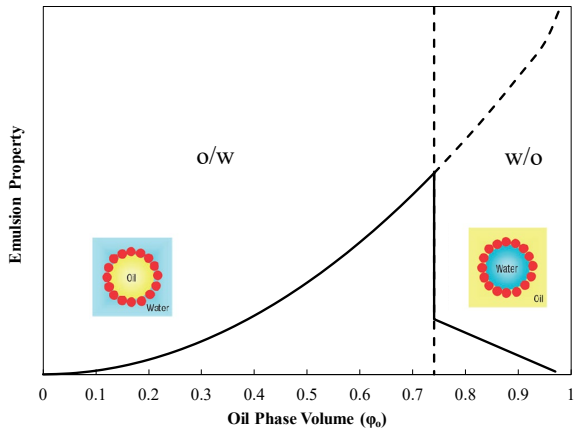

Figure 11. Phase conversion between o/w and w/o emulsions.

One may be concerned that the HHS process may require high reagent (hydrophobizing agent) dosages to obtain $\theta > 90^o$. In general, however, the water contact angles measured using oil drops are nearly twice as high as those measures using air bubbles, as shown in Figure 12. Therefore, the reagent dosages required for the HHS process are substantially lower than required for flotation.

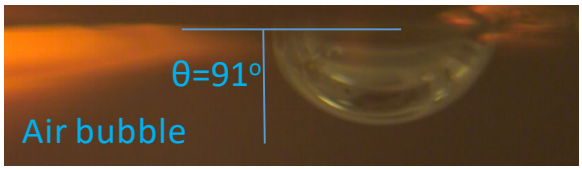

a) $\theta = 91^o$ of air bubble

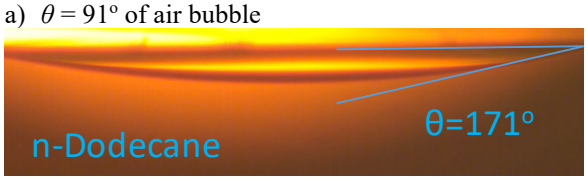

b) $\theta = 171^o$ of octane drop.

Figure 12. Contact angles of air bubble and octane drop on a thiol-coated gold surface.

In this subtask, the hydrophobicity of chalcopyrite particles were controlled as described below. Initially, we used a sample of pure chalcopyrite sample as a model solid emulsifier. In each test, 1 g sample was placed in a 50 ml beaker containing 20 ml KAX solution of known concentration (2.5×10^{-5} M) at pH 9.5 and the mixture was conditioned using an overhead mixer with a 1-inch diameter impeller with 3-twisted blades for 5 min at 800 RPM. After this first hydrophobization step, a hydrophobicity-enhancing reagent (hydrophobic polymer or low HLB surfactant) was added to the beaker before agitating the mixture for another 5 min at the same RPM. After this second hydrophobization step, a volume (20 ml) of heptane was added to the beaker, with the mixture agitated for another 5 min at 1,050 RPM. The mixture was then transferred to a glass vial with a screw cap and allowed to stand. Side view photographs of the vials were taken usually after overnight. In cases where the Pickering emulsions were unstable, photographs were taken sooner.

Recovery of Monazite as Pickering Emulsions

A series of emulsification tests were conducted to recover micronized monazite particles as Pickering emulsions. In a given test, a 20 ml monazite suspension (5% solids) was conditioned with a known amount hydrophobizing agent (fatty acid or hydroxamic acid) at pH 9.7 in a 50 ml beaker for 5 min at 800 RPM. After the monazite particles had been hydrophobized, a volume (20 ml) of heptane was added to the beaker and the mixture agitated at 1,050 RPM for another 5 min. After the agitation, the mixture was transferred to a vial with a screw cap and allowed to settle.

Results and Discussion

Hydrophobic Chalcopyrite Particles as Emulsifier

Effect of Using Hydrophobic Polymers as Hydrophobicity-Enhancing Reagent

A series of emulsification tests were conducted by changing the contact angles of chalcopyrite samples. They were hydrophobized with KAX in the first step and subsequently with four different hydrophobic polymers.

Polybutadiene(dicarboxy terminated)

Figure 13 shows the emulsification tests conducted using first using KAX (2.5×10^{-5} M) in the first step and 0 to 2.8 kg/ton polybutadiene(dicarboxy-terminated) in the second step. All tests were conducted at a phase volume of oil (ϕ_o) at 0.50, i.e., 20 ml water and 20 ml heptane.

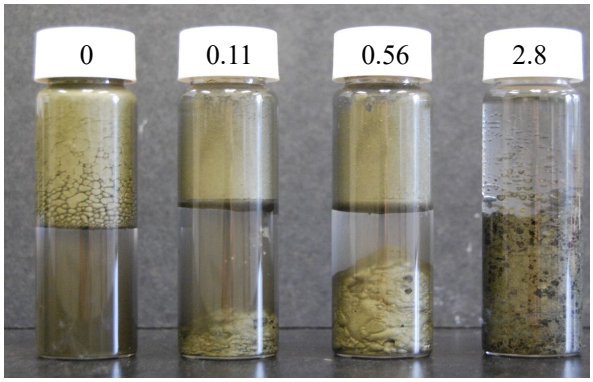

Figure 13. Effect of using polybutadiene (dicarboxy terminated) to increase the hydrophobicity of chalcopyrite particles (d_{80} = 10 µm); dosages in kg/t.

With KAX alone, i.e., at 0 kg/ton polymer, most of the mineral particles were recovered in the oil phase most probably as an o/w emulsion. It appears that $\theta < 90^o$. Under this condition, the particles are hydrophobic enough to be collected on the surface as shown in Figure 14(a).

At 0.11 kg/ton polymer, a large volume of the particles settled at the bottom of the vial, possibly as an w/o emulsion (Figure 14(b)). The emulsion may consist of oil drops loaded with small droplets of water stabilized by hydrophobic chalcopyrite particles. In view of the large SG (=4.2) of the copper mineral, the emulsion drops could not stay in the oil phase. At 0.56 kg/ton polymer, the amount of chalcopyrite particles in the oil drops would be increased, causing them to settle at the bottom even more. As the polymer dosage was increased to 2.8 kg/ton, contact angles may have increased further and allowed more particles to enter the oil droplets in dispersed forms as may be depicted in Figure 14©. In this case, practically all of the mineral particles were recovered by the oil droplets.

The results presented in Figure 13 show that the polybutadiene (dicarboxy terminated) is an efficient hydrophobicity-enhancing agent that can be used to increase the contact angles of chalcopyrite

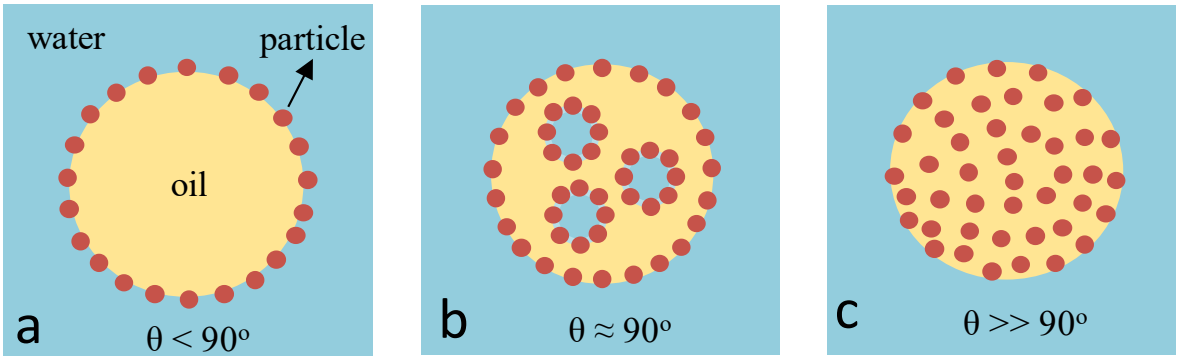

Figure 14. Effect of contact angle on the recovery of fine particles by two-liquid flotation.

above 90°. As has been discussed in conjunction with Figure 14(c), it is necessary to convert an o/w emulsion to w/o emulsion for the HHS process, which is possible at $\theta > 90^o$ and $\phi_o > 0.76$.

Poly(methyl methacrylate) Figure 15 shows the results obtained with chalcopyrite particles using varying amounts of poly(methyl methacrylate) as a hydrophobicity-enhancing reagent. As shown, the use of this polymer failed to increase the contact angles above 90°. Also, the phase volume of oil ($\phi_o = 0.4$) was substantially lower than required ($\phi_o = 0.76$). Under this condition, the mineral particles were recovered as o/w emulsions.

Polymethylhydrosiloxane (PMHS) Figure 16 shows the results obtained using different dosages of PMHS – a water-soluble polymer – as a hydrophobicity-enhancing agent. The results obtained at > 0.5 kg/ton PMCH show clearly that oil drops became too heavy to stay in the oil phase and hence drooped into water. At 2 kg/ton PMCH, oil drops became so heavily loaded with particles that some of them fell to the bottom of the vial. At 10 kg/ton PMCH, the volume of the oil drops protruding from the oil/water interface became smaller, possibly due to the changes in water drops in emulsion droplets. It is hard to see the extent of phase inversion, because $\phi_o = 0.5$, which was substantially lower than required ($\phi_o = 0.76$) (see Figure 11).

Poly(ethyl vinyl ether) Figure 17 shows the effects of using poly(ethyl vinyl ether) as a hydrophobicity-enhancing agent for the KAX treated chalcopyrite particles. The results obtained in the range of 0 to 4 kg/t showed practically no difference, suggesting that the reagent did not work well as a hydrophobicity-enhancing agent. Under this condition, the chalcopyrite particles were recovered as an o/w emulsion.

Figure 18 shows the molecular structure of the hydrophobic polymers tested in this subtask. Of these, polybutadiene(dicarboxy terminated) and PMHS performed well.

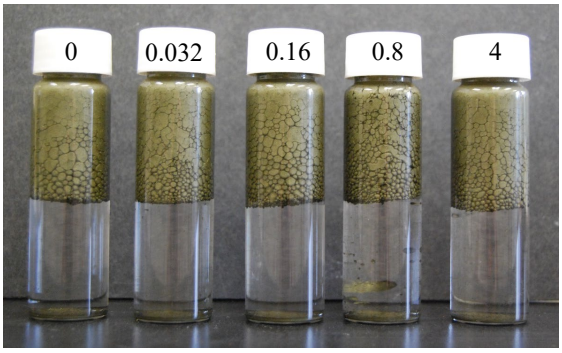

Figure 15. Effect of using poly(methyl methacrylate) for the formation of chalcopyrite particles (d_{80} = 10 µm); dosages in kg/t.

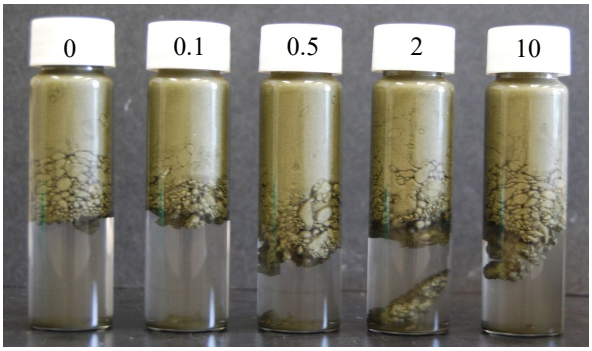

Figure 16. Effect of using polymethylhydrosiloxane (PMHS) to increase chalcopyrite (d_{80} = 10 µm).

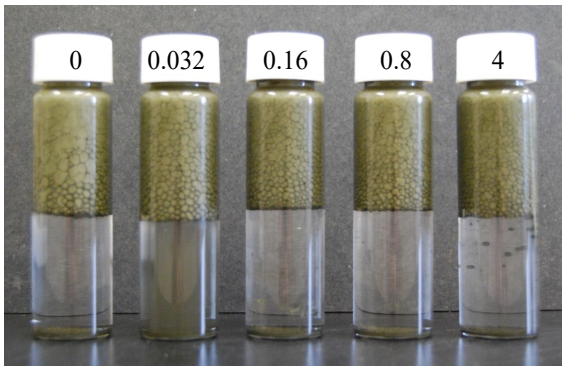

Figure 17. Effect of using poly(ethyl vinyl ether) as a hydrophobicity-enhancing agent for chalcopyrite treated in a $2.5x10^{-5}$ M KAX solution.

Effect of Using Non-ionic Surfactants

It has been shown above that o/w emulsions stabilized by silica particles can be easily transformed to w/o emulsions with the aid of Span 80 (sorbitan monooleate). In the present work, non-ionic surfactants with HLB numbers in the range of 1.0 to 4.3 were tested on chalcopyrite particles hydrophobized with KAX.

Pluronic L101 Pluronic L101 (BASF Care Chemicals) is a difunctional block copolymers of propylene and ethylene oxide with HLB = 1.0. Figure 19 shows the results obtained with KAX-pretreated chalcopyrite particles using Pluronic L101 as a potential hydrophobicity-enhancing agent. It seems that the chalcopyrite particles were recovered as o/w emulsions rather than w/o emulsions, indicating that Pluronic L101 failed to increase the contact angles (θ) of the chalcopyrite particles above 90°. At 10.6 kg/t L101, the surface of the vial was free of particles, indicating that the lamella films of the o/w foam collapsed in the presence of a non-ionic surfactant with an HLB number of 1.

Span 85 A series of emulsification tests were conducted using Span 85 (sorbitan trioleate) with HLB = 1.8. The tests were conducted using KAX-treated chalcopyrite particles as solid surfactant. As shown in Figure 20, the test conducted at 2.2×10^{-5} M Span 85 showed drooping of emulsion drops to the aqueous phase, which became more evident at 5.5×10^{-5} M Span 85. At 8.2×10^{-5} M Span 85 and higher, most of the chalcopyrite particles fell to the aqueous phase, indicating that the reagent caused $\theta > 90°$ and hence allowed the mineral particles to enter the heptane droplets. The oil drops heavily loaded chalcopyrite particles with SG = 4.2 would be too heavy to stay in the oil phase. It appears, therefore, that Span 85 is an excellent hydrophobicity-enhancing agent.

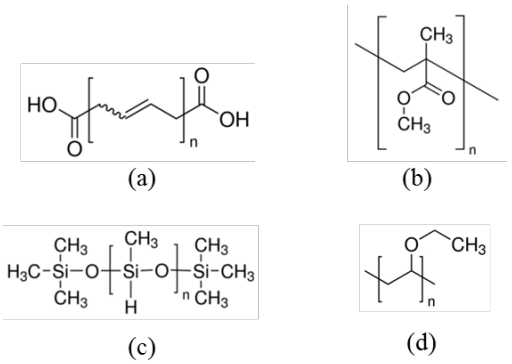

Figure 18. a) polybutadiene(dicarboxy terminated), b) poly(methyl methacrylate), c) polymethylhydrosiloxane (PMHS), d) poly(ethyl vinyl ether).

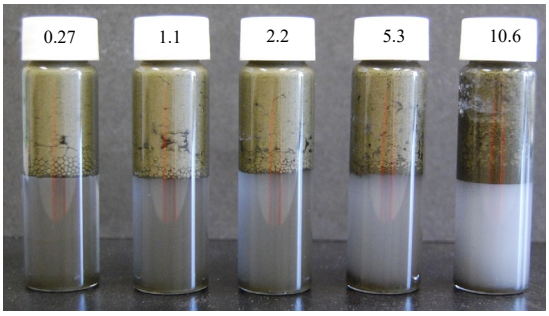

Figure 19. Effect of Pluronic L101 (kg/t) on the formation of heptane-in-water emulsion using KAX-treated chalcopyrite particles as solid surfactant.

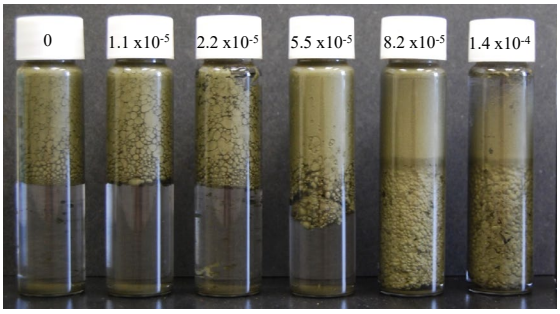

Figure 20. Effect of Span 85 on the formation heptane-in-water emulsion by the KAX-treated chalcopyrite particles.

Pluronic L81 This reagent is another kind of difunction al block copolymer with HLB = 2.0. The results obtained with this reagent are given in Figure 21. At 0.09 kg/t, some emulsions drops were drooping into the water phase. The amount of the drooping emulsion drops became less at higher concentrations, suggesting that the reagent adsorbs on the KAX-treated chalcopyrite surface with inverse orientation. At >0.36 kg/t, there was no evidence for drooping indicating that the contact angles of the particles were less than 90°. It appears, therefore, that Pluronic L181 is not a good hydrophobicity-enhancing agent.

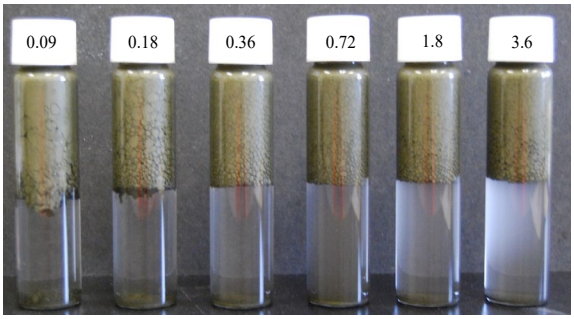

Figure 21. Effect of Pluronic L81 on the emulsification of heptane-in-water emulsions.

Span 65 Figure 22 shows the results obtained with KAX-treated chalcopyrite particles in the presence of Span 65 (sorbitan tristearate, HLB = 2.1). With this reagent, much of the emulsions fell into the water phase, indicating that the reagent is an efficient hydrophobicity-enhancing agent that can increase the contact angle above 90°.

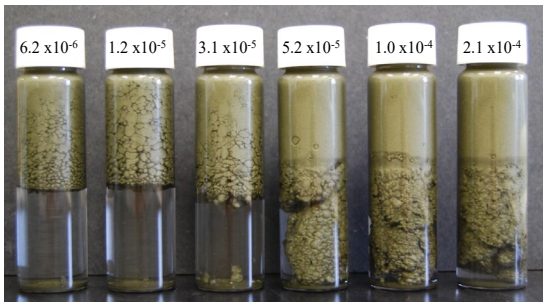

Figure 22. Effect of Span 65 on the formation of water-in-heptane emulsion using KAX-treated chalcopyrite.

Note here that the apparent size of the w/o emulsion droplets obtained at different Span 65 concentrations did not change significantly, which is different from those obtained with Span 85, Span 83 and Span 80, presented in Figure 20, Figure 23, and Figure 26. Also, chalcopyrite particles were uniformly dispersed in the oil phases, which is possible when contact angles are well above 90°. It seems that Span 65 is a very powerful hydrophobicity-enhancing agent.

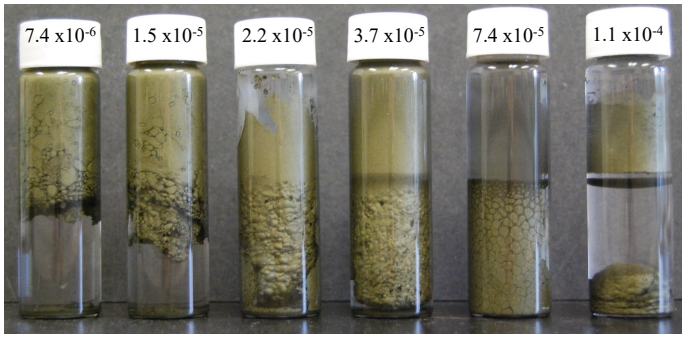

Figure 23. Effect of Span 83 on the formation of water-in-heptane emulsions using KAX-treated chalcopyrite

Span 83 Figure 23 shows the emulsification tests conducted with KAX-treated chalcopyrite particles in the presence of Span 83 (sorbitan sequioleate, HLB = 3.0). The results varied substantially with Span 83 concentration. At $7.4x10^{-6}$ M, most of the chalcopyrite particles were recovered into heptane phase possibly in the form of o/w emulsions. At $1.5x10^{-5}$ M, phase inversion began to occur as θ became larger than 90°. When the concentration was further increased to > $2.2x10^{-5}$ M, the phase inversion became complete with all the particles recovered in water phase in the form of w/o emulsion, which is the most desirable form of minerals recovery for the HHS process.

Genapol PF-20 and Polyethylene-block-poly(ethylene glycol) Both Genapol PF-20 (Clariant Chemicals) and polyethylene-block-poly(ethylene glycol) were surfactants with HLB = 4.0. Figure 24 and Figure 25 show the emulsification test results obtained with Genapol PF-20 and polyethylene-block-

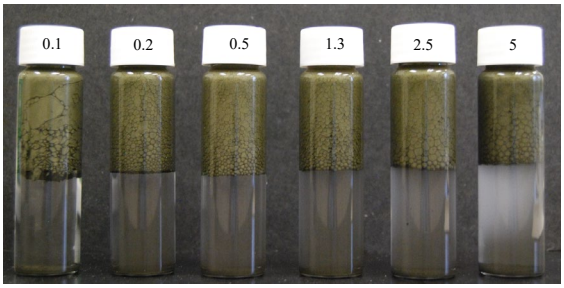

Figure 24. Effect of Genapol PF-20 on emulsification using KAX-treated chalcopyrite as solid surfactant.

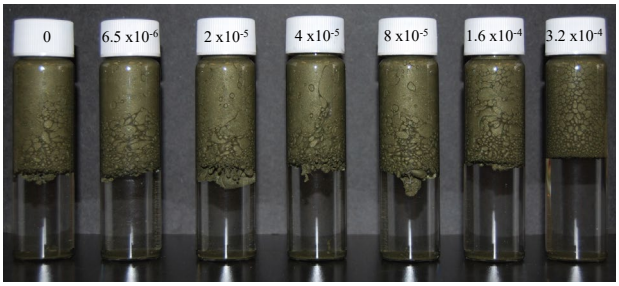

Figure 25. Effect of polyethylene-block-poly(ethylene glycol) on emulsification using KAX-treated chalcopyrite as solid surfactant.

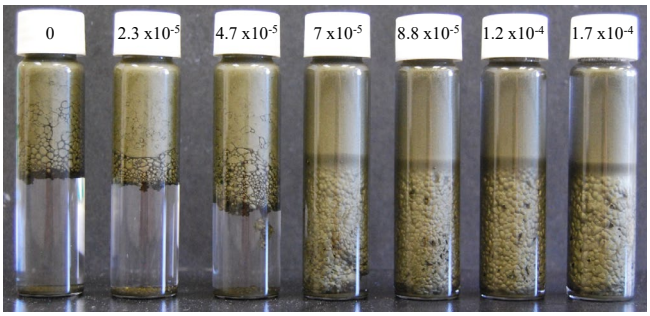

Figure 26. Effect of Span 80 in moles/l on the use of KAX-treated chalcopyrite as surfactant for emulsification.

poly(ethylene glycol), respectively. As shown, chalcopyrite particles were recovered as o/w emulsions rather than w/o emulsions with varying reagent dosages. Apparently, the contact angles of the chalcopyrite particles have not been increased sufficiently in the presence of Genapol PF-20 (Clariant Chemicals) or polyethylene-block-poly(ethylene glycol).

Span 80 This reagent (sorbitan monooleate, HLB = 4.3) is widely used for the formation of w/o emulsions, and we showed its usefulness using hydrophobic silica as solid surfactant. In the current test, Span 80 was used for using KAX-treated chalcopyrite as solid surfactant, with the results presented in Figure 26. As shown, phase inversion began to occur at 2.3×10^{-5} M SMO. As the concentration was increased $>7 \times 10^{-5}$ M, practically all of the mineral particles were recovered as w/o emulsions in water phase.

The results obtained with various non-ionic surfactants presented in the foregoing paragraphs show that the HLB number is a useful guide for choosing appropriate hydrophobicity-enhancing agent. However, it is not an absolute guide for predicting phase inversion. Of the various low-HLB surfactants tested in the present work, Span's low HLB surfactants, particularly Span 65, appears to be the best for phase inversion.

Recovery of Monazite as Pickering Emulsion

Two liquid flotation is capable of recovering ultrafine particles as o/w emulsions as has been demonstrated in the foregoing section with micron-size chalcopyrite particles. Complete recovery is possible regardless of particle size by virtue of the high water contact angles (θ) at the three phase contact line between solid, water, and oil phases involved. The particles can be recovered as either oil-in-water (o/w) emulsion or water-in-oil (w/o) emulsion. In the HHS process, fine particles are recovered in the first step as an o/w emulsion, which is converted to a w/o emulsion in the first step so that the entrapped water drops by destabilizing it *via* a mechanical means along with the unwanted gangue minerals dispersed in the water drops. Thus, phase inversion is critical to obtain high-grade concentrates. It has been shown in the foregoing section that phase inversion requires i) that the contact angle of the particles to be recovered be larger than 90º, and ii) that the phase volume of water be less than 24% **(**see Figure 11**)**.

Based on the data obtained with chalcopyrite, we have conducted a series of Pickering emulsification tests using monazite particles in this subtask. A monazite ore specimen assaying 24.3 %REEs were dry pulverized to d_{80} = 16 μm) using a pug mill at University of Kentucky and hydrophobized using two different types flotation collectors, which included fatty acid salts and octyl hydroxamic acid salts.

Fatty Acid Salts As Hydrophobizing Agent

Sodium Oleate (NaOl) Figure 27 shows the Pickering emulsification test results on the monazite fines hydrophobized by conditioning at NaOl concentrations in the range of $1.4x10^{-4}$ to $1.6x10^{-3}$ M NaOl. The tests were conducted at ϕ_o = 0.50. As shown, the mineral sample was recovered as o/w emulsions at NaOl concentrations below 5.3 $x10^{-5}$ M. Phase inversion was observed at higher concentrations. This finding suggests that the contact angles of the monazite became larger than 90º at >$6.9x10^{-4}$ M NaOl concentration.

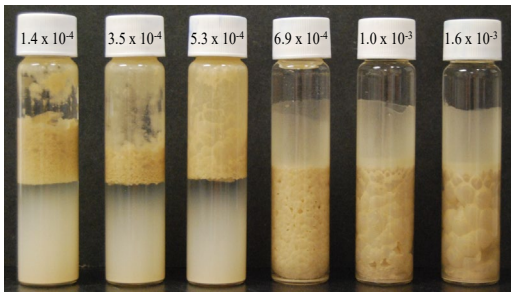

Figure 27. Effect of sodium oleate in moles/l on the recovery of monazite as Pickering emulsions at pH 9.7.

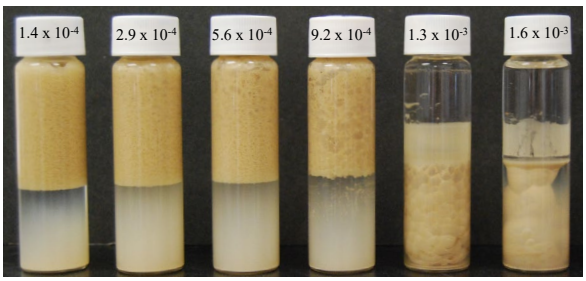

Figure 28. Effect of sodium palmitate in moles/l on the recovery of monazite Pickering emulsions at pH = 9.7.

Sodium Palmitate (NaPl) Figure 28 shows the results obtained with the monazite sample hydrophobized with NaPl at concentrations in the range of $1.4x10^{-6}$ to $2.2x10^{-3}$ M. The mineral was recovered as o/w at concentrations up to $9.2x10^{-4}$ M NaPl, and recovered as w/o emulsion above $1.3x10^{-3}$ M. The critical concentration for the phase inversion is higher than with NaOl, which can be attributed to the hydrocarbon chain length of NaPl, which is shorter than that of NaOl by two CH_2 groups.

Sodium Laurate (NaLa) Figure 29 shows the emulsification test results obtained with monazite particles using NaLa as hydrophobizing agent. The tests were conducted at concentrations in the range of $7.2x10^{-4}$ to $4.5x10^{-3}$ M. As shown, monazite particles were recovered as o/w emulsions

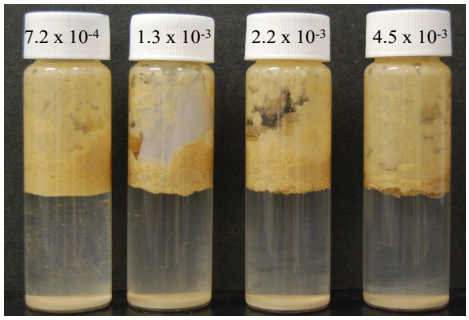

Figure 29. Effect of using sodium laurate in moles/l for the recovery of monazite as Pickering emulsion. Pickering emulsion at pH 9.7.

rather than w/o emulsions. Apparently, the reagent failed to increase contact angles above 90°, which may be ascribed to the relatively short-hydrocarbon chains of NaLa.

Hydroxamic Acids as Hydrophobizing Agent

Octanohydroxamic Acid Figure 30 and Figure 31 show the emulsification results obtained with monazite particles using octanohydroxamic acid as hydrophobizing agent. The tests were conducted in the range of $1.9x10^{-4}$ to $3.6x10^{-3}$ M at $\phi_o = 0.50$. As shown, w/o emulsions were formed at > $7.2x10^{-4}$ M, which is much lower nearly an order of magnitude lower than observed with NaOl (see Figure 27). This finding suggests that hydroxamic acid salts are much more powerful hydrophobizing agents than fatty acids.

Figure 30 shows the images of the Pickering emulsions taken immediately after the emulsification. Note that the oil phases were murky due to the hydrophobic particles dispersed the oil phase. When $\theta >> 90^o$, particles are filly dispersed in oil phase without forming an emulsion as depicted in Figure 14(c). It should be noted here that the oil phase became murkier at higher dosages of octanohydroxamic acid. Figure 31 shows the pictures taken after overnight. As shown, the volume of the w/o emulsions formed in the fifth vial decreased substantially.

Benzohydroxamic acid Figure 32 shows the emulsification results obtained with monazite particles using benzohydroxamic acid as collector. As shown, the monazite particles were recovered as o/w emulsions rather than as w/o emulsions. Apparently, the reagent is inferior to the octanohydroxamic acid.

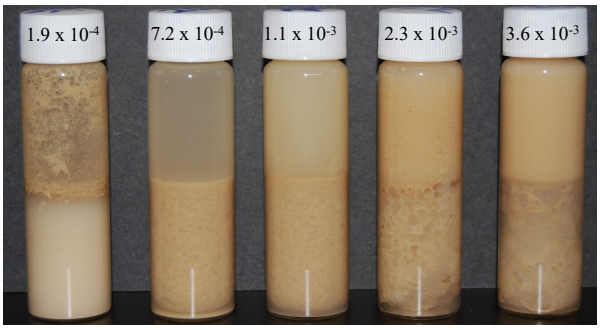

Figure 30. Effect of octanohydroxamic acid in moles/l on the recovery of monazite as Pickering emulsion at pH=9.7. Photos were taken immediately after emulsification.

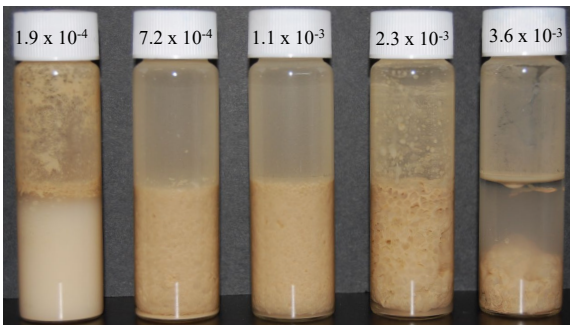

Figure 31. Effect of octanohydroxamic acid in moles/l on the recovery of monazite as Pickering emulsions at pH=9.7. Pictures were taken after setting overnight.

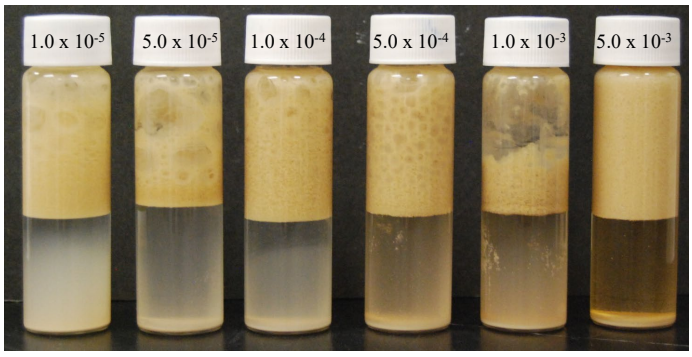

Figure 32. Effect of benzohydroxamic acid in moles/l on the recovery of monazite as Pickering emulsion at pH = 9.7.

Task 3: Control of Surface Hydrophobicity

Subtask 3.1 – Primary Hydrophobizing Agents

Reagent Selection

As part of the current project, several HHS concentrates obtained from the Leatherwood thickener underflow were examined under SEM. The results showed that the concentrates contained a variety of iron-minerals in addition to the monazite – the primary REM in coal and coal byproducts. The reason was probably because the hydrophobizing agent we used, i.e., potassium octyl hydroxamate, was an iron chelate. It was, therefore, decided to use other reagents such as fatty acids as hydrophobizing agent. Although fatty acids are weaker than hydroxamates, they may be more selective and hence produce higher-grade concentrates. C4-C18 alkyl hydroxamates have now been purchased for future testing.

Development of Bench-Scale Semi-continuous HHS system

Figure 33 and Figure 34 show the bench-scale semi-continuous HHS unit. It consists of a *mixing vessel* in which a feed ore (a coal byproduct as slurry) is fed continuously by means of a peristaltic pump while adding appropriate reagents. The mixer discharge is fed to a *separator column*, in which the o/w emulsion dispersed in oil phase is separated from an aqueous phase along with hydrophilic particles. The o/w emulsion is then *phase inverted* to a w/o emulsion in the presence of additional oil. The w/o emulsion is destabilized subsequently in a *Morganizer* separate the hydrophobic particles from the water droplets along with the hydrophilic particles dispersed in them. The Morganizer shown in this picture has been replaced by a packed column, which has no moving parts. The new Morganizer performed well on artificial copper ore samples intermixed with micron-sized particles.

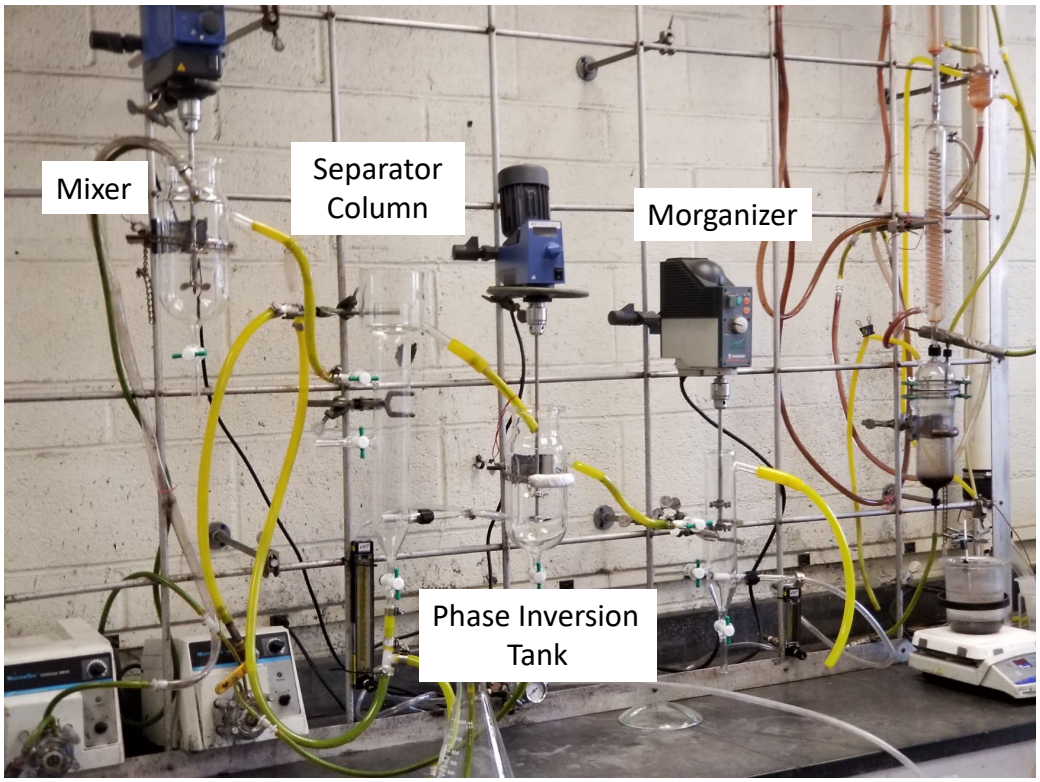

Figure 33. Bench-scale semi-continuous testing circuit for the HHS process.

Artificial Copper Ore Testing 1

Materials and Methods

The artificial copper ore samples were prepared by mixing 10-15 g chalcopyrite sample with d_{80} = 10 µm and 190 g silica particles d_{50} = 5 µm.

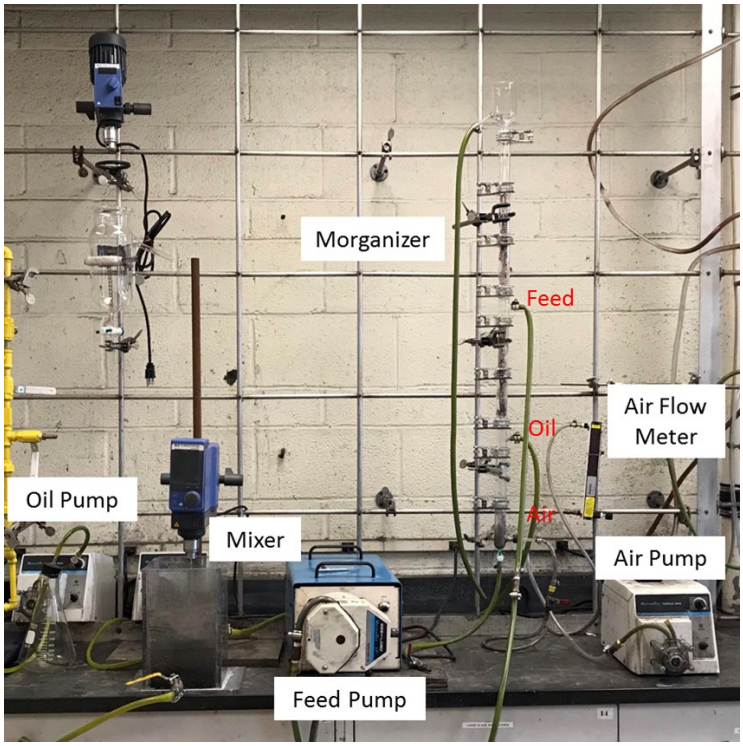

Figure 34. Bench-scale semi-continuous testing circuit for the HHS process.

In a given HHS test, a 3 L of the artificial copper ore slurry at a solid content of 6.8% was conditioned with a hydrophobizing agent, potassium amyl xanthate (KAX) at pH 9.5 in a 5 L mixing tank for 10 min at 650 RPM. After the conditioning, a volume (400 ml) of hydrocarbon oil (heptane) was added to a mixing tank to collect the hydrophobic mineral particles as droplets of an o/w emulsion. The mixture was then fed to the Morganizer by means of a peristaltic pump. The Morganizer, which is a 1-inch diameter column made of glass tubing, has a provision to create an upward flow of pentane to prevent the chalcopyrite particles of SG = 4.1-4.3 from falling by gravity. For this, it was necessary to pump additional heptane to the bottom of the column by means of a peristaltic pump. In the presence of this additional oil, the o/w emulsion is converted to a w/o emulsion – process known as phase inversion. Phase inversion is necessary to be able to liberate the water droplets along with the mineral matter dispersed in them from coal particles. A gentle mixing is required to liberate the water droplets from coal. In the present work, the mixing energy was provided by passing the w/o emulsion through a packing, *e.g.*, copper wool. The water droplets liberated from the copper minerals fall to the bottom, while the hydrophobic chalcopyrite particles dispersed in pentane overflow into a launder.

Results and Discussion

A series of semi-continuous HHS tests have been conducted on the artificial copper ore sample using two different prototype Morganizers. The *first* is made of i.25-inch diameter glass tubing consisting of upper and lower zones filled with copper wools (see Figure 35). An ore slurry is fed to the section in between the two zones, while at the same time heptane is fed to the bottom through an inlet just above the tails pipe. The oil addition serves two purposes: i) phase inversion and ii) create an upward flow to prevent heavy particles with high SG from dropping to the tails. A *second* Morganizer is similar in design except that the column diameter is 1 inch and the column is constructed in divided in many different sections that are connected to each other *via* easy-to-dismantle glass joints so that tests can be conducted by varying column heights (see Figure 36).

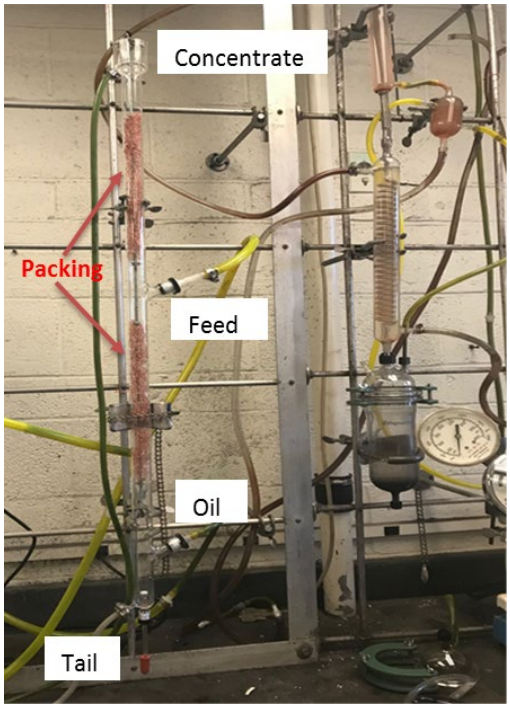

Figure 35. Lab-scale Morganizer 1

Figure 36. Lab-scale Morganizer 2

Table 4 shows the HHS test results obtained with the artificial copper ore sample at 0.3 and 0.4 kg/t of KAX as a primary hydrophobizing agent. The tests were conducted using the first Morganizer described above. The results show that the HHS process is capable of high-grade copper concentrates despite the fact that the size of particles were well below the effective particle size range for flotation. That copper grades were increased from ~1.5 %Cu in the feeds to 25.8- 29.4 %Cu in the concentrates at 86.8-91.9% recoveries in a single-stage operation was far superior to flotation in general. Typically, multiple stages of rougher, scavenger, and cleaning are necessary to produce >20 %Cu concentrates. Furthermore, the products of the HHS process are dry, obviating the needs for costly solid-liquid separation processes. The cost of dewatering increases with decreasing particle size, which has been and still is the reason that the U.S. coal companies discard fine coal to impoundments. In the base metals industry, typically less than 15-20 µm particles are discarded.

It is interesting to note here that copper recovery dropped from 91.6% in

Table 4. Results of the HHS tests conducted on artificial chalcopyrite samples using Morganizer 1: effect of KAX.

Test No.	KAX (kg/t)	Products	Grade (%Cu)	Cu Distribution (Weight %)
1	0.3	Conc	25.91	91.9
		Tails	0.14	8.1
		Feed	1.65	100.0
2	0.3	Conc	25.77	91.3
		Tails	0.13	8.7
		Feed	1.46	100.0
3	0.4	Conc	29.4	86.8
		Tails	0.21	13.2
		Feed	1.52	100.0

Feed: mixture of 15g (23.54%Cu) chalcopyrite (d_{80} = 10µm) and 190 g silica (d_{50} =5 µm); Treated with KAX at pH = 9.5 & 6.8 %solids.

average at 0.3 kg/t KAX to 86.8% at 0.4 kg/t KAX as shown in Table 4, which is counter intuitive. In general, the higher the reagent dosage, the higher the contact angle (θ) and hence recovery in flotation. In the HHS process, contact angles are in general twice as large as in flotation as was shown elsewhere in this report. It was also reported that hydrophobic particles with $\theta > 90^{o}$ can readily enter into an oil drops rather than adsorbing on the surface. It is possible that the oil drops become too heavy to be lifted in the Morganizer if too many particles have entered oil drops. This problem can be easily overcome by optimizing the upward flow velocities of heptane. Note in Table 4 that the grade of the copper concentrate obtained at the higher KAX dosage was substantially higher at the higher KAX dosage. The higher the contact angle, the easier it is to liberate water drops from w/o emulsion drops, which should help achieve higher grade products.

Table 5 shows the effect of varying KAX dosages on the semi-continuous HHS tests conducted using the second Morganizer described above. The tests were conducted on an artificial copper ore assaying 1.06 %Cu. The dosage rates were varied in the range of 0.3 to 0.8 kg/t. The results showed again that the copper recovery decreased with at higher dosages of the primary hydrophobizing agent. As the dosage was increased from 0.3 to 0.4 kg/t, the recovery was reduced from 89% to 87.6% (averaged). As the dosage was doubled to 0.8 kg/t, the copper recovery was decreased to 50.1%, most probably because too many copper minerals were revered into the oil droplets rather than adsorbing to the surface of the droplets. The easiest solution to this problem would, of course, be to reduce the reagent dosage. Another solution would be to use a weaker hydrophobizing agent, *e.g.*, potassium ethyl xanthate (KEX). Still another solution would be to increase the upward velocity of the fluid (pentane) in the Morganizer.

Table 5. Results of the HHS tests conducted on artificial chalcopyrite samples (1.06%Cu) using Morganizer 2: effect of KAX.

Test No.	KAX (kg/t)	Products	Grade (%Cu)	Cu Distribution (Weight %)
1	0.3	Conc	27.7	89.0
		Tails	0.12	11.0
		Feed	1.04	100.0
2	0.4	Conc	32.93	90.6
		Tails	0.11	9.4
		Feed	1.11	100.0
3	0.4	Conc	28.52	87.2
		Tails	0.14	12.8
		Feed	1.07	100.0
4	0.4	Conc	28.39	85.0
		Tails	0.16	15.0
		Feed	1.07	100.0
5	0.8	Conc	28.44	50.1
		Tails	0.53	49.9
		Feed	1.03	100.0

Feed: mixture of 10g chalcopyrite (23.54%Cu, d_{80} = 10μm) and 190 g silica (d_{50} =5 μm); Treated with KAX at pH = 9.5 & 6.8 %solids.

Another set of HHS tests were conducted on an artificial copper feed with a grade of 1.58% (averaged) using 0.45 kg/t KAX. As shown in Table 6, the copper recoveries were in the range of 87.5 to 92.6%, while the grades of the copper concentrates were in the range of 29.03 and 30.39%. These results are superior to those shown in Table 5 in average, which may be attributed to the improvement in our experimental technique.

Table 6. Results of the HHS tests conducted on artificial chalcopyrite samples (1.58%Cu) using Morganizer 2.

Test No.	KAX (kg/t)	Products	Grade (%Cu)	Cu Distribution (Weight %)
1	0.45	Conc	30.39	87.5
		Tails	0.2	12.5
		Feed	1.51	100.0
2	0.45	Conc	29.81	90.9
		Tails	0.17	9.1
		Feed	1.72	100.0
3	0.45	Conc	29.03	92.5
		Tails	0.12	7.5
		Feed	1.51	100.0
4	0.45	Conc	30.17	92.6
		Tails	0.12	7.4
		Feed	1.59	100.0

Feed: mixture of 15g chalcopyrite (23.54%Cu, d_{80} = 10µm) and 190 g silica (d_{50} =5 µm); Treated with KAX at pH = 9.5 & 6.8 %solids;

Artificial Copper Ore Testing 2 & Plant Sample Testing 1

In this subtask, we explored the possibility of producing high-grade rare earth mineral (REM) concentrates using the HHS process. As is well known, the grain sizes of the REMs in coal are <10 µm, which are below the optimal size range for flotation. It has been demonstrated that the HHS process has no lower particle size limit and can recover submicron particles. However, the highest grade REM concentrate obtained until about a year ago was ~2.0% TREEs. It is, therefore, the objective of this subtask is to develop ways to find ways to improve the process to achieve higher grades. As reported above, the key to achieving this objective is to use the Morganizer, for which phase inversion is necessary. Phase inversion is possible when the contact angles of the oil drops in touch with solid particles (θ_o), as measured through the solid-water-oil phase, exceeds 90°. As shown above, the values of θ_o are approximately twice as large as the contact angles of air bubbles (θ_a) in touch with particles, which explains why oil drops are more powerful collectors for hydrophobic particles from water. Note here that θ_a is also referred to as water contact angle (θ_w) in colloid chemistry. In prior testing, most of the HHS test work was conducted with samples of chalcopyrite ($CuFeS_2$) as a model system for monazite ($(Ce,La)PO_4$) to avoid daily contacts with radioactive material. Any results obtained with chalcopyrite should be easily transferable to the recovery of REMs as the separation process is controlled mainly by surface chemistry.

A series of HHS tests were conducted on artificial copper ore samples consisting of pure chalcopyrite and silica in a semi-continuous mode. The results showed that high-grade copper concentrates assaying 27-33 %Cu were obtained from the artificial copper ores consisting of "pure" chalcopyrite (d_{80} = 10 µm) and silica (d_{80} = 5µm) particles. These particle sizes were chosen as the rare earth minerals (REMs) found in coal byproducts are < 10 µm and the gangue minerals are usually clays whose particles sizes are less than 5 µm. During the current study, we conducted tests on both the artificially prepared copper ore samples and the actual copper ore samples taken from operating plants. The copper ore samples were scavenger cleaner tails that are being rejected due to the difficulty of recovering the valuable copper mineral, mostly chalcopyrite, due to the fine particle sizes and/or incomplete liberation by flotation. The samples were obtained through the courtesy of the three largest copper producers in the U.S., *i.e.*, Kennecott, Freeport-McMoRan, and Asarco.

Materials and Methods

Semi-Continuous HHS Tests Figure 33 shows the bench-scale HHS apparatus, which consists of a mixer and a Morganizer (or extraction column). The latter had been modified to prevent the heavy chalcopyrite (or monazite) particles from falling to the bottom by injecting air bubbles to create an upward flow of the fluid in the column with a velocity exceeding the settling velocity of the heavy minerals.

In each HHS test, a volume (3 L) of a copper ore slurry was conditioned with a hydrophobizing agent, *i.e.*, potassium amyl xanthate (KAX), at pH 9.5 in a 5 L rectangular mixing tank for 10 minutes at 650 RPM. A measured volume of hydrocarbon oil (heptane) was then added to the conditioned copper ore slurry to selectively collect the mineral particles rendered hydrophobic. The hydrophobic particles collected on the surface of oil droplets act as solid surfactants (or emulsifiers) and form a stable Pickering emulsion. The o/w emulsion formed in this manner was fed directed to the middle section of a 1-inch diameter glass column, while a volume of oil (pentane) was added to the bottom section of the column. The oil addition at the bottom section of the column serves two purposes. One was to convert the oil-in-water (o/w) emulsion to water-in-oil (w/o) emulsion. The phase inversion occurs when oil becomes the major component of the two-phase mixture as discussed in the preceding section. The other purpose was to create an upward flow of fluid in the column, so that the copper mineral particles detached from the water droplets would not fall to the bottom section of the column.

The top section of the glass column was packed with copper gauze, so that the water droplets coated with hydrophobic particles, *i.e.*, w/o emulsion droplets, lose the hydrophobic particles from the surface due to the turbulence created in the packed zone and coalesce with other water droplets and become larger ones and fall to the bottom. The hydrophobic mineral particles stay dispersed in the organic phase and overflow

the column, while water droplets are collected at the bottom as rejects along with the hydrophilic gangue minerals particles dispersed in them. The column was constructed from a series of 4-inch long glass tubes connected *via* O-ring joints, so that the experiments could be conducted at various column heights.

Relying on a flow of oil to create an upward movement of heavy particles requires a large amount of oil addition. It was, therefore, decided to rely on a bubbly air flow instead, which greatly reduced the amount of oil used in each experiment. On the other hand, it was necessary to use a sufficient amount of oil for phase inversion. In this regard, the semi-continuous HHS circuit has been modified as follows. In the first step, an ore slurry was *conditioned* to selectively render the copper mineral (or REM) particles hydrophobic, followed by the *formation of an o/w emulsion* as a means to collect the hydrophobized particles. The emulsion was *phase separated* from the aqueous slurry and subjected to *phase inversion* to convert the o/w to w/o emulsion. The w/o emulsion was then injected to a glass column (Morganizer), in which the emulsion was destabilized mechanically while passing through the section packed with copper gauge. The water droplets free of the hydrophobic particles coalesce with each other, become larger, and fall to the bottom, while the hydrophobic particles dispersed in the hydrophobic liquid exit the column as an overflow. The materials collected in the overflow and underflow streams were analyzed as concentrate and tails. This procedure was developed using the artificially prepared copper ore samples.

<u>*Batch HHS Tests*</u> A series of batch HHS tests were conducted on the copper scavenger cleaner tail samples taken from the Kennecott copper company, Utah. The sample as-received contained a surprisingly large amount (33.1% wt) of particles larger than 45 μm. It appeared also that the sample was oxidized, which made it difficult to make the chalcopyrite particles hydrophobic with xanthate as a hydrophobizing agent. Therefore, the as-received sample was ball mill ground for 1 hour to obtain ultrafine particles with d_{80}=3 μm. The fine grinding may have exposed fresh chalcopyrite surfaces and improved liberation, which greatly improved the separation process.

In a given test, 100 mL of a copper ore slurry at a solids content of 12% was conditioned with a hydrophobizing agent, potassium amyl xanthate (KAX), at pH 9.5 in a 250 mL separatory funnel for 5 minutes by hand-shaking. After the chalcopyrite particles had been sufficiently hydrophobized, a volume (40 ml) of heptane was added to the separatory funnel and the mixture was hand-shaken again for another 5 minutes. The mixture was allowed to settle to form an o/w emulsion on the top and the aqueous slurry at the bottom. After removing the latter from the separatory funnel, fresh tap water was added to the o/w emulsion left in the funnel, hand-shaken, allowed to settle, and the aqueous slurry was removed from the bottom section of the funnel. This step was designed to remove the entrained gangue minerals from the o/w emulsion phase. After repeating this step once more, additional oil (heptane) was added to increase the volume of oil >76%, so that the o/w emulsion was converted to a w/o emulsion. The latter was then gently agitated by hand-shaking to detach the hydrophobic particles from the water droplets constituting the w/o emulsion. The water droplets free of hydrophobic particles became larger in size by coalescence, while the hydrophobic particles were dispersed in oil phase. Both the hydrophobic mineral concentrate and hydrophilic tail were analyzed for copper to determine the grade and recovery in each test.

Results and Discussion

Artificial Ore Samples

Effect of Packing The top section of the Morganizer was filled with a packing to create a turbulence, in which the hydrophobic particles can be dropped off a w/o emulsion that was fed to the mid-section of a glass column. In this subtask, various packing materials were tested. Figure 37 shows the three different types of packing materials, which included perforated saddles of stainless steel, copper wool, and corrugated stainless steel plate.

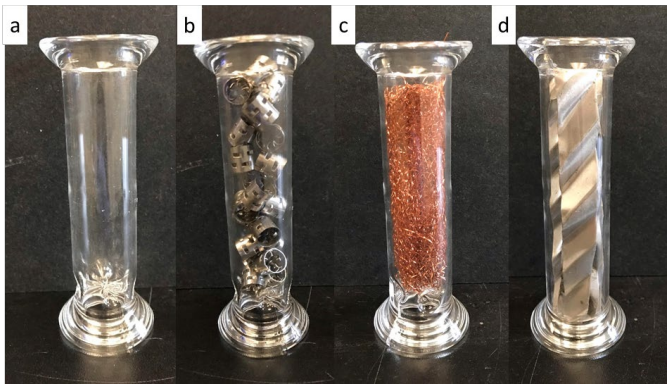

Figure 37. Different packings used for Morganizer; a) no packing, b) stainless saddles, c) copper wool and d) corrugated plate

Table 7 shows the results obtained using different packing materials on an artificial copper ore prepared by blending 15 g chalcopyrite with d_{80} = 10 µm and 190 g silica with d_{50} = 5 µm. The tests were conducted using the semi-continuous HHS test unit described above. The calculated feed grade was 2.29 %Cu except the test conducted with the corrugated stain less steel plate. In all tests, concentrate grades were >32% Cu, which was very close to the theoretical maximum of 34.62% Cu. The copper recoveries were in the range of 78 to 81%, which would have been higher if the test conditions were optimized and a better packing material was used. The results showed that the HHS process can indeed produce high-grade

Table 7. Results of the HHS tests conducted on artificial chalcopyrite samples: effect of packing.

Packing	Products	Grade (%Cu)	Cu Distribution (Weight %)	Conc Moisture (Weight %)
a	Conc	32.66	80.9	33.3
	Tails	0.46	19.1	
	Feed	2.29	100.0	
b	Conc	32.79	81.2	9.6
	Tails	0.46	18.8	
	Feed	2.29	100.0	
c	Conc	32.61	77.2	0.4
	Tails	0.55	22.8	
	Feed	2.29	100.0	
d	Conc	33.23	78.1	2.7
	Tails	0.48	21.9	
	Feed	2.06	100.0	

Feed: mixture of 15g chalcopyrite (d_{80} = 10µm) and 190 g silica (d_{50} =5 µm); Treated with 0.6 kg/t KAX at pH = 9.5 & 6.8 %solids; Feed flow rate: 790 ml/min; Oil flow rate: 210 ml/min; Air flow rate: 92 ml/min.

concentrates. Note here that copper concentrate obtained using copper wool as a packing assayed only 0.4% moisture, which may be attributed to the high surface area of the packing material, on which the water drops freed of hydrophobic particles can coalesce to become larger water drops that are more readily to be separated from the copper mineral particles. The next best packing may be the corrugated stainless plate, which had 2.7% moisture, followed by stainless saddle packing. The results obtained without packing gave 33.3% moisture, suggesting that packing was useful to obtain low-moisture products.

Effect of Oil Flow Rate Oil addition in the bottom of the Morganizer column serves two purposed as noted above. One was to induce *phase inversion*, and the other is to *create an upward flow of fluids* to prevent high SG minerals such as chalcopyrite and REMs from falling to the bottom. Table 8 shows the results obtained at 75 and 210 ml/min oil flow rate. The results obtained at the two different oil flow rates did not show significant differences, which is difficult to explain at this point in time.

Effect of KAX Table 9 shows the effects of varying KAX dosages on the semi-continuous HHS tests conducted using the modified Morganizer packed with copper gauge. The KAX dosage rates were varied in the range of 0.3 to 0.6 kg/t. As the dosage was increased from 0.3 to 0.6 kg/t, the copper recovery was increased slightly from 76.4% to 78.1% and slightly decreased to 77.2%, while maintaining high concentrate grades at 32.4-33.3% Cu and at moistures in the range of 0.4-3.1%.

Table 8. Results of the HHS tests conducted on artificial chalcopyrite samples using: effect of oil flow rate in Morganizer.

Oil Flow Rate (ml/min)	Products	Grade (%Cu)	Cu Distribution (Weight %)	Conc Moisture (Weight %)
75	Conc	32.72	78.2	2.7
	Tails	0.44	21.8	
	Feed	1.94	100.0	
210	Conc	33.23	78.1	2.7
	Tails	0.48	21.9	
	Feed	2.06	100.0	

Feed: mixture of 15g chalcopyrite (d_{80} = 10µm) and 190 g silica (d_{50} =5 µm); Packing: corrugated plate; Treated with 0.6 kg/t KAX at pH = 9.5 & 6.8 %solids; Feed flow rate: 790 ml/min; Oil flow rate: 210 ml/min; Air flow rate: 92 ml/min.

Table 9. Results of the HHS tests conducted on artificial chalcopyrite samples using: effect of KAX.

KAX (kg/t)	Products	Grade (%Cu)	Cu Distribution (Weight %)	Conc Moisture (Weight %)
0.3	Conc	33.21	76.4	3.1
	Tails	0.48	23.6	
	Feed	1.95	100.0	
0.4	Conc	32.45	78.1	2.0
	Tails	0.46	21.9	
	Feed	2.02	100.0	
0.6	Conc	32.61	77.2	0.4
	Tails	0.55	22.8	
	Feed	2.29	100.0	

Feed: mixture of 15g chalcopyrite (d_{80} = 10µm) and 190 g silica (d_{50} =5 µm); Packing: copper wool; Treated with KAX at pH = 9.5 & 6.8 %solids; Feed flow rate: 790 ml/min; Oil flow rate: 210 ml/min; Air flow rate: 92 ml/min.

Effect of Air Flow Rate Table 10 shows the HHS test results obtained with the artificial copper ore sample using bubbly air flow to prevent the high density mineral from being lost. As the air flow rate was increased from 55 to 167 ml/min, the copper grades remained high in the range of 32.45-33.12%, while the copper recovery decreased from 78% to 75.1% at the higher air flow rate. The results show that bubbly air flow is as efficient as oil flow, which will reduce the oil requirement. It appears that air rate required to prevent high density minerals falling is low.

Effect of Feed Flow Rate Table 11 shows the HHS results obtained with the artificial copper ore sample using the Morganizer with a copper gauze packing at 720 and 790 ml/min of slurry feed rate. As the feed rate was increased from 720 to 790 ml/min, the copper recovery was reduced from 80.2 to 75.1%, which may be attributed to the decrease of residence time for emulsion breaking and water coalescence.

Dynamic vs. Static Mixing In a given HHS test, oil is added to a feed slurry tank and mixed to promote collision between hydrophobic particles and oil drops. In the present work, some tests were conducted using an in-line mixer installed on the high-pressure side of a centrifugal pump. The results obtained using the two different mixing techniques are plotted in Figure 37 for comparison. As shown, the inline mixer was substantially more efficient than the dynamic mixer. Both the dynamic mixer and the centrifugal pump were equipped with 0.2 HP motors. With the dynamic mixer, 5 minutes of mixing time was employed. When using the inline mixer, the residence tine was less than 2-3 seconds.

Table 10. Results of the HHS tests conducted on artificial chalcopyrite samples using: effect of air flow rate in Morganizer.

Air Flow Rate (ml/min)	Products	Grade (%Cu)	Cu Distribution (Weight %)	Conc Moisture (Weight %)
55	Conc	33.06	78.0	3.1
	Tails	0.48	22.0	
	Feed	2.07	100.0	
92	Conc	32.45	78.1	2.0
	Tails	0.46	21.9	
	Feed	2.02	100.0	
167	Conc	33.12	75.1	2.8
	Tails	0.49	24.9	
	Feed	1.90	100.0	

Feed: mixture of 15g chalcopyrite (d_{80} = 10µm) and 190 g silica (d_{50} =5 µm); Packing: copper wool; Treated with 0.4 kg/t KAX at pH = 9.5 & 6.8 %solids; Feed flow rate: 790 ml/min; Oil flow rate: 210 ml/min

Table 11. Results of the HHS tests conducted on artificial chalcopyrite samples using: effect of feed flow rate in Morganizer.

Feed Flow Rate (ml/min)	Products	Grade (%Cu)	Cu Distribution (Weight %)	Conc Moisture (Weight %)
720	Conc	32.14	80.2	2.8
	Tails	0.41	19.8	
	Feed	1.96	100.0	
790	Conc	33.12	75.1	2.8
	Tails	0.49	24.9	
	Feed	1.90	100.0	

Feed: mixture of 15g chalcopyrite (d_{80} = 10µm) and 190 g silica (d_{50} =5 µm); Packing: copper wool; Treated with 0.4 kg/t KAX at pH = 9.5 & 6.8 %solids; Air flow rate: 167 ml/min; Oil flow rate: 210 ml/min

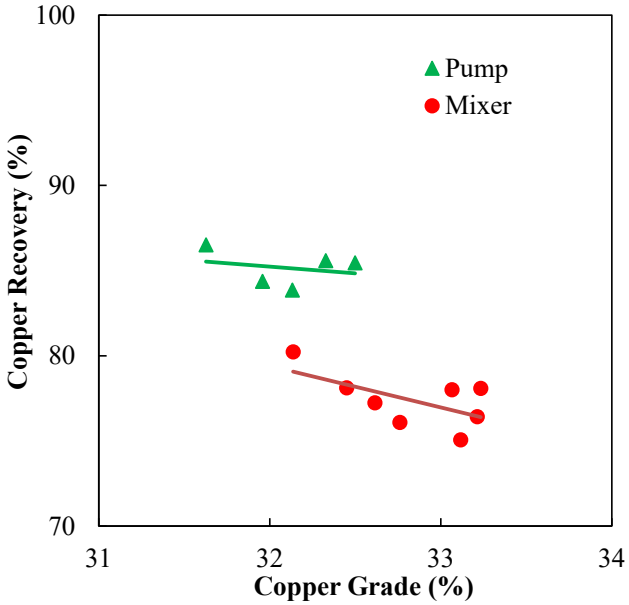

Figure 38. Comparison of HHS tests conducted using different emulsification methods: mixer and pump

Process Modification During the initial stages of the semi-continuous HHS tests, a copper ore slurry was directly injected into the Morganizer as shown in Figure 39a. The process has been evolved to a procedure shown in Figure 39b, in which phase separation and phase inversion steps are added. These changes greatly increased both the recovery and grade for copper minerals as shown in Figure 40. As a result of the modifications, copper recovery was increased by 10-15% and the best copper grade approached the theoretical maximum of 34.6% Cu.

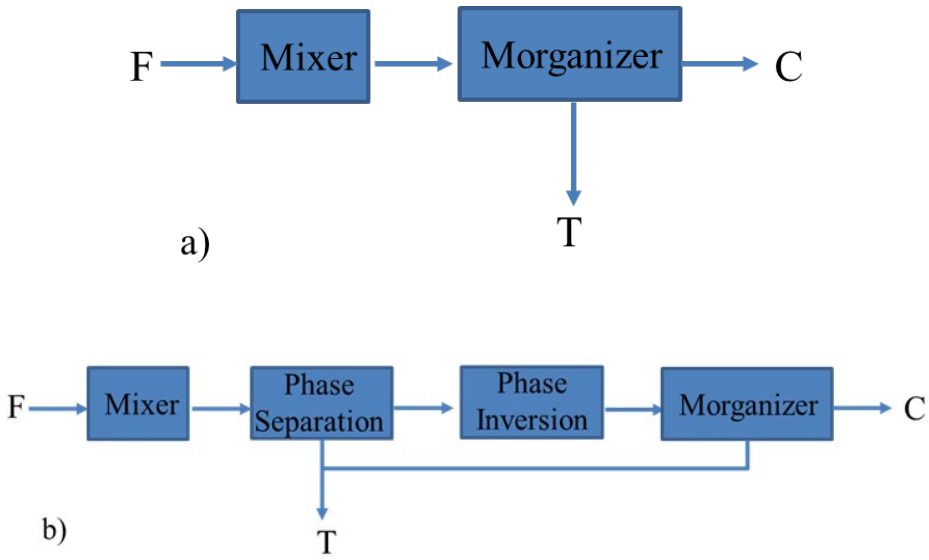

Figure 39. The schematic representation of HHS tests: a) without phase separation; b) with phase separation.

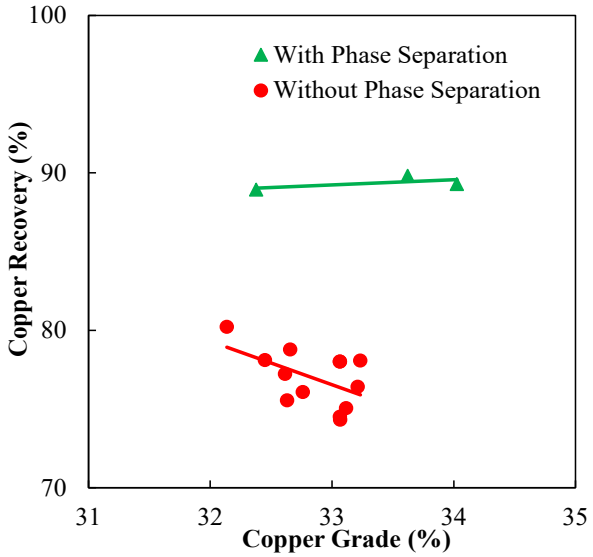

Figure 40. Comparison of HHS tests conducted with and without phase separation on artificial copper ore samples

Effect of Gangue Mineral

Table 12. Results of the HHS tests conducted on artificial chalcopyrite samples using: effect of gangue mineral.

Hydrophilic Gangue	Products	Grade (%Cu)	Cu Distribution (Weight %)	Conc Moisture (Weight %)
Silica	Conc	34.03	89.3	1.0
	Tails	0.25	10.7	
	Feed	2.20	100.0	
Clay	Conc	33.89	66.5	2.1
	Tails	0.84	33.5	
	Feed	2.40	100.0	

HHS test with phase separation; Packing: copper wool; Treated with 0.6 kg/t KAX at pH = 9.5 & 6.8 %solids; Feed flow rate: 790 ml/min; Air flow rate: 167 ml/min; Oil flow rate: 210 ml/min

Table 12 shows the HHS test results conducted on artificial copper ore samples prepared using silica and clay as gangue minerals. As shown, the HHS process was more efficient in removing silica than clay from the copper mineral, which may be attributed to the slime coating associated with submicron clay particles.

Table 12. Results of the HHS tests conducted on artificial chalcopyrite samples using: effect of gangue mineral.

Hydrophilic Gangue	Products	Grade (%Cu)	Cu Distribution (Weight %)	Conc Moisture (Weight %)
Silica	Conc	34.03	89.3	1.0
	Tails	0.25	10.7	
	Feed	2.20	100.0	
Clay	Conc	33.89	66.5	2.1
	Tails	0.84	33.5	
	Feed	2.40	100.0	

HHS test with phase separation; Packing: copper wool; Treated with 0.6 kg/t KAX at pH = 9.5 & 6.8 %solids; Feed flow rate: 790 ml/min; Air flow rate: 167 ml/min; Oil flow rate: 210 ml/min

Plant Samples

Scavenger Cleaner Tail from Kennecott A set of batch HHS tests were conducted on a scavenger-cleaner tail sample at varying KAX dosages. The test procedure was described in the experimental section. The sample assaying 0.55% Cu was wet ground in a ball ground to d_{80} =3 µm to remove the surface oxidation products and also to improve the liberation of chalcopyrite from gangue minerals. As shown in Figure 41, the copper recovery increased with increasing KAX dosage in the range of 0.25 to 1 kg/t. The copper recoveries were 58.3, 59.4 and 62.5% at 0.25, 0.5 and 1 kg/t KAX dosages. The highest copper grade was obtained at 0.5 kg/t of KAX, which was 10.45% Cu. These results show that the HHS process works well for plant samples that are being discarded due to the inefficiencies associated with flotation.

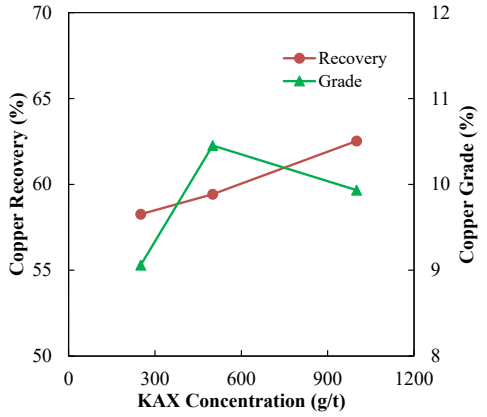

Figure 41. HHS tests conducted on a ground Kennecott copper scavenger cleaner tail sample (d_{80} = 3 µm) at varying KAX dosages.

The data presented in Figure 41 are replotted in Figure 42 and compared with those obtained using flotation. The flotation test was conducted at 0.12 kg/t KAX at pH = 9.5 in a 1.25 liter Denver flotation cell. A 6-minute flotation time was employed due to the slow-floating nature of the ultrafine particles. As shown, the copper recoveries of the flotation and HHS tests were about the same, while the concentrate grades were ~5 times higher. These results demonstrated that the HHS process is superior to flotation in selectivity.

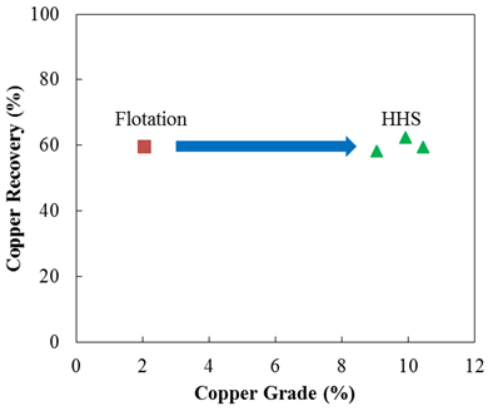

Figure 42. Comparison of flotation and HHS tests conducted on the Kennecott copper scavenger cleaner tail sample.

Freeport copper feed ore A flotation feed, assaying 0.24% Cu, with a top size of 10 mesh, was received from Freeport. The sample was wet-ground by means of a ball mill for one hour to d_{80}=5.8 µm. The ore ground slurry was used for flotation and HHS tests.

Table 13. Results of the flotation test conducted on a ground Freeport copper ore sample

Products	Wt.%		Cu Grade (%)		Cu Recovery (%Wt.)	
	Ind.	Cum.	Ind.	Cum.	Ind.	Cum.
Cleaner Conc	1.2	1.2	16.78	16.78	81.15	81.1
Cleaner Tail	5.5	6.7	0.57	3.44	12.70	93.9
Rougher Tail	93.3	100.0	0.02	0.24	6.15	100.0
Feed	100.0	-	0.24	-	100.0	-

Treated with 0.1 kg/t KAX at pH = 9.5; Flotation time: 2 min; Cleaning for one time; 1 h grinding with d_{80} = 5.8 μm.

Table 13 presents the flotation results obtained using 0.1 kg/t KAX at pH = 9.5 in a 1.25 liter Denver flotation cell. The rougher concentrate was collected for 2 minutes and was cleaned once. As shown, flotation produced a concentrate assaying 16.78% Cu with 81.15% recovery.

Table 14 shows the semi-continuous HHS test results obtained at 0.1 and 0.3 kg/t KAX dosages. The HHS tests were conducted without phase separation (see Figure 39.a). As shown, both the recovery and grade of copper concentrate were increased at a high dosage of KAX. As the KAX dosage was increased from 0.1 to 0.3 kg/t, the copper grade was increased from 34.23% to 36.24% along with the increase of copper recovery from 85.1% to 89% with concentrate moistures in the range of 2.8% to 4.1%. This result shows that the HHS process can produce an almost dry pure chalcopyrite from a feed ore with 0.24% Cu.

Table 13. Results of the flotation test conducted on a ground Freeport copper ore sample

Products	Wt.%		Cu Grade (%)		Cu Recovery (%Wt.)	
	Ind.	Cum.	Ind.	Cum.	Ind.	Cum.
Cleaner Conc	1.2	1.2	16.78	16.78	81.15	81.1
Cleaner Tail	5.5	6.7	0.57	3.44	12.70	93.9
Rougher Tail	93.3	100.0	0.02	0.24	6.15	100.0
Feed	100.0	-	0.24	-	100.0	-

Treated with 0.1 kg/t KAX at pH = 9.5; Flotation time: 2 min; Cleaning for one time; 1 h grinding with d_{80} = 5.8 µm.

Table 14. Results of the HHS tests conducted on a ground Freeport copper ore sample

KAX Kg/t	Products	Grade (%Cu)	Cu Distribution (Weight %)	Conc Moisture (Weight %)
0.1	Conc	34.23	85.1	4.1
	Tails	0.04	14.9	
	Feed	0.24	100.0	
0.3	Conc	36.24	89.0	2.8
	Tails	0.03	11.0	
	Feed	0.24	100.0	

Treated with KAX at pH = 9.5; HHS conducted without phase separation; 1 h grinding with d_{80} = 5.8 µm.

Figure 43 compares the flotation and HHS test results obtained at 0.1 kg/t KAX dosage. It is clear from the figure that the HHS process can produce a copper concentrate with a 4% higher recovery than the flotation, while the grade was doubled to 34.23% from 16.78% with flotation. These results show that the HHS process is far superior to flotation with respect to recovering fine mineral particles.

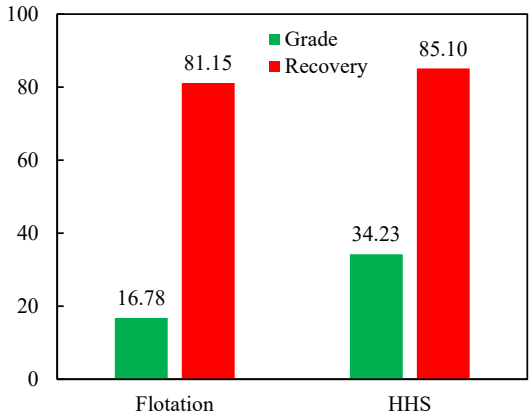

Figure 43. Comparison of flotation and HHS tests conducted on the Freeport copper ore sample

Plant Samples Testing 2

As shown above, the HHS process has been tested on micronized artificial and plant copper samples. We were able to produce high-grade chalcopyrite concentrates, and the scientific information and knowhow gained from this work will be utilized to producing high-grade REM concentrates from coal byproducts. During the current testwork, a series of HHS tests have been conducted actual plant samples, which include the copper scavenger cleaner tails from three operating plants, i.e., Kennecott, Freeport-McMoran, and Asarco.

One of the problems associated with the plant samples appeared to be that the copper-bearing minerals (chalcopyrite) present in the industrial samples were not fully liberated. To overcome this potential problem, we ground the sample in an attrition mill to 3-10 µm size, which vastly improved the separation efficiency. Other approaches are being taken to explore the possibility of improving the HHS recovery without fine grinding.

Based on the information derived from the copper recovery work, we resumed our work on the recovery of REM concentrates. The results obtained on an artificial mixture of micronized monazite and silica particles were encouraging. The samples are currently being analyzed.

Materials and Methods

Batch TLF Tests A series of two-liquid flotation (TLF) tests were conducted on three different copper ore samples from the Kennecott, Freeport-McMoran, and Asarco plants all operating in Arizona. The as-received samples contained significant amounts of coarse particles; therefore, the samples were wet-screened a 45 µm and the screen overflows were discarded prior to the TLF tests. Some of the samples were pulverized to improve the liberation of copper minerals from silica before the TLF tests. The test results obtained with and without the grinding step were compared.

In a given TLF test, 400 mL of a copper ore slurry at a solid content of 10% was agitated in a 1.2 L octagonal mixing vessel for 5 min at 450 RPM in the presence of potassium amyl xanthate (KAX) at pH 9.5. A volume (~200 ml) of heptane was then added to the mixing vessel and the mixture was agitated for 5 min to the oil droplets are selectively collect the micron-sized copper mineral particles hydrophobized by KAX. The mixture was then poured into a 1 L separatory funnel for phase separation, i.e., the oil phase in which the o/w emulsions stabilized by hydrophobic particles rise to the top and the hydrophilic particles dispersed in water settle to the bottom.

After removing the latter from the separatory funnel, fresh tap water was added to the o/w emulsion left in the funnel, hand-shaken, allowed to settle, and the aqueous slurry was removed again from the bottom section of the funnel as cleaner tail. This step was designed to remove the entrained gangue minerals from the o/w emulsion droplets. The water washing step was repeated until the amount of entrained gangue minerals became very small.

Results and Discussion

Scavenger Cleaner Tail from Kennecott Table 15 shows the TLF test results obtained with the *as-received* scavenger cleaner tail with a top size of 45 µm using 1 kg/t KAX as a hydrophobizing agent. The first stage TLF test increased the grade from 0.43 %Cu in the feed to 0.69 %Cu in the concentrate at a recovery of 14.15 %. After three stages of cleaning by water washing, the grade was increased to 2.62 %Cu but at a recovery of 5.56%. These results were inferior to those obtained after grinding the ore to d_{80}=3 µm reported above.

One possible reason for the poor recovery could have been that the copper mineral surface was badly oxidized during recirculation and/or during transportation. One way to overcome this problem may be to use a reducing agent. In the present work, the feed slurry was agitated for 30 min in the presence of 0.55 kg/t Na_2S, which is a well-known reducing agent (or surface cleaning agent). After the conditioning under a reducing condition, the slurry was conditioned again for 5 min in the presence of 1 kg/t KAX at pH 9.5. The conditioned slurry was subjected to a rougher-scavenger TLF tests and the concentrates were

Table 15. Results of the Batch TLF test conducted on an as-received Kennecott Scavenger Cleaner tail sample.

Products	Wt.%	Cu Grade (%)		Cu Distribution (%Wt.)	
		Individual	Cumulative	Individual	Cumulative
Cleaner Conc.	0.9	2.62	2.62	5.6	5.6
Cleaner Tail 3	1.0	0.80	1.67	1.8	7.4
Cleaner Tail 2	1.5	0.47	1.15	1.6	9.0
Cleaner Tail 1	5.5	0.40	0.69	5.2	14.2
Rougher Tail	91.1	0.41	0.43	85.8	100.0
Feed	100.0	0.43	-	100.0	-

Feed size: 100% < 45 μm; Rougher: KAX = 1 kg/t at pH = 9.5; Cleaner: 3 stages cleaning with water.

Table 16. Results of the Batch TLF test conducted on an as-received Kennecott Scavenger Cleaner tail sample.

Products	Wt.%	Cu Grade (%)		Cu Distribution (%Wt.)	
		Individual	Cumulative	Individual	Cumulative
Cleaner Conc.	0.9	2.62	2.62	5.6	5.6
Cleaner Tail 3	1.0	0.80	1.67	1.8	7.4
Cleaner Tail 2	1.5	0.47	1.15	1.6	9.0
Cleaner Tail 1	5.5	0.40	0.69	5.2	14.2
Rougher Tail	91.1	0.41	0.43	85.8	100.0
Feed	100.0	0.43	-	100.0	-

Feed size: 100% < 45 μm; Pretreated with 0.55 kg/t NaHS for 30 min; Rougher: KAX = 1 kg/t at pH = 9.5; Scavenger: 33 g/t SMO; Cleaner: 4 stages cleaning with water.

cleaned four times. For the scavenger flotation, 33 g/t sorbitan monooleate (SMO) was added as a promoter that can increase the hydrophobicity beyond what can be achieved with KAX alone. The results presented in Table 16 show that the Na_2S treatment was not effective for improving the copper recovery, suggesting that it may not be the oxidation that caused the difficulty.

<u>*Scavenger Cleaner Tail from Freeport*</u> Table 17 and Table 18 show the TLF test results obtained on the as-received < 45 μm sample and the ground (d_{80} =5.5 μm) Freeport scavenger cleaner tail, respectively. The tests were conducted under the same experimental procedure which has been described in the experimental section. The only difference between these two tests was that 1 kg/t KAX was employed in the former and 0.6 kg/t KAX was used in the latter. As shown, when the as-received feed was micronized to d_{80} =5.5 μm, both the recovery and grade of copper concentrate were increased despite a much lower dosage of KAX was employed. The copper grade was significantly increased from 0.52% to 25.18% along with the increase of copper recovery from 24.6% to 26.8%.

<u>*Scavenger Cleaner Tail from Asarco*</u> Table 19 shows the result of a batch TLF test conducted on an as-received (< 45 μm) Asarco scavenger cleaner tail. The TLF test was conducted at 0.45 kg/t KAX.

Table 17. Results of the Batch TLF test conducted on an as-received Freeport Scavenger Cleaner tail sample.

Products	Wt. %	Cu Grade%		Cu Distribution (%Wt.)	
		Individual	Cumulative	Individual	Cumulative
Cleaner Conc.	7.0	0.52	0.52	24.6	24.6
Cleaner Tail	0.4	0.47	0.52	1.3	25.9
Rougher Tail	92.6	0.12	0.15	74.1	100.0
Feed	100.0	0.15	-	100.0	-

Feed size: 100% < 45 μm; Treated with 1 kg/t KAX at pH = 9.5; cleaning with water

Table 18. Results of the Batch TLF test conducted on a ground Freeport Scavenger Cleaner tail sample.

Products	Wt. %	Cu Grade%		Cu Distribution (%Wt.)	
		Individual	Cumulative	Individual	Cumulative
Cleaner Conc.	0.1	25.18	25.18	26.8	26.8
Cleaner Tail	0.4	1.59	7.68	4.9	31.6
Rougher Tail	99.5	0.09	0.13	68.4	100.0
Feed	100.0	0.13	-	100.0	-

Feed size: d_{80} = 5.5 μm; Treated with 0.6 kg/t KAX at pH = 9.5; cleaning with water

Table 19. Results of the Batch TLF test conducted on an as-received Asarco Scavenger Cleaner tail sample.

Products	Wt.%	Cu Grade (%)		Cu Distribution (%Wt.)	
		Individual	Cumulative	Individual	Cumulative
Cleaner Conc.	0.6	4.27	4.27	9.2	9.2
Cleaner Tail 3	1.2	1.62	2.48	7.3	16.5
Cleaner Tail 2	3.0	0.60	1.32	6.4	22.9
Cleaner Tail 1	2.7	0.36	0.98	3.4	26.3
Rougher Tail	92.5	0.22	0.28	73.7	100.0
Feed	100.0	0.28	-	100.0	-

Feed size: 100% < 45 μm; Treated with 0.45 kg/t KAX at pH = 9.5; Cleaner: 3 stages cleaning with water

After the rougher flotation, the copper grade was improved from 0.28 %Cu in the feed to 0.98 %Cu in the concentrate with 26.3% recovery. After four stages of cleaning, the copper grade was further increased to 4.27 %Cu but at a recovery of 9.2%.

Table 20 shows the results obtained after grinding the sample to d_{80} = 4 μm. The results were much improved with copper grade increased from 0.39% to 16.29% with a recovery of 37.8% after a single stage

TLF. The improved results seem to suggest that improving mineral liberation may be the key to obtain high-grade copper concentrates.

Table 20. Results of the Batch TLF test conducted on the micronized Asarco Scavenger Cleaner tail.

Products	Cu Grade (%)	Cu Distribution (%Wt.)
Conc.	16.29	37.8
Tail	0.24	62.2
Feed	0.39	100.0

Feed size: d_{80} = 4 µm; Treated with 0.45 kg/t KAX at pH = 9.5

Subtask 3.2 – Secondary Hydrophobizing Agents

Introduction

Adsorption of a primary hydrophobizing agent such as fatty acid or hydroxamate seldom gives close-packed hydrocarbon coating on the surface. The role of secondary hydrophobizing agent is to fill the space the vacant sites to obtain a close-packed mono-layer. In this subtask, work is planned to use hydrophobic polymers as secondary hydrophobizing agents. Four different hydrophobic polymers have been secured for this task.

Contact Angle Measurements and Surface Force Analysis

Adsorption of a primary hydrophobizing agent such as fatty acid or hydroxamate seldom gives close-packed hydrocarbon coating on the surface. The role of a secondary hydrophobizing agent is to fill the vacant sites to obtain a close-packed monolayer. In the present work, the mechanism of how secondary hydrophobizing agents will increase the contact angle of mineral surface has been studied. In this subtask, we used sorbitan monooleate (Span 80, or SMO) as the secondary hydrophobizing agent. Its HLB number is 4.3.

As has been mentioned in Task 2, we can readily transform an o/w Pickering emulsion to w/o Pickering emulsion by using a small amount of SMO. To obtain a better understanding of the mechanism, a series of contact angle measurements were conducted on a hydrophobic quartz plate. When the plate was silylated with octadecyltrichlorosilane (OTS), the contact angles measured with an air bubble and an oil (n-heptane) were 52° and 84°, respectively. When the plate was treated in SMO-in-heptane solutions of different concentrations, the air and oil contact angles changes as shown in Figure 44. As shown, the oil contact angles were substantially larger than the air contact angles, which is a rationale to use oil droplets rather than air bubbles to recover fine particles. At 1.4×10^{-4} M SMO, the oil contact angle became larger than 90°, which is a thermodynamic requirement for phase inversion. After treating the plate in a 5.7×10^{-3} M SMO-in-pentane solution, the oil contact angle became as large as 170°, while air contact angle decreased to 45°. The results presented in Figure 44 shows that SMO is an excellent 'tool' to induce phase inversion, which is essential to use the Morganizer and hence produce high-grade concentrates. The goal of this task to apply this scientific understanding to rare earth minerals recovery using the HHS process.

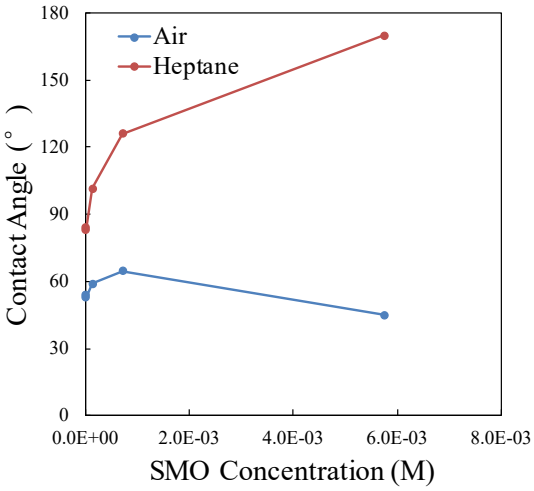

Figure 44. Effect of SMO on the air and oil (n-heptane) contact angles.

The reasons for the large differences between the air and oil contact angles can be explained by means of the Young's equation. For air contact angle (θ_A), one can write the following relation:

$$\cos\theta_A = \frac{\gamma_S - \gamma_{SW}}{\gamma_W} \qquad [3.1]$$

in which is γ_{SW} is the interfacial tension at the solid/water interface, γ_S is the surface tension of the solid, and γ_W is the surface tension of water. For oil contact angle (θ_O), one can write:

$$\cos\theta_O = \frac{\gamma_{SO} - \gamma_{SW}}{\gamma_{WO}} \quad [3.2]$$

in which γ_{SO} is the interfacial tension at the solid/oil interface, and γ_{WO} is the interfacial tension at the water/oil interface.

One can determine the γ_{SW} and γ_{SO} using the acid-base theory (van Oss, 2006) as follows,

$$\gamma_{SW} = \gamma_S + \gamma_W - 2\sqrt{\gamma_S^{LW}\gamma_W^{LW}} - 2\sqrt{\gamma_S^+\gamma_W^-} - 2\sqrt{\gamma_S^-\gamma_W^+} \quad [3.3]$$

$$\gamma_{SO} = \gamma_S + \gamma_O - 2\sqrt{\gamma_S^{LW}\gamma_O^{LW}} - 2\sqrt{\gamma_S^+\gamma_O^-} - 2\sqrt{\gamma_S^-\gamma_O^+} \quad [3.4]$$

in which γ_O is the surface tension of oil, γ^{LW} is the surface tension component due to the Lifshitz-van der Waals interactions (apolar), and γ^+ and γ^- are the surface tension component due to the acid-base interaction (polar). If the oil is *n*-heptane, then the polar parts of oil (γ_o^+ and γ_o^-) will become zero, because *n*-heptane is a completely apolar liquid. Eq. [3.4] can then be simplified as,

$$\gamma_{SO} = \gamma_S + \gamma_O - 2\sqrt{\gamma_S^{LW}\gamma_O^{LW}} \quad [3.5]$$

In general, $\left(\gamma_O - 2\sqrt{\gamma_O^{LW}\gamma_S^{LW}}\right) < 0$,

Therefore,

$$\gamma_{SO} < \gamma_S \quad [3.6]$$

and, hence,

$$\gamma_{SO} - \gamma_{SW} < \gamma_S - \gamma_{SW} \quad [3.7]$$

From Eqs. [3.7], [3.1], and [3.2], one obtains that $\theta o > \theta_A$, which explains the results presented in Figure 44.

SMO is a non-ionic surfactant, which has a polar (hydrophilic) group at one end and an apolar group (hydrocarbon chain) at the other end. If a moderately hydrophobic solid surface with θ_A in the range of 55-65° is treated with a small amount of SMO, γ_S will decrease due to the surfactant adsorption with its polar group in touch with the hydrophilic part of the surface *via* an acid-base interaction, which will lead to a lower γ_{SO}. This will in turn cause the numerator (γ_{SO} - γ_{SW}) of Eq. [3.2] to decrease and hence increase θo.

The SMO adsorption should also increase γ_{SW} by decreasing γ_S^+ and γ_S^- and hence cause the last two terms of Eq. [3.3] to be more negative, while at the same time causing γ_{SO} to decrease as has been noted above. If SMO adsorption continues, the numerator of Eq. [3.2] will become negative and cause θ_O to be larger than 90°. The SMO should also adsorb to the oil/water interface, in which case γ_{WO} will decrease, which should in turn increase θ_O approaching 180° as shown in Figure 44.

According to the acid-base theory, the interfacial tension at the water/oil interface (γ_{WO}) can be written as follows,

$$\gamma_{WO} = \gamma_W + \gamma_O - 2\sqrt{\gamma_W^{LW}\gamma_O^{LW}} - 2\sqrt{\gamma_W^+\gamma_O^-} - 2\sqrt{\gamma_W^-\gamma_O^+} \qquad [3.8]$$

In the absence of surfactant, the last two terms of Eq. [3.8] drop out as both γ_o^+ and γ_o^- are zero. In the presence of SMO, however, they will have finite positive values, causing the interfacial tension to decrease.

As for θ_A, the numerator of Eq. [3.1] can become negative if the wetting tension, i.e., $\gamma_S - \gamma_{SW}$, becomes negative, which should increase the air contact angle above 90°. However, the denominator of Eq. [3.1], *i.e.*, γ_W, is much larger than γ_{OW}. It is, therefore, difficult to increase θ_A close to θ_O, which is a distinct advantage of the HHS process over flotation.

Copper Ore Testing

Materials and Methods

Batch HHS Tests The results obtained on the Kennecott copper sample presented in the foregoing subtask 3.1 show that fine grinding greatly improved the separation process. Therefore, the as-received sample was ball mill ground for 1 hour to obtain ultrafine particles with d_{80}=3 μm and then used for studying the effect of secondary hydrophobizing agents on the HHS process.

In a given test, 100 mL of a copper ore slurry at a solid content of 12% was first conditioned with a hydrophobizing agent, potassium amyl xanthate (KAX), at pH 9.5 in a 250 ml separatory funnel for 5 min by hand-shaking. After the hydrophobizing treatment with KAX, a known amount of a secondary hydrophobizing agent was added to the separatory funnel before hand-shaking the slurry again for 5 min. After the chalcopyrite particles had been sufficiently hydrophobized, a volume (40 ml) of heptane was added to the separatory funnel and the mixture was hand-shaken again for another 5 min. The mixture was allowed to settle to form an o/w emulsion on the top and the aqueous slurry at the bottom. After removing the latter from the separatory funnel, fresh tap water was added to the o/w emulsion left in the funnel, hand-shaken, allowed to settle, and the aqueous slurry was removed from the bottom section of the funnel. This step was designed to remove the entrained gangue minerals from the o/w emulsion phase. After repeating this step once more, additional oil (heptane) was added to increase the volume of oil >76%, so that the o/w emulsion was converted to a w/o emulsion. The latter was then gently agitated by hand-shaking to detach the hydrophobic particles from the water droplets constituting the w/o emulsion. The water droplets free of hydrophobic particles became larger in size by coalescence, while the hydrophobic particles were dispersed in oil phase. Both the hydrophobic mineral concentrate and hydrophilic tail were analyzed for copper to determine the grade and recovery in each test.

Results and Discussion

Effect of Polymethylhydrosiloxane PMHS is a water-soluble hydrophobic polymer, whose role is to enhance the hydrophobicity of a mineral to be floated, e.g., chalcopyrite, beyond the level that could be attained with KAX alone. Figure 45 shows the HHS test results obtained with a ground Kennecott scavenger cleaner copper tail sample using PMHS as a secondary hydrophobizing agent in the presence of 250 g/t KAX as the primary hydrophobizing agent. As shown, both grade and recovery were increased as the PMHS dosages were increased from 0 to 800 g/t. The highest copper grade, which was 12.01 %Cu, was obtained

at 800 g/t of PMHS, which was 1.33 times that of the copper grade obtained without using PMHS. These results show that PMHS is an excellent secondary hydrophobizing agent.

Effect of Polybutadiene(dicarboxy terminated) Figure 46 shows the HHS test results obtained using 250 g/t KAX in the first step and 0 to 800 g/t PBTD in the second step of hydrophobization. As shown, the copper grade of the concentrate was increased with increasing PBTD dosage and then decreased with further increase in PBTD dosage, while the copper recovery decreased with increase PBTD dosage. At 400 g/t PBTD, the HHS test produced a copper concentrate with the highest grade at 10.61 %Cu, which showed only a slight improvement in terms of copper grade in comparison to that obtained without using PBTD. It is obvious that the hydrophobic polymer PBTD can be used to improve the concentrate grade at a suitable dosage but it has deteriorative influence on the recovery.

Comparisons between the results presented in Figure 45 and Figure 46 show that PMHS is a much better secondary hydrophobizing agent than PBTD.

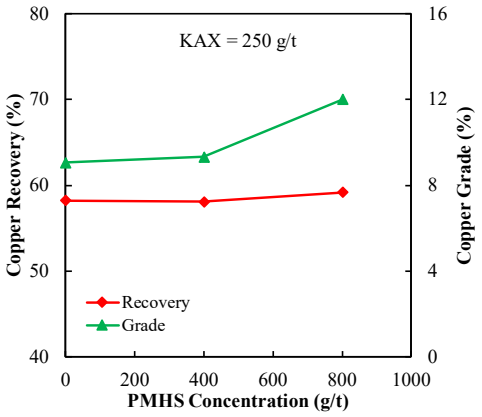

Figure 45. HHS tests conducted on a ground Kennecott copper scavenger cleaner tail sample (d80 = 3 μm) at varying PMHS dosages.

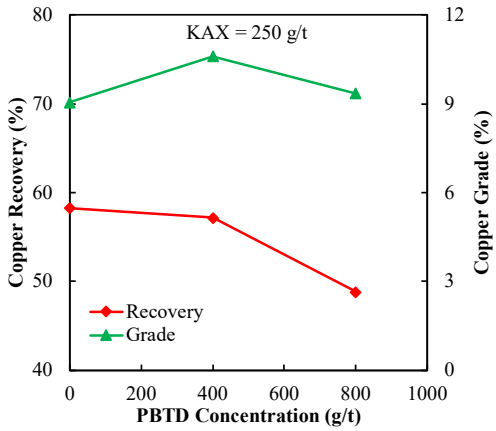

Figure 46. HHS tests conducted on a ground Kennecott copper scavenger cleaner tail sample (d80 = 3 μm) at varying PBTD dosages.

Subtask 3.3 – Depressants

Introduction

One way to produce high-grade concentrates will be to prevent the gangue minerals from reporting to the concentrates. In this subtask, tests will be performed with various depressants to determine the effect of these reagents on separation performance. In this subtask, different depressants including sodium silicate, sodium hexafluorosilicate, lignin sulfonate, sodium carbonate will be tested. Experiments will also be conducted to develop methods of preventing acid-consuming minerals from entering the leaching circuit downstream, which may be achieved by sequestering the hydrolysable cations such as Ca^{2+} and Mg^{2+} ions from solution. At least two different sequestering agents will also be tested in this subtask.

Monazite Testing

In typical coal byproduct streams, *e.g.*, thickener underflows, small amounts of rare earth minerals (REMs) are present amongst large amounts of gangue mineral bearing little or no rare earth elements (REEs). The objective of this subtask is to prevent or minimize the recovery of the gangue minerals from being recovered during HHS tests. In the rare earth minerals industry, sodium silicate and polyphosphate are used to prevent the gangue minerals from being recovered by flotation. In this subtask, the same two reagents have been tested on artificial mixtures of monazite and silica. The role of these reagents is to keep the gangue minerals from becoming hydrophobic inadvertently by the reagents that are used to render the REMs hydrophobic. The former reagents are referred to as depressants and the latter reagents as collectors. In this subtask, sodium oleate (C-18 fatty acid derivative) was used as an REM collector and silica as a gangue mineral.

Materials and Methods

In each test, a mixture of 1 g monazite particles (24.3% REEs, d_{80} = 16 µm) and 1 g silica particles (d_{50} = 5 µm) were placed in a 125 ml separatory funnel containing 20 ml of a depressant solution. The mixture was agitated by hand-shaking for 5 min to allow the depressant to bring the minerals to the right condition. After the conditioning step, a 20 ml of 6.9×10^{-4} M sodium oleate solution was added to the separatory funnel before hand-shaking the mixture again for 5 min. After this hydrophobization step, a volume (40 ml) of heptane was added to the separatory funnel, with the mixture shaken again for another 5 min. The mixture was then allowed to settle for 5 min for phase separation. The concentrate obtained from the two-liquid flotation test and tail were collected and dried for ICP analysis.

Results and Discussion

Effect of Sodium Silicate Table 21 shows the two liquid flotation test results obtained with using sodium silicate as a depressant, with the results plotted in Figure 47. As can be seen, the REE recoveries decreased with the increase of sodium silicate dosages. At dosages of 25-70 kg/t, there was only a slightly reduction in the REEs recovery. Meanwhile, the REE concentrate grades slightly increased from 13.87 to 16.41% with the sodium silicate dosage was increased from 0 to 70 kg/t. These results indicate that sodium silicate has relatively minor negative effects on the recovery of monazite. On the other hand, the reagent is a very efficient depressant for silica.

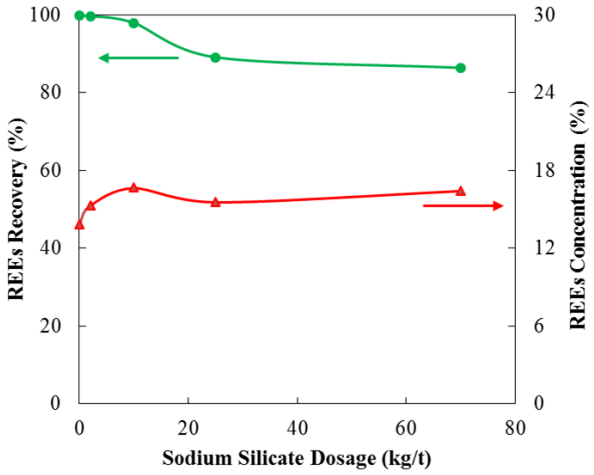

Figure 47. Effect of sodium silicate on grade of REEs concentrate in the two liquid flotation test.

Table 21. Results of the two liquid flotation tests conducted on artificial monazite samples using sodium silicate as a depressant.

Sodium Silicate (kg/t)	Product	wt (%)	REE Assays (%)	REE Distribution (%)
0	Conc	95.4	13.87	99.94
	Tails	4.6	0.18	0.06
	Feed	100.0	13.25	100.00
2	Conc	94.4	15.28	99.77
	Tails	5.6	0.59	0.23
	Feed	100.0	14.46	100.00
10	Conc	92.9	16.64	98.01
	Tails	7.1	4.45	1.99
	Feed	100.0	15.78	100.00
25	Conc	88.6	15.55	89.16
	Tails	11.4	14.63	10.84
	Feed	100.0	15.44	100.00
70	Conc	83.0	16.41	86.43
	Tails	17.0	12.59	13.57
	Feed	100.0	15.76	100.00

Feed: mixture of 1g monazite (d_{80} = 16µm) and 1 g silica (d_{50} = 5 µm); 20 ml 6.9 x 10^{-4} M sodidum oleate, pH = 9.7, 40 ml Heptane.

Effect of Sodium Hexametaphosphate Table 22 shows the results of a set of two-liquid flotation tests conducted on the artificial mixtures of monaztire and silica (1:1 by weight) using sodium hexametaphosphate as a depressant. The effect of the reagent addition on the recovery and grade of the REE concentrate is more clearly shown in Figure 40. The results show firstly that the REE recovery decreased significantly with increasing depressant dosages and secondly that the loss of REE recovery reached a minimum at dosages above 6 kg/t.

The results presented in Figure 40 show that sodium hexametaphosphate is an excellent depressant to be used for the recovery of REMs using the HHS process. As shown, the RRE concentrate grade nearly doubled to 27.08% from 13.87% as the dosage of the depressant was increased from 0 to 10 kg/t. Note here that the grade of 27.08% was higher than the grade (24.3%) of the 'pure' monazite sample used for the HHS tests.

Table 22. Results of the two liquid flotation tests conducted on artificial monazite samples using sodium metahexaphosphate as a depressant.

Sodium Meta Hexaphosphate (kg/t)	Product	wt (%)	REE Assays (%)	REE Distribution (%)
0	Conc	95.4	13.87	99.94
	Tails	4.6	0.18	0.06
	Feed	100.0	13.25	100.00
0.25	Conc	89.9	13.76	98.32
	Tails	10.1	2.09	1.68
	Feed	100.0	12.58	100.00
1	Conc	58.1	18.14	76.90
	Tails	41.9	7.57	23.10
	Feed	100.0	13.71	100.00
2	Conc	46.3	19.70	61.48
	Tails	53.7	10.63	38.52
	Feed	100.0	14.83	100.00
6	Conc	34.0	21.05	46.03
	Tails	66.0	12.72	53.97
	Feed	100.0	15.55	100.00
10	Conc	25.7	27.08	46.62
	Tails	74.3	10.75	53.38
	Feed	100.0	14.95	100.00

Feed: mixture of 1g monazite (d_{80} = 16μm) and 1 g silica (d_{50} = 5 μm); 20 ml 6.9 x 10^{-4} M sodium oleate, pH = 9.7, 40 ml Heptane

Figure 49 compares the results obtained using the two different depressants tested in this subtask. As shown, the concentrate grades achieved by using sodium hexametaphosphate as silica depressant were substantially higher than those achieved using sodium silicate as depressant. The results show clearly that sodium hexametaphosphate is a far superior depressant than sodium silicate that can be used for the recovery of REMs from coal byproducts.

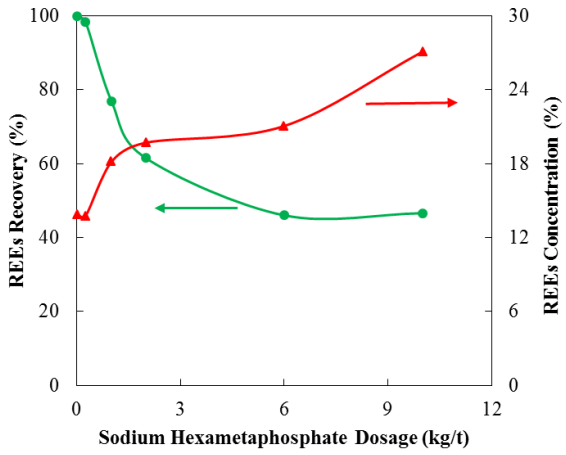

Figure 48. Effect of sodium hexametaphosphate on grade of REEs concentrate in the two liquid flotation test.

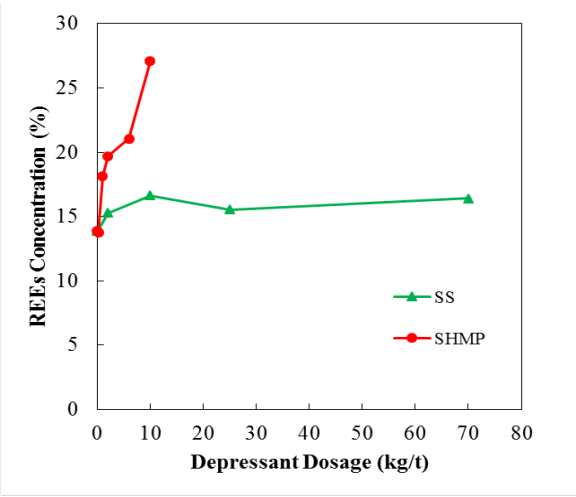

Figure 49. Comparison of the effect of depressants on grade of REEs concentrate in the two liquid flotation test.

Copper Ore Testing

There are two ways to improve the purity of the recovered minerals: one is to use a secondary hydrophobizing agent which has been discussed in Subtask 3.2; another is to use depressant which has a role to keep the gangue minerals from becoming hydrophobic inadvertently by the reagents that are used to render the desirable minerals hydrophobic. In this subtask, a series of HHS tests were conducted for studying the effect of depressants on the recovery of ultrafine copper minerals. The majority of unwanted minerals in the plant copper sample is pyrite, which is also ubiquitous in coal samples and can be detrimental to the recovery of REMs from coal by-products. Therefore, the information about the use of depressants obtained from the HHS tests on a copper sample could be easily applicable to the recovery of REMs from coal.

Materials and Methods

Batch HHS Tests The sample used in this study was a micronized Kennecott scavenger cleaner tail. The d_{80} particle size obtained after 1h ball mill grinding was 3 µm. The test procedure was not too much different from what has been described in Subtask 3.2. In a given test, a certain amount of depressant was added to the copper ore slurry and conditioned for 10 min prior to the addition of KAX. The KAX dosage was kept at 1.3 kg/t for all tests and no secondary hydrophobizing agent was employed in these tests.

Results and Discussion

Effect of Sodium Dithonite Sodium dithionite ($Na_2S_2O_4$) is a reducing agent which may depress the flotation of pyrite by reducing the pulp potential. Kydros et al. (1993) showed also that it can also be used as a depressant for arsenopyrite. Hence, the sodium dithionite was chosen to study in the present work. As shown in Figure 50, the copper recoveries decreased with the increase of $Na_2S_2O_4$ dosages. The recovery was decreased from 66.78% to 48.15% at 30 g/t of $Na_2S_2O_4$.

Copper grades showed a different pattern. The grade first increased from 8.19% to 16.07% as the $Na_2S_2O_4$ dosage was increased from 0 to 16 g/t, and then decreased to 6.83% at a dosage of 32 g/t. These results showed that $Na_2S_2O_4$ is a good depressant for pyrite and the optimal dosage is 30 g/t.

Effect of Sodium Cyanide Cyanide has been regarded as the most effective depressant for iron sulphide minerals including pyrite. In this study, the effect of sodium cyanide (NaCN) on the recovery of copper on the Kennecott copper sample was conducted. As shown in Figure 51, the copper grade was increased with increasing NaCN dosages, while the copper recovery decreased. At a dosage of 32 g/t NaCN, the copper grade reached a maximum at 20.0% at a recovery is 44.4%.

The results presented in the present work show that both $Na_2S_2O_4$ and NaCN are useful for depressing pyrite and, therefore, improving the copper grade. NaCN is superior to $Na_2S_2O_4$ as it gave the highest copper grade among all the tests.

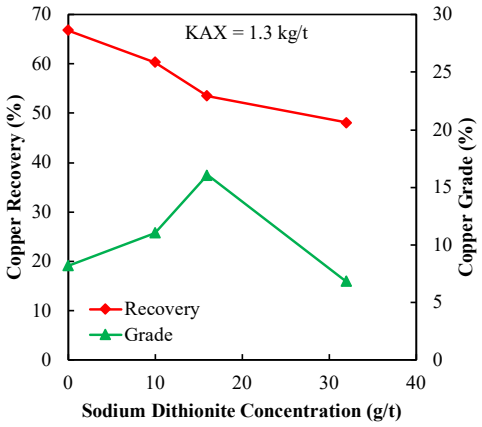

Figure 50. HHS tests conducted on a ground Kennecott copper scavenger cleaner tail sample (d_{80} = 3 μm) at varying $Na_2S_2O_4$ dosages.

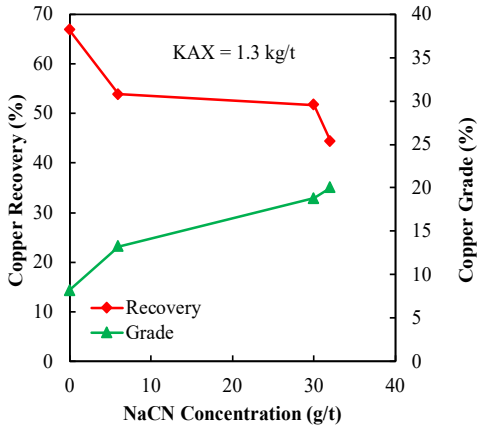

Figure 51. HHS tests conducted on a ground Kennecott copper scavenger cleaner tail sample (d_{80} = 3 μm) at varying NaCN dosages.

Task 4: Study of Thin Liquid Films

Subtask 4.1 –Thin Liquid Film Stability

Introduction

The work performed under Task 4 was designed to measure the surface forces in the thin liquid films (TLFs) of water formed between the two phase, i.e., water and oil. The surface forces control the kinetics of the HHS process, while the particle hydrophobicity (or contact angle) controls its thermodynamics. As outlined in the SOPO, the surface force measurements will be conducted using the force apparatus for deformable surfaces (FADS), which has been developed by the PI (Pan and Yoon, Minerals Eng., 2016). Intially, a cell was designed and constructed that can be used to measure the forces between oil drop and mineral surfaces rather than bubble and mineral surfaces. A series of initial measurements were conducted with this cell using alkanes of different chain lengths. The data collected to date showed that hydrophobic forces increase with decreasing chain lengths, which justifies the use of pentane and heptane in the HHS process.

Study on Gold Hydrophobicity 1

Apparatus

Figure 52 is a schematic representation of the force apparatus for deformable surfaces (FADS), which has been designed to measure the surface forces in the thin liquid films (TLFs) confined between a solid surface and a deformable subject, *e.g.*, oil droplet. In this subtask, the force measurement has been conducted in a liquid cell, which is built with a 2x2-inch glass plate and a 1-inch high glass tube. Three piezo crystals are placed underneath the cell, so that it can move up and down at a desired speed. A hole is drilled at the bottom of the cell, on which a quartz plate is attached and sealed with a vacuum grease. The quartz plate is hydrophobized in an octadecyltrichlorosilane (OTS)-in-toluene solution with an equilibrium water contact angle of ~50º, so that an oil droplet can readily attach to it and give rise to ~ 90º water contact angle. Above the oil droplet, a cantilever spring is fixed on a stem, which in turn is connected to a translational stage that can move in three directions.

The cantilevers are fabricated from thin silicon wafers in class-100 cleanroom. It has the dimensions of 15x3x0.05 mm. In the present work, the cantilevers are coated by a 70 nm thick gold layer and 5 nm thick chrome adhesion layer. The metal deposition is conducted in a $1x10^{-6}$ torr vacuum chamber using e-beam physical vapor deposition technique (PVD-250, Kurt J. Lesker).

An OTS (Acros Organics, 99% purity)-in-toluene (Fisher Chemical, 99.9% purity) solution was used to hydrophobize the lower quartz plate to fixate an oil droplet on the surface. 1-butanethiol (C_4SH) (Sigma Aldrich, 99+% purity) was used as received. The reagent was dissolved in ethanol (200 Proof, Decon Labs) before the hydrophobization of the cantilevers. Potassium amyl xanthate (KAX, >90%, TCI America) was used to hydrophobize the gold surface to study of effect of the hydrocarbon chain

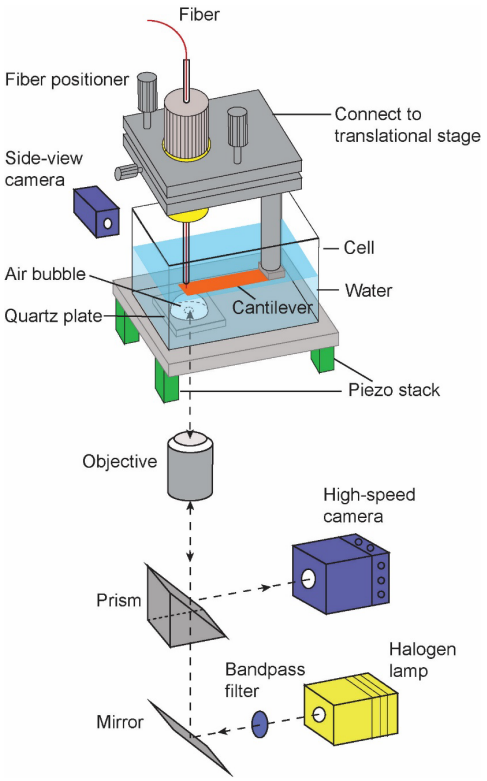

Figure 52. Schematic representation of the force apparatus for deformable surfaces (FADS) developed at CAST.

length. The oils used in the present work were n-octane, n-decane, n-dodecane and n-hexadecane. All experiments were conducted using ultrapure water (>18.2 MΩ/cm) prepared using the Direct-Q water purification system.

Gold-coated cantilevers were cleaned by immersing them in a piranha solution (H_2O_2:H_2SO_4 = 7:3 by volume) for 1 min at 90°C, followed by rinsing with sufficient deionized water. The clean gold-coated cantilevers were hydrophobized by immersing them in the 10^{-5} M C_4SH-in-ethanol solution. Prior to the hydrophobization, the cantilever was removed from water and immersing in the pure ethanol for 10 s to reduce the gold oxide to elemental gold. The hydrophobicity was controlled by varying immersion time. The hydrophobized cantilevers were rinsed with pure ethanol and dried by blowing with ultrapure nitrogen gas. All force measurements were conducted at room temperature.

Procedure

In a given measurement, the stem, on which a cantilever spring was fixed, was lowered by the translational stage until the interference patterns started to appear at film thickness (h) ~ 4 μm. From this point, h was further reduced by slowly lifting the oil droplet at the bottom of the cell using the piezo stack. During the film thinning, the interference patterns were monitored by a high-speed camera, while simultaneously monitoring the deflection of the cantilever spring by means of a fiber optic sensor. The recorded fringes were analyzed offline to determine the film thickness using the micro-interference technique by Sheludko (1967). Once the oil droplet started to deform, the wetting film thinned spontaneously due to the capillary pressure (p_{cur}). On a hydrophilic gold surface, the film thinning stopped at an equilibrium thickness (h_e) when the capillary pressure became equal to the disjoining pressure (Π). On a hydrophobic surface, film thinning continued until the film ruptured at a critical rupture thickness (h_c). In the present work, the approaching speed was set to 1,100 nm/s for all experiments.

Theory

In the FADS measurement, the total interaction force $F(t)$ in the wetting film can be measured directly from the deflection of cantilever, or indirectly determined from the curvature changes of the film using Eq. [4.1] (Pan and Yoon, 2016),

$$\begin{aligned} F(t) &= 2\pi \int_{r=0}^{r_{\max}} p_{cur} r dr \\ &= 2\pi \int_{r=0}^{r_{\max}} \left[p(r,t) + \Pi(r,t) \right] r dr \end{aligned} \qquad [4.1]$$

where p_{cur} is Laplace pressure, p is hydrodynamic pressure, Π is disjoining pressure, r is radial distance from the center of the film and t is the time. Once obtaining the changes of the film profile during film thinning from the interference patterns, one can determine the hydrodynamic pressure (p) using Eq. [4.2],

$$p = 12\mu \int_{r=\infty}^{r} \frac{1}{rh^3} \left[\int_{r=0}^{r} r \frac{\partial h}{\partial t} dr \right] dr \qquad [4.2]$$

in which μ is the viscosity of water and h is the film thickness. The disjoining pressure can be determined by Eq. [4.3],

$$\Pi = \Pi_d + \Pi_e + \Pi_h$$
$$= -\frac{A_{132}}{6\pi h^3} - \frac{\varepsilon\varepsilon_0\kappa^2}{2\sinh(\kappa h)}\left[\left(\psi_1^2 + \psi_2^2\right)\cos ech(\kappa h) - 2\psi_1\psi_2\coth(\kappa h)\right] - \frac{K_{132}}{6\pi h^3} \quad [4.3]$$

in which Π_d, Π_e, and Π_h represent the disjoining pressure contributed from van der Waals force, double-layer force and hydrophobic force, respectively, with A_{132} representing the Hamaker constant, between solid **1** and oil droplet **2**, in water **3**. A_{132} is calculated using the combining rule by Israelachvili (1972). For n-dodecane/water/gold system, A_{132} = 1.38x10^{-20} J. Note here that the A_{132} is positive for this system, while A_{132} is negative for flotation system (air/water/gold). The second term of Eq. [4.3] represents the double-layer interaction, in which ε_o is the permittivity in vacuum, ε is dielectric constant of water, ψ_1 and ψ_2 are the surface potentials at the solid/water interface and oil/water interface, respectively, and κ is the reciprocal Debye length. The third term is the disjoining pressure due to hydrophobic force, with K_{132} representing the force constant. In the present work, ψ_1 and ψ_2 are obtained from the literature (Pan and Yoon, 2016; Stachurski and Michalek, 1996; Djerdjev and Beattie, 2008). κ^{-1} is assumed to be 96 nm, which is equivalent to an electrolyte concentration of 10^{-5} M according to a simplified equation (κ^{-1} =0.304/√Cel nm) given by Butt (1991). The hydrophobic force constant K_{132} is determined by fitting the calculated force *F(t)* in Eq. [4.1] to the force measured directly by the cantilever spring.

Results Obtained with Hydrophilic Gold Surfaces

Figure 53 shows the results of the FADS measurement conducted with an untreated gold surface and an n-dodecane droplet in pure water. The force measurement was initiated by moving the n-dodecane droplet toward the hydrophilic gold surface at an approach speed of 1,100 nm/s, while monitoring the cantilever deflection and interference patterns simultaneously. Deformation of oil droplet was detected by the fringes as in Figure 53(a). By analyzing the fringes, one can readily construct the spatiotemporal film profiles shown in Figure 53(b). During the initial stages of the film thinning, the curvature of the oil droplet did not change significantly. However, at the end of the approaching process (t = 13.78 s), the film became flat and stopped thinning at an equilibrium thickness (he) of 120 nm, indicating that a strong repulsive force existed. Because the gold-coated cantilever was hydrophilic, K_{132} was set to 0 in Eq. [4.3]. All other values of surface chemistry parameters were listed in Table 23. Force vs. time plots are given in Figure 53(c), in which the direct measured force (light blue curve) was in excellent agreement with the total interaction force *F(t)* calculated using Eq. [4.1]. Both surface and hydrodynamic forces were repulsive in this test. The maximum value of the total force was around 790 nN, which appeared after 10 s of film thinning.

Results Obtained with Hydrophilic Gold Surfaces

Figure 54 shows the results obtained with the gold surface hydrophobized with 10^{-5} M C_4SH in ethanol solution for 10 min. The spatiotemporal film profiles were shown in Figure 54(a). The film ruptured at t = 1.86 s with a critical rupture thickness (h_c) equal to 60 nm. The oil droplet became sharp and formed a pimple before it attached onto the hydrophobic gold surface, indicating that the oil/water interface was pulled toward the hydrophobic gold surface. These findings were totally different from what was observed with the hydrophilic gold surface (Figure 53(a)). With the latter, the film became flat and stable. Note here that film thinning rate was much higher than observed with the hydrophilic surface. It took only 1.86 s for the unstable wetting film on the thiol-coated gold surface to thin and to rupture, while for the wetting film formed on the hydrophilic surface, film thinning stopped at t = 13.78 s.

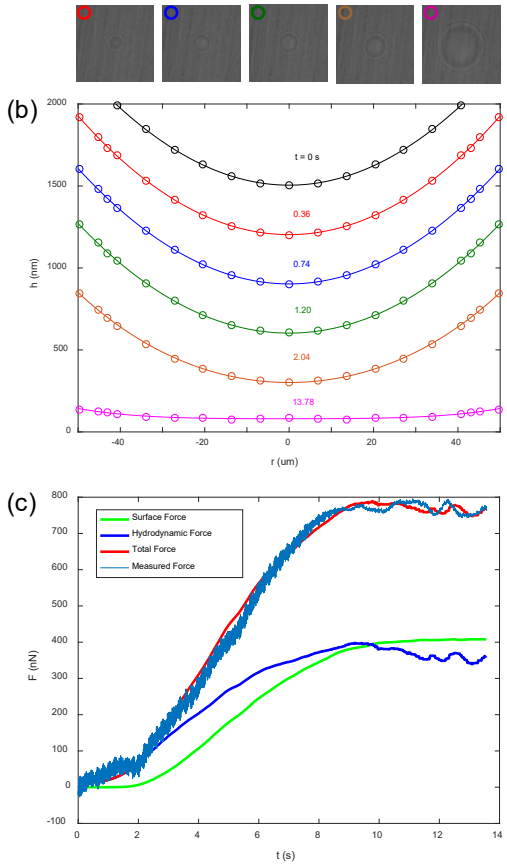

Figure 53. Results obtained for the interaction between an n-dodecane droplet and an untreated gold surface. The optical fringes (a) are used to obtain the spatiotemporal profiles in (b). The Laplace forces (red line) calculated from the data extracted from the film profiles are in good agreement with forces measured directly by the cantilever spring (light blue curve in (c)).

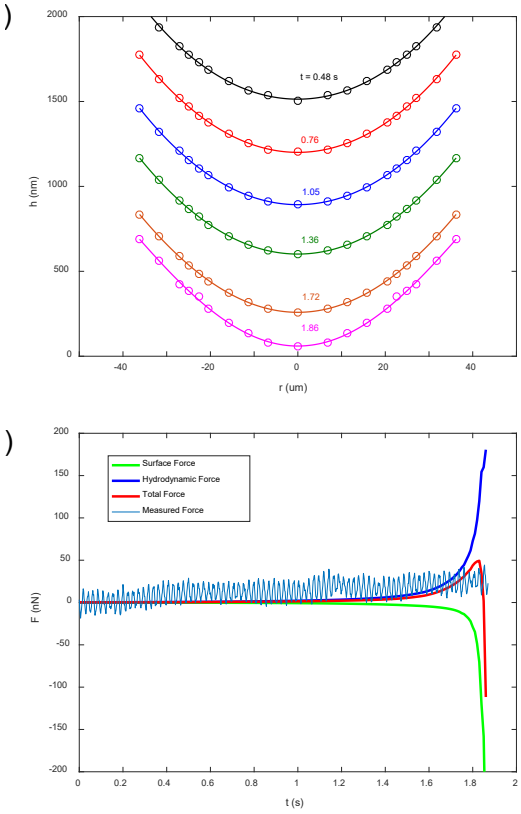

Figure 54. Results obtained for the interaction between an n-dodecane droplet and a gold surface treated in a 10^{-5} M C_4SH solution for 10 min.

In Figure 54(b), the measured force was much weaker than observed with untreated gold surface. In the latter, the maximum force observed was 790 nN, while in the former the maximum force was only 40 nN at t = 1.86 s. It is unlikely that the great decrease in the measured forces was due to the changes of the zeta potential associated with C_4SH adsorption, since C_4SH is an anionic surfactant. The decrease in the measured forces may be due to the appearance of a strong attractive surface force (hydrophobic force) associated with the thiol coating. The green curve represent the surface force obtained by using the surface chemistry parameters listed in the second row of Table 23. The fitting parameter K_{132} had a value of 8.5×10^{-18} J, which was over two magnitudes larger than the Hamaker constant (A_{132}), indicating that the hydrophobic force dominated the stability of the wetting film. The error between the measured force (light blue line) and fitted force (red line) from Eq. [4.1] was reasonable. Also shown in Table 23 were the surface chemistry parameters for the gold surface treated with 10^{-5} M C_4SH for 30 min. With the increase of the immersion time, K_{132} increased along with the increase in the contact angle (θ), implying that the hydrophobicity of gold-coated cantilever increased with the thiol coating time.

With the parameters in Table 23, one can readily plot the disjoining pressure isotherms for each test using Eq. [4.3]. Figure 55 shows the disjoining pressure isotherm for the wetting film of water formed on a gold surface after a 10 min immersion time in a 10^{-5} M C_4SH in ethanol solution. Compared with Π_d and Π_e, Π_h has a dominant effect on the total disjoining pressure Π. Strongly negative Π_h dictates a negative (attractive) Π during the whole film thinning process, which led to a fast film thinning kinetics.

The inset in Figure 55 shows the disjoining pressure isotherm at small film thickness (h < 3 nm). Note here that the short-range hydrophobic interaction and Lennard-Jones interaction will play important roles in the disjoining pressure at such a small h. Therefore, it is necessary to make some modifications in Eq. [4.3]. The modified equation is shown as below,

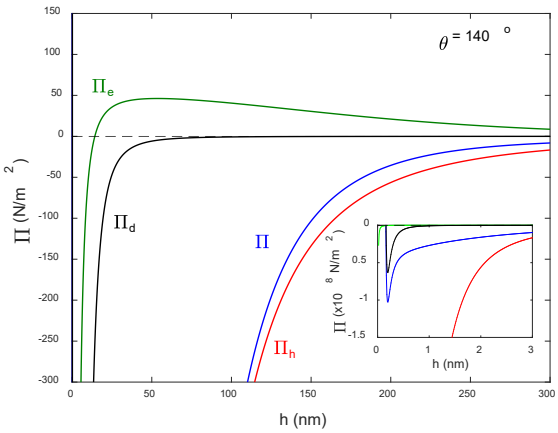

Figure 55. A disjoining pressure isotherm for the wetting film of water formed on a gold surface after a 10 min immersion time in a 10^{-5} M C_4SH in ethanol solution.

$$\Pi = \Pi_d + \Pi_e + \Pi_h$$
$$= -\frac{A_{132}}{6\pi h^3} + \frac{A_{132}\sigma^6}{45\pi h^9} - \frac{\varepsilon\varepsilon_0\kappa^2}{2\sinh(\kappa h)}\left[\left(\psi_1^2 + \psi_2^2\right)\cos ech(\kappa h) - 2\psi_1\psi_2\coth(\kappa h)\right] \quad [4.4]$$
$$+ \frac{C}{2\pi D}\exp\left(-\frac{h}{D}\right)\Big|_{h<h_t} - \frac{K_{132}}{6\pi h^3}\Big|_{h>h_t}$$

in which the second term represents Lennard-Jones interaction and the fourth term represents short-range hydrophobic interaction. In Eq. [4.4], σ is a length parameter related with molecular radius, C is the short-range hydrophobic force constant and D is the decay length. Eq. [4.4] is useful to derive the free energy (G) isotherm using Frumkin-Derjaguin isotherm (Frumkin, 1938; Derjaguin, 1940),

$$\Delta G = -\int_{h=\infty}^{h_0}\Pi(h)dh = \gamma_{wo}(\cos\theta - 1) \quad [4.5]$$

Table 23. Surface chemistry parameters from the FADS measurements conducted on the gold substrates treated in 10-5 M C4SH in ethanol solution with different immersion time.

Immersion Time (min)	A_{132} (10^{-20} J)	ψ_1 (mV)	ψ_2 (mV)	κ^{-1} (nm)	K_{132} (10^{-18} J)	θ (°)
0	1.38	-40.6	-70	96	0	-
10	1.38	-40.6	-70	96	8.5	140
30	1.38	-40.6	-70	96	10.8	145

where h_0 is the thickness of the α-film formed on the gold surface after film rupture, and γ_{wo} is the interfacial tension of the oil/water interface. In this analysis, σ is set to 0.23 nm for n-dodecane. Parameters C and D are determined iteratively by varying them until the ΔG calculated from the integration of Π equals to ΔG obtained from contact angle information. By using Eq. [4.4] and Eq. [4.5], one can obtain the free energy isotherm for the wetting film formed on a gold surface after a 10 min immersion time in a 10^{-5} M C_4SH in ethanol solution, which is plotted in Figure 56. In this specific case, C = -543 mN/m and D = 2 nm.

By comparing the inset of Figure 55 with Figure 56, one can find that at h_0 = 0.16 nm, Π =0, and G reaches its minimum at -90.1 mJ/m^2, indicating that the free energy change (ΔG) for oil-gold attachment is -90.1 mJ/m^2, which is over twice as much as the ΔG for air-gold attachment (ΔG = -40.6 mJ/m^2) reported by Pan and Yoon (2016). As shown in Eq. [4.5], the significant difference of ΔG's may be due to that the large difference of contact angles (θ). θ = 140° for n-dodecane droplets, while for air bubbles, θ is only 64°. Based on the information of ΔG and θ, one may draw a conclusion that oil droplets are superior to air bubbles in the capacity of collecting hydrophobic particles. Note also that no energy barrier is shown in Figure 56, suggesting that oil droplets can spontaneously attach onto the hydrophobic surface with little energy input.

Effect of Carbon Chain Length

FADS measurements were also conducted with different oils. In the present work, n-octane, n-decane, n-dodecane and n-hexadecane were selected to study. In this series of tests, the gold-coated cantilevers were all treated in 5x10^{-5} M KAX solution for 10 min to achieve the same hydrophobicity.

Figure 57 shows the disjoining pressure isotherms in the wetting films of water confined between hydrophobic gold and different oils, with the surface chemistry parameters listed in Table 24. As shown in Figure 57, the disjoining pressure (Π) of n-octane, n-decane and n-dodecane were negative at any film thickness (h). For n-hexadecane, positive Π appeared at h ~ 320 nm, while Π became negative at h < 320 nm. It is interesting that the disjoining pressure became more negative with decreasing the chain length of oil. This observation can be attributed to the fact that CH_3 group is more hydrophobic that CH2 group. In the HHS process, C5 to C7 hydrocarbons are used, which gives an advantage over using longer chain hydrocarbons.

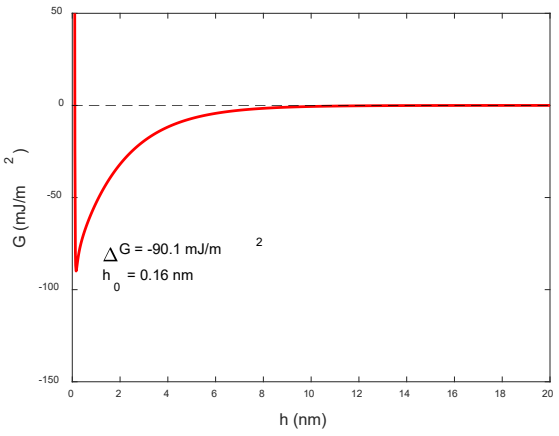

Figure 56. A free energy isotherm for the wetting film of water formed on a gold surface after a 10 min immersion time in a 10^{-5} M C_4SH in ethanol solution.

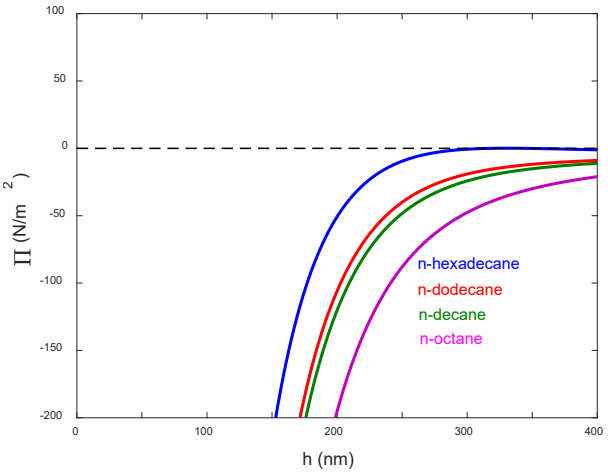

Figure 57. Disjoining isotherms for n-alkanes with varied chain lengths.

The results shown in Figure 57 and Table 24 may support the statement that short chain oils have better performance than the long chain oils in concentrating hydrophobic minerals. The former is more hydrophobic, which will lead to high kinetics of film thinning during the oil-particle interaction. Furthermore, it will be difficult for the short chain oil detaching from a hydrophobic surface, *i.e.*, the probability of oil-particle detachment is significantly low. In addition, short chain oils normally have low boiling point, which can be readily recycled from the slurry/oil mixtures by low temperature heating. n-pentane, therefore, may be the most suitable oil for the HHS process, since it is the shortest n-alkane in liquid state at room temperature.

Table 24. Surface chemistry parameters from the FADS measurements conducted on the oils with different chain lengths.

# of carbons	A_{132} (10^{-20} J)	ψ_1 (mV)	ψ_2 (mV)	κ^{-1} (nm)	K_{132} (10^{-18} J)	θ (°)	γ (mN/m)
8	0.87	-40.6	-115	96	38	141	51.6
10	1.07	-40.6	-124	96	27	137	52.3
12	1.38	-40.6	-130	96	25	133	52.5
16	1.47	-40.6	-144	96	17	130	53.1

Study on Gold Hydrophobicity 2

Materials and Methods

The methods and materials utilized in this study were identical to those of the preceding section. Any differences or deviations are noted in the discussion below.

Results and Discussion

In the present study, a series of FADS measurements have been conducted to study the effect of gold hydrophobicity on the stability of the wetting films. The hydrophobicity of gold-coated cantilevers was controlled by varying the immersion time in a 10^{-5} M *n*-C_4SH-in-ethanol solution. The experiments were conducted at the natural pH. Figure 58 compares the results of the FADS measurements conducted with 5 and 10 min immersion times. The results given in Figure 58-1a show that the forces measured directly by the cantilever spring (green) became negative as an *n*-dodecane drop gradually approached the cantilever by means of a piezo stage. The wetting film ruptured at a critical time (t_c) of 2.34 s. The hydrodynamic forces (red) were calculated by integrating the hydrodynamic pressure (p), which is given by Eq. [4.2], with the kinetic parameters, e.g., $\partial h/\partial t$, derived from the spatiotemporal profiles shown in Figure 58-1b. The surface forces (blue) were obtained by integrating Eq. [4.3]. The calculated total force (black) was determined by summing up the surface forces and hydrodynamic forces, which was in good agreement with the force measured directly with cantilever spring.

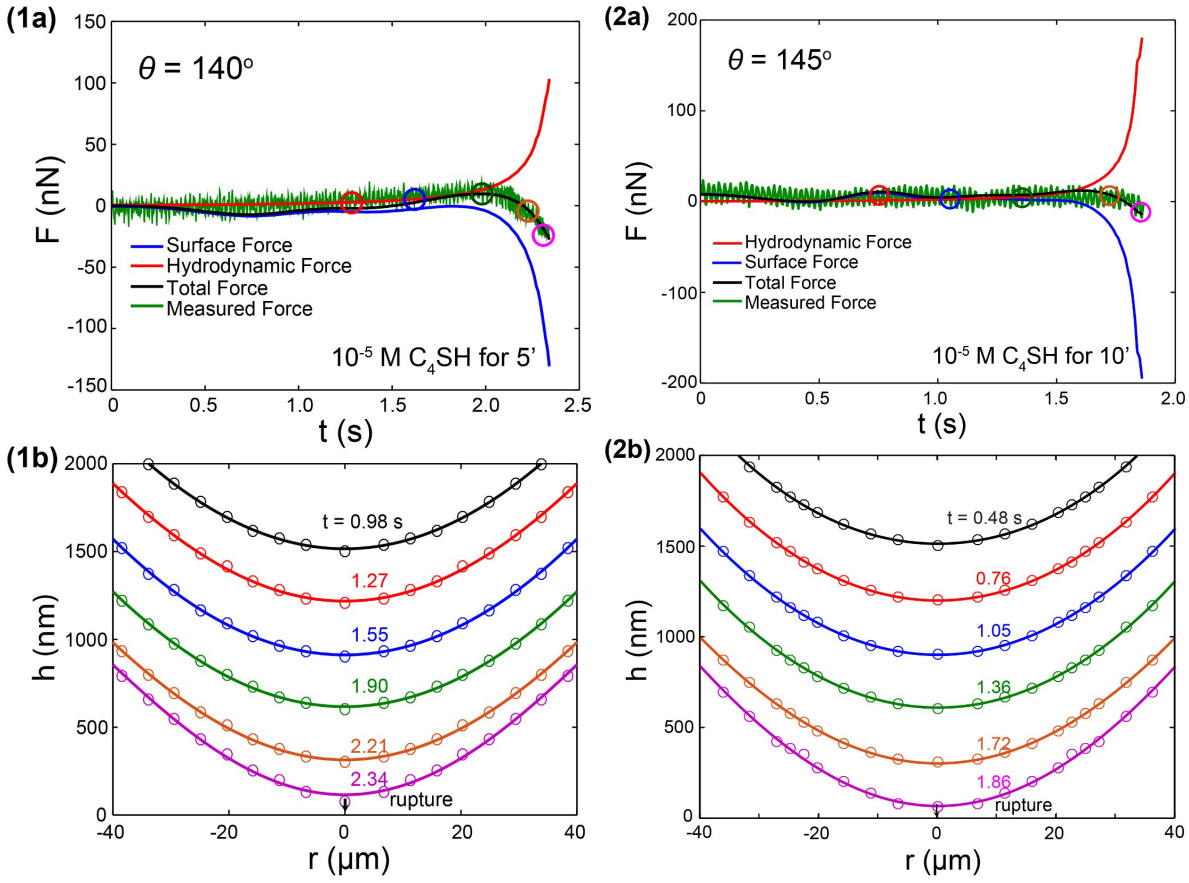

Figure 58. 1a. Force curves obtained for the interactions between an n-Dodecane droplet and a gold surface treated in a 10^{-5} M n-C4SH solution for 5 min, -b, corresponding spatiotemporal film profiles; -2a. Force curves obtained for the interactions between an n-Dodecane droplet and a gold surface treated in a 10^{-5} M n-C4SH solution for 10 min, -2b, corresponding spatiotemporal film profiles.

As shown in Figure 58-1a, the surface force became more and more negative with time, which could be attributed to the strong long-range hydrophobic force. The net negative surface force indicated that the repulsive double layer force was overwhelmed by the strong attractive forces, i.e., hydrophobic force and van der Waals force. In this test, the hydrophobic force constant (K_{132}) was determined to be 8.5 x 10^{-18} J, which was over two orders of magnitudes larger than the Hamaker constant (A_{132}). Therefore, the hydrophobic force was dominating the film thinning process.

Figure 58-2a shows the results obtained after a 10 min immersion time. The surface force curve (blue) became more negative than that after a 5 min immersion time, indicating that the long-range hydrophobic force became stronger with increased immersion time. The larger hydrophobic force was possibly due to that the packing density of *n*-C_4SH on the gold surface increased with increasing the immersion time. The corresponding spatiotemporal film profiles were shown in Figure 58-2b, which showed that the wetting film started to deform (the curvature of film became smaller) at $h < 500$ nm. The film ruptured at $t_c = 1.86$ s, which was 0.48 s faster than the case of 5 min immersion time.

Figure 59 compares the FADS results obtained with 30 and 60 min immersion times. As shown in Figure 59-1a, the measured force (green) increased with decreasing of film thickness. The maximum value of measured force was 26.6 nN, which was repulsive, not attractive. The surface force (blue) became less negative when the immersion time was increased from 10 min to 30 min, indicating that the long-range hydrophobic force decreases at excessively long contact times or conditioning times. The corresponding spatiotemporal film profiles are given in Figure 59-1b. As shown, the deformation of the wetting film was

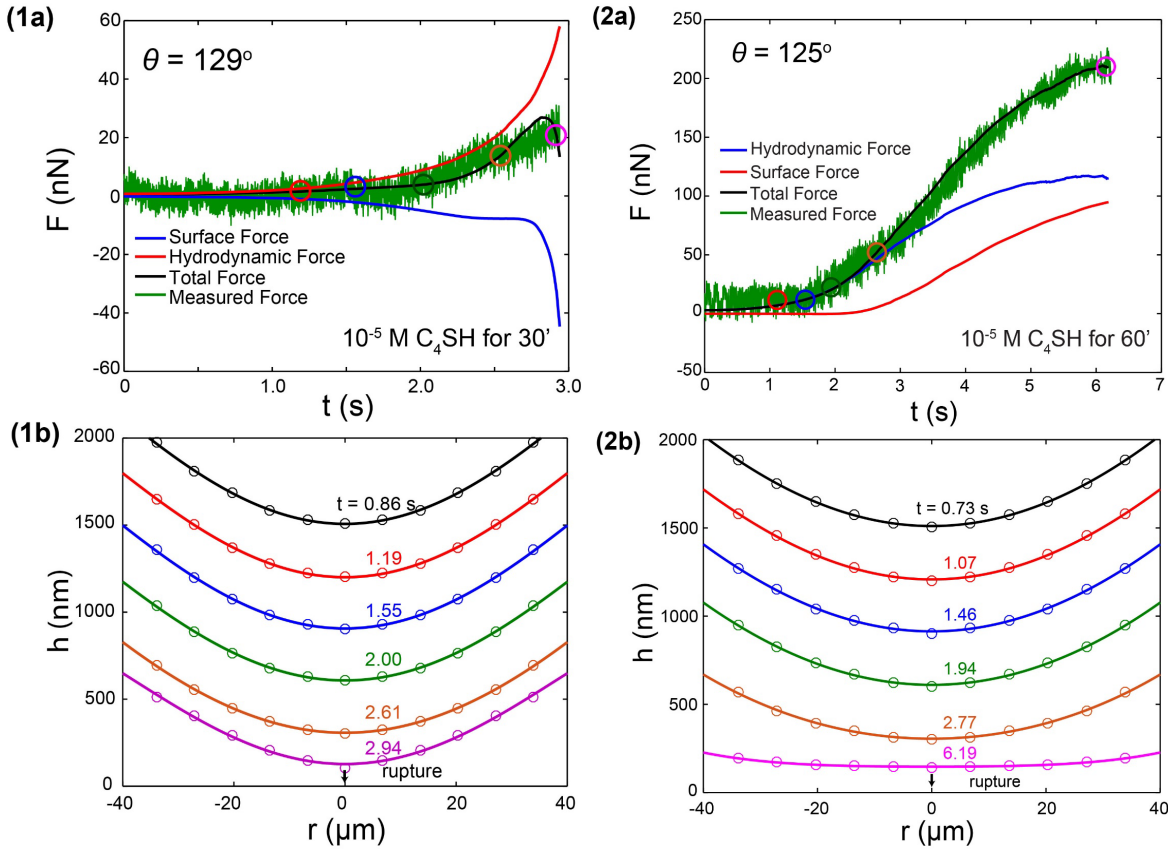

Figure 59. 1a. Force curves obtained for the interactions between an n-Dodecane droplet and a gold surface treated in a 10^{-5} M n-C_4SH solution for 30 min, -b, corresponding spatiotemporal film profiles; -2a. force curves obtained for the interactions between an n-Dodecane droplet and a gold surface treated in a 10^{-5} M n-C_4SH solution for 60 min, -2b, corresponding spatiotemporal film profiles.

not as significant as the case for 10 min immersion time. It took 2.94 s before film ruptured, which was over 1 s longer than the results shown in Figure 58-2b.

The FADS measurement was also conducted after a 60 min immersion time, with the results shown in Figure 59-2a, 2b. It is interesting that the measured force increased a lot during the film thinning process. The maximum value of the measured force was around 200 nN, which was almost 10 times larger than the results obtained after a 30 min immersion time. The surface force also increased with time, which might be due to a further decrease in attractive hydrophobic force. Note in Figure 59-2b that the wetting film became flat before rupture (t_c = 6.19 s), which was consistent with the results obtained in Figure 59-2a. In summary, there is an optimum immersion time (10 min), at which θ and K_{132} reach maxima and t_c reaches a minimum. Above the optimum, *n*-C_4SH may form multilayers with those in the second layer inversely oriented. The –SH and –SAu groups may be exposed toward the aqueous phase, compromising the hydrophobicity. This finding is consistent with the AFM force measurement conducted by Wang and Yoon (2008).

Figure 60 shows the disjoining pressure ($\Pi(h)$) isotherms obtained using the surface chemistry parameters determined from the FADS measurements and given in Table 25. The isotherm obtained with an untreated hydrophilic gold surface is represented as a blue solid line. It is close to the sum of the two DLVO forces, i.e., double-layer (Π_e) and van der Waals-dispersion (Π_d) forces as shown.

On the other hand, the $\Pi(h)$ isotherms obtained with *n*-C_4SH-coated gold surfaces showed substantial deviations from the DLVO theory due to the presence of the hydrophobic force in the wetting films of water confined between a hydrophobic gold and an oil drop. As the immersion time was increased from 5 to 10 min, the hydrophobic force increased. At longer immersion times, however, the hydrophobic force decreased substantially most probably due to the inverse orientation of the thiol molecules on a hydrophobic surface. In general, wetting films thin faster and rupture on a hydrophobic surface, which can be attributed to the strong hydrophobic force.

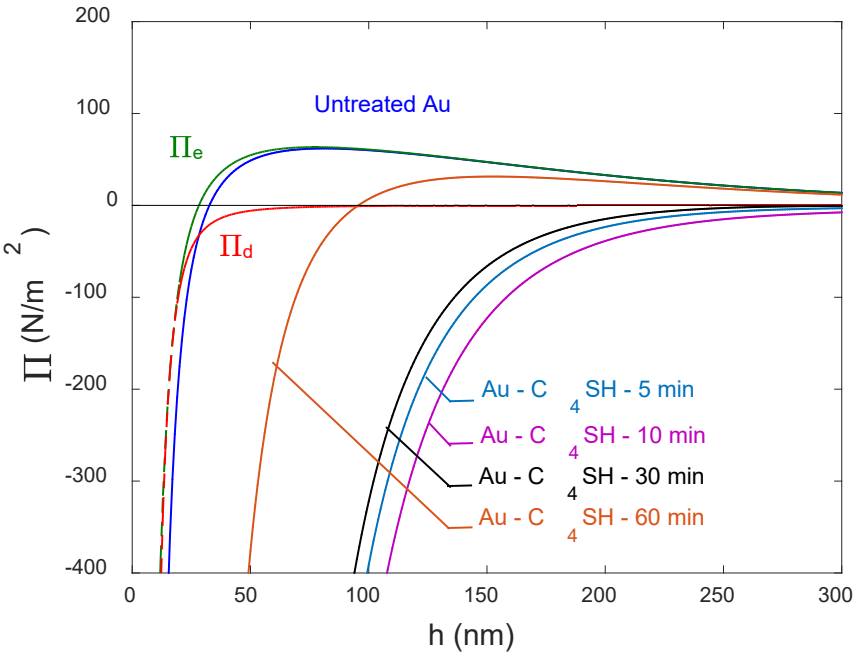

Figure 60. Disjoining pressure isotherms in wetting films formed on gold surfaces treated in a 10^{-5} M n-C_4SH solution for different immersion times. DLVO forces are given as dashed curves.

Table 25. Surface chemistry parameters from the FADS measurements conducted on the gold substrates treated in a 10-5 M C4SH-in-ethanol solution at different immersion time.

Immersion Time (min)	A_{132} (10^{-20} J)	ψ_1 (mV)	ψ_2 (mV)	κ^{-1} (nm)	K_{132} (10^{-18} J)	θ (^{o})	t_c (s)
0	1.38	-40.6	-70	96	0	-	-
5	1.38	-40.6	-70	96	8.5	140	2.34
10	1.38	-40.6	-70	96	10.8	145	1.86
30	1.38	-40.6	-70	96	7.2	129	2.94
60	1.38	-40.6	-70	96	1.0	125	6.19

Air Bubble vs. Oil Droplet

In this study, FADS measurements were also conducted to study the surface forces in the thin liquid films (TLFs) of water confined between air bubble and gold surface. The gold surface was hydrophobized in a 10^{-5} M *n*-C_4SH-in-ethanol solution for 10 min. Measured force was repulsive as shown in Figure 61-1a. It increased linearly after t = ~2 s and reached maximum (460 nN) when the film ruptured. As shown in the inset, the receding contact angle ($\theta = 80^{o}$) measured after the rupture was large despite the appearance of a strong repulsive force. Due to the presence of a strong repulsive force, the film thinning process was slow as shown in the spatiotemporal profiles (Figure 61-1b). It took 5.42 s for thinning before the film ruptured. The flat film appeared at the ending of the thinning process. That the film was flat just before rupture indicated the presence of a strong repulsive force. A question to be raised here is what caused the film rupture at the short range. The answer is the short-range hydrophobic force, which is difficult to measure but can be calculated using the Frumkin-Derjaguin isotherms, as will be shown later.

Figure 61-2a shows the force curves obtained using an *n*-dodecane droplet and a gold surface in water. The gold was hydrophobized in the same manner as for the bubble-surface interaction. One can immediately notice that the measured force curve was more or less flat, indicating practically no resistance

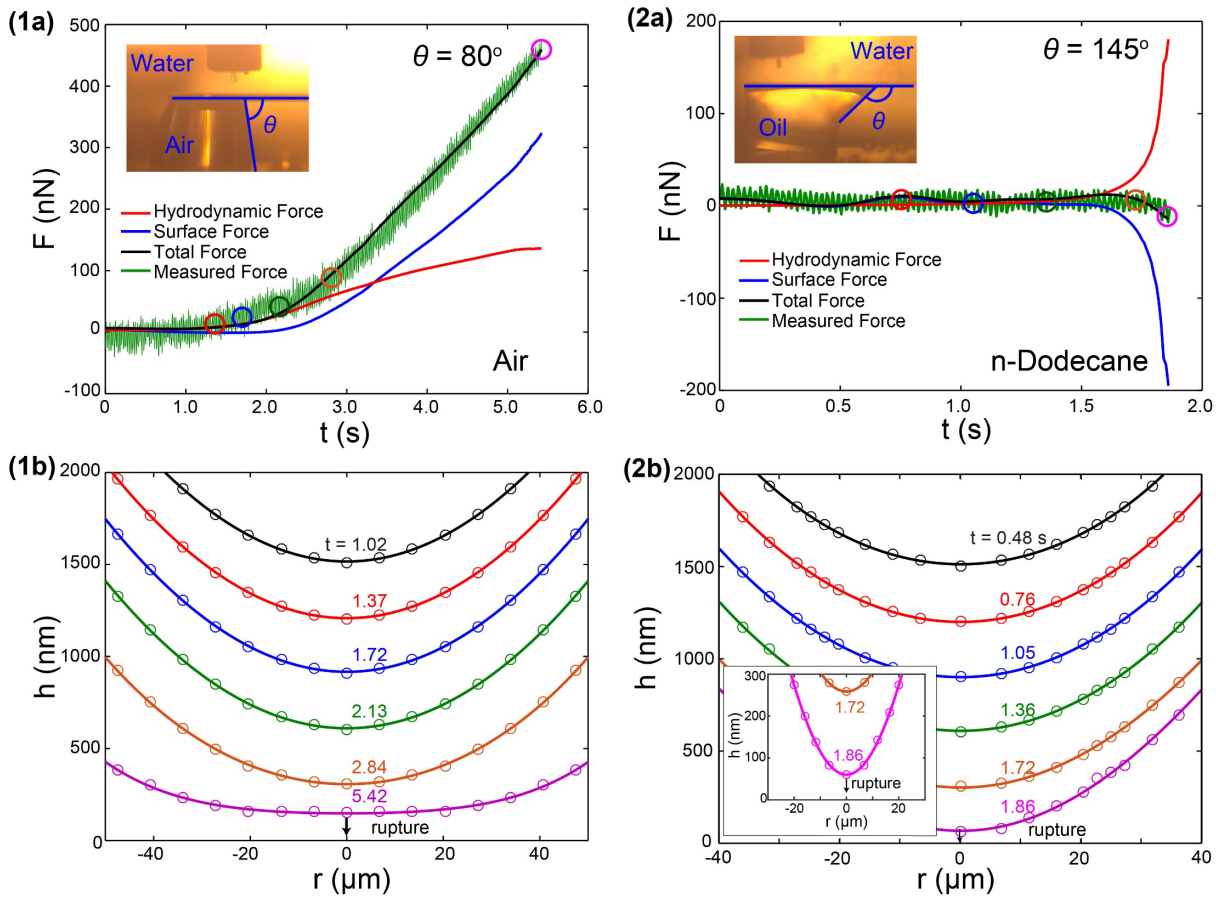

Figure 61. 1a. Force curves obtained for the interactions between an air bubble and an n-C_4SH-coated gold surface in pure water, -b, corresponding spatiotemporal film profiles; -2a. Force curves obtained for the interactions between an n-Dodecane droplet and an n-C_4SH-coated gold surface in pure water, -2b, corresponding spatiotemporal film profiles.

to film thinning. As a consequence, the film thinned much faster than with air bubble as can be seen in the spatiotemporal film profiles shown in Figure 61-1b and -2b. Furthermore, the oil drop exhibits higher curvatures than the air bubble. The inset of Figure 61-2b shows such high curvatures, indicating that it was being pulled toward the hydrophobic surface. Such sharp changes in curvature is referred to as 'pimple'. Note also that the contact angle was 145° as compared to 80° observed with air bubble (see surface force data in Table 26).

The spatiotemporal film profiles shown in Figure 61-1a,b have been analyzed as described previously (Pan and Yoon, 2016) to determine the disjoining pressure ($\Pi(h)$) and the free energy ($G(h)$) isotherms presented in Figure 62-a,b. Eq. [4.3] may be used the $\Pi(h)$ isotherm. However, it includes only the long-range hydrophobic force represented by a parameter K_{132} and does not include contributions from the short-range hydrophobic force. Also, it does not include contributions from the Lennard-Jones interaction between adsorbent and adsorbate at very short-range. Therefore, Eq. [4.3] has been rewritten as follows,

Table 26. Surface chemistry parameters from the FADS measurements conducted on the gold-air and gold-oil interactions.[1]

Material	Surface forces								Free energy		
	van der Waals		Double layer			Hydrophobic					
	A_{132}	σ	ψ_1	ψ_2	κ^{-1}	K_{132}	C	D	θ	γ	ΔG
	(10^{-20} J)	(nm)	(mV)	(mV)	(nm)	(10^{-18} J)	(mN/m)	(nm)	(°)	(mN/m)	(mJ/m^2)
Air bubble	-14.8	0	-40.6	-52	96	0.2	-597	2	80	72.4	-59.6
n-Dodecane	1.38	0.23	-40.6	-70	96	10.8	-543	2	145	52.5	-90.1

[1]Gold surfaces were immersed in a 10^{-5} M C_4SH-in-ethanol solution for 10 min.

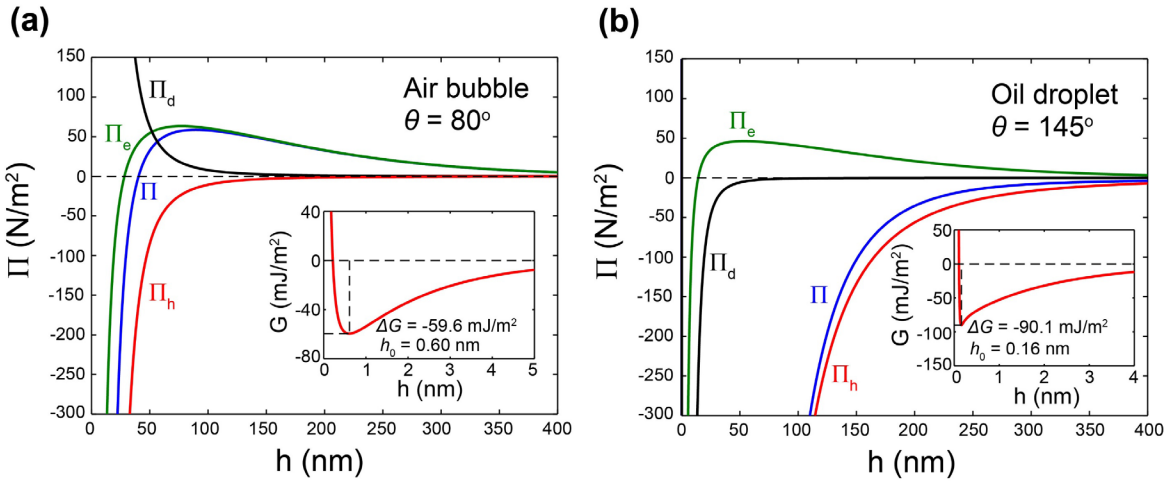

Figure 62. a. The disjoining pressure isotherm obtained for the interactions between an air bubble and an n-C_4SH-coated gold surface in pure water. Inset: the corresponding free energy isotherm; -b. The disjoining pressure isotherm obtained for the interactions between an oil droplet (n-Dodecane) and an n-C_4SH-coated gold surface in pure water. Inset: the corresponding free energy isotherm.

$$\begin{aligned}\Pi(h) &= \Pi_d + \Pi_e + \Pi_h \\ &= -\frac{A_{132}}{6\pi h^3} + \frac{A_{132}\sigma^6}{45\pi h^9} - \frac{\varepsilon\varepsilon_0\kappa^2}{2\sinh(\kappa h)}\left[\left(\psi_1^2+\psi_2^2\right)\cos ech(\kappa h) - 2\psi_1\psi_2\coth(\kappa h)\right] \\ &\quad + \frac{C}{2\pi D}\exp\left(-\frac{h}{D}\right)\Big|_{h<h_t} - \frac{K_{132}}{6\pi h^3}\Big|_{h>h_t}\end{aligned} \qquad [4.6]$$

where σ is the length parameter related to atoms (or molecules) involved; and C is the short-range hydrophobic force parameter and D is its decay length. Note here that we used σ = 0 for bubble-surface interaction because an air bubble represents nothingness, while we used σ = 0.23 nm for oil-gold interaction.

Substituting Eq. [4.6] into the Frumkin-Derjaguin isotherm (Derjaguin, 1940; Frumkin, 1938), one can obtain the free energy (ΔG),

$$\Delta G(h) = -\int_{h=\infty}^{h_0} \Pi(h)\, dh = \gamma(\cos\theta - 1) \qquad [4.7]$$

where h_0 is the thickness of the α-film formed on the gold surface after film rupture, and γ is the interfacial tension of the oil/water interface or air/water interface.

The insets of Figure 62-a,b show the free energy isotherms obtained with an air bubble and an oil droplet, respectively. ΔG for air-gold attachment is only -59.6 mJ/m^2, while ΔG for oil-gold attachment is more negative, which is -90.1 mJ/m^2. Generally, ΔG becomes more negative with increasing of contact angle (θ) as shown in Eq. [4.7]. The more negative ΔG for oil is attributed to that oil can form larger contact angle on a hydrophobic surface than air, which is an important reason that the HHS process developed by CAST should be advantageous over the conventional flotation process.

ζ-potential Study

Introduction

When two macroscopic surfaces interact with each other in water, *e.g.*, a bubble and a particle in flotation and an oil drop and a particle in HHS, the stability of the thin liquid film (TLF) formed in between two surfaces dictates the fate of the interaction. It the film is stable, nothing will happen. If unstable, the film – otherwise known as wetting film – will rupture to form aggregates. The stability is determined by the surface forces in the film, which include the van der Waals, electrical double-layer, and hydrophobic forces. The Yoon's group at Virginia Tech has shown that the hydrophobic force is the major destabilizing force for the wetting films formed on hydrophobic surfaces. On the other hand, both the van der Waals and double-layer forces are stabilizing forces and, therefore, are deterrent to fruitful bubble-particle interaction.

If it is desired to prevent the wetting film from rupture, one should increase its stability by increasing the double-force. A case in point is the depression of the gangue minerals during the process of recovering rare earth minerals (REMs) as has been discussed in the foregoing section of this report. The two depressants we tested, i.e., sodium silicate and sodium hexametaphosphate, are polyelectrolytes that can increase the double-layer forces between the gangue minerals and oil drops.

The work shown in the section above was designed to turn the double-layer force into a destabilizing force such that it can complement the role of the hydrophobic force. The net result will be an acceleration the film thinning and rupture to increase the recovery of REMs.

In the current study, FADS measurements were conducted to study the effects of ζ-potentials on the stability of wetting films confined between an air bubble and a flat silica surface. The results show that one can control the ζ-potentials of air/water and solid/water interfaces to create an attractive double layer force, which will greatly benefit the flotation kinetics and recoveries. The same approach may be taken to improve the kinetics of REM recovery using the HHS process.

Experimental

The Ultrapure water used in the present work was obtained from a Direct-Q water purification system (Millipore) with a resistance of 18.2 MΩ/cm. Sheets of silicon wafers were purchased from University Wafer, Boston, MA, with one side polished. Each sheet was cut into small strips of 15x3x0.05 mm in dimension for force measurement. The cantilevers were cleaned in hydrogen peroxide (H_2O_2, Fisher Scientific, 30-35%) and sulfuric acid (H_2SO_4, Spectrum Chemical, 98%). Dodecylamine hydrochloride (DAH, Sigma Aldrich) and hexadecyltrimethylammonium bromide (CTAB, TCI America) were used as received to hydrophobize the cantilever springs. Hydrochloric acid (HCl, Fisher Scientific) and sodium hydroxide (NaOH, Sigma Aldrich) were used for pH adjustment. The octadecyltrichlorosilane (OTS) from Sigma Aldrich was also used as a hydrophobizing agent in some measurements.

The silicon cantilevers were cleaned by immersing them in a mild piranha solution (H_2SO_4:H_2O_2 = 7:3 by volume) at 90 °C for 1 min, followed by rinsing with ultrapure water and drying in an ultrapure nitrogen gas stream. A layer of silicon dioxide free of organic contaminant forms as manifested by a zero water contact angle measured after the treatment. The majority of the force measurements were conducted using the hydrophilic silicon cantilevers, while in some cases the measurements were conducted after immersion in a $3x10^{-5}$ M OTS-in-toluene solution. The OTS-coated cantilevers were washed with chloroform and dried in an ultrapure nitrogen stream before use.

Figure 52 shows a schematic representation of the force apparatus for deformable surface (FADS), which has been designed to measure the surface forces in wetting films. A detailed description of the instrument has been made previously (Pan and Yoon, 2016, 2018). In a given FADS measurement, one end of a cantilever spring is fixed onto a translational stage by means of an adhesive, so that the cantilever can be moved in 3-directions (*x*, *y*, and *z*). Approximately 10 mL of an aqueous solution is delivered to the liquid cell from the open top. After the cell is filled, an air bubble is formed on the hydrophobic quartz plate

located at the bottom of the cell by means of a syringe pump. The bubble size is controlled by control of air volume being injected.

Initially, the cantilever spring is lowered manually by means of the translational stage until the interference patterns (or Newton rings) begin to appear at $h \approx 10$ μm. From this point and onward, the film thickness is controlled by moving the bubble toward the underside of a cantilever by means of a piezo stage. The approach speed is set at 1,100 nm/s for all tests. During film thinning, the bubble continues to deform and generate Newton rings, which are recorded by means of a high-speed camera, while at the same time a fiber optic sensor is used to monitor the deflection of the cantilever spring. The recorded fringes are analyzed offline using the microinterferometric technique developed by Sheludko (1962) to construct spatiotemporal film profiles. By analyzing the film profiles using the equations presented in the next section, one can determine both the hydrodynamic and surface forces as a function of time (t) and film thickness (h). The forces measured from the curvature changes are then compared with those measured directly using the cantilever spring. The spring constant is determined *in-situ* against the forces determined by analyzing the spatiotemporal film profiles. Since direct force measurement is sensitive to vibration, the entire FADS instrument is placed on a vibration isolation platform (100BM-1, Minus K Technology), which in turn is placed on a Nexus optical table (T46H, Thorlabs).

Theory

When an air bubble in water approaches a flat surface in horizontal disposition, it deforms and creates a capillary pressure (p_c) in the liquid between the two macroscopic surfaces due to the changes in the curvature of the bubble. The liquid drains due the capillary pressure until it becomes equal to the disjoining pressure (Π), *i.e.*, $p_c = \Pi$, to form an equilibrium film thickness (h_e). Both p_c and Π vary with film thickness (h). If $p_c > \Pi$, the film will continue to thin and rupture at a critical thickness (h_c) at which $\Pi < 0$ to form a finite contact angle. Thus, the kinetics of film thinning during bubble-particle interaction is determined by the hydrodynamic pressure, or excess pressure (p),

$$p = p_c - \Pi \qquad [4.8]$$

Once p is known, one can predict the kinetics of film thinning using the Reynolds lubrication theory,

$$\frac{\partial h}{\partial t} = \frac{1}{12\mu r}\frac{\partial}{\partial r}\left(rh^3\frac{\partial p}{\partial r}\right) \qquad [4.9]$$

in which t is time, μ the kinematic viscosity, and r the radial distance from film center. Integrating Eq. [4.9] under the boundary condition that $p_{r=\infty} = 0$ and $\partial p/\partial r|_{r=0} = 0$, one obtains,

$$p = 12\mu\int_{r=\infty}^{r}\frac{1}{rh^3}\left[\int_{r=0}^{r} r\frac{\partial h}{\partial t}dr\right]dr \qquad [4.10]$$

The capillary pressure of Eq. [4.8] can be calculated using the Young-Laplace equation,

$$p_c = \frac{2\gamma}{R} - \frac{\gamma}{r}\frac{\partial}{\partial r}\left(r\frac{\partial h}{\partial r}\right) \qquad [4.11]$$

where R is the bubble radius, while the disjoining pressure can be obtained using the DLVO theory extended to include the contribution from the hydrophobic force as follows:

$$\begin{aligned}\Pi &= \Pi_d + \Pi_e + \Pi_h \\ &= -\frac{A_{132}}{6\pi h^3} - \frac{\varepsilon\varepsilon_0\kappa^2}{2\sinh(\kappa h)}\left[\left(\psi_1^2+\psi_2^2\right)\cos ech(\kappa h) - 2\psi_1\psi_2\coth(\kappa h)\right] \\ &+ \frac{C_1}{2\pi D_1}\exp\left(-\frac{h}{D_1}\right) + \frac{C_2}{2\pi D_2}\exp\left(-\frac{h}{D_2}\right)\end{aligned} \qquad [4.12]$$

In Eq. [4.12], Π_d, Π_e, and Π_h represent the disjoining pressures due to the van der Waals-dispersion force, double layer force, and hydrophobic force, respectively, and A_{132} is the Hamaker constant for the interaction between solid **1**, air bubble **2**, and water **3**.

For the interaction between silica plate and air bubble studied in the present work, A_{132} = -1.2x10^{-20} J (Israelachvili, 2011). Since $A_{132} < 0$, Π_d is repulsive. The Π_e term of Eq. [4.12] represents the Hogg-Healey-Fuerstenau (HHF) approximation (Hogg *et al*., 1966), in which ε_0 is the permittivity of vacuum, ε is the dielectric constant of water, κ is the reciprocal Debye length, ψ_1 is the ζ-potential of the cantilever, ψ_2 is the same of the air bubble. Π_h is given as a double-exponential function, in which C_1 and C_2 represent the short- and long-range hydrophobic force constants, respectively, and D_1 and D_2 represent the corresponding decay lengths.

In the present work, a single bubble is brought to a flat surface from below in the same manner as in captive bubble method of contact angle measurement, while monitoring the changes in bubble curvature as a function of time. The curvature data may be used to determine the bubble-particle interaction force ($F(t)$) at time t by integrating Eq. [4.11] across the film as follows,

$$F(t) = 2\pi\int_0^{r_{\max}} p_c(r,t)\,r\,dr \qquad [4.13]$$

where $r_{\max}$ is the radius of the wetting film. Substituting Eq. [4.8] into Eq. [4.13], one obtains,

$$F(t) = 2\pi\int_0^{r_{\max}} \left[p(r,t) + \Pi(r,t)\right] r\,dr \qquad [4.14]$$

in which the first term on the right represents the hydrodynamic force and the second term represents the surface force that can be calculated using Eqs [4.10] and [4.12], respectively. In the present work, the first two components of Eq. [4.12], *i.e.*, Π_d and Π_e, have been calculated using the parameters, *e.g.*, A_{132} and ζ-

potentials, that are readily available in the literature. The hydrophobic force component, *i.e.*, Π_h, is unknown. The approach taken here is to back-calculate it using Eq. [4.14] from the values of $F(t)$ determined using Eqs. [4.11] and [4.13]. The values of $F(t)$ determined in this manner represents the sum of all the forces operating during bubble-particle interaction. Some of the forces become negative at certain film thicknesses; therefore, $F(t)$ gives net interaction forces, which are also measured directly for comparison with the values calculated using Eq. [4.13].

Results and Discussion – Effect of pH

In the present work, a set of two FADS measurements have been conducted at different pH's with the appearance of 10^{-5} M DAH to measure the hydrodynamic and surface forces in the wetting film, which is confined between an air bubble and the underside of a cantilever spring made from a thin silicon wafer. Since the cantilever has been treated in a mild piranha solution, its surface must be oxidized to a silica (SiO_2) film. The results may be compared with the classic work of Fuerstenau (1957), who showed that flotation recovery reaches a maximum at an alkaline pH where the cationic collector neutralizes the surface charge, which reduces the energy barrier for bubble-particle attachment. In this regard, FADS measurements have been conducted by varying the pH to better understand the role of ζ-potentials in bubble-particle interaction.

Figure 63 shows the FADS measurement results obtained at pHs 5.8 and 9.5. The black force curve represents the Laplace force calculated using Eq. [4.13], while the green curve represents the forces measured directly using the cantilever spring. The two force curves are in reasonable agreements, showing that the method of force measurement using air bubble is valid. The film profiles shown in Figure 63-1b

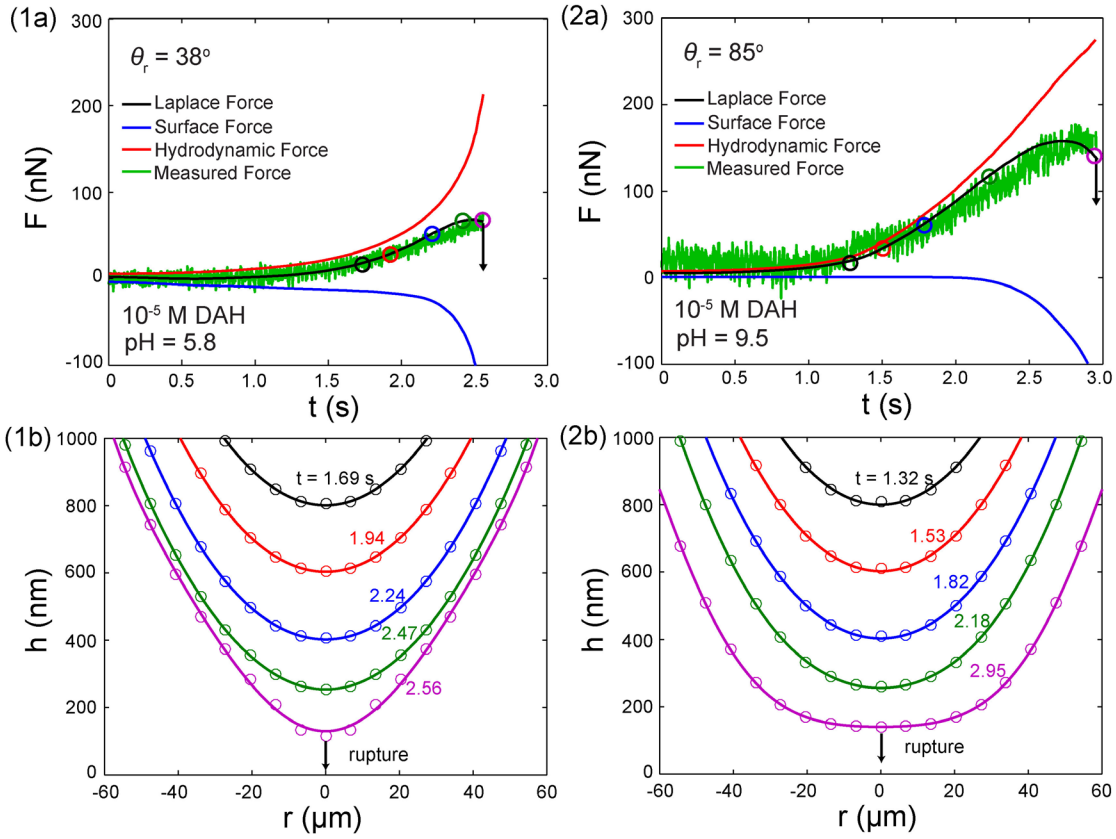

Figure 63. 1a. Force curves obtained for the interactions between an air bubble and a bare silicon surface in 10^{-5} M DAH at pH 5.8, -1b, corresponding spatiotemporal film profiles. -2a. Force curves obtained at pH 9.5, -2b, corresponding spatiotemporal film profiles.

are color-coded to show how the interaction force changes with time (t), film thickness (h), and bubble curvature. As shown, the Laplace force representing the total (or net) interaction force increases slowly with t as the bubble approaches the surface and reaches a maximum of 68.0 nN, which is not very strong. The weak interaction force is due to a strong attractive surface force (blue) counterbalancing the hydrodynamic force. The attractive force becomes stronger with time and hence with decreasing film thickness. Also shown in Figure 63-1a are hydrodynamic (red) and surface (blue) forces as calculated by substituting Eqs. [4.10] and [4.12], respectively, into Eq. [4.14]. The surface force does not change until film thickness (h) is reduced close to ~300 nm, where the net force becomes attractive and causes the film to rupture catastrophically at h_{cr} = 116 nm at the film center and t_{cr} = 2.56 s, where t_{cr} is the critical rupture time.

Table 27 gives the surface force parameters used to obtain force curves. The values of ψ_1 given in the table are actually the ζ-potentials measured in the present work in the presence of 10^{-5} M DAH. The measurements have been conducted on glass spheres with d_{80} = 5 μm using the Malvern Zetasizer NanoZS 90. The ψ_2 values are from Yoon and Yordan (1986), while A_{132} = -1.2 x 10^{-20} J is from Israrelachivili (2011). The surface tension (γ) data are from Finch and Smith (1973). The receding contact angles (θ_r) are from the images recorded during the FADS measurements using the side-view camera. At pH 5.8, θ_r = 38°. According to Churaev (1995), attractive hydrophobic forces appear at θ > 40°; therefore, both C_1 and C_2 are set to zero at pH 5.8 since the contact angle is low.

Note also that in Figure 63-1b the bubble becomes elongated at pH 5.8, as it moves closer to the silica surface. It seems as if the bubble is pulled toward the silica surface, which can be attributed to the stronger double-layer attraction between the two macroscopic surfaces. As shown Table 1, ψ_1 = -40 mV and ψ_2 = 50 mV at pH 5.8, indicating that the double-layer force is attractive. Based on Eq. [4.11], p_c will decrease if $\partial h/\partial r$ increases. $\partial h/\partial r$ describes the shape of the film. When the bubble becomes elongated, $\partial h/\partial r$ increases, which will result in a small p_c and in hence a small Laplace force. The analysis of film profiles is consistent with the small Laplace force shown in Figure 63-1a.

Figure 63-2a shows the results of FADS measurement conducted at pH 9.5. The contact angle measured under this condition is 85°, which is substantially higher than that measured at pH 5.8 (θ_r = 38°). The pKa of DAH is 10.1; therefore, the concentrations of the charged (RNH_3^+) and uncharged (RNH_2) species are the same at pH 10.1. As the pH approaches this value, co-adsorption of the two may occur and

Table 27. Surface force parameters in the wetting films of 10-5 M DAH solutions formed on silicon surface at pHs 5.8 and 9.5.

pH	A_{132} (x10^{-20} J)	ψ_1 [1] (mV)	ψ_2 [2] (mV)	κ^{-1} [3] (nm)	C_1 (mN/m)	D_1 (nm)	C_2 (mN/m)	D_2 (nm)
5.8	-1.2	-40	50	78	0	-	0	-
9.5	-1.2	0	10	20	-350	2	-0.8	35

pH	γ (mN/m)	θ_r (°)	ΔG (mJ/m^2)	h_{cr} (nm)	t_{cr} (s)
5.8	70	38	-14.8	116	2.56
9.5	50	85	-45.6	140	2.95

[1]Measured using Malvern ZetaSizer; [2]Yoon and Yordan, 1986; [3]Claesson *et al.*, 1992; Rutland et al., 1992; [4]Finch and Smith (1973).

give rise to a close-packed monolayer and hence higher contact angles, as suggested by Somasundaran and Ananthapadmanabhan (1979). As shown in Figure 63-2a, the surface force (blue) becomes more and more negative with the time, which is due to the long-range-hydrophobic force present in the wetting films with C_2 = -0.8 mN/m and D_2 = 35 nm. The zeta-potentials for silica/water and air/water interfaces are ψ_1 = 0 mV and ψ_2 = 10 mV, respectively, indicating that the magnitude of double layer force is very small compared with the long-range hydrophobic force. The wetting film ruptures after 2.95 s with a critical rupture thickness h_{cr} = 140 nm, which is longer than the h_{cr} at pH 5.8.

Figure 64 compares the $\Pi(h)$ isotherms obtained at pH 5.8 and 9.5, including the component disjoining pressures, *i.e.*, $\Pi_d(h)$, $\Pi_e(h)$, and $\Pi_h(h)$. Also shown are the free energy isotherms ($G(h)$) as insets. The free energy isotherms are obtained by using Frumkin-Derjaguin isotherm,

$$\Delta G(h) = -\int_{h=\infty}^{h_0} \Pi(h)\, dh = \gamma(\cos\theta_r - 1) \quad [4.8]$$

in which ΔG is the free energy of bubble-surface interaction, γ the surface tension of water, θ_r the receding contact angle, and h_0 is the thickness of the α-film. As shown in Figure 64, the attractive double-layer force (Π_e) at pH 5.8 is longer-ranged than the attractive hydrophobic force (Π_h) at pH 9.5. Should one then expect better flotation results at pH 5.8? The answer is no in view of the fact that the free energy change (ΔG) associated with the bubble-surface interaction at pH 9.5 is three-times more negative than the same at pH 5.8 as shown in the $G(h)$ isotherms shown in the insets. Note also that most of the free energy gained during the bubble-surface interaction is due to the hydrophobic interaction at short-range below ~5 nm.

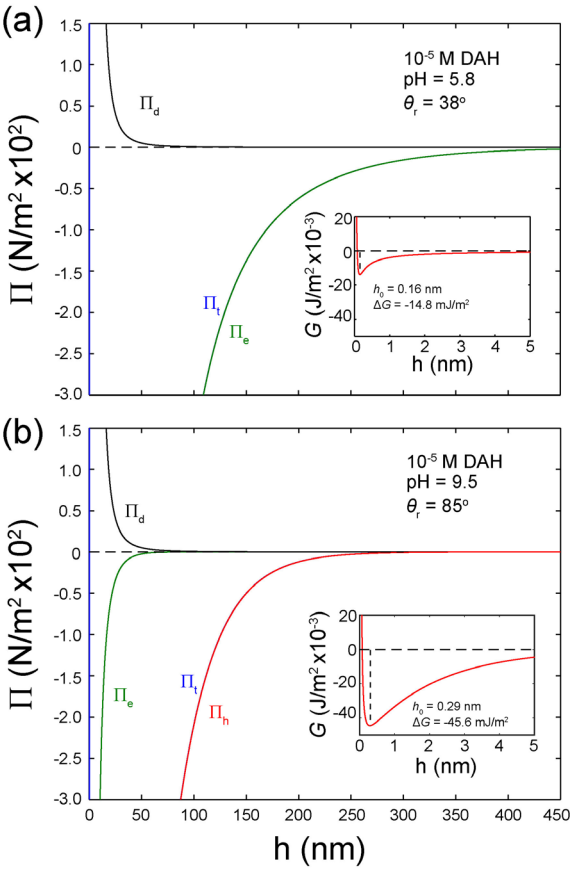

Figure 64. Disjoining pressure isotherms and free energy isotherms constructed for the wetting film of 10^{-5} M DAH solution at (a) pH 5.8, and (b) pH 9.5.

Thus, the data presented in Figure 64 suggests that the long-range hydrophobic force is responsible for film thinning and rupture, while the short-range hydrophobic force is responsible for film retreat (or de-wetting) to create a solid/vapor interface. A wetting film should also retreat due to the double-layer force. The extent of dewetting, however, is a lot greater and its kinetics is a lot faster in the presence of the hydrophobic force as shown in Figure 65. This observation may be explained in view of Eq. [4.8]. The hydrodynamic pressure (p) and hence the dewetting rate should increase when Π becomes more negative. At pH 9.5, the short-range hydrophobic force, which is two-orders of magnitude more negative than the long-range hydrophobic force, accelerates dewetting. The contact area, *i.e.*, the solid/liquid interface created after a bubble-surface interaction, is determined ultimately by the work of adhesion (or -ΔG), which is largely determined by the short-range hydrophobic force (Pan and Yoon, 2016).

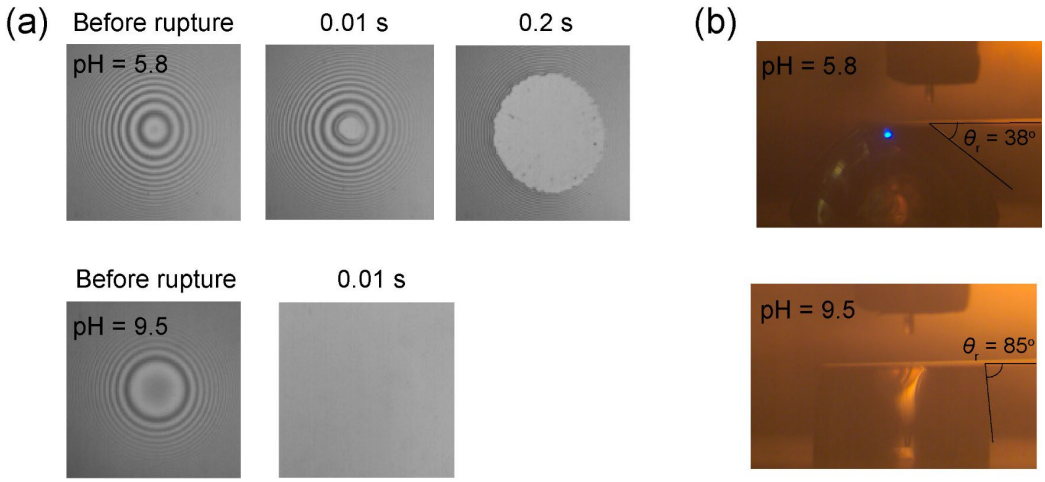

Figure 65. a. Fringes showing that different dewetting rate at pH 5.8 and pH 9.5; -b. Contact angles formed after the film rupture at pH 5.8 and pH 9.5.

Results and Discussion Effect of Addition of CTAB

A set of two FADS measurements are conducted with weakly hydrophobic silica (oxidized silicon cantilever) in the presence and absence of 10^{-6} M hexadecyltrimethylammonium bromide (CTAB) as a means of controlling ψ_2. The silica surfaces have been hydrophobized by immersing the cantilevers in a $3x10^{-5}$ M OTS solution for 30 min to obtain $\theta_r = 30^o$. The results are shown in Figure 66. The force curves obtained in pure water show the presence of a weak attractive force, which may be attributed to a long-range hydrophobic force with C_2 = -0.28 mN/m. Note that the surface force curve turns slightly upward, which can be attributed to the fact that ψ_1 = -40 mV and ψ_2 = -60 mV are of the same sign. Despite the weak surface force, the two surfaces jump into contact at h_{cr} = 81 nm and t_{cr} = 3.46 s.

The surface forces obtained in the presence of 10^{-6} M CTAB are much more attractive, which in turn causes the hydrodynamic force to increase and increases the kinetics of film thinning in accordance to Eqs. [4.8] and [4.9], respectively. The fast kinetics due to the surface force is manifested in changes in bubble profiles and a shorter critical rupture time (see Table 28). One can see that the curvature of the bubble increases significantly, resulting in a decrease in the capillary pressure. In effect, the stronger attractive force (or negative disjoining pressure) reduces the resistance to film thinning and increases the kinetics of bubble-particle interaction.

Table 28. Surface force parameters in the wetting films of water and 10-6 M CTAB solution formed on the OTS-coated silicon surface.

OTS Coating Time	Composition of Solution	θ_r (^{o})	ψ_1[1] (mV)	ψ_2[2] (mV)	κ^{-1} (nm)	C_2 (mN/m)	D_2 (nm)	γ (mN/m)	h_{cr} (nm)	t_{cr} (nm)
30 min	H_2O	30	-40	-60	45	-0.28	55	72	81	3.46
30 min	10^{-6} M CTAB	31	-30	70	70	-0.28	55	72	78	2.43

[1]Measured using Malvern ZetaSizer; [2]From Pan 2013.

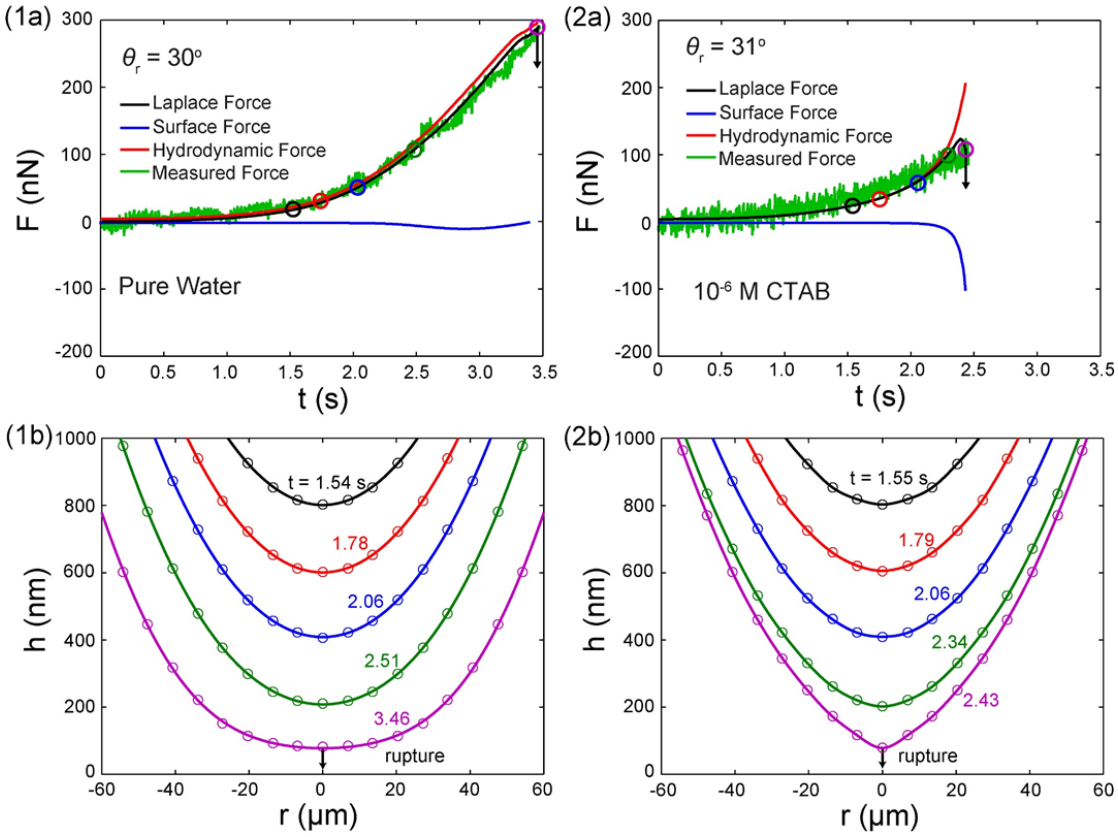

Figure 66. 1a. Force curves obtained for the interactions between an air bubble and an OTS-coated bare silicon surface in deionized water, -1b, corresponding spatiotemporal film profiles. -2a. Force curves obtained with 10^{-6} M CTAB solution, -2b, corresponding spatiotemporal film profiles.

Figure 67 shows the $\Pi(h)$ isotherms corresponding to the results presented in Figure 66 using the surface force parameters given in Table 28. The disjoining pressure due to van der Waals interaction (black) is repulsive. The red curve represents the disjoining pressure due to long-range hydrophobic force with C_2 = -0.28 mN/m, and D_2 = 55 nm. The contact angles do not change significantly with the 10^{-6} M CTAB concentration employed in the FADS measurement. It is assumed, therefore, that C_2 and D_2 remain the same as in pure water. It appears that CTAB cations prefers to be at the air/water interface and impart the bubble positively charged $\psi_2 = 70$ mV while keeping ψ_1 at -30 mV (see Table 28). Thus, the strong attractive surface force observed in the presence of CTAB is due to the double-layer force.

The results presented in this section may have a significant implication on flotation. One can control the ζ-potentials of both air bubbles and mineral particles to achieve high recoveries and selectivity. By analogy, for the HHS process, one may enhance the kinetics of oil-particle interactions and achieve high recoveries simply by controlling the ζ-potentials of oil drops and mineral particles. The attractive double layer force will greatly enhance the thinning of wetting film and simultaneously diminish the energy barrier (E_1) for oil-particle attachment. Usually, both n-alkane drops and mineral particles are negatively charged ($\psi_1 < 0$ and $\psi_2 < 0$) in water. Therefore, it may be of advantage to use positively charged oil drops to improve the separation efficiency. One possible way to obtain the positively charged oil drops is that form a monolayer coating at the oil/water interface by cationic surfactants, such as DAH and CTAB.

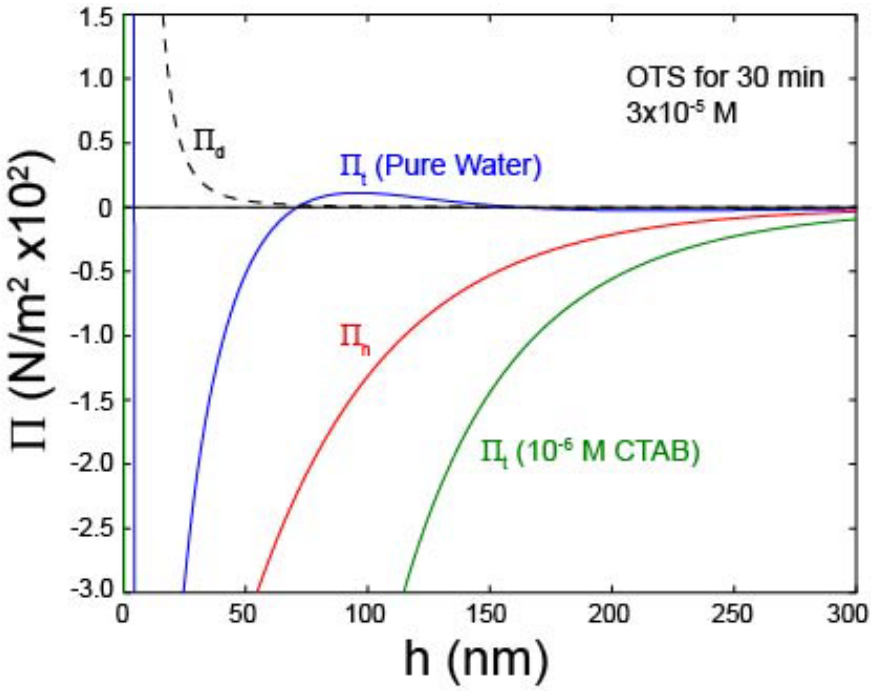

Figure 67. Disjoining pressure isotherms constructed for the wetting film of deionized water and 10^{-6} M CTAB solution confined between an OTS-coated silicon surface and an air bubble at natural pH using the surface chemistry parameters shown in Table 3. The red curve represents the disjoining pressure due to long-range hydrophobic force.

Influence of Dodecylamine Hydrochloride (DAH) Study

Introduction

When an air bubble (or an oil drop) approaches a mineral particle in water, the water film in between will drain due to the capillary pressure (p_c) created by the deformation of the air bubble (or oil drop). As the film thins to ~ 250 nm, the surface forces come into play and create a disjoining pressure (Π). The stability of the thin liquid film is critically dependent on Π. The film will rupture if $\Pi < 0$, indicating a successful flotation or two-liquid flotation. If $\Pi > 0$, however, the film will remain stable and nothing will happen.

The disjoining pressure (Π) is dictated by the surface forces, which includes van der Waals, electric double layer, and hydrophobic forces. In the flotation system, the hydrophobic force is the major contributor to destabilizing the wetting film and leading to a negative Π, while the double layer force is usually repulsive, i.e., stabilizing the wetting film, which is due to the fact that both bubbles and minerals are negatively charged in water. The repulsive double force creates an energy barrier (E_1) for bubble-particle interaction, which impedes the thinning of the wetting film. The research conducted during the current study mainly focuses on turning the double layer force into an attractive force so that the energy barrier is diminished and the wetting film thins faster.

In the present work, surface force measurements have been conducted using force apparatus for deformable surfaces (FADS) to study the interactions between a silica surface and an air bubble with the presence of dodecylamine hydrochloride (DAH). The electric double layer force depends on the ζ-potentials of air bubbles (ψ_2) and mineral surfaces (ψ_1), which are in turn controlled by adjusting the solution pH and DAH concentration. The results show that creating an attractive double layer force by using positively charged bubbles ($\psi_2 > 0$) will greatly benefit flotation kinetics and recoveries. By analogy, we consider that the same method may be applied in the HHS process to improve the recovery and grade of rare earth elements.

Theoretical Background

As has been mentioned in the foregoing section, a capillary pressure (p_c) is created in the liquid film due to the changes in the curvature of the bubble when an air bubble approaches to a flat mineral surface. The liquid film thins due the capillary pressure until it becomes equal to the disjoining pressure (Π), *i.e.*, $p_c = \Pi$, to form an equilibrium film thickness (h_e). If $p_c > \Pi$, the film will continue to thin and rupture at a critical thickness (h_c) at which $\Pi < 0$ to form a finite contact angle. Thus, the kinetics of film thinning during bubble-particle interaction is determined by the hydrodynamic pressure, or excess pressure (p),

$$p = p_c - \Pi \qquad [4.15]$$

Once p is known, one can predict the kinetics of film thinning using the Reynolds lubrication theory,

$$\frac{\partial h}{\partial t} = \frac{1}{12\mu r}\frac{\partial}{\partial r}\left(rh^3\frac{\partial p}{\partial r}\right) \qquad [4.16]$$

in which t is thinning time, μ the kinematic viscosity, and r the radial distance from film center. Integrating Eq. [4.2] under the boundary condition that $p_{r=\infty} = 0$ and $\partial p/\partial r|_{r=0} = 0$, one obtains,

$$p = 12\mu \int_{r=\infty}^{r} \frac{1}{rh^3} \left[\int_{r=0}^{r} r \frac{\partial h}{\partial t} dr \right] dr \qquad [4.17]$$

The capillary pressure of Eq. [4.15] can be calculated using the Young-Laplace equation,

$$p_c = \frac{2\gamma}{R} - \frac{\gamma}{r} \frac{\partial}{\partial r} \left(r \frac{\partial h}{\partial r} \right) \qquad [4.18]$$

where R is the bubble radius, while the disjoining pressure can be obtained using the DLVO theory extended to include the contribution from the hydrophobic force as follows:

$$\begin{aligned} \Pi &= \Pi_d + \Pi_e + \Pi_h \\ &= -\frac{A_{132}}{6\pi h^3} - \frac{\varepsilon\varepsilon_0 \kappa^2}{2\sinh(\kappa h)} \left[\left(\psi_1^2 + \psi_2^2 \right) \cos ech(\kappa h) - 2\psi_1 \psi_2 \coth(\kappa h) \right] \\ &+ \frac{C_1}{2\pi D_1} \exp\left(-\frac{h}{D_1} \right) + \frac{C_2}{2\pi D_2} \exp\left(-\frac{h}{D_2} \right) \end{aligned} \qquad [4.20]$$

In Eq. [4.20], Π_d, Π_e, and Π_h represent the disjoining pressures due to the van der Waals-dispersion force, double layer force, and hydrophobic force, respectively, and A_{132} is the Hamaker constant for the interaction between solid **1** and air bubble **2** in water **3**.

For the interaction between silica plate and air bubble studied in the present work, A_{132} = -1.2x10^{-20} J (Israelachvili, 2011). Since $A_{132} < 0$, Π_d is repulsive. The Π_e term of Eq. [4.18] represents the Hogg-Healey-Fuerstenau (HHF) approximation (Hogg *et al*., 1966), in which ε_0 is the permittivity of vacuum, ε is the dielectric constant of water, κ is the reciprocal Debye length, ψ_1 is the ζ-potential of the cantilever, ψ_2 is the same of the air bubble. Π_h is given as a double-exponential function, in which C_1 and C_2 represent the short- and long-range hydrophobic force constants, respectively, and D_1 and D_2 represent the corresponding decay lengths.

In the present work, a single bubble is brought to a flat surface from below in the same manner as in captive bubble method of contact angle measurement, while monitoring the changes in bubble curvature as a function of time. The curvature data may be used to determine the bubble-particle interaction force ($F(t)$) at time t by integrating Eq. [4.18] across the film as follows,

$$F(t) = 2\pi \int_0^{r_{\max}} p_c(r,t) r dr \qquad [4.21]$$

where $r_{\max}$ is the radius of the wetting film. Substituting Eq. [4.15] into Eq. [4.21], one obtains,

$$F(t) = 2\pi \int_0^{r_{\max}} \left[p(r,t) + \Pi(r,t) \right] r dr \qquad [4.22]$$

in which the first term on the right represents the hydrodynamic force and the second term represents the surface force that can be calculated using Eqs [4.17] and [4.20], respectively. In the present work, the first two components of Eq. [4.20], *i.e.*, Π_d and Π_e, have been calculated using the parameters, *e.g.*, A_{132} and ζ-potentials, that are readily available in the literature. The hydrophobic force component, *i.e.*, Π_h, is unknown. The approach taken here is to back-calculate it using Eq. [4.22] from the values of $F(t)$ determined using Eqs. [4.4] and [4.21]. The values of $F(t)$ determined in this manner represents the sum of all the forces operating during bubble-particle interaction. Some of the forces become negative at certain film thicknesses; therefore, $F(t)$ gives net interaction forces, which are also measured directly for comparison with the values calculated using Eq. [4.21].

Materials and Methods

The ultrapure water used in the present work was obtained from a Direct-Q water purification system (Millipore) with a resistance of 18.2 MΩ/cm. Sheets of silicon wafers were purchased from University Wafer, Boston, MA, with one side polished. Each sheet was cut into small strips of 15x3x0.05 mm in dimension for force measurement. The cantilevers were cleaned in hydrogen peroxide (H_2O_2, Fisher Scientific, 30-35%) and sulfuric acid (H_2SO_4, Spectrum Chemical, 98%). Dodecylamine hydrochloride (DAH, Sigma Aldrich) was used as received to hydrophobize the cantilever springs. Hydrochloric acid (HCl, Fisher Scientific) and sodium hydroxide (NaOH, Sigma Aldrich) were used for pH adjustment.

Apparatus and Procedure

The silicon cantilevers were cleaned by immersion in a mild piranha solution (H_2SO_4:H_2O_2 = 7:3 by volume) at 90°C for 1 minute, followed by rinsing with ultrapure water and drying in an ultrapure nitrogen gas stream. A layer of silicon dioxide free of organic contaminant forms as manifested by a zero water contact angle measured after the treatment. The majority of the force measurements were conducted using the hydrophilic silicon cantilevers, while in some cases the measurements were conducted after immersion in a $3x10^{-5}$ M OTS-in-toluene solution. The OTS-coated cantilevers were washed with chloroform and dried in an ultrapure nitrogen stream before use.

Figure 52 shows a schematic representation of the force apparatus for deformable surface (FADS), which has been designed to measure the surface forces in wetting films. A detailed description of the instrument has been made previously (Pan and Yoon, 2016, 2018). In a given FADS measurement, one end of a cantilever spring is fixed onto a translational stage by means of an adhesive, so that the cantilever can be moved in 3-directions (x, y, and z). Approximately 10 mL of an aqueous solution is delivered to the liquid cell from the open top. After the cell is filled, an air bubble is formed on the hydrophobic quartz plate located at the bottom of the cell by means of a syringe pump. The bubble size is controlled by control of air volume being injected.

Initially, the cantilever spring is lowered manually by means of the translational stage until the interference patterns (or Newton rings) begin to appear at $h \approx 10$ μm. From this point and onward, the film thickness is controlled by moving the bubble toward the underside of a cantilever by means of a piezo stage. The approach speed is set at 1,100 nm/s for all tests. During film thinning, the bubble continues to deform and generate Newton rings, which are recorded by means of a high-speed camera, while at the same time a fiber optic sensor is used to monitor the deflection of the cantilever spring. The recorded fringes are analyzed offline using the microinterferometric technique developed by Sheludko (1962) to construct spatiotemporal film profiles. By analyzing the film profiles using the equations presented in the next section, one can determine both the hydrodynamic and surface forces as a function of time (t) and film thickness (h). The forces measured from the curvature changes are then compared with those measured directly using the cantilever spring. The spring constant is determined *in-situ* against the forces determined by analyzing the spatiotemporal film profiles. Since direct force measurement is sensitive to vibration, the entire FADS instrument is placed on a vibration isolation platform (100BM-1, Minus K Technology), which in turn is placed on a Nexus optical table (T46H, Thorlabs).

Results and Discussion – Effect of pH

In the present work, a series of FADS measurements have been conducted at different pH *e.g.*, 3.0, 10.5 and 12.4 with the appearance of 10^{-5} M DAH to measure the hydrodynamic and surface forces in the wetting film, which is confined between an air bubble and the underside of a cantilever spring made from a thin silicon wafer. Since the cantilever has been treated in a mild piranha solution, its surface must be oxidized to a silica (SiO_2) film. The results may be compared with the classic work of Fuerstenau (1957), who showed that flotation recovery reaches a maximum at an alkaline pH where the cationic collector neutralizes the surface charge, which reduces the energy barrier for bubble-particle attachment. In this regard, FADS measurements have been conducted by varying the pH to better understand the role of ζ-potentials in bubble-particle interaction.

Figure 68 compares the results obtained at pH 3.0 and 10.5. The changes in Laplace forces (black) as calculated using Eq. [4.21] are in good agreement with those measured directly using the cantilever spring (green). The fluctuations in the latter show that direct force measurement is sensitive to vibration. The film profiles are color-coded, so that one can see how the interaction forces change with time (t), film thickness (h), and bubble curvature.

Also shown in Figure 68-1a are the hydrodynamic (red) and surface (blue) forces calculated by substituting Eqs. [4.17] and [4.20], respectively, into Eq. [4.22]. The surface force curve does not change until film thickness (h) is reduced to ~110 nm, where the net force becomes attractive enough to cause the film to rupture catastrophically at h_{cr} = 101 nm at the film center and at t_{cr} = 4.01 s, where h_{cr} and t_{cr} are the critical rupture thickness and time, respectively. The different types of forces plotted in Figure 68-1a are

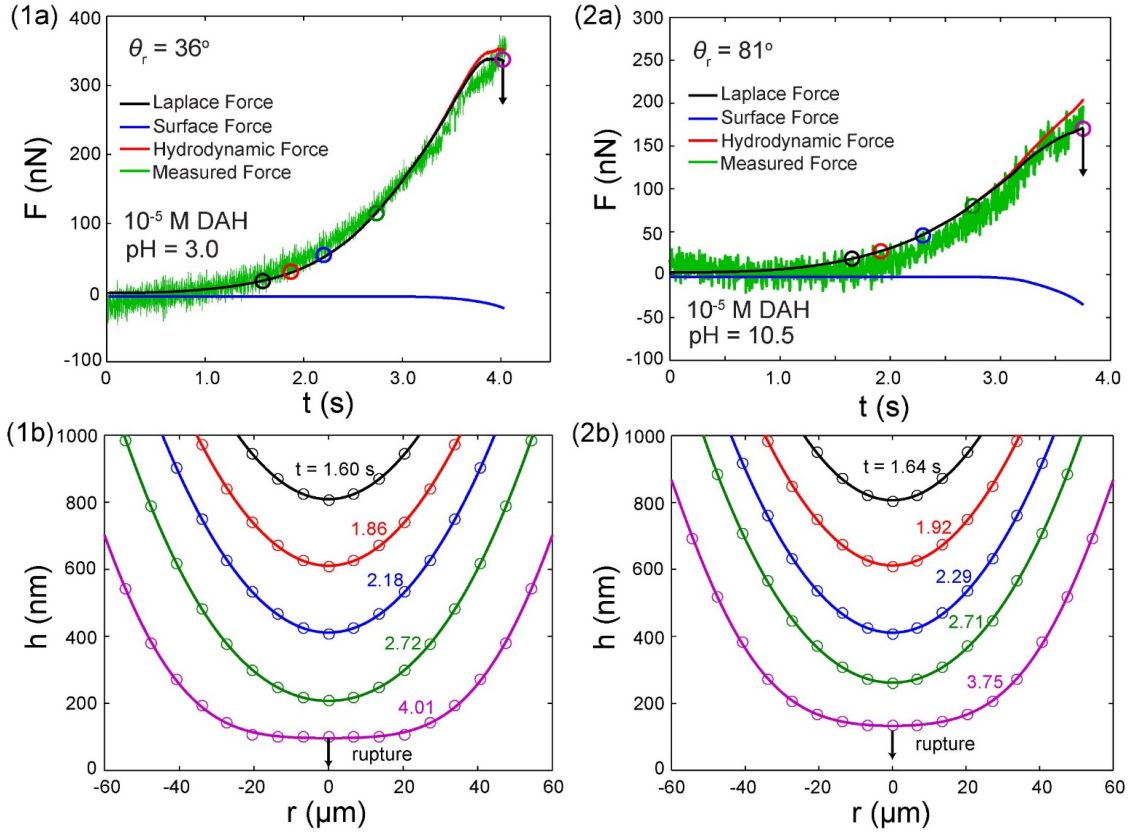

Figure 68. 1a. Forces measured in the wetting films of water formed on a silica surface at 10^{-5} M DAH and pH 3.0, -1b, corresponding film profiles; -2a. Force curves obtained at 10^{-5} M DAH and pH 10.5, -2b, corresponding film profiles.

additive as $p_c = p + \Pi$ (see Eq. [4.15]); therefore, the Laplace (or capillary) force may be referred to as the total (or net) interaction force. Note also that the different types of surface forces, *e.g.*, double-layer, van der Waals, and hydrophobic forces, are also additive. In these regards, the values of $F(t)$ obtained using Eqs. [4.21] and [4.22] should represent the total interaction force at time t.

Table 29 gives the surface force parameters used to obtain the various force curves obtained under different experimental conditions. The values of ψ_1 given in the table are the ζ-potentials of the glass spheres measured in the presence of 10^{-5} M DAH. The measurements have been conducted on glass spheres with d_{80} = 5 μm using the Malvern Zetasizer NanoZS. The ψ_2 values are from Yoon and Yordan (1986), while A_{132} = -1.2 x 10^{-20} J is from Israrelachivili (2011). The surface tension (γ) data for DAH solutions are from Finch and Smith (1973). The receding contact angles (θ_r) are from the images recorded during the FADS measurements using a side-view camera shown in Figure 52. At pH 3.0, 5.8 and 12.4, the values of θ_r are 36°, 38° and 0°, respectively. According to Churaev (1995), attractive hydrophobic forces appear at $\theta > 40°$; therefore, both C_1 and C_2 are considered to be zero at the pHs where contact angles are low. Also shown in Table 29 for comparison are the contact angles predicted using the Frumkin-Derjaguin isotherm. Most of the predictions are in good agreements with those measured except the one measured at pH 3.0. The discrepancy may be due to possible organic contamination of the silica surface or possible errors associated the ζ-potential measurements.

Figure 68-2a shows the results obtained at pH 10.5. The contact angles obtained at this pH are substantially higher than observed at pH 3.0 and 5.8 as shown in Table 29. Fuerstenau (1957) was the first to report the pH sensitivity of quartz flotation using DAA as collector. That the optimal flotation pH is close

Table 29. Effect of pH on the force parameters obtained from the FADS measurements conducted with silica surfaces at 10-5 M DAH.

pH	ψ_1* (mV)	ψ_2† (mV)	κ^{-1} (nm)	C_1 (mN/m)	D_1 (nm)	C_2 (mN/m)	D_2 (nm)	γ‡ (mN/m)
3.0	-10	48	10	0	-	0	-	70
5.8	-60	50	78	0	-	0	-	69
9.5	0	10	20	-350	2	-0.8	35	50
10.5	-30	2	14.5	-301	2	-0.5	30	44
12.4	-60	-30	14	0	-	0	-	70

pH	θ_r (°)		ΔG	h_{cr}	t_{cr}
	Meas'd	Calc'd	(mJ/m^2)	(nm)	(s)
3.0	36	11	-13.4	101	4.01
5.8	38	37	-14.8	116	2.56
9.5	85	85	-45.6	140	2.95
10.5	81	81	-37.1	135	3.75
12.4	0	-	0.0	-	-

* Measured using Malvern ZetaSizer; †From Yoon and Yordan, 1986; ‡From Finch and Smith, 1973.

to the pKa (= 10.1) of the collector, where the concentrations of the RNH_3^+ and RNH_2 species are equal and maximum, led to the co-adsorption mechanism that is conducive to the formation of close-packed monolayers that is required to achieve high contact angles (Somasundaran and Ananthapadmanabhan, 1979).

The wetting film formed at pH 12.4 in the presence of 10^{-5} M DAH is found to be stable and does not rupture, as shown in Figure 69. The stability is due to the fact that the silica (SiO_2) surface is hydrophilic with $\theta_r = 0$. Fuerstenau (1957) showed that contact angle drops precipitously at pH > 11.6, reaching zero by the time the pH is raised to 12.6. At this point, collector adsorption and flotation recovery become zero also. Under these conditions, the hydrophobic force component of the disjoining pressure (Π_h) should be zero. Therefore, the total disjoining pressure (Π) should be the sum of the dispersion (Π_d) and electrostatic force (Π_e) components (see Eq. [4.20]). The former is always positive as A_{132} is negative, and the latter is also positive as both ψ_1 and ψ_2 are negative at pH 12.4 (see Table 29). Thus, the surface forces should be repulsive, which explains why flotation is not possible.

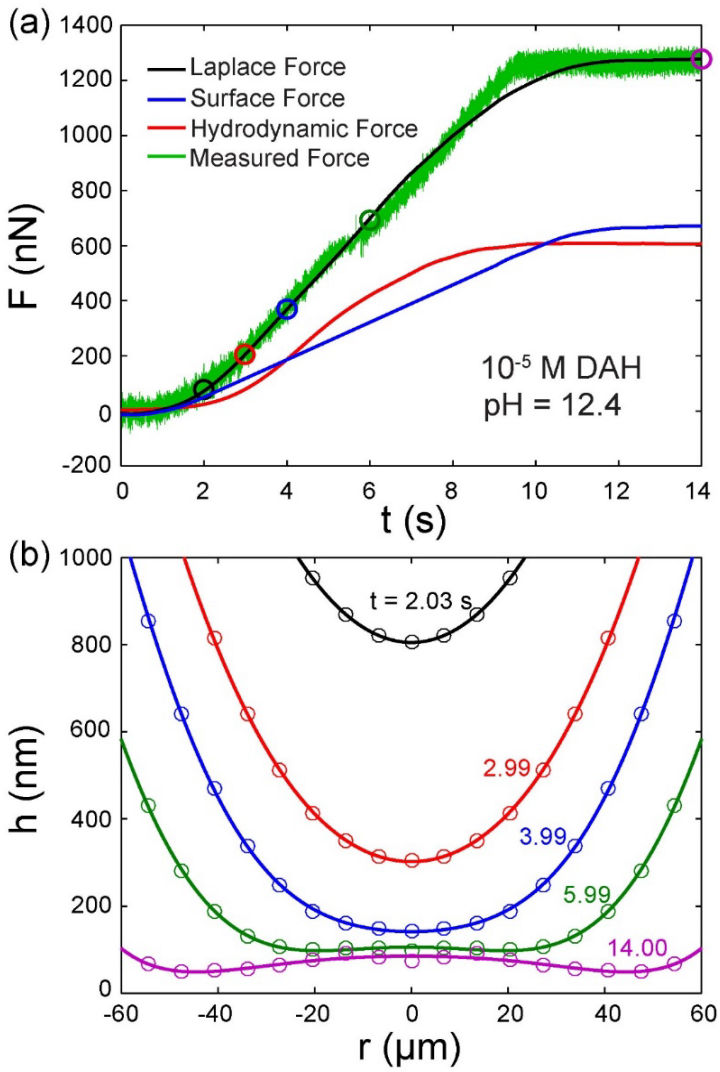

Figure 69. a. Forces measured in the wetting films on a silica surface at 10^{-5} M DAH and pH 12.4; -b, corresponding film profiles. The repulsive surface force is responsible for the slow film thinning kinetics and the dimple formation.

According to Eq. [4.22], the total interaction force as measured by using Eq. [4.21] should be the sum of the hydrodynamic (red) and surface (blue) forces. The force curves plotted in Figure 69-a show that these two forces are about equal. Because of the positive disjoining pressure, the kinetics of film thinning is slow. As shown in the spatiotemporal film profiles, it takes 14 s for the film to form a dimpled film. Dimples form when a film thins much slower at the center than at the barrier rim. Dimpled films are opposite to the pimpled (or elliptical) films observed when the kinetics of film thinning is fast due to the attractive double-layer force created by the ζ-potentials of bubble and silica surfaces that are of opposite sign (see Figure 66).

The disjoining pressure isotherms drawn in Figure 70 show that $\Pi(h) > 0$ at pH 12.4 for the reasons discussed in the forgoing paragraph; therefore, no contact angle is formed at this pH. At pH 3.0, $\Pi(h)$ remains zero at $h > 90$ nm but becomes negative below this distance due to the weak double-layer force. The double-layer force is attractive because ψ_2 becomes positive due to the adsorption of the RNH_3^+ ions at the air/water interface. However, the RNH_3^+ ions do not adsorb on the silica surface because the concentration of the RNH_2 species are too low to warrant co-adsorption. A net result is that silica surface remains negatively charged at -10 mV while air bubble is positively charged at 48 mV. Nevertheless, the double-layer force created under these conditions is weak and becomes discernable only at short range. At pH 5.8, however, ψ_1 becomes -60 mV due to the adsorption of OH^- ions while ψ_2 becomes a little more positive (50 mV) than at pH 3.0. As a consequence, the double-layer force becomes stronger and longer-ranged than at pH 3.0 as shown in Figure 70. The $\Pi(h)$ isotherms obtained at pH 9.5 and 10.5 are also strong and longer-ranged than at pH 3.0. However, they are not as long-ranged as at pH 5.8, which may be surprising and deserve an explanation.

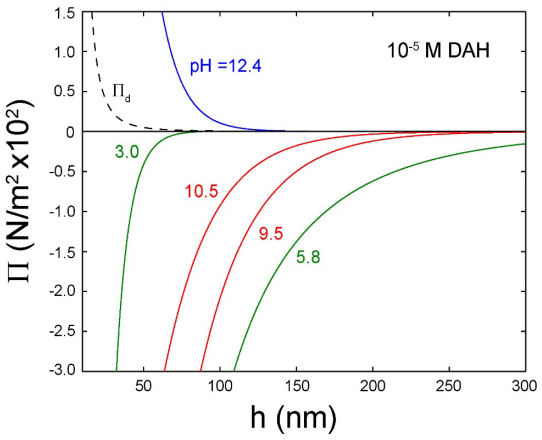

Figure 70. Disjoining pressure isotherms for the wetting films of water formed on silica surfaces at 10^{-5} M DAH and varying pH. The negative disjoining pressures observed at pH 3.0 and 5.8 are due to attractive double-layer forces (green), while those at pH 9.5 and 10.5 are due to hydrophobic forces (red).

The results of the FADS measurements presented hitherto are summarized in Figure 71 for comparison with those reported by Fuerstenau (1957). As pH increases, RNH_3^+ ions adsorb on silica, whose point of zero charge (pzc) is pH 2 (Parks, 1968; Yoon *et. al.*, 1979), *via* columbic attraction and cause θ_r to increase to some extent. Due to the low adsorption density, ψ_1 is largely unaffected and becomes more negative at a higher pH due to the increased adsorption of OH^- ions. On the other hand, the RNH_3^+ ions adsorb more readily on air bubbles and reverse the sign of ψ_2 from negative in pristine water to positive. Thus, wetting films rupture *via* a macroscopic double-layer interaction under these conditions. A maximum

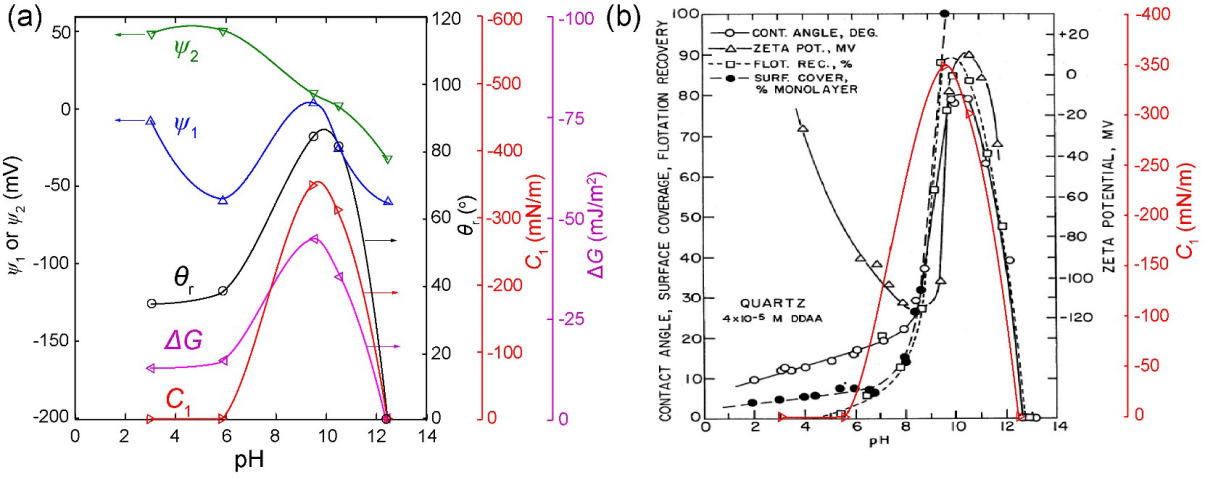

Figure 71. a. Surface force parameters, free energies and contact angles obtained in the present work as a function of pH at 10^{-5} M DAH; -b. A correlation between the short-range hydrophobic force constant (C_1) and the work of Fuerstenau (1957) for quartz flotation at $4x10^{-5}$ M dodecyl ammonium acetate.

receding contact angle (θ_r) of 85° is obtained at pH 9.5, where a strong hydrophobic force has been measured using the FADS. Its long-range hydrophobic component with D_2 = 35 nm is responsible for film thinning and rupture, while its short-range component is responsible for accelerating de-wetting after the rupture and thereby creating a large solid/air interfacial area for a strong bubble-surface attachment. The short-range hydrophobic interaction accounts for most of the free energy change ($\Delta G < 0$) associated with the bubble-surface interaction. At pH 9.5, RNH_3^+ and RNH_2 species co-adsorb on silica, causing the surface charge to be neutralized with ψ_1 = 0 mV, which is conducive to achieving a high bubble-surface attachment kinetics by minimizing the energy barrier. At pH 12.4, the RNH_3^+ ions dissociate further to form phase-separated amines (RNH_2(s)) and thereby deplete the collector from solution.

The FADS data obtained in the present work corroborate well with the work of Fuerstenau (1957). Analysis of the force data suggests that air bubbles can attach to silica surface *via* macroscopic double-layer interactions at pH below 6 and *via* macroscopic hydrophobic interactions at alkaline pH. The latter may be a more desirable mode of bubble-particle interaction in flotation, which can be brought about by formation of a close-packed monolayer.

Results and Discussion – Effect of DAH Concentration

FADS measurements were also conducted by varying DAH concentrations in the range of 10^{-6}-10^{-4} M at the natural pH (≈ 5.7-5.8). The results obtained at 10^{-5} M DAH have already been shown in a prior section, while those obtained at 10^{-6} and 10^{-4} M are compared in Figure 72. The surface forces measured at 10^{-6} and 10^{-5} M DAH are both attractive due to double-layer forces. No hydrophobic forces are considered because contact angles measured at these concentrations are less than 40° (see Table 30). It appears that the surface force measured at 10^{-5} M is a little more attractive. However, the values of h_{cr} are the same.

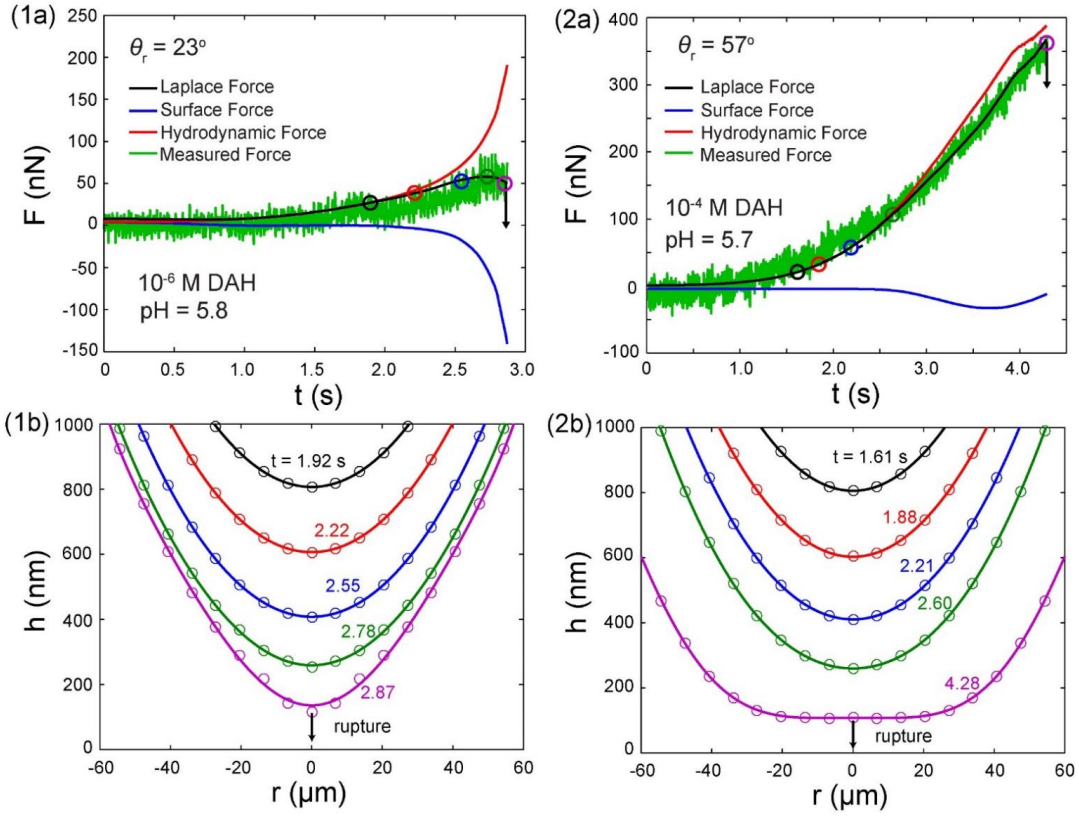

Figure 72. 1a. Force curves obtained for the interactions between an air bubble and a silica surface at 10^{-6} M DAH and pH 5.8, -1b, corresponding spatiotemporal film profiles; -2a. Force curves obtained at 10^{-4} M DAH and pH 5.7, -2b, corresponding film profiles.

The forces measured at 10^{-4} M DAH are quite different. The major difference is the high contact angle of 57°, which according to Churaev (1995) would make it necessary to consider the contribution from Π_h to the total disjoining pressure (Π) of the film (see Eq. [4.20]). Note, however, that the surface force curve (blue) shown in Figure 72-2a is flatter than at 10^{-6} and 10^{-5} M DAH, indicating that Π is less negative. The weakly attractive surface force observed at 10^{-4} M causes h_{cr} to decrease and t_{cr} to increase as shown in Table 30. The weakly attractive surface force is due to the repulsive double-layer force becoming stronger as the film thins further at t > ~3.6. The double-layer force is positive because both ψ_1 and ψ_2 are positive at 10^{-4} M DAH. It appears that RNH_3^+ ions prefer the air/water interface to the silica/water interface at this pH, which may be attributed to the lack of the co-adsorption mechanism at pH 5.7.

Appearance of the weak attractive force discussed above refers to the long-range forces that control film thinning and rupture. The weak long-range hydrophobic force is represented by C_2 (= -0.16 mN/m). Note, however, that the short-range hydrophobic force is strong as represented by C_1 = -234 mN/m. The strong short-range force should also contribute to the kinetics of bubble-surface interaction as discussed in the preceding section.

Using the surface force parameters given in Table 30, the $\Pi(h)$ isotherms obtained at different DAH concentrations have been constructed as shown in Figure 73. At 10^{-5} and 10^{-6} M DAH, disjoining pressures are negative due to the long-range double-layer forces, which is conducive to film thinning and contact angle formation. At 10^{-4} M, Π becomes increasingly negative initially due to the weak long-range hydrophobic force with C_2 = -0.16 mN/m as discussed above. As the film thins further, Π becomes positive due to the appearance of a strong repulsive double-layer force, leading to the formation of a 'secondary minimum' shown as an inset. Although the film ruptures at h_{cr} = 110 nm, which is close to the lower end of the secondary minimum, the kinetics of film thinning is slower than at the lower DAH concentrations due to the presence of the repulsive double-layer force in the wetting film.

Table 30. Effect of DAH concentration on surface force parameters for the wetting films formed on silica surfaces at pH 5.7-5.8

DAH (M)	ψ_1 (mV)	ψ_2‡ (mV)	κ^{-1} (nm)	C_1 (mN/m)	D_1 (nm)	C_2 (mN/m)	D_2 (nm)	γ (mN/m)
10^{-6}	-50*	31	85	0	-	0	-	71
10^{-5}	-60*	50	78	0	-	0	-	69
10^{-4}	40†	60	26	-234	2	-0.16	50	64

DAH	θ_r (°)		ΔG	h_{cr}	t_{cr}
(M)	Meas'd	Calc'd	(mJ/m^2)	(nm)	(s)
10^{-6}	23	20	-5.64	116	2.87
10^{-5}	38	37	-14.8	116	2.56
10^{-4}	57	57	-29.1	110	4.28

A_{132} = 1.2x10^{-20} J; *Measured using Malvern Zetasizer NanoZS; †From Rutland et al., 1992; ‡Estimated from Yoon and Yordan, 1986.

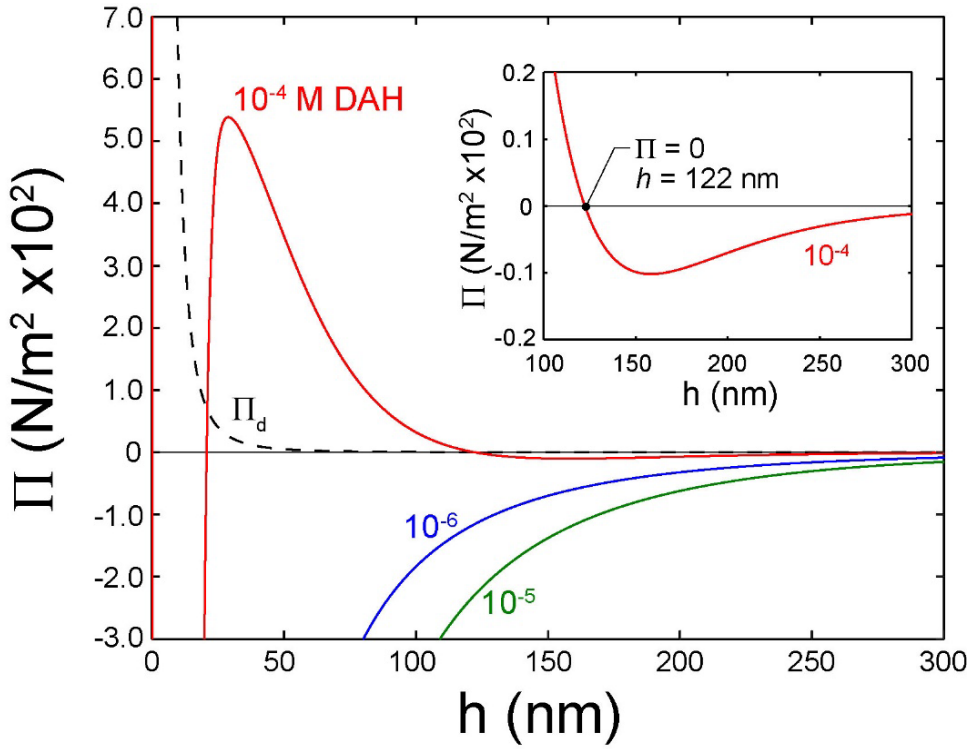

Figure 73. Disjoining pressure isotherms obtained for the wetting film of water formed on silica surfaces at 10^{-6}, 10^{-5}, and 10^{-4} M DAH and the natural pH (5.7-5.8). The negative disjoining pressures observed at 10^{-6} and 10^{-5} M are due to attractive double-layer forces. At 10^{-4} M, a strong repulsive double-layer force appears due to the charge reversal of the silica surface, causing Π to increase but still creates a secondary minimum, as shown at the inset, due to the presence of a strong hydrophobic force created by DAH adsorption.

The findings presented in this task may have a significant implication on flotation. It is of benefit to control the ζ-potentials of both air bubbles and mineral particles to improve the flotation kinetics and efficiency. Analogically, one may also apply the same idea to achieve high recoveries in the HHS process by controlling the ζ-potentials of oil drops and mineral particles. Both mineral particles and oil drops are negatively charged ($\psi_1 < 0$ and $\psi_2 < 0$) in water during the HHS process. Thus, it will be good to use positively charged oil drops ($\psi_2 > 0$) to create an attractive double layer force, which will greatly enhance the thinning of wetting film and simultaneously diminish the energy barrier (E_1) for oil-particle attachment. One simple way to obtain the positively charged oil drops is that form a monolayer coating at the oil/water interface by adding small amount of cationic surfactants, such as primary amines (DAH) and quaternary ammonium cations (cetrimonium bromide, CTAB).

Cationic Surfactant Study

Introduction

The results presented in the prior section showed the advantage of reversing the charge of air bubbles in flotation. By analogy, one can also reverse the charge of oil drops to improve the kinetics of drop-surface interactions and thereby improve the HHS process. During the current study, we have used a cationic surfactant, *i.e.*, alkyltrimethylammonium chloride (C_nTACl), to render an air bubble positively charged and brought it to the vicinity of a hydrophobic surface that is negatively charged. It is possible that the attractive double-layer force between the oppositely charged surfaces may reduce the disjoining pressure (Π) beyond what can be reduced by the hydrophobic force alone and thereby expedite the process of film thinning, rupture, and contact angle formation. In principle, a thin liquid film (TLF) rupture when $\Pi < 0$, which is a prerequisite for contact angle formation.

Theoretical Background

Pressure Balance in a Thin Liquid Film: When an air bubble approaches a flat surface in water, a TLF, also known as wetting (or flotation) film, is formed in between. The curvature changes associated with conforming to the flat geometry creates an excess (or capillary) pressure (p_c) in the film, causing it to thin. As the thinning continues to a film thickness (h) of ~250 nm, surface forces begin to play a role. If they are repulsive, a positive disjoining pressure ($\Pi > 0$) is created and opposes film thinning. The thinning stops at an equilibrium thickness (h_e), at which $p_c = \Pi$. If the disjoining pressure is lower than the capillary pressure ($\Pi < p_c$), the film thins further and ruptures at a critical thickness (h_c), where the disjoining pressure becomes negative ($\Pi < 0$), forming a finite contact angle (θ).

Thus, p_c serves as the driving force for film thinning, while Π offers a resistance by definition. In this regard, one may write a pressure balance in the direction perpendicular to the film as follows,

$$p = p_c - \Pi \qquad [4.23]$$

in which p represents the excess pressure that drives film thinning. The rate of film thinning can be predicted using the Reynolds equation,

$$\frac{\partial h}{\partial t} = \frac{1}{12\mu r}\frac{\partial}{\partial r}\left(rh^3 \frac{\partial p}{\partial r} \right) \qquad [4.24]$$

in which μ is the dynamic viscosity of water and r is the radial distance from the film center. Integrating Eq. [4.24] twice under the boundary conditions that $p_{r=\infty} = 0$ and $\partial p/\partial r|_{r=0} = 0$, one obtains p as follows,

$$p = 12\mu \int_{r=\infty}^{r} \frac{1}{rh^3}\left[\int_{r=0}^{r} r\frac{\partial h}{\partial t} dr \right] dr \qquad [4.25]$$

Integrating Eq. [4.25] over the cross-sectional area of the film gives the force pressing the film.

When a sphere of radius R_p moves slowly in an unbounded viscous liquid, one can use the Stokes' law to calculate the hydrodynamic resistance force ($F_r = 6\pi\mu R_p U$). If the sphere approaches a free surface, *e.g.*, air/water interface, in close proximity, it is necessary to make an appropriate correction as follows,

$$F_r = 6\pi\mu R_p U\beta \quad [4.26]$$

in which U is the particle velocity and β is the correction factor. It has been shown that $\beta \approx R_p/h$, and that the dimensionless correction factor increases sharply at $h < 0.1R_p$ (Brenner, 1961; Mongruel *et al*, 2010). Marston *et al*. (2010) verified Eq. [4.26] by monitoring the motion of a solid sphere in a thin viscous liquid film using an interferometry method. It has been shown also that the lubrication force predicted by Brenner (1961) for a sphere approaching a flat free film is the same as predicted using the Reynolds equation. In this regard, the hydrodynamic pressure given in Eq. [4.25] serves dual roles: i) a driving force away from a surface, and ii) a force resisting to film thinning in close proximity. The latter is the consequence of the fact that p varies as h^{-4} as shown in Eq. [4.25].

Force Measurement: An objective of the present work is to measure the surface forces in wetting films to find ways to improve the bubble-particle attachment and contact angle formation in flotation. To this end, an air bubble is slowly brought to a surface within the distance range where surface forces can cause the bubble to deform. By monitoring the bubble deformation, one can determine the capillary pressure (p_c) using the Young-Laplace equation,

$$p_c = \frac{2\gamma}{R} - \frac{\gamma}{r}\frac{\partial}{\partial r}\left(r\frac{\partial h}{\partial r}\right) \quad [4.27]$$

in which γ is the surface tension of water, and R is the bubble radius. The first term on the right represents the macroscopic capillary pressure, while the second term represents the effects of local curvature changes.

Integrating Eq. [4.27] across a TLF formed at time t will give the force ($F(t)$) exerted on the bubble,

$$F(t) = 2\pi\int_0^{r_{\max}} p_c(r,t)\,r\,dr \quad [4.28]$$

Substituting Eq. [4.23] into Eq. [4.28], one obtains,

$$F(t) = 2\pi\int_0^{r_{\max}} \left[p(r,t) + \Pi(r,t)\right] r\,dr \quad [4.29]$$

The first term on the right of Eq. [4.29] gives the hydrodynamic force, while the second term gives the information on disjoining pressure (Π) (or surface forces).

Mineral flotation is based on controlling the hydrophobicity of minerals to be selectively collected by air bubbles. Therefore, it would be reasonable to use the extended DLVO theory,

$$\Pi = \Pi_d + \Pi_e + \Pi_h$$
$$= -\frac{A_{132}}{6\pi h^3} - \frac{\varepsilon\varepsilon_0\kappa^2}{2\sinh(\kappa h)}\left[\left(\psi_1^2 + \psi_2^2\right)\cos ech(\kappa h) - 2\psi_1\psi_2\coth(\kappa h)\right] \quad [4.30]$$
$$+ \frac{C_1}{2\pi D_1}\exp\left(-\frac{h}{D_2}\right) + \frac{C_2}{2\pi D_2}\exp\left(-\frac{h}{D_2}\right)$$

which includes contributions to Π from the hydrophobic force (Π_h) in addition to those from the van der-Waals (Π_d) and electrical double-layer (Π_e) forces; A_{132} is the Hamaker constant for the interaction between solid **1** and air **2** in water **3**. In wetting films, $A_{132} < 0$, indicating that the water molecules adsorbed on mineral surfaces by the omnipresent van der Waals force cannot be removed by air bubbles. Π_e can be readily predicted using the Hogg-Healey-Fuerstenau approximation (Hogg *et al*., 1966), in which ε_0 is the permittivity of vacuum, ε the dielectric constant of water, κ the reciprocal Debye length, ψ_1 the double-layer potential of the solid surface, and ψ_2 is the same of the air bubble. The values of ψ_1 and ψ_2 are usually substituted by the ζ-potentials that can be readily measured in laboratory experiments.

The hydrophobic disjoining pressure is given as a double-exponential function, in which C_1 and C_2 represent the magnitudes of the short- and long-range hydrophobic forces, respectively, while D_1 and D_2 represent the corresponding decay lengths. One can readily determine the values of C_2 and D_2 by subtracting the hydrodynamic force and two known surface forces, *i.e*., van der Waals and double-layer forces, from the capillary forces the curvature changes using Eq. [4.28]. The values of C_1 and D_1 can be determined from contact angles using the Frumkin-Derjaguin isotherm (Pan and Yoon, 2016). In the present work, however, only the values of C_2 and D_2 have been determined, since the force measurements were conducted in the presence of the reagents that do not significantly affect the short-range hydrophobic forces. The forces measured using air bubble as a sensor have been compared with those measured directly using cantilever springs.

Materials

A Direct-Q water purification system was used to obtain batches of deionized water with a resistance of 18.2 MΩ/cm. Silicon cantilever springs for direct force measurements were fabricated from sheets of silicon wafers purchased from University Wafer, Inc., Boston, MA, with single sides polished. Each cantilever had a dimension of 15x3x0.05 mm. Hydrogen peroxide (H_2O_2, Fisher Scientific, 30-35%) and sulfuric acid (H_2SO_4, Spectrum Chemical, 98%) were used to clean each cantilever before force measurement. n-Dodecyltrimethylammonium chloride (C_{12}TACl), n-tetradecyltrimethylammonium chloride (C_{14}TACl), hexadecyltrimethylammonium chloride (C_{16}TACl), and trimethylstearylammonium chloride (C_{18}TACl) were purchased from TCI America, Inc., which were of >97% purity and used as-received without further purification. In some force measurements, the octadecyltrichlorosilane (OTS, Acros Organics)-in-toluene and methyltrichlorosilane (MTCS, Sigma Aldrich)-in-toluene solutions were used to hydrophobize the cleaned cantilevers. All glassware was cleaned in a saturated potassium hydroxide in 2-propanol solution overnight, rinsed with the distilled water and deionized water, and dried in a laminar fume hood.

Surface Force Measurement

The cantilever springs were cleaned by immersing them in a piranha solution (H_2SO_4:H_2O_2 = 7:3 by volume) for 2 min, followed by rinsing with deionized water and drying in a high-purity N_2 gas stream. After the cleaning step, a layer of silicon dioxide (SiO_2) free of organic contaminants was formed as manifested by a zero water contact angle. The freshly cleaned cantilevers with $\theta = 0$ were then used in the force measurements. In some experiments, the cleaned cantilevers were hydrophobized by immersing them in freshly prepared MTCS-in-toluene or OTS-in-toluene solutions to obtain a receding angle (θ_r) of 40~70°.

In the present work, the force apparatus for deformable surfaces (FADS) was used to measure the surface forces and film profiles. Figure 52 shows a schematic representation of the instrument, which was designed to measure the changes in the capillary, hydrodynamic, and surface forces during bubble-flat surface interactions (Pan *et al*., 2011; Pan and Yoon, 2016). The force measurements were conducted in a liquid cell, in which one end of a cantilever spring was fixed on a translational stage by means of an adhesive, while an air bubble was making a contact with the undersurface of the spring at the other and. The bubble of ~2 mm diameter was formed on a hydrophobic quartz plate located on a Piezo stage. After adjusting the relative positions of the bubble and the spring by means of a translational stage in *x*-, *y*-, and *z*-directions, the Piezo stage was actuated to move the bubble upward at an approach speed of 10-10,000 nm/s. As the bubble changes its curvature during the interaction, a series of optical fringes generated by a monochromatic blue light (λ = 480 nm) were recorded by means of a high-speed camera. While the fringes were being recorded, a fiber optic sensor based on Fabry-Pérot interferometry was used to monitor the spring deflection, and a side-view camera was used to record the images of the bubble to measure dynamic contact angles. The entire FADS unit was placed on a vibration isolation platform (100BM-1, Minus K Technology), which in turn was placed on a Nexus optical table (T46H, Thorlabs).

The optical fringes recorded during the measurement were analyzed using the microinterferometry technique developed by Sheludko (1962) to reconstruct the spatiotemporal film profiles. Analysis of the film profiles using the Matlab gave the parameters, *i.e*., $\partial h/\partial t$ and $\partial h/\partial r$ of Eqs. [4.3] and [4.5], to determine the hydrodynamic and capillary forces, respectively. According to Exerowa and Kruglyakov (1997), the sensitivity limit of the interferometry technique is 0.2 nm, which gives a force sensitivity of $\sim 10^{-11}$ *N* if one considers the bubble as a spring a force spring with a 72 mN/m spring constant. The sensitivity of the cantilever spring used in the present work was $\sim 10^{-9}$ N as measured using an air bubble as a force sensor.

Induction Time Measurement

Figure 74 shows the experimental setup put together to determine the induction time for bubble-surface attachment. It consists of a glass capillary tubing attached to a linear D.C. motor (LVCA-051-051-01, Moticont) controlled by a motion controller (100-1-SRVO, Moticont). In each experiment, a single air bubble of ~2 mm radius was formed at the end of the tubing before it was brought down to a 12x12 mm silicon wafer (coated with an SiO_2 film formed on the surface by oxidation), stayed in contact with the surface for a present period of time, and subsequently retracted while monitoring the bubble-surface

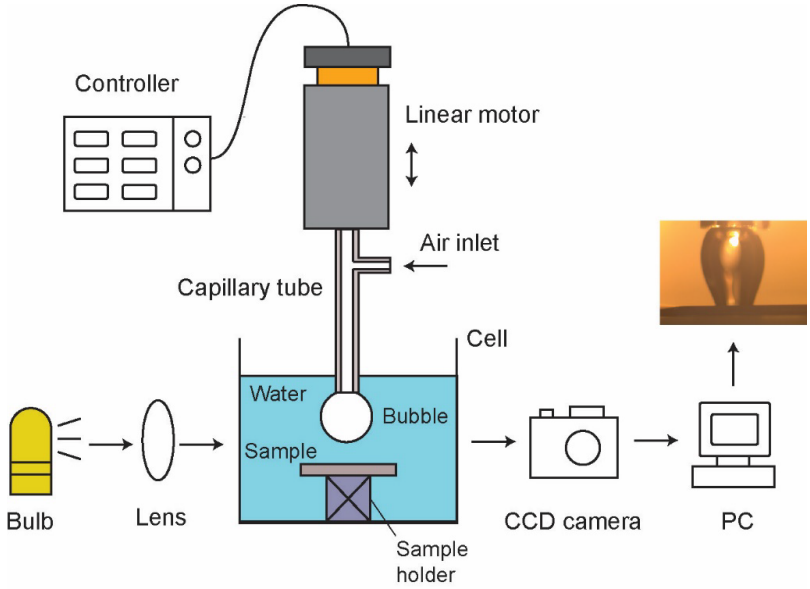

Figure 74. A schematic representation of the experiment set-up for the induction time measurement.

attachment and measuring receding contact angle (θ_r) by means of a high-speed CCD camera. Both the approach and retracting speed were set at 200 cm/s. The induction time was defined as the minimum contact time at which 5 out of 10 contacts as a minimum resulted in successful bubble-surface attachments.

Results and Discussion – Effect of Approach Speed

Figure 75 shows the results of the surface force measurements conducted with OTS-coated silica surfaces with $\theta_r = 70^o$. The silica surfaces were actually the undersurfaces of cantilever springs made from silicon wafers. In each experiment, the air bubble approached the flat silica surface at three different approach speeds, *i.e.*, 100, 1,000, and 3,000 nm/s. Long-range hydrophobic force was observed in all three FADS tests in pure water. The results obtained at low approaching speed (100 nm/s) are shown in Figure 75-1a,b. The hydrodynamic force (red) was calculated using Eqs. [4.24] and [4.29]. The surface force curve (blue) was calculated using Eqs. [4.29] and [4.30]. The Laplace force (black) was the sum of surface force and hydrodynamic force, which agreed well with the force measured directly using a cantilever spring (green). The hydrophobic force constant and its decay length were -1.1 mN/m and 65 nm, respectively, which were determined using the method mentioned in the theory session. The corresponding spatiotemporal film profiles for 100 nm/s approaching speed were shown in Figure 3-1b. The air bubble deformed significantly at the film thickness (h) below 300 nm. A sharp pimple formed due to the strongly attractive hydrophobic force before the film ruptured at a critical film thickness $h_c = 138$ nm.

The two columns on the right in Figure 75 show the results obtained at 1000 and 3000 nm/s approach speed, respectively. At higher approaching speeds, the film thinning becomes much faster as manifested by a shorter critical rupture time (t_c). The magnitude of hydrodynamic force increases significantly as the approach speed increases, which is consistent with Eq. [4.25] showing that hydrodynamic pressure (p) will increase if the approach speed increases ($\partial h/\partial t$). The surface force constants are determined to be the same as those in the first figure, which should be due to that surface force constants are chemical properties that are independent of hydrodynamic conditions. Because the Laplace force is the sum of surface and hydrodynamic forces (Eq. [4.29]), it should also increase with the approach speed, which agrees well with the force curves shown in Figure 75. A large Laplace force indicates

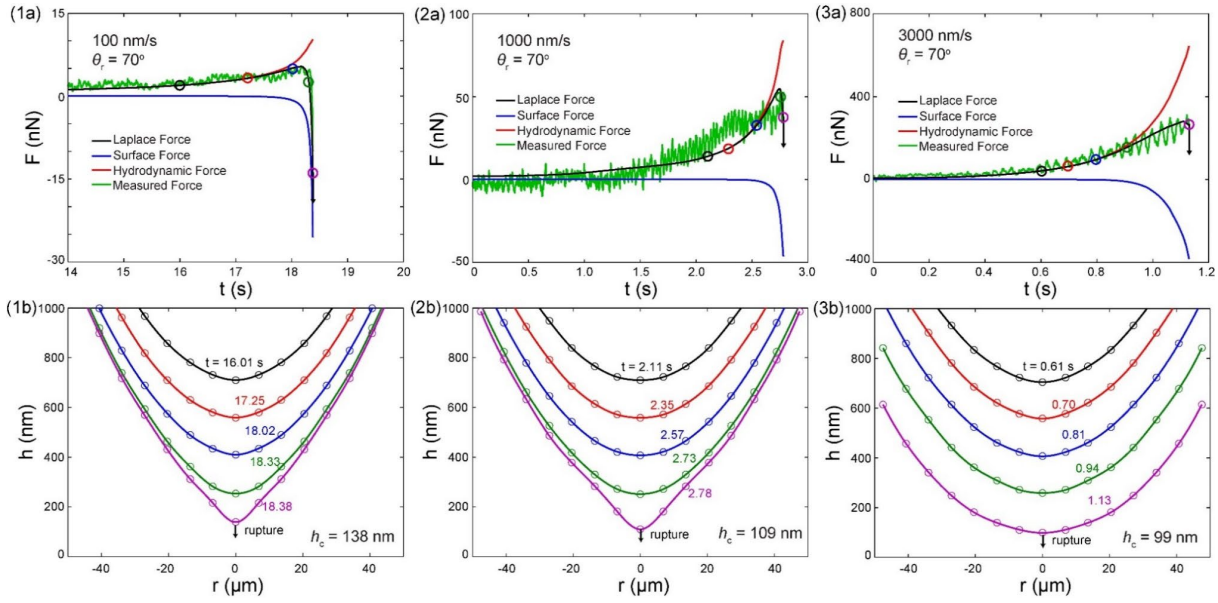

Figure 75. Force curves and spatiotemporal film profiles obtained in the wetting film of water confined between an air bubble and an OTS-coated silica surface with $\vartheta_r = 70^o$ at varied approaching speed, i.e., 100, 1000, and 3000 nm/s. The surface force curves can be fitted using the parameters: $A_{132} = -1.2x10^{-20}$ J, $\psi_1 = -60$ mV, $\psi_2 = -52$ mV, $\kappa^{-1} = 72$ nm, $C_2 = -1.1$ mN/m, and $D_2 = 65$ nm.

a large capillary pressure (p_c). As shown in Eq. [4.27], p_c will decrease if the local curvature change increases, which is the case of forming a sharp pimple as shown in Figure 75-1b,2b. However, a large p_c will be obtained if local curvature change is small, which corresponds to the spatiotemporal film profiles shown in Figure 3-3b. Therefore, to clearly observe the bubble deformation due to the surface forces, it is essential to use a low approach speed in the force measurement.

Results and Discussion – Effect of Adding C_nTACl

A series of FADS measurement have been conducted to study the surface forces in the wetting film between a flat silica surface and an air bubble in the presence of dilute cationic surfactant, i.e., 10^{-6} M alkyltrimethylammonium chloride (C_nTACl), where n = 12, 14, 16, and 18. Since the concentration of surfactant is low, the surface tension (γ) of the C_nTACl solutions is assumed to be the same as the surface tension of pure water (Bergeron, 1997; Zhang et al., 2005).

Figure 76 shows the spatiotemporal film profiles between a hydrophilic silica surface and an air bubble in the presence of 10^{-6} M (a) $C_{12}TACl$, (b) $C_{14}TACl$, (c) $C_{16}TACl$, and (d) $C_{18}TACl$. As shown, the wetting films all ruptured quickly with the addition of a dilute solution of cationic surfactant, although the surface was hydrophilic. The critical rupture time (t_c) for these four surfactants are 3.42, 2.75, 2.67 and 2.59 s, respectively, indicating that the drainage of wetting film becomes faster as the chain length of C_nTACl is longer. It is interesting to study the profile of the air bubble at t_c. With the addition of C_nTACl, the bubble profile becomes sharp instead of flat before the film rupture. One may approximately evaluate the sharpness of the film by calculating dh/dr near the center at t_c. As shown in Table 1, dh/dr increases from 1.59 to 9.87 as the surfactant chain length increases from 12 to 18, meaning that the sharpness of the film increases with

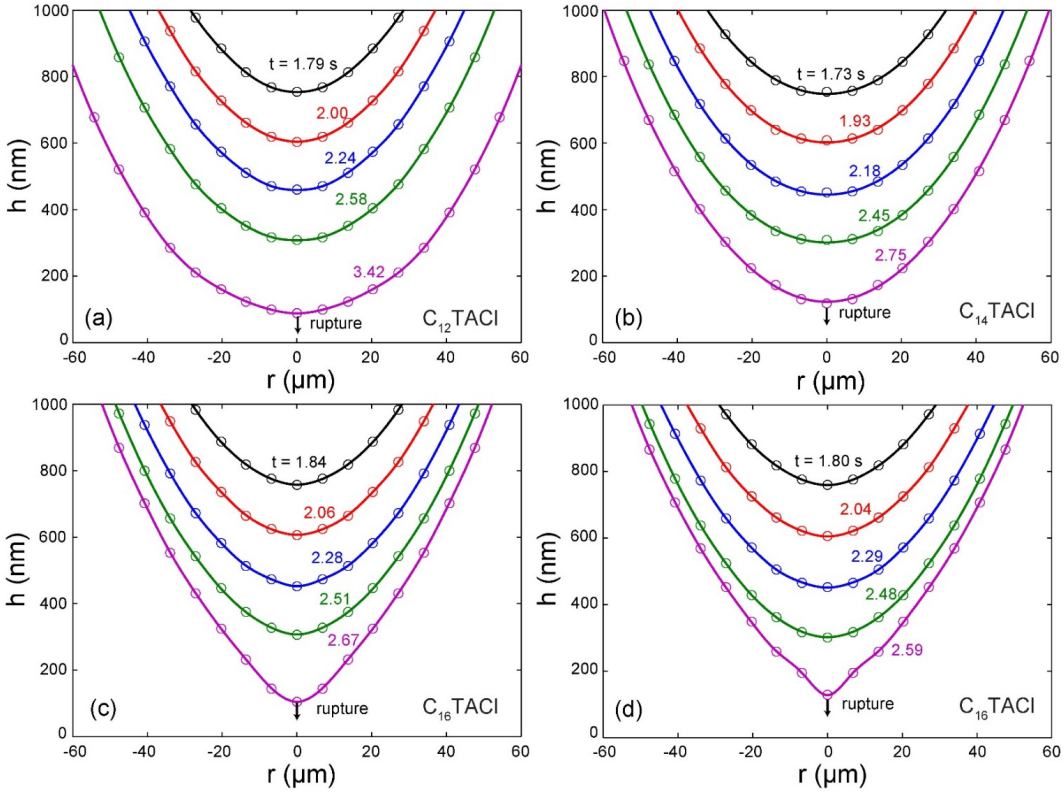

Figure 76. Spatiotemporal film profiles obtained in the wetting film of water confined between an air bubble and a silica surface with appearance of 10^{-6} M C_nTACl , where n = 12 (a), 14 (b), 16 (c) and 18 (d). The sharpness of the air bubble increases with the surfactant chain length.

the surfactant chain length (n). In general, bubble becomes sharp when attractive surface force exists in the wetting film. Note also that critical rupture thickness (h_c) increases with the increasing n.

Figure 77 shows the corresponding force curves obtained with the four C_nTACl surfactants shown in Figure 76. In each force measurement. The calculated Laplace force agreed well with the total force (green) measured by a cantilever spring. The hydrodynamic force increased significantly for C14-, C16-, and C18-surfactants before the film ruptured, which was due to the appearance of attractive surface force. Since the surface used in this series of tests were hydrophilic ($\theta_r < 40^o$), according to Churaev (1995), the contribution of hydrophobic force in Eq. [4.30] should not be considered, i.e., $C_2 = 0$. The parameters for double layer force and van der Waals force were shown in Table 31. As shown, ζ-potential of the air bubble (ψ_2) became positive after adding 10^{-6} M C_nTACl, while ζ-potential of the silica surface (ψ_1) remained negative. Therefore, an attractive double layer force was created, which became the driving force for destabilizing the wetting film. ψ_2 becomes more positive if the surfactant chain length increases, indicating that the long chain cationic surfactant has a better capability of reversing the charge on the air bubble, and in turn results in a more attractive double layer force. The contact angle (θ_r) values were also shown in Figure 77. Instead of $\theta_r = 0$ in the pure water, θ_r increased to ~30° in the presence of 10^{-6} M C_nTACl, which

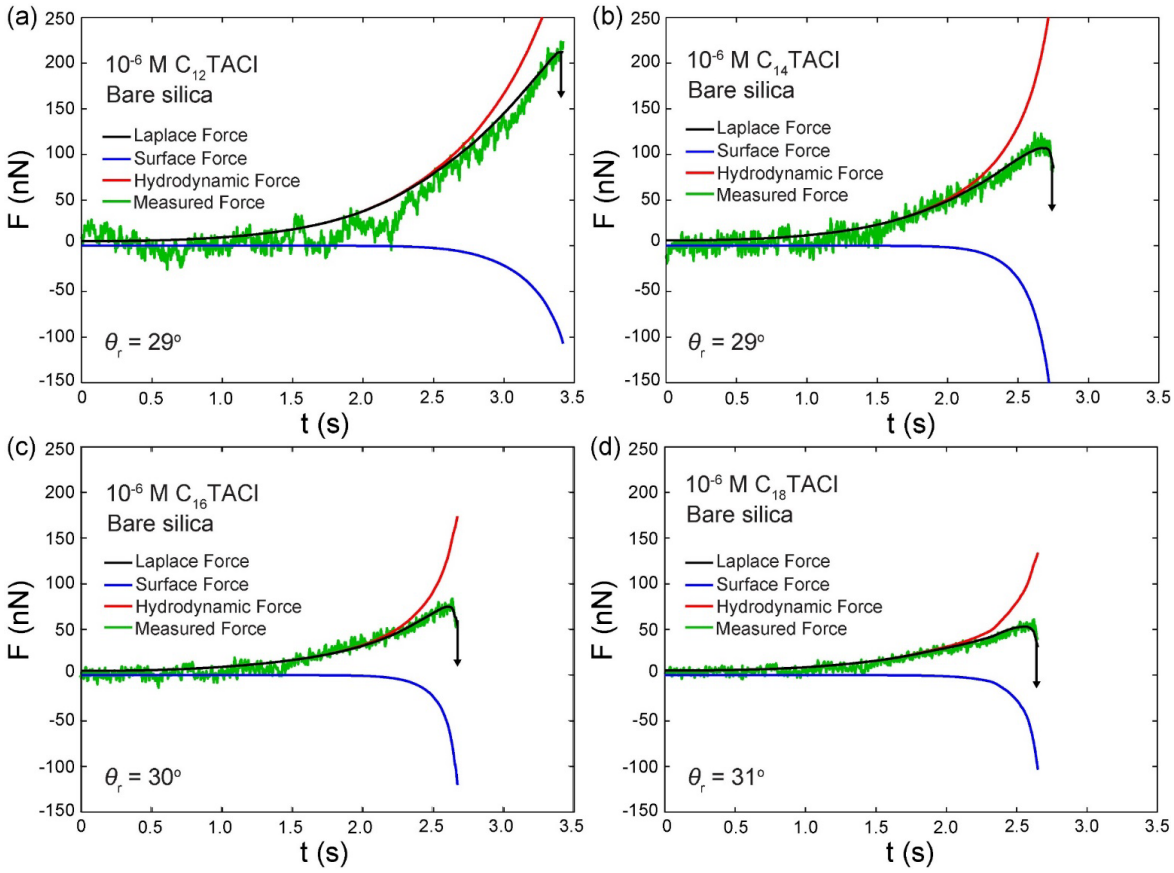

Figure 77. Force curves obtained in the wetting film confined between an air bubble and a bare silica surface at 10^{-6} M C_nTACl, where n = 12 (a), 14 (b), 16 (c) and 18 (d). The contact angle shown in each figure was measured after the film rupture. The non-zero contact angle may be due to the attractive double layer force between air/water interface and solid/water interface.

might be due to the surfactant adsorption on the bare silica surface. The attractive double layer force contributes to the increase of θ_r when surface is hydrophilic.

To clearly present the effect of C_nTACl on the film thinning kinetics, it may be useful to show the relationship between the film thickness as a function of thinning time. Figure 78 is generated in such a way that set the initial film thickness at 500 nm and plot the film thickness at center as a function of time for different surfactants. The slope (dh/dt) of each curve may represent the film thinning rate. As shown, the lowest thinning rate is obtained in the pure water. Adding 10^{-6} M C_nTACl will significantly improve the film thinning. The thinning rate is in an ascending order with increasing the hydrocarbon chain length of C_nTACl. The thinning time for C12-, C14-, C16- and C18-surfactants are 1.26, 0.66, 0.46, and 0.38 s, respectively. Such a big difference in thinning rate may originate from the magnitude of attractive double layer force, which has been discussed in the foregoing session.

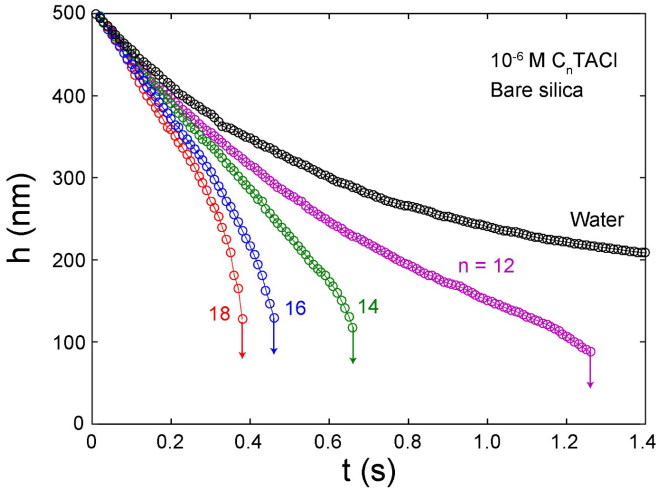

Figure 78. Effect of the different cationic surfactants (C_nTACl) on the film thinning kinetics. The thinning kinetics is promoted when adding 10^{-6} M C_nTACl into the pure water. C_nTACl with longer hydrocarbon chain will lead to a faster film thinning.

Figure 79 shows the disjoining pressure isotherm ($\Pi(h)$) obtained for the wetting film confined between a bare silica surface and an air bubble. $\Pi(h)$ was plotted by plugging the surface force parameters shown in Table 31 into Eq. [4.30]. The disjoining pressure due to van der Waals force (Π_d) was shown in dashed line, which was always positive in the wetting film. The positive Π_d arises from the fact that water molecules are adsorbed on the hydrophobic surface via van der Waals force with $|A_{132}|$ representing the magnitude. To overcome the obstacle by Π_d in the wetting film, one may control the double layer force (Π_e) and hydrophobic force (Π_h) to help destabilize the wetting film. As shown, the disjoining pressure is positive in the pure water, which is due to that Π_e and Π_d are both repulsive. Π becomes, however, negative, in the presence of 10^{-6} M C_nTACl, which is due to the attractive double layer force. According to Table 1, the ζ-potentials of air bubble (ψ_2) become positive in presence of C_nTACl, while the ζ-potentials of the silica surface (ψ_1) stay negative. Since ψ_1 and ψ_2 are in opposite sign, Π_e becomes negative (attractive) at any film thickness (h), which leads to the rupture of the wetting film although the surface is hydrophilic. Note also that Π becomes more negative as n increases, indicating that the capability of reversing bubble charge increases with the surfactant chain length.

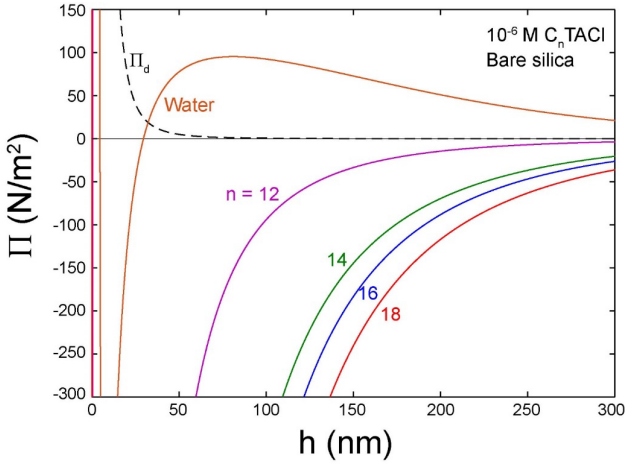

Figure 79. Disjoining pressure isotherm obtained for the wetting films of water and 10^{-6} M C_nTACl solutions formed on the bare silica surfaces (n = 12, 14, 16, and 18).

Table 31. Effect of the chain length of quaternary ammonium salts (CnTACl) on the surface force parameters obtained from the FADS measurements conducted with bare silica surfaces. The surfactant concentration is 10-6 M.

Solution	ψ_1* (mV)	ψ_2† (mV)	κ^{-1} (nm)	θ_r (°)	h_c (nm)	t_c (s)	dh/dr (x10^{-3})
C_{12}TACl	-47.8	10	92	29	88	3.42	1.59
C_{14}TACl	-42.5	65	96	29	117	2.75	1.94
C_{16}TACl	-42.2	80	100	30	129	2.67	4.91
C_{18}TACl	-40.6	98	110	31	130	2.59	9.87
water	-70.0	-52	96	0	-	-	0.02

A_{132} = 1.2x10^{-20} J; * Measured using Malvern Zetasizer NanoZS; † Fitted from surface force measurement.

Results and Discussion – Induction Time Measurement

A prerequisite for a successful flotation is the bubble-particle attachment. Induction time is defined as the minimum time required for the film to drain to a critical thickness and rupture spontaneously to form a stable bubble-particle aggregate (Yoon and Yordan, 1991). In general, a shorter induction time may represent a faster flotation kinetics. In the present work, a series of induction time measurements have been conducted by approaching an air bubble to a flat silica surface in water w/ and w/o 10^{-6} M C_{18}TACl. The contact angles of surfaces are controlled by immersing them in OTS-in-toluene solution at different times.

Figure 80 shows the relationship between the induction time and the contact angle with and without 10^{-6} M C_{18}TACl. As shown, the induction time decreased significantly from 520 ms to 180 ms when the contact angle increased from 57° to 67°. If the contact angle further increased to 105°, the induction time would further decrease to less than 50 ms. A higher contact angle will lead to a shorter induction time, which is possibly due to that the hydrophobic force becomes stronger at a higher contact angle. When the contact angle was less than 80°, the induction time decreased sharply when adding 10^{-6} M C_{18}TACl, which may attribute to the generation of an attractive double layer force that works with hydrophobic force to enhance the film thinning.

The results presented in the present work show that C_nTACl does have the capability to reverse the bubble charge and to create an attractive double layer force to enhance bubble-particle attachment. Among the agents having been tested, C_{18}TACl has the best performance. The induction time was reduced significantly in the presence of 10^{-6} M C_{18}TACl at varied contact angles, indicating that the hydrophobic force is not dampened with the addition of C_nTACl.

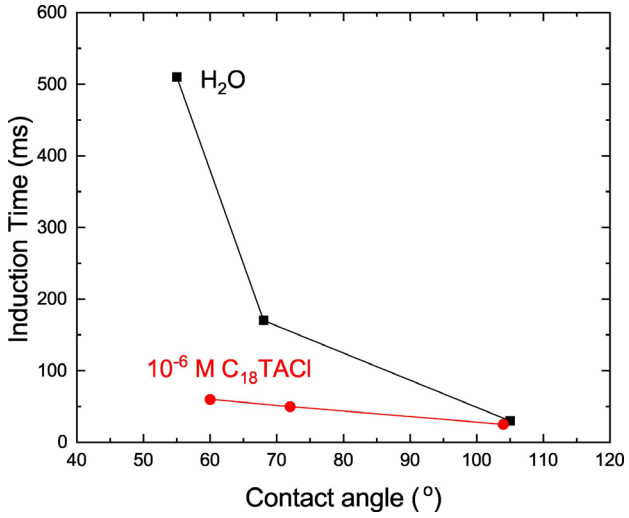

Figure 80. Effect of adding dilute cationic surfactant C_{18}TACl on the induction time. The induction time was measured using OTS-coated silica surfaces with varied contact angles.

Subtask 4.2 – Surface Chemistry Parameter Determination

ζ-potential measurements of the glass spheres used in testing were conducted using a Malvern ZetaSizer NanoZS 90. The results of ζ-potentials of silica spheres have been presented above in Subtask 4.1. See Table 27, Table 28, Table 29, Table 30, Table 31and Figure 71 for the surface chemistry parameters under various treatment conditions and surfactant concentrations.

Subtask 4.3 – Dispersive Liberation of Clay

During the project period, dispersive liberation tests were conducted on two new coal refuse samples, namely the Russellton Pond Fines and the RES fine refuse. Technical detail on the sample acquisition and characterization is given in Subtask 5.1. Upon receipt, the samples were processed using the flowsheet shown in Figure 81 below. After homogeneously mixing the ax-received material, six batch flotation tests were performed to produce sufficient decarbonized clay material. After flotation, the material was adjusted to 30% solids and blunged in a high sheer mixer. Blunging was conducted using 10 lb./ton sodium silicate, 12,000 rpm, pH 9-10 for 5 minutes. In the next step, the blunged slurry was screened at 20 µm to separate the dispersed clay particles from the larger quartz and barren gangue material. Finer size fractions were then obtained using sedimentation with the duration of sedimentation determined by Stoke's Law. Using this process, the Russellton sample was used to generate two fine clay materials with a D_{80} of 9.07 and 5.70 µm, respectively.

After dispersive liberation, the total REE content in the samples were determined by lithium tetraborate fusion followed by inductively coupled plasma mass spectrometry (ICP-MS). Results from this experiment are shown in Figure 82 for both ash-based and whole coal based data. The data indicates that the decarbonization and blunging process was able to increase the whole-coal based REE assay by greater than 2.0x; however, the data also shows that the REE content (particularly the ash based content) tended to decrease with decreasing particle size. This trend is unexpected, and the team intends to investigate other coal samples to see if similar results are obtained. Moreover, the ash-based assay for the as-received material may be misleading given the relatively low ash content of the sample (33%).

Figure 83 shows the assay data on an element-by-element basis. The samples follow a typical, LREE-enriched pattern that is common for coal-based refuse material. Moreover, the distribution pattern does not change significantly as a function of cut size in the blunging process.

Subtask 4.4 – Hydrophobic-Hydrophilic Separation

Experimental Testing

Hydrophobic-hydrophilic separation data has been shown as part of complimentary testing done in Tasks 3 and 5. The reader is referenced to the appropriate sections for the data collected under this task.

Figure 81. Flowsheet diagram of the sample preparation.

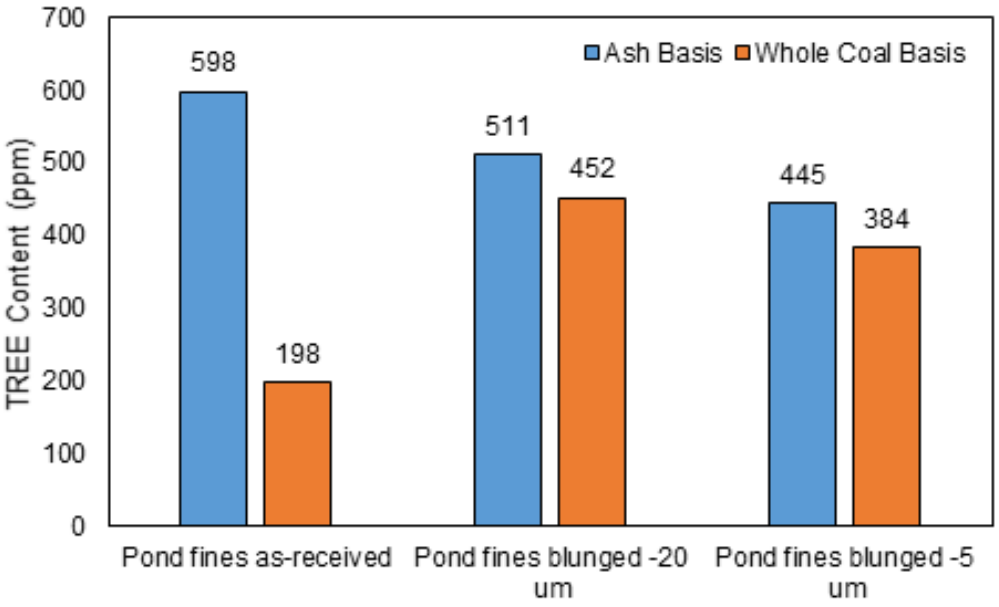

Figure 82. TREE content of Pond Fines and Russellton sample.

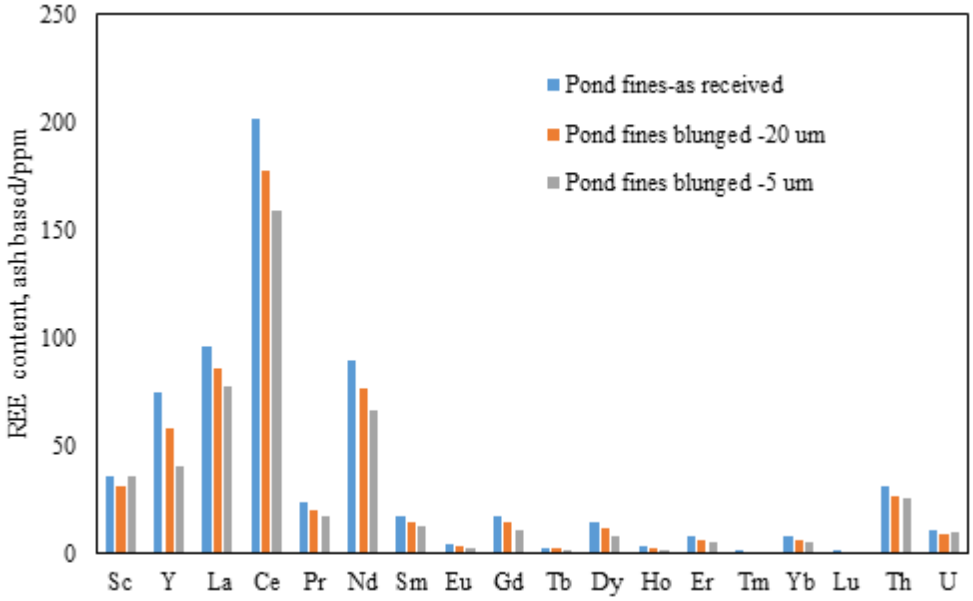

Figure 83. Individual REE distribution of Pond Fines and Russellton sample.

Techno-Economic Analysis

Techno-economic analysis was completed after the analysis and synthesis of the experimental data. The flowsheet evaluated in the study includes the following process modules:

1. Ball mill grinding to reduce the material from 200 to 35 microns.
2. Two liquid flotation to upgrade the REE content of the feed material and reject non-REE bearing gangue
3. An activation circuit to convert the REEs to a more leachable form
4. A tank leaching circuit using ammonium sulfate
5. A neutralization circuit where oxalic acid is used to precipitate rare earth oxalates
6. A roasting unit to convert the rare earth oxalates into a mixed rare earth oxide product

Using this flowsheet, an economic model was generated to determine the itemized CAPEX and OPEX by process module. Each module includes itemized costs for individual equipment, such as tanks mixers, pumps, and filters. Bare equipment costs were determined based on scale models and installation and other direct costs were determined by standard Lang factors. A 2025 construction year was assumed and costs were properly escalated using CEPCI for historical costs and a 3.6% annual capital inflation for projections.

For the economic modeling, the plant was sized to produce 1 metric tonne of MREO per day from a coal-based clay source, and as such, the total plant feed was adjusted based on the feed grade and inputted recovery values. The initial feed grade was assumed to be 450 ppm; however, sensitivity analysis was conducted to evaluate potential variability. REE losses in the activation and oxalate precipitation circuits were assumed to be negligible (<5%), while the recovery of leaching was assumed to be a static 60%. The efficiency of the two liquid flotation circuit (*i.e.* recovery and product grade) were evaluated through sensitivity analysis; with standard values of 50% and 20,000 ppm, respectively.

Using baseline values, the total plant feed rate needed to achieve 1 metric ton per day of product was determined to be 350 tph, with a total capital cost of $44.7 million, excluding the two-liquid flotation process, which was estimated separately. Of the $44.7 million CAPEX, approximately 60% is attributed to the grinding step, 25% to the activation step, and the remainder split between the leaching and oxalate precipitation step. The figures below show the results of the sensitivity analysis. Here, CAPEX (excluding two-liquid flotation) is shown as a function of the two-liquid flotation efficiency (Figure 84) and the initial feed grade (Figure 85). In both cases, the CAPEX follows and exponential trend with increasing efficiency, demonstrating the significant value of the upgrading process.

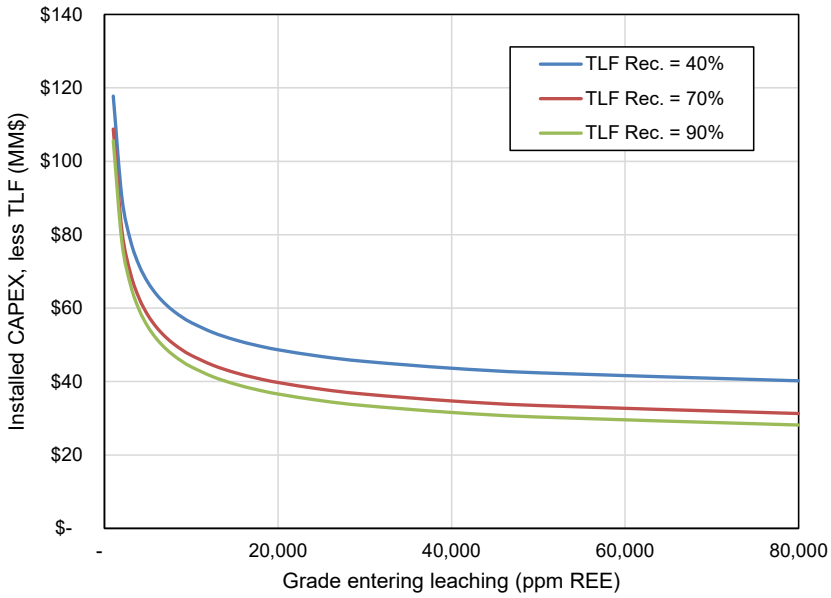

Figure 84. Sensitivity analysis showing installed capex of a 1 metric ton per day REO plant as a function of grade and recovery of the two liquid flotation process. Initial feed grade is fixed at 450 ppm REE.

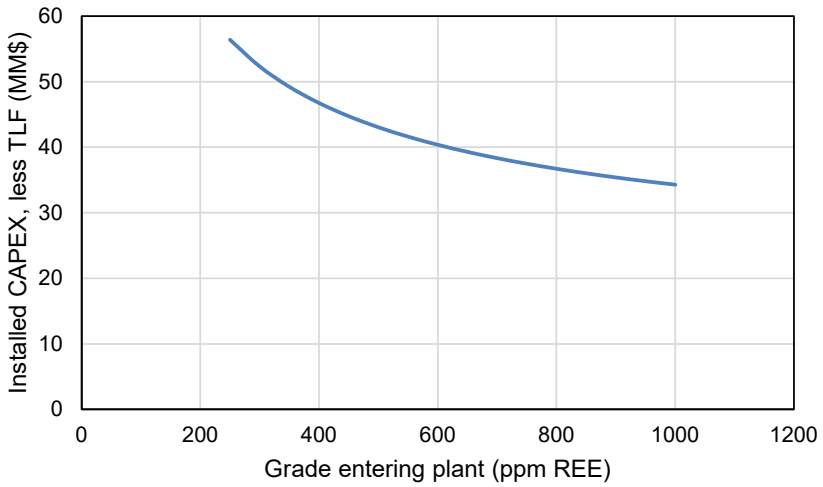

Figure 85. Sensitivity analysis showing installed capex of a 1 metric ton per day REO plant as a function of initial feed grade.

Task 5: Chemical Extraction

Subtask 5.1 – Materials Acquisition and Characterization

Sample Assays

Throughout the project, various coal-based materials were acquired and used in the chemical extraction tests. Table 32 shows the complete sample list as well as pertinent characterization data including ash content and REE concentration. As shown, REE contents (whole sample basis) varied from <60 ppm to over 450 ppm for the samples utilized int his project.

Table 32. Field Sample Assay Summary

Sample ID	Ash Content	Ash-Based REE Assay (ppm)	Whole Coal REE Assay (ppm)
Humphrey Slurry Impoundment	21.00	286.33	60.13
Humphrey Ash Streak	69.00	224.00	154.56
Dry Mercer Clay -#80 w/ RAR	na	na	140.46
Russellton Pond Fines	33.20	597.94	198.52
RES #1 Fine Reject	23.70	452.31	107.20
BRC Underclay	90.17	505.79	456.07
RES #3 Reject Filter Cake	23.85	454.57	108.42
RES #3 Fine Coal Reject	23.14	796.33	184.27
RES #3 Sub 325 Clean Coal	7.65	759.54	58.10
RES #3 Sub 325 Reject	55.85	453.53	253.30
MCMD Underflow	17.94	552.61	99.14
MCMD Middling	18.40	537.46	98.89

XPS Characterization of Kaolinite Contacted with Lanthanum and Phosphate Ions

Initial Studies

As is well known, most of the ion-adsorption clays mined in South China are readily extracted by the ion-exchange mechanism using ammonium sulfate ($(NH_4)_2SO_4$) as lixiviant *via* the following mechanism,

$$2Clay\text{-}Ln + 3(NH_4)_2SO_4 = 2Clay\text{-}3NH_4 + 2Ln^{3+} + 3SO_4^{2-} \quad [5.1.1]$$

For this mechanism to work, it is necessary that the Ln^{3+} ions be adsorbed on clay surfaces as free ions. In general, the ion-exchangeability is determined by conducting experiment using ammonium sulfate as lixiviant as in Reaction [1]. The results obtained by the PIs and others investigators showed disappointing results, which led to the possibility that lanthanides may be present in a colloidal form, *e.g.*, (Fe,Ln)(OOH). PIs developed during the first year of this project a reductive leaching process to extract the Ln^{3+} ions into solution at a neutral pH. However, the method worked well only on a limited number of samples. It was, therefore, suggested that Ln^{3+} ions may be passivated by the PO_4^{3+} ions from solution during the geological time scale. The objective of this subtask is to test this premise.

During the current study, a kaolinite sample received from the Thiele Kaolin Company, Sandersville, GA, was contacted with a 10^{-3} M $LaCl_3$ (1,000 ppm) solution with and without 10^{-2} M NaH_2PO_4 (1,000ppm $H_2PO_4^-$). After a 24 hrs of contact time at a room temperature, the clay sample was separated from the solution by centrifugation, washed with deionized water, and dried overnight at 60°C. The dried samples were subjected to surface analysis using the PHI VersaProbe III scanning XPS microscope equipped with a monochromatic Al K-alpha X-ray source (1,486.6 eV) with a base pressure of 3×10^{-8} Pa. The XPS Spectra were acquired with 200 µm/50 W/15 kV settings over a 200 µm×200 µm sample area using 69 eV pass energy, which gives a Ag $3d_{5/2}$ full-width at half maximum of 0.69 eV. All binding energies were referenced to Al *2p* peak at 74.6 eV.

Knowing that the adsorption of the La^{3+} ions depend on the surface charge density of the clay minerals, the kaolinite samples were contacted with the $LaCl_3$ solutions at three different pHs, *i.e.*, 2.0, 5.0, and 6.0. As is generally known, the basal surface of kaolinite particles are negatively charged at any pH, while the edge surfaces are positively charged at a pH below the point of charge (pzc) of the edge surface and negatively charged at pH above the pzc. It has been shown previously that the pzc of the edge surface of kaolinite is pH 6.1 (Huang *et al*., 2018; Yoon *et al*., 1979).

Figure 86 shows the XPS spectra of the kaolinite samples contacted with the La- and/or P-doped kaolinite samples at pH 2. After doping in a 1,000 ppm La^{3+} solution, XPS spectra of the sample (Figure 86a) show evidences of La adsorption on the surface of kaolinite, with a La $3d_{5/2}$ photoemission peak at 836.5 eV and a satellite peak at 840.1 eV. An F *KLL* feature is also present in this region, similar to that on previous artificial ion-adsorption clay samples. The three characteristics of the La $3d_{5/2}$ feature, *i.e.* the photoemission peak at 836.5 eV, the multiplet splitting of 3.6 eV, and the satellite/peak intensity ratio of 0.90, do not have an exact match with those of relevant La-bearing compounds (Table 33) suggesting that the chemical bonding of the La species is different from that of listed La compounds (e.g., monazite). It is possible that La binds to the surface of kaolinite *via* electrostatic attraction between the predominant La^{3+} ions at this pH and the negatively charged basal planes of kaolinite. P signals are not detected on the surface of kaolinite as anticipated.

After doping in the 1,000 ppm $H_2PO_4^-$ solution, the XPS spectra of the sample (Figure 86c) show the P adsorption with a P $2p_{3/2}$ peak at 133.9 eV, which is presumably bound to the protonated hydroxyl groups on the edge surfaces of kaolinite particles at pH 2. The P $2p_{3/2}$ binding energy falls within the range of phosphates but is 0.9 eV higher than that of PO_4^{3-} (as in $LaPO_4$ in Figure 86), resulting from the protonation of PO_4^{3-} to $H_2PO_4^-$. After a sequential doping, first in the 1,000 ppm La^{3+} solution then in the 1,000 ppm $H_2PO_4^-$ solution (Figure 86b), the La $3d_{5/2}$ feature exhibits the same characteristics as those of the sample that was not introduced to $H_2PO_4^-$, and P is still absent on the sample surface, suggesting that

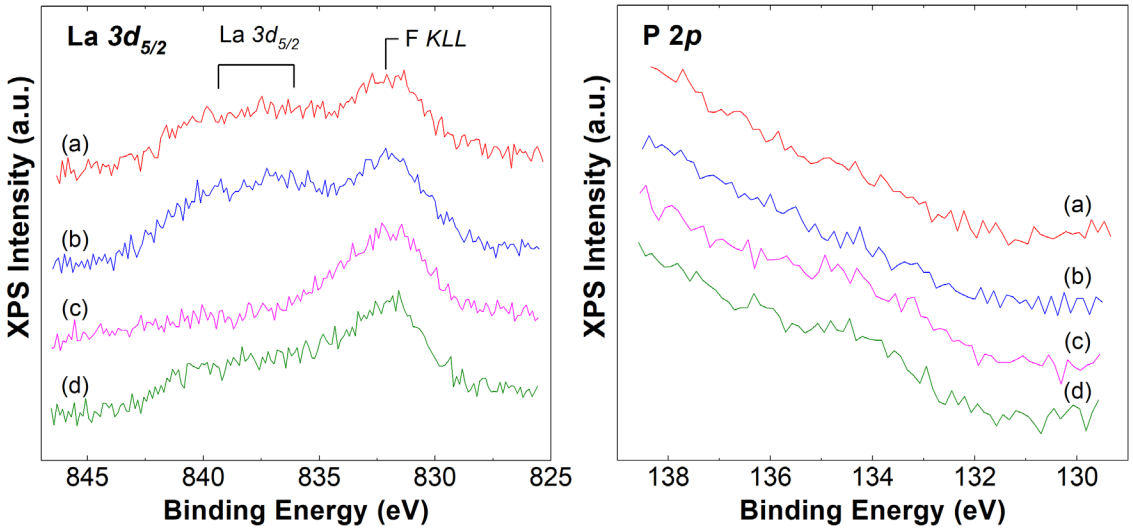

Figure 86. La 3d5/2 and P 2p XPS spectra of kaolinite sequentially doped with La3+ and H2PO4- at pH 2. (a) 1000 ppm La3+; (b) 1000 ppm La3+, then 1000 ppm H2PO4-; (c) 1000 ppm H2PO4-; (d) 1000 ppm H2PO4-, then 1000 ppm La3+.

the pre-adsorbed La may not bind to $H_2PO_4^-$ ions and perhaps blocks the adsorption of $H_2PO_4^-$ onto the kaolinite surface. When the order of reagent contact was reversed, i.e., when kaolinite was first introduced to $H_2PO_4^-$ then to La^{3+}, both La and P are present on the surface of kaolinite with similar concentration as that on the sample synthesized in the La^{3+} or $H_2PO_4^-$ solution respectively, suggesting that the pre-adsorbed $H_2PO_4^-$ does not affect the uptake of La^{3+} on kaolinite. These results suggest that La^{3+} might adsorb on the basal surface of the clay mineral and hinder the adsorption of the $H_2PO_4^-$ ions on the edges.

Figure 87 shows the XPS spectra of the La $3d_{5/2}$ and P *2p* on the La- and/or P-doped kaolinite samples at pH 5. When kaolinite was first introduced to La^{3+}, La adsorbs onto the surface of kaolinite presumably *via* electrostatic attraction and blocks the adsorption of $H_2PO_4^-$ ions, same as observed at pH 2 (Figure 86 a and b). After doping in the 1,000 ppm $H_2PO_4^-$ solution, the concentration of P is much lower than that on the sample synthesized at pH 2, most probably because the surface charge of the edge surfaces are less positive than at the acidic pH. After doping the clay with $H_2PO_4^-$ ions first before doping with La^{3+} ions (Figure 86d), the signal intensity of the La $3d_{5/2}$ feature was greatly attenuated as compared to that on the sample without pre-doped $H_2PO_4^-$, indicating that the pre-doped $H_2PO_4^-$ suppresses the uptake of La onto the kaolinite surfaces. It is possible that the $H_2PO_4^-$ ions adsorb on the edges and thereby prevent the adsorption of the La^{3+} ions.

Figure 88 shows the XPS spectra of La $3d_{5/2}$ and P *2p* on the La- and/or P-doped kaolinite at pH 6. The adsorption behavior of La and P are similar to those observed at pH 5, except that the pre-doped $H_2PO_4^-$ does not affect the uptake of La onto the kaolinite surfaces. This finding suggests that both P and La adsorb on the edges, and that La adsorption hinders the adsorption of the P adsorption.

The XPS data presented in this section is consistent with the heats of adsorption data (ΔH_i) obtained for the $H_2PO_4^-$-kaolinite system (Penn and Warren, 2009). These investigators showed that the $H_2PO_4^-$ ions adsorb on clay surfaces exothermically at pH < 5.6 which corresponds to the pzc of edge surfaces of kaolinite and endothermically at pH > 5.6. Most of the data obtained to date were obtained at pH 2, which is not a realistic pH. If XPS is not sensitive enough to detect the small amounts of phosphor adsorbed on clay surfaces, we will increase the concentration of the phosphate ions.

Clay minerals, *e.g.*, kaolinite, have been formed from the weathering of feldspar, which is the major component of granite. The REE ions released from the weathering of the RE-bearing minerals such as

Table 33. Characteristic XPS values for the synthesized REE clay samples and several reference La compounds.

Spectra	La $3d_{5/2}$ BE (eV)		ΔE (eV)	satellite:peak ratio	P $2p_{3/2}$ BE (eV)	Atomic Ratio	
	peak	satellite				La/Al	P/Al
5-1(a)/5-2(a)	835.7	839.3	3.6	0.77	-	0.0067	-
5-1(b)	-	-	-	-	-	-	-
5-2(b)	835.4	839.0	3.6	0.66	133.7	0.0043	0.021
5-2(c)	835.6	839.0	3.4	0.86	134.0	0.0049	0.013
5-3(a)	-	-	-	-	-	-	-
5-3(b)	-	-	-	-	133.7	-	0.048
5-3(c)	-	-	-	-	133.8	-	0.031
5-4(a)	-	-	-	-	133.7	-	0.047
5-4(b)	835.3	838.7	3.4	0.51	133.7	0.0023	0.044
5-4(c)	835.3	838.8	3.5	0.68	133.8	0.0018	0.043
$LaPO_4$	835.3	838.6	3.3	0.71	133.0	-	-
$LaCl_3$	835.6	839.1	3.5	1.43	-	-	-
La_2O_3	834.1	838.6	4.5	0.77	-	-	-
$La_2(CO_3)_3$	834.5	838.1	3.6	1.01	-	-	-
$La(OH)_3$	834.7	838.4	3.7	0.71	-	-	-

allanite, titanite, apatite, and/or flurocarbonate may adsorb to the clay surfaces, forming ion-adsorption clays. It has been shown that weathered granites of high phosphate contents exhibit low percentages of ion-exchangeable REE+Y, which may be due to passivation by the phosphate ions as discussed above. It is also possible, however, that the REE+Y species may be associated with the residual RE-bearing minerals such as monazite and xenotime which are resistant to weathering (Sanematsu *et al*., 2015; Bern *et al*., 2017). In the present work, methods of extracting REE+Y from both of these sources have been explored.

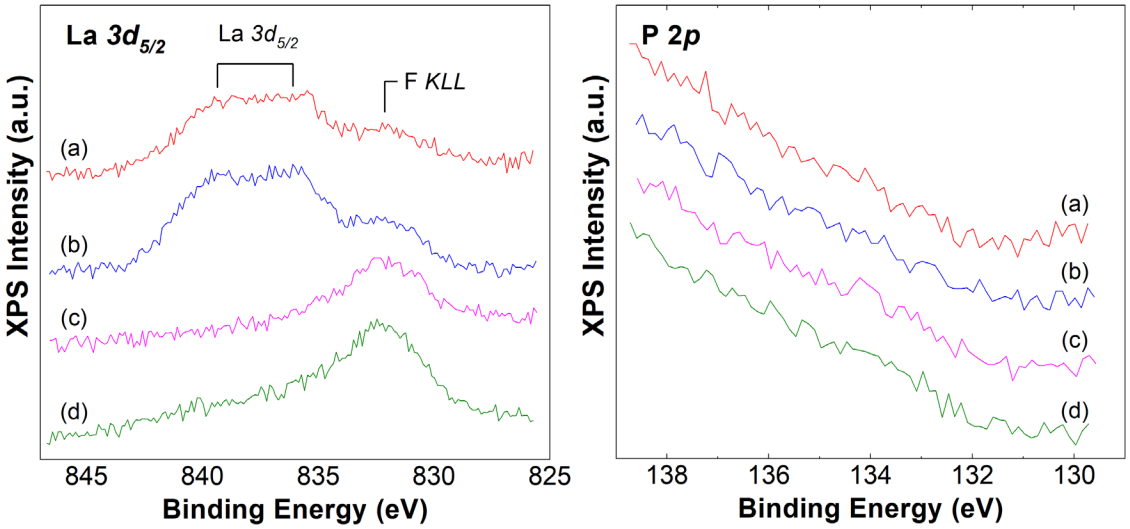

Figure 87. La $3d_{5/2}$ and P 2p XPS spectra of kaolinite sequentially doped with La^{3+} and $H_2PO_4^-$ at pH 5. (a) 1000 ppm La^{3+}; (b) 1000 ppm La^{3+}, then 1000 ppm $H_2PO_4^-$; (3) 1000 ppm $H_2PO_4^-$; (4) 1000 ppm $H_2PO_4^-$, then 1000 ppm La^{3+}.

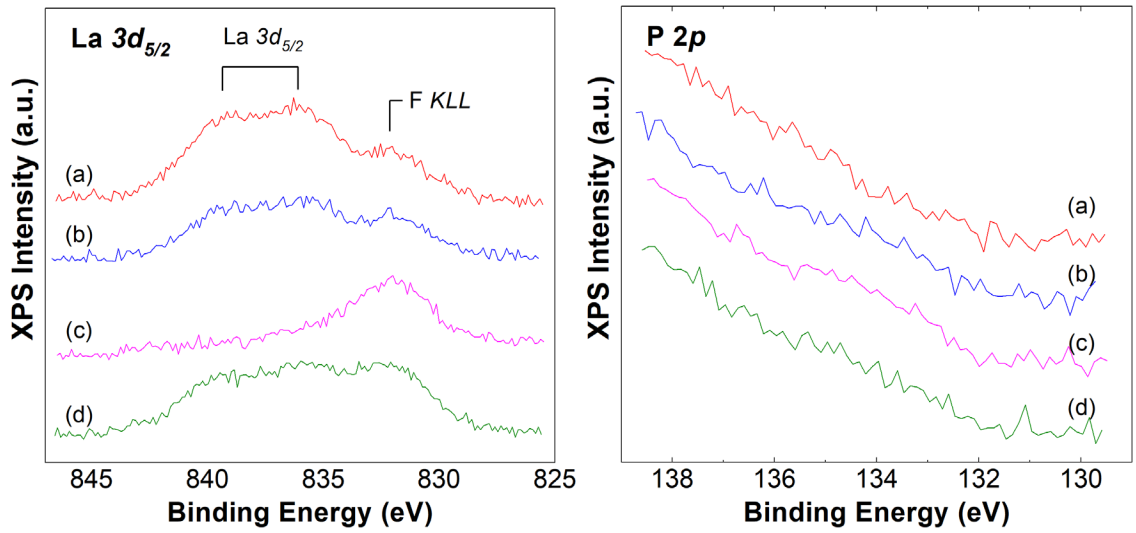

Figure 88. La $3d_{5/2}$ and P 2p XPS spectra of kaolinite sequentially doped with La^{3+} and $H_2PO_4^-$ at pH 6. (a) 1000 ppm La^{3+}; (b) 1000 ppm La^{3+}, then 1000 ppm $H_2PO_4^-$; (c) 1000 ppm $H_2PO_4^-$; (d) 1000 ppm $H_2PO_4^-$, then 1000 ppm.

Detailed Studies and Ion Exchange Leaching

Sample preparation and experimental procedure

Kaolinite (Kaogloss, Thiele Kaolin Company) was conditioned in an NaOH solution at pH 12 for 1 h before use to remove native phosphates on the as-received surface of kaolinite. No phosphorus signals were detected by X-ray photoelectron spectroscopy (XPS) on the surface of kaolinite after this pretreatment. Subsequently, 0.5 g kaolinite was treated by (a) 0.36 mM $LaCl_3$ at pH 4, then (b) 0.5 M $(NH_3)_2SO_4$ at pH 4; *or* (a) 0.36 mM $LaCl_3$ at pH 4, then (b) 0.025 M NaH_2PO_4 at pH 4, then (c) 0.5 M $(NH_3)_2SO_4$ at pH 4. Wet solids were centrifuged and washed with deionized water prior to the next treatment. Samples were collected after each treatment and dried at 70 ºC.

In a separate experiment, Alumina (Al_2O_3, 99.999%, MSE supplies) was used as received. No phosphorus signals were detected by X-ray photoelectron spectroscopy (XPS) on the as-received surface of alumina. In these tests, 0.5 g alumina was subsequently treated by (a) 0.36 mM $LaCl_3$ at pH 4, then (b) 0.025 M NaH_2PO_4 at pH 4, then (c) 0.5 M $(NH_3)_2SO_4$ at pH 4; *or* (a) 0.025 M NaH_2PO_4 at pH 4, then (b) 0.36 mM $LaCl_3$ at pH 4, then (c) 0.5 M $(NH_3)_2SO_4$ at pH 4. Wet solids were centrifuged and washed with deionized water prior to the next treatment. Samples were collected after each treatment and dried at 70 ºC.

Results of the effect of phosphate on the ion-exchangeability of La on kaolinite

Figure 89 shows the XPS spectra of La $3d_{5/2}$ and P *2p* on kaolinite subsequently treated by (a) 0.36 mM $LaCl_3$ at pH 4, then (b) 0.5 M $(NH_3)_2SO_4$ at pH 4. Table 34 summaries characteristic XPS values for synthesized REE clay samples. After doping in the $LaCl_3$ solution, XPS shows La adsorption on the surface of kaolinite (Figure 89a), with a La $3d_{5/2}$ photoemission peak at 835.7 eV and a satellite peak at 839.3 eV. A small fluorine feature (F *KLL*) is also present in this region, which is commonly seen on synthetic REE clay samples. The three characteristics of the La $3d_{5/2}$ feature, *i.e.* the photoemission peak at 835.7 eV, the multiplet splitting of 3.6 eV, and the satellite:peak intensity ratio of 0.77, do not have an exact match with those of relevant La-bearing compounds suggesting that the chemical bonding of this La species is different from that of reference La compounds. After the La-doped kaolinite was subsequently treated in the $(NH_3)_2SO_4$ solution, La $3d_{5/2}$ signals were not detected (Figure 89b), indicating that the previously adsorbed La species were completely removed from kaolinite by $(NH_3)_2SO_4$. No P signals were detected on both samples. These results suggest that La were adsorbed on kaolinite at pH 4 *via* electrostatic attraction, which can be easily displaced by $(NH_3)_2SO_4$ with ion-exchange mechanism.

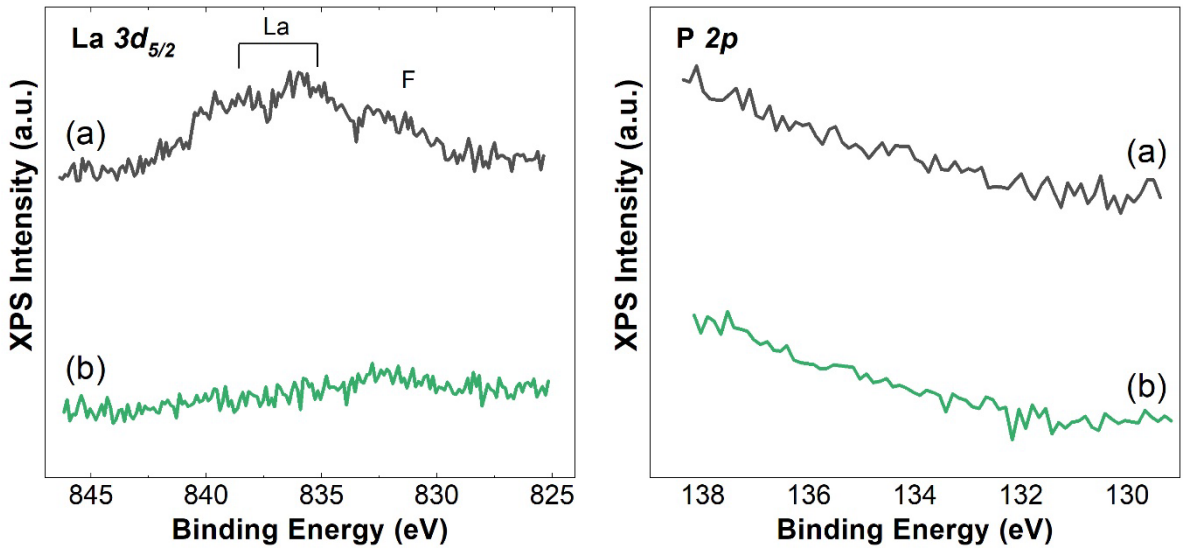

Figure 89. La $3d_{5/2}$ and P 2p XPS spectra of kaolinite (a) doped with 0.36 mM $LaCl_3$ at pH 4, then (b) leached by 0.5 M $(NH_3)_2SO_4$ at pH 4.

Table 34. Characteristic values obtained from La 3d5/2 and P 2p XPS spectra for kaolinite doped in various combination of LaCl3 and/or NaH2PO4 solutions at pH 2, 5 and 6, and those of several standard La compounds.

pH	Solution	La $3d_{5/2}$ BE (eV)		ΔE (eV)	Satellite/ Peak ratio	P $2p_{3/2}$ BE (eV)	Atomic Ratio	
		Peak	Satellite				La/Al	P/Al
pH 2	(a) La^{3+}	836.5	840.1	3.6	0.90	-	0.003	0.000
	(b) La^{3+}+$H_2PO_4^-$	836.5	840.2	3.7	0.80	-	0.005	0.000
	(c) $H_2PO_4^-$	-	-	-	-	133.9	0.000	0.005
	(d) $H_2PO_4^-$+La^{3+}	836.0	839.9	3.9	0.88	133.9	0.003	0.004
pH 5	(a) La^{3+}	835.9	839.4	3.5	0.87	-	0.006	0.000
	(b) La^{3+}+$H_2PO_4^-$	836.1	839.7	3.6	0.91	-	0.008	0.000
	(c) $H_2PO_4^-$	-	-	-	-	-	0.000	0.001
	(d) $H_2PO_4^-$+La^{3+}	836.2	840.2	4.0	0.67	-	0.003	0.002
pH 6	(a) La^{3+}	835.9	839.5	3.6	0.90	-	0.008	0.000
	(b) La^{3+}+$H_2PO_4^-$	835.7	839.3	3.6	0.92	-	0.006	0.001
	(c) $H_2PO_4^-$	-	-	-	-	-	0.000	0.002
	(d) $H_2PO_4^-$+La^{3+}	835.9	839.6	3.7	0.85	-	0.008	0.000
Standard	$LaPO_4$	835.3	838.6	3.3	0.71	133.0	-	-
	$LaCl_3$	835.6	839.1	3.5	1.43	-	-	-
	La_2O_3	834.1	838.6	4.5	0.77	-	-	-
	$La_2(CO_3)_3$	834.5	838.1	3.6	1.01	-	-	-
	$La(OH)_3$	834.7	838.4	3.7	0.71	-	-	-

Figure 90 shows the XPS spectra of La $3d_{5/2}$ and P $2p$ on kaolinite subsequently treated by (a) 0.36 mM $LaCl_3$ at pH 4, then (b) 0.025 M NaH_2PO_4 at pH 4, then (c) 0.5 M $(NH_3)_2SO_4$ at pH 4. Figure 90a demonstrates the same La adsorption feature on kaolinite as Fig5-1a after doping in the $LaCl_3$ solution. After the La-doped kaolinite was subsequently treated in the NaH_2PO_4 solution (Figure 90b), small variations in La $3d_{5/2}$ photoemission peak position and the satellite:peak intensity ratio were observed, indicating a subtle change in La chemical environment upon phosphate adsorption. P $2p$ signals were detected with a P $2p_{3/2}$ peak at 133.7 eV, which falls within the range of $H_2PO_4^-$ and is substantially higher than that of $LaPO_4$, suggesting that some kaolinite-La-H_2PO_4 complexes were formed rather than the precipitation of $LaPO_4$. Only 36% of pre-adsorbed La were removed in the presence of NaH_2PO_4, indicating that the adsorption of La and phosphates on kaolinite is largely a non-competitive process. After the La- and P-doped kaolinite was subsequently treated in the $(NH_3)_2SO_4$ solution (Figure 90c), no La were removed from kaolinite by $(NH_3)_2SO_4$, indicating that the phosphates inhibit the ion-exchangeability of pre-adsorbed La on kaolinite.

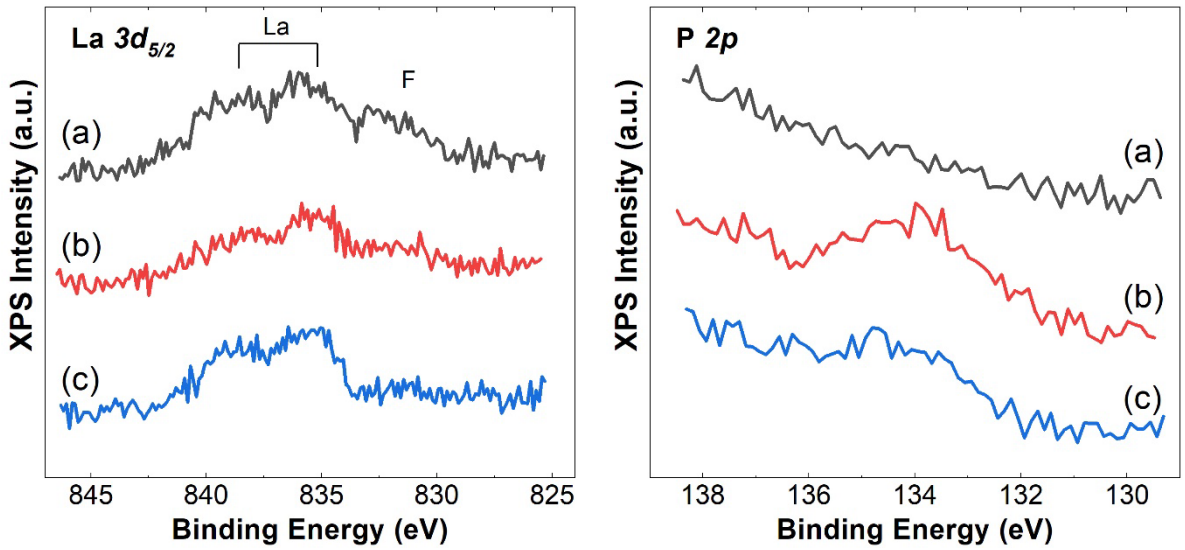

Figure 90. La $3d_{5/2}$ and P 2p XPS spectra of kaolinite (a) doped with 0.36 mM $LaCl_3$ at pH 4, then (b) doped with 0.025 M NaH_2PO_4 at pH 4, then (c) leached by 0.5 M $(NH_3)_2SO_4$ at pH 4.

Results of the effect of phosphate on the ion-exchangeability of La on alumina

We have found that the presence of phosphates prevents La from being removed by ion-exchange mechanism from kaolinite, however it is unknown if this phosphate passivation occurs at particular sites on kaolinite. It is commonly acknowledged that the basal plane of kaolinite exhibits a permanent, negative charge density resulting from the isomorphic substitution of Si^{4+} or Al^{3+} by cations of lower valency, while the charge density on the edge sites arises from aluminol and silanol groups and thus is pH-dependent. Under our treatment conditions at pH 4, the edge sites of kaolinite should exhibit a positive charge density resulting from the protonation of aluminol groups. Therefore, alumina was used to probe the effect of phosphate on the ion-exchangeability of La on the edge sites of kaolinite at pH 4.

Figure 91 shows the XPS spectra of La $3d_{5/2}$ and P $2p$ on alumina subsequently treated by (a) 0.36 mM $LaCl_3$ at pH 4, then (b) 0.025 M NaH_2PO_4 at pH 4, then (c) 0.5 M $(NH_3)_2SO_4$ at pH 4. After doping in the $LaCl_3$ solution, no La signals were detected (Figure 91a), indicating that La is not favored to adsorb on alumina under this condition, presumably due to the electrostatic repulsion between La^{3+} ions and a positive charge density on the surface of alumina at pH 4. No P signals were detected. After the La-doped alumina was subsequently treated in the NaH_2PO_4 solution (Fig 5-3b), no La was detected, while a P $2p_{3/2}$ peak at 133.7 eV was observed, which matches that of $H_2PO_4^-$. After the La- and P-doped alumina was subsequently treated in the $(NH_3)_2SO_4$ solution (Figure 92c), no La was not detected, while 35% of the pre-adsorbed phosphates were removed.

Reversing the order of $LaCl_3$ and NaH_2PO_4 treatments, Figure 92 shows the XPS spectra of La $3d_{5/2}$ and P $2p$ on alumina subsequently treated by (a) 0.025 M NaH_2PO_4 at pH 4, then (b) 0.36 mM $LaCl_3$ at pH 4, then (c) 0.5 M $(NH_3)_2SO_4$ at pH 4. After firstly doping in the NaH_2PO_4 solution (Fig 5-4a), no La was detected, while a P $2p_{3/2}$ peak at 133.7 eV similar to that of Figure 91b was observed, indicating phosphate adsorption on the surface of alumina. After the P-doped alumina was subsequently treated in the $LaCl_3$ solution (Fig 5-4b), the P $2p$ feature remain unchanged, while a La $3d_{5/2}$ photoemission peak at 835.3 eV and a satellite peak at 838.7 eV were detected. The three characteristics of this La $3d_{5/2}$ feature, *i.e.* the photoemission peak at 835.3 eV, the multiplet splitting of 3.4 eV, and the satellite:peak intensity ratio of 0.51, do not match those of the La- and P-doped kaolinite (Figure 90b), indicating that the chemical bonding of this La species is different from that on kaolinite, *i.e.* alumina-H_2PO_4-La vs. kaolinite-La-H_2PO_4. After the P- and La-doped alumina was subsequently treated in the $(NH_3)_2SO_4$ solution (Figure 92c), only 22%

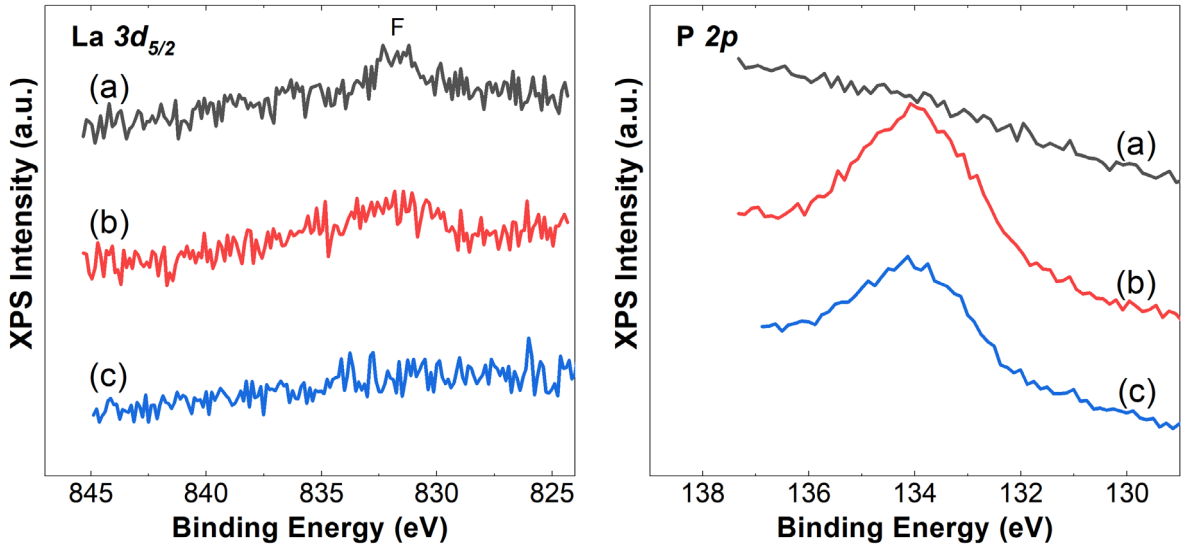

Figure 91. La $3d_{5/2}$ and P 2p XPS spectra of alumina (a) doped with 0.36 mM $LaCl_3$ at pH 4, then (b) doped with 0.025 M NaH_2PO_4 at pH 4, then (c) leached by 0.5 M $(NH_3)_2SO_4$ at pH 4

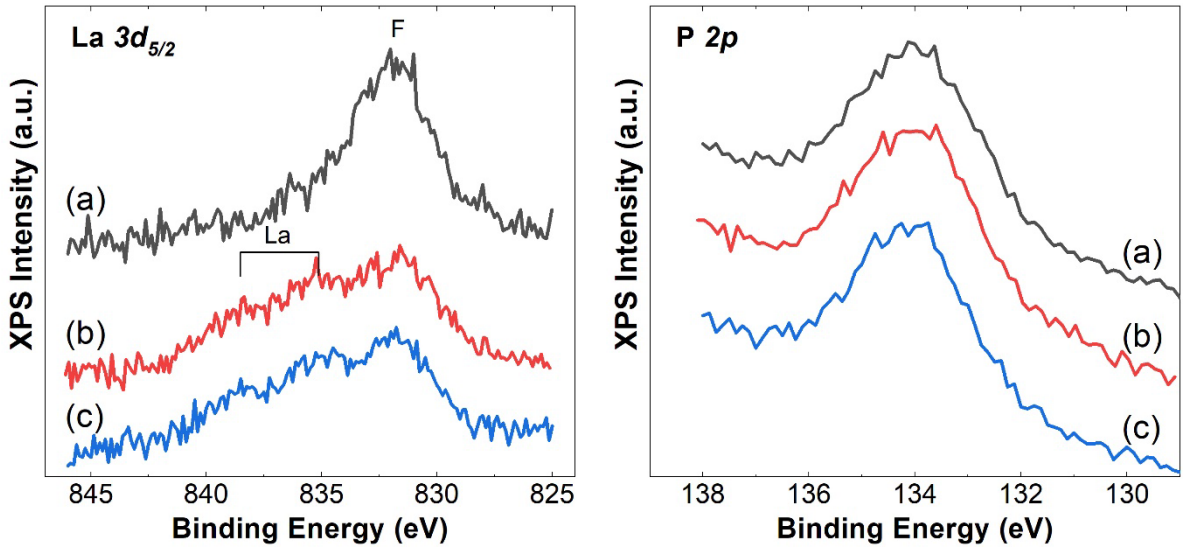

Figure 92. La $3d_{5/2}$ and P 2p XPS spectra of alumina (a) doped with 0.025 M NaH_2PO_4 at pH 4, then (b) doped with 0.36 mM $LaCl_3$ at pH 4, then (c) leached by 0.5 M $(NH_3)_2SO_4$ at pH 4.

of pre-adsorbed La were removed from alumina by $(NH_3)_2SO_4$, indicating that the formed alumina-H_2PO_4-La complexes respond poorly to ion-exchange mechanism.

Mechanism of phosphate passivation on synthesized REE clays

We have concluded that when La are adsorbed on kaolinite *via* electrostatic attraction at pH 4, subsequently introduced phosphates inhibit the ion-exchangeability of pre-adsorbed La on kaolinite, presumably due to the formation of kaolinite-La-H_2PO_4 complexes. This particular type of phosphate passivation is not observed on alumina, as a phosphate passivation of La on alumina only occurs when phosphates are present on alumina prior to La adsorption. Since the behavior of alumina mimics the edge

sites of kaolinite, these results indicate that the phosphate passivation on La occurs predominantly on the basal plane of kaolinite. Figure 93 is a cartoon illustration of a proposed mechanism of phosphate passivation on La on kaolinite. La are adsorbed on the basal plane of kaolinite at pH 4 *via* electrostatic attraction and can be effectively displaced by cations governed by ion-exchange mechanism. However, if La-kaolinite is exposed to phosphates at pH 4, kaolinite-La-H_2PO_4 complexes are formed on the basal plane of kaolinite and responds poorly to ion-exchange lixivants.

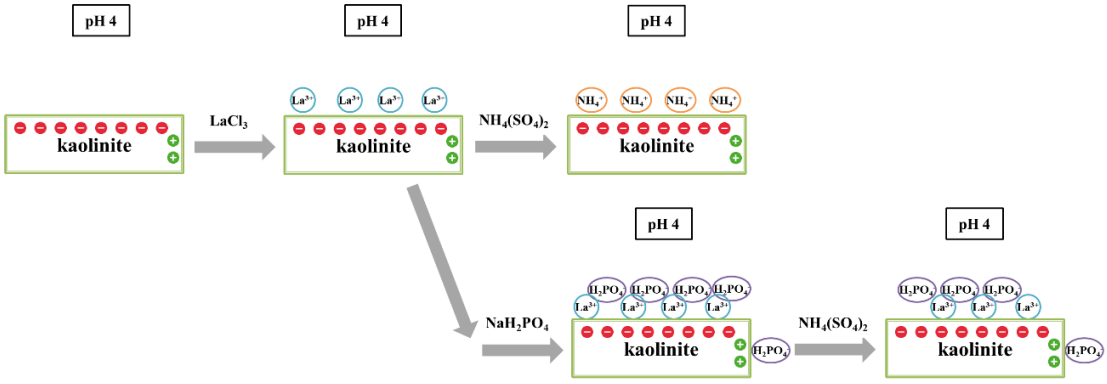

Figure 93. Proposed mechanism of phosphate passivation on La on kaolinite.

XPS Characterization of Chinese Ion Adsportion Clays

Sample preparation and experimental procedure

Rare earth ion adsorption clays (IACs) were obtained from an undisclosed site in South China. As-received IACs were sieved through a 100-mesh screen (150 μm) before use. Phosphate-passivated IACs were prepared by treating IACs in 0.5 M NaH_2PO_4 solution at pH 4 for 1h at room temperature, then washed with deionized water and dried at 70 ºC before use.

After preparation, ion-exchange leaching tests were performed by treating IACs or phosphate-passivated IACs in 0.5 M ammonium sulfate (AS) solution at pH 4 for 1h at room temperature. Leaching tests using ethylenediaminetetraacetic acid (EDTA) were performed by treating phosphate-passivated IACs in 0.0575 M EDTA solution at pH 10 for 1h at room temperature.

Elemental concentrations in leaching solution were analyzed by inductively coupled plasma mass spectrometry (ICP-MS). Elemental concentrations in IACs before and after treatments were analyzed by lithium tetraborate fusion followed by ICP-MS.

Results of the effect of phosphates on the ion-exchangeability of REEs on IACs

As discussed in prior sections, we hypothesize that phosphates bind to REEs on IACs to form more stable REE phosphate species, which in turn lead to poor leaching recovery when using ion-exchange lixiviants. Figure 94(a) shows the percentage of rare earth elements (REEs) and phosphorus (P) that were extracted from IACs in a 0.5 M ammonium sulfate (AS) leaching solution. For the as received clay material, 74% of total REE content (TREE) were extracted into the leaching solution with individual REE extraction efficiency in the range of 63-82%, indicating that this sample responds well to ion-exchange mechanism. This result is consistent with the definition of IACs where REE ions adsorb on the negatively charged clay surface *via* electrostatic attraction and can be readily displaced by monovalent cations such as NH_4^+. Negligible amount of Ce was extracted since Ce(III) is easily oxidized to Ce(IV) on IACs in the form of CeO_2/$Ce(OH)_4$, which is difficult to be extracted by ion-exchange leaching. No P was liberated into the leaching solution, suggesting that P species in IACs are not associated with ion-adsorbed REEs.

Figure 94(b) shows the percentage of rare earth elements (REEs) and phosphorus (P) that were extracted from phosphate-passivated IACs in a 0.5 M ammonium sulfate (AS) leaching solution. Only 3% of total REE content (TREE) in this sample were extracted into the leaching solution, indicating that the phosphates inhibit the ion-exchangeability of REEs on IACs. This result support our proposed phosphate passivation mechanism, where clay-REE-H_2PO_4 complexes are formed in the presence of phosphates which do not respond to ion-exchange lixiviants. The data indicates that 21% of the total P content in the phosphate-passivated IACs were liberated into the leaching solution, presumably from the excess amount of phosphates that were initially doped onto the IACs. In summary, phosphates are detrimental to the ion-exchangeability of REEs on IACs likely due to the formation of clay-REE-H_2PO_4 complexes.

Results of phosphate-passivated IACs leached by EDTA

After observing the detrimental effectives of phosphate, additional experiments were conducted to identify methods of restoring the leachability of REEs. EDTA has been widely used to chelate or complex metal ions due to its high density of ligands and resulting affinity for metal ions with binding typically occurring through its two amines and four carboxylate groups. In addition, EDTA has been reported as an effective reagent to dissolve metal phosphates due to the formation of more stable metal-EDTA complexes (Lazo et al., 2018; Paschalidou and Pashalidis, 2019). Figure 95 shows a speciation diagram of $LaPO_4$-EDTA system as a function of pH, which suggests that high concentrations of EDTA can dissolve $LaPO_4$ and form soluble La-EDTA complexes at pH > 4. We hypothesize that EDTA can dissolve clay-REE-H_2PO_4 complexes that are formed on IACs in the presence of phosphates and chelate REEs in the solution in the form of soluble REE-EDTA complexes.

Figure 94(c) shows the percentage of rare earth elements (REEs) and phosphorus (P) that were extracted from phosphate-passivated IACs in a 0.0575 M EDTA leaching solution at pH 10. 91% of total REE content (TREE) were extracted into the leaching solution with individual REE extraction efficiency in the range of 79-100%, indicating that EDTA is very effective to dissolve clay-REE-H_2PO_4 complexes and chelate REEs. Furthermore, 100% of P content in the phosphate-passivated IACs were also liberated into the leaching solution, which supports the dissolution of clay-REE-H_2PO_4. In summary, preliminary results show that EDTA is a promising lixiviant to extract REEs from phosphate-passivated REE clays. Further studies will be performed to gain full understanding of the extraction mechanism by EDTA from phosphate-passivated REE clays.

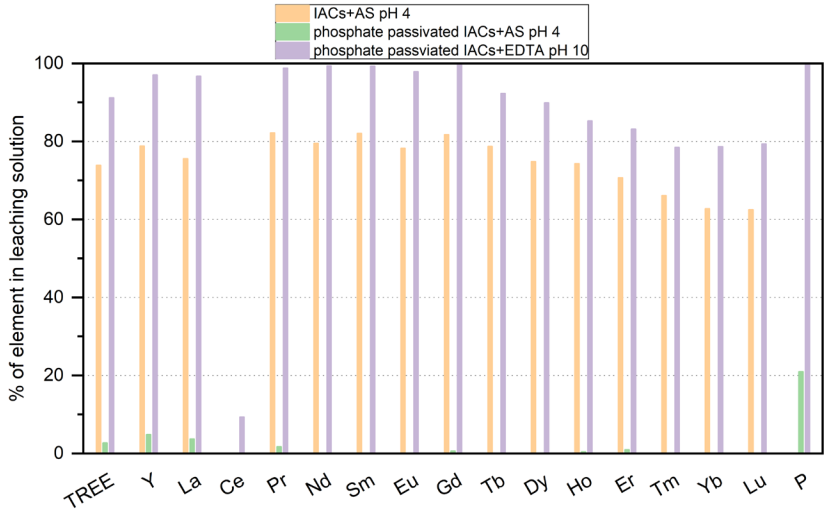

Figure 94. Percentage of REE+P in leaching solution from IACs treated in 0.5 M ammonium sulfate (AS) solution at pH 4 for 1h; (b, orange bar) phosphate passivated IACs treated in 0.5 M ammonium sulfate (AS) solution at pH 4 for 1h; phosphate passivated IACs treated in 0.0575M EDTA solution at pH 10 for 1h.

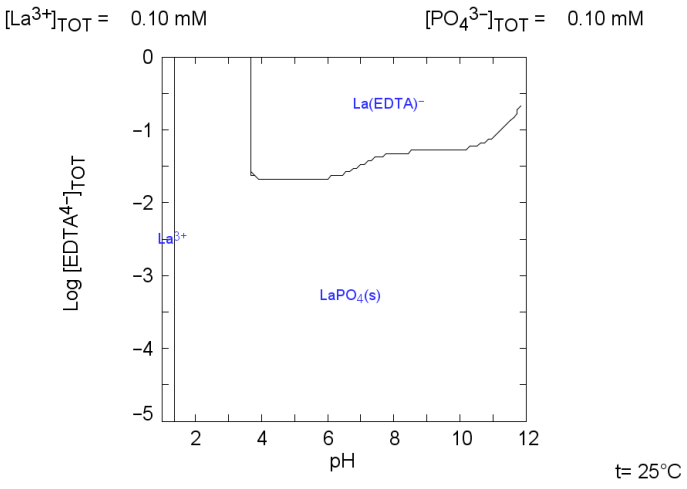

Figure 95. Speciation diagram of $LaPO_4$-EDTA system as a function of pH.

Subtask 5.2 – Enhanced Leaching and Liberation of REEs: Pretreatment/Activation

Thermodynamic Simulation of Chelating Agents

Background

In Subtask 5.4, we employed the standard ion-exchange leaching method, used in South China, on the clay samples isolated from the coal byproducts (fine coal refuse) by blunging. The results gave us 2-5% recovery, which suggested immediately that the nature of the REEs present on the surface of the clay samples we tested were very different from those mined in South China. At the same time, our XPS work showed the presence of a large amount of iron (Fe) on the surface of clay, which led us to believe that the REEs are in the form of mixed oxy-hydroxide, possibly in the form of (Fe,RE)(O,OH), which is generically referred to as "colloidal form of REEs" in the literature. We addressed this problem by developing a *reductive leaching* process, in which the colloidal form is dissolved in water under reducing conditions. This increased the REE recoveries to 10-13% range from the from the 2-5% range noted above.

It was, therefore, decided to consider the possibility that the REEs on the surface the clay may exist in different colloidal forms. Recognizing the fact that apatite ($(Ca_5(PO_4)_3(F,Cl,OH)$) monazite ($LaPO_4$) are present in U.S. coals, we thought that the colloidal form may be a RE phosphate, *e.g.*, $LaPO_4$, which can be hydroxylated to from $La(OH)_3$ via the following reaction,

$$LaPO_4 + 3NaOH \rightarrow La(OH)_3 + PO_4^{3-} + 3Na^+ \qquad [5.2.1]$$

The $La(OH)_3$ formed in this manner can be readily dissolved by acid leaching. In the present work, the blunged clay samples were subjected to ion-exchange leaching using NH_4SO_4 as a lixiviant at pH 4, which is more economical and environmentally acceptable. In some experiments, we used $CO_2(g)$ to reduce the pH to 4, which is another way to minimize the environmental impact.

The second approach to addressing the passivating effect PO_4^{3-} ions worked well with all the clay samples isolated from coal byproducts, which gave rise to ~80% recovery. Also, the recoveries of the medium and heavy REEs+Y were high, which was typical of the ion-exchange leaching process for Chines clays. The only concerns were that the initial tests were conducted at high NaOH concentrations and high temperatures. At lower concentrations and the room temperature, the recoveries dropped to the 40-50% range.

It appears that the REEs adsorbed on the surface of the ion-adsorption clays found in the U.S. coal are partitioned into two different colloidal forms, one as (Fe,RE)(O,OH) and another as $LaPO_4$. The former accounts for 10-14% of the total REEs+Y, and the latter account for ~80%. If a commercial entity employs both of these approaches sequentially, the company should be able to achieve 90-93% REE recoveries. It is possible to even make a profit while addressing the national security issue.

During the second year of the ongoing project, we are exploring a new approach, in which a chelating agent is used to increase the solubility of the $LaPO_4$ as articulated in the second-year proposal. A challenge is to identify a suitable reagent that can give rise to a maximum REE+Y recovery at a minimum cost. Toxicity of the reagent should be another selection criterion. We met the challenge by conducting a series of thermodynamic simulations using the MEDUSA software (Puigdomenech, 2013), which is capable of predicting the reactivity in the form of stability diagrams under different conditions, *e.g.*, reagent dosage, pH, PO_4^{3-} concentration, *etc*. It is also possible to predict the fractions of different REEs extracted into solution. It is, of course, necessary to have appropriate thermodynamic data. Initially, we carried our simulations using the thermodynamic data available in the literature. Once promising groups of chelating agents have been identified, we can readily determine the thermodynamic data experimentally.

Input Parameters

Most of simulations were carried out at a 10^{-5} M La^{3+} ion concentration. In so doing, the La^{3+} ion was considered to represent the behavior of other Ln^{3+} ions. The simulations were also carried out in the

presence PO_4^{3-} ions to study the effect of passivation. When studying the effect of $LaPO_4(s)$, the La^{3+} ion concentrations were increased to increase the solids content in the system.

Simulation Results

La-PO_4 System Due to the negative charge of the clay surface, resulting from the isomorphous substitution of cations with lesser formal charge, REE ions absorb on the surface *via* coulombic attraction. The stability diagram of the La^{3+} ions in water system is shown in Figure 96, which also explains how the Ln^{3+} ions are extracted by NH_4^+ ion *via* an ion-exchange mechanism. As shown, at acidic and near neutral pH, lanthanum exists as La^{3+} ions. As the pH is raised, $La(OH)_3(s)$ is formed. The critical pH, at which the free La^{3+} ions transforms to Lanthanum hydroxide decreases with La^{3+} ion concentration. This finding is consistent with how REE ions adsorb on clay surfaces. Specifically, the dominant species of REEs is "clay-REE" or "clay-REE $(H_2O)_n$" at acidic and near neutral pH conditions (Papangelakis et al., 2014). In this case, REEs can be readily extracted at acidic pH by using monovalent cations like NH_4^{3+} as lixiviant. In neutral and alkaline pH, REEs occur as "clay-O-REE^{2+}" species by complexing with the amphoteric surface hydroxyl groups, which will make it difficult to be extracted by the ion-exchange mechanism. Therefore, REEs are extracted at near neutral pHs.

The stability diagram changes drastically in the presence of PO_4^{3-} ions as shown in Figure 97. Even at 10^{-6} M PO_4^{3-} ions, free La^{3+} ions exist only at pH < 2.5, suggesting that REE ions can be extracted only by acid leaching, which explains why we were able to extract only 2-5% of the REEs from the surface of the clays isolated from coal byproducts by ion-exchange leaching using $(NH_4)_2SO_4$ as lixiviant. Note also that as the PO_4^{3-} ion concentration increases, the free La^{3+} ions disappear almost completely, suggesting that most of the REEs on the surface exists as phosphates, *e.g.*, $LaPO_4(s)$. One way to undo the passivating effect would be to convert phosphates it to hydroxides by an alkali treatment as shown by Reaction [1]. The conversion from phosphate to hydroxide is possible, because the OH^- ions are more basic than the PO_4^{3-} ions, whose pK_b's are 1.7 and 0, respectively. With the approach, we obtained 80% recovery.

Effect of Citrate Various organic acids were used to improve the extraction of REEs from ion-adsorption clay by ion-exchange leaching (Wang *et al.*, 2017). Of the various reagents tested, the authors found that citric acid was most efficient. One of the mechanisms suggested was that organic acids form soluble complexes, which should increase the extraction efficiencies. In the present work, we explored the possibility of rendering $LaPO_4(s)$ water soluble using citric acid as a complexing agent.

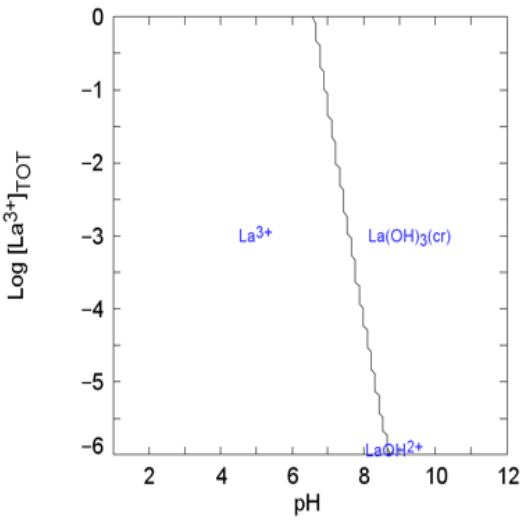

Figure 96. Stability diagram for the La^{3+}-H_2O system at at $[La^{3+}]=10^{-5}$ M and $[PO_4^{3-}]=0$.

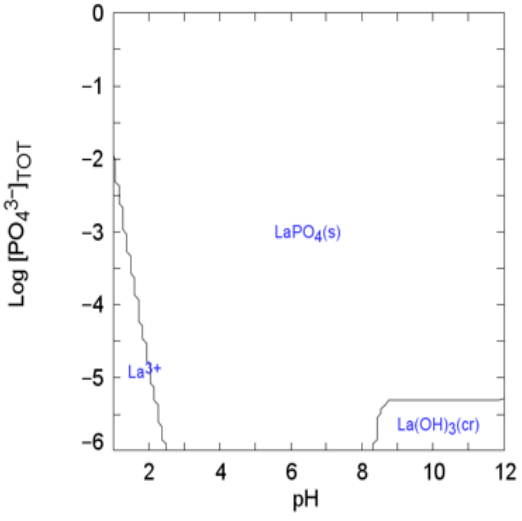

Figure 97. Stability diagram for the La^{3+}-PO_4^{3-}-H_2O system at $[La^{3+}]$ and $[PO_4^{3-}] =10^{-5}$ M.

Figure 98 shows the stability diagram of the La^{3+} ion-PO_4^{3-}-H_2O system in the presence of citric acid ($C_6H_8O_7$). As shown, there is an island on the upper-left corner of the diagram, where La-citrate complex is formed. The 1:1 complex is neutral, as the citric acid has three carboxyl groups. Yet, the complex is water soluble due to the presence of one OH group in the molecule.

Figure 99 shows the fraction diagram constructed for the La^{3+} ions at a 10^{-3} M citrate concentration. The results show that the La^{3+} ions on clay surface are not passivated in the presence of 10^{-3} M PO_4^{3-} ions in acidic solutions. As the pH is raised above 2, however, it will be difficult to extract the La^{3+} ions from the clay surface as they precipitate as $LaPO_4$(s). Nevertheless, approximately 25oN % of the lanthanum in the system can be extracted at pH 4 using 10^{-3} M of citric acid as a complexing agent.

Effect of Other Organic Acids On the basis of the encouraging results obtained with citric acid, thermodynamic simulations have also been conducted for using other organic acids as complexing agents for La^{3+} ions. Table 35 shows a list of the reagents used for the simulation, while Table 36 and Table 37 shows their stability constants (pKa) and the stability constants (log K) with lanthanum, respectively, that were used for the simulations. Figure 100 shows the chemical structures of the organic acids, and Figure 101 through Figure 106 show the stability diagrams obtained from the simulations.

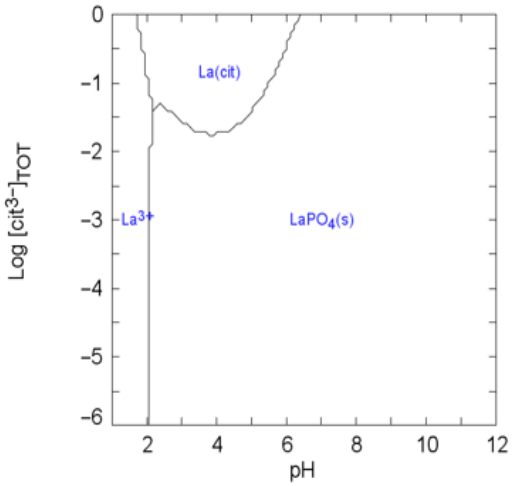

Figure 98. Stability diagram for the La^{3+}-citric acid-H_2O system at $[La^{3+}]$, $[PO_4^{3-}]=10^{-5}$ M.

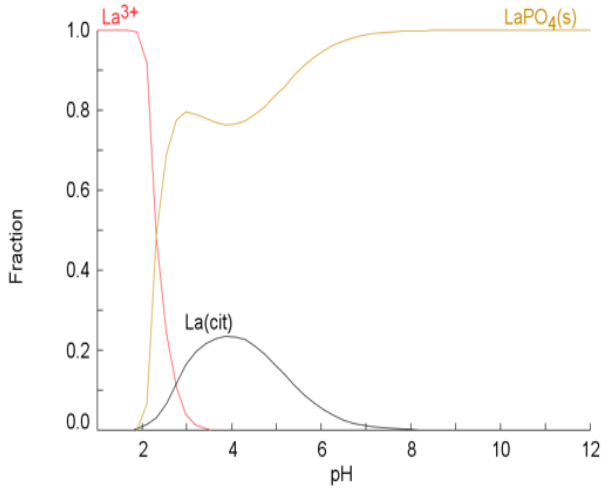

Figure 99. Fraction diagram at 10^{-3} citric acid at $[La^{3+}]$, $[PO_4^{3-}]=10^{-5}$ M.

Table 35. Organic acids used for simulation

Organic acid	Abbreviation	Ligand form
Triethylenetetramine-N,N,N',N'',N''',N'''-hexaacetic acid	TTHA	H_6L
Diethylenetriaminepentaacetic acid	DTPA	H_5L
trans-1,2-Diaminocyclohexane-N,N,N',N'-tetraacetic acid, monohydrate	CyDTA	H_4L
Ethylene glycol-bis(β-aminoethyl ether)-N,N,N′,N′-tetraacetic acid	EGTA	H_4L
N,N'-Dihydroxyethyl Glycine	DHEG	HL
2-Aminoethanoic acid	Gly	HL

Note: Information from Demonstration CD-ROM of the IUPAC stability Constants Database

Table 36. Acid dissociation constants of organic acids used in this study (Metal Chelates, 2012

pKa	TTHA	DTPA	CyDTA	EGTA	DHEG	Glycine
a1	2.42	2.14	2.43	1.90	8.14	9.78
a2	2.95	2.38	3.52	3.34		
a3	4.16	4.26	6.12	9.36		
a4	6.16	8.60	11.70	10.17		
a5	9.40	10.53				
a6	10.19					

Table 37. Stability constants of La and the organic ligands used in this study (Metal Chelates, 2012)

Stability constant (Log K)	TTHA	DTPA	CyDTA	EGTA	DHEG	Gly
La	22.22(25.62)	19.48	16.75	18.23	7.3	3.75

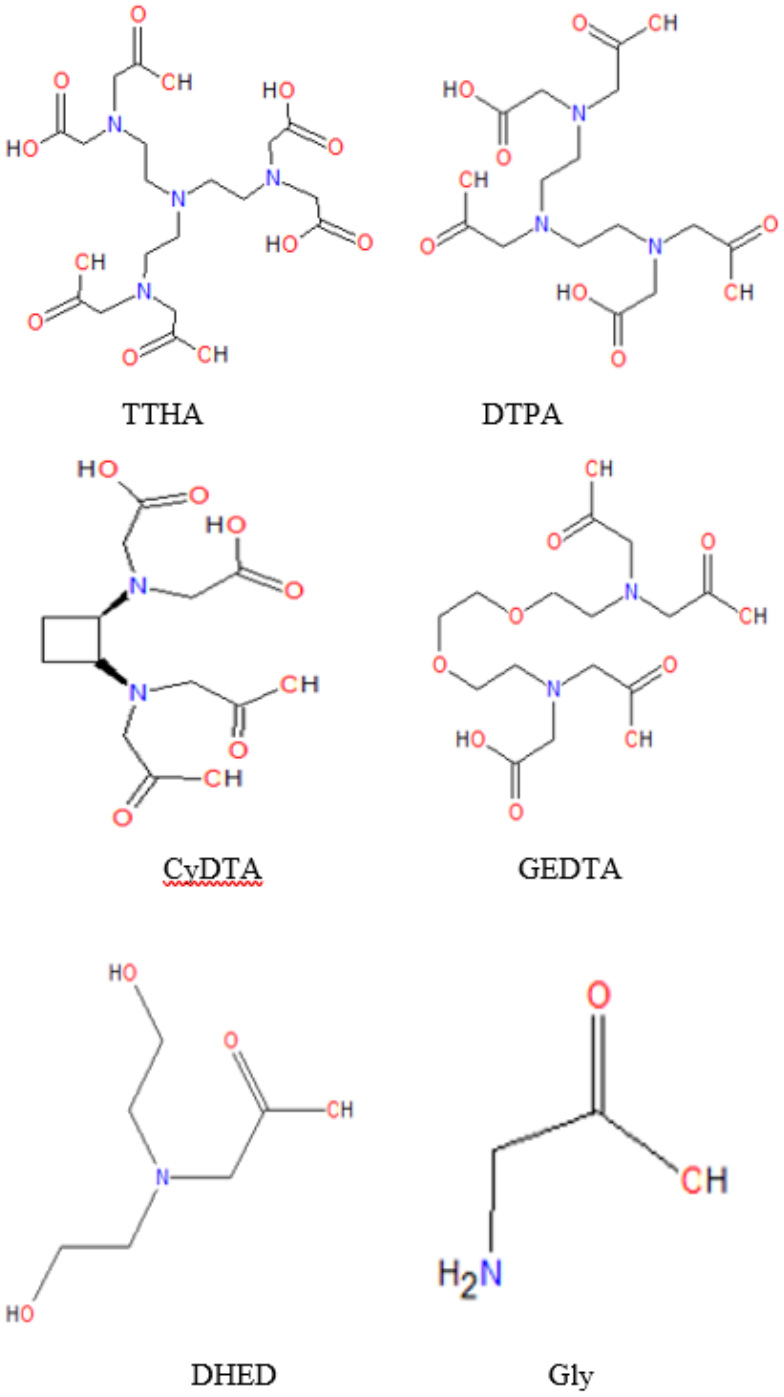

Figure 100. Chemical structure of the organic acids used Note (Pictures from Demonstration CD-ROM of the IUPAC stability Constants Database).

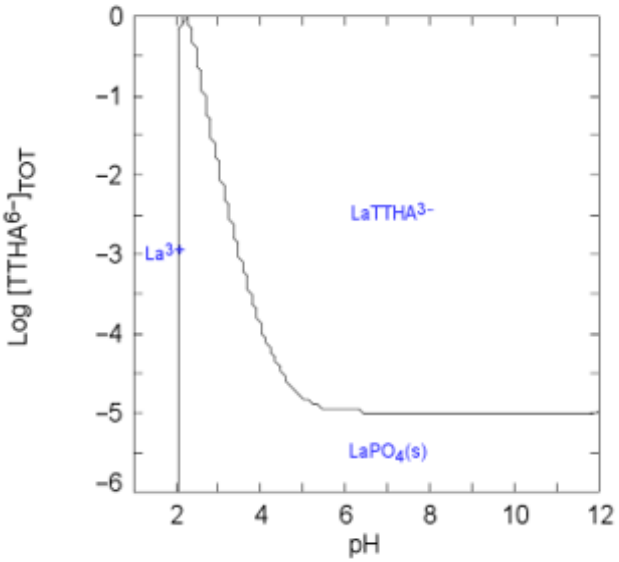

Figure 101. Stability diagram of La^{3+}- PO_4^{3-} -TTHA-H_2O system as a function of pH and concentration of TTHA, conditions: $[La^{3+}] = [PO_4^{3-}] = 10^{-5}$ M.

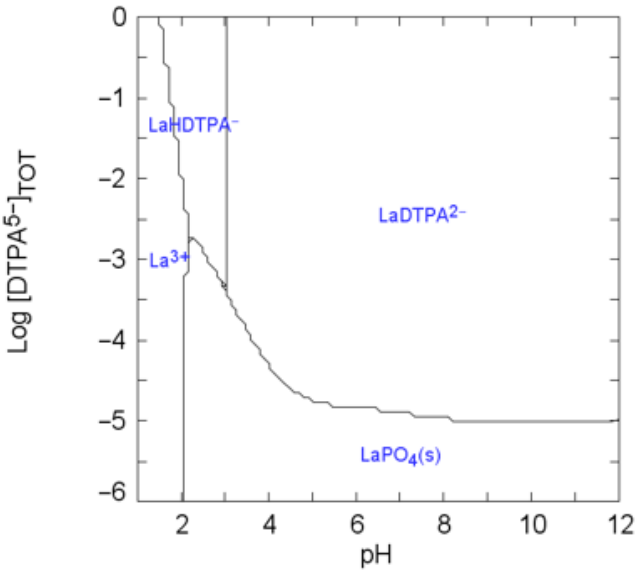

Figure 102. Stability diagram of La^{3+}- PO_4^{3-} -DTPA-H_2O system as a function of pH and concentration of DTPA, conditions: $[La^{3+}] = [PO_4^{3-}] = 10^{-5}$ M.

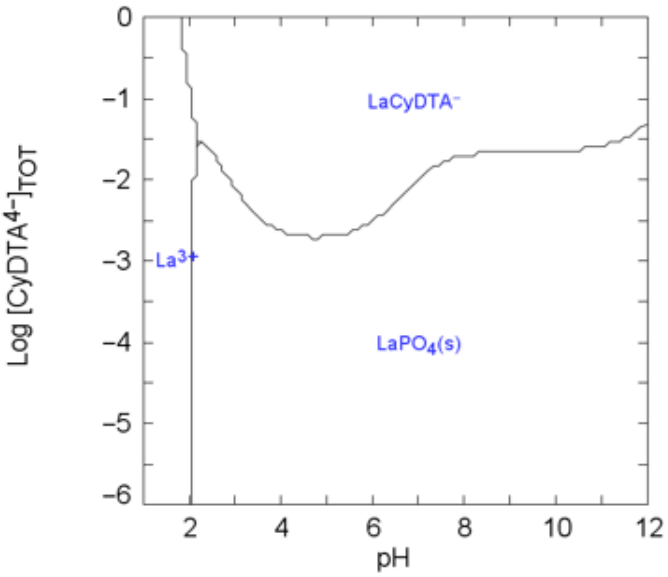

Figure 103. Stability diagram of La^{3+}- PO_4^{3-} -CyDTA-H_2O system as a function of pH and concentration of CyDTA, conditions: $[La^{3+}] = [PO_4^{3-}] = 10^{-5}$ M.

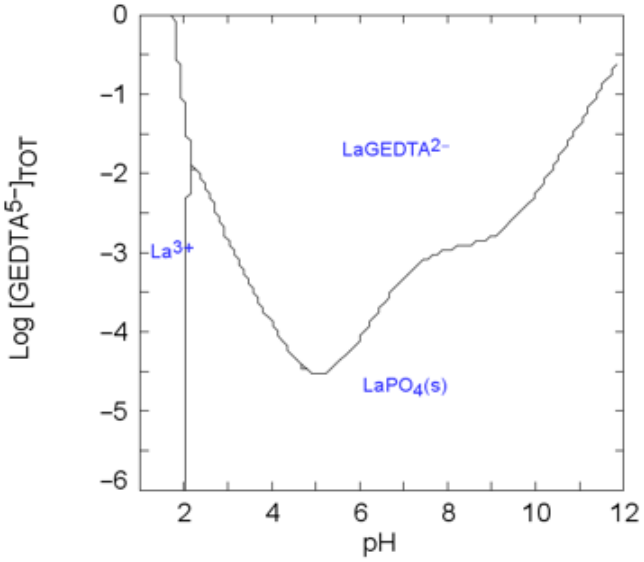

Figure 104. Stability diagram of La^{3+}- PO_4^{3-} -GEDTA-H_2O system as a function of pH and concentration of GEDTA, conditions: $[La^{3+}] = [PO_4^{3-}] = 10^{-5}$ M.

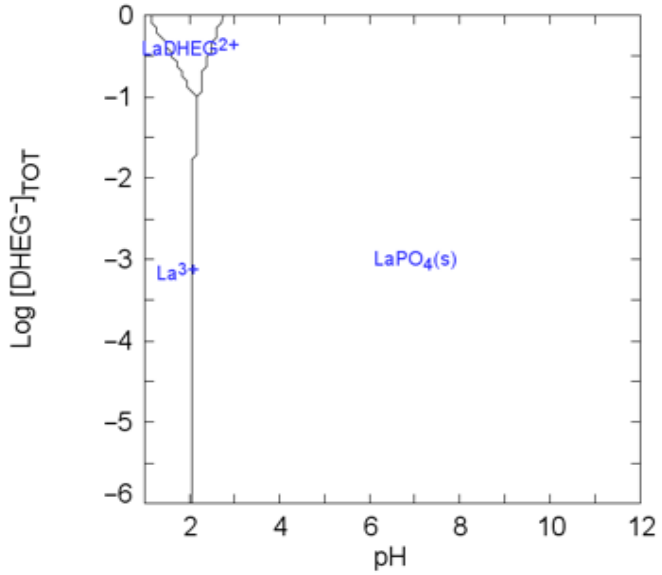

Figure 105. Stability diagram of La^{3+}- PO_4^{3-} -DHEG-H_2O system as a function of pH and concentration of DHEG, conditions: $[La^{3+}] = [PO_4^{3-}] = 10^{-5}$ M.

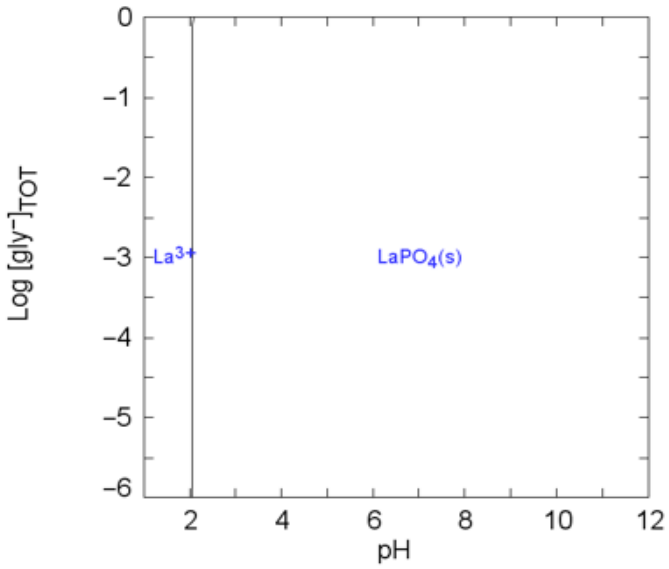

Figure 106. Stability diagram of La^{3+}- PO_4^{3-} -Gly-H_2O system as a function of pH and as a function of gly, conditions: $[La^{3+}] = [PO_4^{3-}] = 10^{-5}$ M.

Discussion

According to the Pearson's hard and soft acid base principle (HSAB), hard acids prefer to coordinate with hard bases, while soft acids preferentially complex with soft bases (Perumareddi et al., 2003). REE ions belongs to hard acids and oxygen containing ligands like carboxylic acids are hard bases. In this case, REE ions prefer to coordinate with chelating ligands.

Stability constants, also known as equilibrium constants, measure the ability of a ligand to form a complex with a mental ion. In other words, the stability constant can be used to evaluate the affinity of the metal ion for a chelating ligand. Based on Bauer's study (1996), the selection of chelating agents for solvent extraction is determined by several factors, one of them is the magnitude of the stability constants of the REEs and organic ligands that need to be selected. Generally, a higher stability constant implies stronger complexing ability of an organic ligand with metal ion. Another factor mentioned by Bauer is the solubility of the chelating agents in water system. In this study, the six organic acids studied in the present work were classified as good, medium, and poor based on the above-mentioned factors. Figure 101 and Figure 102 show two good chelating agents, with which $LaPO_4$(s) can be dissolved at a wide pH range (4-6) and at a low concentration (10^{-5} M). Two chelating agents with medium complexing ability are shown in Figure 103 and Figure 104. With these two ligands, $LaPO_4$ can be dissolved in a wide pH range but the minimum concentration of ligands is around 10^{-3} M, which is higher than that of the two good chelating agents. However, for the poor chelating agents shown in Figure 105 and Figure 106, $LaPO_4$(s) dissolves only at small regions of the stability diagrams in the presence of DHEG, and glycine has no impact on the dissolution of $LaPO_4$(s), indicating that their complexing ability is not strong enough. Therefore, TTHA and DTPA will be selected as two promising chelating agents for the REEs extraction from coal-based sources.

Synergistic Effect Development of new extractants in solvent extraction of REEs is of great importance. In addition to the single organic acids, synergistic extraction, which is a combination of two different extractants, of rare earth has been well studied (Rehman et al., 2015; Sun et al., 2006; Matsumoto et al., 2001; Reddy et al., 1999). The extraction efficiency of metal ions and chelating agents could be enhanced significantly by using two extractants. Normally, most of the synergistic systems in solvent extraction of REEs consist of acidic extractants (like diketones, carboxylic, organophosphorus acids) and neutral extractants (*e.g*. TBP, TOPO, Cyanex923, crown ethers, *etc*.). The mixture of two acidic extractants were also reported by Sun *et al*. (2006). Zabiszak investigated a new synergistic system with a combination of citric acid and polyamines for the treatment of cancer disease and determined the stability constants of lanthanum and the synergistic extractant developed. The results showed that the stability constants of lanthanum and citrate-spermine ranges from 27.20 to 61.24, which are largely higher than that in a single organic acid. Based on the stability constants reported in that study, the stability and fraction diagrams of lanthanum are shown in Figure 107 and Figure 108, respectively. As shown, $LaPO_4$(s) can be fully dissolved in acidic condition (especially when pH is less than 4.5). From the perspective of the concentration of spermine, it may be even less than the initial concentrations of La^{3+} and PO_4^{3-} ions, indicating the lower consumption of chelating agents compared with single organic acids.

Experimental Validation with Synthetically-Prepared Clays

To evaluate the impact of phosphate as a passivating ion, the research team prepared samples of purified kaolinite clay with known concentrations of exogenous anions, such as phosphate, and known concentrations of lanthanum (III) to compare the binding of lanthanum to these materials with that of unmodified clay. The samples serve as models of ion-absorption clays and will be examined by XPS and ion-exchanged using ammonium sulfate.

XPS analysis of Georgia commercially available "Kaofine" kaolinite clay samples showed that, as received, these materials had low levels of intrinsic phosphorus as phosphate (protonated at some unknown level). Attempting to increase the level of phosphate with aqueous sodium phosphate, Na_3PO_4, surprisingly removed this native phosphate without binding additional phosphate as shown in Figure 109 (blue). This experiment consisted of mechanical shaking of clay and aqueous solutions of phosphate for 24 hours,

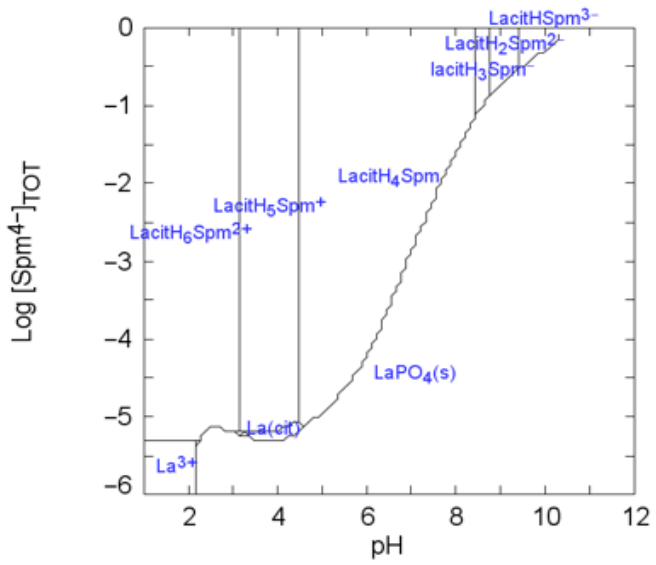

Figure 107. Stability diagram of La^{3+}-PO_4^{3-}– Citrate^{3-}- Spm^{4-}-H_2O system as a function of pH and as a function of Spm, $[La^{3+}] = [PO_4^{3-}] = 10^{-5}$ M, $[Citrate^{3-}] = 10^{-2}$ M.

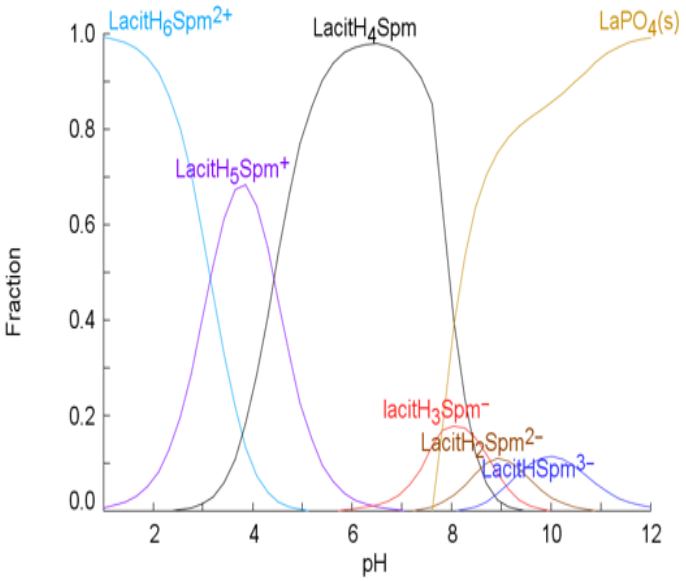

Figure 108. Fraction diagram La^{3+} in La^{3+}-PO_4^{3-}– Citrate^{3-}- Spm^{4-}-H2O system as a function of pH. $[La^{3+}] = [PO_4^{3-}] = 10^{-5}$ M, $[Citrate^{3-}] = [Spm^{4-}] = 10^{-2}$ M.

followed by washing with DI water. This result was understood to mean that sodium phosphate raises the pH substantially, making the surface of the clay more negative by deprotonation of O-H groups, which repel the phosphate, making binding unfavorable.

In contrast, adding surface phosphate as sodium dihydrogen phosphate, NaH_2PO_4, a weakly acidic form, was successful as determined by XPS (Figure 109 – green). The research team is testing this hypothesis by using sodium hydroxide to wash the as received clay to remove the native phosphate.

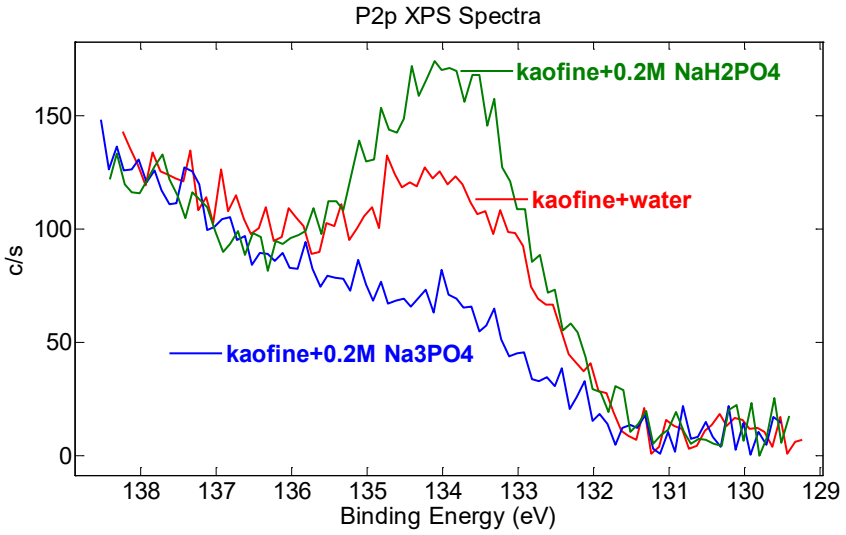

Figure 109. XPS Analysis of commercial Kaofine Kaolinite sample with and without added phosphate.

Activation and Leaching of Natural Monazite (Exploratory Study)

At present, the major sources of light REEs are the rare earth minerals (REMs) that are usually mined as carbonates (bastnaesite) and phosphates (monazite and xenotime). In industry, monazite concentrates are subjected to an acid (con. H_2SO_4) treatment at 200°C,

$$2RE(PO_4)_{(s)} + 3H_2SO_4 = RE_2(SO_4) + 6H^+ + PO_4^{3} \quad [5.2.2]$$

or to an alkali treatment at high (~73%) NaOH concentrations and high temperature (140°C),

$$RE(PO_4)_{(s)} + 3NaOH = RE(OH)_3 + 3Na^+ + PO_4^{3-} \quad [5.2.3]$$

These methods may be useful for extracting REEs from high-grade monazite concentrates with ~65% TREE but not for processing the low-grade feedstocks such as coal byproducts. The latter typically have two-orders of magnitudes lower RE grades. Processing such low-grade feedstocks using the aggressive processes will not only incur high processing costs but also generate large amounts of toxic wastes.

It may be necessary, therefore, to find ways to overcome the passivation effect of the phosphate ions and/or extracting REEs from the residual un-weathered REMs that may be present in coal byproducts. As discussed in the foregoing section, it is also possible that the REEs may be present as secondary RE-bearing phosphate minerals such as rhabdophane and carnallite. In both cases, it will be necessary to find ways to remove phosphate in a manner similar to those described by Reactions [2] and [3] above. In these regards, our research has directed toward addressing two issues, *i.e.*, extracting REEs from passivated ion-adsorption clays and extracting REEs from the residual and/or secondary phosphate minerals in a manner that is cost effective and environmentally benign. For the latter, we used a sample of cerium-monazite ($(Ce,La,Nd,Th)PO_4$) assaying 24.3% TREE. The as-received sample was ground to d_{80} = 14.61 µm and upgraded to 48.94% TREE, which was equivalent to 75.3%-pure monazite. Figure 110 and Figure 111 represent elemental and particle size distributions of the upgraded monazite sample.

In a given experiment, 0.25 g of the upgraded monazite sample was placed in a 50 ml alkaline-resistant polytetrafluoroethylene (PTFE) beaker in the presence of known amount of NaOH. The beaker was placed on a hotplate agitated at 600 rpm by means a Teflon-coated magnetic stirrer for 24 hrs. One set of measurements were conducted at 60°C and another at 80°C. The temperature was monitored within ± 1°C by means of a temperature probe. The beaker was covered by paraffin film to minimize the loss of water vapor *via* vaporization. The pretreated monazite sample was then separated from the supernatant solution by centrifugation. The solid residue left in a 50 ml centrifuge tube was agitated with 45 ml of deionized water and centrifuged again for solid/liquid separation. This rinsing step was repeated three times.

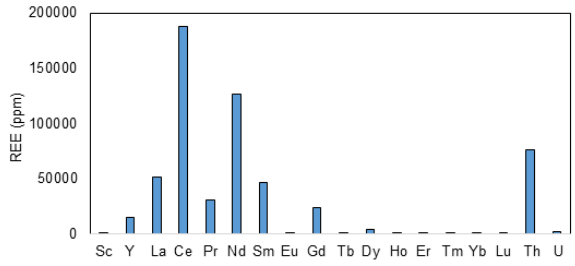

Figure 110. Individual REE distribution for upgraded monazite sample.

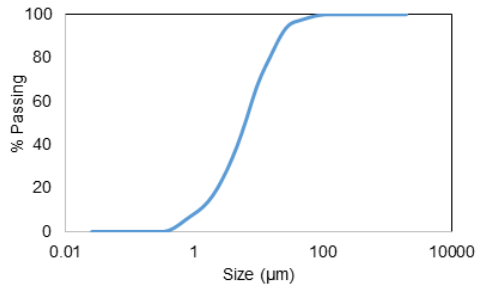

Figure 111. Particle size distribution curve for upgraded monazite sample.

Leaching Monazite Using Ammonium Sulfate Under Mild Conditions

The NaOH pretreatment may convert the natural monazite sample to rare earth hydroxide as follows,

$$RE(PO_4)(s) + 3NaOH = RE(OH)_3(s) + 3Na^{+} + PO_4^{3-} \quad [5.2.4]$$

which can be readily dissolved in a strong sulfuric acid solution at pH < 2 (Kumari *et al*., 2015). In the present work, the pretreated monazite was dissolved at pH 4 using ammonium sulfate $(NH_4)_2SO_4$ as a lixiviant. The extraction tests were carried out at room temperature, with the results presented in Figure 112 and Figure 113. Aliquots (0.5 ml) of the leach liquor were taken at regular time intervals and analyzed using the ICP-MS analysis to obtain kinetic information.

The extraction tests were conducted by varying the NaOH concentrations in the range of 10 to 50% w/v concentrations at 60 and 80ºC. As shown in Figure 112, the REE recoveries increased substantially as the NaOH concentrations were increased sequentially from 10, 30 and 50% NaOH. At 60ºC, it was necessary to increase the NaOH concentration to 50% to achieve >60% REE recovery (Figure 112). At 80ºC, it was possible to achieve 40% REE recovery at 10% NaOH (Figure 113). At 50% NaOH, it was possible to obtain >65% REE recovery at a relatively short treatment time. At longer treatment times, much higher recoveries would have been achieved. An equally important parameter would be the particle size.

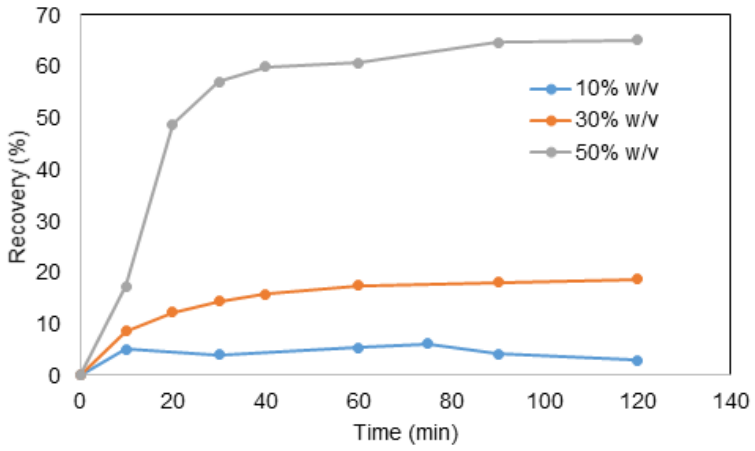

Figure 112. $(NH_4)_2SO_4$ leaching at pH 4 after NaOH pretreatment at 60 ℃ for 24 h.

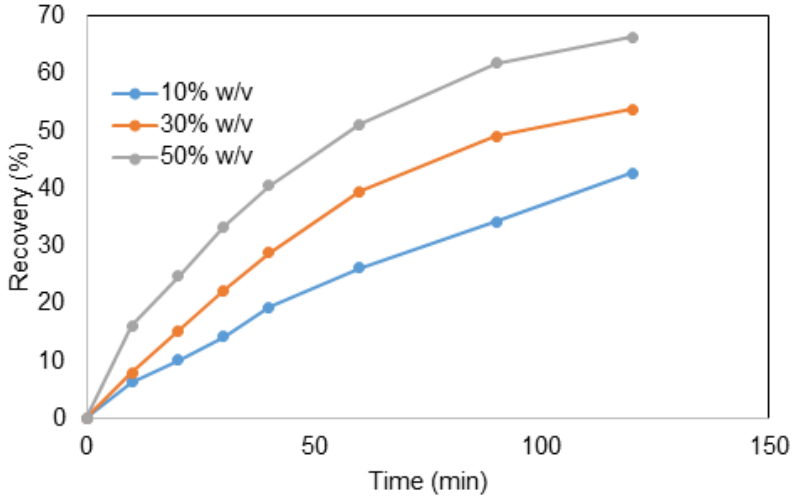

Figure 113. $(NH_4)_2SO_4$ leaching at pH 4 after NaOH pretreatment at 80 ℃ for 24 h.

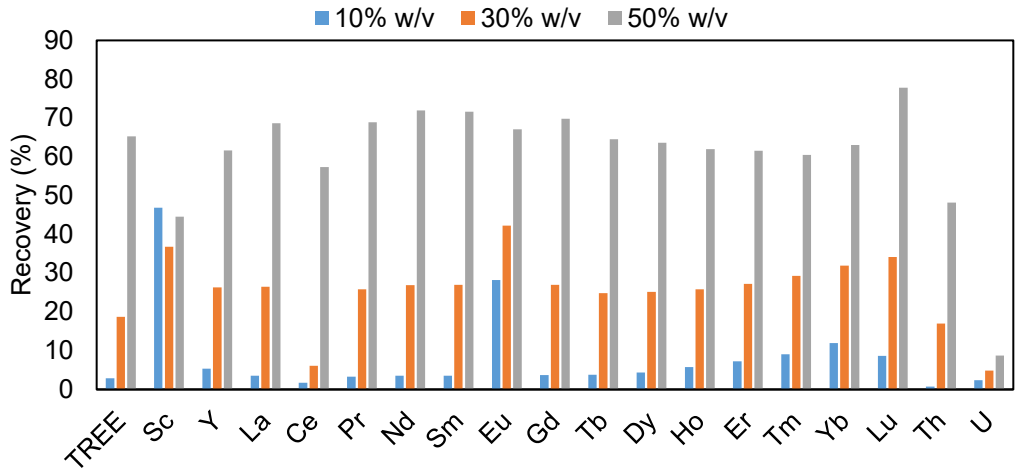

Figure 114. Rare earth distribution for $(NH_4)_2SO_4$ leaching at pH 4 after 24h NaOH pretreatment at 60 ℃

Had we used finer monazite samples for the leaching experiments, both the kinetics and ultimate recoveries would have been substantially higher. The particle size of the samples we used in the present work was larger than those used in industry.

The effects of NaOH concentration and pretreatment temperature on individual rare earth extractions are shown in Figure 114. and Figure 115 . As shown, the REE extractions are sensitive to NaOH concentration and have similar extraction levels. The recovery of Sc was ~46% (much higher than other elements) even when treated at a 10% NaOH concentration and no noticeable change was observed for 50% NaOH group except a decrease for 30% NaOH group. This finding is likely due to the fact that Sc has a different mode of occurrence as compared to the REEs in monazite, leading to different leaching behaviors. In Figure 115 , however, the recovery of Sc was zero, which is inconsistent with the results presented in Figure 114. . The possible reason can be the errors in ICP-MS analysis or small variations in feed sample.

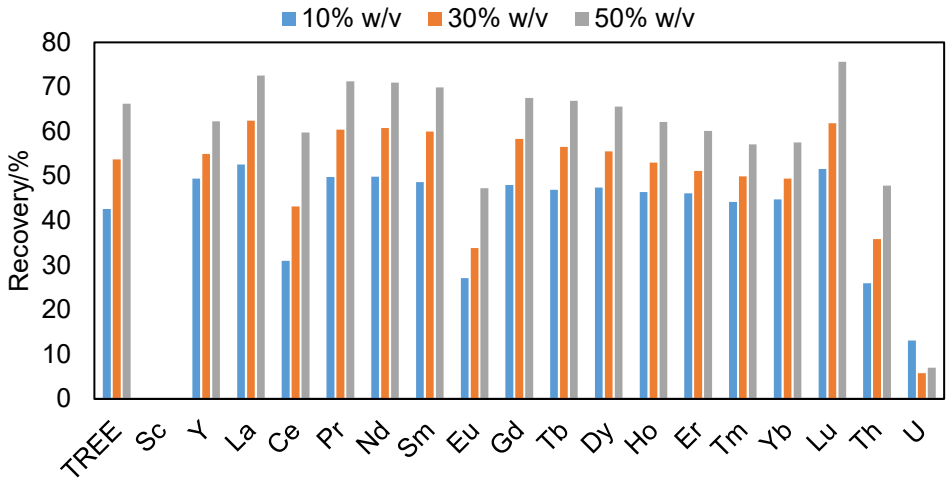

Figure 115. Rare earth distribution for $(NH_4)_2SO_4$ leaching at pH 4 after 24h NaOH pretreatment at 80 ℃

The relatively low recovery of Ce in both figures may be explained by Ce oxidation, a phenomenon that was commonly found in the dissolution of NaOH treated monazite sample by acid (Kumari *et al.*, 2019). During the NaOH pretreatment step, the Ce^{3+} ions are readily oxidized to Ce^{4+} ions and subsequently to CeO_2, which is sparingly soluble in acidic condition (Kumari *et al.*, 2019; Abreu and Morais, 2010). It has been shown that reduction of Ce (IV) to Ce (III) can increase the recovery of Ce (Kumari *et al.*, 2019).

Leaching Monazite Using Other Lixiviant Under Mild Conditions

The significance of the results presented in the foregoing Section may be that one can extract REEs from monazite under milder conditions than using the conventional processes embodied by Reactions [2] and [3]. Encouraged by the promising results obtained using ammonium sulfate, we tested another ammonium salt, *i.e.*, ammonium formate (NH_4HCO_2), with the results shown in Figure 116. Also shown in this was the results obtained with ammonium sulfate ($(NH_4)_2SO_4$) for comparison. Both tests were conducted after NaOH treatment at a 30% w/v concentration and 80°C. As shown, the former exhibited substantially faster leaching kinetics than the latter. It is possible that anions may play a significant role in leaching NaOH treated monazite. Further investigation is planned to study the effect of anions.

During the first year, we studied fundamental mechanisms of the ion-exchange leaching process u sing a series of ion-adsorption clays prepared by contacting known amount of REE ions with kaolinite, which was referred to as 'artificial' ion-adsorption clay samples. The samples were prepared at pH in the range of pH 3 to 10.5. It was found that the adsorption of REE ions increased with increasing pH, most probably as mono- or di-hydroxy species, *i.e.*, $LnOH^{2+}$ and $Ln(OH)_2^{+}$, respectively.

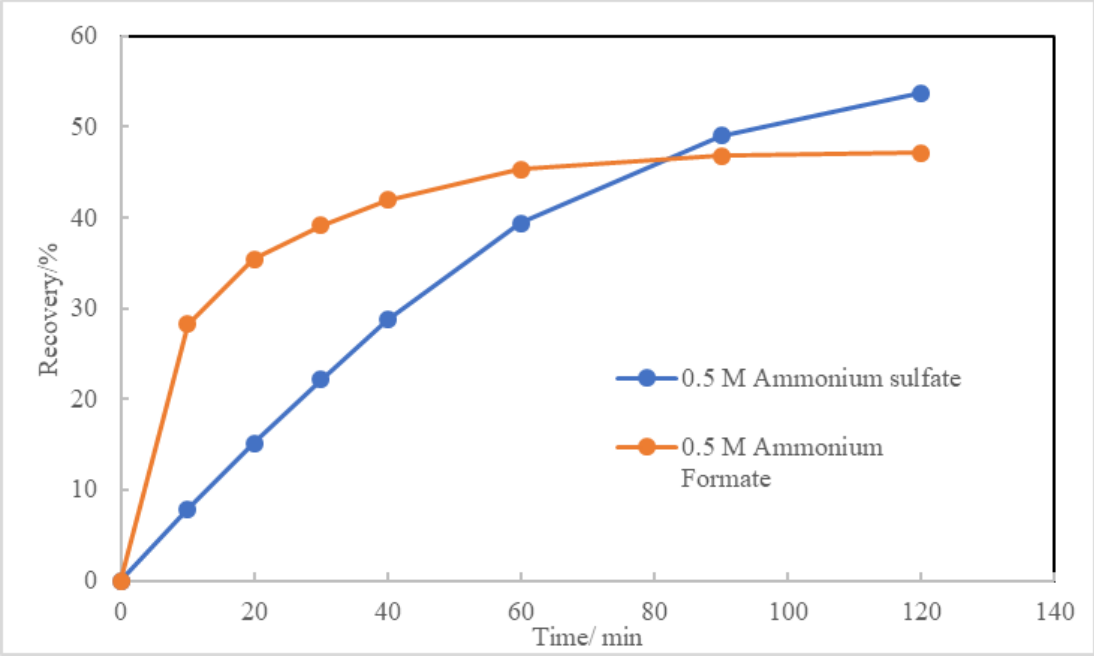

Figure 116. Effects of Using Three different lixiviants for leaching a natural monazite at pH 4 after NaOH pretreatment at 80 ℃ for 24h

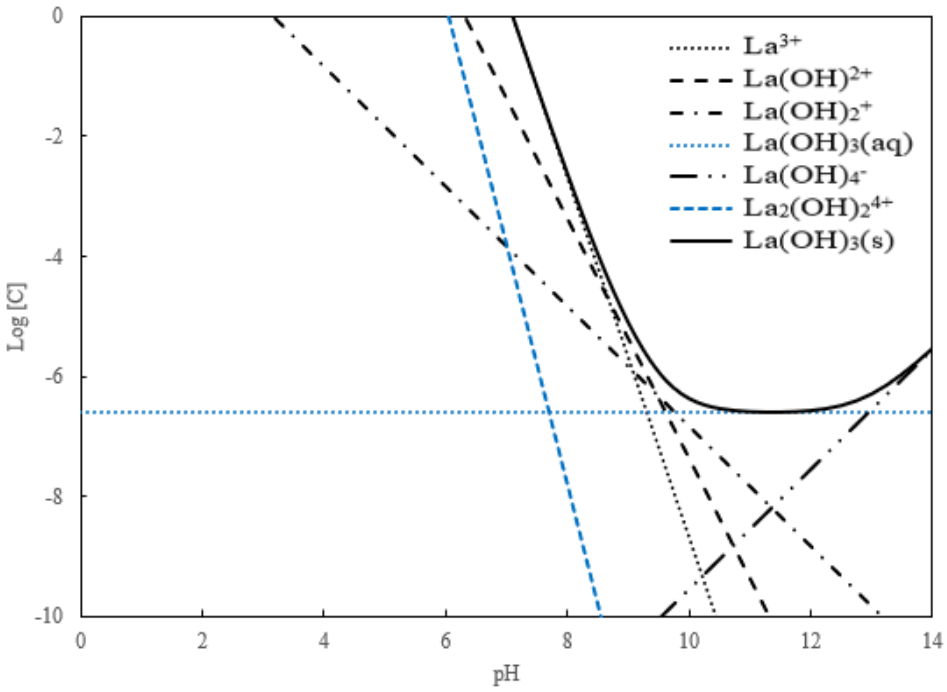

Figure 117. Solubility diagram for La(III) hydroxide in pure water at 298.15 K

The solubility diagram for lanthanum hydroxide ($La(OH)_3$) constructed in the present work and presented in Figure 117 may provide an explanation for the mechanisms involved in the leaching of NaOH-treated monazite. As shown, the solubility of the $La(OH)_3(s)$ increases sharply at pH < 10. At pH 4, where most of our ammonium sulfate leaching experiments were conducted, the hydroxide will be dissolved as La^{3+}, $LaOH_2^+$, $LaOH^{2+}$, $La2(OH)_2^{4+}$species. The role of the NH_4^+ ions may be to displace these cationic species from the surface and, thereby, facilitate the leaching kinetics. As is well known, the heat of hydration of the NH_4^+ ions (322 kJ/mol) is less than that of the La^{3+} ions (3285 kJ/mol), which explains why the former displaces the latter from the surface of the ion-exchange clays. At this point in time, we do not have the values of the heats of hydration of the various lanthanum hydroxo-complexes. The Eh-pH diagram given in Figure 118 also shows that $La(OH)_3(s)$ should dissolve at pH < 10. Why it is necessary to use a lixiviant at all is not clearly understood at this point in time. Regardless of the reasons, work is continuing to better understand the mechanism while testing a variety of different lixiviants for the dissolution of $Ln(OH)_3$ *via* the ion-exchange mechanism discussed above.

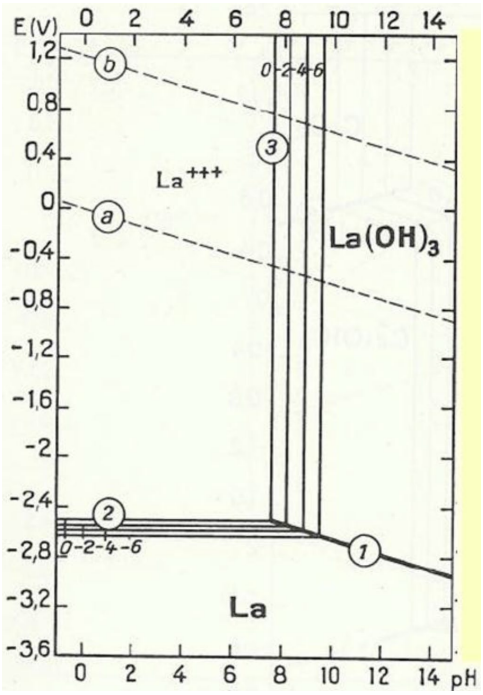

Figure 118. Eh-pH diagram of Lanthanum in water at 25°C (Garnier, 2013).

Activation and Leaching of Natural Monazite (Detailed Study)

Sample preparation and experimental procedure

A Ce-type monazite ((Ce, La, Nd, Th) PO_4) sample assaying 24.3% total REE (TREE) content was used for all the experimental work. The REE contents of the samples were determined using the lithium tetraborate fusion method with the addition of Na_2CO_3 to enhance the dissolution of monazite at 1000°C. The as-received sample was ground initially to d_{80} = 14.61 µm using a motor-driven mortar-and-pestle grinder (Mahendra Automatic Agate Mortar Pestle). To mitigate the impact of impure elements (undesired components), *e.g.*, Fe, Si, Al, *etc*., on the extraction tests, the as-received sample was upgraded by multiple stages of flotation to 48.9% TREE, which was equivalent to a 75.3%-pure monazite sample. Table 38 shows the elemental composition of the upgraded monazite sample.

Most of the experimental work was conducted on the upgraded monazite sample after grinding it d_{80} = 14.6 µm to establish the optimal chemical conditions for the extraction of REEs by the ion-exchange leaching process being developed in the present work. Part of the sample was further ground to d_{80} = 6.99 µm to study the effect of particle size on extraction kinetics and REE recovery. Figure 119 shows the particle size distributions of the two micronized monazite samples.

A 50% w/v sodium hydroxide solution was used for the NaOH pretreatment step. Acids of trace metals grade were purchased from Fisher Scientific. All other chemicals and regents used in this study were of analytical grade. Deionized water with a resistivity of 18.2 MΩ·cm at 298.15 K was used for all solution preparations and leaching tests.

NaOH pretreatment

In a given NaOH pretreatment step, 0.5 g of the upgraded monazite sample (48.9% TREE) was placed in a 50 ml alkaline-resistant polytetrafluoroethylene (PTFE) beaker at a solid concentration of 25 g/L. The beaker was placed on a hotplate (Super-Nuova Multi-place Stirrer and Stirring Hot plates), and agitated at 600 rpm *via* a Teflon-coated magnetic stirrer for 24 hrs. One set of measurements were conducted at 60°C and another at 80°C. The temperature was monitored within ±1°C by means of a temperature probe. During the entire NaOH pretreatment step, the beaker was covered by paraffin film to minimize the loss of water vapor through vaporization. The loss of water *via* evaporation was less than 1.0 ml in each

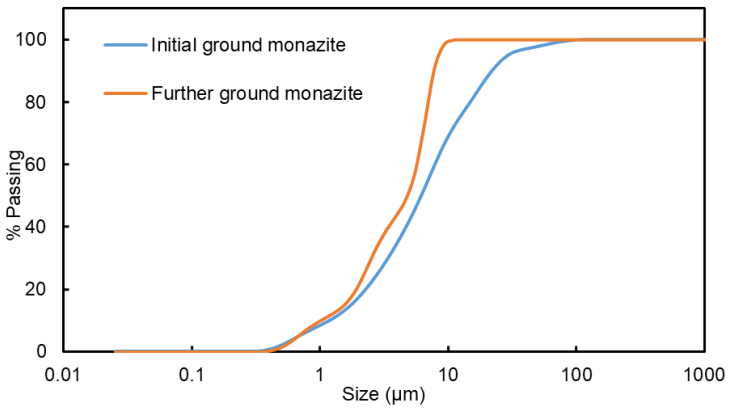

Figure 119. Particle size distribution curve for upgraded monazite sample.

Table 38. Elemental composition of the upgraded monazite sample

Element	Grade (wt%)
Ce	18.80
Nd	12.68
La	5.18
Sm	4.68
Pr	3.06
Gd	2.38
Y	1.49
P	9.57
Total Other REEs	0.66

experiment. At the end of an NaOH pretreatment step, the sample slurry was subjected to solid-liquid separation by centrifugation at 5,000 rpm for 10 mins. The solid residue in a 50 mL centrifuge vial was washed with a volume of deionized water and centrifuged again. This rinsing step was repeated three times. The amounts of REE ions dissolving during the NaOH pretreatment step is much smaller than those extracted during the ensuing ion-exchange step.

Extraction tests

The leaching tests were carried out at room temperature as a function of lixiviants. An NaOH-treated monazite sample was washed into a 50 ml beaker (disposable polypropylene) using 40 ml of a lixiviant solution. The solid content of the sample in the beaker was 12.5g/L. The sample suspension was agitated magnetically by means of a magnetic stirring bar for 120 min. The pH of the sample suspension was maintained at 4 (±0.1) by adding small drops of HCl and NaOH solutions while monitoring the pH continuously. Small volumes (0.4 ml) of the sample suspension were taken from the leaching solution by means of disposable syringes at regular intervals analyzed for REE concentrations. When a leaching experiment was finished, the leachate was diluted 2000 times in an acidic solution (2.5% HNO_3 and 0.5% HCl) for analysis by using an Inductively Coupled Plasma Mass Spectrometry (ICP-MS). The REE recovery (extraction efficiency) was calculated using the formula below,

$$Recovery\ (\%) = 100\ \times \frac{c_l \cdot v}{c_f \cdot m} \qquad [5.2.4.]$$

where c_l and c_f is the REE assays of leaching liquor and feed sample respectively, m is the feed mass, v is the volume of the leaching liquor.

Zeta potential measurement

Zeta (ζ) potential measurements were performed to better understand the mechanism of $(NH_4)_2SO_4$ leaching. The measurements were conducted using a Zs90 Zeta Spectrometer (Nano series, Malvern Instruments, UK). The ζ-potentials of monazite (initial sample), NaOH-treated monazite, NaOH-treated monazite in the presence of water or 0.5 M $(NH_4)_2SO_4$ solution at pH 4 and 25ºC were measured. The measurement was also conducted after adding a predetermined amount of $(NH_4)_2SO_4$ into a monazite suspension at pH 6. In each measurement, 0.05 g sample was mixed with 40 ml deionized water and the slurry was agitated by means of a magnetic stirring bar. Once the pH reached the desired values, 1 ml slurry was sampled for zeta potential measurements. At given pH the ζ-potentials were measured three times and averaged.

X-ray diffraction (XRD) Characterization

To characterize the mineralogical changes of monazite during NaOH pretreatment and leaching steps, the initial ground monazite, NaOH treated monazite, and NaOH-treated monazite, and $(NH_4)_2SO_4$-treated monazite samples were subjected to XRD analyses. The latter two samples were dried in an oven overnight at 60 °C. The XRD analyses were performed using a Rigaku Miniflex 600 instrument with Cu-K-α radiation (λ = 1.54 Å). The XRD spectra were recorded over a 2θ range of 10° to 80° with a step size of 0.04° and a dwell time of 2 seconds.

X-ray photoelectron spectroscopy (XPS) Characterization

The monazite samples were also subjected to XPS characterization to investigate the variations of chemical state of Ce during the NaOH pretreatment and leaching steps. The samples and sample preparation method for XPS measurements were the same as those for the XRD analyses. A PHI VersaProbe III scanning XPS microscope, which was equipped with a monochromatic Al K-α X-ray source (1486.6 eV) with a base pressure of 3×10^{-8} Pa. As for the spectra, they were acquired over a 1,400 µm×00 µm with the settings of 100 µm/100 W/20 kV. Adventitious carbon peak at 248.8 eV was used as a reference for all binding energies.

Table 39. Reactions and corresponding stability constants used for solubility diagram construction

Reactions	Stability constants	ΔG^o (kJ/mol)
$La(OH)_3(s) = La^{3+} + OH^-$	$10^{-21.22}$	121.12
$La(OH)^{+2} = La^{3+} + OH^-$	$10^{-4.83}$	27.57
$La(OH)_2^+ = La^{3+} + 2OH^-$	$10^{-9.86}$	56.28
$La(OH)_3(aq) = La^{3+} + 3OH^-$	$10^{-14.09}$	80.42
$La_2(OH)_2^{4+} = 2La^{3+} + 2OH^-$	$10^{-9.59}$	54.71
$La(OH)_4^- = La^{3+} + 4OH^-$	$10^{-15.14}$	86.13
$La^{3+} + Citrate^{3-} = La\text{-}Citrate(aq)$	$10^{10.82}$	-61.76
$La^{3+} + DTPA^{5-} = La\text{-}DTPA^{-2}$	$10^{19.48}$	-111.19

(Data sources: MINEQL+ 5.0 and HSC 10 thermodynamic database)

Construction of Solubility diagram

Solubility diagrams for La(III) hydroxide both in pure water was constructed to better understand the mechanisms involved in the ion-exchange leaching of NaOH-treated monazite. By constructing such diagrams, the concentrations of each different species at different pHs can be seen graphically. Table 39 shows the reactions involved in the solubilization of the $La(OH)_3(s)$, which represents one of the lanthanum hydroxides formed on the surface of monazite after the NaOH pretreatment step.

Results of ion-exchange leaching tests conducted on natural monazite

Effect of NaOH concentration on recovery

The extraction tests were conducted by varying the NaOH concentrations in the range of 10 to 50% and temperatures in the range of 60 to 80°C. As shown in Figure 120, the REE recoveries increased substantially as the NaOH concentrations were increased from 10, 30, and 50%. At 60°C, more than 50% REEs were recovered at 50% NaOH. At 80°C, the recovery was increased from 21 to 60% as the NaOH concentration was increased from 30 to 50%. These results suggest that of the two process variables, i.e., NaOH concentration and temperature, the former is more important than the latter. Panda *et al*. (2014) showed that the concentration of PO_4^{3-} ions in solution increases sharply at NaOH concentrations above ~40% at 150°C. The release of phosphor into solution may be an indicator for monazite cracking, which is a prerequisite for monazite leaching.

The process of extracting REEs from monazite has been in industry for the past 60 years so so without major changes. In general, finely ground monazite is cracked in 60-70% NaOH solutions at 140-150°C to form insoluble REE hydroxide, followed by an acid leaching in HCl, HNO_3, H_2SO_4 to prepare REE solutions for solvent extraction (Krishinamurthy and Gupta, 2016; Qi, 2018; Zhang and Zhao, 2016). It is common to use 1 to 6 N NaCl and HNO_3 for the acid leaching (Kumari *et al*., 2014; Zhang and Lincoln, 1994). It has been reported that an increase in NaOH concentration from 50 to 60% at 140°C reduced the reaction time from 5 to 1 hr, resulting in a substantial savings in NaOH consumption (Zhang and Zhao, 2016). Also, much of the spent NaOH can be recycled (Qi, 2018) after a simple solid-liquid separation.

Figure 121 shows the XRD spectra of the monazite sample before and after the NaOH pretreatment as well as the spectrum of the residue left after the ion-exchange leaching using $(NH_4)_2SO_4$ as a lixiviant. The results show that monazite had been converted to rare earth hydroxide after the NaOH pretreatment. After the $(NH_4)_2SO_4$ leaching, most of the hydroxide formed on the monazite surface was removed, leaving unreacted monazite as a residue.

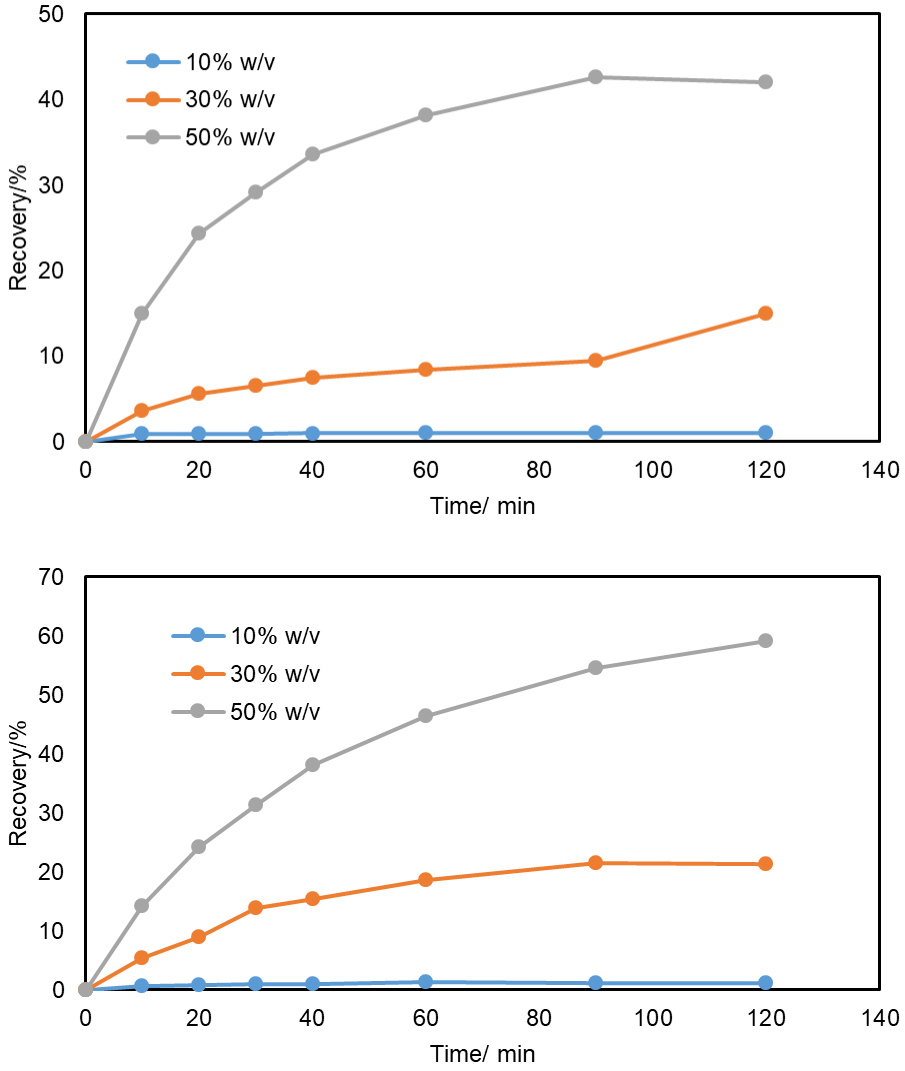

Figure 120. Ion-exchange leaching of monazite using $(NH_4)_2SO_4$ as lixiviant at pH 4 after NaOH pretreatment at 60 (top) and 80 (bottom) ℃ for 24 hrs.

Figure 122 shows the element-by-element recoveries of REEs from the monazite after pretreating the mineral concentrate at 10 and 30% NaOH, followed by the ammonium sulfate leaching at 60 and 80°C for 2 hrs. The results show that the ion-exchange leaching process developed in the process is good for extracting heavy rare earth elements (HREEs), which is an advantage of using the novel process. Note also that the recoveries of Ce and U are low. The low U recovery is a distinct advantage from an environmental point of view. The low Ce recovery may be attributed to the possibility that Ce^{3+} is oxidized to Ce^{4+} during the NaOH pretreatment step. As is well known, Ce^{4+} ions form CeO_2, which cannot be extracted by an ion-exchange mechanism, which works for free ions.

The relatively low Ce recovery in Figure 122 can be explained by oxidation, a phenomenon that has been recognized in the dissolution of alkali-treated monazite samples by acid (Kumari *et al*. 2019). The oxidation mechanism can be expressed in by Zhang *et al*., 1998).

$$4Ce(OH)_3 + O_2 + 2(2n-3)H_2O = 4CeO_2 \bullet nH_2O \qquad [5.2.5]$$

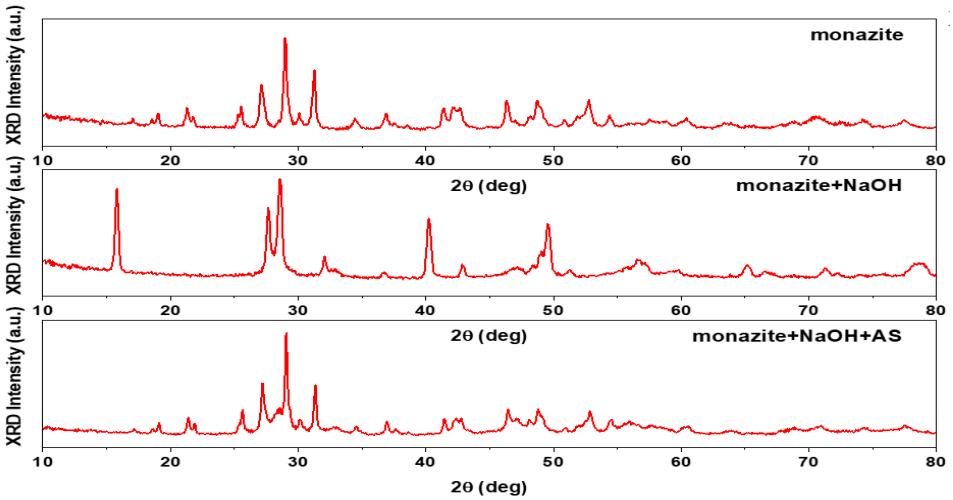

Figure 121. XRD spectra of i) monazite, ii) monazite pretreated in a 30% NaOH solution at 80°C for 24 hrs, and iii) of the leach residue.

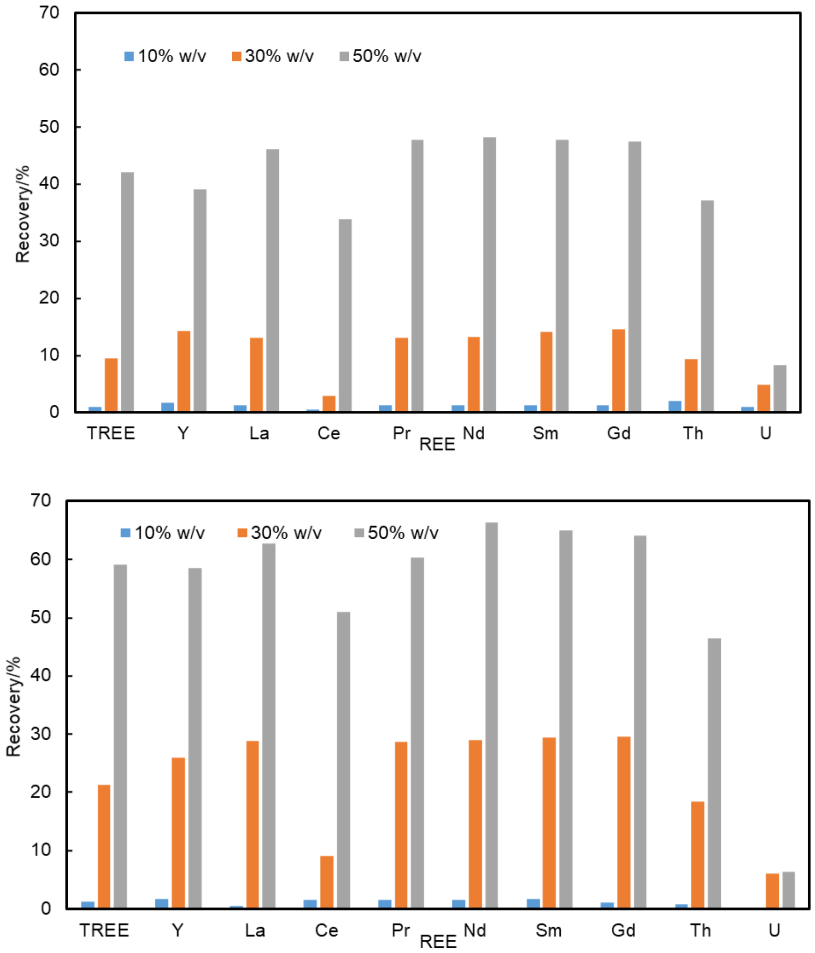

Figure 122. Element-by-element recovery of REEs for the $(NH_4)_2SO_4$ leaching of monazite at pH 4 after the pretreatments in NaOH solutions at 60 (top) and 80°C (bottom) for 24 hrs.

Li *et al*. (2017) reported that Ce (VI) is difficult to be extracted at an ambient temperature, and decent Ce recoveries can only be achieved under aggressive conditions (*e.g*., high temperatures and high acid concentrations). This explanation is well supported by the Ce3d XPS spectra of our test samples (same as those used in the XRD analyses) presented in Figure 123. The oxidation state of Ce in the feed monazite sample was Ce (III) and no Ce^{4+} satellite peak (916.3 eV) was observed, suggesting that Ce is associated in monazite crystals. A noticeable Ce^{4+} satellite peak was found in both the XPS spectra of the NaOH-treated monazite sample and the leaching residue. It indicates that Ce (III) was oxidized during processing. So, during the NaOH pretreatment step, part of the $Ce(OH)_3$ was oxidized to Ce(VI) by the oxygens present in the alkaline solution and became CeO_2, which is sparingly soluble in weakly acidic condition (Kumari *et al*., 2019; Abreu *et al*., 20108). It appears that only part of the Ce in the hydroxide cake has been oxidized to Ce(IV) in a sense that bulk of the Ce has been recovered particularly when the mineral sample was pretreated at 50% NaOH and 80°C. Under these conditions, the hydroxide layer may be thick; therefore, only the elements close to the surface have been expose to oxygen.

Effect of particle size on recovery

Other than the NaOH concentration and reaction temperature, particle size is another important process variable that can be controlled to further improve the process of extracting rare earth from monazite by leaching. In industry, monazite concentrates are micronized before NaOH treatment. Figure 124 compares the extraction tests conducted on monazite particles with d_{80} = 14.61 µm and d_{80} = 6.99 µm. The tests were conducted by varying the NaOH concentrations in the range of 10-50% at 80°C for 24 hrs. As expected, the REE recoveries increased substantially by decreasing the particle size. The largest improvements were observed at 30% NaOH, with the recoveries being doubled by reducing the particle size to below 10 µm. At 50% NaOH, the REE recovery reached ~80%, which represented ~10% increase.

Figure 125 shows the element-by-element recoveries plotted for the test conducted on the monazite sample that was ground to d_{80} = 6.99 µm, pretreated in a 50% NaOH solution at 80°C for 24 hrs, and was leached in a 0.5 M $(NH_4)_2SO_4$ solution of pH 4 for 2 hrs at room temperature. The overall recovery of TREEs was 80%. Note the recoveries of La, Pr, and Nd were over 80%, while the recoveries of Sm and Gd were close to 80%.

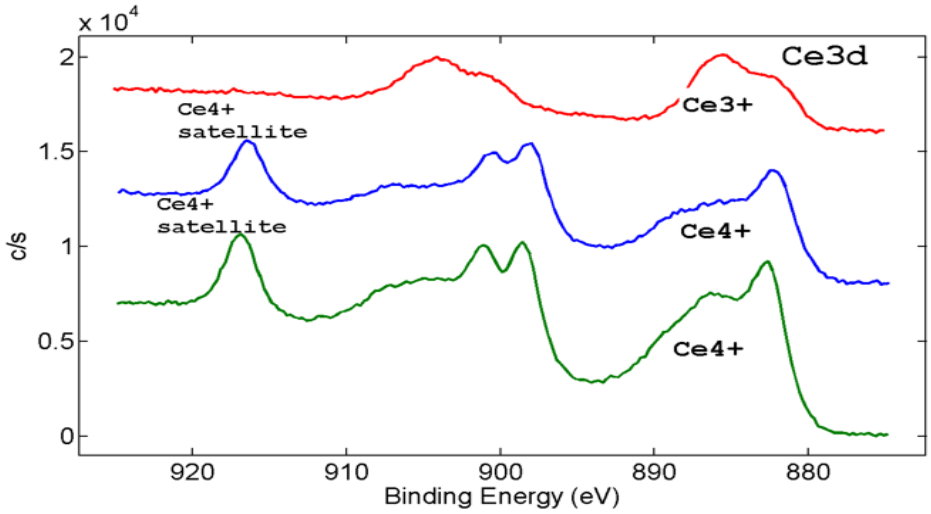

Figure 123. Ce3d XPS spectra of feed monazite (red line), NaOH-treated monazite (blue line, treated by 30% NaOH, 80°C, 24 h), and leaching residue (green line).

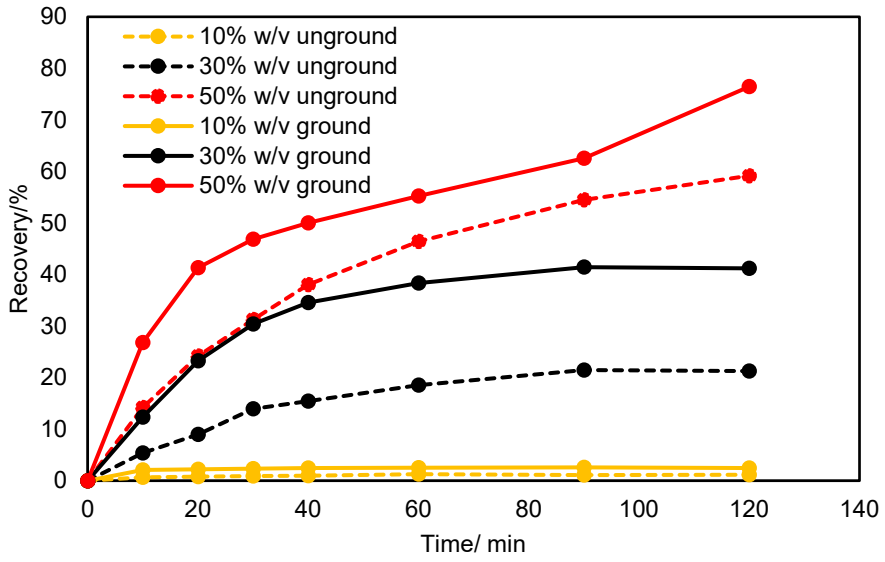

Figure 124. Effects of grinding on the $(NH_4)_2SO_4$ leaching of monazite at pH 4. A monazite sample with d_{80} = 14.6 µm was further ground to d_{80} = 6.99 µm before NaOH pretreatment in 10-50% NaOH solutions at 80°C for 24 hrs.

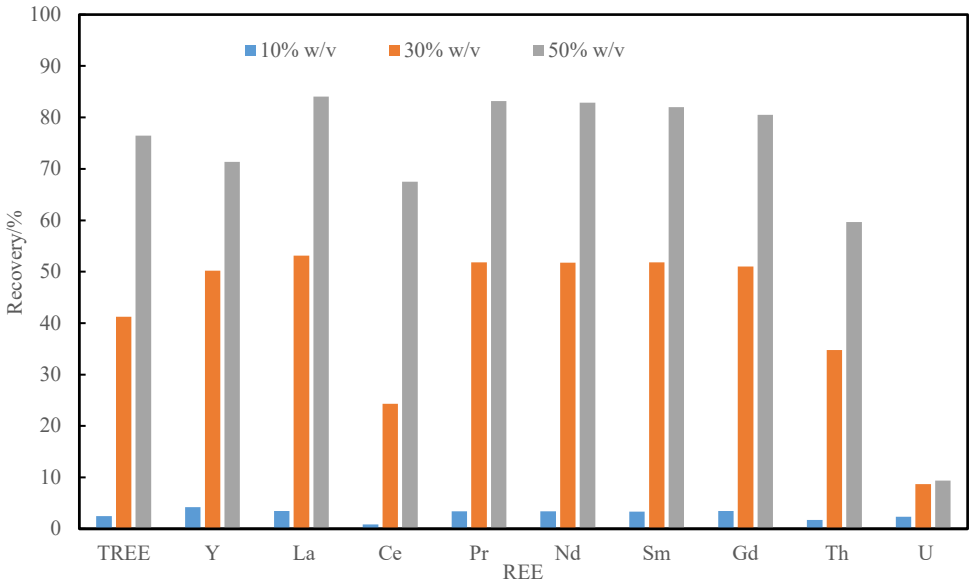

Figure 125. Element-by-element recovery of REEs for the $(NH_4)_2SO_4$ leaching of monazite of d_{80} = 6.99 µm at pH 4 after treating the mineral in 10-50% NaOH solutions for 24 hrs at 80°C.

Comparison between ammonium sulfate and acid leaching

Monazite is a stable compound formed between strong acids (Ln^{3+}) and a strong base (PO_4^{3}). Therefore, it takes a stronger base to displace the phosphate from the mineral lattice, a process known as "alkaline cracking." It happens that the OH^- ions, whose $pK_b = 0$, are stronger base than the PO_4^{3-} ions whose $pK_b = 1.7$. In industry, the $Ln(OH)_3$ formed by the NaOH treatment is dissolved in acid solutions, while in the present work we use $(NH_4)_2SO_4$ as lixiviant.

Figure 126 compares the results obtained using the two different methods of dissolving the $Ln(OH)_3$ residue, which was formed by dissolving the unground monazite with $d_{80} = 14.61$ µm in 30 and 50% NaOH solutions for 12 hrs at 80ºC. Also, the results obtained at the higher NaOH concentration performed better. On the other hand, the differences between the two different methods become less significant when the results are compared on the basis of the element-by-element recoveries shown in Figure 127. This observation may be attributed to the likelihood that $Ce(OH)_2$ is more readily dissolved in 6M HCl than in the 0.5M $(NH_4)_2SO_4$. The monazite sample we used for the extraction tests was essentially a cerium monazite, meaning that Ce was the dominant lanthanide.

Note also that the recoveries of the major REEs, *e.g.*, La, Pr, Nd, Sm and Gd, were ~76%, while those obtained with the micronized monazite using $(NH_4)_2SO_4$ as lixiviant were ~80% (see Figure 125). Thus, the ammonium sulfate leaching was actually better than the acid leaching when the mineral was micronized to $d_{80} = 7.6$ prior to the NaOH pretreatment step. A problem associated with the acid leaching in general is the production of excessive waste water containing high concentrations of various toxic elements.

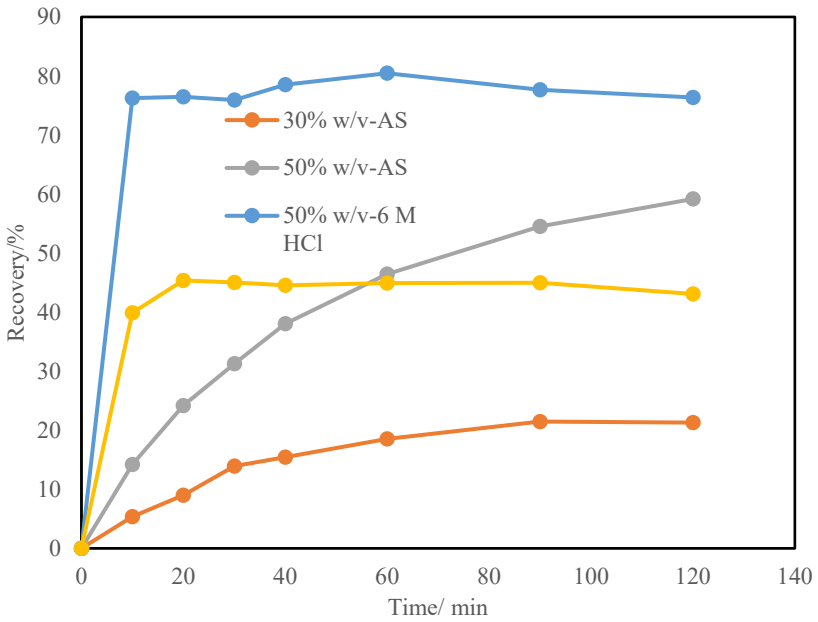

Figure 126. Comparison between extracting REEs from the NaOH treated monazite i) by ion-exchange leaching using 0.5 M $(NH_4)_2SO_4$ at pH 4 and ii) by acid leaching in a 6 M HCl solution.

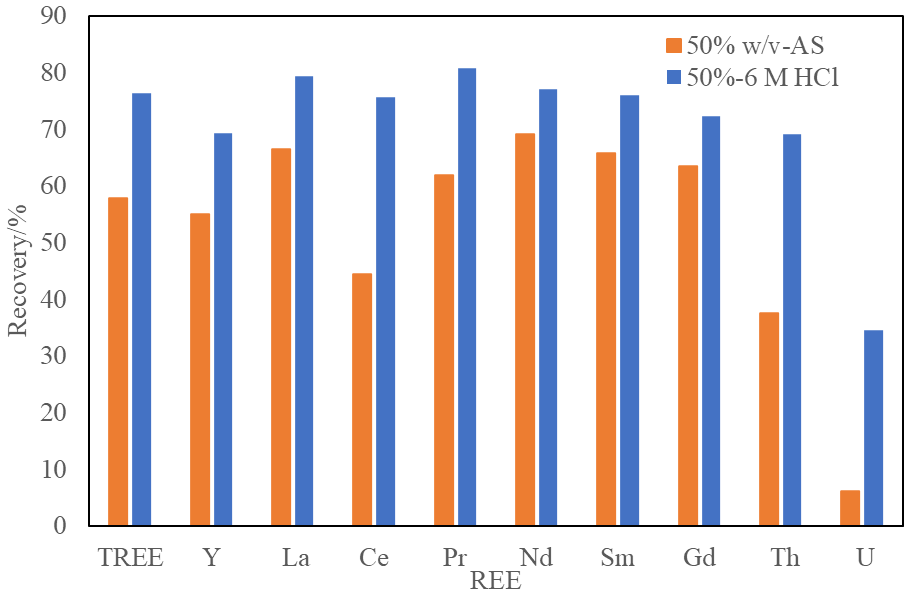

Figure 127. Element-by-element REE recoveries in the 0.5M $(NH_4)_2SO_4$ and 6M HCl leaching of monazite (d_{80} = 14.6 µm) pretreated in 50% NaOH solutions at 80°C for 12 hrs.

Comparison between Natural and Artificial Monazite Samples

Figure 128 shows the results obtained with a pure $LaPO_4$(s) sample obtained from Fisher Scientific. Its d_{80} particle size was 6.8 µm as received. The sample was pretreated in 10, 30, and 50% NaOH solutions at 80°C for 24 hrs before being subjected to ion-exchange leaching in a 0.5 M $(NH_4)_2SO_4$ solution for 2 hrs at ambient temperatures. As discussed in the foregoing sections, the REE recoveries from the pure $LaPO_4$(s) were considerably higher than those obtained with the natural monazite samples with d_{80} = 14.61 and 6.99 µm.

The most noticeable difference between the artificial and natural monazite samples was that the kinetics of leaching was much faster with the former. One possible explanation may be that the bond energy of the $LaPO_4$(s) is lower than those of natural monazite due to the presence of heavy REEs in the latter. It has been shown that rhabdophanes and hydrated rare earth phosphates varied with ionic radii of the cations (Sheylug *et al*., 2018).

The fact that the pure $LaPO_4$(s) (artificial monazite) dissolves more readily well and its kinetics is faster is an encouraging sign that we can eventually find ways to do the same with natural monazite.

Mechanisms of ammonium sulfate leaching of NaOH treated monazite

Ion-Exchange Leaching The results presented heretofore showed that $(NH_4)_2SO_4$ can be used as a lixiviant for the $Ln(OH)_3$ formed on the surface of NaOH-treated monazite. The new process can potentially substitute the traditional acid leaching, which is costly and can create toxic wastes. Its kinetics may to be slower than the acid leaching as shown in Figure 126. It is possible, however, to improve the kinetics by understanding the role of ammonium sulfate as a lixiviant.

As is well known, ammonium sulfate is used as a lixiviant for the ion-exchange leaching of the ion-adsorption clays mined in South China. The mechanism may be explained as flows:

$$\text{Clay-}Ln^{3+} + 3NH_4^+ \rightarrow \text{Clay-}3NH_4^+ + Ln^{3+} \qquad [5.2.6]$$

in which one mole of Ln^{3+} ions are displaced by three moles of ammonium ions. The kinetics is fast, which is generally attributed to the simple ion-exchange mechanism. It is generally believed that the Ln^{3+} ions are adsorbed on the basal surface of clay minerals by the weak coulombic attraction; therefore, they can be

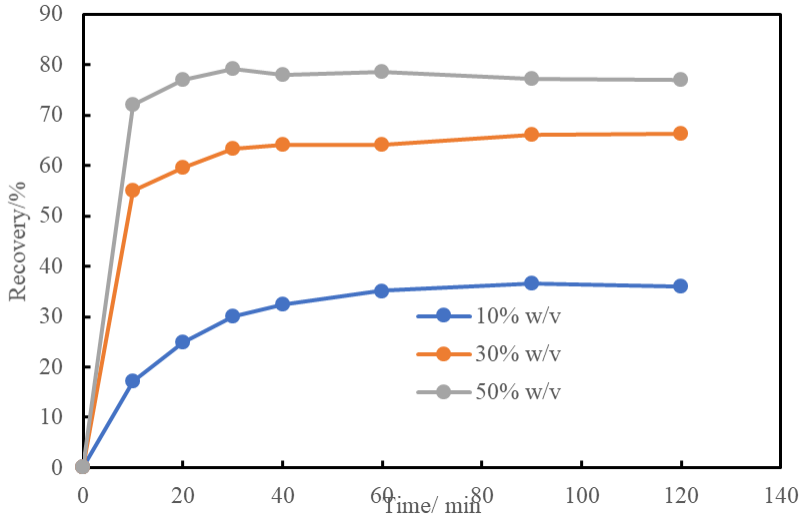

Figure 128. Ammonium sulfate leaching of an artificial monazite (pure $LaPO_4$) at pH 4 after the NaOH pretreatment at 80°C. The artificial sample responded better than the natural monazite.

substituted by the ammonium ions that are weakly hydrated in solution than the lanthanum ions. Borst *et al*. (2020) confirmed that Y^{3+} and Nd^{3+} ions are present on the surface of kaolinite as free ions with 8-9 outer-layer hydrated water molecules. However, some of the Ln^{3+} ions are adsorbed as hydroxo-complexes, in which case the ion-exchange leaching becomes difficult. The Ln^{3+} ions adsorbed in this manner is referred to as 'colloidal form of REEs.

Since we are using the same reagent, *i.e*., NH_4^+ ions, for the extraction of Ln^{3+} ions from the NaOH-treated monazite, it may be reasonable to assume that the extraction mechanism may be the same, *i.e*., ion-exchange leaching. The solubility diagram for the $La(OH)_3$, shown in Figure 129, may show the concentrations of La-bearing species present on the surface of the $Ln(OH)_3(s)$ formed after NaOH treatment of monazite. It shows that the concentration of the free La^{3+} ions is higher than those of any other La-bearing cations at pH 4. It would, therefore, be reasonable to assume that La^{3+} ions adsorb on the surface of La(OH)(s) in the same manner as they would on clay and be subjected to an ion-exchange leaching as follows,

$$La(OH)_3(s)\text{-}La^{3+} + 3NH_4^+ \rightarrow La(OH)_3\text{-}3NH_4^+ + La^{3+} \qquad [5.2.7]$$

which is akin to Reaction [3]. The driving force for the leaching mechanism is the difference in the enthalpy of hydration (ΔH_{hyd}) between La^{3+} and NH_4^+ions, *i.e*., -3,285 and -322 kJ/mole, respectively (Moldovenau and Papangelakis, 2012). Thus, La^{3+} ions have a higher propensity to stay in water than NH_4^+ ions do.

One difference between the two different mechanisms is that the NH_4^+ ions are consumed *via* adsorption in processing ion-adsorption clays (Reaction [3]), while the lixiviant is released back into solution as the La^{3+} ions are released into solution. Once released, Reaction [4] repeats itself with another set of La^{3+} ions adsorbed on the fresh surface of $La(OH)_3(s)$ below. The leaching mechanism is akin to the shrinking core model of leaching.

One of the major concerns associated with the leaching ion-adsorption clays (Reaction [3]) is the high reagent consumption, which arises from the facts that three moles of NH_4^+ ions are consumed for each

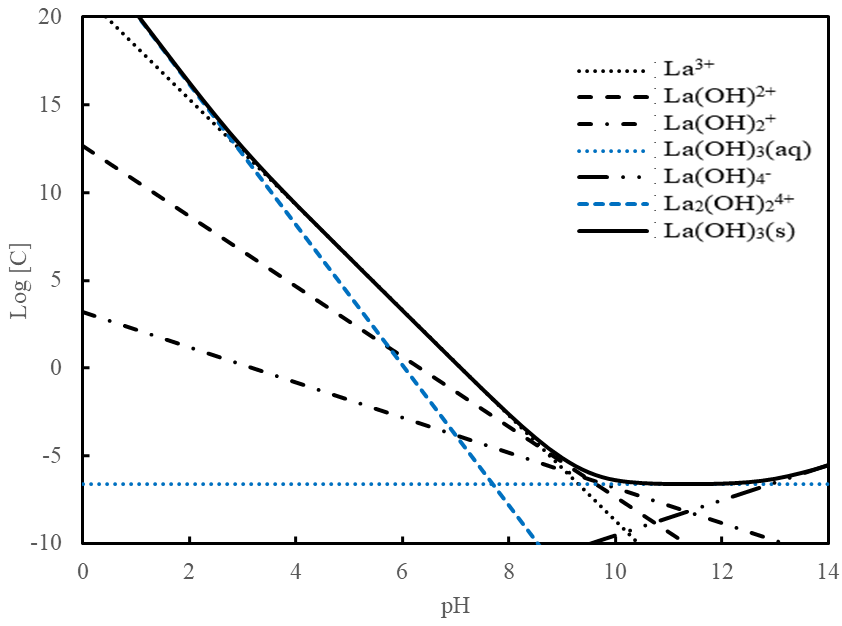

Figure 129. The solubility diagram $La(OH)_3(s)$ in water at 25°C. At pH 4. The concentration of the on-exchangeable free La^{3+} ions is higher than those of the La hydroxo-complexes.

mole of Ln^{3+} ions and that the surface area of clay minerals are large due to the small particle sizes. Some

of the NH^{4+} ions are eventually released to the environment, creating serious pollution problems. For this reason, the use of ammonium ions as lixiviant is banned in China unless they are used for *in-situ* leaching only.

As the La^{3+} ions are released into solution *via* reaction [4], the hydroxo-complexes, will dissociate as follows,

$$La_x(OH)_y^{(3x-y)+} + yH^+ \rightarrow xLa^{3+} + yH_2O \qquad [5.2.8]$$

to generate free and ion-exchangeable La^{3+} ions. In effect, the ion-exchange leaching mechanism for the NaOH-treated monazite (Reactions [4.2.7] and [5.2.8]) represents a mild acid leaching of $Ln(OH)_3$, which is environmentally acceptable in terms minimizing the generation of waste water containing large amounts of toxic elements and savings in lixiviant cost.

Acid Leaching vs. Ion-exchange Leaching Figure 130 shows the results of leaching the monazite pretreated in 10, 30, and 50% NaOH solutions at 80°C for 24 hrs. The experiments were conducted at pH 4 without using $(NH_4)_2SO_4$) to see the role of the lixiviant. Indeed, REE ions were extracted without using the lixiviant; however, the recoveries were substantially lower than the case of using the lixiviant.

Another set of leaching experiments were conducted on a monazite sample pretreated at 30% NaOH at 80°C for 24 hrs without using $(NH_4)_2SO_4$ (Figure 131). The results obtained in an HCl solution of pH 1 were substantially lower than those obtained using the lixiviant at pH 4.

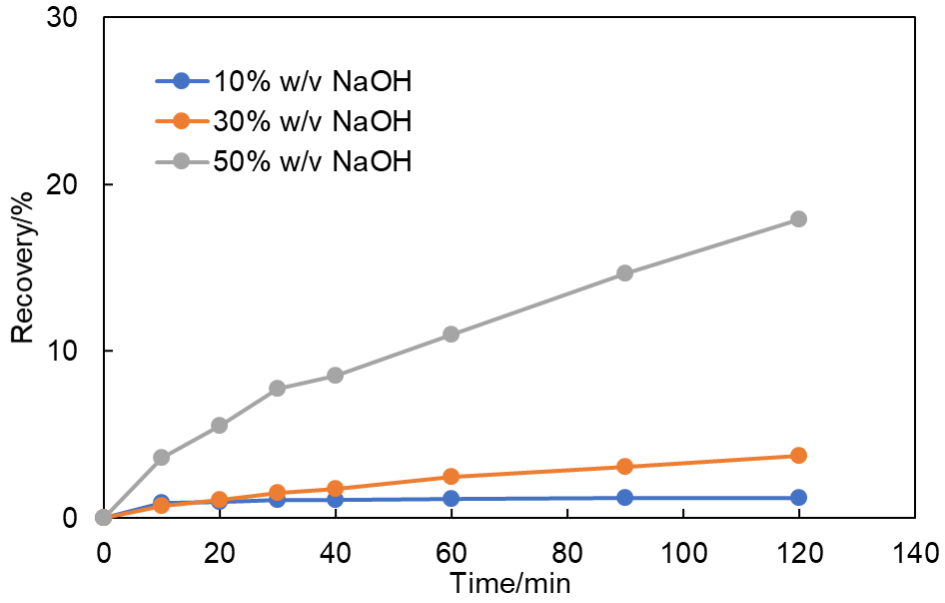

Figure 130. Results of HCl leaching without $(NH_4)_2SO_4$ at pH 4 after pretreatment in 10-50% NaOH solution at 80°C for 24 hrs.

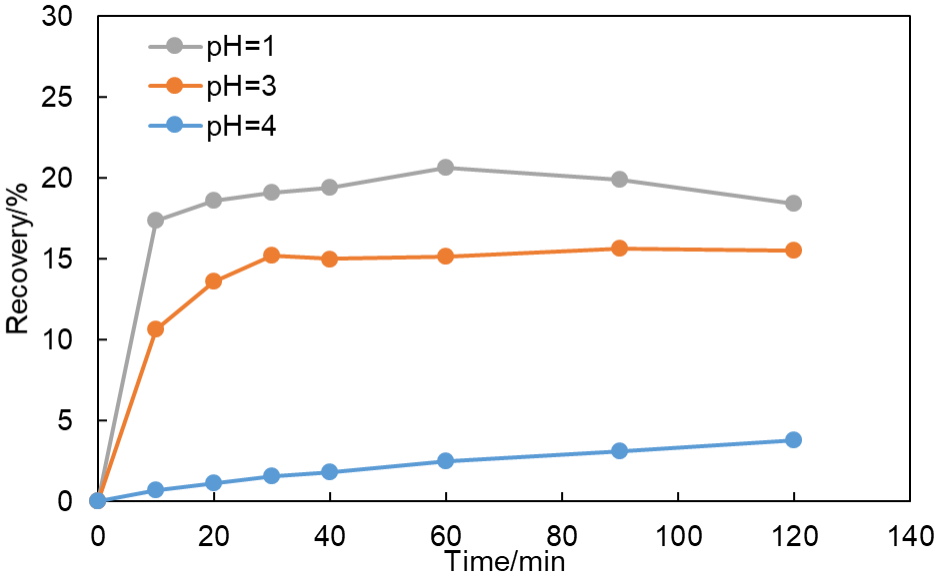

Figure 131 Results of HCl leaching at different pHs after 30% NaOH pretreatment at 80°C for 24 hrs.

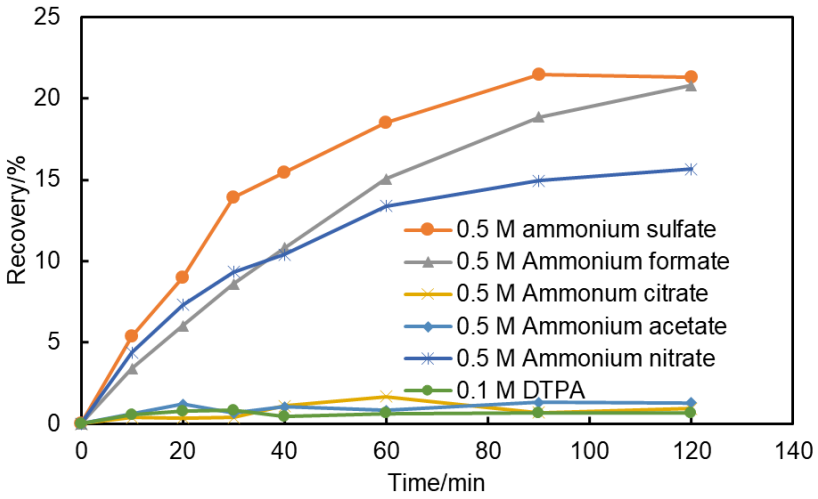

Figure 132. Effect of different anions of NH_4 salts after NaOH pretreatment (30%) at 80°C for 24 hrs.

Effect of Anions It is possible that the SO_4^{2-} ions coming into the leaching system along with the NH_4^+ ions of the lixiviant may play a role in the extraction process. In an effort to better understand the role of anions a serious of leaching experiments were conducted on the monazite sample pretreated in a 30% NaOH solution at 80°C for 24 hrs using ammonium sulfate ($(NH_4)_2SO_4$), ammonium formate ($(NH_4)OCOH$), ammonium citrate ($(NH_4)_3(COO)_3C_3OH$), ammonium acetate ($(NH_4)CH_3COO_2$), and ammonium nitrate ($(NH_4)NO_3$). The results of the leaching experiments are presented in Figure 132. As shown, the sulfate (SO_4^{2-}) performed the best, followed by formate, and nitrate. Ammonium citrate and acetate did not perform well and neither DTPA did. On the contrary, chelating and complexing agents improved significantly for the recovery of REEs from the colloidal forms of REEs on clays. Therefore, the

poor performance suggests that the reagent amount used in these experiments were too small to make impacts in leaching a bulk rather than surface compounds.

Effect of Cations Another series ion-exchange leaching experiments were conducted using sulfate salts of different cations, which included NH_4^+, Na^+, Mg^{2+}, and Al^{3+}. The results presented in Figure 133 show that the NH_4^+ ions gave substantially higher recoveries than the other cations. This observation can be explained on the basis of the heats of hydration ($-\Delta H_{hyd}$) of the cations involved, which represent the propensity of the ions to be hydrated. It has been shown that the heat of hydration of NH_4^+ ion is 322 kJ/mol, which is smaller than most other cations, which is the reason that NH_4^+ can displace Ln^{3+} ions and other cations of higher heats of hydration from the surface of ion-adsorption clays (Moldoveanu and Papangelakis, 2012). Thus, the experimental results presented in Figure 132 and Figure 133 show that $(NH_4)_2SO_4$ may be the best lixiviant of choice. Nevertheless, we are continually search for better lixiviants that are more powerful and requires less dosages.

Proposed Model When monazite undergoes different chemical treatment steps, *e.g.*, NaOH pretreatment and ammonium sulfate (AS), the ζ-potentials of the mineral and its reaction products will change. Therefore, a series of ζ-potential measurements have been conducted, with the results presented in Figure 134. At pH 4, the ζ of monazite was 11.93 mV. When the mineral was pretreated with NaOH, its ζ-potential was increased to 40.60 mV, indicating that the surface is coated with $Ln(OH)_3$, whose p.z.c. is higher than that of monazite. When the NaOH-treated monazite was treated with AS, the ζ-potential was reduced to -17.77 mV at pH 6.7, suggesting that t he SO_4^{2-} ions adsorb to the surface. As the pH decreased to 4.0, the ζ-potential became a little less negative due to the adsorption of H^+ ions. These findings suggest that SO_4^{2-} ions adsorb on the NaOH-pretreated surface, which is reasonable, because the surface was positively charged due to the adsorption of the free Ln^{3+} ions on the Ln(OH)3(s) surface,

Based on the ζ-potential data presented in Figure 134, an ion-exchange leaching mechanism may be proposed as depicted in Figure 135. The model suggests that an NaOH-treated monazite is converted to Ln(OH)(s). As the pH is reduced to 4, free Ln^{3+} ions would adsorb onto the surface, as indicated by the highly positive ζ-potential. As the $(NH_4)_2SO_4$ lixiviant is added to the system, SO_4^{2-} ions would adsorb on to the Ln(OH)(s) surface as indicated by the sharp decrease in ζ-potentials. The adsorbed SO_4^{2-} ions will reduce the electrostatic energy barrier for the Ln^{3+} ions to accumulate on the Ln(OH)(s) surface and be displaced by the NH_4^+ ions *via* an ion-exchange mechanism.

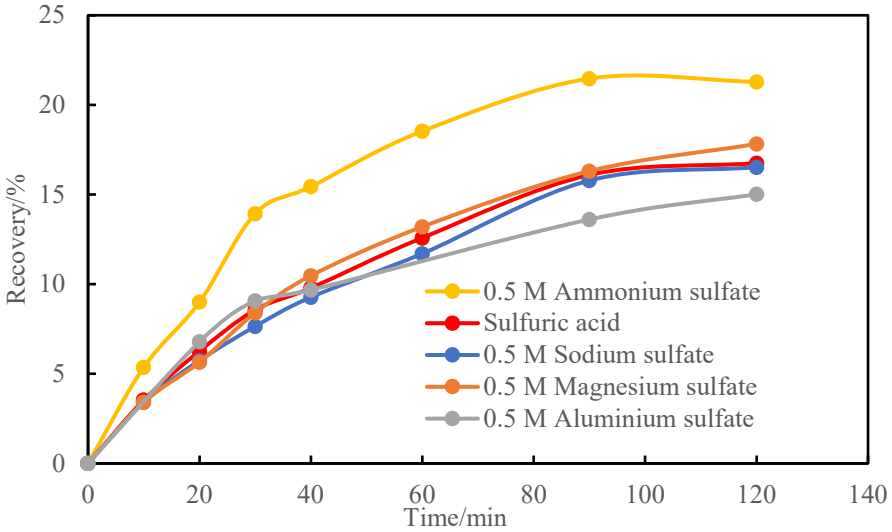

Figure 133. Effects of using sulfate salts of different cations as lixiviant at pH 4 after NaOH pretreatment (30%) at 80°C for 24 hrs.

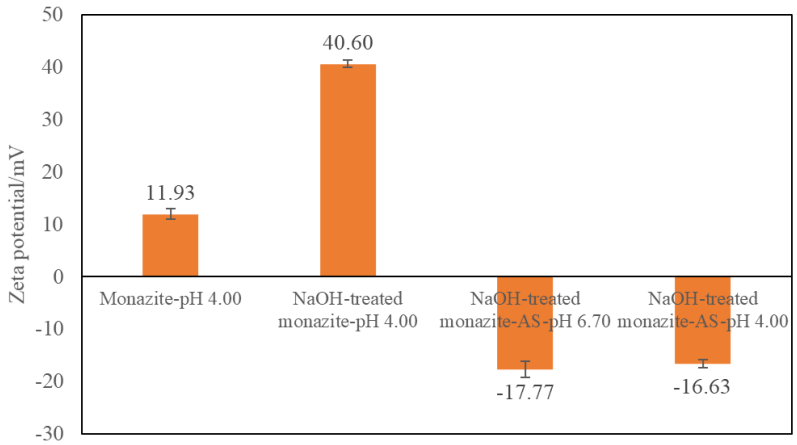

Figure 134. Changes in the ζ-potentials of a monazite sample subjected to different chemical treatments.

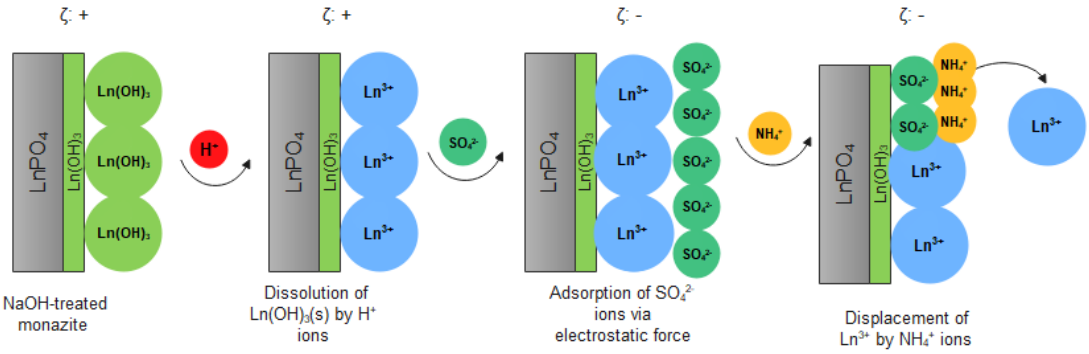

Figure 135. A proposed ion-exchange leaching mechanism for the extraction of NaOH-treated monazite using $(NH_4)_2SO_4$ as lixiviant.

Developing novel lixiviants

In search of lixiviants better than the $(NH_4)_2SO_4$, we have tested three different amines shown in Table 40. A series of leaching tests were conducted on a monazite sample treated in a 30% NaOH solution at 80°C for 24 hrs, with the results presented in Figure 137. A shown, diethylamine gave higher recoveries than the $(NH_4)_2SO_4$. A reason for this improvement may be that its pK_b (= 2.94) is lower than the pK_b (= 4.7) of the NH_4^+ ions. Since the Ln^{3+} ions are strong Lewis acids, a stronger base may serve as a better lixiviant.

Table 40. Amine-based lixiviants used in the present study

Chemical	Formula	pKb	Chemical structure
1-propylamine	C_3H_9N	3.33	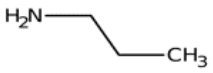
Diethylamine	$C_4H_{11}N$	2.91	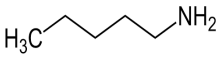
Pentylamine	$C_5H_{13}N$	3.37	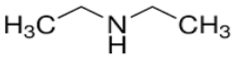

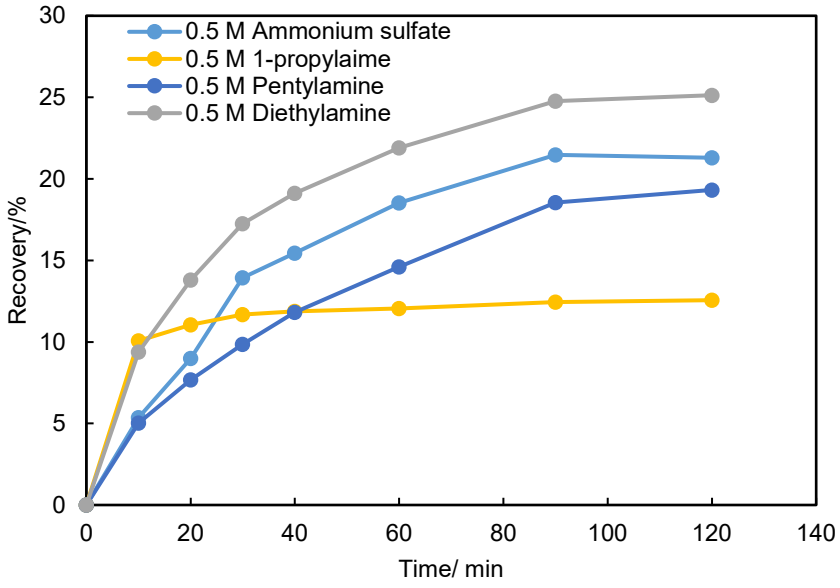

Figure 137. Effect of using different amine-based lixiviants at pH 4 after NaOH pretreatment (30%) at 80°C for 24 hrs.

Activation and Leaching of Natural Monazite and Coal Underclay (Kinetics of Activation)

Introduction

In last prior section, ammonium sulfate leaching (0.5 M ammonium sulfate concentration, pH 4) of NaOH treated monazite was found to be an effective process for extracting REEs, achieving >60% recovery of REEs from a monazite sample. At the time, we proposed a leaching mechanism based on the difference of zeta potential; however, the kinetics of the ammonium sulfate leaching process were not well studied. In the literature, few studies have been conducted on the leaching kinetics of monazite as well as NaOH treated monazite. Panda et al examined the kinetics of phosphate dissolution during the NaOH pretreatment stage (50% w/v NaOH, 170° C for 4 h) as a function of leaching temperature [4]. The results show that chemical-reaction-controlled model can describe the kinetics of phosphate dissolution and the calculated activation energy is 58.04 KJ/mol. Unlike our process, which uses ammonium sulfate, studies in the literature typically leach NaOH treated monazite with mineral acids, such HCl, HNO_3, H_2SO_4 at high concentrations (≥ 1.0 M) and elevated temperatures (e.g., 80° C) [4,14]. At such conditions, the rapid leaching kinetics prohibit a well-controlled experimental study; however, the more mild conditions used in our process do allow such a study to be conducted.

In addition, the testing to date has not evaluated the effects of leaching temperature and particle size on the process efficiency. Given these knowledge gaps, the aims of this study were to investigate the leaching kinetics of NaOH treated monazite with ammonium sulfate based on the shirking core model. In addition to this, the leaching kinetic of a NaOH treated underclay sample (BRC underclay from central PA) with ammonium sulfate was also investigated. The leaching mechanism was also explained based on the results of chemical sequential extraction tests.

Experimental

Sample preparation and reagents

The monazite sample utilized in the current study was the same material introduced elsewhere. The material has a TREE content of 48.9% after upgrading by flotation. The D_{80} of the sample is 14.61 μm. In order to investigate the effects of particle size on the leachability of the monazite sample, the monazite samples was further ground in a PBM-04 planetary ball mill for increments up to 2 hours. The measured D_{80} of the ground samples were 8.25, 4.95, and 4.22 μm. In addition, the BRC underclay sample with a dry ash content of 91.03% was also selected as a feed material for rare earth extraction tests. A representative sample of approximately 200 g was collected from the as-received bulk sample. The sample was ground to 5.03 μm by using a laboratory attrition mail. The total REE content, as determined by lithium tetraborate fusion was 416.85 ppm. As shown in Figure 138 the samples follow a typical LREE-enriched pattern that is common for coal-based refuse material.

Methods

NaOH pretreatment

This procedure of this section is the same as the one described in the prior report section.

Leaching kinetics

The leaching tests were performed in a five-neck round bottom flask, which was heated to the desired temperature (Accuracy: ±1° C) by a digital magnetic stirring heating bath. To avoid the loss of leaching solution through evaporation during leaching process, a water-cooled reflux condenser was connected with the middle neck of the flask. The temperature and the pH value of the leaching solution was monitored through a pH meter. Each leaching test was repeated three times and the average values are reported.

At the beginning of each leaching test, 40 ml deionized water and the water bath were heated to the desired temperature, and 0.5 g of the NaOH-treated material was added into the flask. When the temperature of the solution reached the desired temperature, ammonium sulfate solid of known mass was added to the flask so as to create a 0.5 M concentration in solution. During the test, 0.5 M HCl, which was added by an

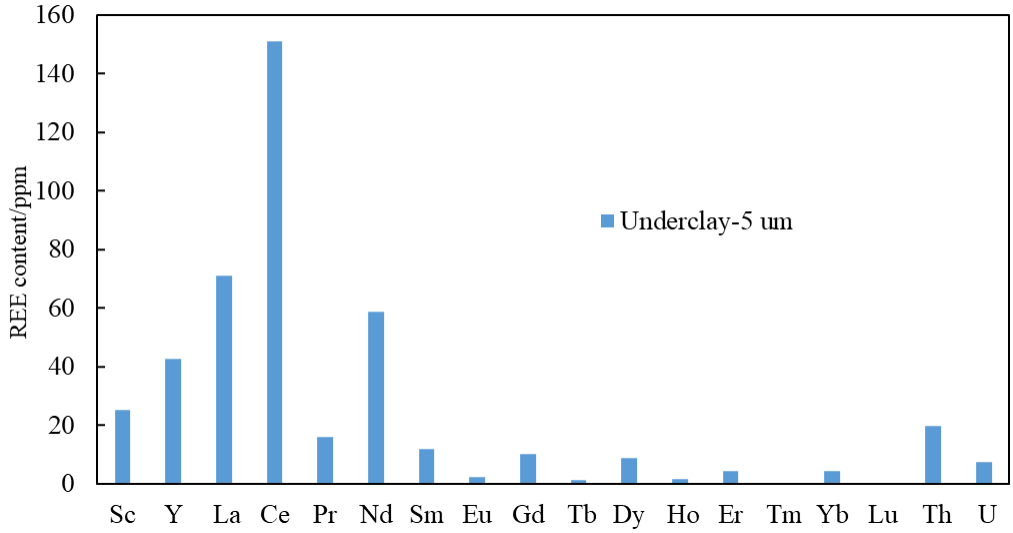

Figure 138. Individual rare earth element distribution of Underclay sample.

electronic pipette to adjust the pH of the leaching solution to a desired value of 4. After reaching the pH set point, the leaching test was started, and samples were subsequently collected by a disposable 1 ml syringe at time intervals, of 10, 20, 30, 40, 60 90, 120 min. After extracting the sample, a PTFE syringe filter (0.22 μm) was immediately used to stop the leaching reaction and separate the leachate and leaching residue. For the leaching tests conducted at 55 and 65° C, additional sampling points were taken at 4 min and 1, 2, 4, 7 min respectively. The volume of the acid consumed at each sampling point was recorded for the purpose of tracking the actual volume of the leaching solution. Since the leaching kinetics of clay samples is fast, the sampling points were selected at 1, 2, 4, 7, 10, 20, 30, 60 min.

At the end of leaching tests, the leaching solution was transferred into a 50 ml centrifuge tube for solid-liquid separation and the volume of the leaching liquor was measured by a graduated cylinder (±0.5 ml). Each solution sample was diluted 2000 (monazite samples) and 100 (underclay samples) times by an acidic solution (2.5% HNO_3 and 0.5% HCl) for Inductively Coupled Plasma Mass Spectrometry (ICP-MS) analysis. The extraction recovery was calculated based on the eqn. (4),

$$Recovery\ (\%) = 100 \times \frac{c_l \cdot v}{c_f \cdot m} \qquad [5.2.9]$$

where c_l and c_f is the REE assays of leaching liquor and feed sample respectively, m is the feed mass, v is the volume of the leaching liquor.

Chemical sequential extraction test

To identify and quantify the fraction of each mode of occurrence of rare earth elements in the underclay sample and the its variation after NaOH pretreatment and leaching, a chemical sequential extraction method was used based on the reagents and conditions shown in Table 41. In a sequential extraction test, 1.0 g underclay samples (untreated, NaOH-treated, NaOH-treated and ammonium sulfate leached) was reacted with the lixiviants in step 1 and 4. At the end of each extraction step, the same procedure as described in the leaching kinetic test was followed to prepare the final samples for ICP-MS analysis. To eliminate the impact of residual reagents on the next step, the leaching residue of each step was washed by 45 ml deionized water three times, and then the washed residue was dried in an oven at 60° C overnight before it was subjected to the next step.

Table 41. Procedure of the chemical sequential extraction used in this study

Step	Target fraction	Regents and volume	Temperature/°C	pH	Reaction time/hr(s)
1	Ion-exchangeable	1 M $MgCl_2$,40 ml,	22	8.20	1
2	Carbonates	1 M CH_3COONa, 40 ml	22	5.00	5
3	Metal oxides	0.04 M $NH_2OH{\cdot}HCl$ in 25% Acetic acid, 100 ml	95	-	3
4	Acid soluble	2 M HNO_3 solution, 40 ml,	22	-	18
5	Insoluble/Silicates	$LiBO_2$ fusion	1000	-	-

Results and Discussion

Effect of leaching temperature on the leaching kinetics of NaOH-treated monazite

Previous study shows that the leaching process of NaOH treated monazite by ammonium sulfate have two steps, *i.e.*, the dissolution of rare earth hydroxide and the displacement of La^{3+} ions by NH_4^+ ions. The related leaching reactions are listed as follows:

$$La_x(OH)_y^{(3x-y)+} + yH^+ \rightarrow xLa^{3+} + yH_2O \quad [5.2.10]$$

$$La(OH)_3(s)\text{-}La^{3+} + 3NH_4^+ \rightarrow La(OH)_3\text{-}3NH_4^+ + La^{3+} \quad [5.2.11]$$

The above reactions show that the leaching process is a non-catalytic heterogeneous reaction in liquid-solid systems, which is similar with the leaching of IACs by ammonium sulfate. To have a better understanding about the mechanism of the leaching process, the leaching kinetics of NaOH-treated monazite was analyzed based on the shirking core model for spherical particles of constant size. Initially, the effect of leaching temperature on the leaching efficiency was investigated in the range of 25-65° C with all other conditions held constant (*i.e.*, 0.5 M ammonium sulfate concentration, 1:80 solid: liquid ratio). As is shown in Figure 139, not only the recovery of total rare earth elements increases with the increasing of leaching temperature, the leaching kinetics was also significantly accelerated, suggesting that kinetics controls the leaching process. For example, the leaching equilibrium was not approached even after 120 min when the leaching temperature was at 25° C temperature; however, at 65° C, the recovery remained stable only after 8 min. With respect to the major REEs, 10-15% improvements in recovery were observed for La, Ce, Pr, Nd when the leaching temperature increased from 25 to 65° C (see Figure 140).

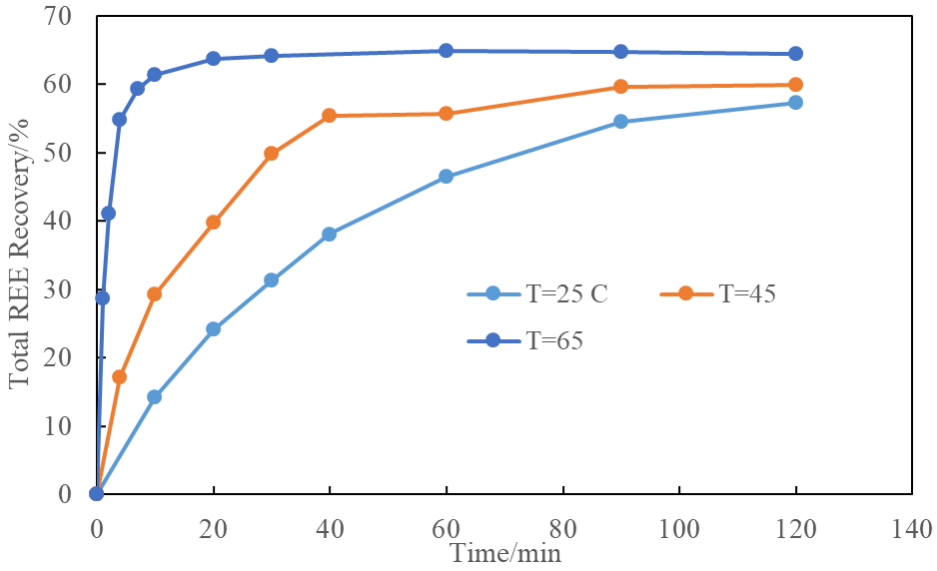

Figure 139. Total REE recovery of NaOH-treated monazite (50% NaOH, 80 ℃, 24 h) leached by $(NH_4)_2SO_4$ at pH 4 as a function of leaching temperature.

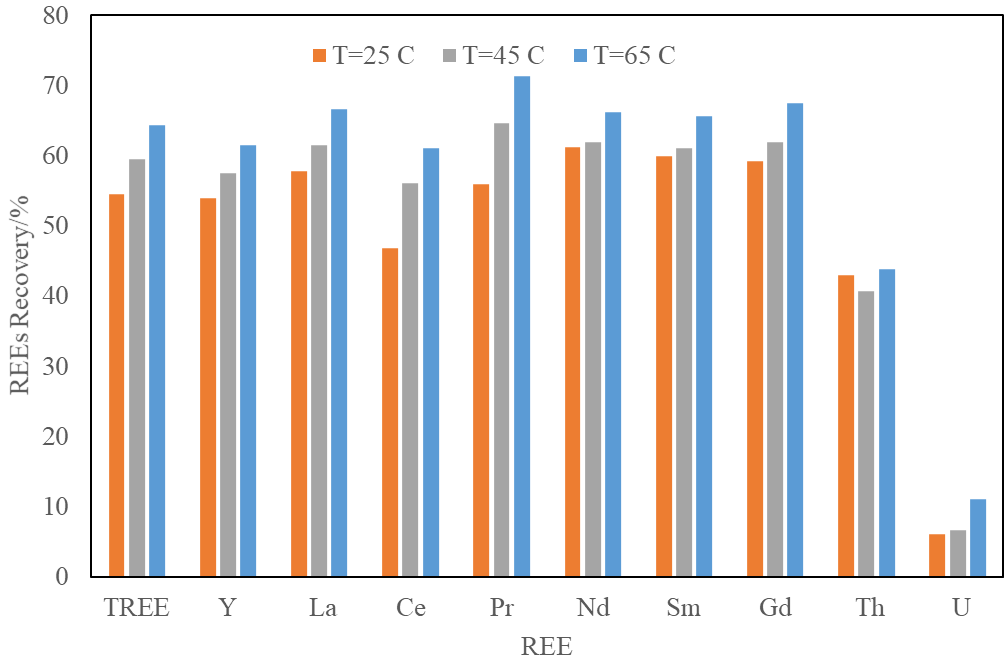

Figure 140. Recovery values of major REEs of NaOH-treated monazite (50% NaOH, 80 ℃, 24 h) leached by $(NH_4)_2SO_4$ at pH 4 as a function of leaching temperature.

The shrinking core model assumes that the leaching process is dependent either on the diffusion of reactants through an ash layer (or through the solution boundary or through a solid product layer) or on the surface chemical reaction rate [5]. The standard equations of shirking core kinetic models are shown as follows [2, 4]:

(1) Chemical reaction controls:

$$1-(1-x)^{\frac{1}{3}}=k_1 t \quad [5.2.12]$$

(2) Outer diffusion controls

$$1-(1-x)^{\frac{1}{3}}=k_2 t \quad [5.2.13]$$

(3) Inner diffusion controls

$$1-\frac{2}{3}x-(1-x)^{\frac{2}{3}}=k_3 t \quad [5.2.14]$$

(4) Mixed controls:

$$1-(1-x)^{\frac{1}{3}}=k_4\frac{C_0 M}{r_0 p}t \quad [5.2.15]$$

where x is the fraction of TREEs leached (% recovery/100), k_1, k_2, k_3, k_4 are chemical constants for different control steps; t is the leaching time; C_0 is the initial concentration of the lixiviant used; r_0 is and p are the initial radius and the molar density of the ore sample particle respectively; M is the mass of the sample particle.

Analysis of the NaOH treated monazite leaching data as a function of time and temperature indicates that the plot of $1-(1-x)^{\frac{1}{3}}$ vs. time produced the best fit to the experimental data as indicated by the regression coefficient. Figure 141 shows the linear fit, while Table 42 includes the linear regression values. This result suggests that the chemical reaction control or outer diffusion control model best describes the leaching mechanism. To further distinguish between these two models, an analysis of the reaction activation energy is required. Normally, chemical controlled reaction exhibit a reaction energy larger than 42 KJ/mol, while the the activation energy of mixed controlled reaction is between 20-34 KJ/mol. To further confirm the leaching kinetic model for the current data, the k_1 values and the temperatures were used to calculate the activation energy (Ea), which can be determined based on the Arrhenius equation:

$$k_1 = \mathrm{A}e^{-\frac{E_a}{RT}} \quad [5.2.16]$$

The Arrhenius plot of ln *k* versus 1/T is shown in Figure 142. Based on this assessment, the calculated Ea was found to be 61.28 KJ/mol, indicating the leaching process is a chemical-controlled reaction. This finding is consistent with the proposed leaching mechanism, as is shown in reaction [5.2.12] and [5.2.13]. Therefore, the first step of the leaching process can be considered as the dissolution of $Ln(OH)_3(s)$ and then followed by a ion-exchange process. At higher leaching temperature, the dissolution rate of $Ln(OH)_3(s)$ is dramatically accelerated, thereby facilitating the entire leaching kinetics.

Table 42. Linear regression results of leaching results at different temperatures for monazite sample

T/°C	k	b	R^2
25	0.0031	0.0080	0.9863
45	0.0064	0.0241	0.9515
65	0.0551	0.0285	0. 9255

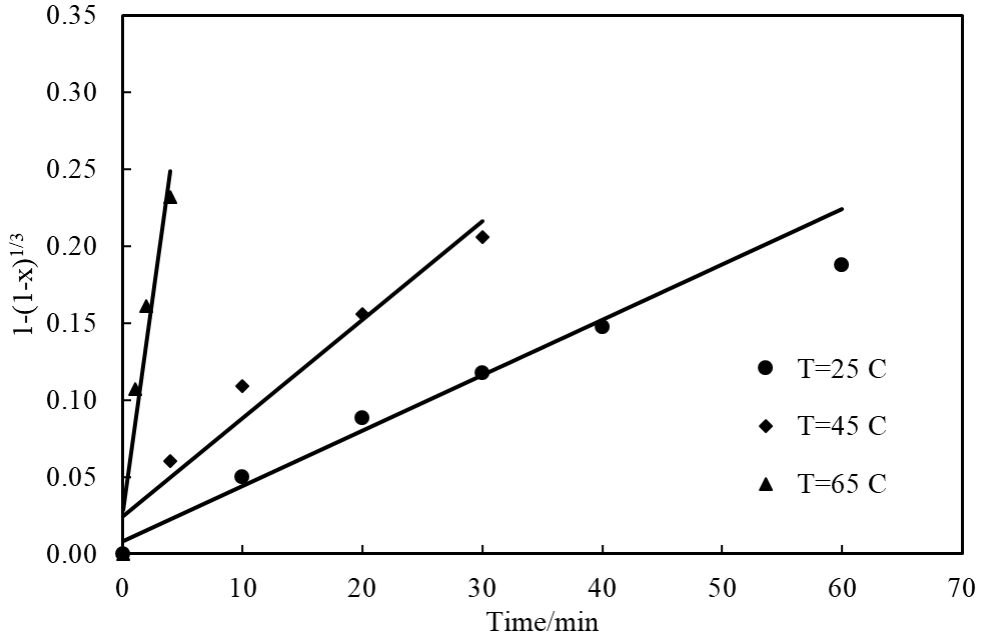

Figure 141. Plots of $1-(1-x)^{1/3}$ vs. time for different temperatures.

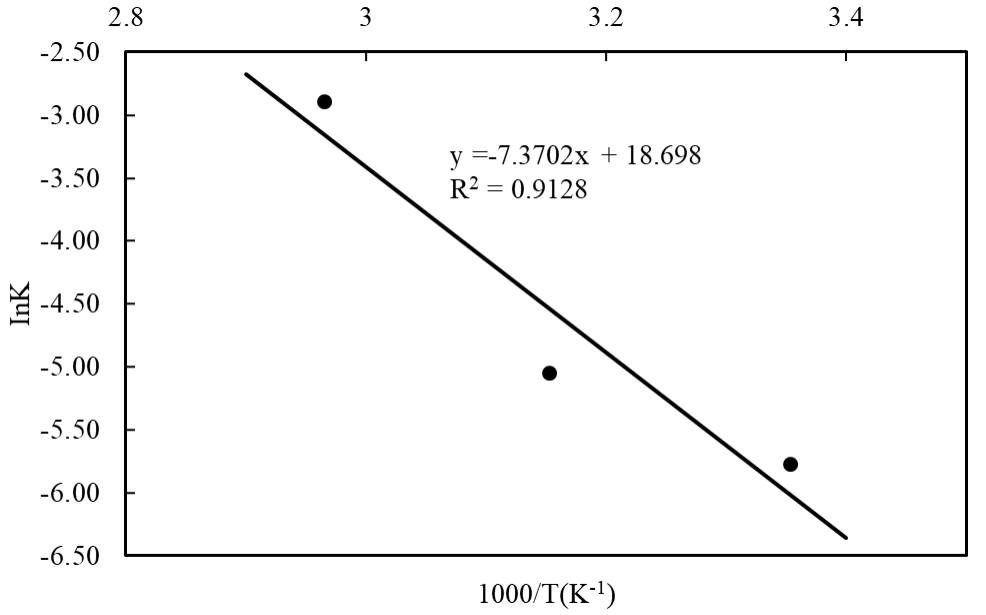

Figure 142. Arrhenius plot of leaching kinetics of NaOH-treated monazite by $(NH_4)_2SO_4$ at different temperatures.

Effect of particle size on the leaching kinetics of NaOH-treated monazite

In addition to the leaching temperature, particle size is another important process variable that can be controlled to further improve the performance of leaching process in terms of leaching kinetics as well as extraction recovery. This improvement is primarily due to the larger surface area that is created with the reduction of particle size. To further to understand the effects of particle size on the leaching process, monazite samples with three different size distributions (i.e. D80 = 14.69, 8.25, 4.95, µm) were used as feed for the NaOH pretreatment and ammonium sulfate leaching process. Each size fraction was treated by 50% w/v NaOH at 80° C for 24 h and subsequently leached by 0.5 M ammonium sulfate at 25° C and pH 4 for 2 h.

Results from this study are shown in Figure 143 as total REE recovery versus reaction time and in Figure 144 as individual REE recovery for major REEs. The reduction in particle size prompted a substantial increase in TREE recovery, as reducing the size from 14.61 µm to 4.95 µm led to an improvement in recovery from ~50% to ~76%. Moreover, the recoveries of major REEs (e.g., La, Pr, Nd) were increased to around 85% for the finest size tested.

In addition to the equilibrium recovery, the leaching kinetics were also increased due to the reduction in particle size. For the sizes evaluate din this experiment, the leaching needed to reach equilibrium shortened from 120 min to ~20 min at 25 ºC. To quantify the variation of leaching kinetics during the reduction of particle size, the Arrhenius equation introduced in Eq. [5.2.16] was modified as follows to incorporate the radius of the particle size:

$$k_1 = A' \mathrm{r}_0^n e^{-\frac{E_a}{RT}} \qquad [5.2.17]$$

where r_0 is the radius of particle size and n is the order of the particle size. This equation can be linearized to produce:

$$Ink_1 = \mathrm{n} \cdot Inr_0 - InA' \qquad [5.2.18]$$

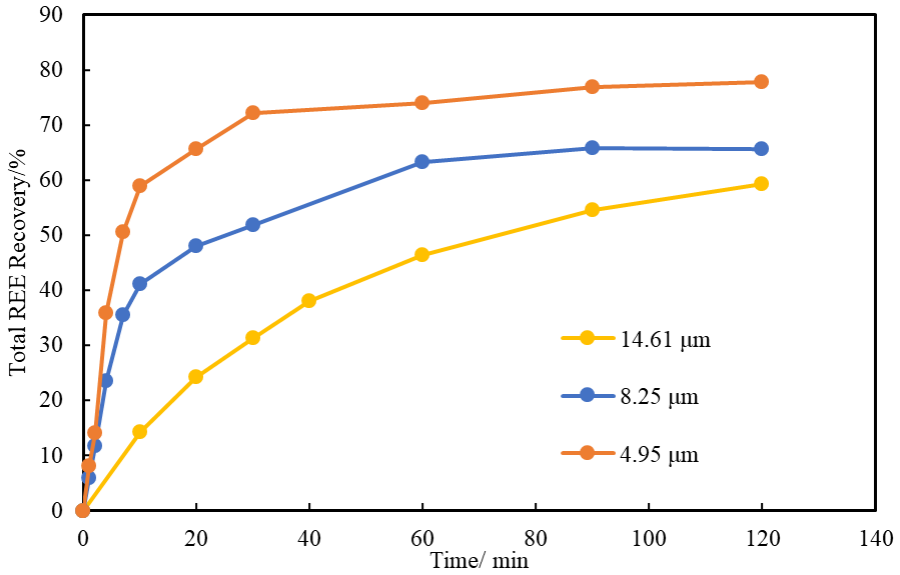

Figure 143. Total REE recovery of NaOH-treated monazite (50% NaOH, 80 ºC, 24 h) leached by $(NH_4)_2SO_4$ at pH 4 and 25 ºC as a function of particle size.

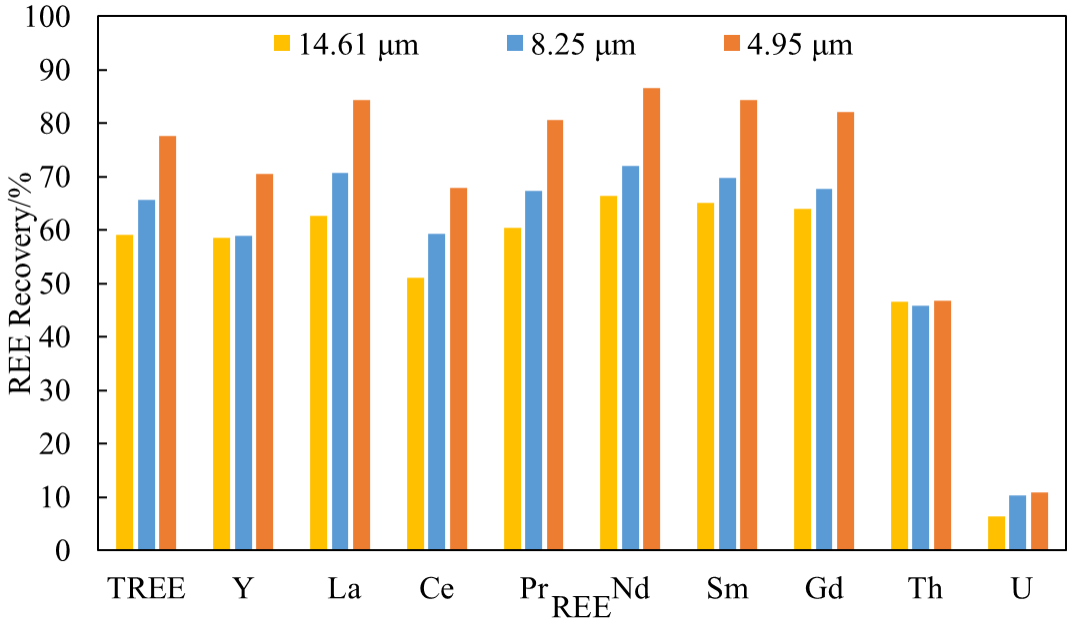

Figure 144. Recovery values of major REEs of NaOH-treated monazite (50% NaOH, 80 °C, 24 h) leached by $(NH_4)_2SO_4$ at pH 4 and 25 °C as a function of particle size.

The k values for each size fraction were calculated from the plots of of $1-(1-x)^{\frac{1}{3}}$ vs. time, which are straight lines as shown in Figure 145. The corresponding regression coefficients are summarized in Table 43. Based on this linear regression, a plot of ln k and ln r_0 can be constructed (Figure 146) and used to determine n and A'. From this analysis, the n and A' were determined to be -2.0335 (n ≈2) and 4.79, respectively. As a result, Eq. [5.2.17] can be rewritten as follows:

$$k_1 = 4.79 \cdot r_0^{-2} e^{-\frac{61280}{RT}} \quad [5.2.19]$$

After combining Eq. 5.2.12 and Eq. 5.2.19 together, the empirical equation of the leaching kinetics can be expressed as:

$$1-(1-x)^{\frac{1}{3}} = 4.79 \cdot r_0^{-2} e^{-\frac{61280}{RT}} \quad [5.2.20]$$

Table 43. Linear regression results of leaching results as a function of particle size (D_{80}) on the monazite sample.

D_{80}/um	k	b	R^2
14.61	0.0031	0.0162	0.9695
8.25	0.0167	0.0162	0.9760
4.22	0.0314	0.0065	0.9899

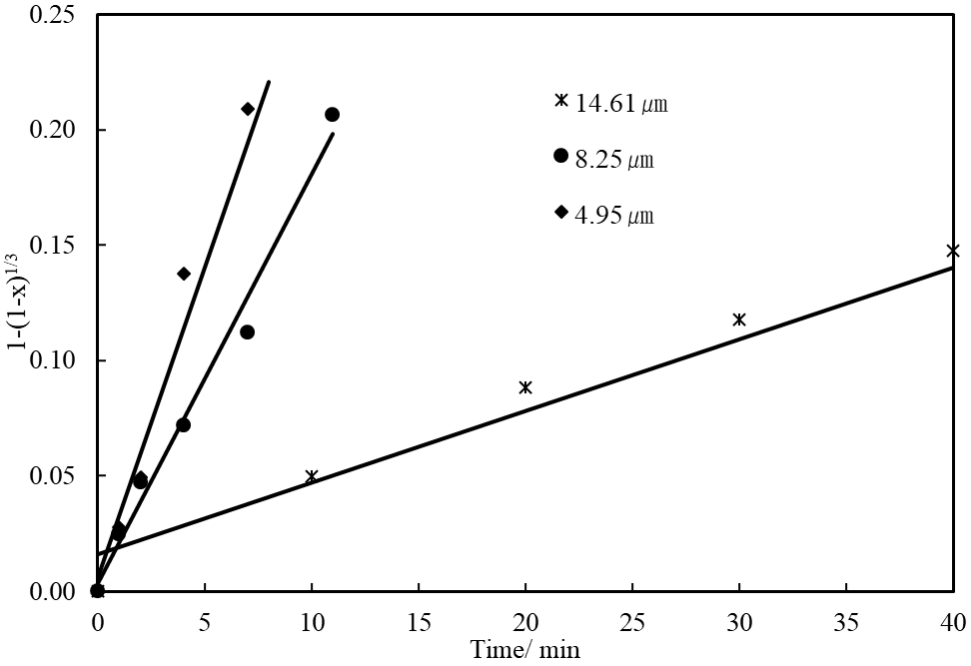

Figure 145. Plots of $1-(1-x)^{1/3}$ vs. time as a function of particle size (D_{80}) at 25 °C.

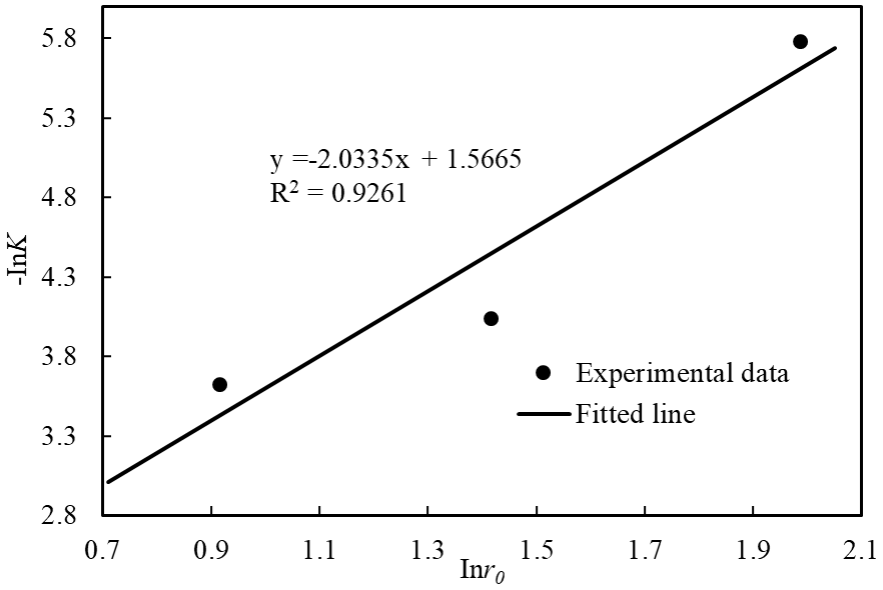

Figure 146. Plots of lnK vs. lnr_0 at 25 °C.

Effect of leaching temperature on the leaching kinetics of NaOH-treated underclay sample

The effect of temperature on the ammonium sulfate leaching efficiency of an NaOH-treated underclay sample was conducted at 25, 35, 45° C. Experimental data from this test is shown in Figure 147 as total REE recovery versus time and as individual REE recovery in Figure 148. When the leaching temperature was increased from 25 to 45° C, the extraction increased from 34% to 43% (~9% improvement on recovery), revealing that ammonium sulfate leaching of NaOH treated clay samples is only slightly sensitive to leaching temperature. In all tests, the leaching kinetics was rapid in the first 10 minutes and subsequently followed by a very slow leaching process, which is consistent with the results from literature. Individual REE values indicate that the recoveries of LREEs (La, Ce, Pr, Nd, Sm) and Eu, Gd are relatively more sensitive to leaching temperature, whereas the recoveries of the rest of HREEs have smaller improvement as the temperature increased from 25 to 45° C.

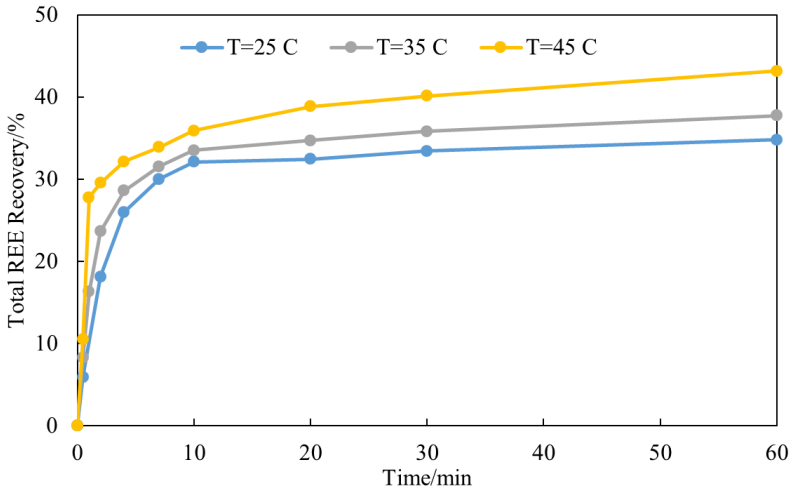

Figure 147. Total REE recovery of NaOH-treated underclay (30% NaOH, 80 °C, 24 h) leached by $(NH_4)_2SO_4$ at pH 4 and 25 °C as a function leaching temperature.

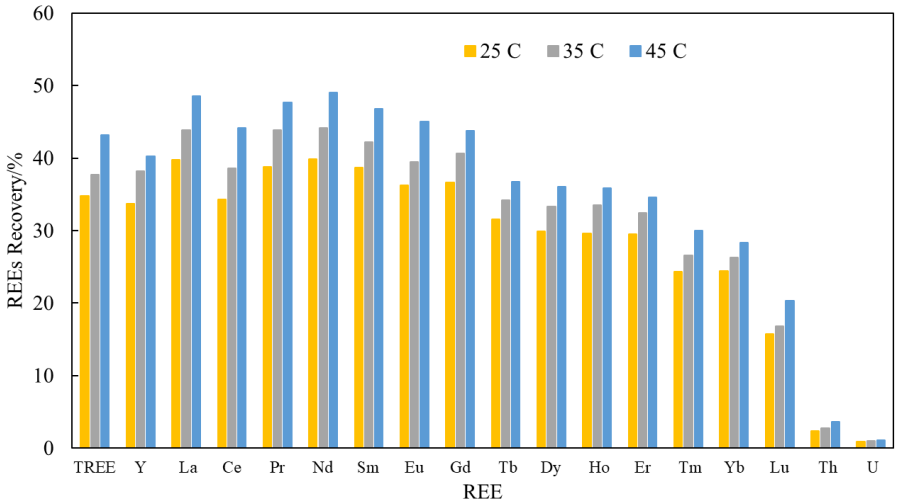

Figure 148. Recovery values of major REEs of NaOH treated underclay (30% NaOH, 80 °C, 24 h) leached by $(NH_4)_2SO_4$ at pH 4 as a function leaching temperature.

As in the monazite testing shown above, a kinetic study was also conducted on the leaching of the NaOH pretreated underclay materials. After fitting the experimental data according to the standard leaching kinetic models, it was found that $1-(1-x)^{\frac{1}{3}}$ is still the model that gives the highest values of regression coefficients (see Figure 149 and Table 44). In addition, the calculation based on the Arrhenius plot in Figure 150 shows that the activation energy for this material is 29.36 KJ/mol. This result suggests that the leaching process belongs to a mixed controlled leaching reaction, the same conclusion was drawn from the leaching kinetic study on a fire clay seam coal sample, which was leached by 1.2 M sulfuric acid [9]. This mixed-control leaching kinetic is resulted from the existence of different modes of occurrence of REEs in coal-based clay samples, thereby several reactions were involved in the leaching process.

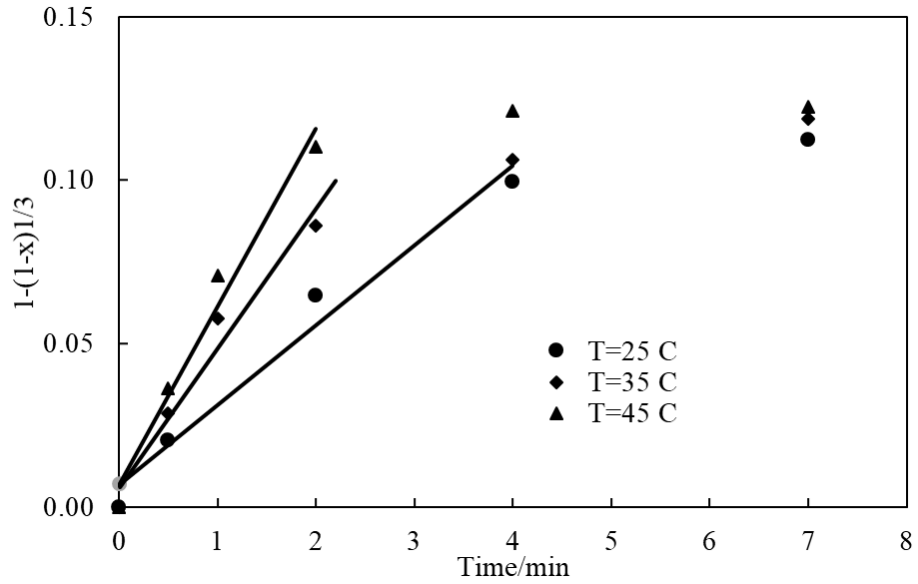

Figure 149. Plots of 1-(1-x)$^{1/3}$ vs. time of NaOH-treated underclay by $(NH_4)_2SO_4$ at different temperatures.

Table 44. Linear regression results of leaching results at different temperatures for the Underclay sample.

T/°C	k	b	R^2
25	0.0249	0.0049	0.9715
35	0.0423	0.0048	0.9627
45	0.0522	0.0121	0.8611

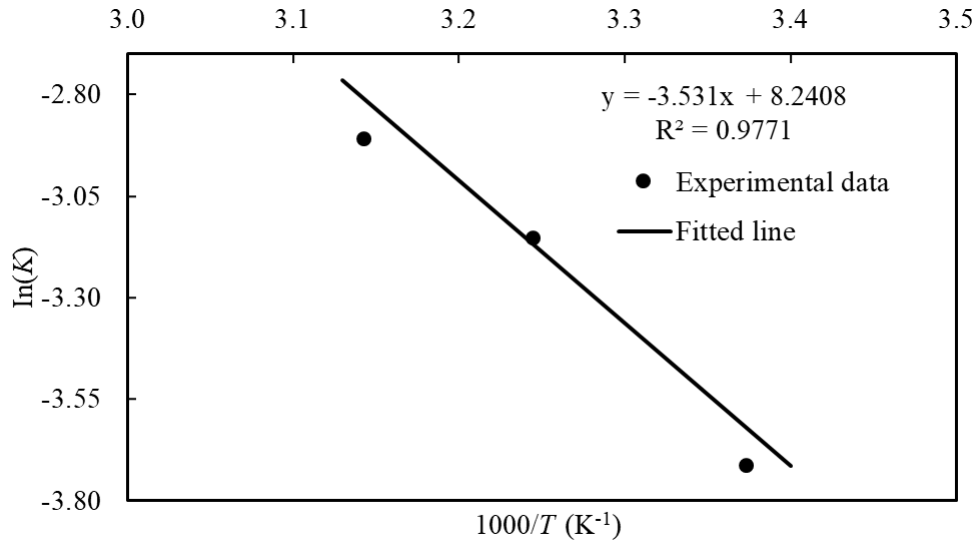

Figure 150. Arrhenius plot of leaching kinetics of NaOH-treated underclay by $(NH_4)_2SO_4$ at different temperatures.

Characterization of underclay sample by chemical sequential extraction

Generally, REEs in coal-based sources can be categorized into ion-exchangeable form, carbonate form, metal oxide form, acid soluble form, and insoluble/silicate form [11]. A 5-step chemical sequential extraction method was applied to quantify the changes of rare earth partition among different forms during NaOH pretreatment and leaching process (including the feed sample, NaOH treated sample, and leaching residue). Chemical sequential extraction tests were conducted on the three samples, (i.e., the underclay samples that were not treated, NaOH treated, NaOH-treated and ammonium sulfate leached), so as to quantify the variations of each form of REEs.

As is shown in Figure 151, without any pretreatment, only 0.14% of REEs were extracted in the first step, i.e., ion-exchangeable form, and the majority (81.26%) of REEs exist in the insoluble/silicate form (e.g., monazite, xenotime etc.), which is not able to be extracted under the mild conditions like those used for the leaching of IACs. Only 2.13% and 6.43% are associated with carbonates and metal oxides, which are the forms that can be dissolved in weak acid condition [11]. The fraction of REEs in acid soluble forms is 10.08%, which can be dissolved by strong acid. The above results indicate that significant amounts (81.26%) of REEs in the underclay sample are in hard-to-leach forms.

However, the modes of occurrence changed significantly after the material was treated by 50% NaOH at 80^{o} C for 24 hours. After treatment, only 17.14% of REEs reported to insoluble/silicate from, and REEs in metal oxide form increased from 6.43% to 44.44%, nearly seven times higher. A large improvement (from 2.13% to 22.25%) in the fraction of REEs in carbonate form was also observed. This result demonstrate that NaOH pretreatment is able to activate those REEs exist as insoluble/silicate form.

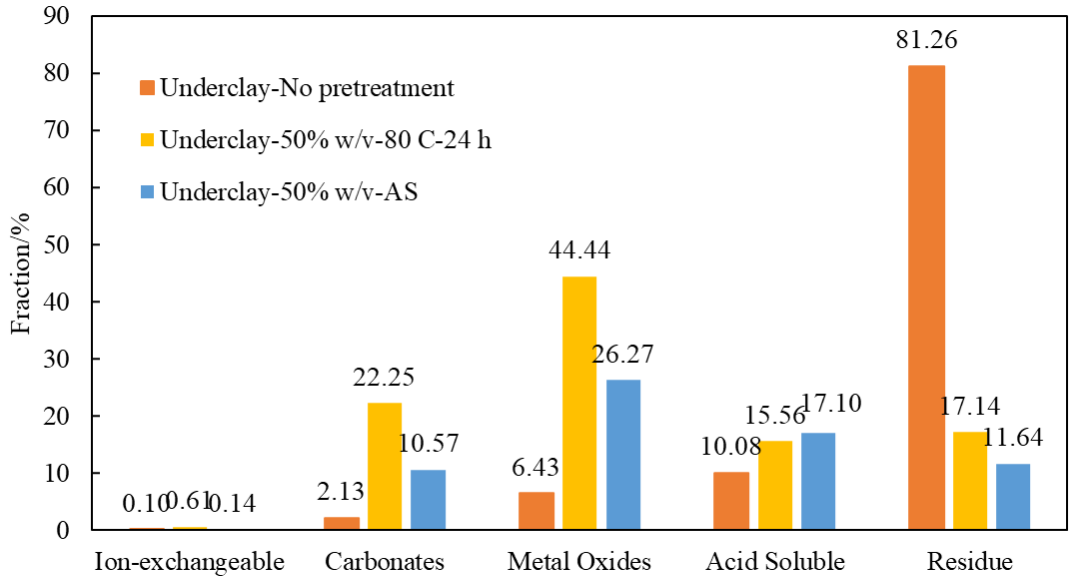

Figure 151. Leaching results of NaOH-treated underclay sample by $(NH_4)_2SO_4$ at pH 4 as a function of leaching temperature 50% NaOH, 80 ℃, 24 h.

After leaching by ammonium sulfate at 25° C, the fractions of REEs in carbonate and metal oxide of the leach residual was found to be nearly half of the amount prior to leaching. This result indicates that most of REEs recovered by ammonium sulfate were from REEs in carbonate and metal oxide form, which is why the leaching kinetics of NaOH-treated underclay sample is so rapid in the first 10 mins.

Comparison of leaching kinetics of ammonium sulfate leaching on different ores (monazite, coal-based clay, ion adsorption clay)

Many studies have been published related to the REE extraction from IACs. The leaching kinetics of IACs by ammonium sulfate was investigated by Tian et al. It was found that the leaching process is an inner diffusion kinetic controlled model . The activation energy is only 9.24 KJ/mol. This result is due to the fact that the REEs adsorb on the surface of clays through electrostatic force and therefore lower energy is required for the diffusion of the reactants and products through the porous solid layer.

In the present study, the ammonium sulfate leaching kinetics of NaOH-treated monazite and underclay were investigated. The leaching kinetic models of different ores with ammonium sulfate are summarized in Table 45 for a comparison purpose. As is shown, three different leaching kinetic models were established for NaOH treated monazite, NaOH treated underclay, and IACs. These results show that the ammonium sulfate leaching has a strong adaptability to different ores. With regard to NaOH treated monazite, the outer surface of unreacted monazite is coated with a layer of rare earth hydroxide with a certain thickness, this product layer is thicker than the one of IACs, in which the REEs only reported to the surface of clay minerals. In this case, ammonium sulfate plays a role in the leaching process by displacing the soluble REE species by ammonium ions after the dissolution of the outmost layer of rare earth hydroxide. The high activation energy is mainly consumed to overcome the energy barrier of the dissolution of rare earth hydroxide, which is the rate limiting step of the leaching process.

As for the underclay samples, the mixed-control kinetic model can be attributed to its various REE associations, thereby several reactions are involved during the ammonium sulfate leaching process. The ammonium sulfate leaching conditions used is a mild condition thus only those easy-to-leach REEs, which are mainly converted from insoluble/silicate form, were recovered, leading to a rapid leaching kinetics in the first 10 min. REEs in acid soluble and insoluble/silicate form were difficult to be extracted is such

condition. Therefore, the steps that constrain the leaching process are the chemical reaction as well as interfacial transfer of products and reagents. Based on the current research, leaching kinetics of ammonium sulfate leaching is dependent on the type of ores.

Conclusions

In this study, the leaching kinetics of NaOH treated monazite and NaOH treated underclay sample with ammonium sulfate were examined based on the shirking core model. It was found that chemical-reaction-controlled and mixed-controlled model fitted the leaching process (the rapid reaction stage) of NaOH treated monazite and underclay respectively, and the corresponding activation energy calculated from Arrhenius equation are 59.21 and 29.36 KJ/mol respectively. The established empirical equation for the NaOH treated monazite is given by:

$$1 - (1-x)^{\frac{1}{3}} = 4.79 \cdot r_0^{-2} e^{-\frac{61280}{RT}}.$$

This study revealed that leaching kinetic of ammonium sulfate is dependent on the specific ore. When the monazite sample was ground from D_{80} = 14.69 to 4.95 μm, the TREE recovery was 76%, among which over 80% of La, Pr, and Nd extracted. For NaOH treated underclay sample, when the leaching temperature changed from 25 to 45 ºC. the TREE recovery increased from 34% to 43% whereas the recoveries for La, Pr, Nd, Sm were close to 50%. The sequential extraction test results revealed that after treated by 50% NaOH at 80ºC for 24 h, the fraction of REEs in insoluble/silicate decreased from 81.26% to 17.14%. ~66% of REEs were converted to carbonate and metal oxide form, which are leachable at weak acid contrition. ~65.42% of this easy-to-leach REEs were extracted by ammonium sulfate leaching. The result shows that ammonium sulfate is a promising lixiviant for both NaOH treated monazite and underclay samples.

Table 45. Comparison of reaction types by using ammonium sulfate as a lixiviant on different samples.

Sample	Ea KJ/mol	Reaction type	Kinetics equation
NaOH-treated monazite	59.21	Chemical reaction controlled	$1-(1-x)^{1/3} = kt$
NaOH-treated underclay	29.36	Mixed controlled	$1-(1-x)^{1/3} = kt$
IACs[2]	9.24	Inner diffusion controlled	$1 - 2/3x-(1-x)^{2/3} = kt$

Activation and Leaching of Natural Monazite (Leaching Kinetic Study)

Samples and reagents

The monazite sample used in this study is a Ce-type monazite purchased from Khyber Mineral Co., Westmont, IL. The specific procedures for the sample preparation (grinding, upgrading by flotation) are the same with those described in earlier section of this report. For leaching tests here, the froth product assaying 48.9% of REEs with d_{80} = 14.6 µm was used. Reagent grade NaOH and HCl from Fisher Scientific were used for leaching experiments, while all other regents were of analytical grades. Deionized water with a resistivity of 18.2 MΩ·cm at 298.15 K was used in all solution preparation and leaching tests.

NaOH pretreatment and leaching test protocol for Monazite Samples

The specific procedures for the NaOH pretreatment of the monazite sample was also described above. The conditions for NaOH pretreatment were: 30% NaOH, 80 ºC, 24 h, S/L = 0.5 g/20 ml, 600 rpm. After pretreatment, the samples were leached by various lixiviants including amines and carboxylic acids. The specific conditions for the leaching tests are as follows: S/L = 0.5 g/ 40 ml, pH 4 (± 0.1), room temperature, 2 h, 600 rpm. The REE content was measured by ICP-MS.

Leaching test protocol for pure $La(OH)_3$ solid

To avoid the interference of impure elements on the leaching results, pure $La(OH)_3$(s) was also evaluated as an ideal model for the NaOH-treated monazite (i.e., rare earth hydroxide). Pure $La(OH)_3$(s) was leached by 0.5 M ammonium acetate and 0.1 M EDTA respectively at pH 4 as a function of temperature, so as to determine the leaching kinetics. The leaching tests were performed in a Soxhlet extraction apparatus (the temperature was maintained by a water bath equipped with a magnetic stirrer). In the first step, he leaching solution was pre-heated to the desired temperature, and 0.5 g of pure La(OH)3(s) power was added into the flask. Subsequently, 0.5 M HCl and NaOH were used to adjust the pH of the solution to 4 (±0.1). The temperature (±0.1 oC) and the pH value (±0.1) of the leaching solution were monitored through a pH meter. Similar with the ammonium sulfate leaching, samples of the slurry were taken at specific time intervals and assayed for REE content by means of a 1 ml disposable syringe. At the end of each test, the same procedure with ammonium sulfate leaching was followed to prepare the samples for ICP-MS analysis. The recovery (R) of an REE species was determined using the following equation:

$$R = 100 \times \frac{C_l V}{C_f M} \qquad [2]$$

in which C_l and V are the REE concentration and volume of the leach liquor, respectively; and C_f and M are the REE concentration and weight of the sample, respectively.

FTIR analysis procedures

FTIR analysis (Varian 670 FTIR spectrometer) was performed to characterize the variation of $La(OH)_3$(s) before and after leaching especially the formation of surface complexes. The spectral resolution of the device is less than 0.07 cm^{-1}. The samples were pure $La(OH)_3$(s) powder, $La(OH)_3$(s) leached by ammonium 0.5 M ammonium sulfate, ammonium formate, and ammonium citrate, and 0.1 M EDTA and DTPA at pH 4 at room temperature. The leaching residues were rinsed with deionized water for three times and then dried in an oven at 60 ºC overnight. Additionally, the FTIR spectra of 0.5 M ammonium citrate before and after leaching was also collected for a better understanding of the leaching mechanism.

Leaching results with carboxylate anions

In this section, several other ammonium-based organic ligands with different carboxy numbers (from 1 to 3), Ethylenediaminetetraacetic acid (EDTA), and diethylenetriamine pentaacetic acid (DTPA) were selected as lixiviants for the NaOH-treated monazite. These acids and their respective pKa values are shown in Table 46. Considering the low solubilities of DTPA (4.8 g/L at 25 oC) and EDTA in water at room temperature, their concentrations were 0.1 M for the leaching tests.

Table 46. Organic acids and their pKa Values (Data from Banerjee et a., 2021).

Organic acids	pK_a
Formic acid	3.75
Acetic acid	4.75
Citric acid	3.14, 5,77, 6.4
EDTA	0.0, 1.5, 2.0, 2.69
DTPA	1.68, 2.1, 2.6, 4.15, 8.2, 9.9

Prior to the leaching tests, a series of thermodynamic calculation was conducted to predict the feasibility of dissolving rare earth hydroxide by organic ligands. The stability diagrams of $La(OH)_3(s)$ in the presence of formate, acetate, citrate and EDTA were created and are shown in Figure 152. The stability diagram of each ligand shows that the dissolution of $La(OH)_3(s)$ by organic ligands is thermodynamically

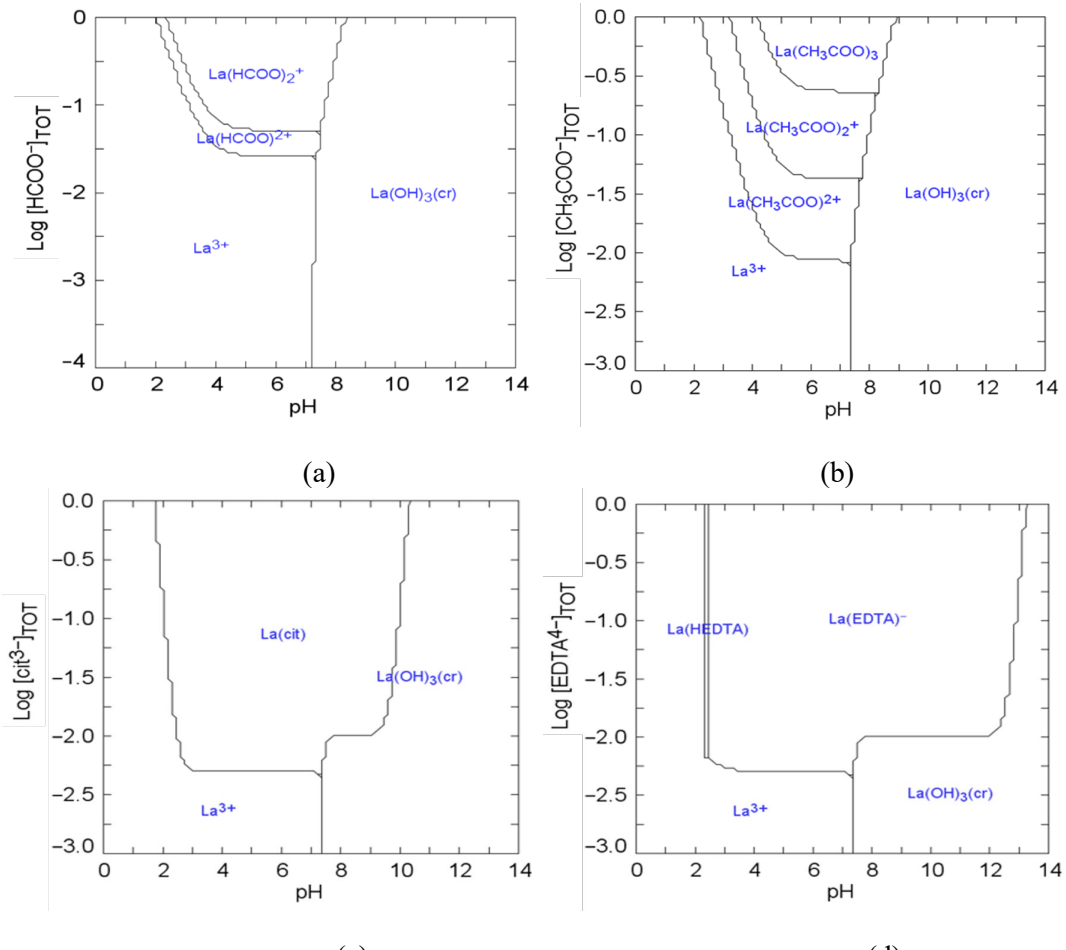

Figure 152. Stability diagrams of La in different leaching systems of NaOH-treated monazite samples (created by Meduda and its database), (a): ammonium formate; (b): ammonium acetate; (c): ammonium citrate; (d): EDTA, [La3+] = 0.01 M.

favored at acidic pH range. With the increase of the stability constant (from formate to EDTA), the region of La-ligand complexes also increases, In the presence of EDTA, La forms soluble La-EDTA complexes (i.e., La-EDTA$^-$) from pH 2.0 to 12.0 even when the concentration is around 0.01 M. This range is significantlywider than that of acetate at 0.01 M, which only formed soluble La-acetate complexes from pH 5.0 to 7.5. This finding suggests that ligands with stronger complexing ability are more capable of enhancing the dissolution process.

Notwithstanding these findings, the experimental leaching results typically follow thE opposite trend of that predicted by the thermodynamic simulations (with the exception of formate). As shown in Figure 153, very poor leaching efficiencies were achieved by most lixiviants at room temperature with formate being the only outlier. Similar to acetate, less than 3% of REEs were extracted by citrate, EDTA, and DTPA.

Effect of pH on the leaching efficiency of DTPA

During the leaching process of NaOH-treated monazite by the organic ligands, the coordination of REEs and ligands may have two possibilities (i.e., aqueous and/or surface complexation). On one hand, the complexation may occur between the free RE^{3+} ions and the chelating ligands (known as aqueous complexation). In such case, both the dissolution of $RE(OH)_3(s)$ (i.e., the release of free RE^{3+} ions) and the dissociation a of chelating ligands are required for the proceeding of the leaching process. On the other hand, organic ligands can directly complex with the REEs on the solid surface, and then the surface complexes dissolve (i.e., surface complexation). In both cases, the dissociation of the organic ligands is critical to the leaching process. As organic ligands with more than one COOH group, their speciation in solution is pH-dependent since the protonation and deprotonation. The dissociation of a chelating agent increases with the pH, thereby the deprotonated free ligands would be more available (Moldoveanu et al., 2021). According to above analysis, the degree of the dissociation of organic ligands, which in turn affects the availability of the ligands in leaching solutions, might be one of the possible reasons for the poor leaching results achieved by those organic ligands.

In this section, the effect of pH on the leaching efficiency of NaOH-treated monazite by 0.1 M DTPA as a function of pH (from 2 to 10) was investigated. Data from these experiments are shown in Figure 154, and largely indicate that the leaching efficiencies are very low (<2%), despite changes in pH.

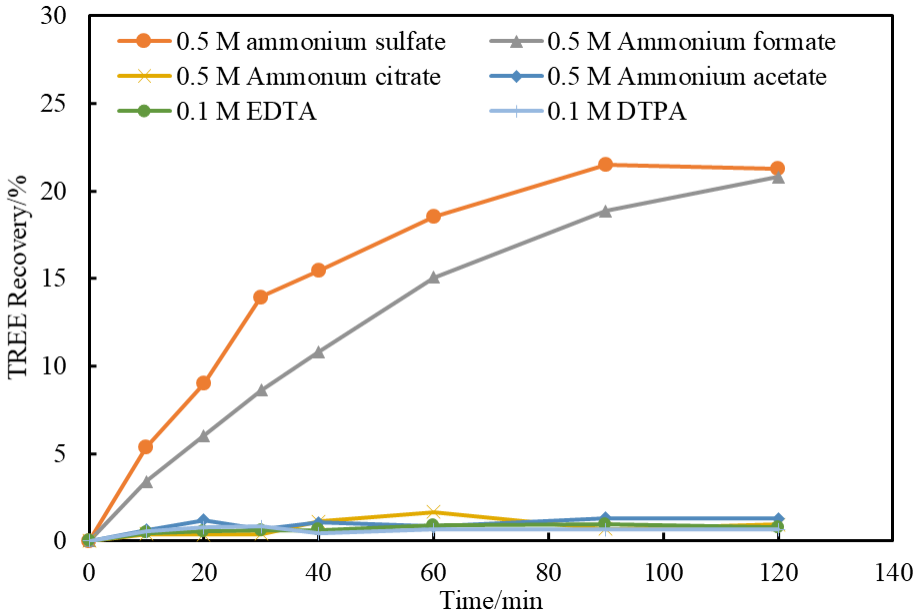

Figure 153. Effect of different anions on the total REE recovery of monazite after NaOH pretreatment (30%) at 80 ℃ for 24 h, d_{80} = 14.61 µm.

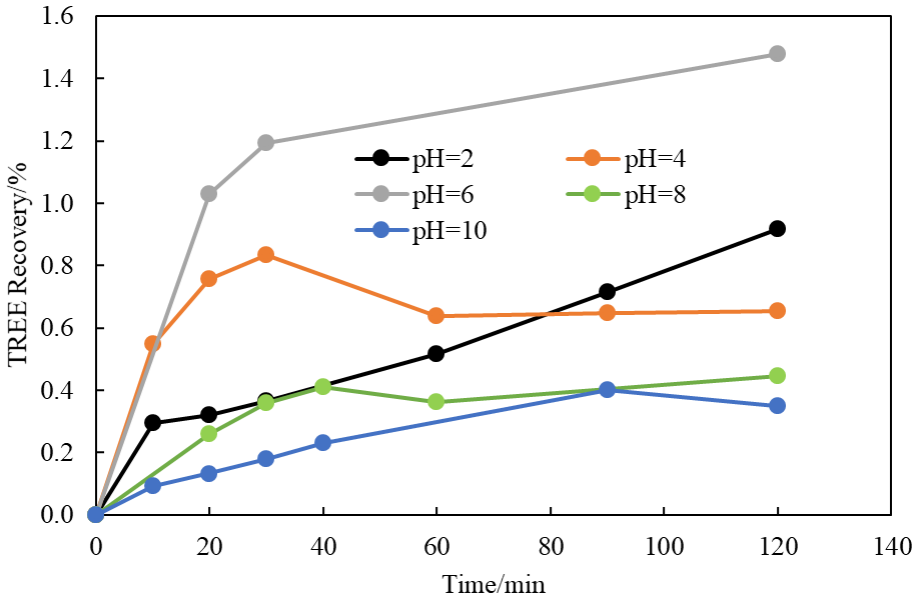

Figure 154. REE recovery leached by 0.1 M DTPA at various pH values after 30% NaOH pretreatment at 80 °C for 24 h.

This finding suggests that the availability of the dissociated ligands in solution did not affect the leaching process. Among the tested pH values, relatively higher recoveries were obtained at pH 4 and 6. Under these two weakly acidic conditions, the deprotonation of DTPA and the dissolution of the $RE(OH)_3(s)$ may be both enhanced, thereby benefiting the extraction process. At pH 8 and 10, the deprotonation of DTPA was enhanced since these two pH values are close to the pKa values that DTPA can lose its fifth and sixth hydrogen. However, the solubility of $RE(OH)_3(s)$ is close to its minimum values at this pH according to the solubility diagram of $La(OH)_3(s)$ constructed elsewhere. This explanation may be the reason for its low leaching efficiency. In one industry practice, the leaching of NaOH-treated monazite can be performed by HCl at around pH 3, indicating that $RE(OH)_3(s)$ can be dissolved at that pH (Qi, 2018). However, with the addition of DTPA, the recovery even at pH 2 was only 0.8%. This observation indicated that the hydrogen ions may be mainly consumed by the protonation of DTPA rather than the dissolution of $RE(OH)_3(s)$. If $RE(OH)_3(s)$ was dissolved at pH 2, higher leaching efficiency should have been achieved. Therefore, it suggested that the surface coordination is more likely to occur directly on the surface of $RE(OH)_3(s)$. As such, there should be other factors that constrained the leaching process.

Passivation of organic ligands by surface complexation

In the previous section, data showed that pH has a minor impact on the leaching efficiency, indicating that the process is less likely to be controlled by aqueous coordination. For most of the tested ligands (especially for citrate, EDTA, and DTPA), they are more complicated than ammonium formate in terms of molecular structures, which may have other interactions that deteriorate the leaching efficiency.

The leaching process of the NaOH-treated monazite by organic ligands can be simplified as the dissolution of $La(OH)_3(s)$ in the presence of various organic ligands. Several studies have reported the influences of organic ligands on the dissolution of oxide minerals. Bondietti et al. (1993) investigated the effect of several organic and inorganic ligands on the dissolution of Fe(III) (hydr)oxides. This author postulated that the formation of mononuclear surface complexes (monodentate and bidentate) can enhance the mineral dissolution, while the existence of bidentate binuclear surface complexes inhibits the dissolution process. This finding is due to the fact that the removal of two metal ions from the surface requires greater energy for the latter one. The adsorption of EDTA and the complexes of EDTA-metal (metal: Ca, Zn, Ni,

et al.) on goethite was investigated by Nowack et al. (1996). In the aqueous system of EDTA and goethite, the adsorption of EDTA at the low pH is in the manner of binuclear complexes, while the mononuclear type was found at the high pH values. Because of the type of surface complex varies with pH (from binuclear to mononuclear one), the dissolution of goethite was low at the low pH due to the inhibitory effect of binuclear complex, whereas the dissolution rate gradually increased with pH and maximized at pH 8. Chin et al. (1991) examined the dissolution kinetics and mechanisms of kaolinite in the presence of protons, low molecular weight organic ligands, and soil humic acid, etc., it was found that organic ligands markedly accelerate the dissolution rates of Al and Si, whereas the soil humic acid and stream water dissolved organic matter didn't enhance the dissolution process under the experimental conditions. The proposed surface coordination model shows that the formation of binuclear surface complexes can block the dissolution process (shown as below reaction).

$$2\equiv M\text{-}OH + H_2B = \equiv M_2B + 2H_2O \qquad [5.2.21]$$

This study indicated that the kinetics of the surface-controlled dissolution reactions are also slow. Additionally, Eick et al. (1999) proposed that oxyanions (chromate and arsenate) inhibited the oxalate-promoted dissolution of goethite by competitive adsorption (those two oxyanions compete the goethite surface site with oxalate). According to the above studies, the dissolution of oxide minerals can be accelerated or inhibited in the presence of organic ligands. The organic ligands-promoted or inhibited dissolution depends on the type of surface complexes and the strength of the bond (Eick et al., 1999) in the competitive sorption reactions. The similar reason may also apply to the dissolution of $La(OH)_3(s)$ in the presence of various organic ligands (acetate, citrate, EDTA, and DTPA). To confirm this hypothesis, FTIR was used to characterize the variations of surface composition of the sample before and after leaching.

Since the composition of natural monazite sample is complicated, a standard $La(OH)_3(s)$ chemical was used to replace the actual NaOH-treated monazite sample for the FTIR analysis, so as to minimize the interference of other impure elements. Firstly, the ammonium citrate solution and $La(OH)_3(s)$ were analyzed by FTIR respectively before and after leaching. As is shown in Figure 155, similar spectra were observed for the ammonium citrate solution before and after leaching. Both spectra show the existence of

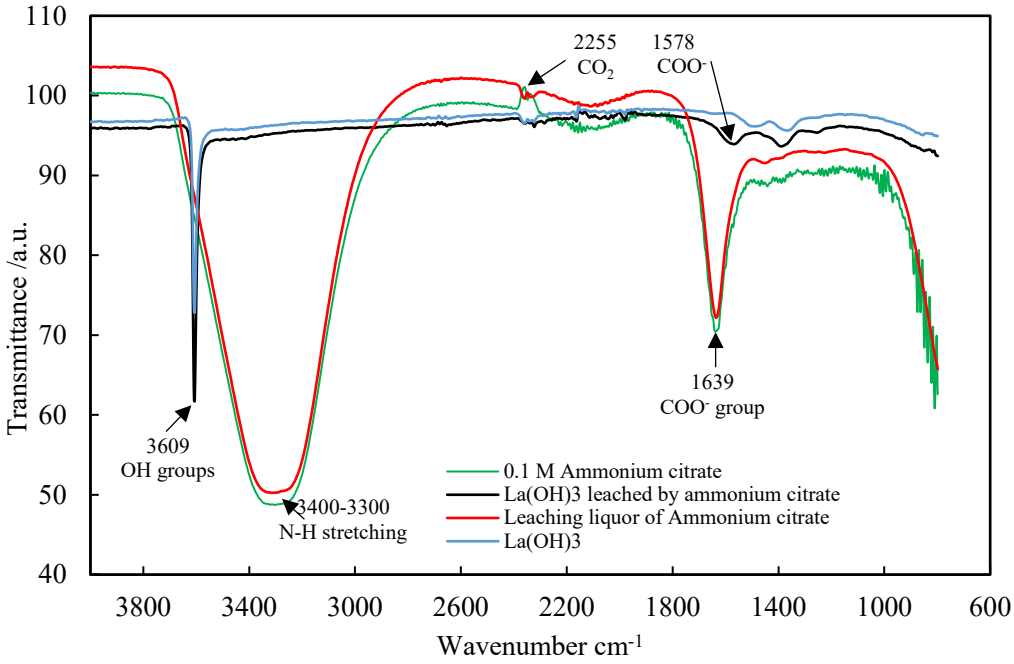

Figure 155. FTIR results of the ammonium citrate and $La(OH)_3(s)$ before and after leaching respectively.

CO_2, which is supported by the O=C=O stretching at peak 2255 cm^{-1} (2400-2000 cm^{-1}) (Vanderah et al., 2012). The peak at 3303 cm^{-1} was assigned to the N-H stretching of ammonium citrate. The existence of carboxyl group was confirmed by the peak at 1639 cm^{-1}.

In the leaching residue, the peak at 1639 cm^{-1} shifted toward lower wave numbers (1578 cm^{-1}), compared with that of the ammonium citrate solutions (Sun et al., 2014). This change was produced from the chemical bonds formed between hydroxy group and La(III). This change was not found in the spectra of $La(OH)_3(s)$ feed sample. Therefore, the results suggests that the interaction between citrate and the surface of $La(OH)_3(s)$ is inner-sphere coordination bond and with the surface complexes being generated on the surfaces of $La(OH)_3(s)$.

The same characteristic was found in the leaching residues leached by other ligands. The spectra of the leaching residues after being leached by other organic ligands also show the similar behavior. As is shown in Figure 156, the peak at 1578 cm^{-1} was observed for all the lixiviants with carboxyl group in their molecules, while no peaks were found for the feed sample and the one leached by ammonium sulfate. Above results indicate that the formation of surface complexes on the surface of $La(OH)_3(s)$ when organic ligands with carboxyl group. Among these surface complexes, bidentate binuclear complexes maybe the dominant species, and thus inhibits the further dissolution. Though the peak at 1578 cm^{-1} was also observed in the residue leached by ammonium formate, the peak intensity was weaker than its counterparts. This might be due to the likelihood that only a small proportion of formate adsorbs on the surface via binuclear bidentate complexes, while most of the complexes are in mononuclear. As such, ammonium formate is still an effective lixiviant for the leaching of $La(OH)_3(s)$.

The results of FTIR analysis in this section indicate the formation of surface complexes when $La(OH)_3(s)$ was leached by various organic ligands with (e.g., citrate, EDTA, DTPA). Among those complexes, the binuclear bidentate may be the dominant species and inhibit the dissolution of $La(OH)_3(s)$,

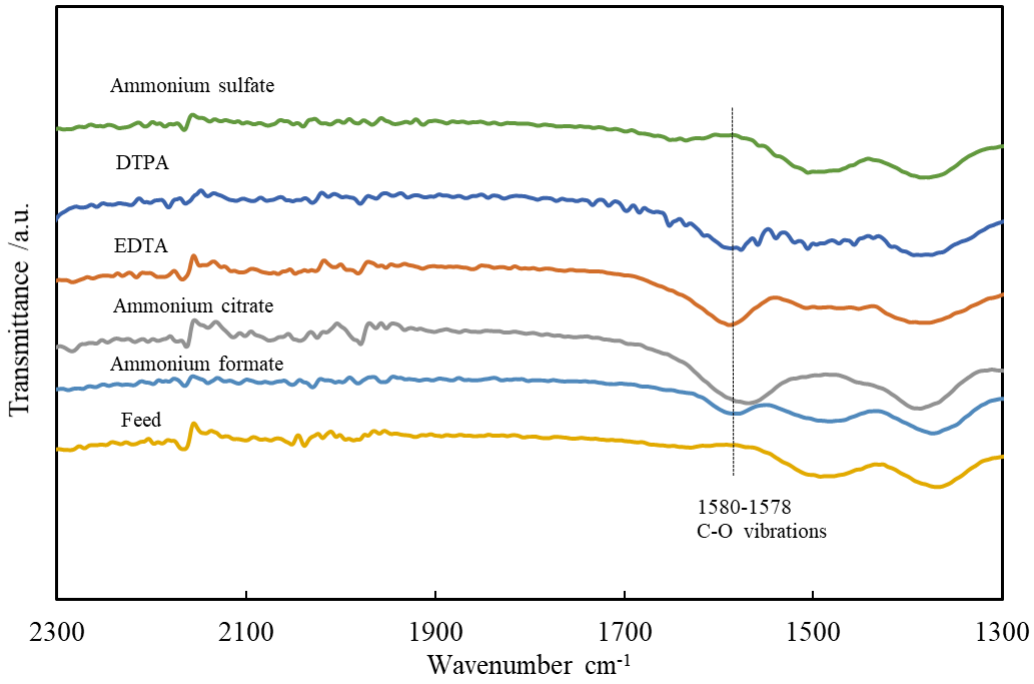

Figure 156. FTIR analysis of the leaching residues of the $La(OH)_3(s)$ standard after leached by various lixiviants. (After mixing the $La(OH)_3(s)$ with organic ligands, the stretching band of $-COO^-$ at 1662-1620 cm^{-1} of the leaching liquor shifted to 1590 cm^{-1} of the leaching residues, suggesting the coordination of La^{3+} and $-COO^-$) (He et al., 2014).

thereby poor leaching efficiencies were achieved by them. This observation is consistent with the conclusion reported in previous studies: organic ligands can facilitate or inhibit the dissolution of minerals depending on the type of surface complexes. On the other hand, the surface-coordinated organic ligands have a buffering effect. When the pH was adjusted to 4 during the leaching tests, the consumption of HCl (used for pH adjustment) by protonation of those ligands also prevented the dissolution of the $La(OH)_3(s)$. The invalidation of the thermodynamic prediction (Figure 152) is mainly attributed to the fact that the inhibition of surface complexes to the dissolution of rare earth hydroxide was not considered.

Without the presence of organic ligands, surface hydrolysis reactions of $La(OH)_3(s)$ occur as follows (Fang et al., 2017):

$$\equiv LaOH + H^+ = \equiv LaOH_2^+ \qquad \text{Log K} = 6.9 \qquad [5.2.22]$$

$$\equiv LaOH = \equiv LaO^- + H^+ \qquad \text{Log K} = -10.9 \qquad [5.2.23]$$

The stability constants suggest that reaction [5.2.22] is the dominant reaction for the dissolution of $La(OH)_3(s)$ by acids. This is why $La(OH)_3(s)$ can be well dissolved by mineral acids.

However, in the presence of organic acids (e.g., citrate and EDTA), the dissolution of $La(OH)_3(s)$ becomes a surface-controlled dissolution reaction. Organic ligands can adsorb on the surface of $La(OH)_3(s)$. The surface complexation of $La(OH)_3(s)$ and EDTA can be described by the following reactions:

$$\equiv LaOH + L^{4-} + H^+ \rightleftharpoons \equiv LaL^{3-} + H_2O \qquad [5.2.24]$$

$$2\equiv LaOH + L^{4-} + 2H^+ \rightleftharpoons \equiv La_2L^{2-} + 2H_2O \qquad \text{blocking} \qquad [5.2.25]$$

$$2\equiv LaOH + L^{4-} + 3H^+ \rightleftharpoons \equiv La_2LH^- + 2H_2O \qquad \text{blocking} \qquad [5.2.26]$$

In which "L" represents EDTA. Reaction (5) and (6) indicate the formation of binuclear surface complexes, which are difficult to dissolve, thereby inhibiting the dissolution of rare earth hydroxide.

Effect of leaching temperatures on the leaching efficiency

Previous results indicate that inhibition of surface complexes is the reason for the poor leaching efficiencies achieved by acetate, citrate, EDTA, and DTPA. The rate-determining step for them was found to be the dissolution of surface complexes, which is a slow process at room temperature. By using DTPA as a lixiviant, Gado et al (2019) selectively recovered Th and REEs from NaOH-treated monazite, leaving U as a precipitate in the leaching residue. Such unique property enables DTPA to be a promising lixiviant in terms of separation radioactive elements from REEs. The optimal conditions for the DTPA leaching were: DTPA concentration: 20%, 100 ºC, 8 h, and S/L = 1:30. Under the optimal conditions, the recoveries of REEs and Th can be 99 and 98% respectively. As such it is still necessary to further explore the leaching characteristic of $La(OH)_3(s)$ by organic ligands. Therefore, the motivation of this section is to examine the effect of temperature on leaching of $La(OH)_3(s)$ by organic ligands. Ammonium acetate (0.5 M) and EDTA (0.1 M) were used as lixiviants for the standard $La(OH)_3(s)$ respectively as various leaching temperatures. The leaching kinetics was also analyzed based on the shirking core model.

As is presented in Figure 157, the leaching kinetics of TREE by ammonium acetate was significantly improved by increased temperature. At 40 ºC, the recovery of La was only 40.70%; however, it increased to 76.27% when the leaching temperature increased to 70 ºC. Figure 158a and b replot this data and are used to determine the kinetics type and activation energy, respectively. This analysis suggests that the leaching rate of ammonium acetate is an inner diffusion-controlled reaction (eqn. 7). The kinetics parameters of ammonium acetate leaching are listed in Table 47. Large activation energy (77.95 KJ/mol) was determined for the reaction, suggesting that the leaching process is highly temperature-dependent. On the other hand, the leaching equilibrium was achieved within 60 min at 70 ºC.

$$1 - \frac{2}{3}x - (1-x)^{\frac{2}{3}} = k_3 t \tag{7}$$

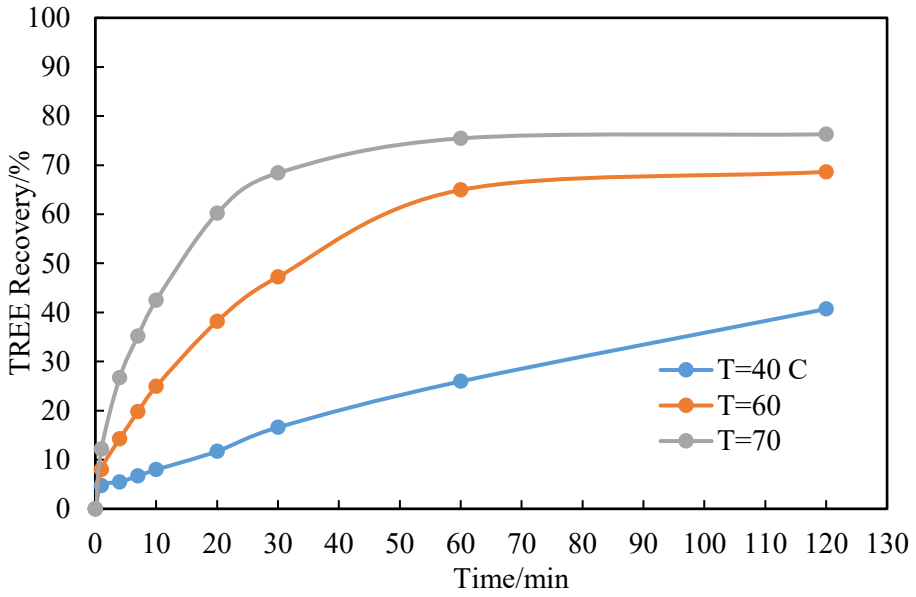

Figure 157. Leaching behavior of TREE from the standard La(OH)3(s) by 0.5 M ammonium acetate at different temperatures.

Table 47. Linearly regression results of 0.5 M ammonium acetate leaching at different temperatures from standard $La(OH)_3$(s)(21-118 R).

T/ºC	k	b	R^2
40	0.0006	-0.0031	0.9768
60	0.0035	-0.0068	0.9955
70	0.0083	-0.0038	0.9962

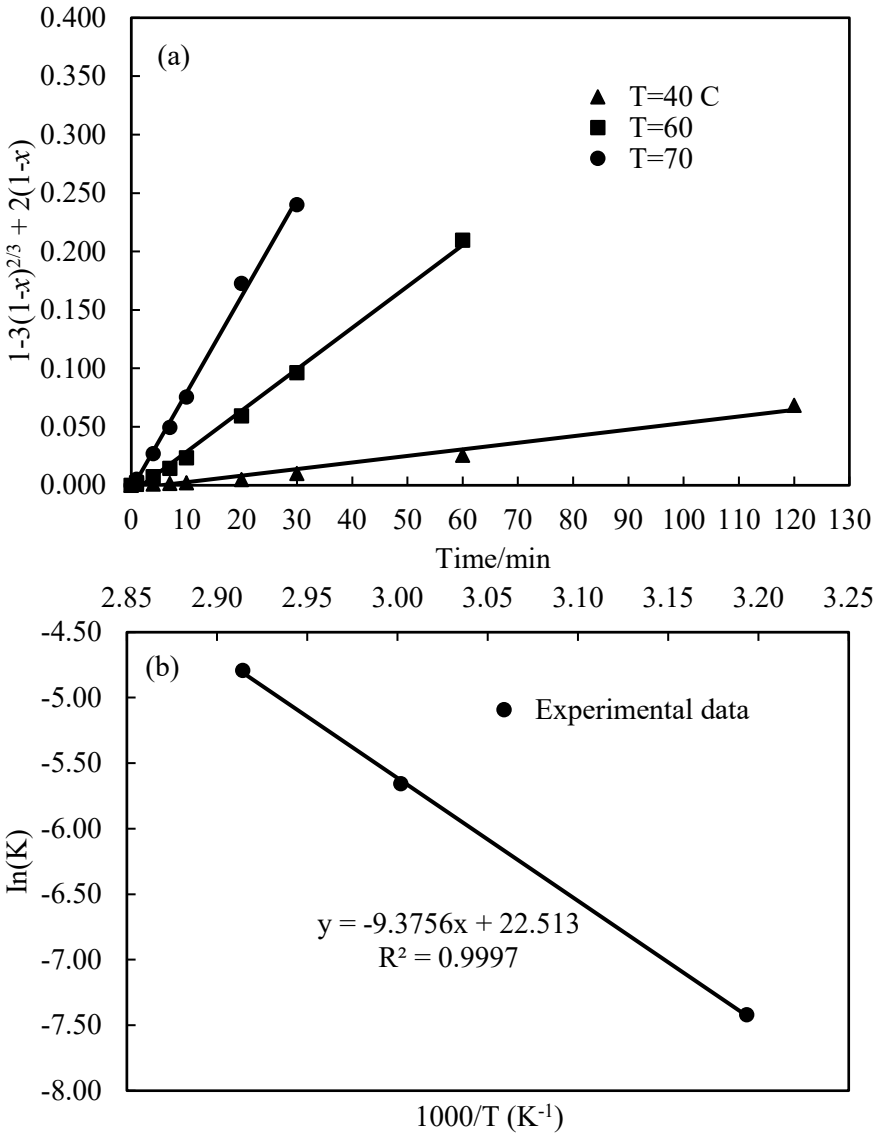

Figure 158. Plot of (a) $1-3(1-x)^{2/3} + 2(1-x)$ vs. time and (b) Arrhenius plot of leaching kinetics of $La(OH)_3(s)$ by 0.5 M ammonium acetate at pH 4 and different temperatures.

A similar leaching characteristic was found for the EDTA leaching. As shown in Figure 159, temperature was a significant factor in overall REE recovery with increases of temperature from 60 to 80 ºC prompting an increase in REE recovery from 20% to nearly 60% . The related analyses are shown in Figure 160a and b, which were used to determine the kinetic model and activation energy, respectively. Table 48 shows the related kinetics parameters. Based on these results, again, the kinetics type is an inner diffusion-controlled reaction, and a large activation energy (101.87 KJ/mol) was determined. As can be seen, the apparent activation energy determined for ammonium acetate was smaller than that of EDTA. This finding suggests that the adsorption of EDTA is stronger than that of acetate as the former has more COOH groups. As such, the removal of the surface complexes consumes more energy.

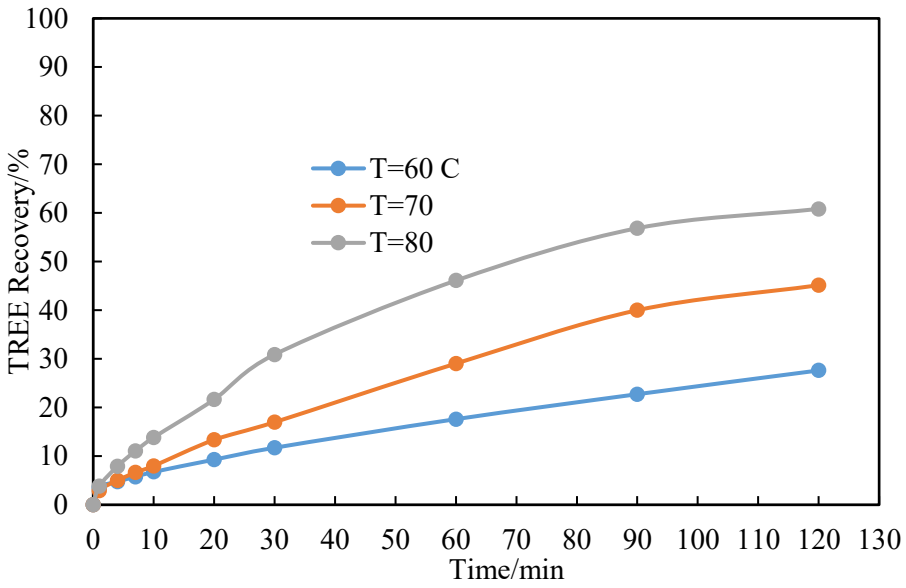

Figure 159. Leaching behaviors of TREE from standard La(OH)3(s) by 0.1 M EDTA at different temperatures.

The diffusion-controlled reaction with high activation energy has been reported by several studies. The apparent activation energy determined for the leaching of Ce from an oxidation roasted Baotou mixed rare earth concentrate was found to be 76.78 KJ/mol, and the kinetics type is both the interfacial transfer and diffusion through the product layer (Li et al., 2019). And the authors think the kinetics type is better to be predicted by kinetic equations rather than the activation energy. Kim et al (2007) studied the leaching kinetics of nickel from waste multi-layer ceramic capacitors. The determined activation energy is 37.6 KJ/mol, which is slightly higher than the values that normally reported for the diffusion-controlled leaching process. Such high value was attributed to certain surface diffusion in the thin channels formed between the multi-layer. Hernández et al (1986) also reported a high activation energy (63.5 KJ/mol) for the magnesium extraction from sepiolite by sulfuric acid, the corresponding leaching kinetic model is diffusion-controlled. Moreover, Paspaliaris et al (1987) found that the activation energies for the leaching of iron oxides from diasporic bauxite by HCl, which is also described by the diffusion-controlled kinetics model, changes from 62 to 79 KJ/mol depending on the size fractions of the sample. The above analysis indicated that the dissolution of rare earth hydroxide in the presence of these chelating ligands is inhibited by the surface complexation.

Table 48. Linearly regression results of 0.1 M EDTA leaching at different temperatures from standard $La(OH)_3(s)$.

T/°C	k	b	R^2
60	0.0002	-0.0008	0.9847
70	0.0007	-0.0045	0.9788
80	0.0016	-0.0056	0.9904

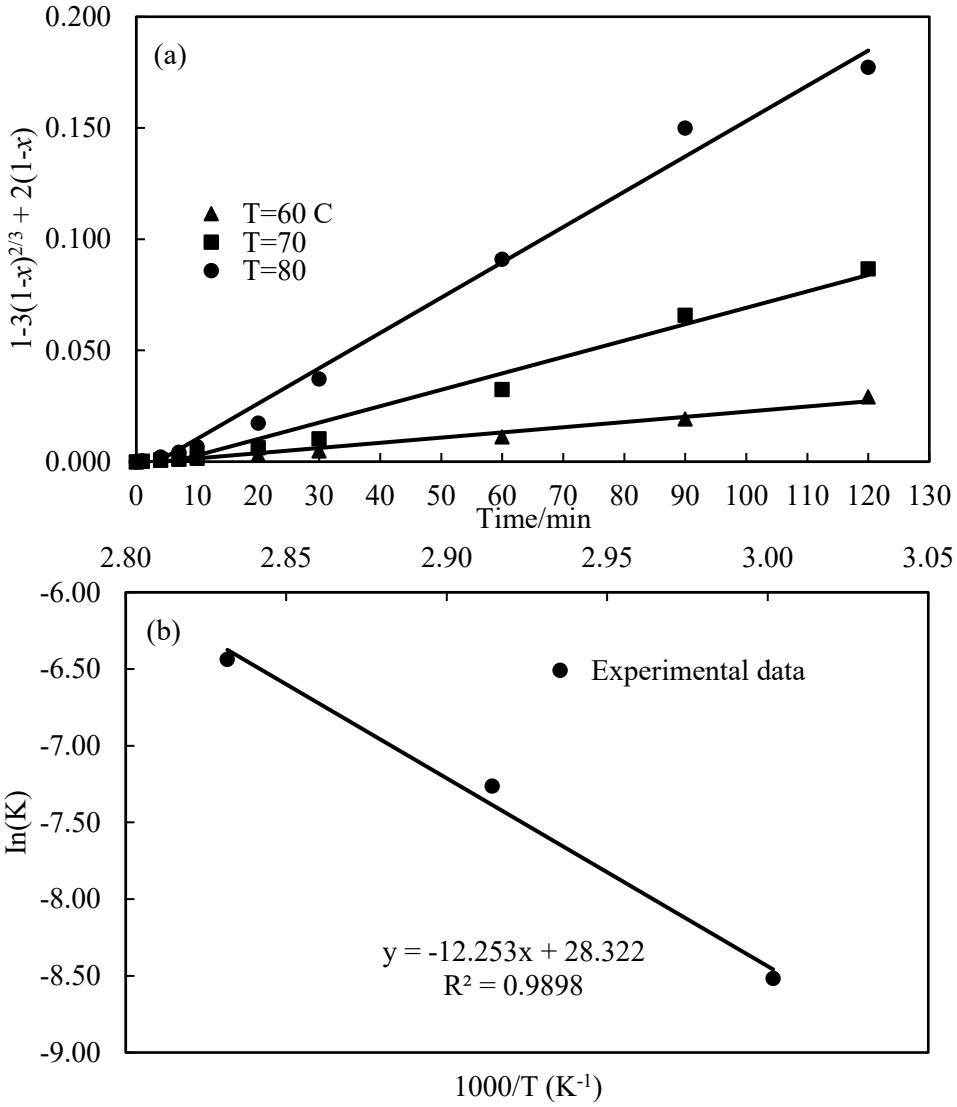

Figure 160. Plot of (a) 1-3(1-x)$^{2/3}$ + 2(1-x) vs. time and (b) Arrhenius plot of leaching kinetics of La(OH)$_3$(s) by 0.1 M EDTA at pH 4 and different temperatures.

Activation and Leaching of Passivated Ion Adsorption Clays

Sample preparation and experimental procedure

Rare earth ion adsorption clays (IACs) were obtained from an undisclosed site in South China. Phosphate-passivated IACs were prepared by treating IACs in 0.5 M NaH_2PO_4 solution at pH 4 for 1 h at room temperature, then washed with deionized water and dried at 70 ºC before use. Leaching tests using ethylenediaminetetraacetic acid (EDTA) were performed by treating phosphate-passivated IACs in various concentrations of EDTA solution at desired pH for 1 h at room temperature. Elemental concentrations in leaching solution were analyzed by inductively coupled plasma mass spectrometry (ICP-MS).

The effect of EDTA concentration and pH on the extraction efficiency of phosphate-passivated IACs

We have shown that organic chelating agents, such as EDTA, are effective lixiviants to extract REEs from phosphate-passivated IACs at pH 10. High concentrations of EDTA dissolve clay-REE-H_2PO_4 complexes on phosphate-passivated IACs and chelate REEs in the solution in the form of soluble REE-EDTA complexes. This section further investigates the dependency of REE extraction efficiency on EDTA concentration and leaching solution pH for phosphate-passivated IACs.

Figure 161 shows representative predominance area diagrams of REE^{3+}(La, Sm, Dy and Yb)-PO_4^{3-}-$EDTA^{4-}$ systems. The initial concentrations of REE^{3+} and PO_4^{3-} in the system are set to account for the full amounts of individual REE and P in the phosphate-passivated IACs, while the presence of other elements are not considered for the calculation. Three common phases, including REE^{3+}(aq), $REE(EDTA)^-$(aq) and (REE)PO_4(s), are observed in these diagrams in the pH range of 0 to 12. These diagrams demonstrate that high concentrations of $EDTA^{4-}$ in the leaching solution favors the formation of soluble REE-EDTA complexes over (REE)PO_4 precipitates under basic pH conditions, which is in excellent agreement with our previous experimental findings that EDTA has superior REE extraction efficiency for phosphate-passivated IACs at pH 10. Furthermore, the EDTA concentration at the phase equilibrium of $REE(EDTA)^-$(aq) and (REE)PO_4(s) decreases with increasing REE atomic numbers as shown in Figure 162, indicating that heavier REEs requires lower EDTA concentrations in the leaching solution to form soluble REE-EDTA complexes other than $REEPO_4$ precipitates. In addition, these diagrams also suggest that EDTA remains high effective under weak and mild acidic pH conditions, with the working pH range wider for heavier REEs.

Phosphate-passivated IACs were leached in a 0.5 M and 0.0005 M EDTA leaching solution at pH 10 respectively. Based on the predominance area diagrams in Figure 161, we hypothesize that high EDTA concentrations will yield similar extraction efficiency for individual REE, while a much lower EDTA concentration will result in lower extraction efficiency for lighter REEs. Figure 163 shows the extraction percentage of REEs and P for phosphate-passivated IACs that were leached by the two EDTA leaching solutions. After being leached in a 0.5 M EDTA solution for 1 h, 55% of the total REE content (TREE) was extracted into the leaching solution. Similar extraction efficiencies were observed for individual REE in the range of 45-61% (excluding Ce), while a slight decline in extraction % was present for heavier REEs. By contrast, after being leached in a 0.0005 M EDTA solution for 1 h, only 15% of total REE content (TREE) were extracted. This result is possible due to an insufficient amount of EDTA molecules and slower kinetics. Most importantly, an attenuation in extraction % for lighter REEs (La-Gd) were observed, with La suffering the largest decline. These results are in good agreement with the predominance area calculations, indicating that a low EDTA concentration is more detrimental to the extraction of lighter REEs from phosphate-passivated IACs.

Phosphate-passivated IACs were also leached in a 0.05 M EDTA leaching solution at pH 10 and 2.8 respectively. Based on the predominance area diagrams in Figure 161, we hypothesize that EDTA would be ineffective to extract lighter REEs at pH 2.8. Figure 164 shows the extraction percentage of REEs and P for phosphate-passivated IACs that were leached by the two EDTA leaching solutions. After being leached in a 0.05 M EDTA solution at pH 10 for 1 h, 51% of total REE content (TREE) were extracted into the leaching solution and similar extraction efficiencies were observed for individual REE in the range of

41-58% (excluding Ce). After being leached at pH 2.8 for 1 h, a mild decrease in TREE extraction % was observed (39%); however, as opposed to the predominance area prediction, EDTA remains equally effective to extract all REEs under this strong acidic condition. These results reveal the limitation of our current thermodynamic calculations, and a more sophisticated model system is desired.

In summary, EDTA is an effective lixiviant to extract REEs from phosphate-passivated IACs under both acidic and basic conditions. The extraction efficiency of Lighter REEs is more sensitively to the EDTA concentration in the leaching solution.

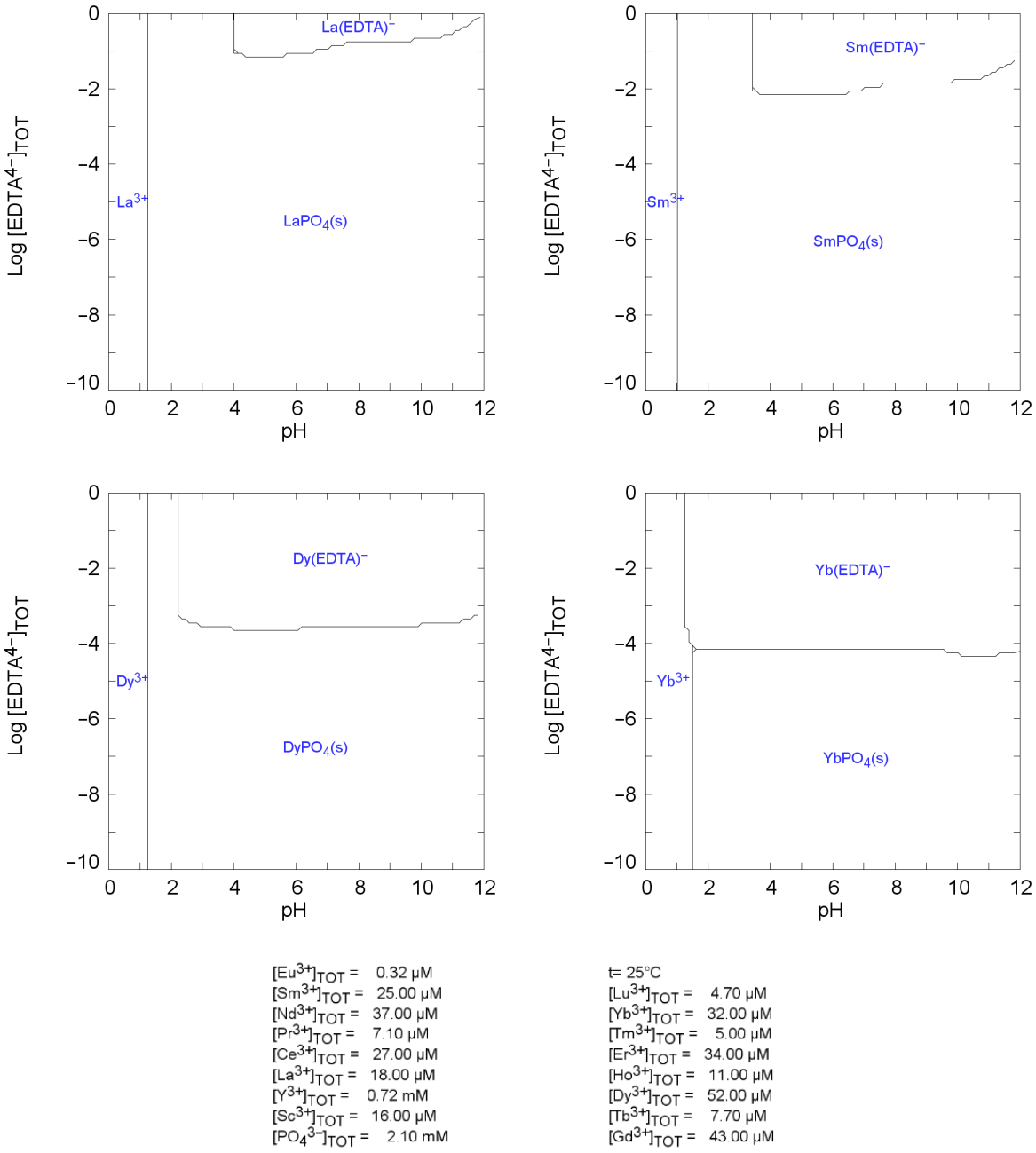

Figure 161. Predominance area diagrams of $REEPO_4$-EDTA systems (La, Nd, Dy, Yb).

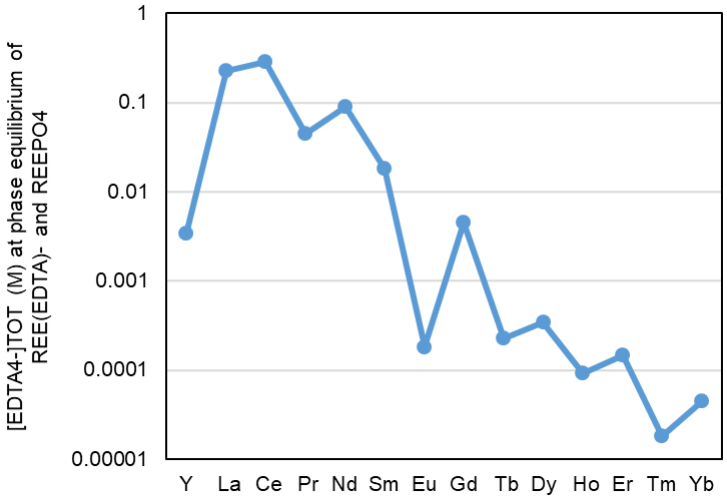

Figure 162. Concentration of $EDTA^{4-}$ to achieve phase equilibrium of $REE(EDTA)^{-}(aq)$ and $(REE)PO_4(s)$.

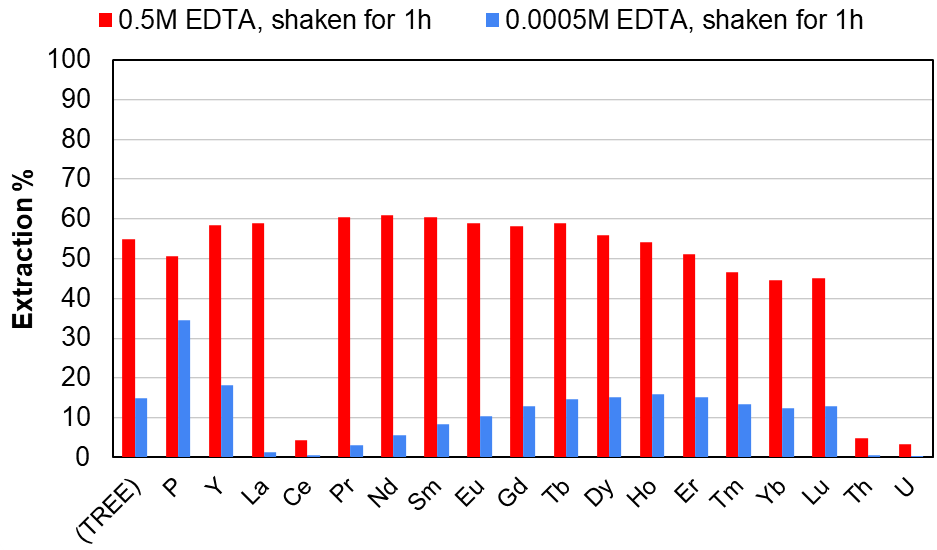

Figure 163. REE+P extraction % for phosphate-passivated IACs leached by various EDTA concentrations at pH 10.

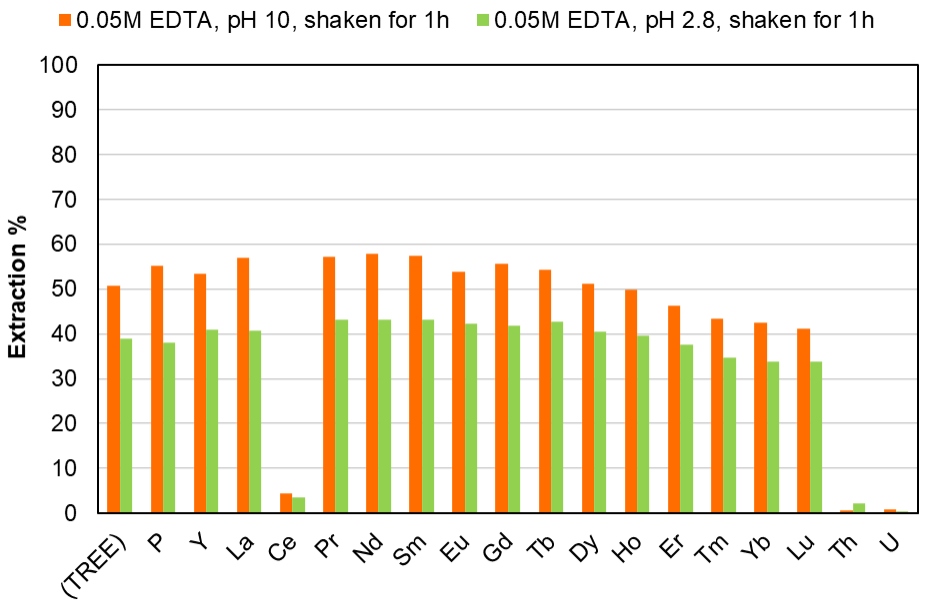

Figure 164. REE+P extraction % for phosphate-passivated IACs leached by 0.05 M EDTA under various pH conditions.

Subtask 5.3 – Chemical Leaching and Selective Liberation of Colloidal Phase REEs

Solubility of $LaPO_4$

Thermodynamic simulation

The effect of the chelating agent, EDTA, on the dissolution of a pure $LaPO_4$(s) standard was studied as part of our effort to improve the extraction of REEs from the surface of the clays isolated from coal byproducts (refuse). The EDTA was chosen as it has large stability constants with lanthanides, is widely used in industry for other purposes, and is readily available at commercial scale. Unless otherwise noted, all experiments were conducted in 0.1 M EDTA solutions prepared from the disodium salt of EDTA.

Initially, the EDTA leaching was simulated using the MEDUSA software, with the results in Figure 165. The simulations were carried out under conditions of 10 µM $LaPO_4$ in the presence of 0.1M EDTA. As shown, La(PO_4)(s) dissolves at pH < 2 to release bare La^{3+} ions into solution. As the pH is increased above 2, it produces LaEDTA(aq) into solution, its fractional distribution reaching a maximum at pH 2.5. The complex is neutral as one of the four carboxylic acid groups of the chelating agent is not ionized. As the pH further increased, all four carboxylic acid groups are fully ionized and form $La(EDTA)^-$.

Effect of pH on the $LaPO_4$ dissolution in EDTA solution

In an effort to validate the simulation results shown in Figure 165, a series of leaching experiments was conducted on the neat $LaPO_4$(s) standard at room temperature. The experiment started at a high pH (= 10) to negate the acidic dissolution effects, while the solution was being titrated using a dilute hydrochloric acid (HCl) solution to reduce the pH. Disposable magnetic polytetrafluoroethylene (PTFE) stir-bars were utilized for constant stirring of the suspension. Disposable polypropylene (PP) syringes were used to draw sample aliquots, which were then filtered through 0.22 µm polyvinylidenedifluoride (PVDF) membranes directly into the 2% w/v nitric acid (HNO_3) + 0.5% w/v HCl diluent for ICP-MS analysis. Samples were taken intermittently as the pH decreased, and done quickly as a means of reducing the leaching kinetics extraction bias for any specific pH value. As shown in Figure 166, approximately 1% or less of the total $LaPO_4$(s) was dissolved across the pH range at room temperature. However, the amount of La^{3+} ions extracted into solution increased drastically below pH 2. While the increase at low pH values is consistent with the simulation model of La^{3+} formation, the low recoveries at high pH were not, suggesting that the leaching efficiency may be rate limited at high pH.

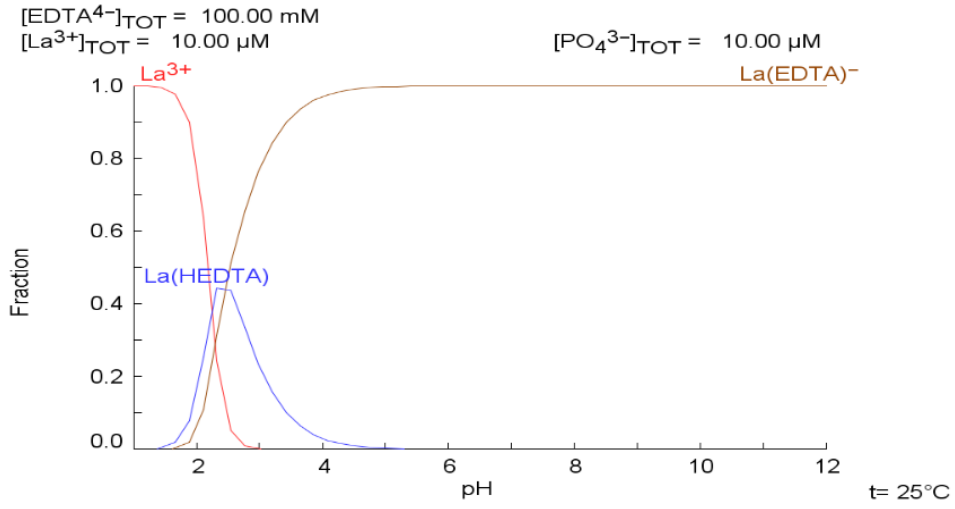

Figure 165. Hydra and Medusa simulation showing the species of 10 µM $LaPO_4$ in the presence of 0.1M EDTA.

A temperature of 80 °C was used in all subsequent experiments in an attempt to accelerate the leaching kinetics in the alkaline pH range. Individual experiments targeting improved kinetics at specific pH values were performed in an effort to identify the optimal leaching pH. The pH probe used was calibrated between pH 7 and 10 using fresh buffer solutions prior to beginning each experiment, and the probe was set to account for temperature variations. The target pH values above pH 8.5 were obtained by titration with a dilute sodium hydroxide (NaOH) solution, while the target pH values below 8.5 were achieved by titration using dilute HCl. Even though the simulation data had shown that $LaPO_4$ leaching would be negligible under alkaline conditions, a blank run of the same extraction at ~pH 10 was also included to further show that EDTA was the cause of the $LaPO_4$ dissolution. The results for this set of experiments can be found in Figure 167. The optimal leaching kinetics for the highest percentage of La extracted over time was shown to be at approximately pH 8, with approximately 86% of the La was extracted in the presence of 0.1 M EDTA after 5 hours or more of reaction time. While the extractions tests conducted at pH 7, 9, and 10 exhibited similar initial extraction kinetics, they ultimately had lower total extraction efficiencies of approximately 70%, 57%, and 35% over the same time period, respectively.

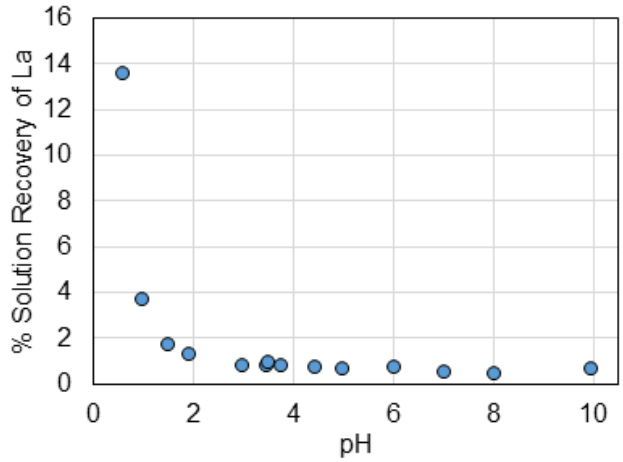

Figure 166. Initial pH screening for the dissolution of neat $LaPO_4$ standard by 0.1M EDTA.

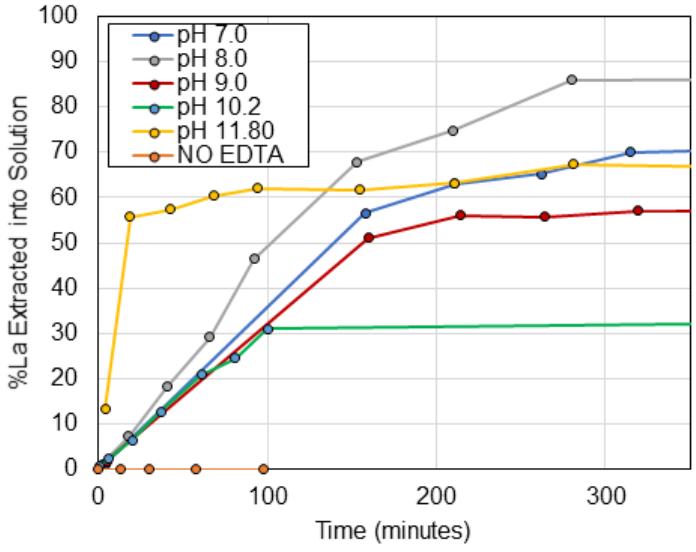

Figure 167. % Extraction of $LaPO_4$ at 80°C with 0.1M EDTA at various pH.

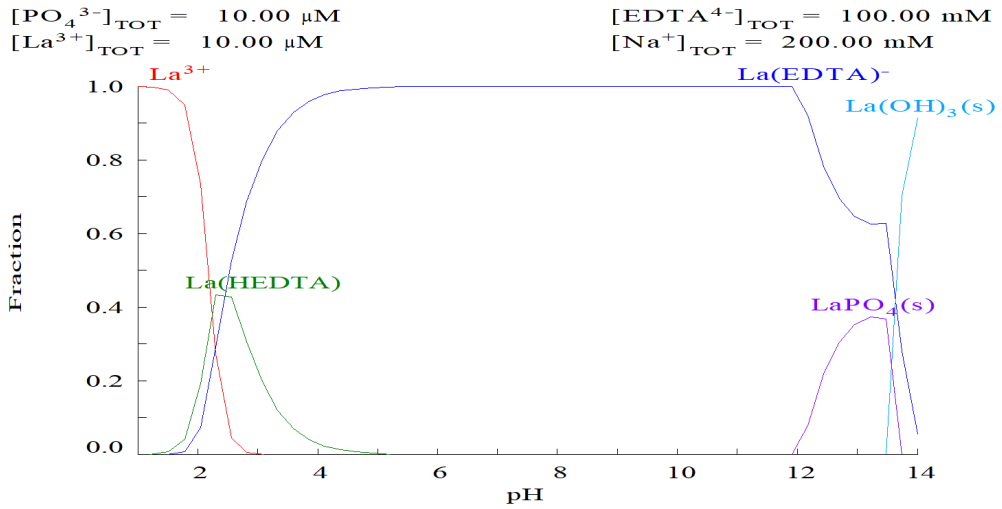

Figure 168. Thermodynamic simulation showing the species of 10 µM $LaPO_4$ in the presence of 0.1M EDTA.

One major outlier observed was the dissolution experiment performed at pH 11.8. The initial leaching kinetics was extremely rapid with 56% La extraction in just 20 minutes, but then leveled off quickly before reaching total extractions of about 68% in five hours. This may be partially explained due to the relatively large amount of NaOH required to reach pH 11.8 *vs*. the amounts used for lower pH extractions. The drastic increase in localized NaOH content, and therefore the pH as well, may have contributed to the partial alkaline hydrolysis of the $LaPO_4$ to $La(OH)_3$, which may have been more easily dissolved into the EDTA solution. The simulation data presented in Figure 168 also show that the stability of the $La(EDTA)^-$ species was reduced at this pH and above, as $LaPO_4(s)$ is predicted to begin precipitating. Given the high NaOH consumption required to reach these pH values, stability concerns, and the lower overall recovery of La into solution, pH 8 was ultimately chosen to be used in subsequent leaching experiments. The experimental results presented in Figure 167 clearly show the benefits of using EDTA for leaching $La(PO_4)(s)$ at alkaline pH, which in turn suggests that the passivation effect of PO_4^{3-} ions may be readily overcome by using a chelating agent.

Effects of solids content in EDTA leaching

Leaching tests with the pure $LaPO_4(s)$ standard described in this section were performed at pH 8 and at a temperature of 80°. Disposable magnetic PTFE stir bars were utilized for constant stirring of the particle suspensions. The solids content of $LaPO_4(s)$ in the 0.1 M EDTA solution was varied from approximately 0.00025% w/v to 1% w/v. The sample suspensions with solids contents below 0.1% w/v were obtained by suspending a known mass of $LaPO_4(s)$ standard in water, and then aliquoting known volumes of said suspensions immediately after being thoroughly shaken directly into the EDTA solutions. Total La contents of the individual leach liquor (or pregnant solution) were determined *via* direct acid digestion of the final leach liquor to account for any variations in the $LaPO_4(s)$ concentrations of the dispensed standard solution suspensions. Samples with solids content greater than 0.1% w/v had known amounts of the neat standard weighed directly into the extraction vessels.

These measurements were performed by preparing a series of solutions with known solids concentrations. The pH probe used was calibrated between pH 7 and 10 using fresh buffer solutions prior to beginning the experiment, and the probe was set to account for temperature variations. Samples were allowed to reach their target temperatures over approximately 10 minutes before being titrated with a dilute HCl solution to reach the target pH of 8.0. Solution pH was regularly monitored, and the probe was rinsed with deionized water and cleaned with dilute HCl between samples to prevent transfer of any $LaPO_4$ potentially adsorbed to the probe. Samples were collected intermittently over the course of approximately

24 hours. Disposable PP syringes were used to draw sample aliquots which were filtered through 0.22 µm PVDF membranes directly into the 2% w/v nitric acid (HNO_3) + 0.5% w/v HCl diluent used for ICP-MS analysis. The results of this analysis can be found in Figure 169.

As expected, the extraction efficiency decreased as the solids content increased. The highest leaching efficiency of approximately 80% was obtained with the 0.00025% w/v sample, while the lowest extraction efficiency was obtained with the 1% w/v sample. A plot of the extraction efficiency *vs*. solids content is shown in Figure 170 on the basis of the data presented in Figure 169.

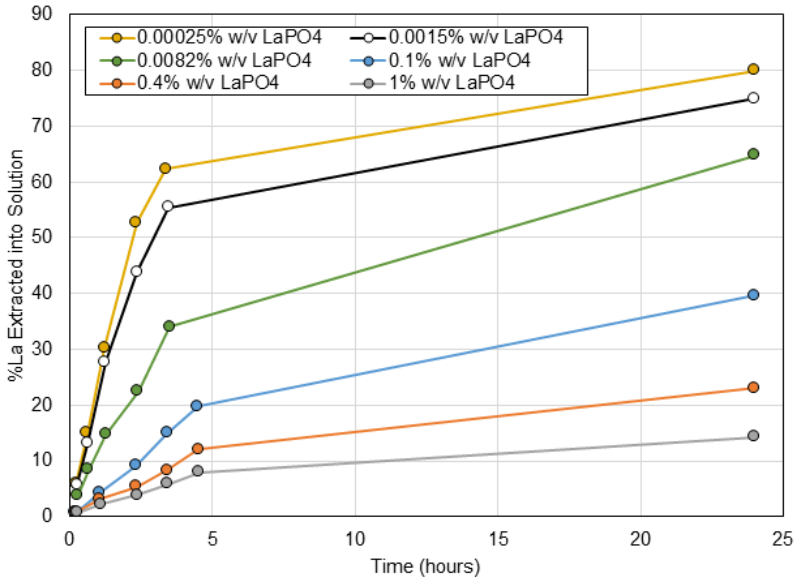

Figure 169. % Extraction of La from $LaPO_4$(s) over time at 80°C with EDTA solution at pH 8.0 with varying % $LaPO_4$ solids.

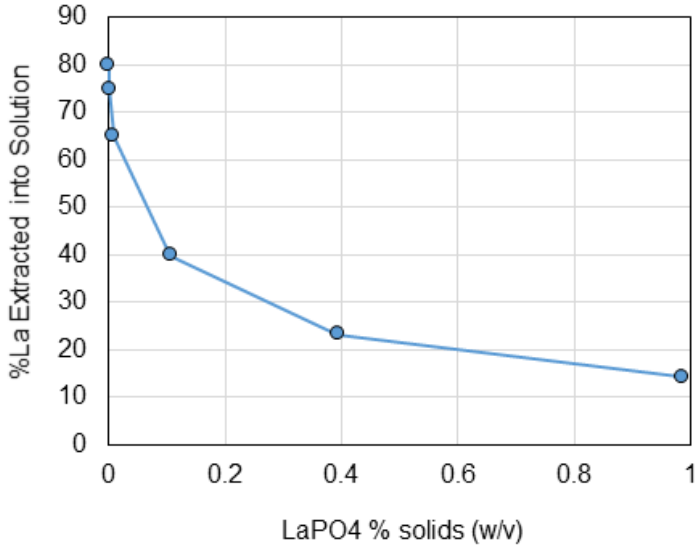

Figure 170. % Extraction of LaPO4 over 24 hours as a function of % solids in solution.

EDTPO Leaching

The leaching kinetics of a neat $LaPO_4$ standard, *i.e.*, an "artificial monazite" purchased from a chemical company, were used as a means of direct comparison to the leaching of a naturally occurring monazite. EDTPO was used in the chelation experiments after EDTA due to its large stability constants with lanthanides, and its ability to highly negatively charged ligand species up to $(EDTPO)^{8-}$. Unless otherwise noted, EDTPO solution is prepared from the free acid of EDTPO. A simulation of EDTPO speciation in aqueous solution is shown in Figure 171.

A neat $LaPO_4$ standard was leached at 80°C as a means of attempt to accommodate for the much slower leaching kinetics in the alkaline pH range. EDTPO concentration was kept constant at 0.1M. The $LaPO_4$ standard was weighed directly into extraction vessels to obtain a solids ratio of 0.1% (w/v), and this ratio was kept constant for the experiment. Individual experiments targeting the leaching kinetics at specific pH values were performed in an effort to identify the optimal leaching pH with EDTPO. The pH probe used was calibrated between pH 7 and 10 using fresh buffer solutions prior to beginning the experiment, and the probe was set to account for temperature variations. Target pH values were obtained *via* titration with dilute sodium hydroxide (NaOH). The results for this set of experiments can be found in Figure 172 and Figure 173.

The optimal leaching kinetics for the highest percentage extracted over time was shown to be at approximately pH 11, with approximately 11% of the $LaPO_4$ extracted into solution over 70 hours. A trend emerged indicating that EDTPO leaching efficiency increased with pH.

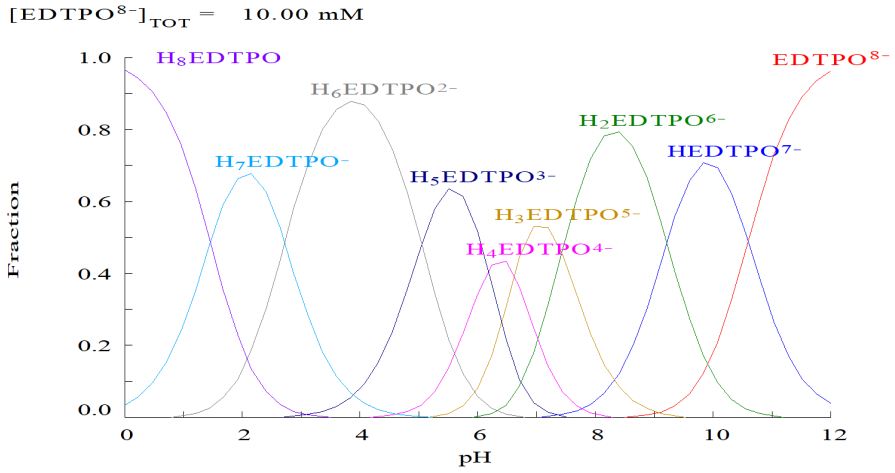

Figure 171. Hydra and Medusa simulation showing EDTPO speciation in aqueous solution based on pKa values.

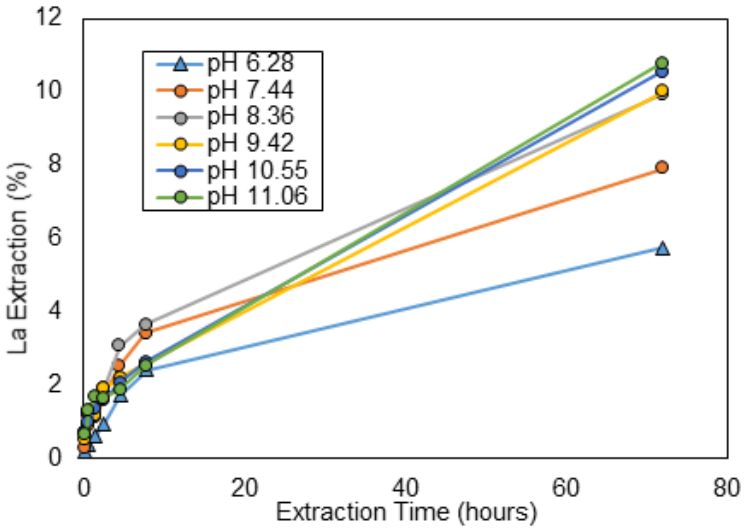

Figure 172. % Extraction of $LaPO_4$ at 80°C with 0.1M EDPO at various pH.

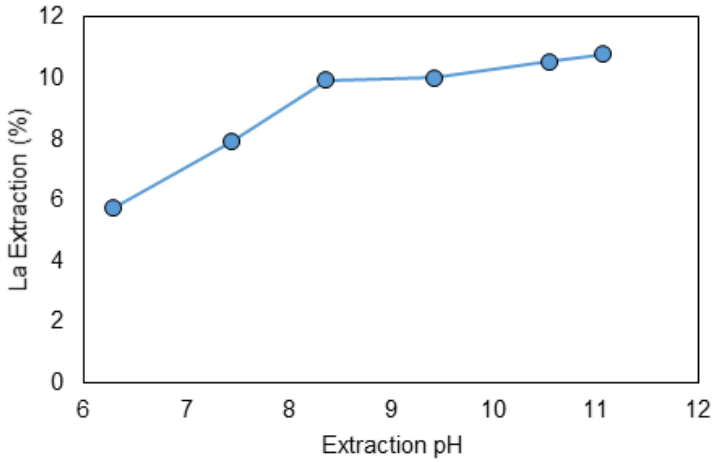

Figure 173. % Extraction of $LaPO_4$ at 80°C with 0.1M EDPO at various pH.

Methanol Leaching

A neat powder of anhydrous lanthanum phosphate ($LaPO_4$) was used to compare pretreatment methodologies prior to leaching with ammonium sulfate (AS). Pretreatment solutions of 20% (w/v) NaOH in water, water + sodium ascorbate, and dry methanol were compared. Approximately 6 mg of the standard was pretreated by 20 mL alkaline solution at a temperature of 60 °C for 22 hours. The lower temperature was used to minimize evaporation effects from the methanol. The pretreated samples were then washed with either water, or dry methanol prior to leaching. Samples were leached in 25 mL of 0.5M AS at pH 4.0 and 80°C. The $LaPO_4$ standard that had not been pretreated was also leached in the same manner and used as a control test.

Assuming that the standards were completely dissolved at this point, the concentration of La^{3+} ions in solution would be approximately 1 mM. Disposable magnetic PTFE stir bars were utilized for constant stirring of the samples. Samples were taken periodically during the course of 2 hours. Disposable polypropylene (PP) syringes were used to draw sample aliquots which were filtered through 0.22 µm PVDF membranes directly into the 2% w/v nitric acid (HNO_3) + 0.5% w/v HCl diluent used for ICP-MS analysis.

The results of this analysis can be found in Figure 174. Aqueous NaOH was found to be more effective than methanolic NaOH as a pretreatment solution meant to enhance the leaching efficiency of 0.5M AS at pH 4.

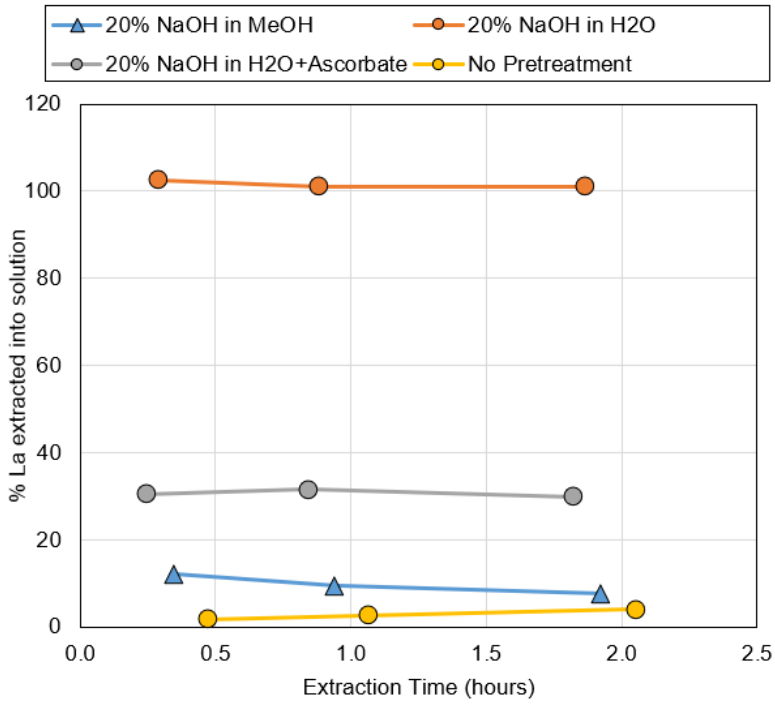

Figure 174. %$LaPO_4$ standard extracted into solution using 0.5M AS at pH 4 after various alkaline pretreatment methods.

Ion-exchange leaching

A neat powder of lanthanum hydroxide, $La(OH)_3$, was used to simulate sample material containing La species that had been successfully converted to $La(OH)_3$ via alkaline pretreatment processes. An example of this reaction is shown below,

$$LaPO_{4\,(s)} + 3\ NaOH_{\,(s)} \rightarrow La(OH)_{3\,(s)} + Na_3PO_{4\,(aq)} \qquad [5.3.1]$$

where 3 mols of NaOH convert 1 mol of lanthanum phosphate to lanthanum hydroxide and trisodium phosphate.

As such, this allows for a rapid means of direct comparison of lixiviants without requiring a time-consuming pretreatment process. The lixiviants chosen were ammonium sulfate, ammonium formate, and oxalic acid. Approximately 6 mg of the standard was directly leached in 25 mL of lixiviant which would make a concentration of approximately 1 mM La in solution assuming 100% dissolution of the standard. Simulations using the Hydra/Medusa software indicated that each of the reagent was capable of dissolving the La standard, with both the ammonium sulfate and ammonium formate utilized at pH 4, and oxalic acid at pH 6. The simulation diagrams for these conditions can be found in Figure 175 to Figure 177.

The extraction experiments were carried out at 80°C and using a disposable magnetic PTFE stir bars to provide constant stirring of the samples. Samples were taken at 30 minutes and 18 hours. Disposable polypropylene (PP) syringes were used to draw sample aliquots, which were subsequently filtered through 0.22 µm PVDF membranes directly into the 2% w/v nitric acid (HNO_3) + 0.5% w/v HCl diluent used for ICP-MS analysis. The results of the extraction tests are shown in Figure 178.

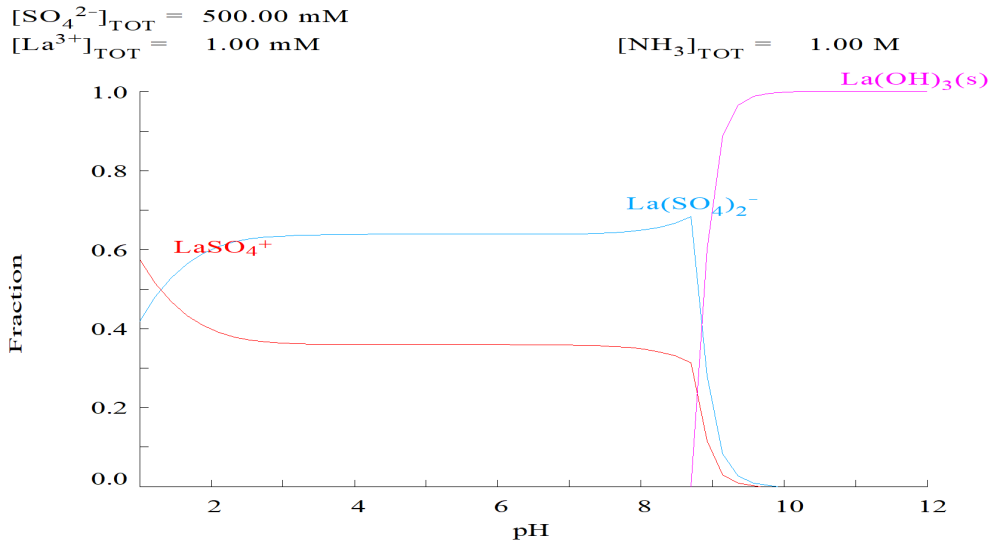

Figure 175. Hydra/Medusa simulation of La speciation in 0.5M AS; [La] = 1 mM.

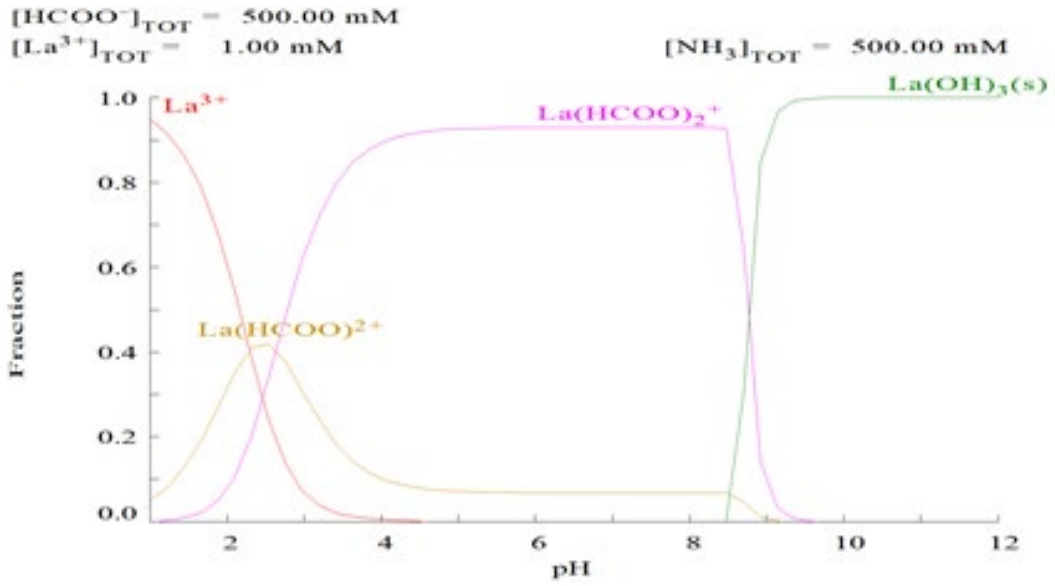

Figure 176. Hydra/Medusa simulation of La speciation in 0.5M ammonium formate; [La] = 1 mM.

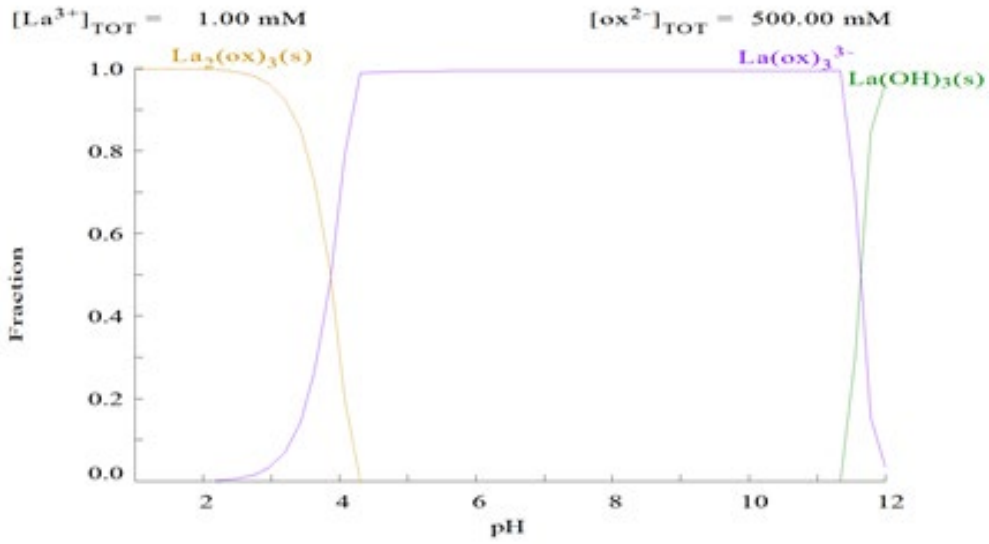

Figure 177. Hydra/Medusa simulation of La speciation in 0.5M oxalic acid; [La] = 1 mM.

Under the conditions employed in the present work, ammonium formate was found to be just as effective or more effective for the initial dissolution of the standard reagent, although the efficiency dropped over time due to precipitation observed at the final time point. This was likely due to the formation of formamide caused by the heating of ammonium formate solution over time. This could be beneficial in that direct precipitation of the dissolved REE species could be achieved by controlling temperature gradients over time.

Oxalic acid was also found to solubilize the standard at a pH of 6 to a lesser degree than either AS or ammonium formate, but at a much higher pH with the final pH of the solution drifting closer to 7. Future tests utilizing the oxalate ion at weakly acidic to alkaline pH values should incorporate ammonium oxalate rather than the oxalic acid used in this experiment to minimize the amount of a acid to bring the pH down to 4 after an NaOH pretreatment. If the new concept is proven, the ion-exchange leaching of pond fines can be done without using an acid at all.

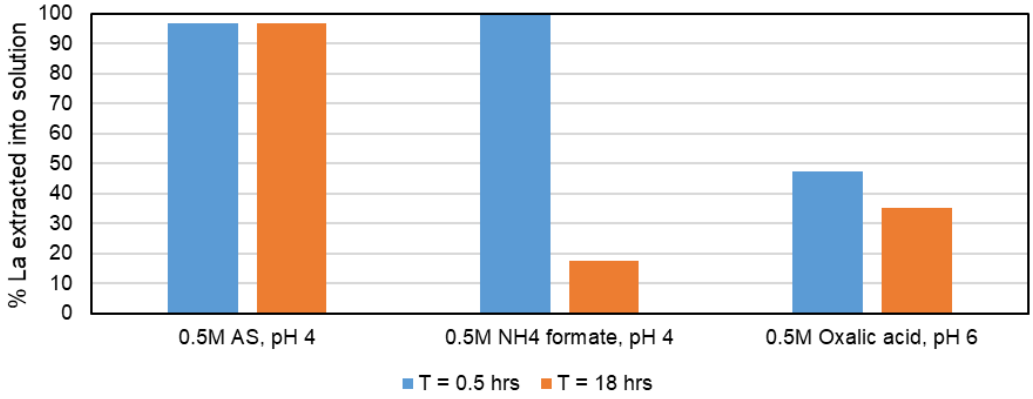

Figure 178. %$La(OH)_3$ standard extracted into solution using various lixiviants; [La] = 1 mM.

EDTA and EDTPO Leaching Studies

EDTA Leaching Kinetics

The results presented heretofore appear to support our basic premise that the REEs present on the surface of the clay particles isolated from fine coal refuse are passivated by the PO_4^{3-} ions present in the system. As suggested by the thermodynamic analysis, we may be able to overcome the problem using a chelating agent. Therefore, we conducted a set of ion-exchange leaching tests on the as-received Russellton sample with and without using EDTA. The sample assayed 598 ppm TREE on mineral basis. In one test, a sample was subjected to a standard ion-exchange leaching test using NH_4SO_4 as lixiviant at 0.5 M at pH 4 without using EDTA. In another test, the same sample was conditioned in a 0.1 M EDTA solution. As shown in Figure 179, Both experiments were conducted at 80ºC to improve the kinetics. The standard technique gave ~7% recovery after 4 hours, while the use of EDTA gave recoveries in the range of 12- work is continuing using stronger chelating agents and other ion-adsorption clay samples.

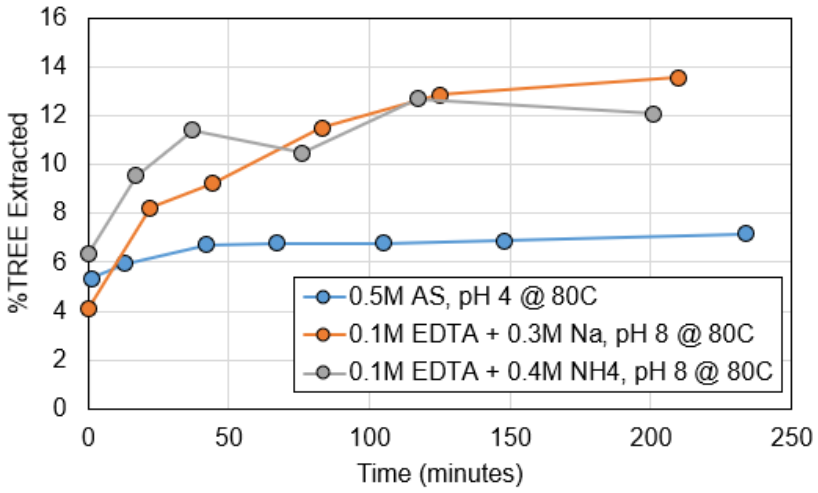

Figure 179. % Extraction over time of total rare earth elements (TREE) from the as-received Russellton clay sample at 80°C using 0.5M AS at pH 4, and 0.1M EDTA. Compares salt exchange efficiency and the effect of the sodium vs. ammonium cation for EDTA.

Influence of NaOH concentration on EDTPO Leaching

Leaching tests in this section with the as-received Russellton clay were performed at a temperature of 80°C. Disposable magnetic PTFE stirbars were utilized for constant stirring of the samples. Approximately 1 gram of wet sample was leached in 25 mL of 0.1M EDTPO with various concentrations of NaOH added. A moisture content of the solids was found to be approximately 26.9% by lyophilization at the time of sampling. NaOH content was tested at 2.8, 4.6, 6.2, and 10.4% NaOH (w/v). Leaching kinetics samples were collected intermittently over the course of approximately 150 hours. Disposable polypropylene (PP) syringes were used to draw sample aliquots which were filtered through 0.22 µm PVDF membranes directly into the 2% w/v nitric acid (HNO_3) + 0.5% w/v HCl diluent used for ICP-MS analysis. The results of this analysis can be found in Figure 180 and Figure 181.

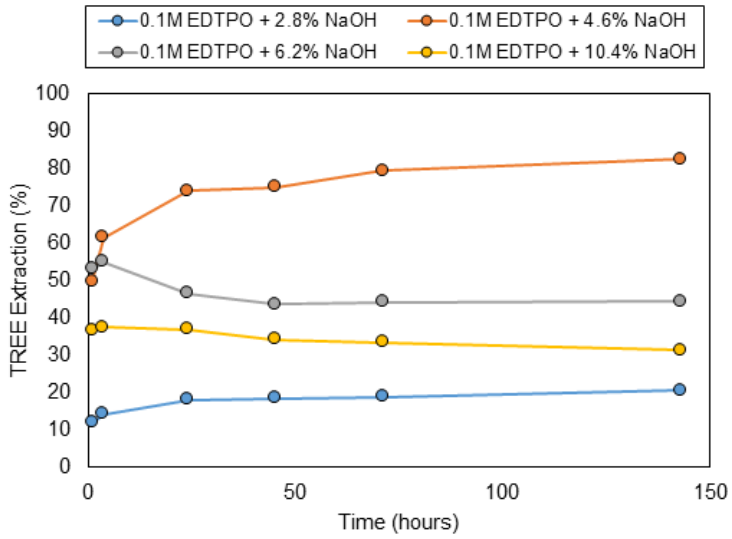

Figure 180. % TREE Extracted from as-received Russellton clay over time at 80°C with varying NaOH concentrations in 0.1M EDTPO solution.

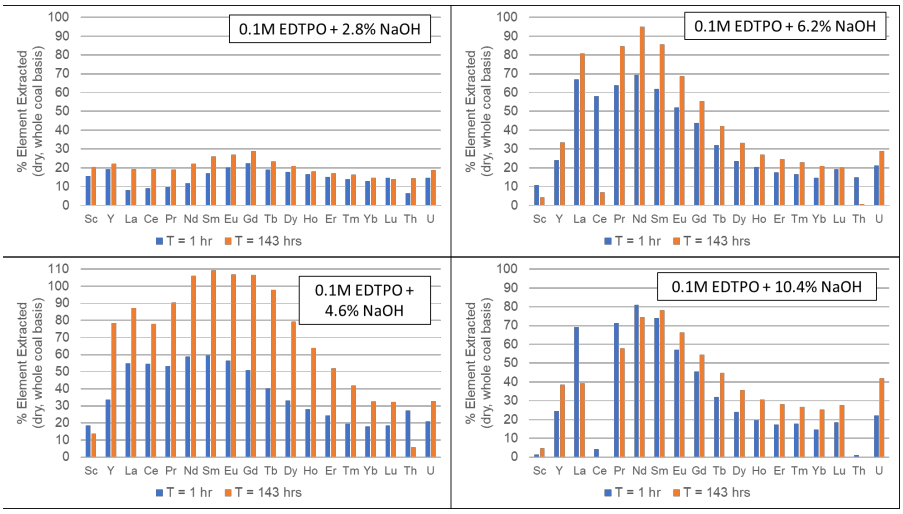

Figure 181. % Individual REE extracted from as-received Russellton clay over time at 80°C with varying NaOH concentrations in 0.1M EDTPO solution.

The total REE concentrations extracted were found to be optimal at around 4.6% NaOH (w/v), with approximately 81% extracted over 140 hours. Lower concentrations were extracted at both lower and higher NaOH concentrations. Lower recoveries at lower pH were expected based on the previous experiments, and the lower recoveries at higher pH values indicate a tipping point where Ce begins to precipitate. Recoveries of individual REE peak at around 100% and slightly higher for certain REE including Nd, Sm, Eu, and Gd. This can be explained by these leachates being directly compared to microwave leaching in nitric and sulfuric acids.

Influence of EDTPO Concentration

Leaching tests in this section with the as-received Russellton clay were performed at a temperature of 80°C. Disposable magnetic PTFE stirbars were utilized for constant stirring of the samples. Approximately 1 gram of wet sample was leached in 25 mL of solution with various concentrations of EDTPO used for leaching. The NaOH concentration was kept constant at 4.6% NaOH (w/v). A moisture content of the solids was found to be approximately 26.9% by lyophilization at the time of sampling. EDTPO concentrations were tested at 0.001, 0.005, 0.01, 0.02, 0.05, and 0.1M. Leaching kinetics samples were collected intermittently over the course of approximately 122 hours. The results of this analysis can be found in Figure 182.

The TREE content extracted was found to increase with increasing EDTPO concentrations in the extraction solution, with an upward trend appearing to continue on past the highest concentration of EDTPO tested at 0.1M. Cerium precipitation was again observed but a trend emerged where it was occurring in extracts with lower EDTPO concentrations. This indicates that higher EDTPO concentrations will stabilize against Ce precipitation, and that it may be possible to obtain similar extraction results at lower EDTPO concentrations with lower NaOH concentrations.

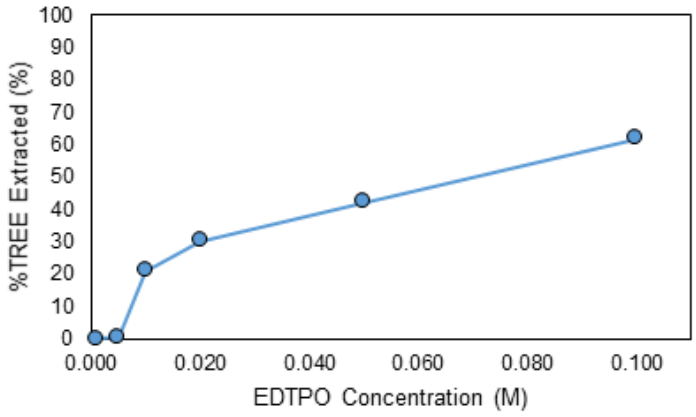

Figure 182. % TREE Extracted from as-received Russellton clay at 80°C with varying EDTPO concentrations in 4.6% NaOH (w/v).

Influence of Methanol (MeOH) Concentration on EDTPO Leaching

Alkoxide is a strong base that can exist in non-aqueous solutions and is considered a stronger base than hydroxide, and as such it was speculated that it could be used in place of NaOH at even lower concentrations. The effectiveness of the simplest alkoxide, methoxide (CH_3O^-), was tested by varying the concentration of methanol during the extraction of the as-received Russellton sample with 0.1M EDTPO. Potassium hydroxide (KOH) was used instead of NaOH due to its higher solubility in methanol. Leaching tests in this section with the as-received Russellton clay were performed at a temperature of 50°C to minimize evaporation effects due to the boiling point of methanol being approximately 65°C. KOH concentrations were kept constant at 5% (w/v). MeOH concentrations were tested at 0, 10, 20, 50, 75, and 100% MeOH (v/v) in the leaching solution. A freshly opened bottle of LC-MS grade methanol with a known moisture content was used to minimize the effect of any water in the methanol. Leaching kinetics samples were collected intermittently over the course of approximately 95 hours. The results of this analysis can be found in Figure 183.

The TREE content extracted was found to decrease with increasing MeOH concentrations in the extraction solution. This indicates that while methoxide may be a more powerful base than hydroxide, it does not enhance the leachability of the REE with EDTPO under this methodology. A darker color was observed in the methanolic KOH extracts, and it was speculated that this came from the alkaline saponification or methyl esterification of organic compounds present within the as-received Russellton clay sample, and that this may have taken away from the methoxide's ability to act as a strong base for the lower prevalence REE. Additional tests utilizing a pure standard of $LaPO_4$ or monazite could be beneficial in proving this theory in the future if needed.

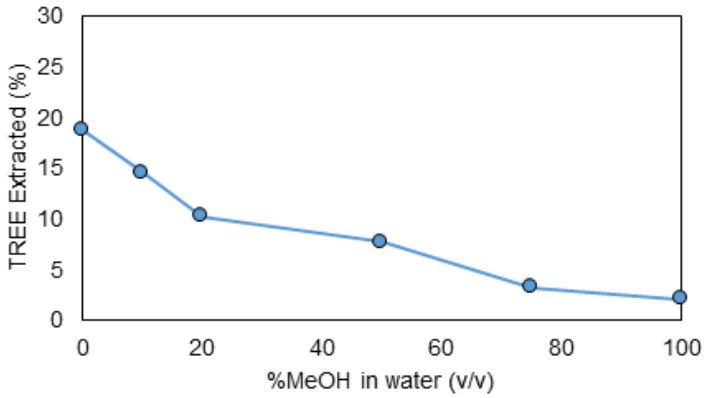

Figure 183. TREE Extracted from as-received Russellton clay at 50°C with varying MeOH concentrations in 5% KOH (w/v).

Ammonium Fluoride Pretreatment

Ammonium fluoride (NH_4F) was another base that was investigated as a means of potentially increasing the TREE extraction efficiency while using EDTPO. Various fluorides have been used in previous tests to enhance extraction efficiency under highly acidic conditions. In this instance, fluoride was used as a pretreatment as means of assisting to etch the clay surfaces and potentially precipitate any liberated REE as REE-F_3. Ideally, these REE fluorides would then be directly leached and converted to hydroxides prior to leaching with alkaline EDTPO.

Pretreatment and leaching tests in this section with the as-received Russellton clay were performed at a temperature of 80°C. Approximately 1 gram of wet sample was pretreated in 25 mL of NH_4F solution over the course of 96 hours. NH_4F concentrations were tested at 0, 0.01, 0.025, 0.05, 0.1, and 0.2M. After pretreatment, samples were centrifuged and their supernatants removed. The pellets were then washed twice with deionized water prior to proceeding with the leaching tests. Leaching was then performed using 25 mL of 0.1M EDTPO+4.6% NaOH using the same methodology as previous experiments. The results of this analysis can be found in Figure 184.

The use of NH_4F during pretreatment was found to cause unwanted leaching of REE into the pretreatment solution. This effect was made worse with increasing concentrations of NH_4F and affected scandium extraction in particular. The additional extraction of scandium was to be expected as it has been observed in previous tests utilizing fluorides. Minimal gains were observed through the use of fluoride with this extraction methodology, and no additional testing with fluorides was performed with this methodology. However, it is speculated that fluoride pretreatment may have a more significant effect on samples with higher clay content. It should also be noted that residual fluoride in solution may still be actively competing with EDTPO and NaOH to form insoluble REE-fluorides. This effect could be minimized/removed via the use of boric acid complexation with free fluorides.

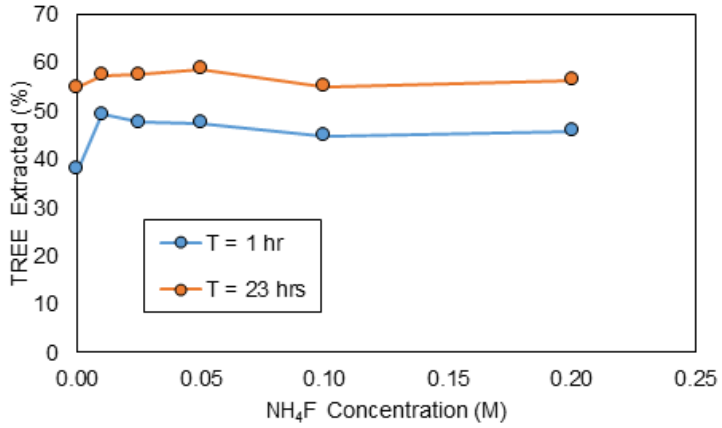

Figure 184. TREE extracted into an EDTPO and NaOH solution from as-received Russellton clay after C after NH4F pretreatment at 80°C.

Influence of Chelating Agents

Various chelation reagents were tested in combination with EDTPO as a means of enhancing the extraction efficiency of TREE from clay samples while potentially reducing EDTPO consumption. The reagents chosen were citrate, ascorbate, gluconate, oxalate, and tripolyphosphate. Each reagent is commonly used in industry for a variety of chelation purposes. Ascorbate, oxalate, and gluconate are also commonly used as reducing agents.

This is the first leaching study section to utilize the blunged Russellton Pond Fines clay, which is different from the as-received Russellton clay that has been utilized in all previous tests described above. The experiment was performed at a temperature of 80°C. Approximately 1 gram of dry, -20 µm sample was extracted in 25 mL of 0.1M EDTPO+0.1M chelation reagent+4.9% NaOH (w/v) over the course of approximately 282 hours using the same methodology as in the previous experiments. During the experiment, additional NaOH was incrementally added after reaching the 168 hour mark. An additional 1% NaOH (w/v) was added for three days after this mark, until a total of 7.9% NaOH (w/v) was present in solution. The results of this analysis can be found in Figure 185.

The use of citrate appears to have had a negative effect on the TREE extraction efficiency, however it was also the only reagent to utilize an ammonium cation as opposed to a sodium or potassium cation in each of the others tested. Higher pH values contributed to the formation of ammonia gas that may have had a negative effect on the extraction efficiency, but further follow-up tests to that speculation have not been tested. Oxalate and tripolyphosphate did not appear to play a significant role under the conditions tested as their added use did not affect the extraction efficiency *vs*. EDTPO alone. Ascorbate and gluconate both enhanced the TREE extraction efficiency, particularly after the addition of more NaOH since these were the only two to continue on a positive trend *vs*. the others which exhibited the same negative trend after increasing beyond 4.9% NaOH (w/v) in solution. This can likely be explained by a combination of their reducing agent properties and formation of soluble REE complexes under the alkaline conditions. Additional experiments utilizing ascorbate or other similar chelation agents at higher concentrations are planned for future analyses. Gluconate may also be considered, though its ability to chelate thorium extremely well in addition to many other elemental impurities may reduce its potential for usage.

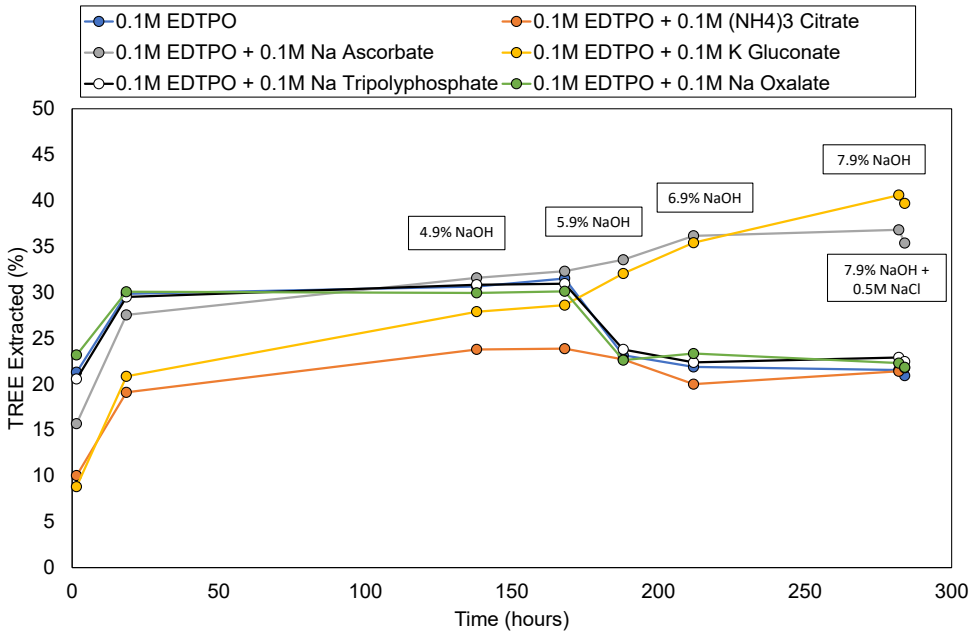

Figure 185. % TREE Extracted from blunged Russellton Pond Fines clay at 80°C with 0.1M EDTPO + 0.1M various chelation reagents + 4.9% NaOH (w/v).

Influence of NaOH Concentrations on EDTPO Leaching of Blunged Fines

Leaching tests were conducted on the blunged Pond Fines at 80°C. Disposable magnetic PTFE stir bars were used for constant stirring of the samples. Approximately 1 gram of dry sample was leached in 25 mL of 0.1 M ethylenediaminetetra(methylenephosphonic)acid (EDTPO) with various concentrations of NaOH added. The NaOH concentrations were varied in the range of 2 to 6% (w/v). A sample was taken after 96 hours of extraction. Disposable polypropylene (PP) syringes were used to draw sample aliquots which were filtered through 0.22 µm PVDF membranes directly into the 2% w/v nitric acid (HNO_3) + 0.5% w/v HCl diluent used for ICP-MS analysis.

The results presented in Figure 186 show that the REE recovery increased with increasing NaOH concentration. Note here that the NaOH concentration required to extract of the REEs from the ion-adsorption clays in coal was substantially (by an order of magnitude) less than those required to extract the REEs from monazite by the $(NH_4)_2SO_4$ leaching. This finding suggests that the Ln^{3+} ions on clay may not be as strongly bonded to the PO_4^{3-} ions as those in monazite. Another major difference between the two different REE sources is that the REE extraction increased with pH until the it reached 12.9, where Ce recovery dropped due to precipitation. At the optimal conditions, REE recovery reached 31% maximum under the relatively mild conditions employed in these experiments (See Figure 187). As shown in a previous report, we achieved >80% recoveries in the presence of 0.1 M EDTPO as a chelating agent.

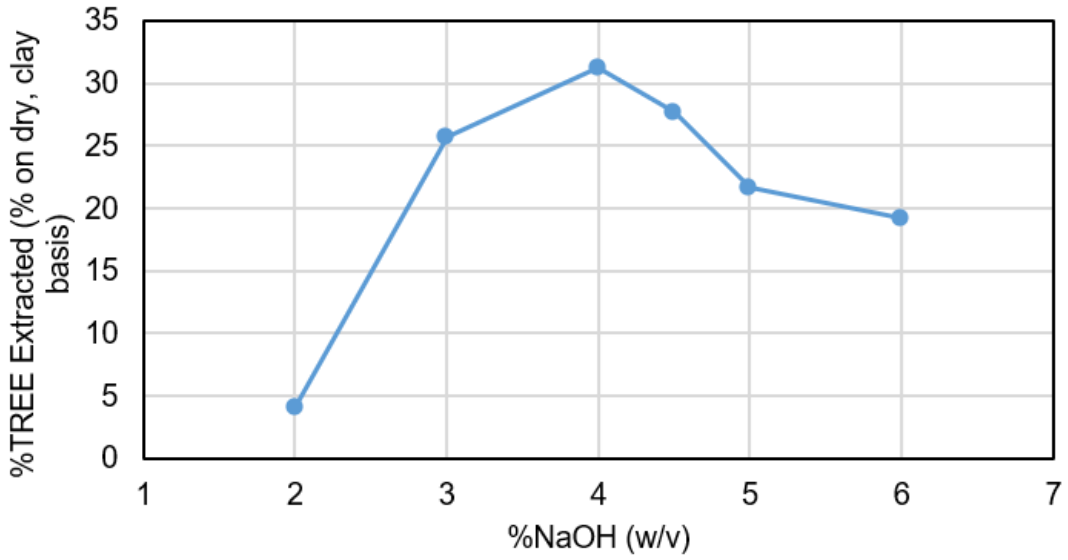

Figure 186. %TREE extracted from blunged pond fines in 96 hours at 80°C with varying NaOH concentrations in 0.1M EDTPO solution.

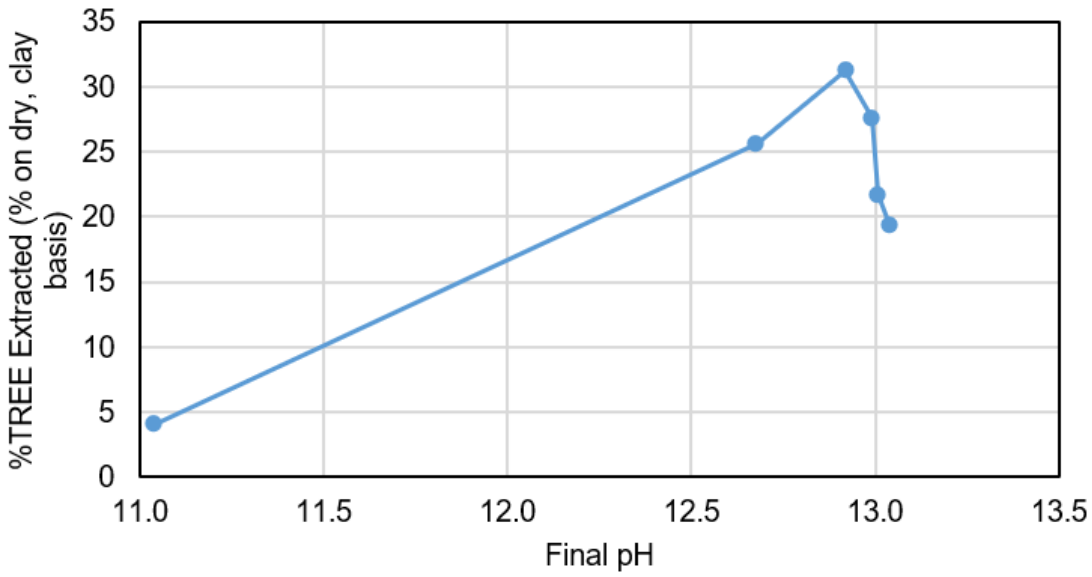

Figure 187. %TREE extracted from blunged pond fines in 96 hours at 80°C with varying NaOH concentrations in 0.1M EDTPO solution, represented as pH to illustrate the pH drop-off of TREE concentration.

EDTPO leaching after NaOH Pretreatment with Additives

Leaching tests were performed on the blunged Pond Fines. Approximately 0.5 g of dry sample was pretreated with 10 mL of 25% (w/v) NaOH and 1 g of either potassium gluconate, sodium ascorbate, or sodium chloride as pretreatment additives. The first two reagents were complexing agents that can facilitate the dissolution of the Ln^{3+} ions. The samples were microwave treated by ramping the temperature to 100°C over 5 mins, held for 5 mins, then ramped again to 160°C over 5 mins and held 5 mins prior to cooling to room temperature for subsequent leaching experiments. The pretreated samples were washed with deionized water prior to leaching with 25 mL of 0.1M EDTPO + 3% (w/v) NaOH. Sample extractions were performed at a temperature of 80°C. Disposable magnetic PTFE stir bars were utilized for constant stirring of the samples. Samples were taken periodically over the course of 7 days. Disposable polypropylene (PP) syringes were used to draw sample aliquots which were filtered through 0.22 µm PVDF membranes directly into the 2% w/v nitric acid (HNO_3) + 0.5% w/v HCl diluent used for ICP-MS analysis. The results of this analysis can be found in Figure 188.

Extracted TREE concentrations increased, as a result of NaOH pretreatment prior to EDTPO leaching, with ~46% TREEs extracted with the pretreatment *vs*. ~31% TREE extracted without. Pretreatments with organic ligands as additives also showed leaching patterns similar to salt exchange mechanisms in that they did not increase after 1 hr of leaching time, whereas pretreatment with NaOH alone continued to increase over time and took approximately 1 week to reach the same levels. Increasing the pH after extraction also appears to keep REEs in solution while precipitating Fe, Mn, Mg and possibly other elements that may make it beneficial for downstream processes and/or purification *via* chromatographic separation of REE-EDTPO chelates.

Figure 188 shows the element-by-element REE recoveries obtained under different conditions. The results obtained in the presence of NaOH and NaCl were about the same as obtained with NaOH alone. However, the results obtained in the presence of the two organic ligands, *i.e.*, K gluconate and Na ascorbate, showed improved recoveries for some elements.

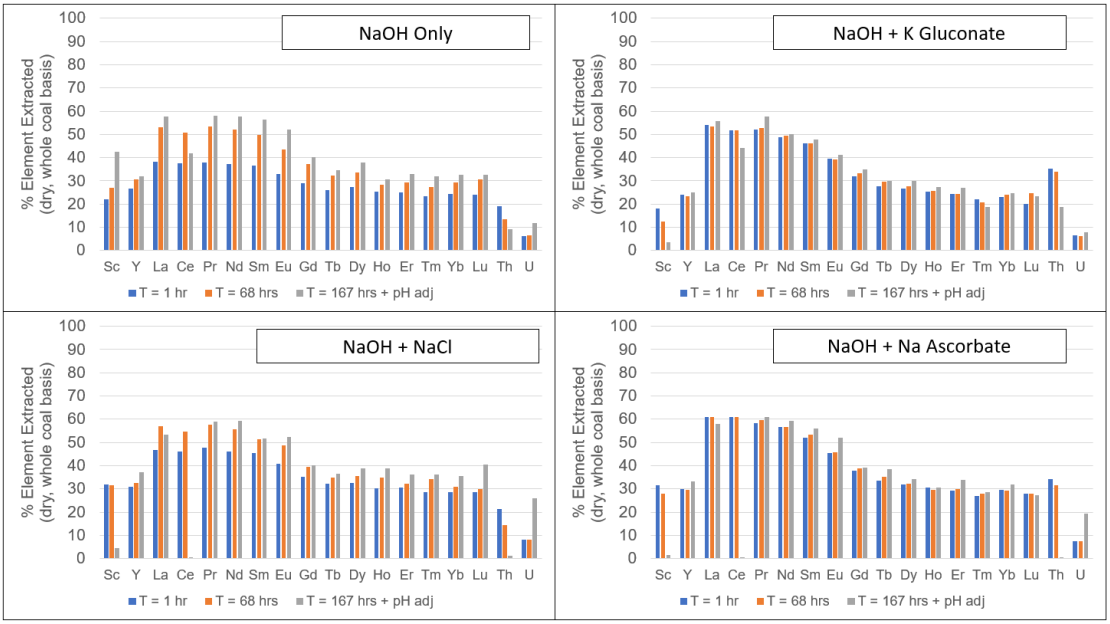

Figure 188. %Individual REE extracted from blunged pond fines over time at 80°C with various NaOH pretreatment additives prior to leaching in 0.1M EDTPO solution.

EDTPO leaching after NaOH Pretreatment with Sodium Ascorbate

Leaching tests in this section were performed using blunged Pond Fines. Approximately 1 gram of dry sample was pretreated with 20 mL of 25% (w/v) NaOH and sodium ascorbate was added with varying amounts of samples in the range of 0 to 4 grams. The samples were pretreated at 80°C with constant stirring over 67 hours. The pretreated samples were washed with deionized water prior to leaching with 25 mL of 0.1M EDTPO + 3% (w/v) NaOH. Sample extractions were performed at a temperature of 80°C. Disposable magnetic PTFE stir bars were utilized for constant stirring of the samples. Samples were taken periodically over the course of 21 hours. Disposable polypropylene (PP) syringes were used to draw sample aliquots which were filtered through 0.22 µm PVDF membranes directly into the 2% w/v nitric acid (HNO_3) + 0.5% w/v HCl diluent used for ICP-MS analysis. The results of this analysis can be found in Figure 189 and Figure 190.

NaOH pretreatment in the presence of ascorbate was found to increase the initial TREE recovery *vs*. NaOH alone, but decreased the heavy REE recoveries. The pretreatments with ascorbate alone showed leaching patterns similar to that of salt exchange kinetics. A precipitation event was also observed during the initial pH adjustment with NaOH at ~pH 12 for all ascorbate treated samples. This may have been caused by the precipitation of sodium ascorbate or ascorbate chelates that may have formed *via* adsorption of ascorbate to the sample surfaces at a high pH. This approach may be beneficial with ascorbate and possibly other ligands that have optimal extraction efficiencies at less extreme pH conditions than those that are used here.

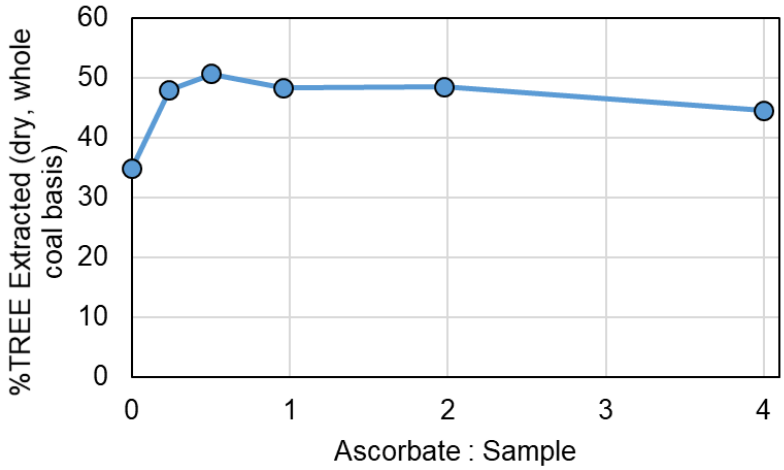

Figure 189. REE recovery from NaOH + ascorbate pretreated pond fines over 21 hours at 80°C in 0.1M EDTPO solution, showcasing the effect of varying the ascorbate-to-sample ratio.

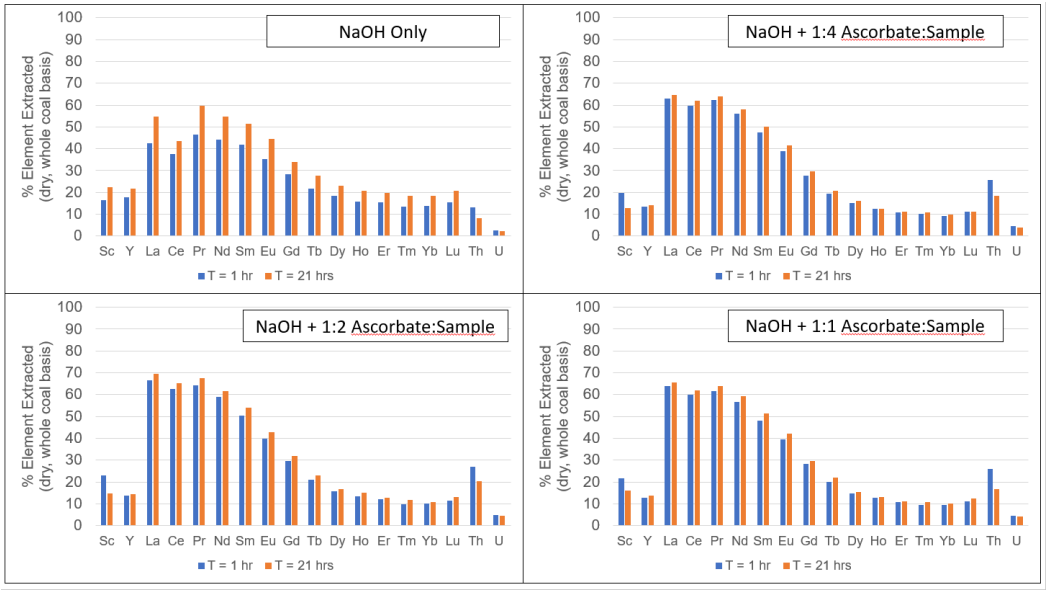

Figure 190. %Individual REE extracted from NaOH+ascorbate pretreated blunged pond fines over 21 hours at 80°C in 0.1M EDTPO solution.

Investigation of Leaching Additives

Ion-exchange leaching of Russellton pond fines with different additives

Leaching tests in this section were performed using the blunged pond fine sample. Approximately 1 gram of dry sample was pretreated with 20 mL of 20% (w/v) NaOH. The samples were pretreated at 80°C with constant stirring over 22 hours. The pretreated samples were washed with deionized water prior to leaching with 25 mL of various lixiviants at room temperature. The lixiviants compared were 0.5M AS, 0.5M ammonium formate, 0.25M AS + 0.25M ammonium formate, 1M NH_4OH, 0.5M oxalic acid, and 0.5M ammonium persulfate. Each of these reagent solutions was adjusted to pH 4 with dilute HCl with the exception of the oxalic acid, which was adjusted using NH_4OH.

Disposable magnetic PTFE stir bars were utilized for constant stirring of the samples. Samples were taken periodically over the course of 24 hours. Disposable polypropylene (PP) syringes were used to draw sample aliquots, which were filtered through 0.22 µm PVDF membranes directly into the 2% w/v nitric acid (HNO_3) + 0.5% w/v HCl diluent used for ICP-MS analysis. The results of this analysis can be found in Figure 191.

Leaching with ammonium formate yielded identical results to those obtained with ammonium sulfate, indicating that the NaOH pretreatment process is the limiting step for the TREE extraction process.

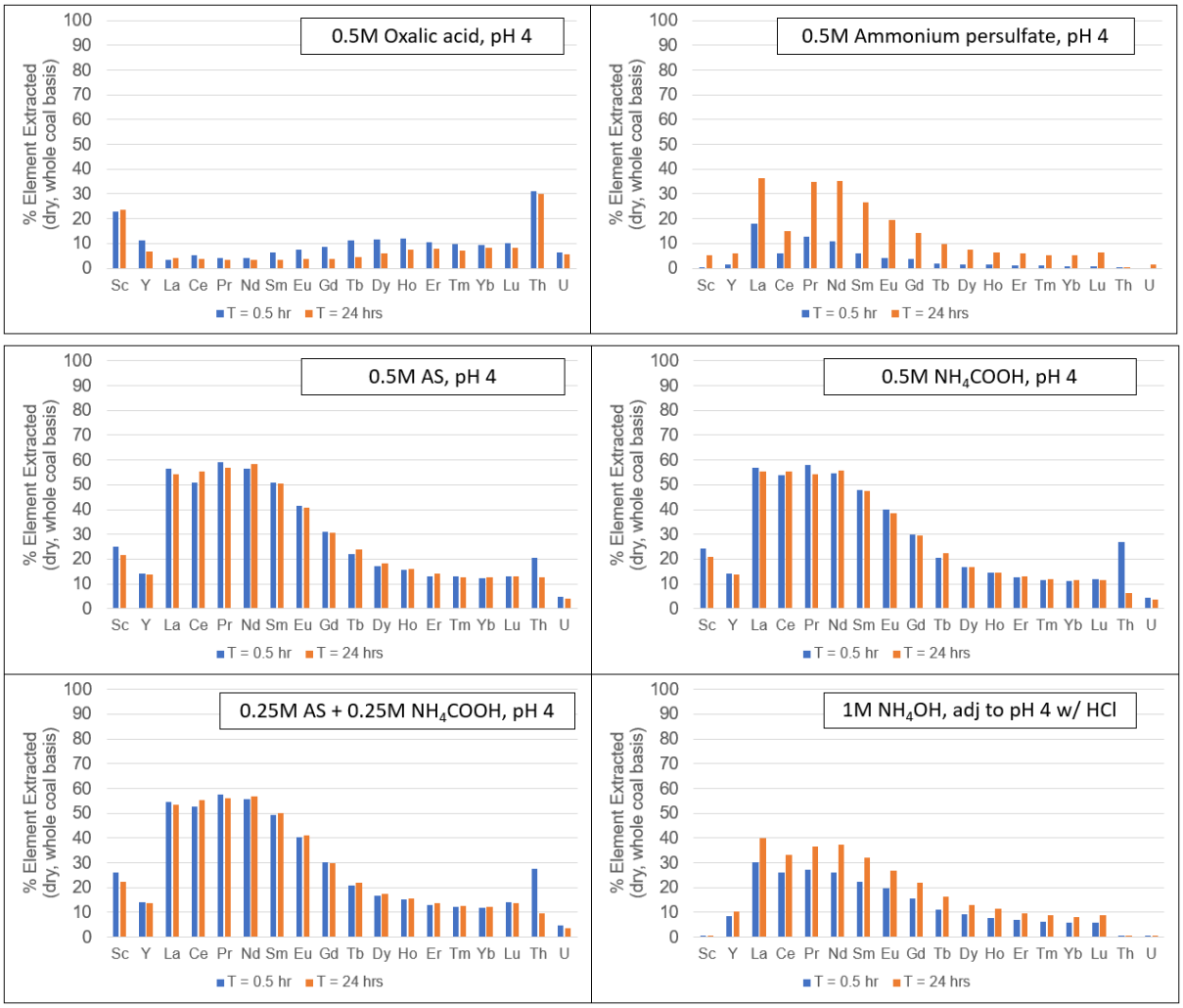

Figure 191. %Individual REE extracted from NaOH pretreated blunged pond fines. Extractions performed over 24 hours at room temperature in various lixiviants

Addition of other reagents during the pretreatment process may help minimize the NaOH consumption or catalyze the reactions.

Leaching with NH_4OH with pH adjusted to 4 with HCl, as well as with oxalic acid with pH adjusted with NH_4OH, and with ammonium persulfate were all less effective than either ammonium sulfate or ammonium formate. This finding indicates that the lixiviant anion also plays a major role in the dissolution of exchangeable REE species, rather than just the ammonium cation alone.

Ion-exchange leaching of Russellton pond fines with NaOH pretreatment

Leaching tests in this section were performed using blunged pond fines. Approximately 1 gram of dry sample was pretreated with 20 mL of 20% (w/v) NaOH and approximately 1 g of various additives were added for comparison. The additives tested were sodium carbonate, sodium nitrate, sodium metasilicate, sodium sulfate, and sodium tetraborate. A sample without additives was also used as a control. The samples were pretreated at 80°C with constant stirring for 43 hours. The pretreated samples were washed with deionized water prior to leaching with 25 mL of 0.5M AS, adjusted to pH 4. Disposable magnetic PTFE stir bars were utilized for constant stirring of the samples. Samples were taken periodically over the course of 4 hours. Disposable polypropylene (PP) syringes were used to draw sample aliquots which were filtered through 0.22 µm PVDF membranes directly into the 2% w/v nitric acid (HNO_3) + 0.5% w/v HCl diluent used for ICP-MS analysis. The results of this analysis can be found in Figure 192.

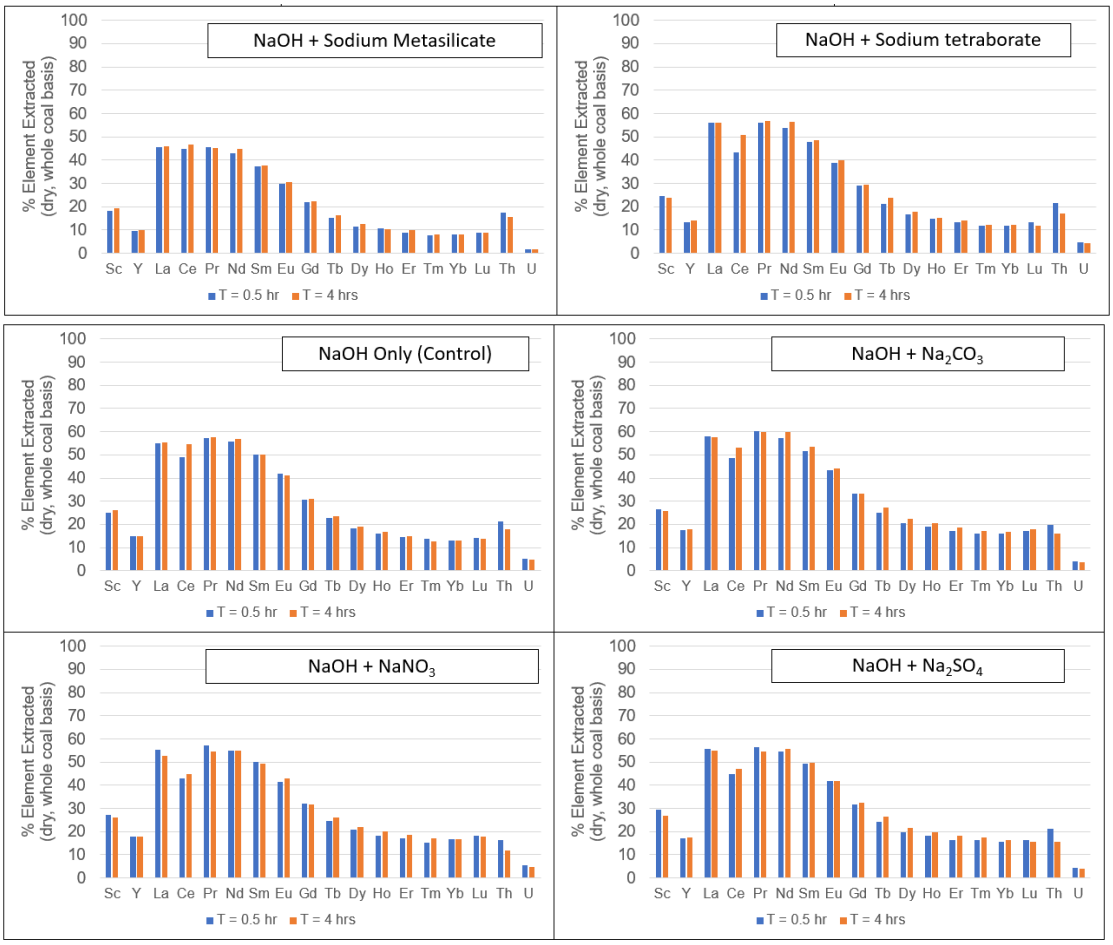

Figure 192. %Individual REE extracted from blunged pond fines pretreated with NaOH and various additives. Extractions performed over 4 hours at room temperature in 0.5M AS, pH 4.

Slight increases in middle and heavy REE extraction efficiency were observed in samples pretreated with both NaOH and the sodium salts of carbonate, nitrate, and sulfate. This may be due to the anions adsorbing to the surface of the clays and forming additional soluble sites at high pH, thereby increasing the total surface area that is accessible to the NaOH pretreatment process. Alternatively, the added anions may also be directly forming other complexes that are not soluble at high pH but are then soluble in 0.5M AS at pH 4.

Significant decreases in leachable REEs were observed when combining sodium silicate with the NaOH pretreatment process. Adsorption of the silicate to clay surfaces combined with higher concentrations of Si dissolved in solution is likely inhibiting the dissolution or alkaline hydrolysis of the clay surfaces during pretreatment. This can possibly be explained by the dissolution of silicon in NaOH solution, which forms sodium silicate as shown in the reaction below. Increasing solution concentrations of sodium silicate (Na_2SiO_3) pushes the equilibrium further left towards the reactants, thereby inhibiting the NaOH pretreatment process.

$$SiO_2 + 2\ NaOH \leftrightarrow Na_2SiO_3 + H_2O$$

Comparison of control samples from several of the aforementioned extraction tests showed that essentially identical results were obtained with samples that had been pretreated in NaOH solution for 22, 43, and 68 hours (Figure 193). This finding indicates that the NaOH pretreatment process was reaching equilibrium at or before the 22-hour mark under the conditions chosen up to this point. The blunging was done at a 20 µm top size.

Dilute HCl titration of the NaOH lixiviant after pretreatment appeared to indicate that negligible amounts of the base were being consumed, and in some cases a higher concentration of base was found to be more efficient than what was used to begin with. This finding may be explained by the possibility that other cations may be dissolved from the sample matrix and enter the NaOH solution that then go on to react and form other alkaline hydroxide compounds that stay in solution but don't react further with the sample matrix, thereby creating an equilibrium. These extraneous complexes in solution may consume acid in a

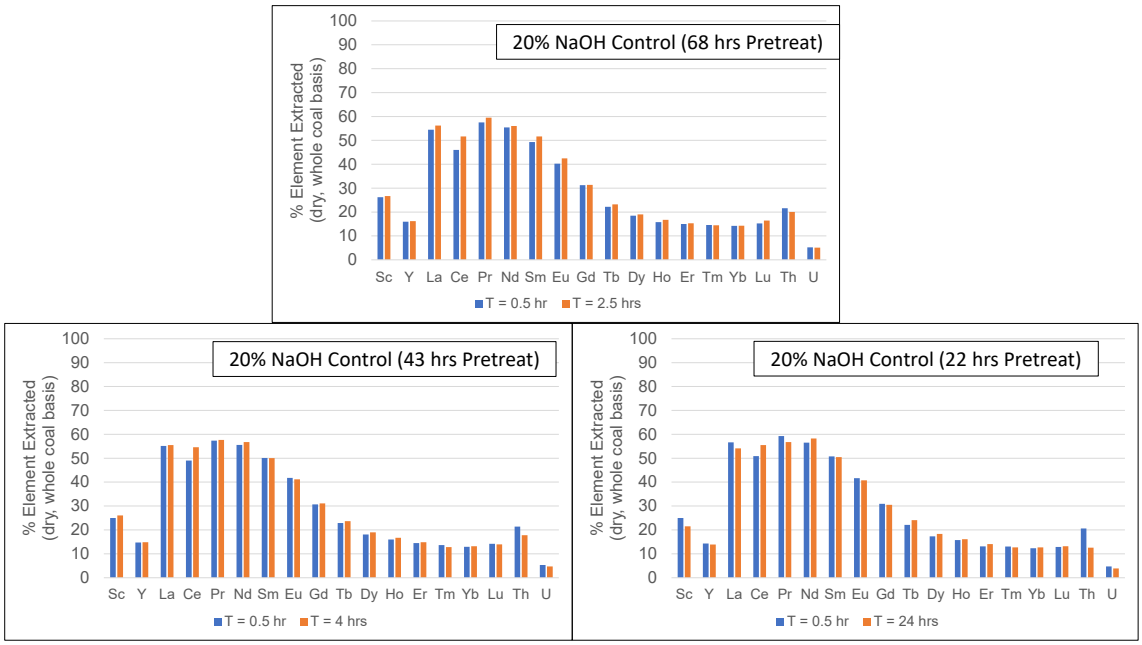

Figure 193. %Individual REE extracted from the control samples of blunged pond fines pretreated with 20% (w/v) NaOH. Increasing the pretreatment times between 22 and 68 hours did not yield a significant increase in extraction efficiency.

manner similar to NaOH, thereby giving the appearance of limited NaOH consumption to the non-selective strong acid-strong base titration that was used here. Alternatively, a product of the NaOH pretreatment process, such as the sodium silicate equilibrium shown above, may be inhibiting the NaOH pretreatment process. To test this theory, a comparison of sequential NaOH pretreatments were used prior to leaching with 0.5M AS at pH 4.

Leaching tests in this section were performed using the blunged pond fines. Approximately 1 gram of dry sample was pretreated with 20 mL of 20% (w/v) NaOH. The samples were pretreated at 80°C with constant stirring over 120 hours. The first sample was pretreated over 120 hours with the same NaOH solution and was utilized as a control sample. The second was treated with the first NaOH solution for 24 hours, and then a second fresh solution for the next 96 hours. The third solution had a first treatment for 24 hours, a second for 24 hours, and a third for 72 hours. Each was treated with NaOH solution for a total of 120 hours.

The pretreated samples were not washed between sequential NaOH treatments. After the final NaOH pretreatment samples were washed with deionized water prior to leaching at room temperature with 25 mL of 0.5M AS, adjusted to pH 4. Disposable magnetic PTFE stir bars were utilized for constant stirring of the samples. Samples were taken periodically over the course of 47 hours. Disposable polypropylene (PP) syringes were used to draw sample aliquots which were filtered through 0.22 µm PVDF membranes directly into the 2% w/v nitric acid (HNO_3) + 0.5% w/v HCl diluent used for ICP-MS analysis. The results of this analysis can be found in Figure 194 and Figure 195.

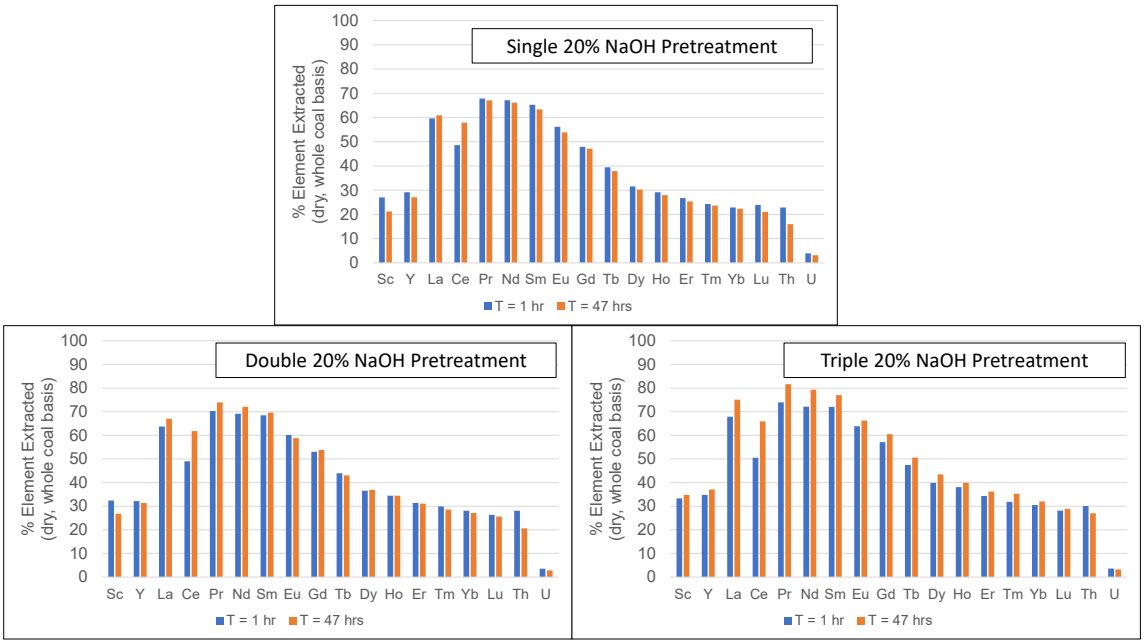

Figure 194. %Individual REE extracted from blunged pond fines sequentially pretreated with 20% (w/v) NaOH prior to leaching with 0.5M AS, pH 4.

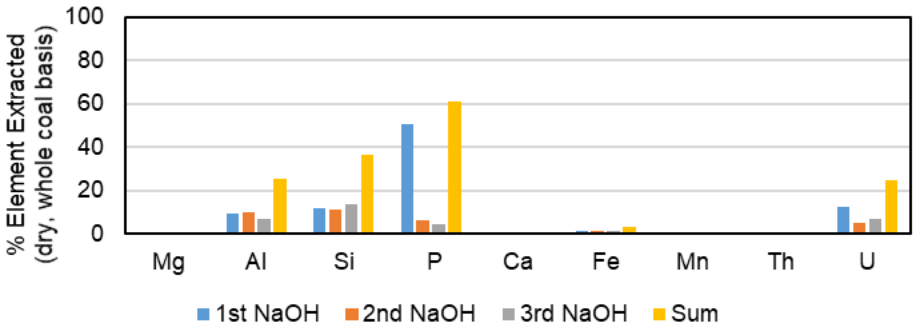

Figure 195.%Individual non-REE extracted directly into the sequential NaOH pretreatment solutions from blunged pond fines.

Sequential NaOH pretreatments prior to AS leaching were found to increase the TREE extraction efficiency, with ~53, 58, and 64% TREE extracted using single, double, and triple NaOH pretreatments, respectively. Analysis of the sequential NaOH pretreatment solutions also yielded findings that the concentrations of dissolved Mg, Al, Si, Ca, Fe, and Mn remained relatively constant for each pretreatment solution, indicating that a single NaOH pretreatment may be saturated with these cations. It is interesting that most of the phosphor is removed during the first step NaOH pretreatment. If indeed, the REEs on the clay surface are passivated by the PO_4^{3-} ions, most of them can be removed by the single-stage NaOH pretreatment. It will be of interest to find other ways to desorb the PO_4^{3-} ions from the REEs on the surface of clay.

Ammonium sulfate leaching of blunged thickener underflow, effect of cation chloride additives during NaOH pretreatment

Leaching tests in this section utilized blunged samples of thickener underflow from a mine operating in the Lower Kittaning seam and were performed at a temperature of 80°C. Approximately 1 gram of dry sample and 1 gram of the various individual cation chlorides were pretreated in 20 mL of 20% NaOH (w/v) for 91 hours prior to leaching with 0.5M ammonium sulfate (AS), pH 4 at room temperature. The cation chlorides tested were $MgCl_2$, KCl, $CaCl_2$, $FeCl_2$, and $AlCl_3$. The results of this test can be found in Figure 196.

No major increases in extracted TREE were observed with any of the additives. Calcium caused a major decrease in TREE but an unexplained increase in the extracted Y and HREE content. Both magnesium and calcium chloride caused in increase in acid consumption attributed to the conversion of the chloride salts to low solubility hydroxides during NaOH pretreatment.

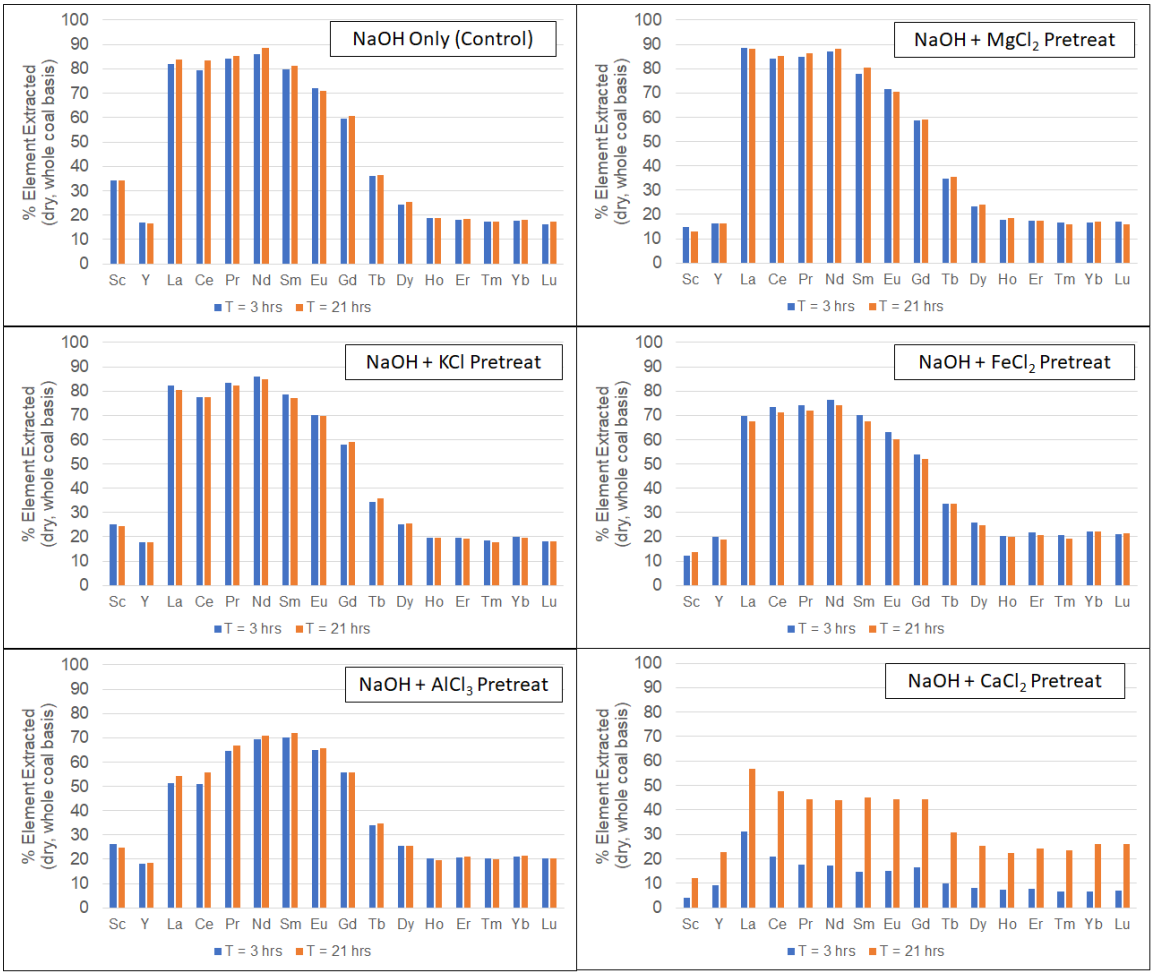

Figure 196. % Individual REE extracted from blunged LEER using AS after NaOH pretreatment with various cation chloride additives.

Ammonium sulfate leaching of Underclay, effect of multiple bases during NaOH pretreatment

Leaching tests in this section utilized the BRC underclay 5 µm sample and were performed at a temperature of 80°C. Approximately 1 gram of dry sample and 0.2 gram of either calcium hydroxide or potassium hydroxide were pretreated in 20 mL of 20% NaOH (w/v) for 64 hours prior to leaching with 0.5M ammonium sulfate (AS), pH 4 at room temperature. The results of this analysis can be found in Figure 197.

The addition of calcium hydroxide again increased the extracted concentrations of Y and HREE, and potassium hydroxide decreased the acid consumption during AS leaching, consistent with findings and hypothesis from the previous test.

Ammonium sulfate and ammonium formate leaching of Underclay, effect of sequential NaOH pretreatments and leaching

A new series of tests was conducted using a combination of recycled NaOH solution and lixiviant solution. Leaching tests in this section utilized BRC underclay 5 µ samples and were performed at a temperature of 80°C. Approximately 1 gram of dry sample were pretreated in 20 mL of 20% NaOH (w/v) for ~24 hours prior to leaching with 0.5M ammonium sulfate (AS) or ammonium formate (NH_4HCO_2), pH 4 at 80°C. The pretreatment / leaching cycle was repeated three times, with the base or lixiviant being replaced with fresh or recycled at various points in the process. Table 49 shows the experimental matrix for this test, a the experimental results are shown in Figure 198.

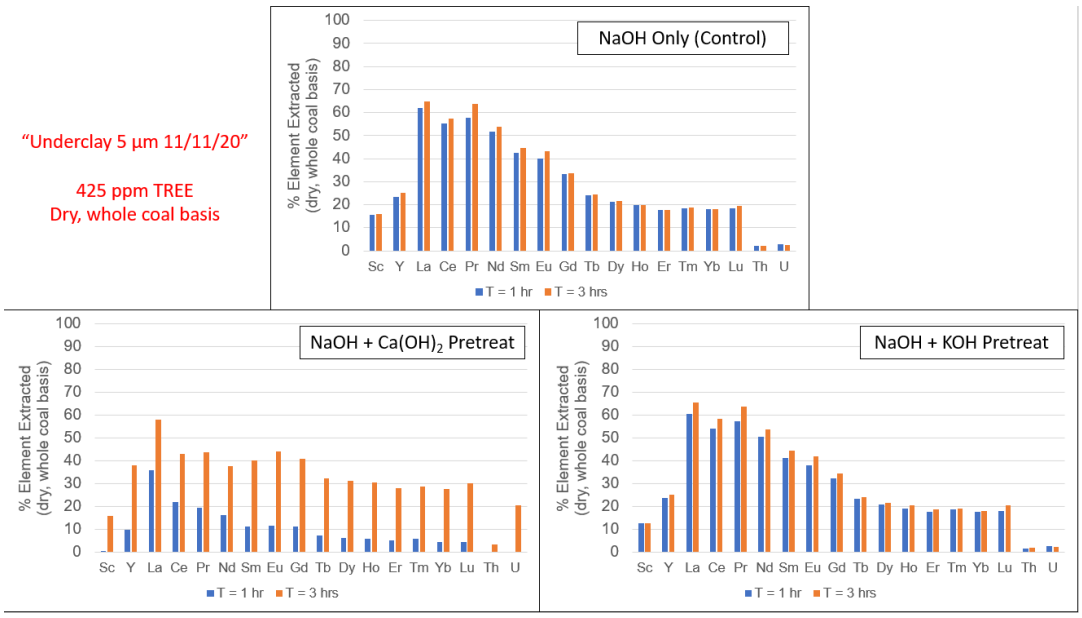

Figure 197. % Individual REE extracted from Underclay 5um using AS after NaOH pretreatment with various base additives.

Table 49. Steps and fresh/recycled reagent use during sequential pretreatment and extraction experiments.

Sample #	Pretreat 1	Lix. 1	Pretreat 2	Lix. 2	Pretreat 3	Lix 3.
129	Fresh NaOH	Fresh AS	Fresh NaOH	Fresh AS	Fresh NaOH	Fresh AS
130	Fresh NaOH	Fresh AS	Fresh NaOH	Recycle AS	Fresh NaOH	Recycle AS
131	Fresh NaOH	Fresh AS	Recycle NaOH	Recycle AS	Recycle NaOH	Recycle AS
132	Fresh NaOH	Fresh NH_4HCO_2	Fresh NaOH	Fresh NH_4HCO_2	Fresh NaOH	Fresh NH_4HCO_2
133	Fresh NaOH	Fresh NH_4HCO_2	Fresh NaOH	Recycle NH_4HCO_2	Fresh NaOH	Recycle NH_4HCO_2
134	Fresh NaOH	Fresh NH_4HCO_2	Recycle NaOH	Recycle NH_4HCO_2	Recycle NaOH	Recycle NH_4HCO_2

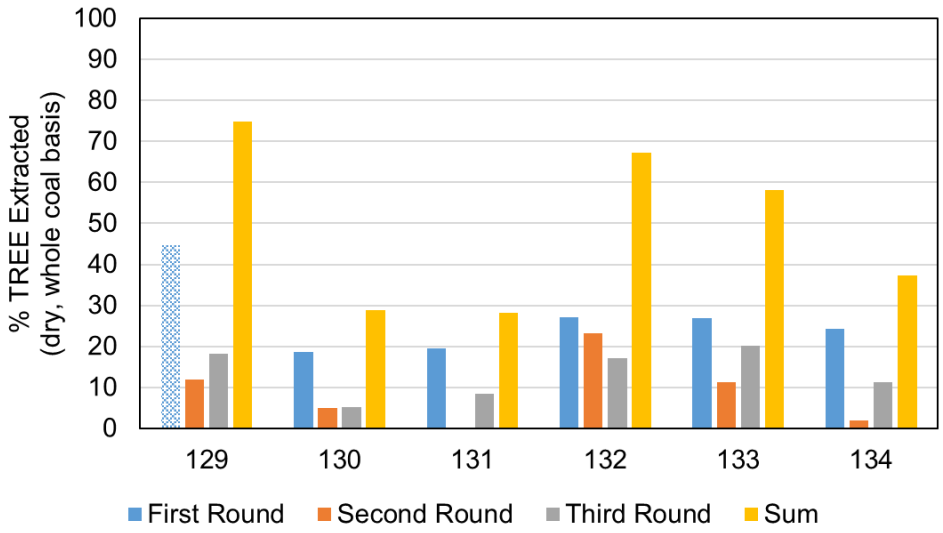

Figure 198. %TREE extracted from Underclay 5um during sequential pretreatment and leaching tests.

For sample 129, the pH was inadvertently overshot to 3.2, resulting in a drastically increased TREE extraction vs. the other samples in this series of tests. Ammonium formate was found to perform better for TREE extraction than AS at 80° C. Fresh NaOH was found to have the largest impact on the extracted TREE concentrations.

Ammonium formate leaching of underclay with ammonium formate after alkaline pretreatment, effect of adding $Ca(OH)_2$

Leaching tests in this section utilized the BRC Underclay 5 µm samples and were performed at a temperature of 80°C. Approximately 1 gram of dry sample and 10, 25, and 48 milligrams of calcium hydroxide (0.05, 0.1, 0.24% w/w, respectively) were pretreated in 20 mL of 20% NaOH (w/v) for 96 hours prior to leaching with 0.5M ammonium formate, pH 4 at room temperature for 22 hours. The results of this analysis can be found in Figure 199.

Adding lower concentrations of $Ca(OH)_2$ than had been used in previous tests drastically increased the extracted TREE concentrations vs. NaOH pretreatment alone. Addition of the $Ca(OH)_2$ also drastically increased the TREE leaching kinetics, with identical results observed at both 1 and 22 hour extraction times for optimal $Ca(OH)_2$ concentrations of approximately 0.24% w/v in the pretreatment solution vs. a steadily increasing TREE content in the NaOH only control. Adding more than the optimal amount of $Ca(OH)_2$ resulted in decreasing extraction efficiency or precipitation over time as seen in previous tests that utilizing too much $Ca(OH)_2$.

Other than assisting in the alkaline decomposition of the samples, adsorbed Ca may also be altering the mineral structure of aluminosilicates present within the sample. The addition of calcium is likely also helping to shift the equilibrium of aluminosilicate dissolution, in particular of dissolved weathered silicon minerals or quartz via precipitation of dissolved silicon and regeneration of consumed NaOH according to the following reactions.

$$SiO_2\,(s) + 2\,NaOH\,(aq) \leftrightarrow Na_2SiO_3\,(aq) + H_2O\,(l)$$

$$Na_2SiO_3\,(aq) + Ca(OH)_2\,(aq) \leftrightarrow CaSiO_3\,(s) + 2\,NaOH$$

Other divalent and trivalent hydroxides of Ba, Mg, Sr, and Al were also investigated as additives during NaOH pretreatment, but none yielded similar results to Ca.

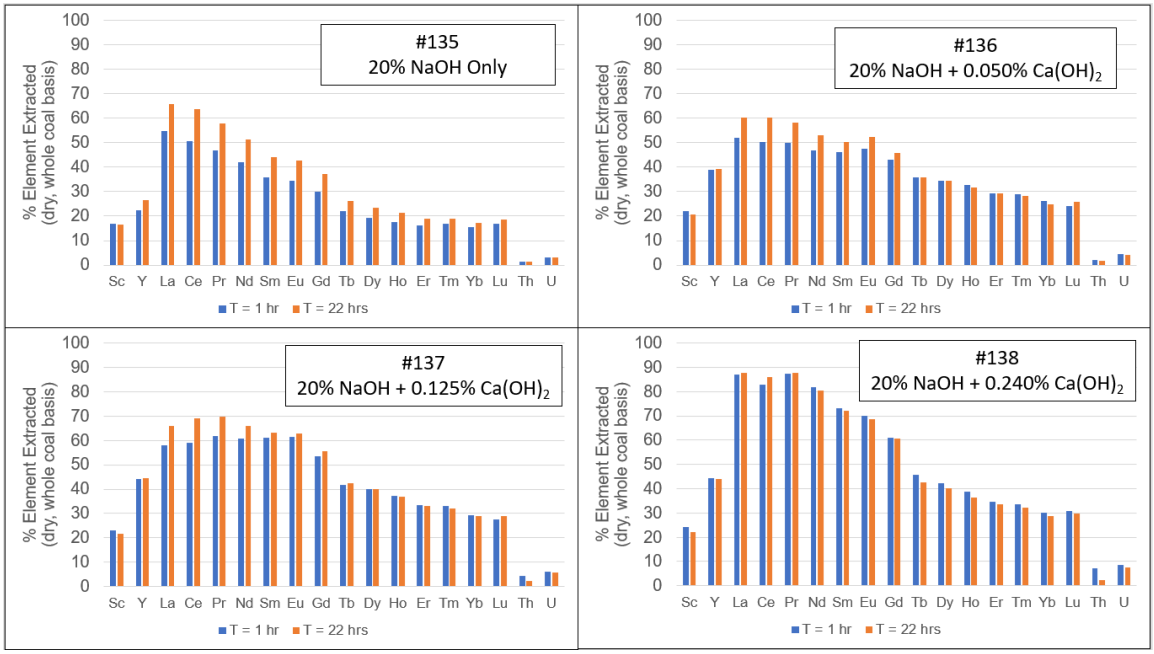

Figure 199. % Individual REE extracted from Underclay 5um using ammonium formate after NaOH + Ca(OH)2 pretreatment.

Ammonium formate leaching of underclay with ammonium formate after alkaline pretreatment, effect of varying NaOH and $Ca(OH)_2$

As in prior tests, leaching tests in this section utilized the BRC Underclay 5 µm samples and were performed at a temperature of 80°C. Approximately 1 gram of dry sample were pretreated in various NaOH + $Ca(OH)_2$ solution concentrations and ratios for 72 hours prior to leaching with 0.5M ammonium formate, pH 4 at room temperature for 72 hours. The results of this analysis can be found in Figure 200 and Figure 201.

The addition of $Ca(OH)_2$ during pretreatment again showed rapid exchange kinetics during leaching, but adding too much will also cause co-precipitation of extracted REE over time. Extracted TREE increased proportionally with NaOH pretreatment concentrations.

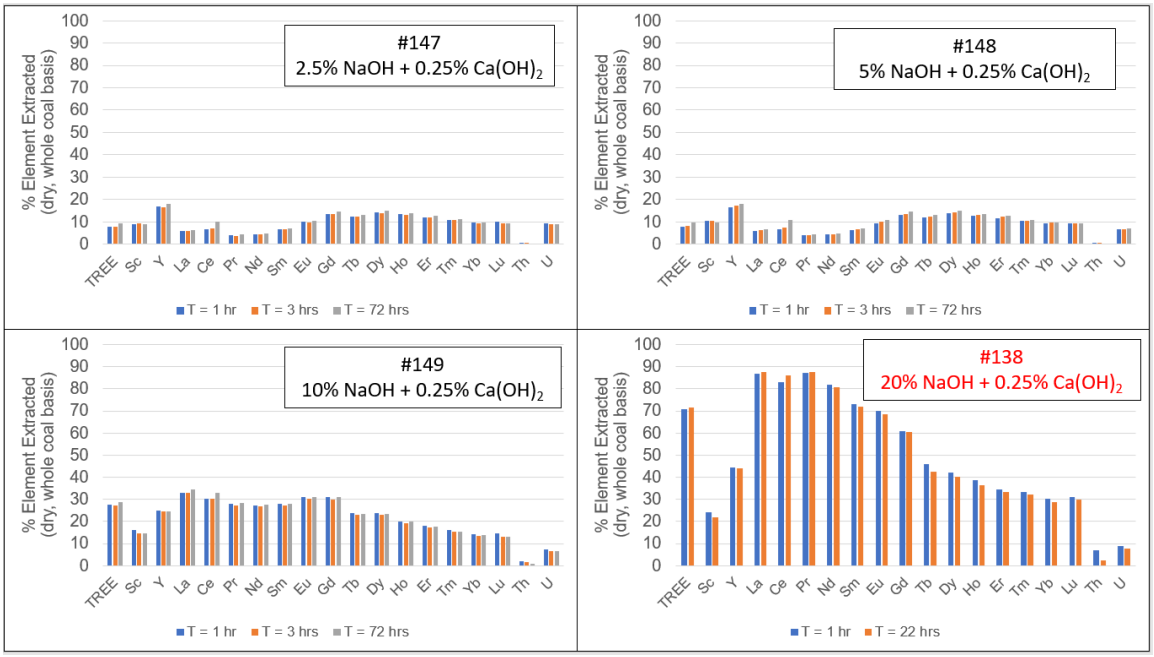

Figure 200. % Individual REE extracted from Underclay 5um using ammonium formate after NaOH + Ca(OH)2 pretreatment. Demonstrates effect of varying [NaOH] with constant [Ca(OH)2].

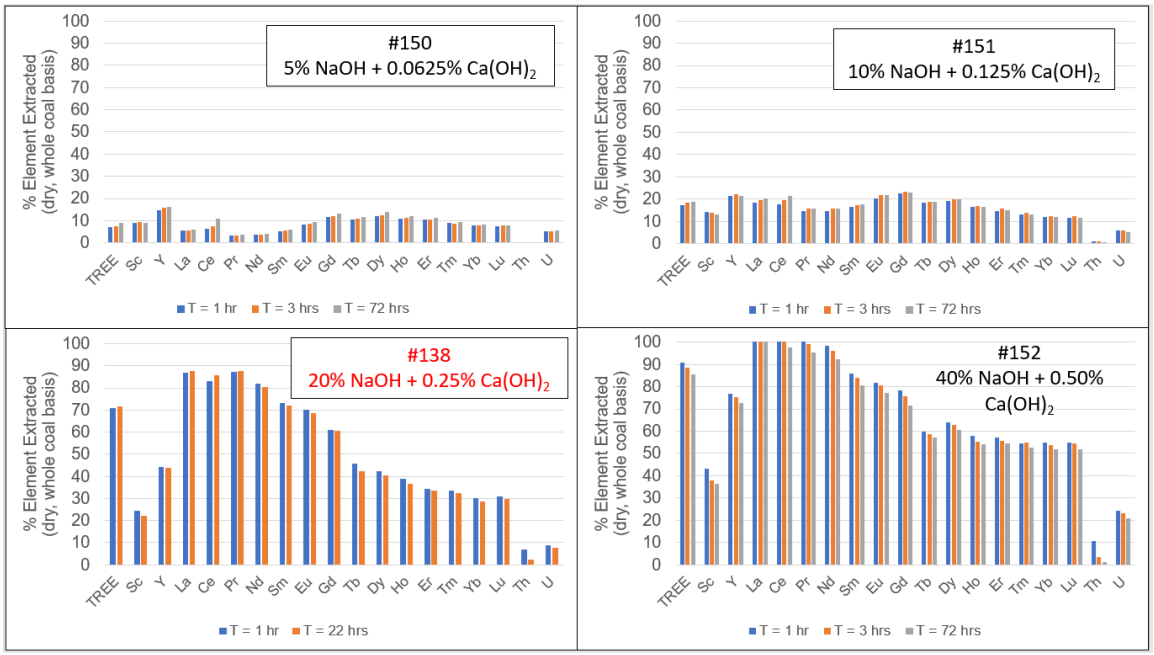

Figure 201. % Individual REE extracted from Underclay 5um using ammonium formate after NaOH + Ca(OH)2 pretreatment. Demonstrates effect of varying [NaOH] with constant NaOH : Ca(OH)2.

Ammonium formate leaching of underclay with ammonium formate after alkaline pretreatment, effect of liquid to solid ratio during alkaline pretreatment

Leaching tests in this section utilized BRC Underclay 5 µm samples and were performed at a temperature of 80°C. Approximately 1 gram of dry sample were pretreated in various ratios of 20% NaOH (w/v) + 50 mg $Ca(OH)_2$ for 66 hours prior to leaching with 25 mL of 0.5M ammonium formate, pH 4 at room temperature for 24 hours. The results of this analysis can be found in Figure 202 and show an inverse relationship between TREE extracted and L/S ratio during leaching. Note the compressed y axis in the figure.

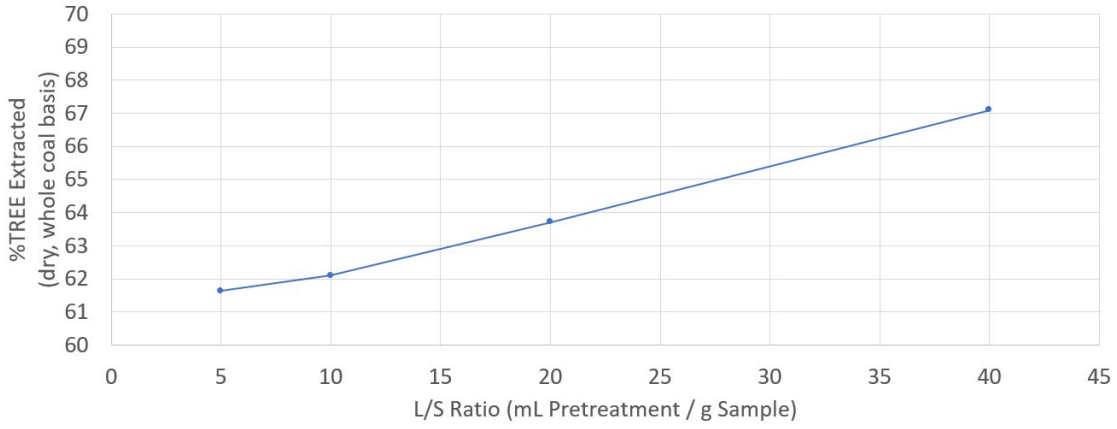

Figure 202. % TREE extracted from Underclay 5um using various L/S ratios during alkaline pretreatment.

Alkaline extraction of underclay with organic acids at pH 13

Leaching tests in this section utilized Underclay 5 µm samples and were performed at a temperature of 80°C. Approximately 1 gram of dry sample were extracted in 0.5M of either potassium gluconate, sodium glucoheptonate, tartaric acid, or glycolic acid at pH 13 +/- 0.15 for 72 hours. The results of this analysis can be found in Figure 203. The samples were then acidified to lower pH values and left to extract for approximately 24 hours at each pH point and the results of this can be found in Figure 204.

Glucoheptonate was found to have the best REE extraction efficiency at pH 13, but only with a recovery of approximately 15%. Glucoheptonate and gluconate had approximately the same extraction efficiencies as their pH decreased, potentially indicating that these ligands would not extract better at lower pH, but also that they can stabilized dissolved REE while lowering the pH (Figure 204). This could be useful for removal of dissolved Al and Si impurities in the leach liquor.

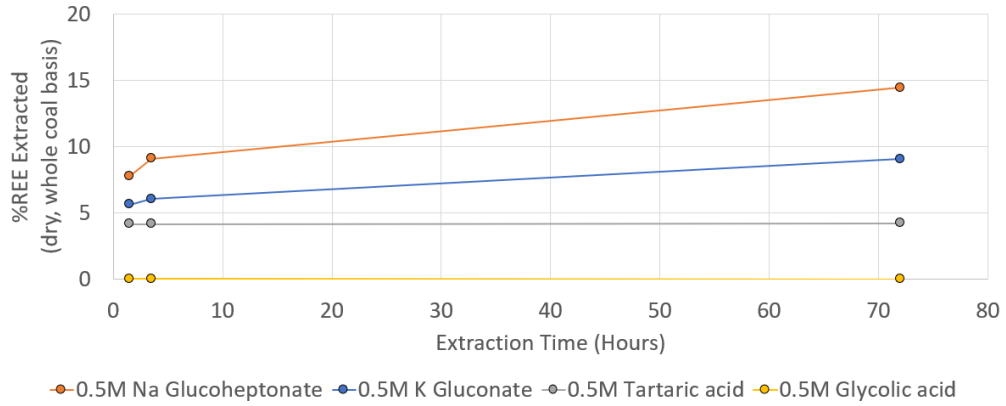

Figure 203. % TREE extracted from Underclay 5um using various organic acids at pH 13.

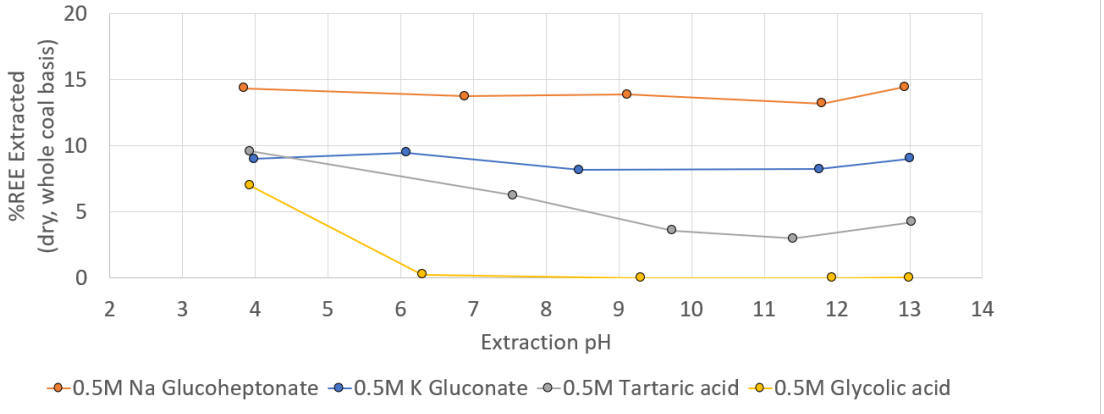

Figure 204. % TREE extracted from Underclay 5um using various organic acids starting at pH 13 and then acidifying to lower pH values.

Alkaline extraction of underclay with organic acids in dilute NaOH

Leaching tests in this section utilized underclay 5 um samples and were performed at a temperature of 80°C. Approximately 1 gram of dry sample were extracted in 0.25M of either ethylenediaminetetra(methylene phosphonic) acid) (EDTPO), ethylenediaminetetraacetic acid (EDTA), diethylenetriaminepetaacetic acid (DTPA), potassium gluconate, sodium glucoheptonate, or calcium gluconate with 5% (w/v) NaOH added for 120 hours. The results of this analysis can be found in Figure 205.

Both potassium gluconate and sodium glucoheptonate were found to have the best REE extraction efficiency under these conditions. However, calcium gluconate was found to have a lower extraction efficiency, likely due to precipitation or inhibition as a direct result of the calcium ion concentration in solution. Despite having these high concentrations of chelation agents in solution, high pH is still needed to facilitate REE extraction from Underclay samples.

REE-organic acid stability after alkaline extraction of underclay

The potassium gluconate and sodium glucoheptonate extracts from the previous section were used to test the stability of REE-organic acid complexes after alkaline extraction. The samples started at pH 12.4 and 12.7 for the gluconate and glucoheptonate, respectively, and these were both acidified to pH ~8 and allowed to stir for 24 hours at 80 °C. The results of this analysis can be found in Table 50.

After acidifying the alkaline extracts to pH 8, both potassium gluconate and sodium glucoheptonate were found to efficiently keep REE-organic acid complexes in solution while simultaneously precipitating out almost all of the dissolved Al and Si. Fe was only partially precipitated by glucoheptonate. This finding may indicate that other organic acids, or a mixture of various organic acids could be used to alter the selectivity of elements that are retained in solution by simple pH modification. The ability of these two organic acids to keep REE in solution at slightly alkaline pH may also allow for them to function as efficient REE lixiviants at pH 7-9 after an NaOH pretreatment procedure.

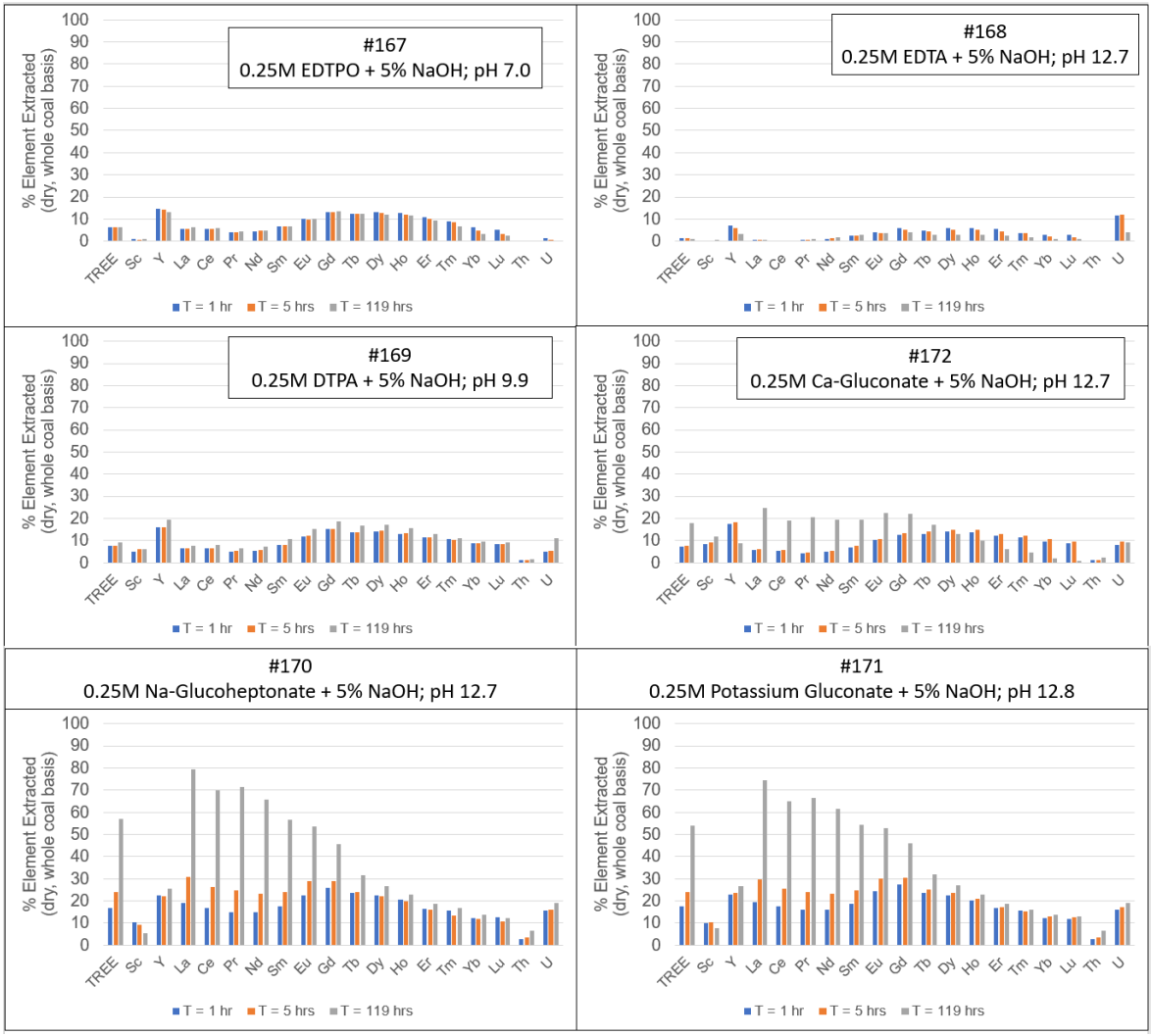

Figure 205. % Individual REE extracted from Underclay 5 um using 0.25M organic acid in 5% NaOH.

Table 50. REE-organic acid complex stability vs. pH compared with the stability of Al, Si, and Fe in solution under the same conditions.

Reagent	Initial / Final pH	[TREE] (µg/g)	[Al] (µg/g)	[Si] (µg/g)	[Fe] (µg/g)
Na-Glucoheptonate	12.73	242	11,646	56,830	23,080
	8.19	224	84	1,473	11,674
K-Gluconate	12.43	229	21,184	46,637	20,296
	7.99	225	871	260	19,244

Alkaline extraction of underclay with glucoheptonate – effect of alkaline pretreatment and washing

Leaching tests in this section utilized Underclay 5 um sample. As in prior tests, approximately 1 gram of dry sample were pretreated in 20 mL of 20% (w/v) NaOH at 80°C for 24 hours. Two of the four samples included 0.25% (w/v) $Ca(OH)_2$ in their alkaline pretreatment. One set of samples was washed with deionized water after pretreatment while the other was not. After pretreatment and washing, the samples were then extracted in 25 mL of 0.25M sodium glucoheptonate at room temperature over 96 hours. The results of this analysis can be found in Figure 206 though Figure 208.

Washing after alkaline pretreatment was found to remove excess NaOH as well as a portion of the sodium salts of Al, Si, and Fe that are formed during the alkaline pretreatments. These may also be removing small amounts of NaOH liberated REE. Water washing of the NaOH only pretreated sample had a slower extraction rate than the same sample without water washing, which may be explained by the removal of adsorbed salts or the drastic change in the ionic strength of solution. Future tests incorporating washes with dilute salt solutions or ammonium hydroxide may be beneficial instead of water washing. The extraction rate for the $Ca(OH)_2$ added samples was unaffected by the washing, which may support the adsorption of calcium or other ions during alkaline pretreatment.

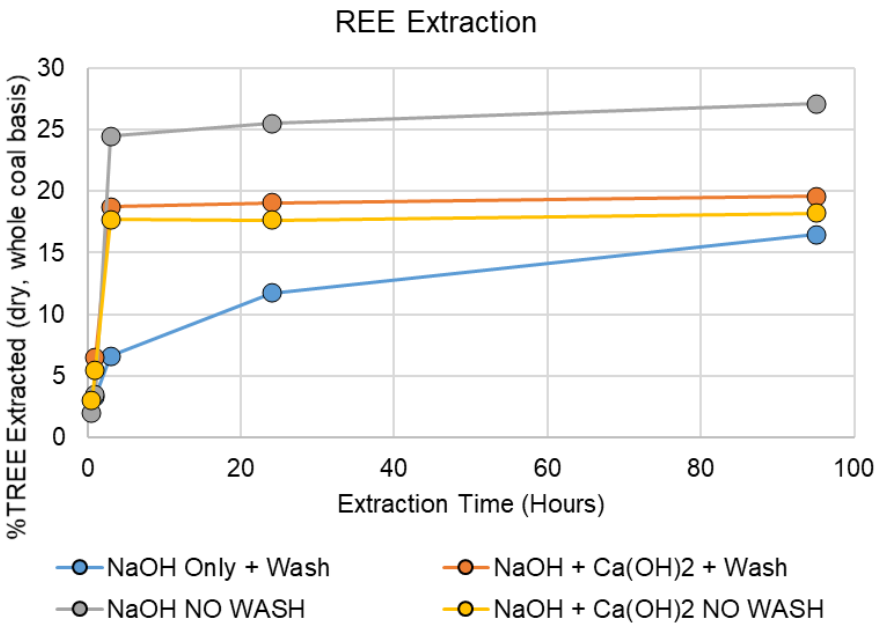

Figure 206. %TREE extracted from Underclay 5um using sodium glucoheptonate, pH 9 after NaOH + Ca(OH)2 pretreatment, with and without washing.

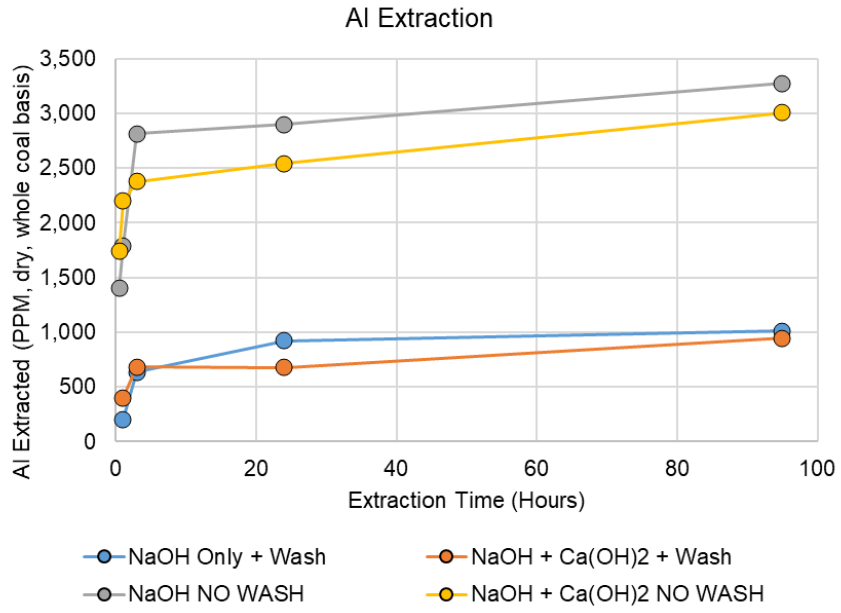

Figure 207. Aluminum extracted from Underclay 5um using sodium glucoheptonate, pH 9 after NaOH + Ca(OH)2 pretreatment, with and without washing.

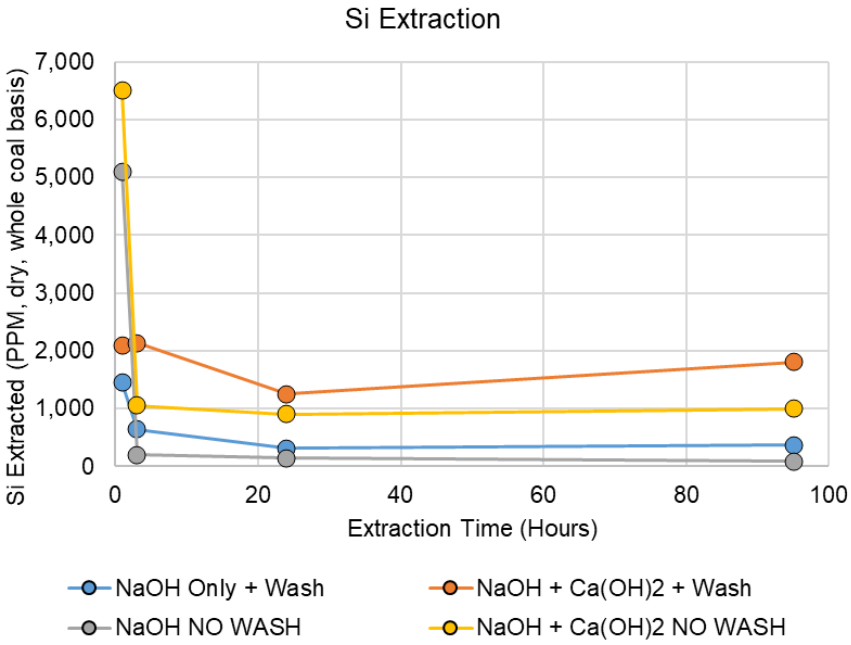

Figure 208. Silicon extracted from Underclay 5um using sodium glucoheptonate, pH 9 after NaOH + Ca(OH)2 pretreatment, with and without washing.

Extraction of fine coal refuse in 0.1M EDTPO, effect of L/S ratio

Leaching tests in this section utilized a thickener underflow sample from the lower kittaning coal, which was blunged and screened to -20 microns. Dry samples were leached directly in 0.1M EDTPO at pH 12.5 and 80 °C for approximately 72 hours. L/S ratios of approximately 5, 10, 25, and 50 were compared. The results of this analysis can be found in Figure 209 and Table 51.

The TREE extraction efficiency appears to decrease with decreasing L/S ratios. However, decreasing L/S increases the concentration of TREE in the leach liquor solution and increases the ratio of TREE / (Al+Si+Fe). Higher concentrations of calcium in solution were also found to correlate with lower Ce, Al, Si, and Fe in solution due to precipitation, as expected due to similar to observations in previous experiments. Reductive leaching conditions combined with lower L/S ratios may help increase the TREE concentrations in the leach liquor but will also increase dissolved Fe, Mn, Cr, among others, as a result.

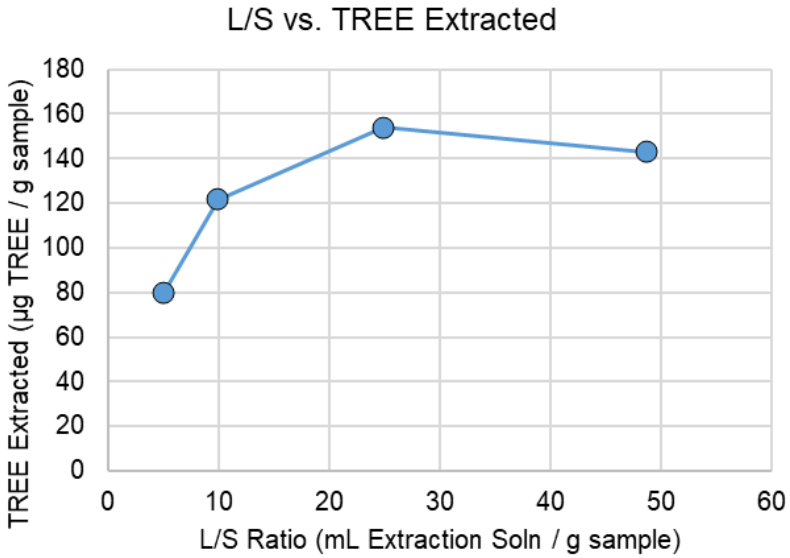

Figure 209. TREE (PPM) extracted from LEER using 0.1M EDTPO at pH 12.5, varying L/S ratios.

Table 51. Effect of L/S ratio on extraction of LEER with 0.1M EDTPO, pH 12.5

Ext. #	Time (hrs)	L/S	TREE : (Al+Si+Fe)	Concentration (µg element / mL extract)					
				[TREE]	[Cerium]	[Calcium]	[Al]	[Si]	[Fe]
181	72	50	0.0051	2.87	1.21	56	187	232	140
182	72	25	0.0080	5.82	2.45	109	292	348	84
183	72	10	0.0096	10.63	4.07	239	512	564	29
184	72	5	0.0259	12.30	3.21	401	205	263	6

Effect of free phosphate on REE standard solutions at pH 4

A simple experiment demonstrating the effect of free phosphate in solution has on REE standards in solution was performed. An REE standard solution comprised of approximately 10 µg/mL of Sc, Y, La-Lu, Th, U that is typically used for ICP-MS standard analysis was diluted in 0.5M ammonium chloride at pH 4 and kept constant at a concentration of approximately 400 ng/mL per element (sum of individual REE = 6.4 µg/mL). A stock solution of sodium phosphate (NaH_2PO_4) was made up and diluted into three of the four sample replicates at concentrations of approximately 1.1, 11, and 110 µg/mL PO_4^{3-}. The experiment was performed at room temperature, and a pH of 4.0 was kept constant. Samples were taken over approximately 1.5 hours with no pH adjustment needed between samples. The results of this analysis are shown in Figure 210.

REE concentrations in solution decreases with increasing phosphate concentrations in solution due to precipitation of REE-PO_4 solids according to the following.

$$REE^{3+}_{(aq)} + PO_4^{3-}_{(aq)} \leftrightarrow REE\text{-}PO_{4(s)} \qquad [5.3.2]$$

This precipitation occurs even whenever REE concentrations in solution are greater than those of phosphate. This indicates that any residual phosphate left in solution has the ability to re-precipitate extracted REE. A specific precipitation order was also observed as Th > Sc > U > REEs, with thorium being the first to precipitate under these conditions. An anomalous dip in the lanthanide series like that observed in extraction experiments spiked with $LaPO_4$ solid standards was also observed.

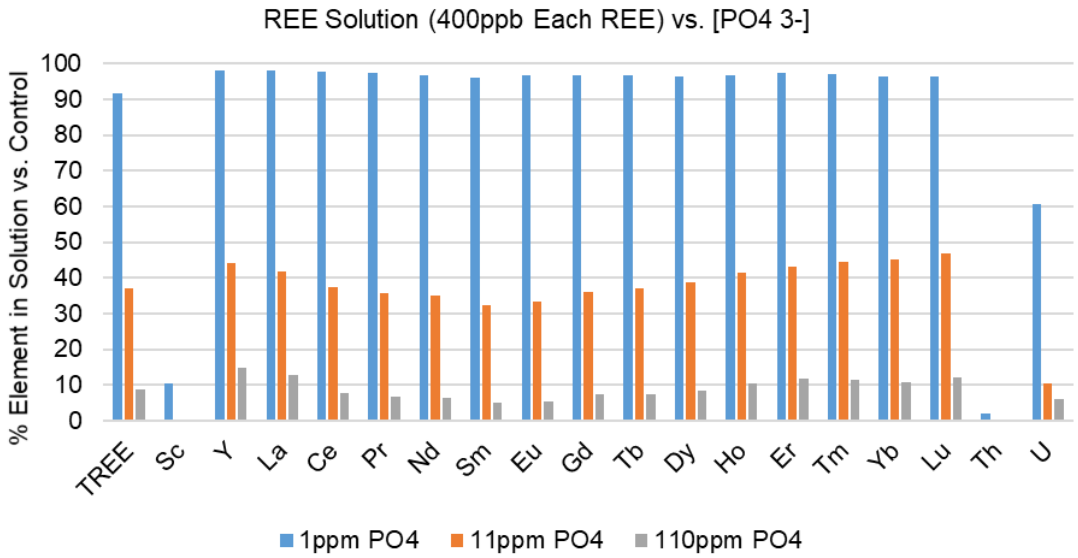

Figure 210. % Individual REE remaining in solution vs. [PO4 3-]. Control sample is at 100% with 400 ng/mL per element (Sc, Y, La-Lu; Sum of REE = 6.4 µg/mL)

Alkaline Extraction of LEER with EDTA + Organic Acids

Leaching tests in this section utilized blunged LEER samples and were performed at a temperature of 80°C. Disposable magnetic PTFE stirbars were utilized for constant stirring of the samples. Approximately 1 gram of dry sample were extracted in 25mL of 0.1M ethylenediamine tetraacetic acid (EDTA) with various organic acids at a concentration of 0.1M added to evaluate potential synergistic effects of extraction efficiency while varying pH over 120 hours. Organic acids tested were potassium gluconate, sodium citrate, and sodium ascorbate. The results of this analysis can be found in Figure 211 and Figure 212.

TREE extraction efficiency with EDTA was found to increase with pH as expected, with total NaOH concentrations reaching approximately 2.5% (w/v) at the highest pH values tested. The added NaOH is likely lower concentration than that of the previous free acid EDTPO tests due to the EDTA used here being a disodium, dihydrate salt rather than the free acid. A drop off in extraction efficiency was found for EDTA between pH 12 and 12.5 and was mostly due to the loss of La, Ce as expected. EDTPO exhibits a similar drop off point but at a higher pH of about pH 13.

Addition of organic acids was found to modified the TREE extraction and selectivity. Gluconate and ascorbate help to keep La, Ce in solution at pH > 12 *via* reducing and chelation effects as expected. Citrate may also help with TREE chelation and extraction efficiency but only at pH < 12. Drastic increases in dissolved Fe, Si and slight increases in Cr, Mn were observed with the chelation agents.

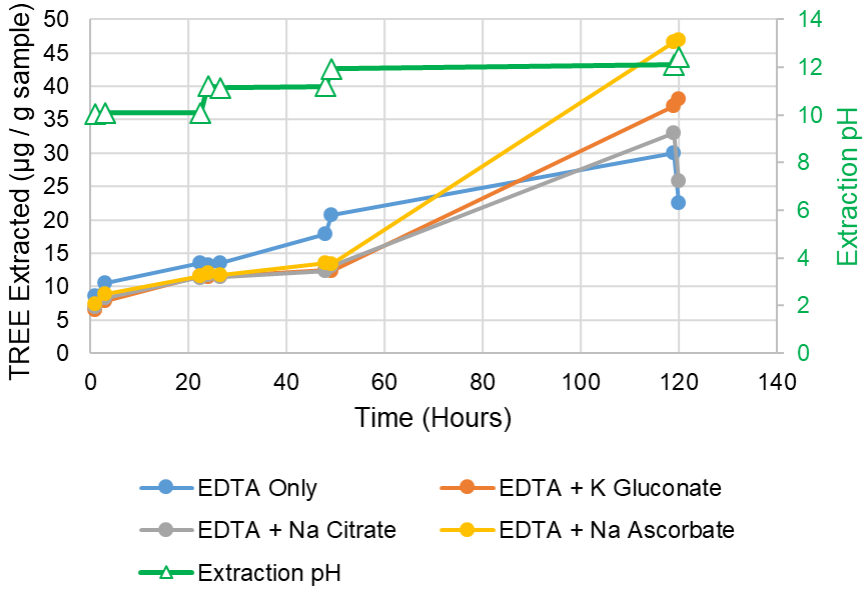

Figure 211. TREE extracted vs. pH for blunged Leer using 0.1M EDTA + various organic acids while modifying pH over time.

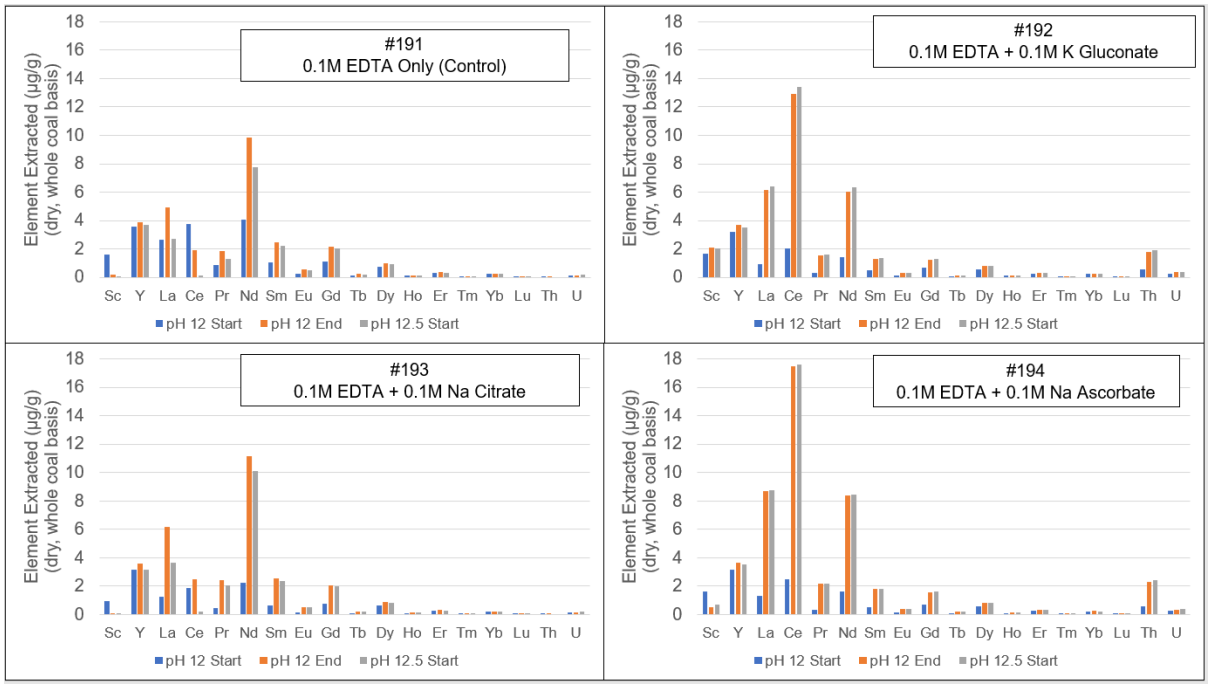

Figure 212. % Individual REE extracted from blunged Leer using 0.1M EDTA + various organic acids between pH 12 and 12.5.

Extraction of As-Received Russellton in Ammonium Oxalate

Leaching tests in this section utilized As-received Russellton samples and were performed at a room temperature. Disposable magnetic PTFE stirbars were utilized for constant stirring of the samples. Approximately 1 gram of dry sample were extracted in 25mL of 0.3M ammonium oxalate with pH values tested at 3,4, and 5 to evaluate direct TREE extraction efficiency. The results of this analysis can be found in Figure 213.

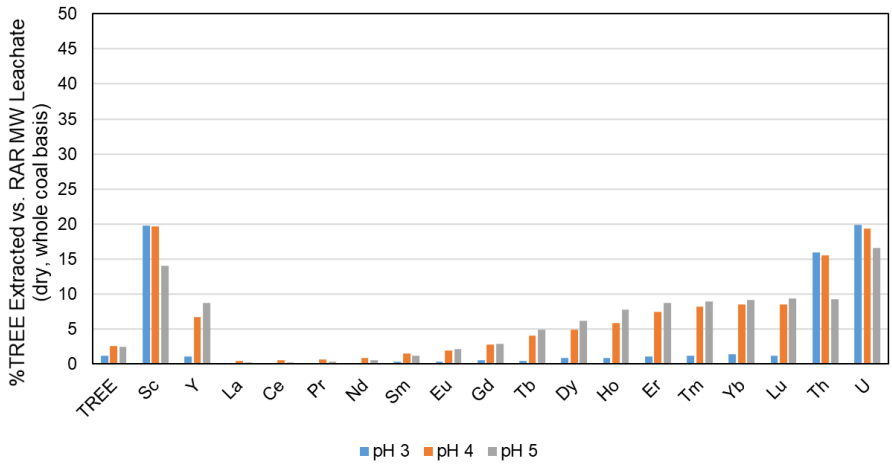

Figure 213. % Individual REE and P extracted from As-received Russellton using 0.3M oxalic acid while varying pH between 3 and 5.

Extraction with ammonium oxalate at room temperature yielded low %TREE but recovered Sc, Y, and HREE despite very high recoveries of P content. Extraction at pH 3 may be too low for this approach and may possibly be in equilibrium with solid REE-oxalates. The extraction of REEs, particularly LREEs, have also been shown in previous experiments to be inhibited by free phosphate in solution which fits the observed extraction patterns.

Extraction of As-Received Russellton in EDTA/Ammonium Oxalate

Leaching tests in this section utilized As-received Russellton samples and were performed at a room temperature. Disposable magnetic PTFE stirbars were utilized for constant stirring of the samples. Approximately 1 gram of dry sample were extracted in 25mL of 0.1M EDTA*2Na*2H2O for 23 hours. After 23 hours, solid ammonium oxalate was added to make 0.1M EDTA + 0.1M ammonium oxalate solution, with pH values tested at 4,5, and 6 to evaluate direct TREE extraction efficiency. The results of this analysis can be found in Figure 214.

Initial EDTA extractions only removed ~8% TREE after 23 hours at room temperature. Higher temperatures and longer extractions times would be required to optimize the EDTA extraction efficiency. Addition of oxalate in a 1:1 molar ratio with EDTA caused pH sensitive precipitation of LREE and Ca. Oxalate does not appear to have a synergistic extraction effect with EDTA under the conditions tested.

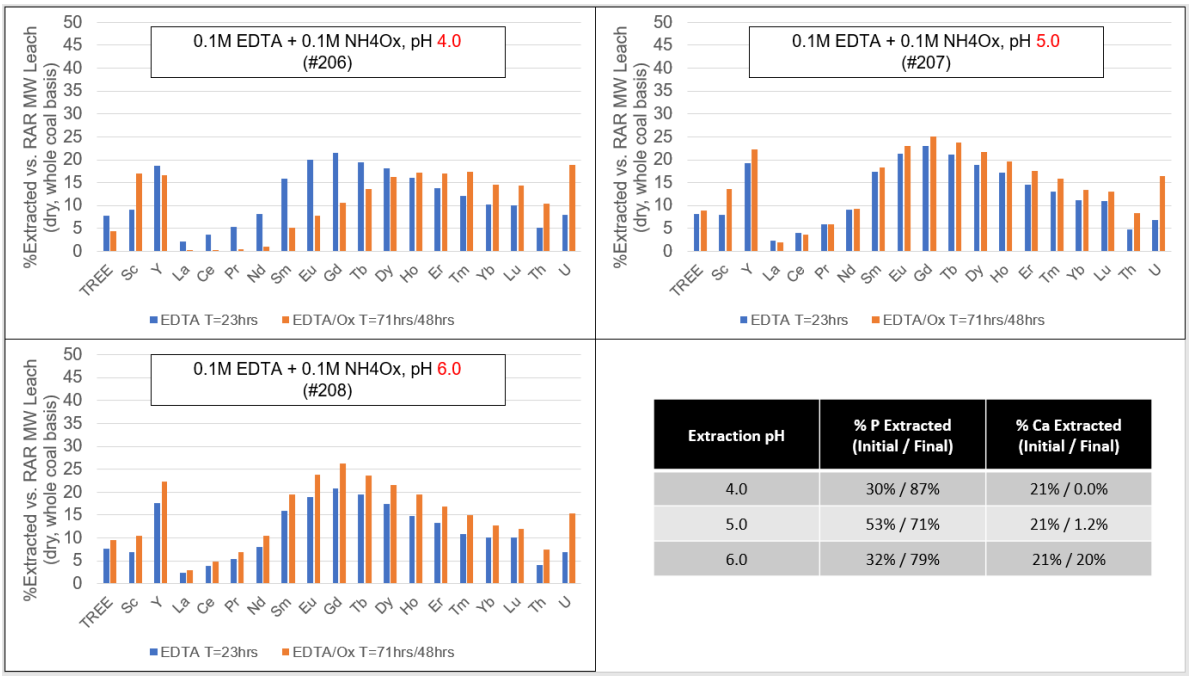

Extraction pH	% P Extracted (Initial / Final)	% Ca Extracted (Initial / Final)
4.0	30% / 87%	21% / 0.0%
5.0	53% / 71%	21% / 1.2%
6.0	32% / 79%	21% / 20%

Figure 214. % Individual REE, Ca, and P extracted from As-received Russellton using 0.1M EDTA + 0.1M ammonium oxalate between pH 4 and 6.

Extraction of As-received Russellton in Ammonium Sulfate + Free Acid Chelation Agents

Leaching tests in this section utilized As-received Russellton samples and were performed at a room temperature. Disposable magnetic PTFE stirbars were utilized for constant stirring of the samples. Approximately 1 gram of dry sample were extracted in 25mL of 0.25M ammonium sulfate with 0.25M various organic acid chelation agents for 24 hours. The pH of the experiment was not controlled and allowed to drift freely but was measured intermittently. The results of this analysis are shown in Figure 215.

A follow-up on this experiment where the pH was adjusted to include extraction time points from where they naturally drifted after 24 hours and up to pH 10 was performed. Each pH point was allowed to extract for 24 hours prior to sampling. The results of this analysis can be found in Figure 216 and Figure 217.

Extraction of TREE with ammonium sulfate and free acid chelation agents at room temperature is dominated by rapid acid leaching kinetics at low pH and when the pH < pKa of the specific chelation reagent. Increased temperatures, and extraction pH values > the pKa of the chelation agent of interest should be used to accommodate the much slower chelation kinetics and allow for these reagents to properly function as ligands to assist in TREE extraction efficiency.

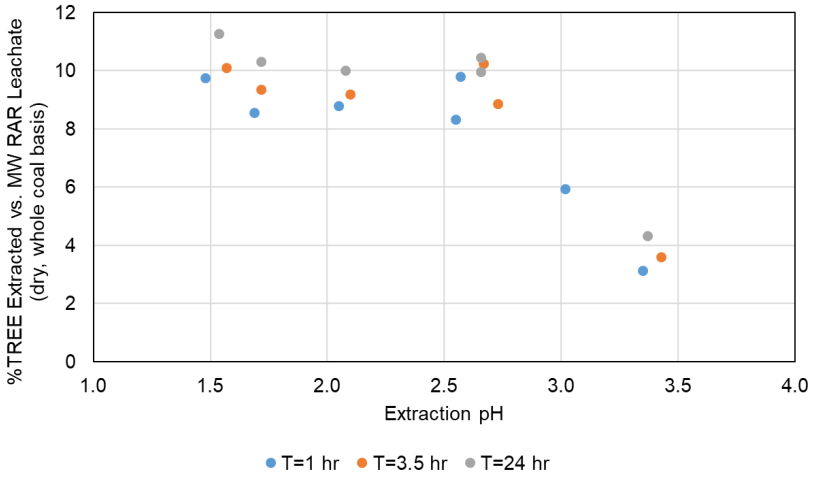

Figure 215. %TREE extracted vs. pH for As-received Russellton using 0.25M ammonium sulfate + 0.25M various organic acids extracting over 24 hours.

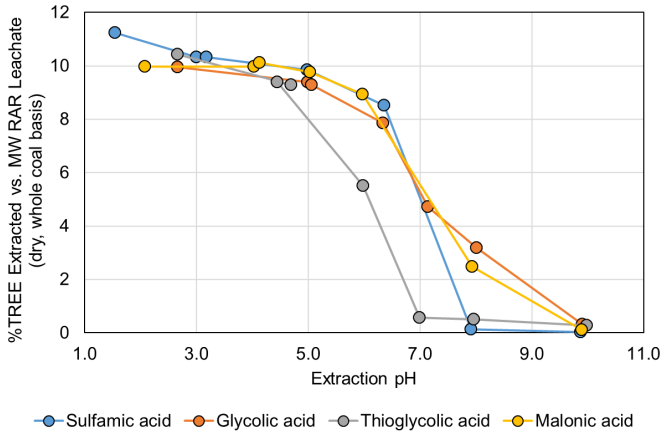

Figure 216. %TREE extracted vs. pH for As-received Russellton using 0.25M ammonium sulfate + 0.25M various organic acids, with higher pH values extracting for 24 hours prior to sampling.

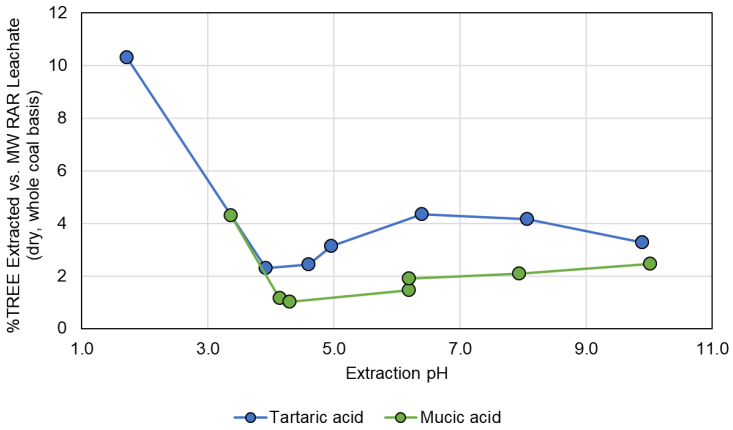

Figure 217. %TREE extracted vs. pH for As-received Russellton using 0.25M ammonium sulfate + 0.25M various organic acids, with higher pH values extracting for 24 hours prior to sampling.

Microstructural and Mineralogical Studies

In previous reports, we showed that ammonium sulfate leaching after NaOH treatment is an effective method to leach monazite and can potentially replace traditional acid cracking, which is commonly used in industry. Considering that rare earth phosphates are the dominant REE-bearing minerals in coal materials, the application of ammonium sulfate leaching on an NaOH-treated underclay sample was systematically studied in this report section. Second, other lixiviants include organic ligands and compound lixiviants (i.e., combining ammonium sulfate and other organic ligands) were also investigated. Thirdly, the effect of NaOH pretreatment and leaching on the mineralogical changes of the sample were characterized by X-ray diffraction (XRD) and X-ray photoelectron spectroscopy (XPS). Scanning electron microscopy-energy dispersive X-ray spectrometer (SEM-EDX) was applied to study the morphological variations of the sample before and after NaOH pretreatment.

Experimental

A representative underclay sample from the northern Appalachian Basin was collected as the feed material for leaching tests. The as-received sample was crushed into less than 1 mm in a ball mill and then was further ground to 5 μm in an attrition mill. The ground sample was dried in an oven with 60 ºC overnight. The TREE assay of the sample is 416.85 ppm, as determined by lithium tetraborate fusion and ICP-MS. Analytical grade chemicals and reagents were used in this study. Deionized water was used for all solution preparation and leaching tests.

To characterize the mineralogical changes before and after NaOH pretreatment as well as leaching, the untreated underclay sample, NaOH-treated underclay sample, and NaOH-treated plus ammonium sulfate leaching residues of the underclay samples were analyzed by a Bruker D8 discover plus instrument with Cu-K α radiation. The leaching residues and NaOH-treated samples were dried in an oven overnight at 60 °C before analyses. XRD spectra were recorded over a 2θ range from 5° to 70° with a step size of 0.04°.

The morphology of the untreated and NaOH-treated sample was characterized by a field emission SEM (JEOL IT500 SEM) under high vacuum conditions at 20 kV. The elemental composition of particles interested was analyzed by an energy dispersive X-ray spectrometer (EDX) detector with accelerating voltage 20 kV. XPS analysis of also performed on the above samples as well as the leaching residues.

Results and Discussion

Sample characterization

XRD analysis was conducted to characterize the compositions of the untreated and NaOH-treated samples and the mineralogical changes during NaOH pretreatment stage. The results are shown in Figure 218. It was found that quartz, illite, kaolinite were the dominant minerals in the untreated sample. For the samples treated by 30% w/v NaOH at 25 and 40 ºC, there was nearly no XRD-detectable mineralogical change. However, the diffraction peaks of kaolinite disappeared for the samples treated at 60 and 80 ºC. This result indicates that the decomposition of kaolinite by NaOH occurred between those two temperatures.

To provide additional insight on the dissolution of kaolinite at high pH, the solubility diagram of kaolinite was constructed (Figure 219). The results show that the total amount of dissolved kaolinite increases with the increase of pH values even at 25 ºC. $Al(OH)_4^-$ and $H_3SiO_4^-$ are the two major soluble species in the solution at alkaline pH values. The chemical reaction for the dissolution of kaolinite in NaOH solution can be described as (Wang et al. 2016):

$$Al_2O_3 \cdot 2SiO_2 \cdot 2H_2O + 2OH^- + 5H_2O = 2Al(OH)_4^- + 2H_4SiO_4 \quad [5.3.3]$$

$$2NaOH + SiO_2 = Na_2SiO_3 + H_2O \quad [5.3.4]$$

Under the aggressive conditions used in this study, the dissolution of kaolinite is inevitable. In addition, the peak intensities of quartz gradually decreased with the increase of pretreatment temperature (as shown in equation [5.3.4], demonstrating that a proportion of quartz also reacted with NaOH and is likely being dissolved. The solubility diagram of quartz was also constructed (see Figure 220). A new mineral, i.e., zeolite, was formed in the sample treated at 80 ºC. the formation of zeolite can be expressed as equation (3) (Wang et al. 2016) follows:

$$Na^+ + 6Al(OH)_4^- + 2SiO_3^{2-} + 2X \leftrightharpoons Na_6(AlSiO_4)_6 2NaX \cdot nH_2O + (6\text{-}n)H_2O + 12OH^- \quad [5.3.4]$$

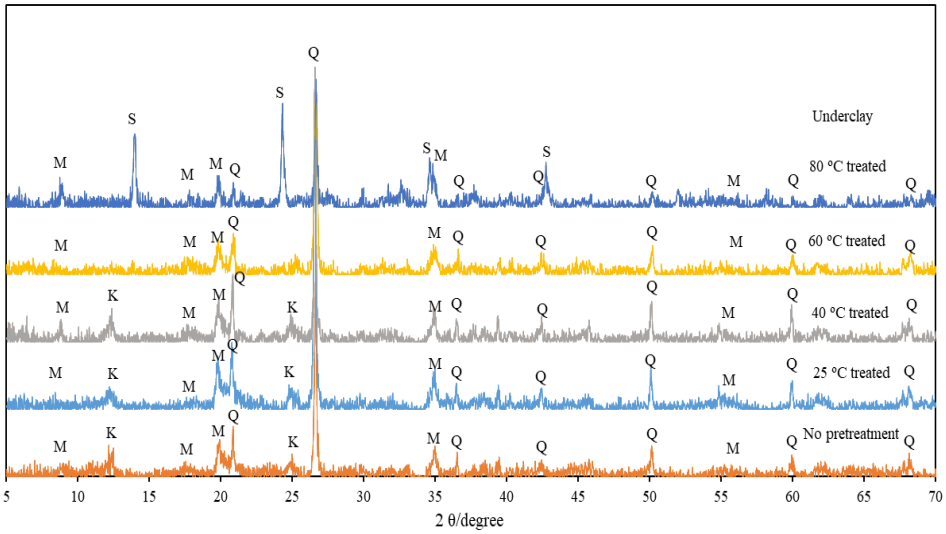

Figure 218. XRD patterns of the underclay sample and its NaOH-treated samples at different temperatures. (30% NaOH, 24 hrs) (Q: quartz; M: Muscovite/Illite; K: kaolinite; S: zeolite).

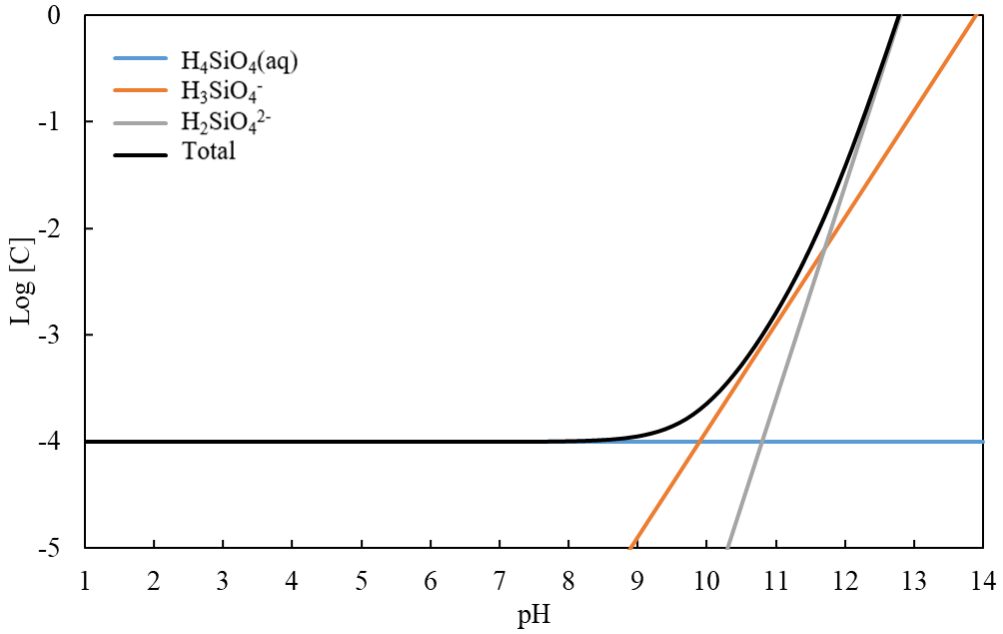

Figure 219. Solubility diagram of quartz in pure water at 298.15 K.

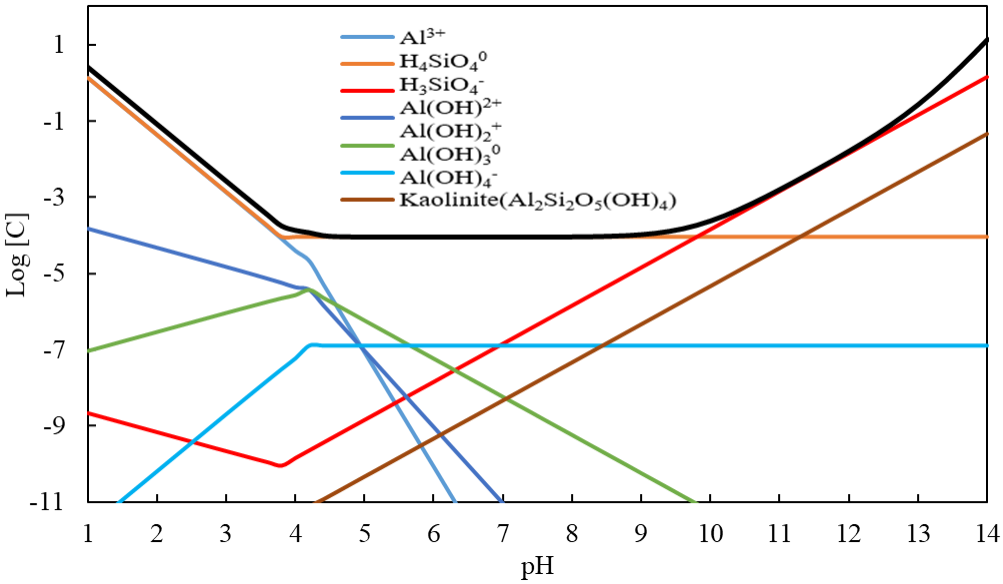

Figure 220. Solubility diagram of kaolinite in pure water at 298.15 K.

in which X can be $\frac{1}{2}CO_3^{2-}$, $\frac{1}{2}SO_4^{2-}$, Cl^-, OH^- respectively. Once kalinite was dissolved, the number of monomers (e.g., $[Al(OH)_4]^-$, $[SiO_2(OH)_2]^{2-}$ increased and these monomers can react with each other, leading to the formation of zeolite (Want et al., 2016; Gougazeh et al., 2014). From the above XRD patterns, the mineralogical variations during NaOH pretreatment stage at different temperatures were well recorded. During the dissolution of clay matrix, the REE-bearing minerals (e.g., apatite, rare earth phosphate,

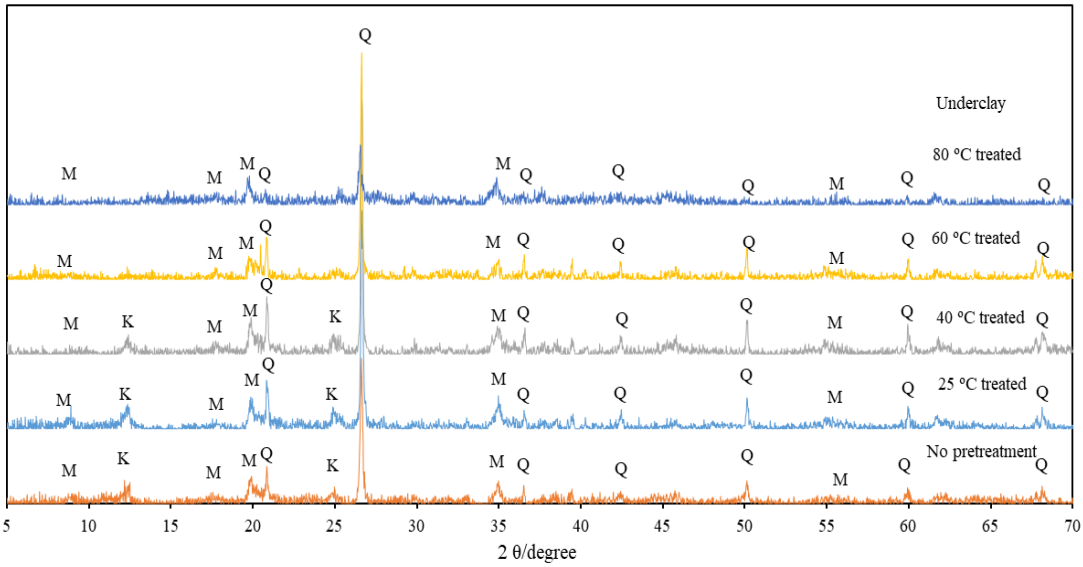

Figure 221. XRD patterns of the leaching residues of the NaOH-treated Underclay samples by ammonium sulfate, the feed sample with no pretreatment was shown for comparison purpose. (Q: quartz; M: Muscovite/Illite; K: kaolinite).

xenotime, bastnaesite) can also reacted with NaOH and converted to some easy-to-leach forms (e.g., rare earth hydroxide, rare earth oxide).

The XRD patterns of the leaching residues by 0.5 M ammonium sulfate at pH 4 are shown in Figure 221. As is shown, a similar mineralogical composition was found for each sample and the peak intensities are increasingly weaker as the pretreatment temperature increasing. This finding suggests that additional clay minerals as well as other minerals were dissolved during the ammonium sulfate leaching process, which was conducted at pH 4. For the sample treated by NaOH at 80 ºC, the diffraction peaks of zeolite were no longer present after leaching; the corresponding reactions (Wang et al. 2016) can be expressed as below:

$$Na_6(AlSiO_4)_6 2NaOH + 24HCl \rightarrow 8NaCl + 6AlCl_3 + 6Si(OH)_4 + H_2O \quad [5.3.5]$$

$$NaOH + Fe_2O_3 = 2NaFeO_2 + H_2O \quad [5.3.6]$$

$$FeS_2 + 4OH^- + 15/4O_2 = FeOOH + 2SO_4^{2-} + 3/2\ H_2O \quad [5.3.7]$$

Morphological analyses vis SEM were performed to characterize the changes of the sample before and after NaOH pretreatment. For the untreated sample (Figure 222) the micrograph (a) showed that many irregular-shaped ultrafine particles coexisted (covered or surrounded) with larger particles, indicating the heterogeneous composition of the sample. At higher magnifications (see subplots b, c, and d), lamellar structure of clays was observed. After NaOH pretreatment (Figure 223), the dominant minerals showed signs of NaOH corrosion. For instance, more fresh surfaces were formed and exposed to the air after NaOH pretreatment. The majority of those irregular-shaped ultrafine particles were dissolved and a considerable number of protuberant particles were formed at subplot (a). A common characterization for the NaOH-treated and untreated is that many cracks were found on the clay surfaces (Figure 222 and Figure 223), which was formed during grinding. Based on the XRD and SEM analyses, we found that NaOH pretreatment at 30% NaOH and 80 ºC for 24 hours does cause significant mineralogical and morphological changes to the sample.

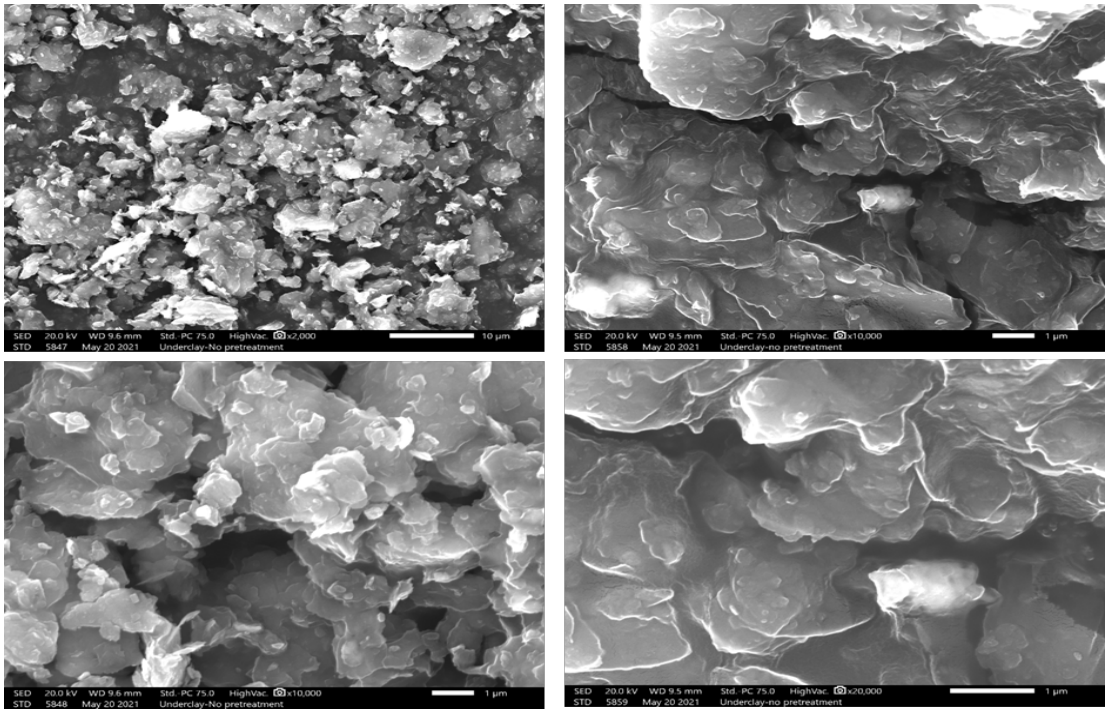

Figure 222. SEM images of the underclay feed sample without pretreatment at different magnification: (a) ×2k; (b) ×10 k; (c) ×10 k; (d) ×20 k.

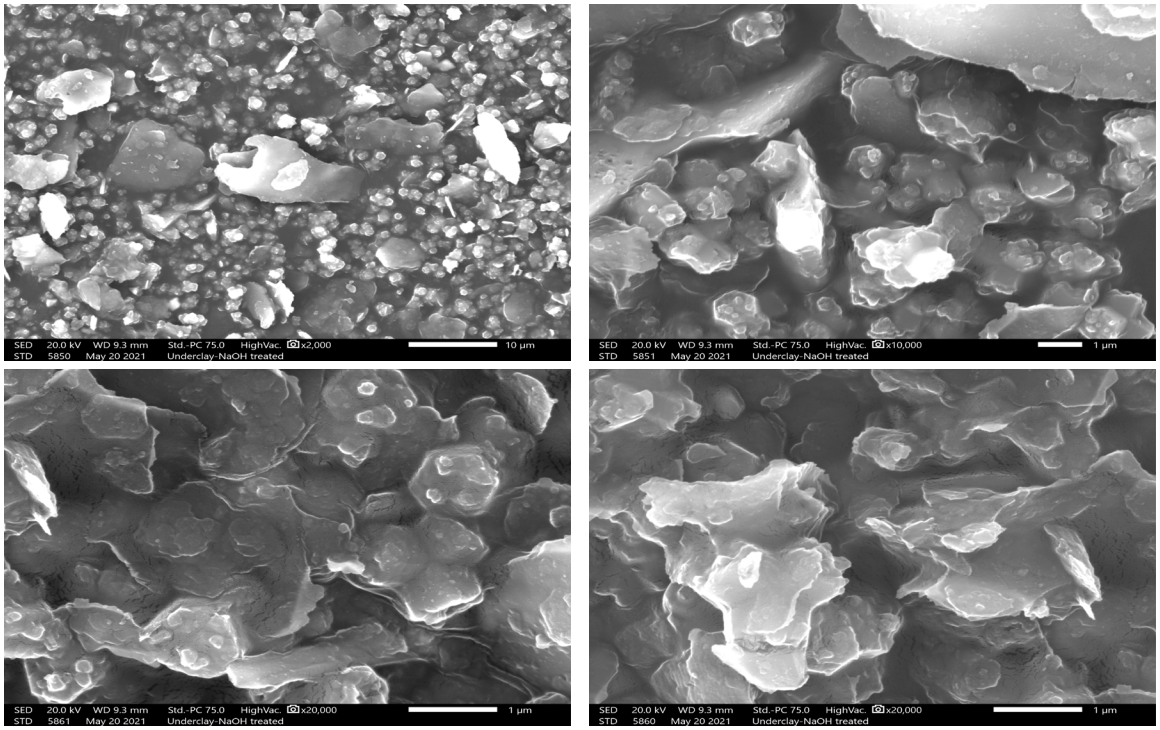

Figure 223. SEM images of the NaOH treated underclay samples at different magnification (pretreatment: 30% w/v NaOH, 80 ^{o}C, 24 hrs., 0.5 g/20 ml, d_{80} = 5.0 um): (a) × 2k; (b) ×10 k; (c) ×20 k; (d) ×20 k.

Effects of pretreatment temperature and leaching pH on the REE recovery of ammonium sulfate

The NaOH-treated underclay samples at different temperatures were leached by 0.5 M ammonium sulfate at pH 4. As is shown in Figure 224, pretreatment temperature had a significant impact on the TREE recovery, an improvement from 20 to 40% was noticed when the temperature increased from 25 to 80 ºC. A relatively small improvement on the TREE recovery was found with increasing temperature especially from 60 to 80 ºC. The leaching curves of those samples treated at 60 and 80 ºC were close to each other within the first 10 mins, thereafter only ~5% more REEs were extracted from the sample treated at 80 ºC. As is shown by the XRD patterns, clay minerals and quartz can be destroyed by the chemical attack of NaOH solutions. In addition to REE recovery, the ratio of TREE/(Al + Si + Fe) can be used to evaluate the selectivity of the leaching methods proposed in this study. As shown in Table 52, the ratio of TREE/(Al + Si + Fe) exhibited an increasing trend (from 0.06741 to 0.12226) as the pretreatment temperature increased from 25 to 60 ºC. However, for the sample treated at 80 ºC, the ratio of TREE/(Al + Si + Fe) decreased ~50 times compared with that of 60 ºC, indicating only minor dissolution of clays and quartz in these samples.

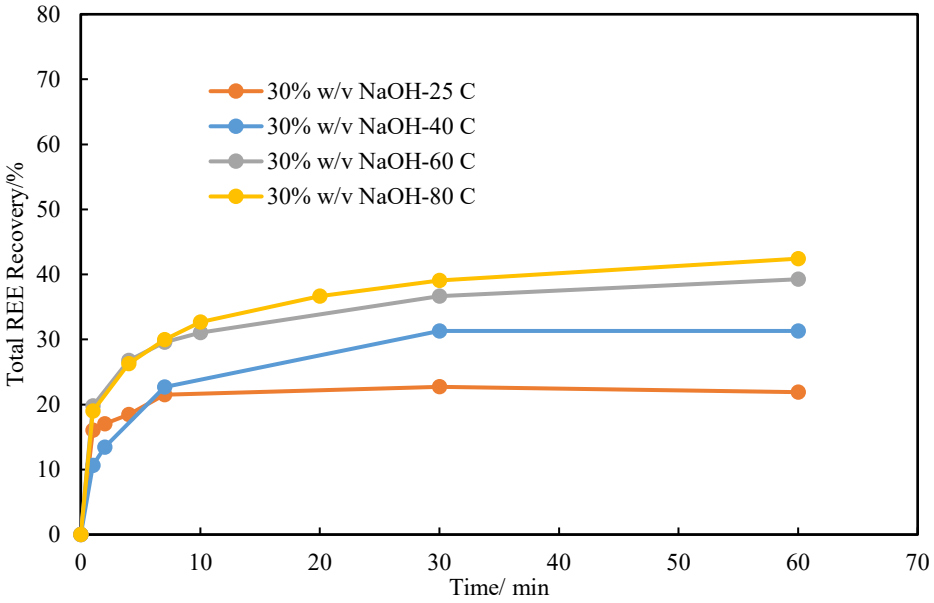

Figure 224. Effects of NaOH pretreatment temperature on total REE recovery leached by 0.5 M ammonium sulfate at pH 4 after treated at different temperatures for 24 hrs.

The effect of temperature on the individual REE recovery was also analyzed. The leaching behaviors of LREEs and HREEs were also analyzed and compared to better understand the associations of REEs in the underclay sample. As is presented in Figure 225 and Table 52, the recoveries of LREEs were generally higher than those of HREEs. At 40 ºC, for instance, the LREE recovery was 33.61%, which is 10% higher than that (23.53%) at 25 ºC; however, a relatively small improvement (from 14.00 to 20.33%) on the HREE recovery were noticed. Relatively large LREE recovery values were also noticed when the temperature changed from 40 to 60 ºC and 60 to 80 ºC respectively, indicating that HREEs and LREEs had different associations in this sample.

At 80 ºC, the LREE recovery was 43.08%, the HREE recovery also increased to 38.99% which is more than twice as high as the one (14.00%) at 25 ºC. For the samples treated over 25 ºC, relatively lower Ce recovery was notice, which is probably ascribed to the fact that Ce(IV) is difficult to be extracted by weak acid. The oxidization of Ce(III) to Ce(IV) have occurred during NaOH pretreatment, which is very similar with the leaching of NaOH-treated monazite by ammonium sulfate.

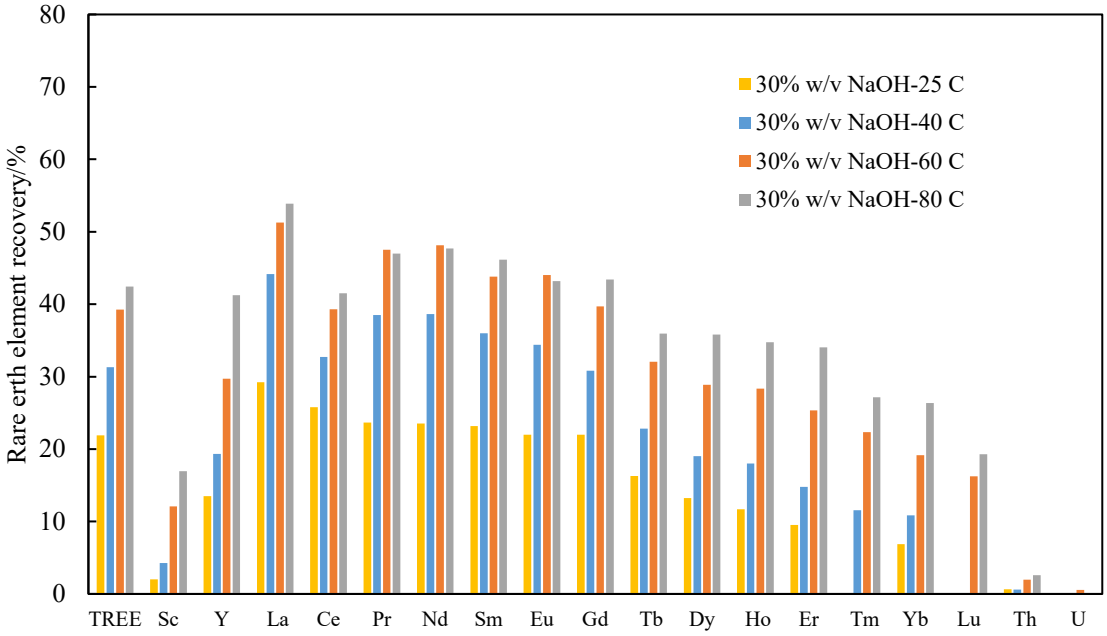

Figure 225. Effects of NaOH pretreatment temperature on the individual REE recovery leached by 0.5 M ammonium sulfate at pH 4 after treated at different temperatures for 24 hrs.

To verify this hypothesis, ammonium sulfate leaching tests at lower pH values as well as HCl (1 M) leaching test were performed on the samples treated by 30% NaOH at 80 ºC. The 1 M HCl leaching test was designed to serve as a reference line, which was assumed to recovery nearly all the easy-to-leach REEs due to its strong acid attack (see Figure 226). When pH was reduced from 4 to 2, the TREE recovery of ammonium sulfate leaching increased to 60%, which was close to the TREE recovery obtained by 1 M HCl (68.22%). The elemental recovery (Figure 227) indicated that LREE recovery contributed more to the

Table 52. Leaching results of ammonium sulfate from 30% NaOH-treated Underclay samples at different pretreatment temperatures and leached at different pH values, 1 M HCl leaching results were used as a reference.

Lixiviant	NaOH pretreatment temperature	pH during leaching	Recovery/%			TREE (Al + Si + Fe)
			TREE	LREE	HREE	
0.5 M Ammonium sulfate	25	4	21.88	23.53	14.00	0.06741
	40	4	31.31	33.61	20.33	0.10230
	60	4	39.26	41.10	30.33	0.12226
	80	4	42.42	43.08	38.99	0.00240
	80	3	51.54	52.90	44.71	0.00224
	80	2	60.37	64.21	45.95	0.00273
1 M HCl	80	0	68.22	72.79	46.38	0.00336

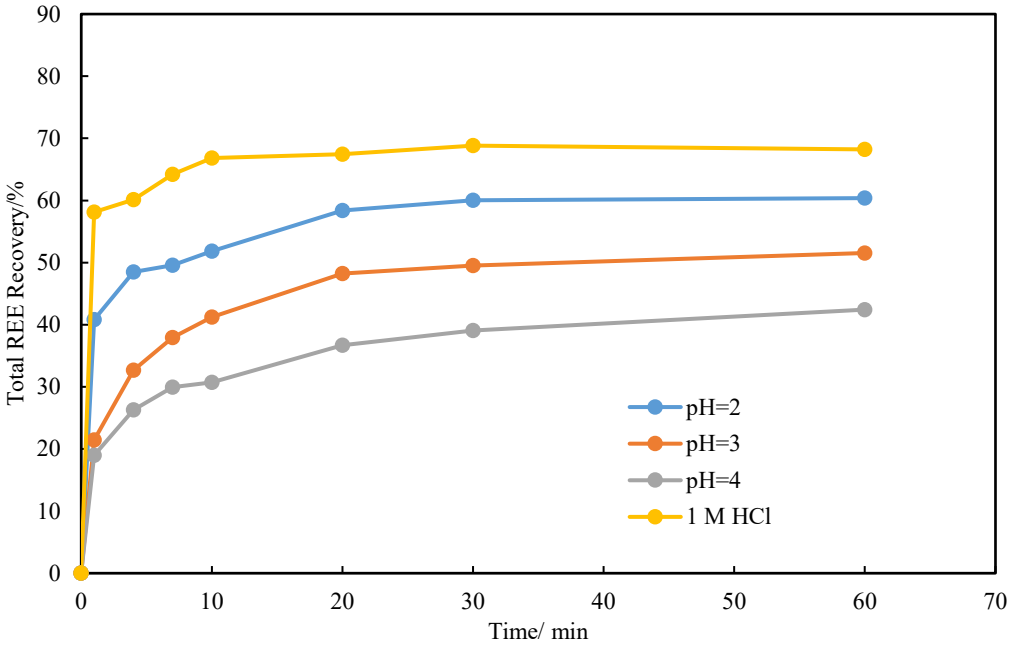

Figure 226. Effects of pH on total REE recovery leached by ammonium sulfate at various pH values and 1 M HCl after treated at different temperatures for 24 hrs.

TREE recovery at lower pH values. At pH 2, the LREE recovery increased from 45.97 to 69.31%, whereas the improvement on HREE recovery was only from 38.99 to 45.95%. Even by using 1 M HCl, 46.38% of HREEs were extracted, suggesting that HREEs should exist in or associate with some difficult-to-leach phases, which needs higher pretreatment temperatures and NaOH concentrations. The improvement on

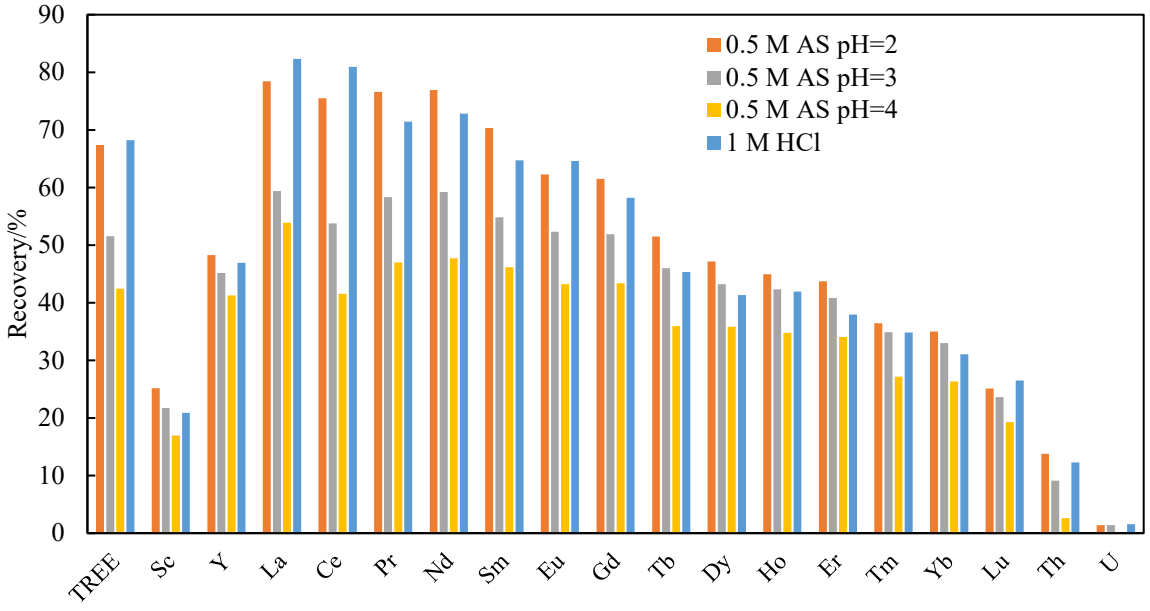

Figure 227. Effects of pH on individual REE recovery leached by ammonium sulfate at various pH values and 1 M HCl after treated at different temperatures for 24 hrs.

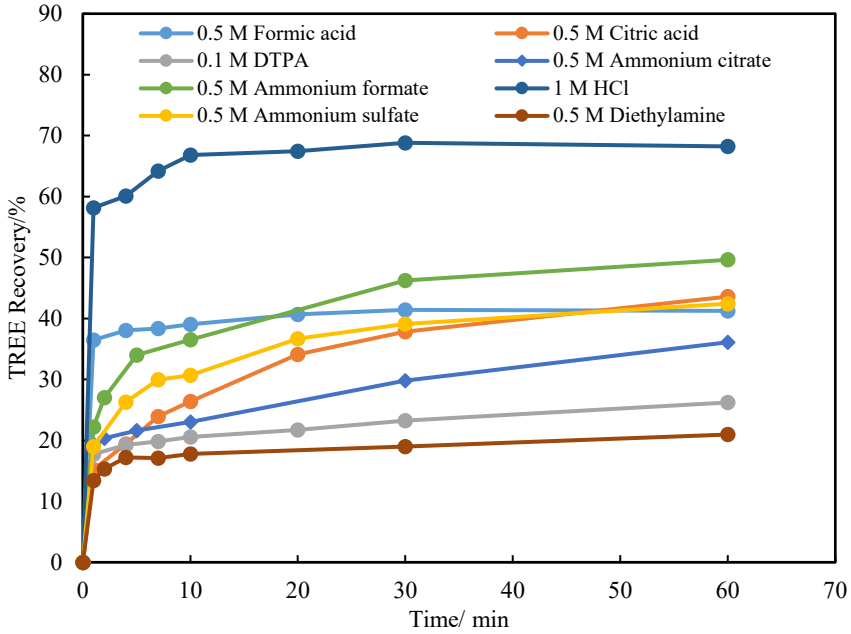

Figure 228. Effect of different lixiviants on total REE recovery from the NaOH-treated underclay sample (pretreatment: 30% w/v NaOH, 80 °C, 24 hrs, 0.5 g/20 ml, d_{80} = 5.0 um, leaching conditions: room temperature, 0.5 g/40 ml, pH = 4 (except for the lixiviant of 1 M HCl).

LREE recovery was achieved by the complete dissolution of the rare earth hydroxide especially for Ce through hydrogen attack. Therefore, the recovery of Ce was close to the recoveries of other LREEs (e.g., La, Pr, Nd) with the reduction of the pH value. Meanwhile, the ratio of TREE/(Al + Si + Fe) remained in a similar level with the decrease of pH from 4 to 2, which is slightly lower than that of 1 M HCl. There is a significant improvement on the leaching of impure elements for the samples treated at 80 °C. The recoveries of Al and Si increased from 27.83 to 35.98% and from 18.85 to 22.68% respectively when pH decreased from 4 to 2, while the dissolution of iron was also increased from 5.13 to 34.01%, suggesting that more iron-bearing minerals were also dissolved. Since more clay minerals and/or aluminosilicates, and iron-bearing species were dissolved at lower pH values, REEs associated with clay and/or REE-bearing minerals encapsulated by clays can be well dissolved, thereby leading to higher TREE recovery (Zhang et al., 2020). The aforementioned results indicated that ammonium sulfate is an effective lixiviants especially at lower pH values (e.g., pH =2) since it can extract similar level of TREE recovery with that of 1 M HCl.

Leaching characteristics of rare earth element by different lixiviants

Other than ammonium sulfate, different chemicals were also selected as lixiviants to maximize the TREE recovery. The leaching behaviors of the rare earth and major elements were also investigated to understand the leaching mechanisms. In this study, four types of lixiviants were used: (1) ammonium sulfate, which is a common lixiviant for the leaching of Chinese ion-adsorption clays. (2) ammonium salts of chelating ligands (ammonium formate, ammonium citrate); (3) chelating ligands (formic acid, citric acid, DTPA, diethylamine); (4) the leaching results of 1 M HCl used in previous section were used for a comparison purpose. The pH value of each lixiviant during leaching process was adjusted to 4 before mixing with NaOH-treated samples.

The TREE recovery of each lixiviant is shown in Figure 228. As indicated, the highest TREE recovery (68.21%) was still achieved by 1 M HCl. The sample leached by ammonium formate had 49% TREE recovery, which is higher than that of formic acid, though it had a slower leaching kinetics. An opposite trend was observed on ammonium citrate and citric acid with higher recovery being achieved by citric acid. This result may indicate that the presence of ammonium ions can only enhance the coordination

of organic ligands with less COOH groups. Also, it might also be that case that the leaching mechanisms of citrate (by coordination) and formate (by ion exchange) are largely different. In this case, the existence of ammonium ions can promote the ion-exchange leaching process and had no enhancement on the coordination between citrate and REEs.

Ammonium sulfate, formic acid and citric acid had similar extraction efficiencies, ranging from 41.26 to 43.59%. In addition, 36.10 and 26.21% of TREE recoveries were achieved by ammonium citrate, DTPA respectively, indicating that ligands having stronger complexing ability did not enhance the leachability of NaOH-treated samples as expected. One possibility is that the impure elements (e.g., Al, Si, Fe, Ca, Mg etc.) in the leaching system compete with REEs for organic ligands, thereby leading to a lower leaching efficiency compared with inorganic lixiviants. This possibility is supported by the stability diagrams with and without the presence of 0.1 M Al^{3+} ions (Figure 229), which were constructed by the chemical equilibrium software MEDUSA (Puigdomenech, 2013). The $LaPO_4(s)$ was assumed as a starting material (with the concentration being 10^{-5} M) since rare earth phosphate is the dominant REE-bearing phase in the Underclay sample. With the presence of 0.1 M Al^{3+} ions, the domain of La-citrate shrinks and the range of $LaPO_4(s)$ increases. It indicates a tendency that a negative impact can be exerted by the existence of Al^{3+} ions in the leaching system, though La-citrate still exists at pH 4 and 0.5 M citrate.

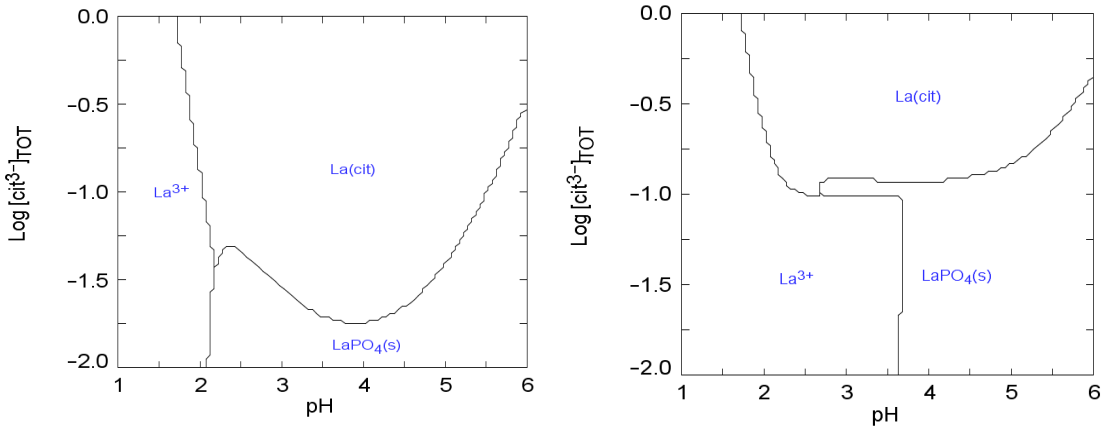

Figure 229. Stability diagrams of lanthanide as a function of pH and total citrate concentration, in the absence (left) and presence (Right) of 0.1 M Al^{3+} ions. Conditions: $[La^{3+}] = [PO_4^{3-}] = 10^{-5}$ M.

Another reason may be attributed to the increasingly stronger steric effect due to the increase of the number of COOH groups, when the lixiviant varies from formate (1 COOH group) to citrate (3 COOH groups) to DTPA (6 COOH groups) (Husin et al., 2013; Su et al., 2017). The stronger complexing ability of chelating ligands was counterbalanced by the increasing steric hinderance effect. Diehtylamine, which can complex with REEs through Lewis acid (REEs) and base (diehtylamine) interaction, achieved only 20.95% TREE recovery. The leaching curves of HCl, ammonium formate, ammonium sulfate, citric acid displayed a similar trend, which were relatively slower at the beginning and then followed by a slight increase thereafter. However, for the rest lixiviants especially for formic acid, the leaching equilibrium was achieved within the first 2 minutes, after that the leaching curve almost remained stable.

A similar trend was found for the LREE recovery achieved by each lixiviant but it is higher than that of TREE (Figure 230), indicating that LREE-bearing species (e.g., monazite) was converted to easy-to-leach forms. This is because the majority of REEs contained in the sample belongs to LREEs (Zhang, 2019). For 1 M HCl, the LREE recovery was 78.54%, which is 10% higher than that of TREE. For the rest of the lixiviants, the increments of LREE recovery ranged from 2 to 5% compared with their corresponding TREE recovery. However, relatively lower HREE recovery was extracted by each lixiviant compared with

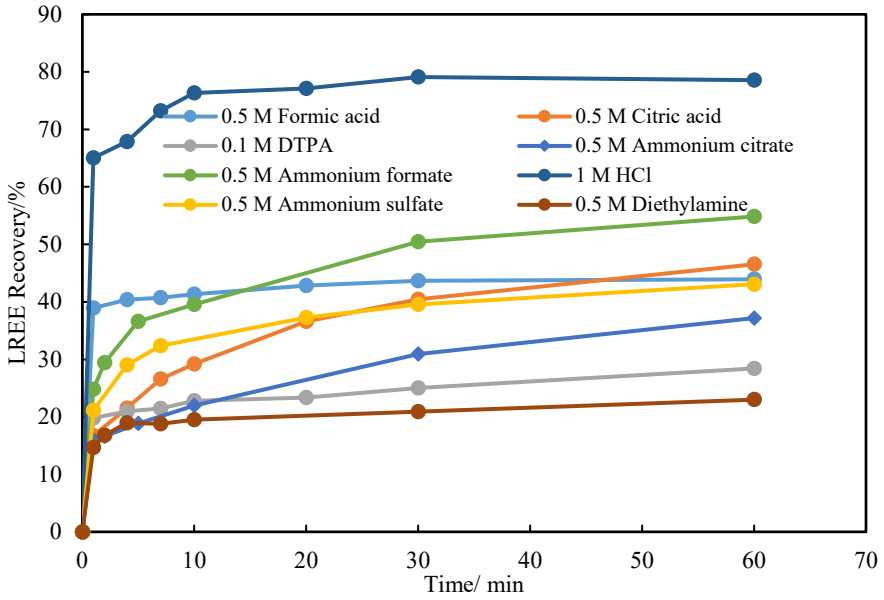

Figure 230. Effect of different lixiviants on LREE recovery from the NaOH-treated underclay sample (pretreatment: 30% w/v NaOH, 80 °C, 24 hrs, 0.5 g/20 ml, d_{80} = 5.0 um, leaching conditions: room temperature, 0.5 g/40 ml, pH = 4 (except for the lixiviant of 1 M HCl).

that of TREE recovery (Figure 231), similar findings have been reported by other researchers (Zhang et al. 2020). Again, this finding indicated that most of the HREEs are in hard-to-leach species.

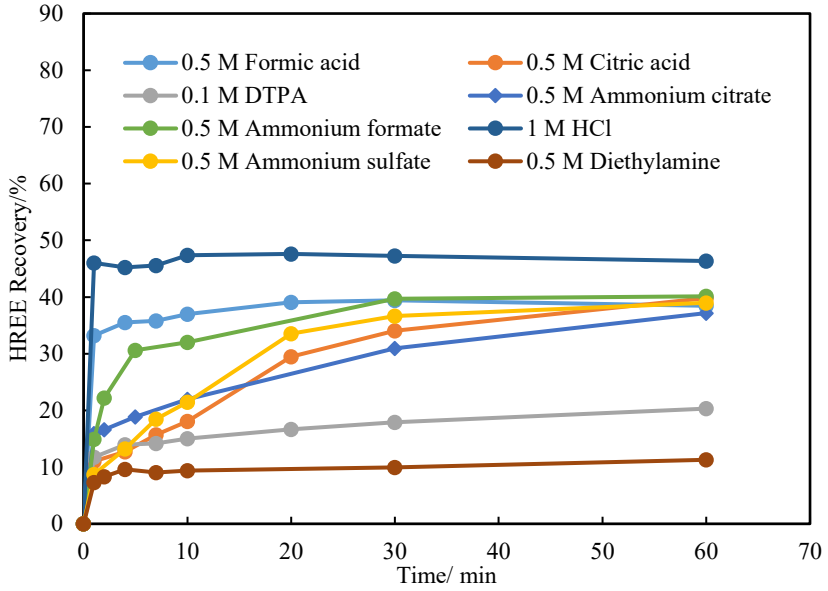

Figure 231. Effect of different lixiviants on HREE recovery from the NaOH-treated underclay sample (pretreatment: 30% w/v NaOH, 80 °C, 24 hrs, 0.5 g/20 ml, d80 = 5.0 um, leaching conditions: room temperature, 0.5 g/40 ml, pH = 4 (except for the lixiviant of 1 M HCl).

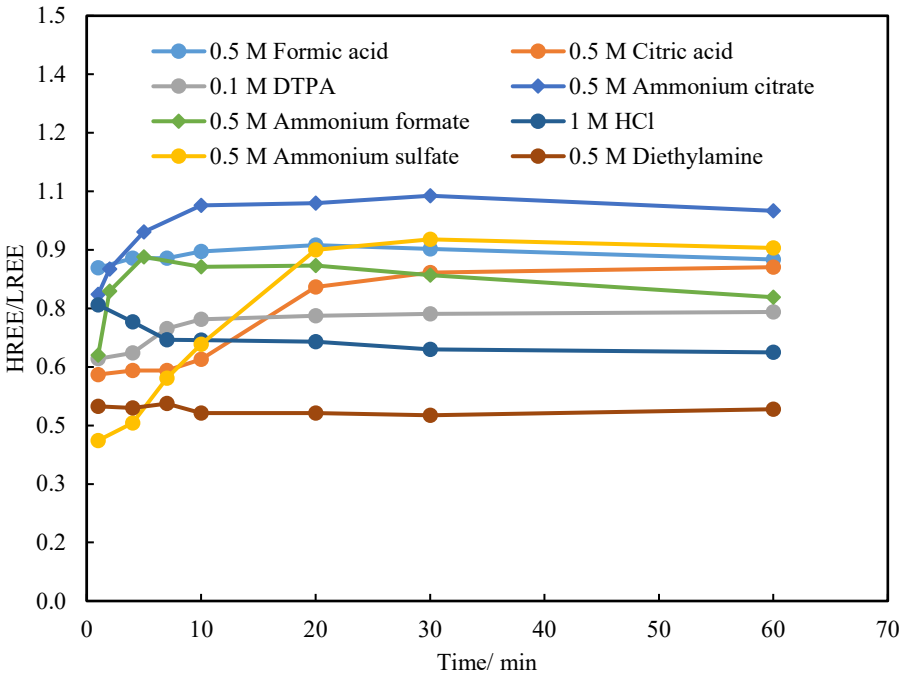

Figure 232. HREE/LREE ratios in the leachates of different lixiviants from the NaOH-treated underclay samples as a function of time. (pretreatment: 30% w/v NaOH, 80 °C, 24 hrs, 0.5 g/20 ml, d80 = 5.0 um, leaching conditions: room temperature, 0.5 g/40 ml, pH = 4 (except for the lixiviant of 1 M HCl).

Considering that HREEs differ from LREEs from a perspective of modes of occurrence, the ratio of HREE recovery over LREE recovery (H/L ratio) for each lixiviant was compared for further understanding the leaching characteristic of each lixiviant. As is shown in Figure 232, for the samples leached by HCl and diethylamine, the H/L ratio gradually decrease within the first 10 mins, and then remained stable. This trend suggests that HREEs were more preferentially leached compared with LREEs. The reason was more likely since HREEs have higher hydration energy and it is easier to be released from the clay surfaces (Zhang et al., 2019) compared with LREEs. On the contrary, a gradual increase in the H/L ratio within the first 10 mins was found for other lixiviants except ammonium sulfate and citric acid, though the climbing speed varied from each other. It revealed that LREEs were preferentially leached at the earlier leaching stage. Assume the leaching mechanism of organic ligands is dependent on the complexation, this increasing trend may be explained by comparing the stability constants of HREEs and LREEs. Larger stability constants of HREEs with the chelating ligands (citrate and DTPA) were noticed (Table 53). The log K values of La and Y with citrate are 9.18 and 9.42 respectively, suggesting that those ligands have more affinity to complex with HREEs compared with LREEs. Therefore, higher H/L ratios were achieved by organic ligands at the end of leaching compared with that of HCl. As such, the difference in stability constants may be the reason that causing the increasing trend of H/L ratio. The H/L ratio of ammonium

Table 53. Stability constants of REEs and chelating ligands.

	Log K		
	Citrate	DTPA	Sulfate
La	9.18	19.48	5.3
Y	9.42	22.05	5.2

Note: the data above were from the database of Visual MINTEQ 3.1

sulfate gradually climbed from the lowest (0.41) at the first min to 0.9 at the 20 min, suggesting that LREEs were preferentially extracted, then HREEs were gradually extracted This is consistent with the relative magnitude of the stability constants of sulfate and REEs, the Log K value of La-sulfate is a little higher than that of Y-sulfate, thereby LREEs have more tendency to complex with sulfate ions.

The H/L ratio at the end of leaching (i.e., at t=60 min) was used to evaluate the ability of each lixiviant to recovery HREEs since they are more critical elements compared with LREEs. The TREE recovery of HCl was 68.21%, however, its corresponding H/L ratio was 0.64. The lowest H/L ratio was achieved by diethylamine, revealing that it has weak affinity with HREEs. While ammonium citrate only recovered 36.10% of REEs, it had the highest H/L ratio (1.00) among all the tested lixiviants. Ammonium sulfate, formic acid, citric acid achieved similar level of H/L ratio (~0.9), which are slightly higher than those (~0.8) of ammonium formate and DTPA. Based on above analysis, ammonium sulfate and ammonium formate are better lixiviants that maintain relatively higher TREE recovery and H/L ratio than those of other lixiviants.

Leaching characteristics of major element by different lixiviants

Coal-based clays normally are more complicated in composition and rare earth associations than those of ion-adsorption clays. The leaching behaviors of major elements (Al, Si, Fe, Mn, Ca, Mg) in the leachates were also analyzed to understand the leaching mechanism of each lixiviant. If large number of impure elements are in the leachates, it can severely impact the following stream.

The Al recovery is presented in the Figure 233, it can be seen that HCl and ammonium sulfate achieved the lowest Al receives (27.83%), while much higher Al were extracted by other chelating ligands (36.45 to 42.33%) especially for DTPA (47.84%), which is likely due to their stronger complexing ability. The lower Al recovery obtained by HCl, revealing that there should be other Al-bearing species that didn't exist in acid-leachable forms, it is more likely that a proportion of Al has affinity to bound with organic ligands. With such high (30-40%) Al recoveries, the dominant clay structures of the samples have been altered.

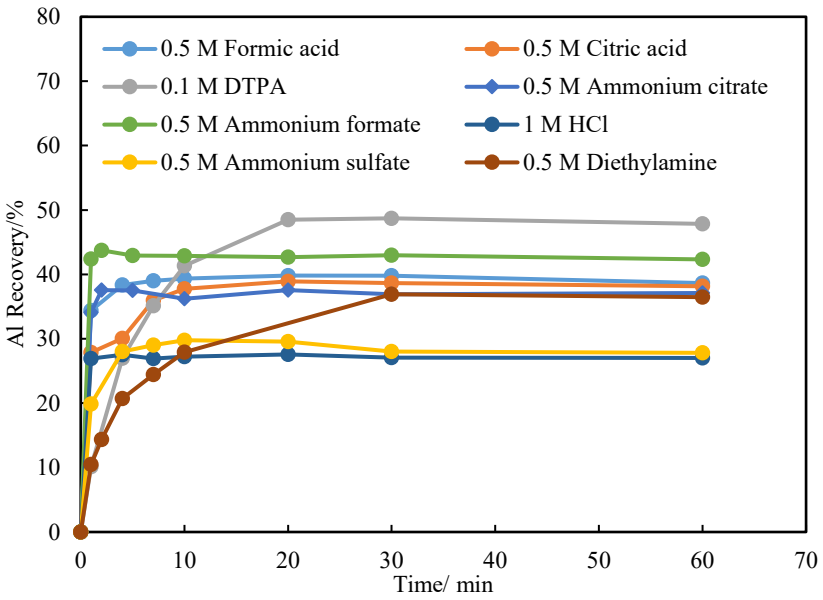

Figure 233. Leaching behaviors of aluminum in the leachates of different lixiviants from the NaOH-treated underclay samples as a function of time.

It has been reported that in the Chinese ion-adsorption clays, there are seven existing statuses of Al, which are soluble, exchangeable, adsorption inorganic hydroxyl, iron oxide combined, interlaminar, non-crystalline metasilicate, and mineral Al (Chi and Tian, 2008). Among them, Al in soluble and exchangeable forms can be easily recovered, while Al in adsorption inorganic hydroxyl and iron oxide combined phases can be dissolved by HCl leaching but the latter one is un-leachable by ammonium sulfate (Chi and Tian, 2008). Higher Al recovery should be extracted from the last three forms out of the seven, which normally requires the decomposition of the dominant Al-bearing minerals (such as kaolinite, muscovite, etc.) to some extent. Therefore, one disadvantage of using organic ligands is that a large amount of Al was extracted and reported to the leachates.

The composition of Si is less complicated than that of Al. In this sample, quartz and clay minerals (kaolinite and muscovite) are two major sources of Si. The recovery of Si in the leachate can be taken as an indicator of the degree of decomposition of the dominant minerals. As is displayed (Figure 234), other than DTPA, the Si recovery ranges from 16.75 (by HCl) to 23.57% (by ammonium formate), which is around half amount of Al recovery. DTPA achieved the highest Al and Si recovery, indicating it has a stronger ability to recover Al and Si.

The leaching curves of Al by DTPA, citric acid especially for diethylamine showed a slower kinetics compared with their counterparts. A similar trend was also found for the leaching curves of Si. This finding may suggest that the complexing process between these two elements and those lixiviants are relatively slower. For other lixiviants especially for HCl and ammonium formate, however, Al and Si recovery maximized immediately at the beginning of the leaching process. Due to the strong hydrogen attack, acid leachable Al and Si were released immediately once the NaOH-treated samples mixed with HCl solution.

Additionally, the analysis of the used NaOH solution indicated that 28.30% Al partitioned into NaOH solution after NaOH pretreatment (Table 54), the value for Si was 56.34%. Considering the partition of Al and Si in the leachates, the data shows that the dissolution rate of Al and Si were in a similar level (~70%) during both NaOH pretreatment and leaching process, with more Al reported to the leachates but

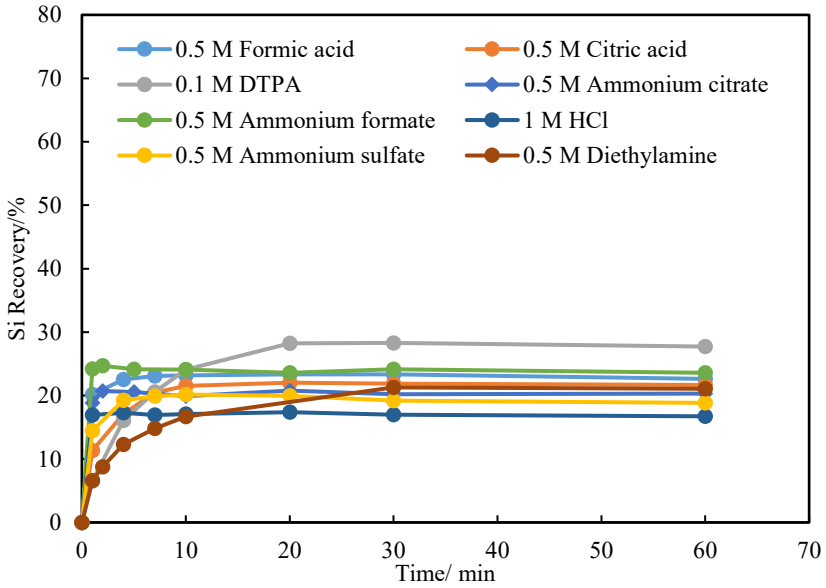

Figure 234. Leaching behaviors of silicon in the leachates of different lixiviants from the NaOH-treated underclay samples as a function of time.

Table 54. Partition of major elements and scandium in the NaOH solution after NaOH pretreatment (Pretreatment conditions: 0.5 g/20 ml, 30% NaOH, 80 °C, 24 hrs.)

Element	Mg	Al	Si	Ca	Sc	Fe	Mn
Recovery/%	0.00	28.30	56.34	0.00	5.71	13.34	0.00

more Si stayed in the used NaOH solution. The Si in the NaOH solution should mainly exist in the form of sodium silicate gel $(Na_2O)_x{\cdot}SiO_2$, a product resulted from the reaction of quartz and NaOH. As for Al, it may stay as $Al(OH)_4$. This high level of Al recovery has also been reported by other studies (Zhang et al. 2019).

SEM-EDX analyses were performed to understand the modes of occurrence of Fe in the treated and untreated underclay samples. In the untreated sample, the detected iron-bearing minerals including pyrite. Fe(III) associated with clays and quartz were detected by SEM-EDX analyses (see Figure 235 to Figure 240). In Figure 236, several EDX spectrums showed strong Fe and S peaks, which should be pyrite particles (Figure 235). Furthermore, the associations of illite (one of the major minerals in the Underclay sample) and minor amount of Fe (with and without S) were also observed. The mode of occurrence of Fe with no sulfur should be the goethite (FeOOH) and/or hematite (Fe_2O_3) coexisted with illite (Dong et al 2003), and a quartz particle with minor amount of Fe was also observed (Tuncuk et al. 2014).

After NaOH pretreatment (Figure 239 and Figure 240), the majority of Fe in minor amount was found to be associated with other minerals since a proportion of Fe (e.g., pyrite) was dissolved during NaOH pretreatment stage, As is shown in (Table 54), 13.34% of Fe was found to partition into the used NaOH solution. Other than the original FeOOH associated with clays and quartz, a proportion of Fe reported to the surfaces of the minerals (e.g., quartz and clays) may also be resulted from the reaction product (i.e., secondary FeOOH or Fe_2O_3) after pyrite reacted with NaOH. Spectrum 57, 58, and 62 in Figure 240Figure 240 revealed that Fe was associated with illite, but it is difficult to determine whether the particles where spectrum 57, 58, and 62 are located were independent particles like 63 or they were associated together with the substrate particle. Above observation indicated the diverse associations of Fe in the untreated and treated Underclay sample.

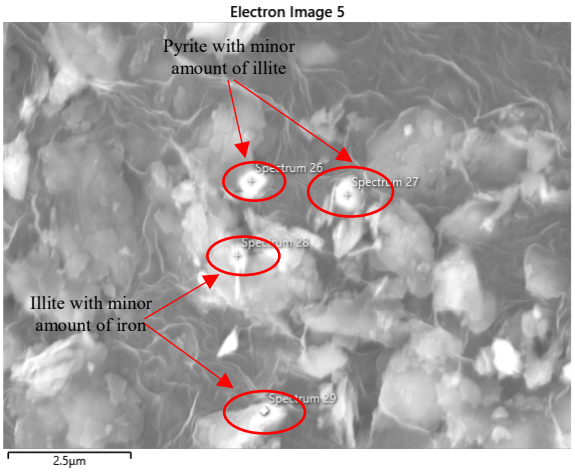

Figure 235. A back-scattered SEM image of particles enriched iron in the untreated Underclay sample. Spectrum 26 and 27 (red circles) are pyrite particles with minor amount of illite, while spectrum 28 and 29 are illite with minor amount of pyrite.

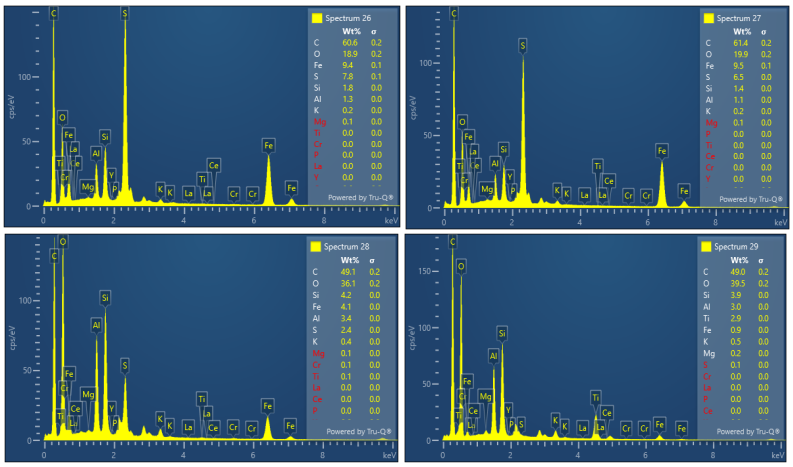

Figure 236. Representative EDX patterns of the spectrum 26 to 29 in the untreated Underclay sample.

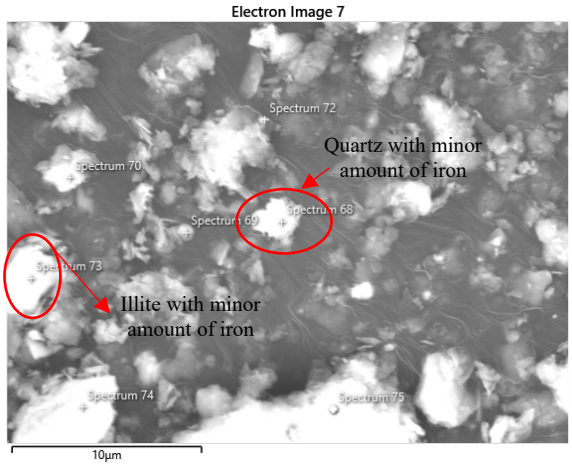

Figure 237. A back-scattered SEM image of particles enriched iron in the untreated sample. Spectrum 68 is a quartz particle with minor amount of iron. Spectrum 73 is an illite particle with minor amount of iron. (Note: Spectrum 75 is an illite particle associated with pyrite again)

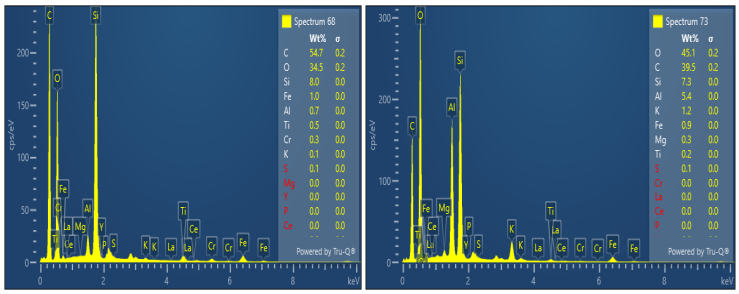

Figure 238. Representative EDX patterns of the spectrum 68 (similar with spectrum 69,70) and 73 (similar with spectrum 72, 74, and 75) in the untreated Underclay sample.

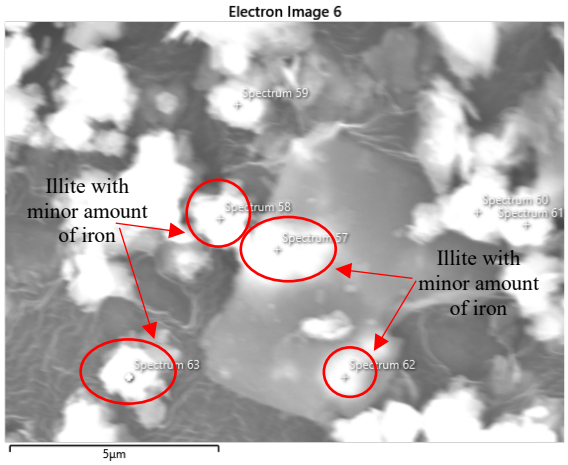

Figure 239. A back-scattered SEM image of particles enriched iron in the NaOH treated sample (30% NaOH, 80 ^{o}C, 24 hrs.) in the NaOH-treated Underclay sample. Spectrum 57, 58, 62, and 63 iron enriched particles.

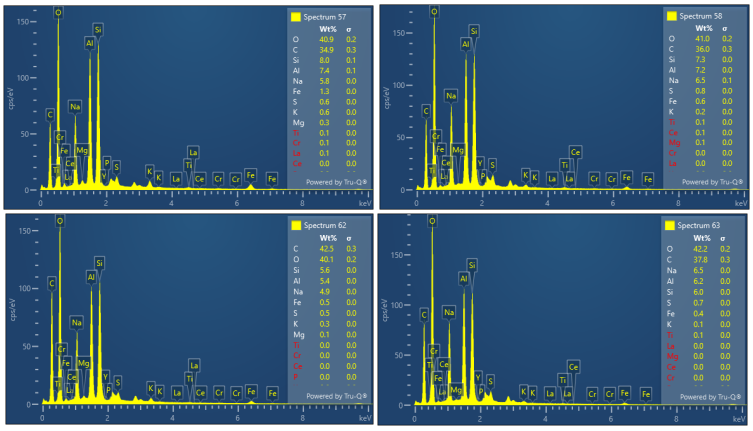

Figure 240. Representative EDX patterns of the spectrum 57, 58, 62, and 63 in the NaOH-treated Underclay sample. Spectrum 57 and 62 are spots with minor amount of iron and that existed together with an illite particle. Spectrum 58 and 63 are independent spots with minor amount iron and associated with illite.

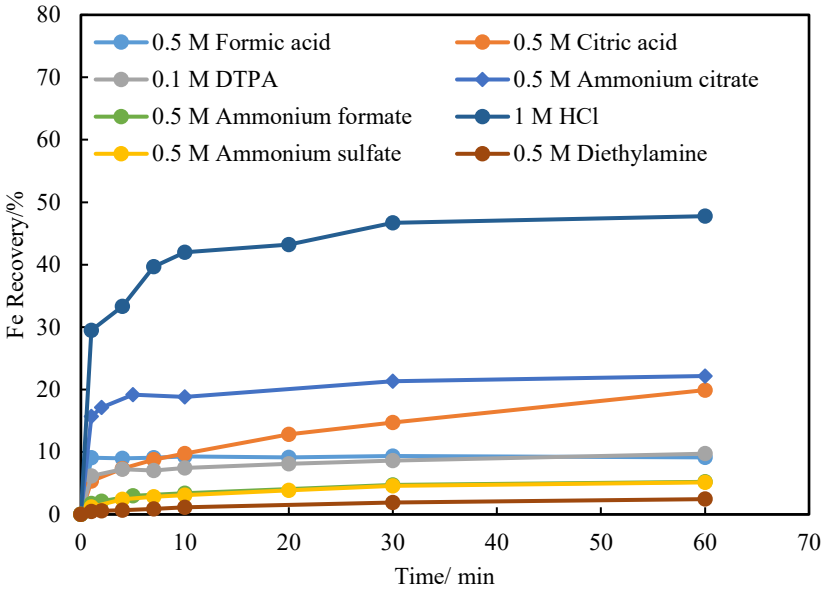

Figure 241. Leaching behaviors of iron in the leachates of different lixiviants from the NaOH-treated underclay samples as a function of time.

The leaching characteristics of Fe are shown in Figure 241. It showed that ~50% of Fe was dissolved by HCl, which is consistent with the yellow-green color observed in the leachate. Such high Fe recovery, which was two times higher than that of ammonium citrate, matched with the highest TREE recovery achieved by HCl. It indicated that a proportion of REEs associated with Fe were also dissolved by HCl. The associations of REEs with Fe (e.g., Fe-Mn oxyhydroxide, iron oxide, pyrite) in coal-based clays have been reported in previous study (Finkelman et al., 2018; Zhang et al., 2019). The Fe recovery (22%) obtained by ammonium citrate and citric acid were around 2 times higher than those achieved by DTPA and formic acid. Less than 5% of Fe was obtained by ammonium sulfate and ammonium formate, then followed by diethylamine, which recovered 2.44% of Fe, which was consistent with its low TREE recovery. Ammonium sulfate and ammonium formate achieved over 40% TREE recovery but only extracted around 5% of Fe, suggesting they are outperformed from other tested lixiviants in terms of economy and environment.

Mn in this sample is only 129 ppm, which is largely lower than that of Fe (3.60%). It has been reported that Mn in the high rank coals of North American are mainly associated with calcite (50%), clays (25%), and siderite (15%), the remaining 10% of Mn is organically associated, which is less likely to occur for the Underclay sample with very high ash content (91%) (Finkelman et al., 2018). As such, the modes of occurrence of Mn in this sample should mainly bound to calcite, clays, and siderite. The leaching behaviors of Mn were similar with those of Fe (Figure 243). It was HCl and diethylamine that achieved the highest (40.39%) and lowest (11.14%) Mn recovery respectively, which were 10% lower and 8% higher than their corresponding Fe recovery. It revealed that around 40-50% of Fe and Mn were in HCl-leachable

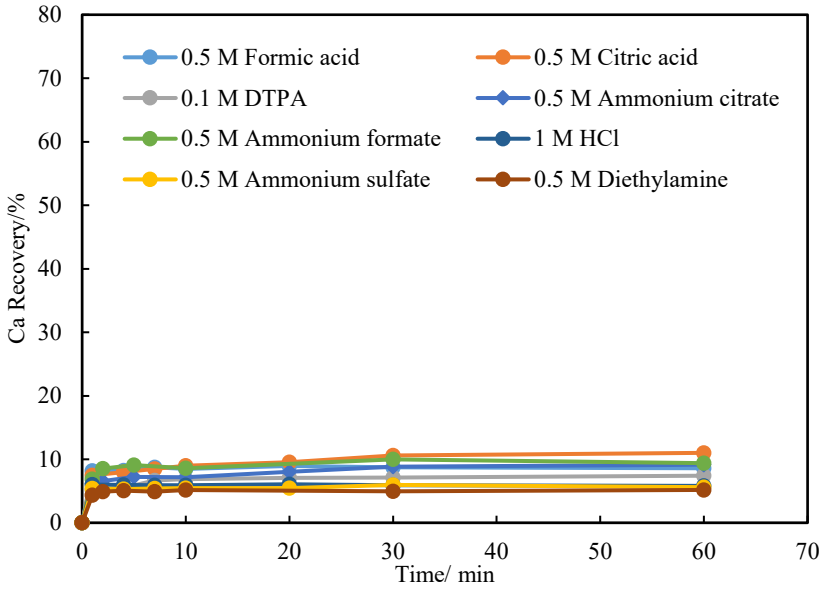

Figure 242. Leaching behaviors of calcium in the leachates of different lixiviants from the NaOH-treated underclay samples as a function of time.

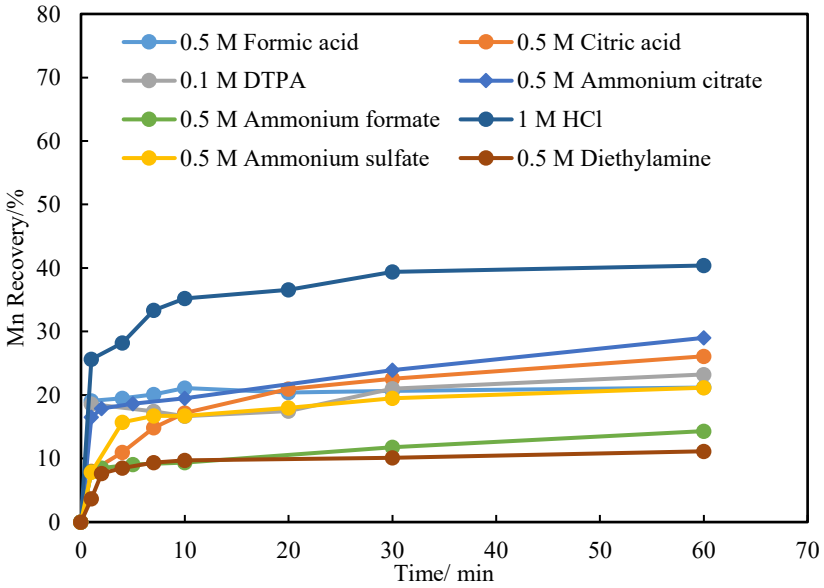

Figure 243. Leaching behaviors of manganese in the leachates of different lixiviants from the NaOH-treated underclay samples as a function of time.

forms. The total amount of The Mn recovery obtained by ammonium formate (14.32%) was lower than ammonium sulfate (21.15%) and other organic ligands (21.15 to 29.01%). Based on the above analysis as well as the leaching behaviors of Fe, ammonium formate and ammonium sulfate displayed better selectivity of REEs over Fe and Mn than other lixiviants tested.

As two important alkali-earth metal elements, the leaching behaviors of Ca and Mg were also studied. The recoveries of Ca ranged from 5.18 to 11.02%, indicating that the leachability of Ca was slightly

affected by different lixiviants, which is distinct with other impure elements mentioned before (Figure 242). Even with 1 M HCl, the Ca recovery was only 5.82%, which was lower than the values (9.26 and 9.14 respectively) of ammonium formate and ammonium citrate. This demonstrated that Ca has a stronger affinity to chelating ligands. It revealed that the associations of the majority of calcium were in stable forms and the dissolved calcium may be resulted from some easy-to-dissolve minerals like calcite, though no XRD-detectable Ca (e.g., calcite) was found in this sample. The major associations of Ca may bound to silicate and phosphate etc. (Finkelman et al., 2018).

The leaching behaviors of Mg were also slightly influenced by the lixiviants except diethylamine (Figure 244). The lowest Mg recovery (9.35%) was also obtained by diethylamine due to its low reactivity with the sample. The Mg recovery also focused a narrow range (from 20.38 to 29.53%). In this range, organic ligands also achieved higher levels of magnesium recovery than those of HCl and ammonium sulfate, which is similar with the case of the leaching characteristics of Ca. It suggested that a part of Ca and Mg in this sample tend to have more affinity to organic ligands rather than inorganic lixiviants.

Based on the analysis of the leaching behaviors of impure elements of different lixiviants and the ratio of TREE/(Al + Si + Fe) (see Table 55), it can be seen that HCl leaching achieved the highest TREE recovery but also dissolved a large amount of Fe among other lixiviants. However, it didn't extract too much Al and Si, which is contrary to expectation. Among the tested organic ligands, only ammonium formate outperformed others by achieving the highest TREE recovery and low Fe recovery, but it achieved second high Al in the leachate. The performance of DTPA didn't match with its strong complexing ability since it gave low TREE recovery as well as high impure element recovery. This demonstrated that strong chelating ligands are not promising lixiviants for NaOH-treated clays. Diethylamine also showed weak reactivity to the NaOH-treated clay samples because it achieved low TREE recovery but relatively high Al and Si recovery, though it had the lowest recoveries for other impure elements. Combing with the ratios of TREE/(Al + Si + Fe), ammonium sulfate and ammonium formate were two promising lixiviant among all the tested lixiviants. DTPA and diethylamine are the lixiviants that gave low TREE recovery but high recoveries of impure elements.

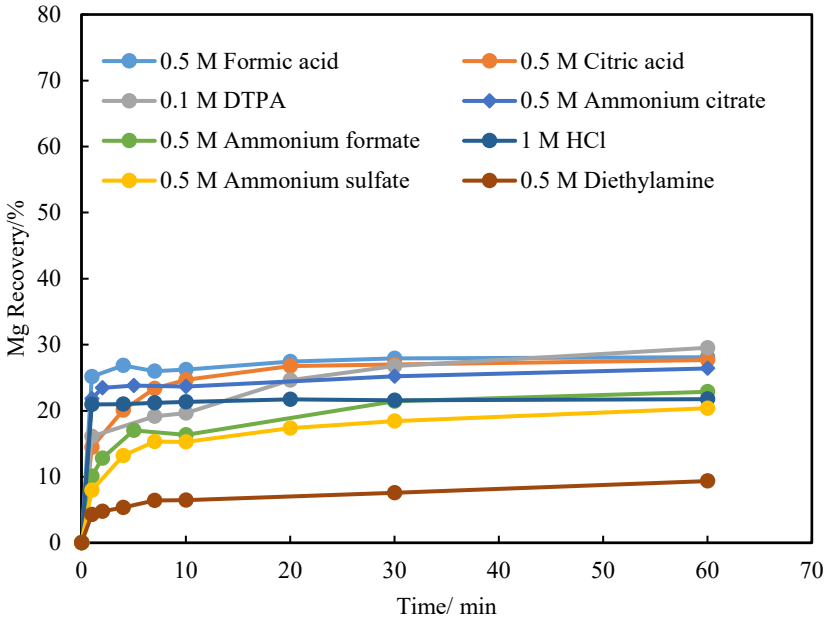

Figure 244. Leaching behaviors of magnesium in the leachates of different lixiviants from the NaOH-treated underclay samples as a function of time.

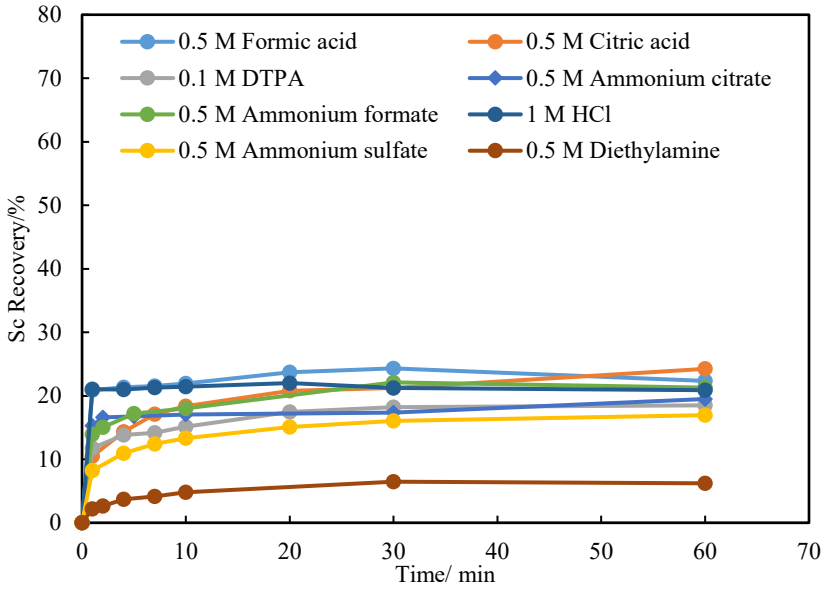

Figure 245. Leaching behaviors of scandium in the leachates of different lixiviants from the NaOH-treated underclay samples as a function of time.

Table 55. TREE recovery and the ratio of TREE/(Al+Si+Fe) of different lixiviants from 30% NaOH-treated Underclay samples at 80 °C.

Lixiviant	Concentration/M	TREE recovery/%	TREE/(Al+Si+Fe)
HCl	1.0	68.22	0.00336
Ammonium sulfate	0.5	42.42	0.00240
Ammonium formate	0.5	49.62	0.00204
Ammonium citrate	0.5	36.10	0.00164
Formic acid	0.5	41.26	0.00178
Citric acid	0.5	43.59	0.00185
DTPA	0.1	26.21	0.00092
Diethylamine	0.5	20.95	0.00099

As an element with much smaller ionic radius compared with other REEs, scandium normally exists independently (Zhang et a., 2019). Finkelman et al (2018) reported that mineral and organic matter associated scandium are the two main modes of occurrence of scandium. Arbuzov et al. (Arbuzov et al., 2015) reviewed the associations of scandium in coals and peats, and found that the mineral matter includes silicates, aluminosilicates, phosphates, and aluminophosphates. Compared with the organic matter, the association of scandium with inorganic minerals are more likely to be the occurrence of scandium in the underclay sample studied. Since scandium is associated with mineral matters and a proportion of clays and quartz were dissolved during NaOH pretreatment stage, the 5.7% of scandium (see Table 54) found in the used NaOH solution.

As is shown in Figure 245, a narrow range of Sc recovery (16.95 to 24.24%) was also achieved by the lixiviants except diethylamine (6.23%), this range is very close to the Si recovery (18.85 to 24.33%). These two similar ranges may indicate that the extracted Sc was resulted from clays and quartz. Those un-leachable Sc may primarily exist in insoluble minerals (e.g., Sc-containing zircon etc.) (Arbuzov et al., 2014), which require higher temperatures (above 200 °C) to be decomposed and then release Sc (Sun et al. 2019).

Compound leaching after NaOH pretreatment

Compound leaching is a type of leaching method by using more than one (normally 2 lixiviants) lixiviants together (e.g., chelating or reducing agent) in each leaching test. The additional lixiviant added is served as an assisting lixiviant. By virtue of the complexing and reducing ability of those assisting lixiviants, higher leaching efficiency of IACs can be achieved, since REEs associated with colloidal phase or other difficult-to-leach forms can hardly be recovered by only using the common lixiviants such as ammonium sulfate. Moreover, in the presence of the assisting lixiviant, the consumption of the common lixiviants (e.g., ammonium sulfate, magnesium sulfate) can be reduced and thus, the environmental pollution caused by the massive usage of ammonium sulfate can also be alleviated, which are the advantages of compound leaching.

Several studies have been reported about the application of compound leaching on REE extraction from IACs. Feng et al combined 0.1 M ammonium sulfate with 0.032 M ammonium formate and used them as a compound lixiviant, the results showed that 92.97% and 37.79% TREE and aluminum were extracted respectively at pH 5.0 to 8.0, and faster leaching kinetics was observed compared with that of the leaching tests by using ammonium sulfate only (Feng et al., 2018). Lai et al investigated the mixture of magnesium sulfate and ascorbic acid together to deal with IACs, and 86.2% TREE recovery and 57.1% REEs in colloidal sediment phase were recovered under optimal conditions (0.15 M magnesium sulfate and 1.0g/L ascorbic acid, initial pH 2.50) (Lai et al., 2018). In another study, Lai et al used the same combination (0.15 M magnesium sulfate and 1.0g/L ascorbic acid) for IACs, and 85.7% REEs in colloidal sediment phase was extracted at pH 2 (Lai et al., 2018). Tang et al developed a lixiviant by combining 0.2% ammonium sulfate with 0.005 M EDTA, the results showed that over 90% La was extracted, which was in a similar level with the recovery achieved by only using 2.0% ammonium sulfate (Tang et al., 2018). The compound leaching tests by using magnesium-ferrous and magnesium-ascorbic acid tests have been reported by Xiao et al respectively, both of them can also serve as potential alternatives for the traditional leaching agent, i.e., ammonium sulfate (Xiao et al., 2016; 2017).

Since the addition of organic ligands can further improve the leaching efficiency, compound leaching tests were carried out on the NaOH-treated underclay samples. The compound leaching agents used are ammonium sulfate (served as a major lixiviant) and other organic ligands (served as an assisting lixiviant), including ammonium formate (AF), EDTA, ascorbic acid (ASA), sulfur salicylic acid (SSA). Two concentration levels (low and high lev el respectively) of the organic ligands were used (see Table 56), the low concentration level of each organic ligand was the optimal concentration from literature (ammonium formate from Feng et al., 2018, EDTA from Tang et al., 2018), which was carried out on the IACs. Different concentrations were used since their difference in molecule weight. The high concentration level was two times higher than the that of low concentration level. The leaching curves of ammonium sulfate and 1 M HCl were still used as two references, so as to compare the performance of each compound leaching agent. As presented in Table 56, other than AF (at both 0.032 and 0.064 M) and SSA (at 0.01 M), the TREE recoveries achieved by the addition of other organic ligands at both concentration levels were higher than that of using AS only. 52.49 and 56.81% TREE recovery were obtained by the addition of 0.05 and 0.1 M ASA respectively. A slightly increase (from 45.24 to 46.42%) on TREE recovery was observed when the addition of EDTA increased from 0.005 to 0.01 M. Among those tested reagents, ASA and SSA can improve the TREE recovery to above 50%. The leaching curve of each reagent at the high concentration

Table 56. Compound leaching results with different assisting lixiviants at two concentration levels from 30% NaOH-treated Underclay samples at 80 °C..

Assisting lixiviant	Concentration/M	TREE Recovery/%	TREE/(Al+Si+Fe)
Ammonium formate (AF)	0.032	18.58	0.000940
	0.064	23.15	0.000990
Ascorbic acid (ASA)	0.050	52.49	0.002078
	0.100	56.81	0.002045
Sulfur salicylic acid (SSA)	0.010	32.02	0.001720
	0.050	52.68	0.002153
EDTA	0.005	45.24	0.001986
	0.010	46.42	0.002166

(Note: AS: ammonium sulfate; AF: ammonium formate; ASA: ascorbic acid; SSA: sulfur salicylic acid; EDTA: ethylenediaminetetraacetic acid, similarly hereinafter.)

is shown in Figure 246. A similar trend, which had a rapid leaching rate within first 10 mins and followed by a slight increase thereafter was observed for all tests.

Figure 247 showed the individual REE recoveries of each reagent at the high concentration. Compared with AS, the improvements of LREE (especially Ce) recovery were more apparent than those of HREE recovery. In the AS leaching, the Ce recovery was only 41.53%, which is 12% lower than that of La. However, for ASA and SSA, the Ce recovery increased by 58.07 and 42.20% respectively (calculated based on the Ce recovery of AS at 60 min). Moreover, the improvements on the TREE recovery of ASA and SSA were 33.90 and 24.17% respectively compared with that of AS leaching. Again, this is more likely due to be the fact that CeO_2, which is difficult to be dissolved by weak acid, was reduced to Ce^{3+} by those two ligands. As a dominant REE (36.27% out of TREE content) in the Underclay sample, Ce recovery has a stronger influence on the leaching efficiency of TREE than other REEs. As such, the TREE recovery is more dependent on Ce recovery relative to the recoveries of other REEs. The HREE recoveries of ASA and SSA were very close to those of 1 M HCl, indicating that the extraction of HREEs have reached a plateau that almost all the leachable HREEs were recovered. The rest of HREEs should exist as more hard-to-leach species and more aggressive conditions are required to convert them into easy-to-leach species.

The ratio of HREE/LREE as a function of leaching time for each reagent is shown in Figure 248. Other than 1 M HCl, an increase of the ratio at the beginning followed by a level-off trend was found for other reagents. At the end of the leaching tests, the ratios of ASA, SSA, and EDTA were lower than that AS but higher than that of 1 M HCl. It suggested that the leachability of LREEs was enhanced to a greater extent than that of HREEs by combining AS with organic ligands. For AF, the very slight increasing trend was observed during the whole leaching process compared with its counterparts.

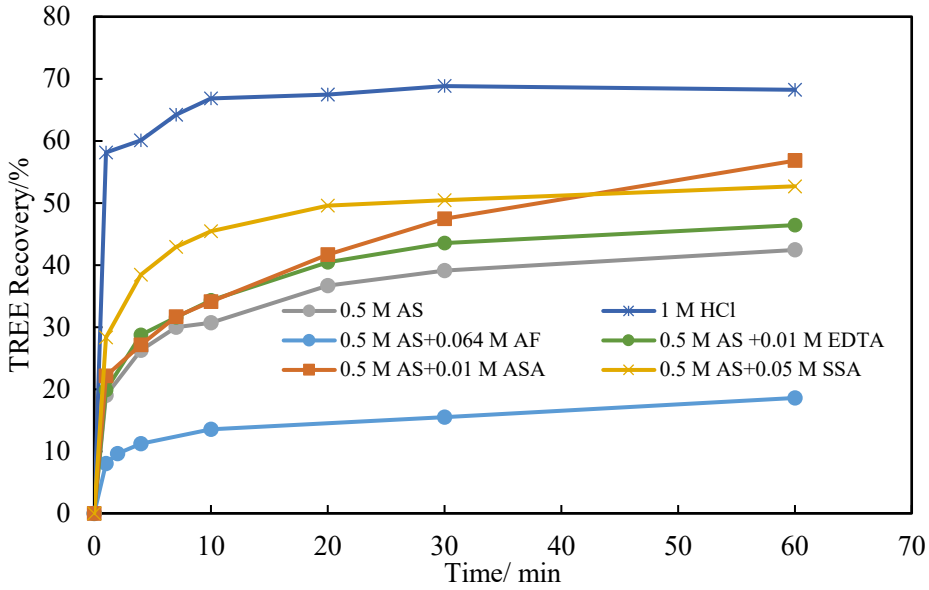

Figure 246. Leaching behaviors of TREE from the NaOH-treated underclay samples by different lixiviants.

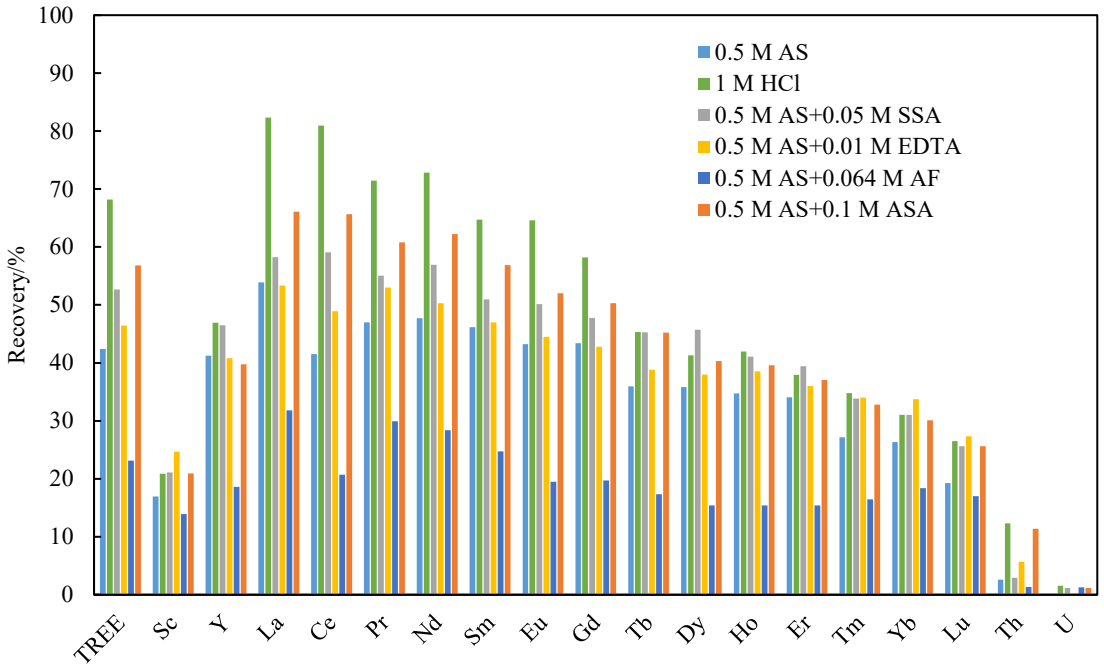

Figure 247. Leaching results of individual REE recoveries from the NaOH-treated underclay samples after treated by 30% NaOH at 80 °C for 24 h

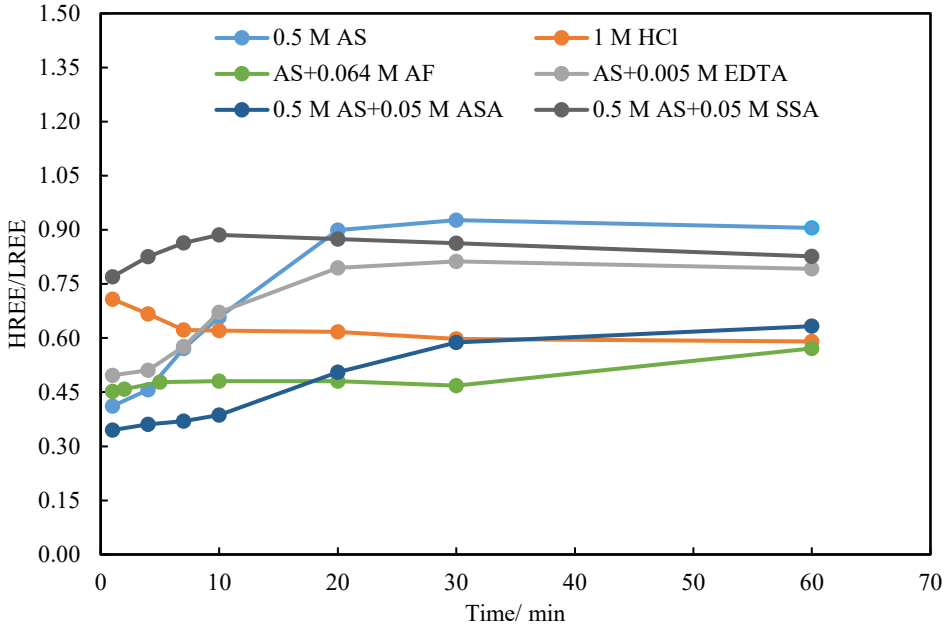

Figure 248. HREE/LREE ratios in the leachates of different lixiviants from the NaOH-treated underclay samples as a function of time.

The leaching behaviors of Al and Fe were presented in Figure 249 and Figure 250. Similar with the conclusions obtained in the previous section, the leaching tests in the presence of organic ligands normally had higher Al recovery than those of AS and HCl leaching, which is likely due to the fact that Al^{3+} ions can also form complex with those ligands. The highest aluminum recovery was achieved by AF (45%), and ~10% less aluminum was recovered by EDTA, ASA, and SSA. As for the Fe recovery, ASA (38.77%), SSA (21.09%), and EDTA (13.60%) had relatively higher values than AS and AF, but lower than that of HCl leaching (47.76%). The addition of AF had the 2 times lower ratios of TREE/(Al + Si + Fe) at both concentration levels than other combinations, suggesting that the mixture has no selectivity for REEs. The ratios of TREE/(Al + Si + Fe) for other combinations (except SSA at 0.01 M) were close to each other, ranging from 0.001986 to 0.002166, which were in a similar level with the ratios of using ammonium sulfate and ammonium formate only as lixiviants.

The SEM analyses in previous section identified the existence of iron in pyrite (Fe(II)) and iron associated with clays and quartz. XPS (Figure 251) analyses of different Underclay samples indicated that iron (III) oxide, i.e., Fe (III) is the dominant species on the surfaces of each sample. The ferric iron in coal-based materials and clays includes goethite and hematite etc., (Zhou et al., 2014; García et al., 2016). In the Underclay sample, the Fe(III) is more likely to be goethite due to no magnetic iron was removed by a magnetic separation test. García et al found that goethite is more abundant than hematite in the clay tractions of a soil chronosequence in South Spain. The goethite on the clay surfaces, consisting of original goethite and goethite formed during NaOH pretreatment and leaching stage, was dissolved by those assisting ligands (reduced and/or complexed). Without the removal of those goethite, the leaching of REEs can be passivated since the contact of REEs and lixiviant molecules is inhibited (Lin et al., 2021). The presence of the reducing and complexing ligands enhanced the extraction of those Fe compounds and REEs (CeO_2), leading to relatively higher Fe and TREE recovery than that of only using AS.

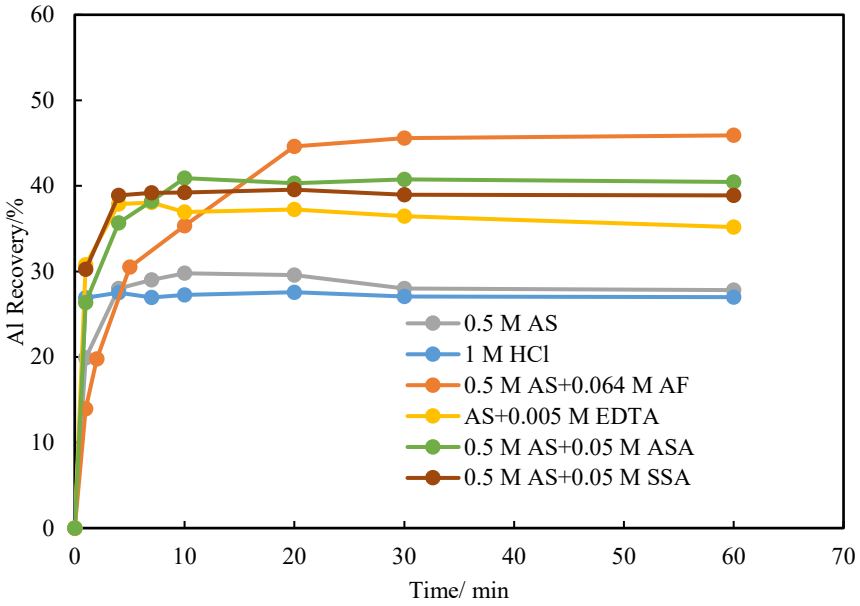

Figure 249. Leaching behaviors of Al in the leachates of different lixiviants from the NaOH-treated underclay samples by different lixiviants.

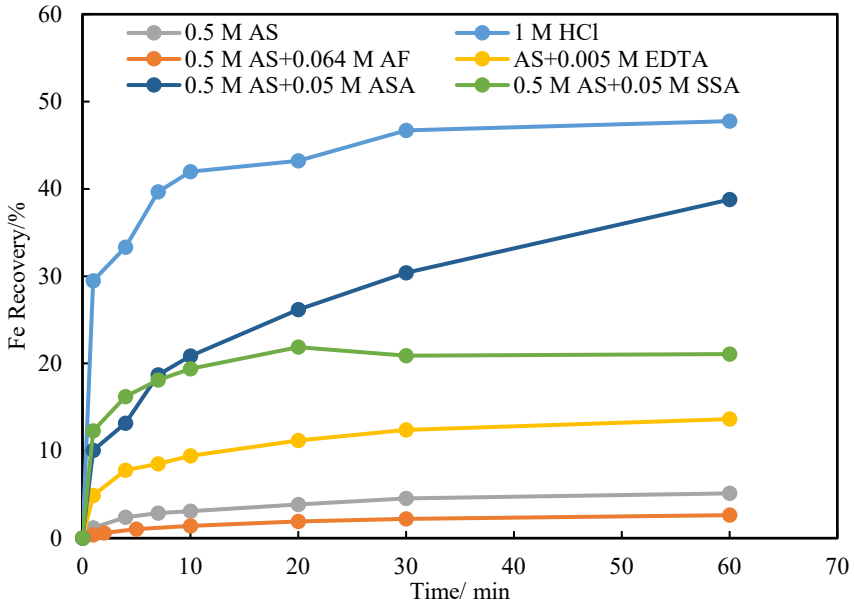

Figure 250. Leaching behaviors of Fe in the leachates of different lixiviants from the NaOH-treated underclay samples by different lixiviants.

In order to investigate the significance of the correlation between REY and major elements (Al, Si, Fe, Mn), as well as the correlation between impure elements (Al-Si and Fe-Mn), the TREE recovery versus major-element recovery (Figure 253 and Figure 252), Al versus Si (Figure 254), and Fe versus Mn (Figure 255), were plotted for each leaching test. Also, the Pearson correlation analyses were performed to quantify the corrections. The positive and negative correlation can be determined based on the Pearson correlation

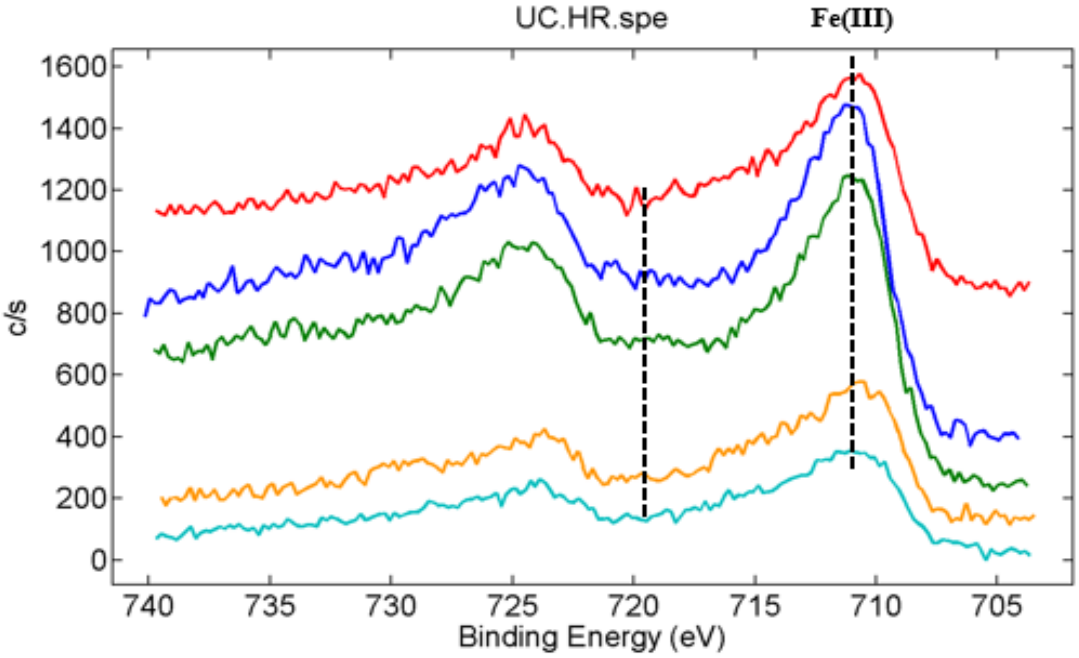

Figure 251. XPS spectra of different samples, the spectra from the top to the bottom are: feed Underclay sample (red line); NaOH-treated Underclay sample (dark-blue line); leaching residue of AS (green line); leaching residue of HCl (orange line); and leaching residue of 0.5 M AS +0.1 M ASA) (light-blue line).

coefficient. As is shown (Table 57), higher degree of linearity was found on TREE versus Fe recovery, compared with that of TREE versus Al. This may demonstrate that a proportion of REEs associated with Fe. However, another possibility is that iron-bearing species in the sample may only contain minor amount of REEs (less than 15%), the reducing and chelating agents added reduced and/or complexed both REEs and those iron-bearing species, leading to a similar leaching characteristic of REEs and iron.

As can be seen from Figure 254, all the data points of Al and Si recovery can be well described by a linear trend, indicating that these two elements have a similar association, which were mainly resulted from clay and/or other aluminosilicate minerals. Since more than half of the Si (56.13%) was partitioned into the used-NaOH solution, higher Al recovery was observed in the leachates, which is why the slope of the regression line of Al versus Si is less than 1 (~0.56). Linear trends were also found for the Fe and Mn recovery, but the slope of each trend line varied from lixiviant to lixiviant, indicating diverse associations of Fe and Mn. The five-step sequential extraction tests of the Underclay sample indicated various modes of occurrence of REEs and impure elements (see Figure 256). Around 60% of Fe existed as metal oxide (33.83%) and acid-soluble (24.96%) forms, while 27% of Mn associated with carbonates and then followed by Mn in metal oxide (11.80%) and acid-soluble (21.53%) forms. As is presented in Figure 255, 1 M HCl and ASA achieved relatively high Fe and Mn recovery due to the acidity of HCl and reducibility of ASA respectively. for other lixiviants, less than 23% of Fe and 30% Mn were extracted, which may mainly result from Fe and Mn in easy-to-leach forms (e.g., Fe in metal oxides and Mn in carbonates). The above linear analyses of TREE recovery and recoveries of impure elements revealed the complexity of the Underclay sample in terms of REEs and impure elements.

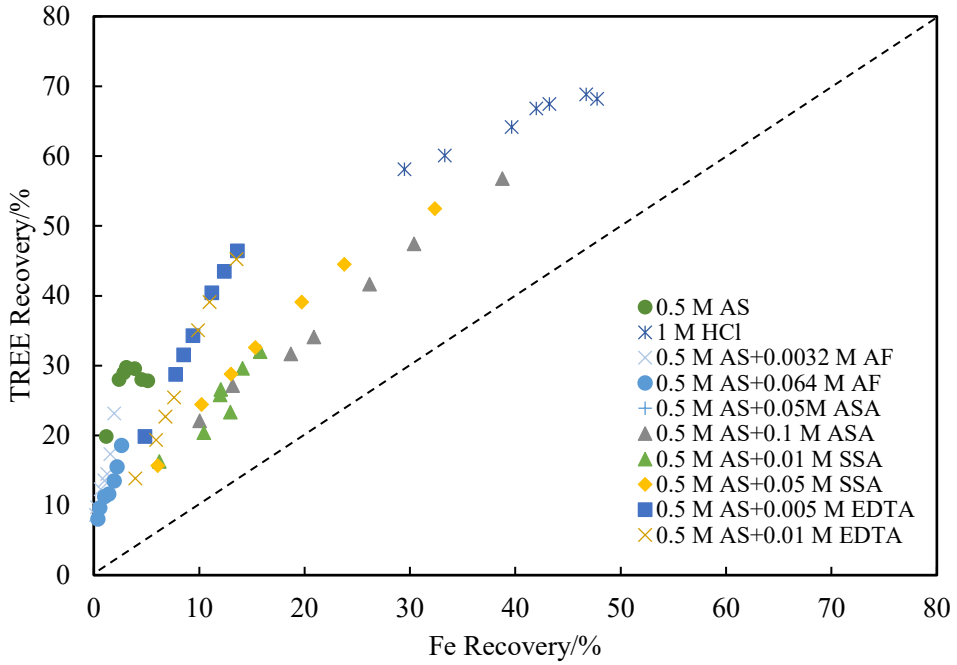

Figure 252. The correlation between TREE recovery vs. Fe recovery in the leachates of different lixiviants.

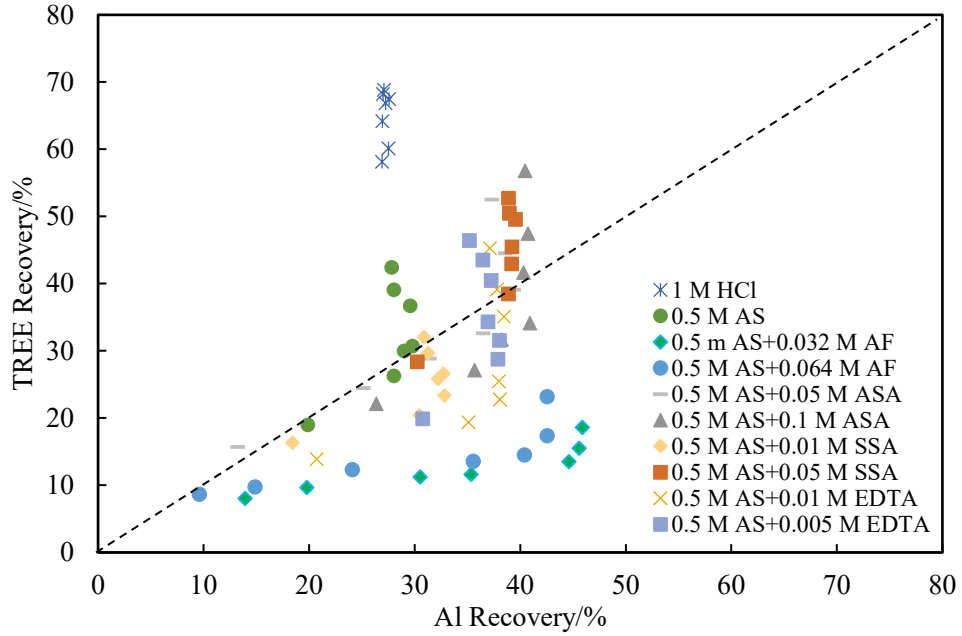

Figure 253. The correlation between TREE recovery vs. Al recovery in the leachates of different lixiviants.

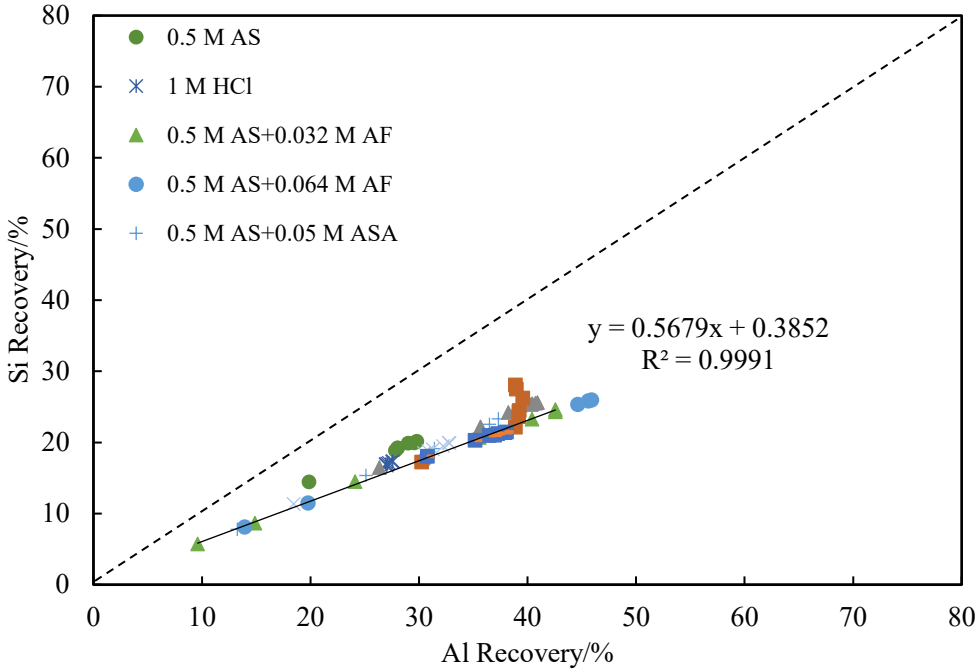

Figure 254. The correlation between Al recovery vs. Si recovery in the leachates of different lixiviants.

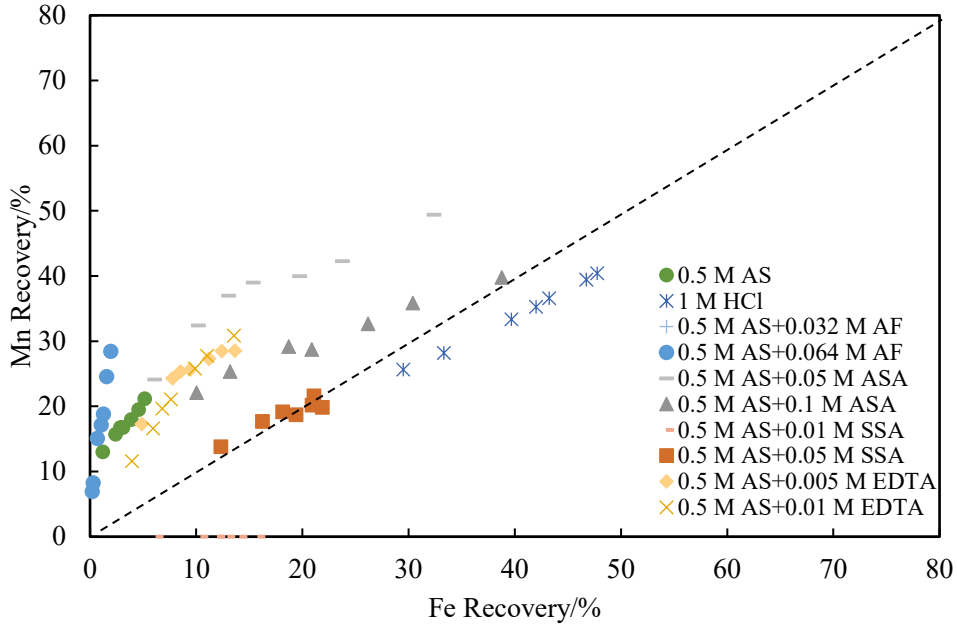

Figure 255. The correlation between Fe recovery vs. Mn recovery in the leachates of different lixiviants.

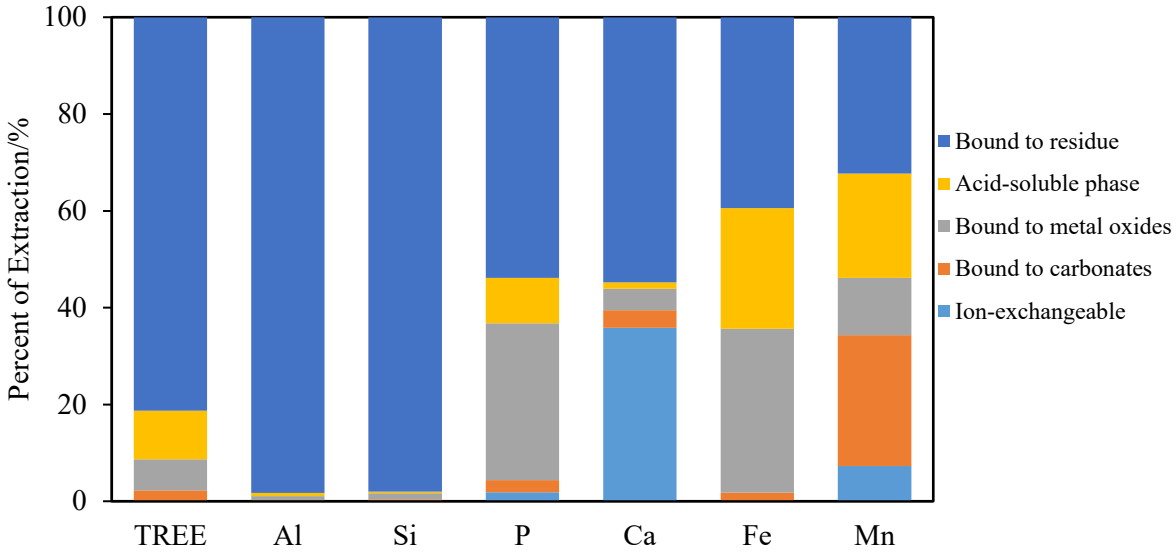

Figure 256. Sequential results of TREE and impure elements from the Underclay sample.

Table 57. Pearson's correlation coefficient between the fraction of REEs and major elements.

Lixiviant	Concentration/M	Al	Si	Fe	Mn	Al-Si	Fe-Mn
HCl	1.0	0.07	-0.08	0.98	0.98	0.94	1.00
AS	0.5	0.65	0.62	1.00	0.99	1.00	0.99
SSA	0.01	0.68	0.68	0.94	--	1.00	--
	0.05	0.82	1.00	0.98	0.98	0.82	0.94
ASA	0.05	0.86	0.87	0.99	0.97	1.00	0.95
	0.10	0.72	0.72	1.00	0.99	1.00	0.99
EDTA	0.005	0.43	0.50	1.00	0.94	1.00	0.93
	0.010	0.62	0.63	1.00	0.99	1.00	0.99
AF	0.032	0.85	0.85	0.97	0.97	1.00	0.99
	0.064	0.90	0.90	0.98	--	1.00	--

Mode of Occurrence Studies

Introduction

The modes of occurrence of REEs in coal samples are generally classified into five phases: water soluble, ion-exchangeable, carbonates, organic matter, and aluminum-silicates (Dai *et al.*, 2012). The standard chemical sequential extraction test is used to determine the fraction of each phase; however, for coal-based clays of bituminous origin, the fractions of REEs in the water-soluble phase and the organic matter phase are very minor or even negligible in most cases. As a result, the REEs in metal oxide and acid-soluble forms are normally used to replace the REE forms in water soluble and organic matter in the chemical sequential extraction procedure (Zhang *et al.*, 2019). REEs in carbonates and oxides are readily leachable, whereas REEs associated with aluminosilicates and phosphates are hard-to-leach (Yang *et al.*, 2020). As previously mentioned, the majority of REEs in coal-based clays is in the insoluble form such as aluminosilicate and rare earth phosphates, REE extraction from these two forms normally requires the dissolution of the dominant host minerals. Accordingly, REEs in coal-based clays can also be simply categorized into two parts: *i.e.,* readily leachable and hard-to-leach REEs. The former refers to the REEs that can be extracted with only minor or negligible damage of the crystal structures of the dominant minerals, while the latter requires more aggressive conditions that often dissolve major fractions of the host rock. In this study, the leaching behaviors of REEs and impure elements were compared and disused, in an attempt to understand the associations of REEs.

Experimental

Sample preparation and reagents

A coal underclay sample from central Pennsylvania was used for all the leaching tests involving NaOH pretreatment in this study. For direct leaching tests, the underclay sample as well as several other coal-based clay samples were selected to investigate the dependence of the fraction of readily leachable REEs on sample. In an attempt to isolate mineral matter from the as-received samples, the hydrophobic - hydrophilic separation (HHS) process was performed to remove the coal in a step denoted as *decarbonization* (Gupta *et al.*, 2016). The as-received underclay sample was initially crushed by a mortar and pestle, followed by a further grinding to 5 micron by an attrition mill. The ground sample was dried in an oven at 60 ^{o}C overnight before being used as a feed for the leaching test. Regarding the Leer and WY sample, both from West Virginia, the coal was first removed by HHS without grinding. For the RB (from Pennsylvania), MCMDM, and MCMDU (both from Maryland) samples, they were ground in a ball mill for 2 h for better liberation of coal and inorganic mineral matter. The ground samples were subjected to HHS separation for decarbonization, the tailing products were collected and dried in an oven. The dry tailing products are the feed samples for leaching tests. The chemical used in this study were all in analytical grade. Deionized water was used for all the solution preparation.

Direct acid leaching tests

In this study, the quantification of the fraction of REEs in readily leachable form was performed by direct HCl leaching without chemical or thermal pretreatment. The acid leaching tests were conducted by using 1 and 6 M HCl at room temperature for 1h and 18 h respectively. Several studies have examined the leachability of coal and coal refuse by conducting direct acid leaching tests at pH 0, which is equivalent to 1 M HCl (Honaker *et al.,* 2017; Yang *et al.,* 2019; Laudal *et al.,* 2018). As a commonly used method, the aim of 1 M HCl leaching for 1 h is to initially measure the amount of easy-to-leach REEs. However, 1 M HCl may not be sufficient for the recovery of all the REEs in readily leachable forms. As such, a longer contact time (18 h) and higher acid concentration (6 M HCl) were selected. With such a long leaching time, the leaching equilibrium is able to be reached. It is, therefore, reasonable to assume that the easy-to-leach REEs can be fully extracted by such a long contact time and high acid concentration.

Several coal-based clay samples were leached by 6 M HCl at room temperature for 18 h. In each test, 0.5 g sample was mixed with 20 ml HCl solution. To determine leaching kinetics, 0.3 ml leaching solution samples were taken at specific time intervals (0.167 , 0.5, 1, 3, 5, 7, 18 h, etc.) during each leaching

experiment. 1 ml disposable syringes were used to take liquid samples, and then transferred the solution samples into 1.5 ml centrifuge tubes. The tubes with liquid samples were immediately centrifuged at 3000 rpm for 5 min. The supernatant in each tube was diluted 50 times by an acidic solution (2.5% HNO_3 and 0.5% HCl) before it was subjected to Inductively Coupled Plasma Mass Spectrometry (ICP-MS) analysis. The extraction recovery was calculated based on:

$$Recovery\ (\%) = 100 \times \frac{c_l \cdot v}{c_f \cdot m} \quad [5.3.8]$$

where c_l and c_f is the REE assays of leaching liquor and feed sample respectively, m is the feed mass, v is the volume of the leaching liquor.

Ammonium sulfate and 1 M HCl leaching after NaOH pretreatment

The procedure for ammonium sulfate and 1 M HCl leaching was similar to the one used for NaOH-treated monazite at room temperature. No pH adjustment was required for the 1 M HCl leaching tests. Unlike the leaching of NaOH-treated monazite samples, the leaching time was set as 1 h, and thus different time intervals (*i.e.,* 1, 4, 7, 10, 20, 30, 60 min) were used for ammonium sulfate and 1 M HCl leaching here. After leaching, the same procedure as described in section 2.2.1 was used to prepare samples for ICP-MS analysis and recovery calculations.

Results and Discussion

Leaching behaviors of REEs and impure elements (Fe Mn) by 1 M and 6 M HCl

The leaching behaviors of TREE and impure elements of the 1 and 6 M HCl leaching are plotted in Figure 257 and Figure 258 respectively, As shown, only 10.10% TREE recovery was obtained by the 1 M HCl leaching. Even by using 6 M HCl and extending contact time to 18 h, the TREE recovery was slightly climbed to 13.91%. These results indicated that the majority (> 80%) of REEs in the Underclay sample exists in the difficult-to-leach phase. These low recovery values are consistent with the results of

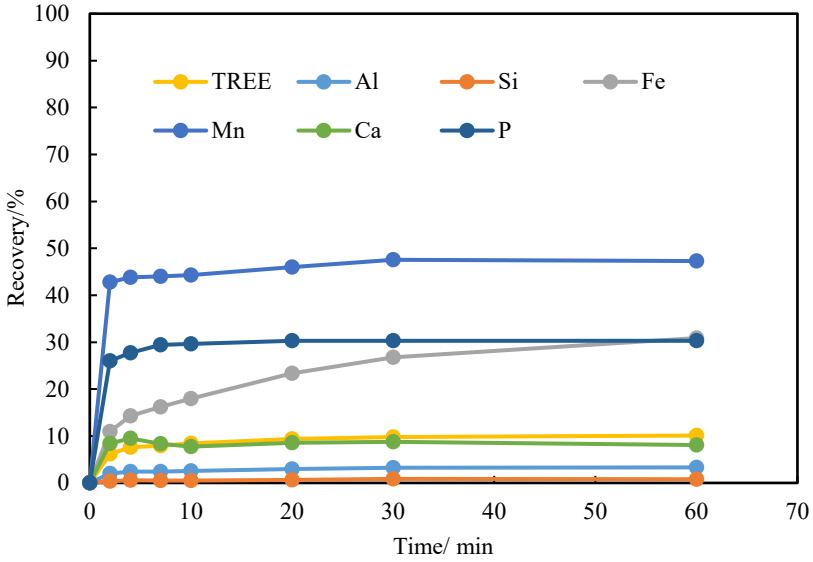

Figure 257. Leaching results of TREE and impure elements by 1 M HCl, condition: 0.5 g/20 ml, room temperature, 1 h.

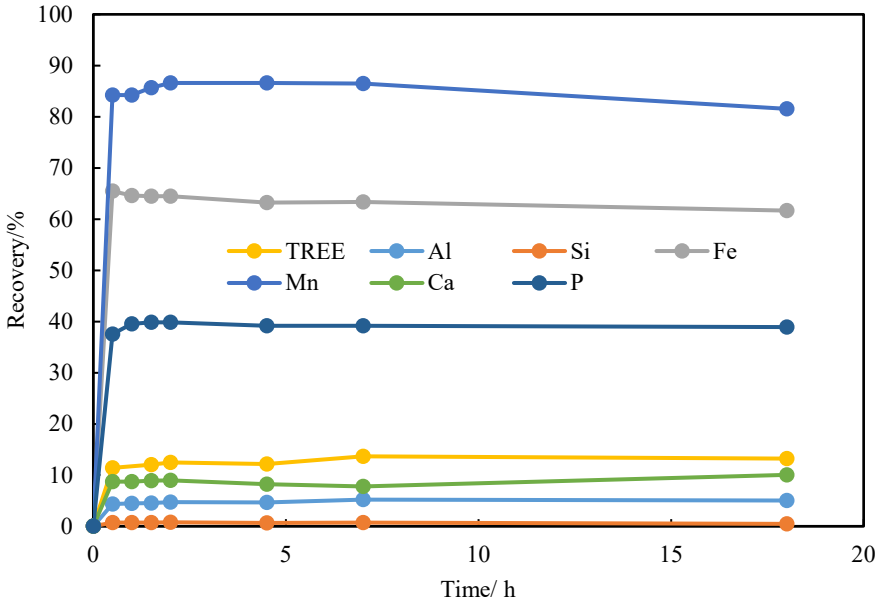

Figure 258. Leaching results of TREE and impure elements by 6 M HCl, condition: 0.5 g/20 ml, room temperature, 18 h.

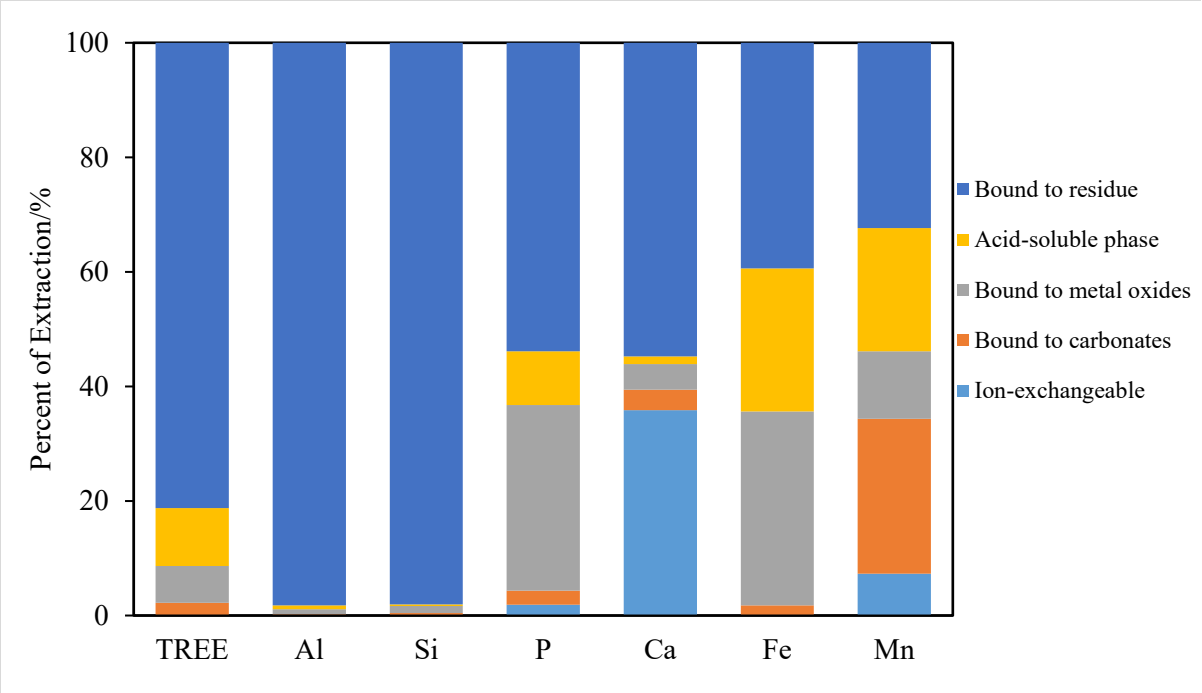

Figure 259. Sequential results of TREE and impure elements from the Underclay sample.

the chemical sequential extraction test performed on the same sample (Figure 259), which indicated that ~81.26% of REEs are associated with insoluble and residual matters (*e.g.,* monazite, aluminosilicates, etc.).

The individual REE recoveries of both acid leaching tests were analyzed and compared (see Figure 260). The similar REY patterns suggest that similar REE-bearing phases were extracted by the 1 and 6 M HCl leaching. Both distributions show that the REE recovery peaked at gadolinium (Gd), and the recoveries for REEs (except Y) on both sides of Gd gradually decreased, exhibiting typical MREE-enriched REY patterns. This MREE-enriched REY pattern is further confirmed by the Upper Continental Crust (UCC)-normalized REE distributions (see Figure 261) (Taylor *et al.,* 1985), though an Eu negative anomaly was noticed in the REY pattern of 1 M HCl leaching. The MREE-enriched pattern represents the distribution characteristics of the readily leachable REEs in the Underclay sample.

In geochemistry, MREE-enriched patterns have been found in acidic terrestrial waters, such as acid mine drainage precipitates (Wang *et al.,* 2021), acidic lakes, and their clastic sedimentary rocks (Johannesson *et al.*, 1999). According to Johannesson *et al.,* (1999), the formation of the MREE-enriched signatures in acidic aqueous can be ascribed to the dissolution of Fe-Mn oxides/oxyhydroxides mineral/amorphous phase, including Fe-Mn oxide/oxyhydroxide cements, coating on sedimentary rock grains, and/or possibly Fe oxides (hematite) that enriched MREEs. Since clay minerals are typical sedimentary rocks, the Fe-Mn oxides/oxyhydroxides species may also exist in the Underclay sample and possibly in a manner of coating on the surface of clays. The SEM and XPS analysis in the last report found the Fe (III)-bearing clay particles, which maybe Fe(O, OH) and or Fe_2O_3. However, the direct observation of Fe-Mn species is difficult due to the very low Mn content.

As can be seen in Figure 257 and Figure 258, relatively high Fe and Mn recovery values were observed for both leaching tests. Regarding to the 1 M HCl leaching, when the TREE recovery increased from 0 to 8.41% at 10 min, the recovery of Fe increased from 0 to 17.97%. After 10 min, only a slight improvement for the TREE recovery (from 8.41 to 10.10%) was found, while the recovery of Fe (from 17.97 to 30.87%) nearly doubled. This indicated that the Fe extracted in the later stage didn't contribute

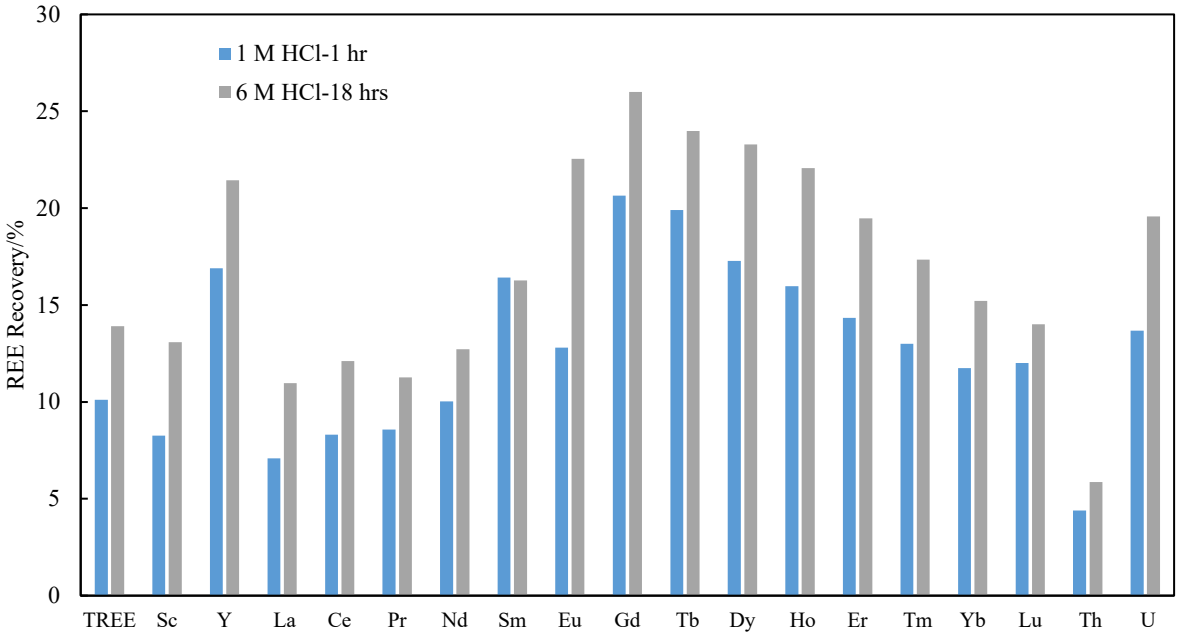

Figure 260. Individual REE distributions of the Underclay sample leached by 1 M and 6 M HCl.

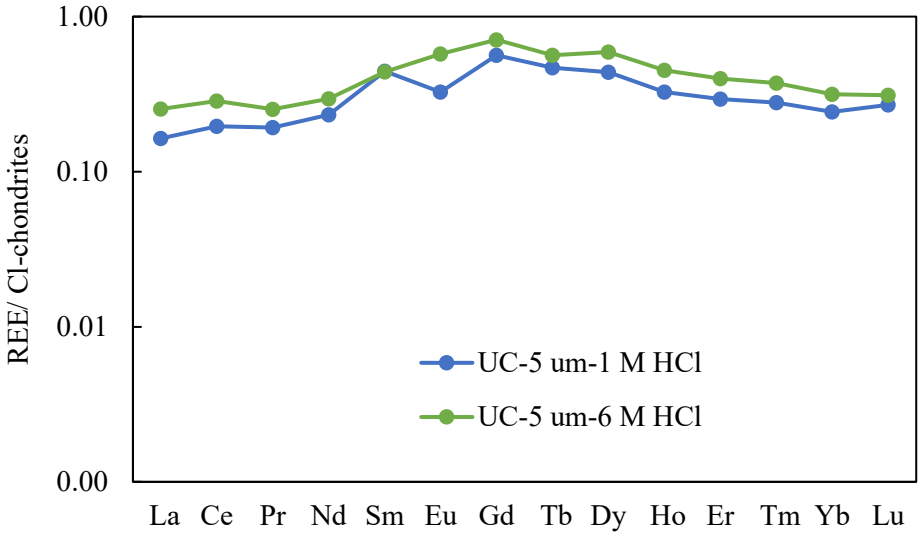

Figure 261. UCC-normalized REE distribution of the REEs extracted by 1 and 6 M HCl from the Underclay sample.

much to the TREE recovery. The leaching curve of Mn reached equilibrium rapidly in the first 10 min and remained stable thereafter, revealing the majority of Mn exists in an acid-soluble form.

In the sequential extraction test, the fractions of REEs bound to ion-exchangeable, carbonates, metal oxides, and acid soluble phase were 0.10, 2.13, 6.43, and 10.08% respectively, while the corresponding recovery values of Fe were 0.10, 1.70, 33.83, and 24.96% respectively (Figure 259). As can be seen, the amounts of REEs in ion-exchangeable and carbonate forms are negligible in this sample. This result is consistent with the relatively small fractions of those two forms found in the Fire clay coal samples

(less than 2%) (Zhang *et al.,* 2019). Also, relatively low fractions (0.3-7.5%) of ion-exchangeable REEs were extracted from four Underclay samples from Appalachian coal seams (Montross *et al.,* 2020).

On the other hand, it can be seen that the extraction of REEs in ion exchangeable and carbonate forms only resulted in minor dissolution of Fe-bearing spices. More Fe-bearing species is released in the third and fourth step of the sequential extraction test. The Eh-pH diagrams of Fe_2O_3 (Figure 262) indicate that iron exists in its soluble species (Fe^{3+}/Fe^{2+} ion) when the pH is less than 1.0. The domain of soluble iron species of Fe(O, OH), created by Langmuir *et al. (2004)* (in Figure 263), is similar with that of Fe_2O_3. It is, therefore, reasonable to derive that the Fe_2O_3 and Fe(O, OH) in the Underclay sample should be dissolved during the 1 M and 6 M HCl leaching, and the REEs bound to Fe-Mn oxy/hydroxides is also released. Moreover, 47.27% of Mn was extracted in the first three steps, with more Mn was released from the

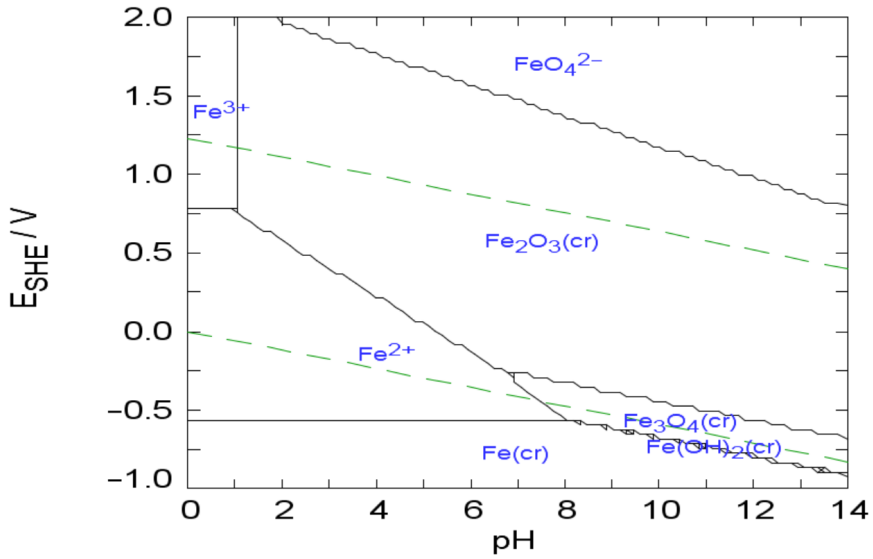

Figure 262. Eh-pH diagram of the Fe^{3+}-H_2O system at 25 °C created by Medusa software (Puigdomenech, 2013), [Fe^{3+}] = 0.001 M.

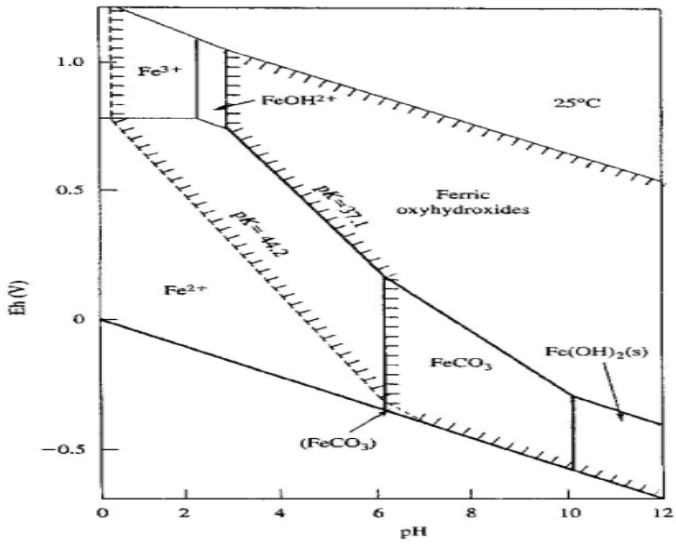

Figure 263. Eh-pH diagram of the Fe-O_2-CO_2-H_2O system at 25 °C constructed by Langmuir et al. (2004). Total dissolved combinate and iron equal 10^{-3} mol/Kg.

carbonate form compared with that of Fe. The co-extraction of Fe-Mn indicate these two elements have similar leaching behaviors.

At the same time, the 10.10% of TREE obtained by the 1 M HCl leaching should be dominantly resulted from the carbonates and metal oxides, and a small fraction of (1.54%) of REEs from the acid-soluble phase. This finding is consistent with the results reported by Montross *et al.* (2020). In the study, four underclay samples from Central Appalachian coal seams were sequentially leached by $(NH_4)_2SO_4$, HCl, H_2SO_4 respectively, which correspondingly aimed to recover REEs bound to exchangeable, colloid, and colloid + mineral forms. $LiBO_2$ digestion tests were performed to quantify the fractions of REEs in mineral and residual form. The fractions of HCl-extractable REEs ranged from 10.1 to 31.1%, the occurrences of those REEs were ascribed to the REEs associated with clays (on the surface), carbonates and Fe-oxides (*i.e.,* colloidal). As such, it is the dissolution of REEs associated with carbonates, metal oxides, and a proportion of REEs in acid-soluble form in the Underclay sample that contributed to the formation of the MREE-enriched pattern.

In the 6 M HCl leaching, the TREE recovery only raised from 0 to 11.38% in the first 30 min, after which, it only increased from 11.38 to 13.22% (Figure 258). This recovery value was higher than the TREE recovery obtained in the first-three step of sequential extraction. Similar with the 1 M HCl leaching, a part of the REEs in acid-soluble form was extracted and contribute to this increment of the TREE recovery. The rest of the un-leached REEs supposed to be bound to acid-soluble and mineral/residue forms. When the HCl concentration changed from 1 to 6 M, the recovery of Fe jumped from 30.87 to 65.47%, which was higher than the total fraction (58.2%) of Fe in the first-four step of the sequential extraction. However, such significant dissolution of Fe only led to an increment of the TREE recovery by 3 absolute percentage points It suggested that other Fe-bearing species was dissolved by the 6 M HCl. Since another important iron-bearing mineral in the Underclay sample is pyrite, which was confirmed by SEM-EDS analysis. Hence, the additional 35% of Fe extracted is highly likely resulted from the dissolution of pyrite by HCl (as shown in eq. 5.3.9).

$$FeS_2 + 2HCl = FeCl_2 + H_2S\uparrow + S\downarrow \qquad [5.3.9]$$

Around 85% of Mn was transferred to the leachate of 6 M HCl, it revealed that most of the Mn-bearing species were dissolved, and thus the REEs associated with Fe-Mn species have been extracted.

Leaching behaviors of other impure elements (Si, Al, Ca, and P) by 1 M and 6 M HCl

The leaching behaviors of other impure elements of the 1 and 6 M HCl leaching were also analyzed and compared. Because the predominant components of the feed sample are aluminosilicates (mainly clays and quartz), the fractions of the Al and Si dissolved during leaching process indicate the degree of decomposition of the feed sample. As can be seen, only small amounts (< 0.8%) of Si were extracted in both cases, revealing that the dissolution of quartz and clay matrix by HCl solutions was negligible. The surface morphology of the leaching residue of 6 M HCl leaching was characterized by a SEM analysis (see Figure 264). The SEM images demonstrate only small irregularly-shaped ultrafine particles (floccule) disappeared (probably being dissolved during the leaching process). Other than that, no visible corrosion can be observed on the leached residue, which agrees with the low dissolution rate of Si.

Alternatively, relatively higher Al recoveries (3.31 and 5.05% by 1 and 6 M HCl respectively) demonstrated the Al in other associations were dissolved. This result is due to the various modes of occurrence of Al in clays such as soluble, exchangeable, iron oxide combined Al, etc. (Chi and Tian, 2008). It has been reported that there is a proportion of Fe was substituted by Al in Fe-Mn oxyhydroxide (Gasparatos *et al.*, 2013) and iron oxides (Fontes et L., 1992). As mentioned previously, the Underclay sample has clay particles that associated with iron. Considering the high dissolution rate of Fe, it can be concluded that a proportion of the HCl-leachable Al was dissolved with the dissolution of Fe-Mn oxyhydroxide and/or iron oxides. Xiao *et al*. (2017) performed reductive leaching on the ion-adsorption clays from South China, it was found that more Al was released with the increase of acidity, which was

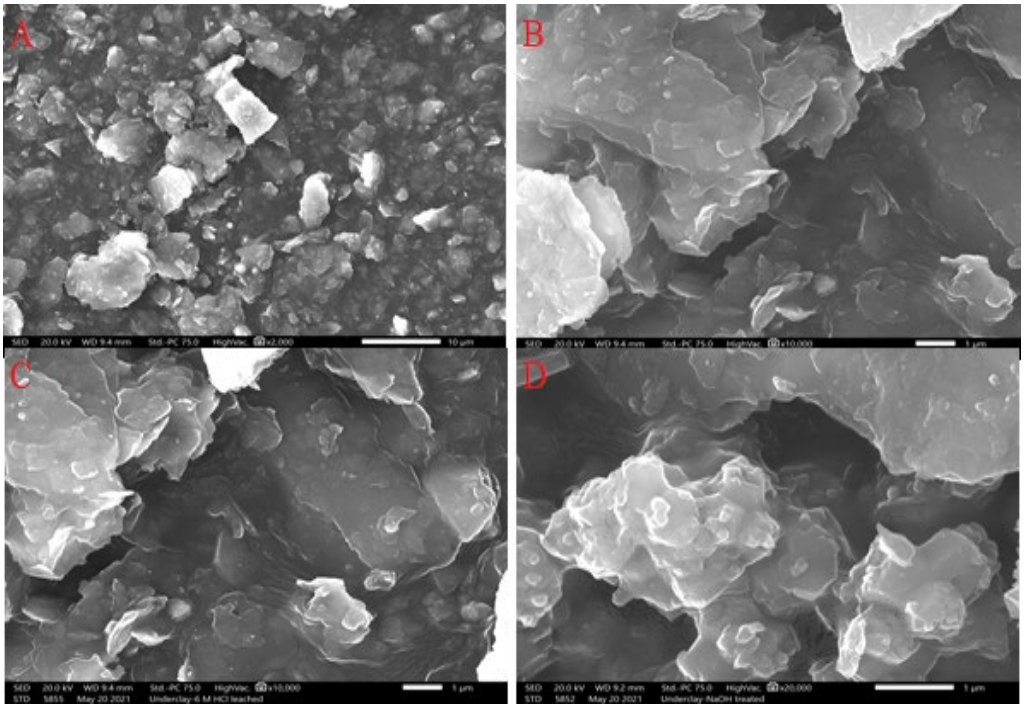

Figure 264. SEM images of the underclay sample leached by 6 M HCl at different magnification (6 M HCl, 0.5 g/20 ml, 18 h, d_{80} = 5.0 um): A: × 2k; B: ×10 k; C: ×10 k; D: ×20 k.

ascribed to the dissolution of the hydroxy-aluminum phase. As such, it is reasonable to attribute the majority of the dissolved Al to Al in other occurrences rather than the clay matrix.

For Ca and P, as is shown, the dissolution of Ca increased from 8.08 to 10.04% as the acid concentration varied from 1 to 6 M. At the same time, the recovery of P increased from 30.29 to 38.91%, suggesting that Ca and P have similar responses to the variation of acid concentration. The low Ca recoveries demonstrated that the majority of Ca-bearing species in this sample is not in acid-soluble carbonates (*e.g.,* calcite and dolomite, etc.) (Zhang *et al.*, 2019). It has been reported that the majority of P in coal-based clays is associated with phosphorus minerals (*e.g.,* rare earth phosphates, crandallite group minerals, and apatite) (Finkelman *et al.*, 2018). However, it is difficult to dissolve rare earth phosphate minerals such as monazite and xenotime by acid leaching at room temperatures, they are slightly dissolved in warm concentrate HCl (Sinkankus 1972). In this study, A Ce-typed monazite sample was also subjected to the 6 M HCl leaching under the same conditions with the Underclay being leached, the result shows that only 5% of REEs were dissolved, suggesting that only a minor amount of monazite was dissolved. Since the recoveries of LREEs were around 10% by the 6 M HCl leaching, the HCl-extractable REEs did not resulted from the dissolution of rare earth phosphates in the Underclay sample.

As such, the similar leaching behaviors of Ca and P may indicate the presence of apatite and crandallite group minerals in this sample. Those two minerals were also found to contain REEs. The associations of REEs with those two types of minerals were identified in coal samples from West Kentucky (Bin *et al.*, 2022). To verify this assumption, SEM/EDS analysis was conducted on the ashed-Underclay sample (Figure 265). A fluorapatite particle that associated with clays (probably be apatite) was identified, however, no REEs was detected by SEM-EDS in it. Also, a Ca-P enriched particle with no REEs was found, which may be a crandallite or hydroxyapatite particle. These results indicate that the dissolved Ca and P is more likely to be attributed to the dissolution of apatite and/or crandallite group minerals, but it is not sure whether there are REEs in those two minerals and contribute to the formation of the MREE-enriched

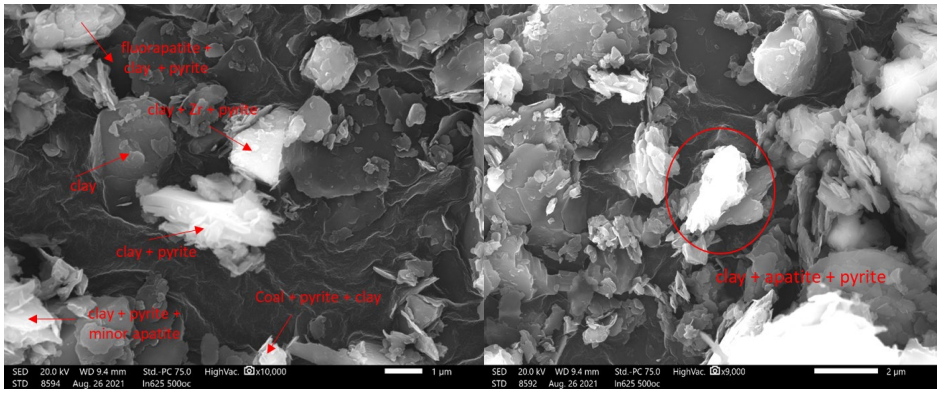

Figure 265. Back-scattered SEM images of apatite particles in the ashed Underclay sample, however, no REEs were detected by SEM-EDS.

pattern. It might be the case that the REE content in the apatite is lower than the detection limit of SEM/EDS, or other REE-bearing apatite and crandallite particles were not found in the Underclay sample.

In apatite, its individual REE distribution also exhibits a MREE-enriched pattern (Johannesson *et al.*, 1999; Bingen *et al.*, 1996), as well as a negative Eu anomaly. It has been reported that the dissolution of three different apatite ores normally occurs in a pH range of 1.0 to 3.2 (Kim *et al.*, 2016). This pH range is higher than that of the HCl leaching in this study. A negative Eu anomaly was found in the REY pattern of the 1 M HCl leaching. An additional feature of REE-bearing apatite is its association with Th and U (Slobodnik *et al.*, 2020). Though monazite is also a Th and U-bearing mineral, as mentioned earlier, it is weakly soluble in concentrate HCl solution. Accordingly, the presence of Th and U in the leachates may result from other sources such as apatite in the Underclay sample. The above characteristics may indicate the existence of REE-bearing apatite in the sample.

According to the above data, only 13% of the TREE recovery was achieved even by 6 M HCl at room temperature. The results of a five-step sequential extraction indicated that those HCl-leachable REEs were primarily attributed to the readily leachable and a proportion of acid-soluble REEs. The REEs reported to the surface of clays should also be released by such a strong acid. Though such low TREE recovery led to negligible dissolution of clays and quartz, it caused relatively high dissolution rates of other impure elements, including 65 of Fe, 85% of Mn, 10.04% of Ca, and 38.91% of P. The dissolved Fe was ascribed to the dissolution of Fe-Mn oxides/oxyhydroxide and pyrite, the dissolved Ca and P can be explained by the existence and apatite ad crandallite. The REE-bearing Fe-Mn oxides/oxyhydroxide is more likely to be an outer layer coated on the surface of clays. More aggressive conditions (*e.g.,* higher temperature, stronger acid) are required to achieve TREE recoveries higher than 13%. However, those conditions would lead to the dissolution of monazite as well as clays, a similar conclusion has been drawn by Montross *et al.* (2020). Therefore, the 13% TREE recovery represents the maximum amount of REEs that can be extracted without the dissolution of clays in the Underclay sample.

Effect of particle size on the TREE recovery of the 6 M HCl.

In the last section, the modes of occurrence of acid-leachable REEs were initially determined by analyzing the leaching behaviors of impure elements as well as SEM analysis. However, the dependence of the partition of HCl-leachable REEs on the particle size in the Underclay sample is still unknown. As such, another two Underclay samples with different particle sizes (d_{80} =7, 10 μm respectively) were also leached by 6 M HCl for 18 h at room temperature. The TREE contents of those two new samples (415 and 410 ppm respectively) are close to each other, suggesting that nearly no enrichment of REEs in the finer size fractions. A similar observation was reported by Lin *et al.* (2017), the results indicated that REEs were uniformly distributed in the inorganic part of coal samples with various particle size fractions.

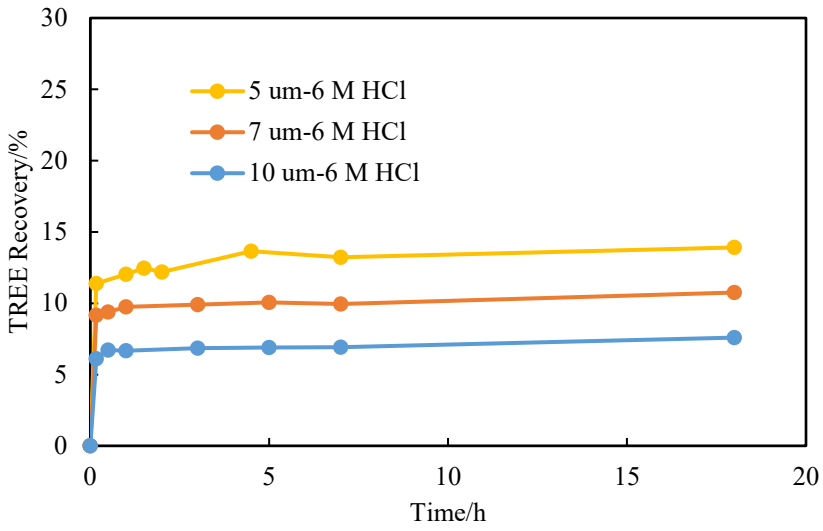

Figure 266. Effect of particle size on the leaching performance of 6 M HCl leaching on the Underclay samples with different particle size.

The TREE recovery of each size fraction as a function of leaching time is shown in Figure 266. With the reduction of particle size, the TREE recovery increased from 7.59 to 13.91%. Moreover, similar leaching curves of TREE were also observed for different size fractions, with the leaching equilibrium being reached in the first 30 min. The rapid leaching kinetics revealed that the leaching rate was a diffusion-controlled process, which is consistent with the fact that the 6 M HCl leaching is mainly aimed to extract REEs reported to the surface of clays. Additionally, the assessment of the elemental recovery reveals that a similar MREE-enriched pattern was found for each size fraction (Figure 267). The recovery of each REE gradually increased with the reduction of particle size, which was resulted from a better liberation of REE-

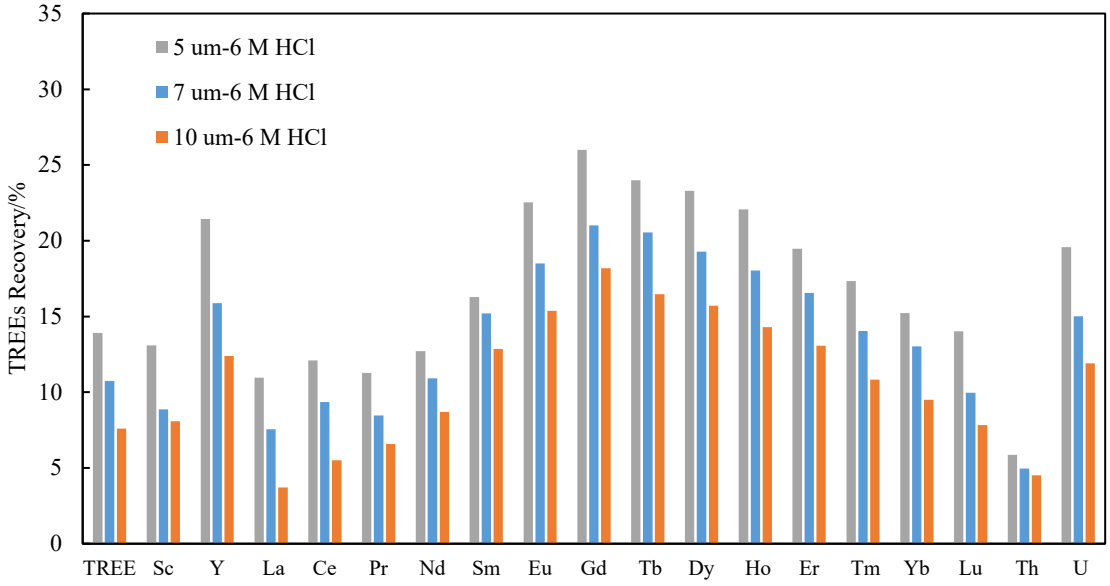

Figure 267. Effect of particle size on elemental recovery of 6 M HCl leaching on the Underclay samples with different particle size.

bearing species. With the reduction of particle size, the liberation of REE-bearing species was enhanced, and thus more specific surface area was created. In the meantime, REEs in nano-size and associated with oxides can be liberated during grinding, thereby leading to better leaching performance (Yang *et al.*, 2020). The above analysis demonstrated that size reduction is able to enhance the leachability of the HCl leachable REEs.

The correlations among TREE versus impure element recoveries and impure element versus impure element recoveries (*i.e.,* Al versus Si and Fe versus Mn) were also plotted and compared (see Figure 268). Due to the fast leaching kinetics, the recovery values of the TREE and impure elements reached their corresponding maximum values in a very short time relative to the whole leaching process. It is, therefore, unable to study their correlations as a function of time. Instead, the correlations were analyzed as a function of particle size. The recoveries of TREE and impure elements used here were the final values of each test. However, according to the findings in the previous section, only a small proportion of REEs was found to be bound to Fe-Mn oxide. Thus, it should be noticed that not all the dissolved Fe and Mn by the 6 M HCl led to the releasing of REEs into the leachates. As such, the regression analysis did here can help understand the relationship between the fraction of acid-soluble REEs versus the recoveries of the impure elements, as well as effect of particle size on the leaching behaviors of Fe and Mn in the Underclay sample.

As can be seen in Figure 268, the TREE recovery was positively proportional to those of Fe, Mn, and Al respectively. Among those three impure elements, the fractions of the dissolved Fe and Mn were much higher than that of Al for each size fraction. The increasing trends of TREE versus Fe, Mn, and Al indicate that the fractions of acid-leachable TREE, Fe, Mn, and Al increase as the particle size reduces. From a perspective of REE leaching, this observation indicated that extraction of readily leachable REEs by strong acid will bring much Fe and Mn to the leachates. Moreover, the slopes of the fitted lines of TREE versus those three impure elements were compared. The Al had a much larger slope than those of Fe and Mn, which suggests that the releasing of Al is more sensitive to particle size than Fe and Mn do during the 6 M HCl leaching. For the sample with d_{80} = 10 um, the recoveries of Fe and Mn were close to each other, whereas the discrepancies of their recoveries gradually became larger with the reduction of particle size. The

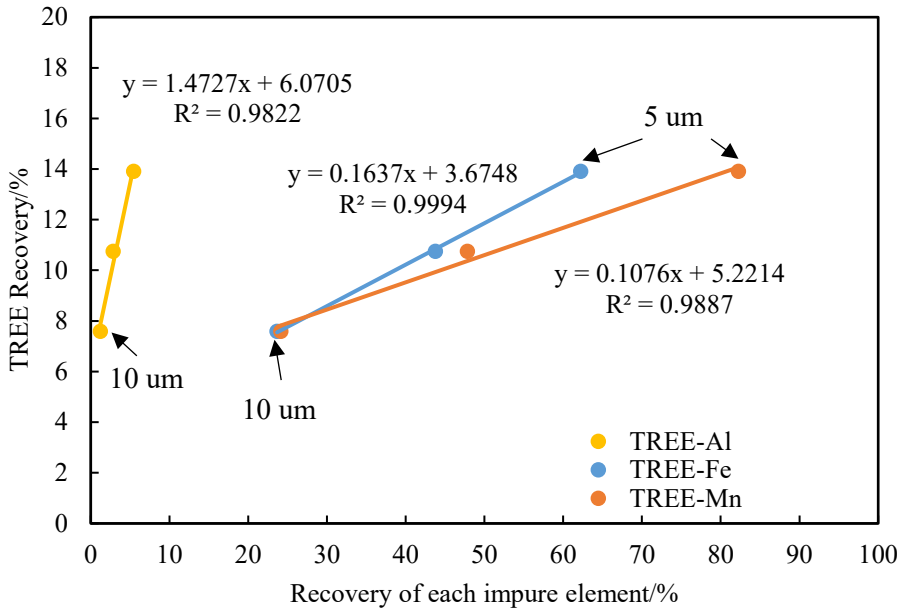

Figure 268. Correlation of TREE recovery versus Al, Fe, and Mn recovery in the leachates of 6 M HCl as a function of particle size.

smaller slope of TREE versus Mn indicated that TREE recovery is relatively more correlated to the releasing of Fe rather than Mn at a smaller size fraction.

The recovery of Si only ranged from 0.3 to 0.8%, while the Al recovery increased from 1.01 to 5.45% when the particle size (d_{80}) reduced from 10 to 5 μm (Figure 269). No specific correlation was found between Al and Si, which again confirmed the hypothesis that Si and Al were extracted from different sources. However, differing from Al versus Si, a pronounced linear correlation between Fe and Mn was noticed as a function of particle size (Figure 270). It revealed that the recoveries of Fe and Mn increased as the decreasing of particle size. However, as mentioned in last paragraph, this linear correlation between Fe

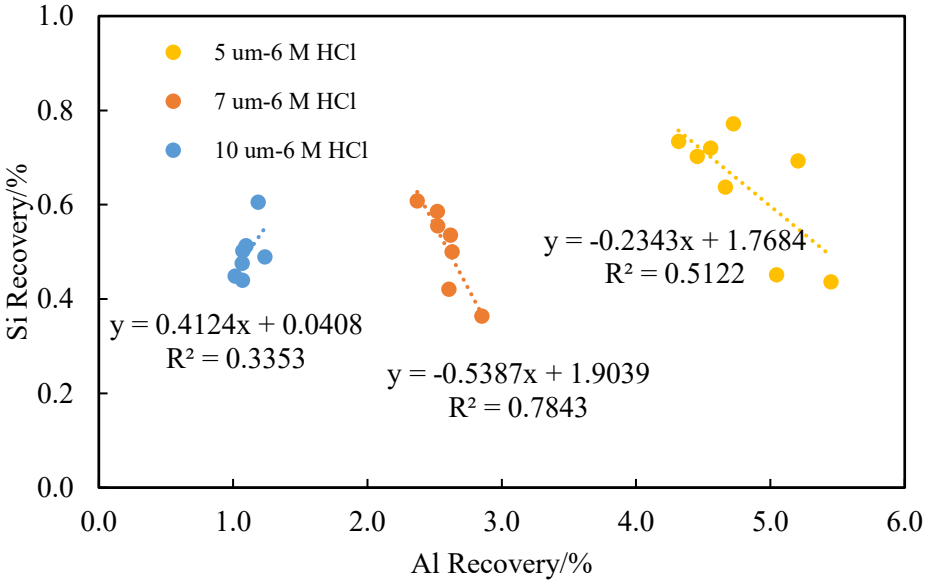

Figure 269. Correlation of Si versus Al recovery in the leachates of 6 M HCl as a function of particle size.

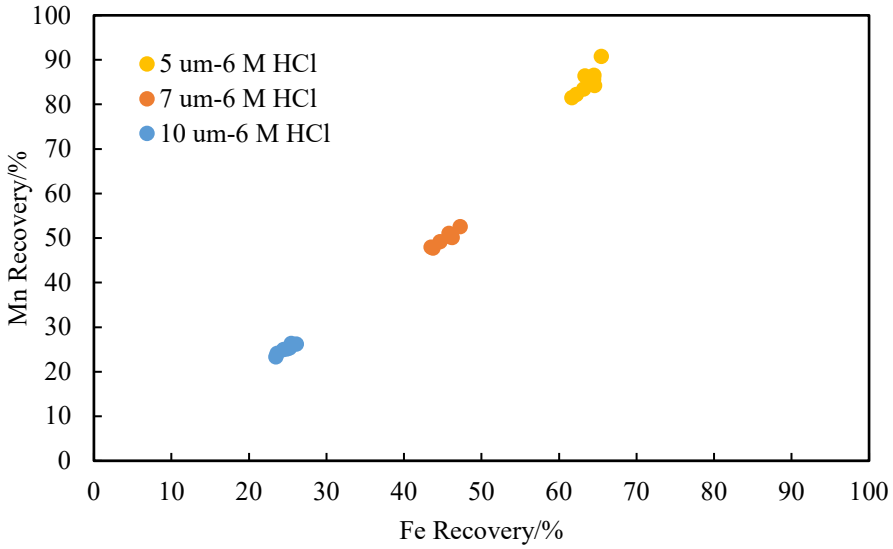

Figure 270. Correlation of Mn versus Fe recovery in the leachates of 6 M HCl as a function of particle size.

and Mn didn't necessarily mean that all the extracted Fe and Mn have exactly the same associations. We prefer to interpret this correlation in the way that Fe and Mn have similar leachability when they are exposed to 6 M HCl leaching.

Partition of HCl-leachable REEs in different coal-based clay samples.

In addition to the underclay sample, five other coal-based clay samples were also subjected to the 6 M HCl leaching, aimed to investigate the partition of HCl-leachable REEs as a function of sample. The information of TREE content, ash content, and particle size of each tested sample is summarized in Table 58. As is shown, the RB and MCMDU samples have relatively lower ash contents than other samples which are due to their poor floatability (Chen., 2013). The leaching characteristic of each sample is shown in Figure 271. Other than the MCMDM and MCMDU samples, the rest of the samples had similar fractions of HCl-leachable REEs. Additionally, similar UCC-normalized REE patterns (MREE-enriched distributions) were found in the leachates of nearly all the samples tested (Figure 272). This finding demonstrated that the MREE-enriched REE pattern prevalently exists in the coal-based clays. though the

Table 58. The samples used for 6 M HCl leaching.

Sample	Sample source	TREE (in whole basis)/ppm	Dry ash content/%	Particle size/um
WY	West Virginia	298.87	88.61	13.50
RB	Pennsylvania	250.10	76.16	7.10
MCMDM	Maryland	278.50	86.64	4.78
Leer	West Virginia	424.34	90.35	9.03
MCMDU	Maryland	247.80	56.85	6.13
Underclay	Pennsylvania	418.85	91.17	5.02

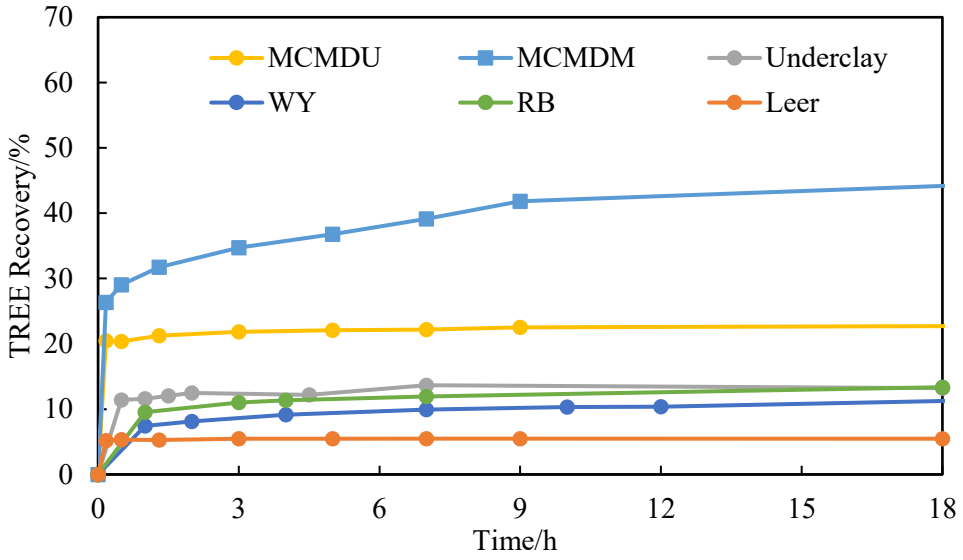

Figure 271. Dependence of the fraction of HCl-leachable REEs on different coal-based clay samples, leached by 6 M HCl at room temperature for 24 h.

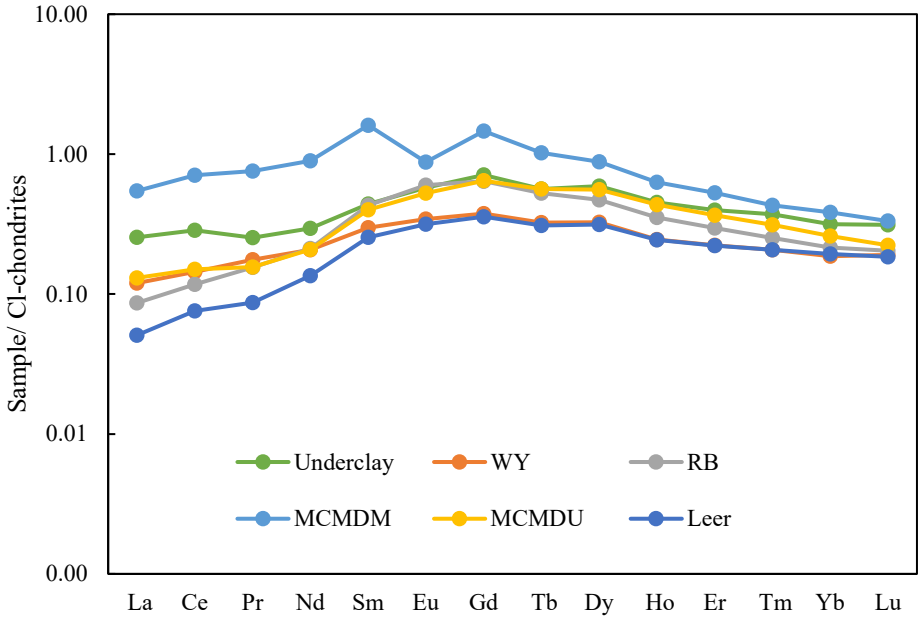

Figure 272. UCC Normalized HCl-soluble REEs from different samples.

fractions of HCl-leachable REEs are sample-dependent. In addition, the relatively larger particle sizes of the WY and Leer may also be a factor that led to the relatively lower fractions of the HCl-extractable REEs.

As indicated above, the UCC-normalized REE distribution of the MCMDM sample shows a relatively higher values of LREEs and a negative Eu anomaly. The leaching behaviors of the impure elements in the MCMDM sample show high fractions of dissolved Ca (88.31%) and P (71.21%) (Figure 273). This result demonstrates that the majority of minerals that contain Ca and P in the MCMDM sample is acid-soluble. Mineralogical analysis by SEM-EDS was performed on the MCMDM sample, and several apatite and Ca-P-bearing particles were identified (Figure 274). As the cases in the Underclay sample, the dominant minerals that contain Ca and P should also be hydroxyapatite and/or crandallite group minerals (Figure 275). The slightly decreasing trend of these two elements may be ascribed to the re-precipitation of secondary calcium phosphates.

The high fraction of HCl-extractable REEs determined in the MCMDM sample may be explained by the fact that the sample has more readily leachable REEs. Another scenario is that the rare earth phosphates in the sample have relatively lower crystallinity, which is more leachable by the HCl than monazite crystals with high crystallinity (Yang *et al.*, 2021; Lim *et al.*, 2012). However, the first scenario is excluded by the results of sequential extraction tests (Figure 276). Compared with the Underclay sample, the MCMDM sample only has slightly higher fractions of REEs in the first 4 steps. Around 77% of the REEs were still in the residue form (*i.e.,* rare earth phosphates and aluminosilicates). The minor increments of the readily leachable REEs are not able to explain the relatively high fraction of HCl-extractable REEs in the MCMDM sample. If REE-bearing apatite and crandallite group minerals exist in the sample, most of them should be dissolved by the 2 M HNO_3 in the fourth step of the sequential extraction test. However, the REEs extracted in the fourth step were similar to that of the Underclay, suggesting that the dissolution of apatite and crandallite group minerals did not release much REEs and led to the high fraction of HCl-leachable REEs in the MCMDM sample.

Furthermore, two ascorbic acid leaching tests, with different pH values and leaching temperatures, were performed on the MCMDM sample. It can be seen that similar TREE recovery values (~13%) were obtained for both tests, which are around 30% lower than that of 6 M HCl leaching (FIGURE). Even for the one leached under more aggressive conditions (*i.e.,* pH 2 and 60 °C), only a minor improvement on the

TREE recovery was noticed compared with the one conducted at pH 3 and 25 °C. Pronounced decrements on the recoveries of the elements from La to Sm in the leachates of the two ascorbic acid leaching tests were noticed. In the meantime, the recoveries of HREEs (especially for REEs from Dy to Lu) of both ascorbic acid leaching tests were only 3% lower than those of the 6 M HCl leaching, which was at similar level with those of the Underclay sample (see Figure 267), It can be concluded that the dissolution of the rare earth phosphates was depressed under mild conditions, and the fraction of readily leachable REEs in the MCMDM sample is similar with its counterparts. As such, the uniqueness of the MCMDM sample is more likely to be the lower degree of crystallinity of rare earth phosphates.

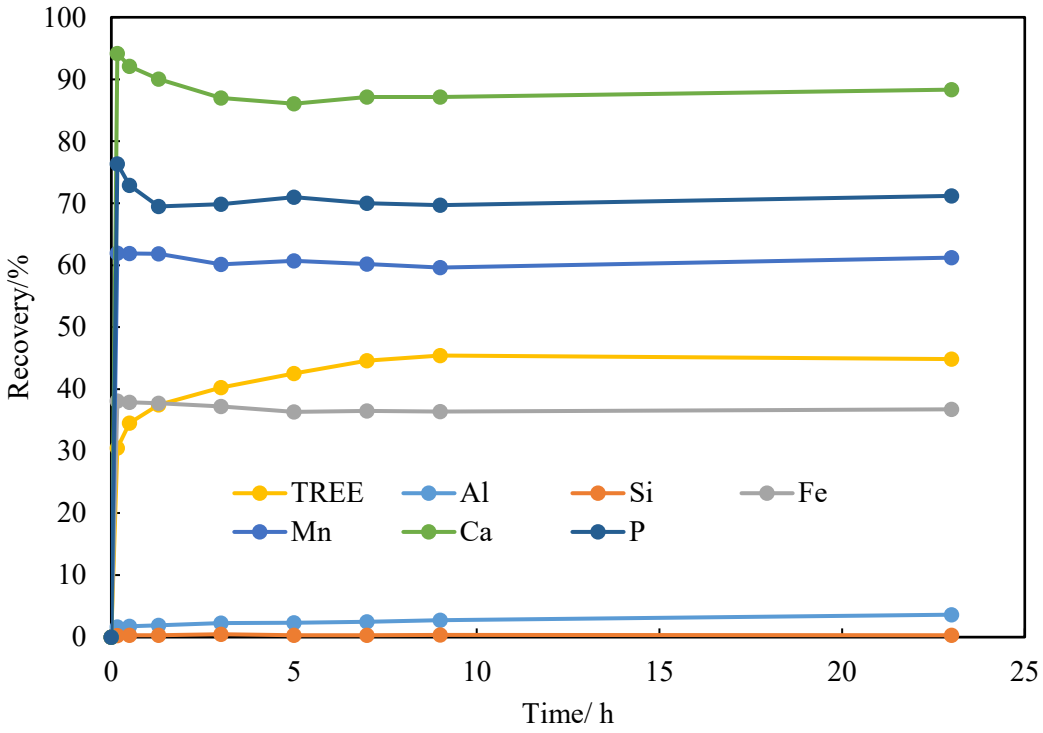

Figure 273. Leaching results of TREE and impure elements by 6 M HCl from the MCMDM sample, condition: 0.5 g/20 ml, room temperature, 18 h.

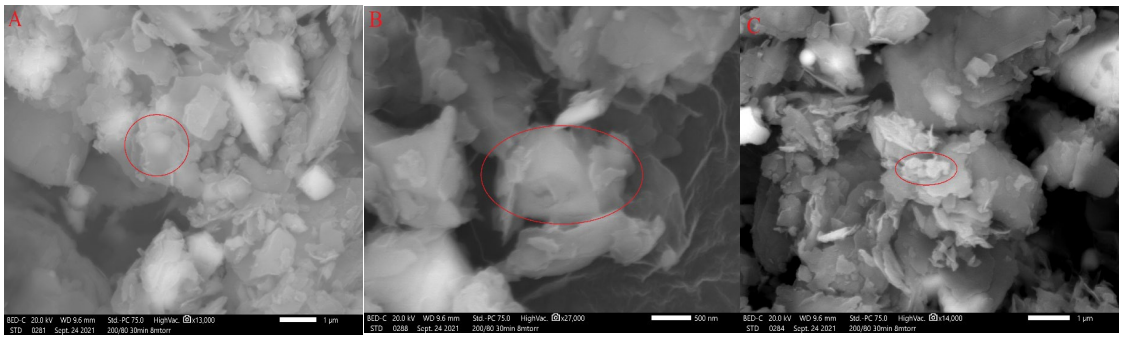

Figure 274. SEM images and their corresponding EDS spectra of fluorapatite particles found in the MCMDM sample.

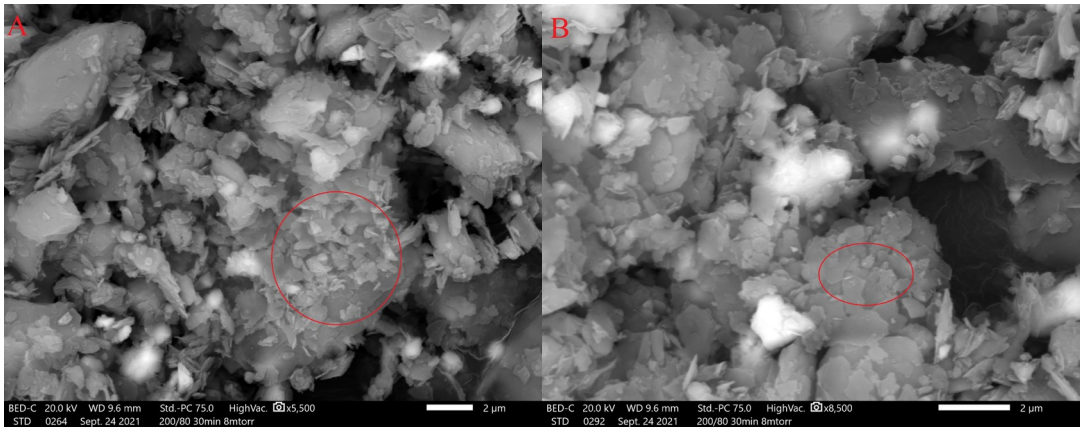

Figure 275. SEM images and their corresponding EDS spectra of Ca-P bearing particles found in the MCMDM sample.

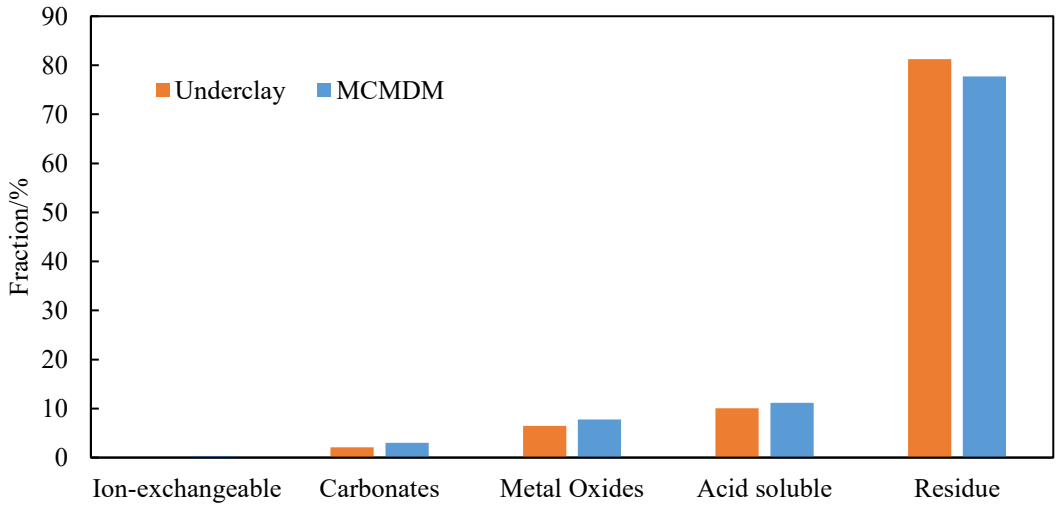

Figure 276. Comparison of sequential extraction results of the MCMDM and Underclay samples.

Several rare earth phosphate particles were found by SEM-EDS (Figure 278). Particles A and B are two single rare earth phosphate particles, which appears to be rare earth phosphates with high degree of crystallinity, whereas particle C and D are rare earth phosphate that associated with other minerals (*e.g.,* clay, pyrite), which are more likely to have poor crystal structures. The existence of particles such as C and D with lower crystallinity (*e.g.*, rhabdophanes, etc.) are more likely to be dissolved by the 6 M HCl. As such, the high fraction of HCl-extractable REEs of the MCMDM sample is more likely to be explained by the dissolution of rare earth phosphates with low crystallinity by 6 M HCl. This explanation is consistent with the fact that LREEs (La, Ce, Nd, Pr, Sm) contributed most to the higher TREE recovery.

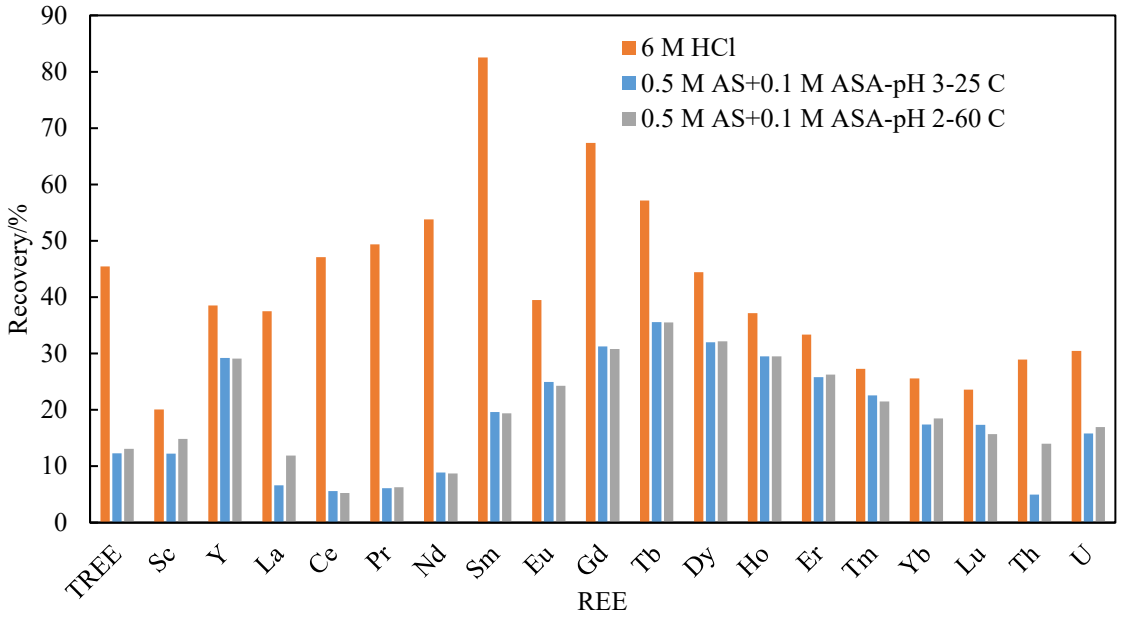

Figure 277. Comparison of the individual REE distributions from the MCMDM sample after leached by two different ascorbic acid leaching and 6 M HCl leaching. (101)

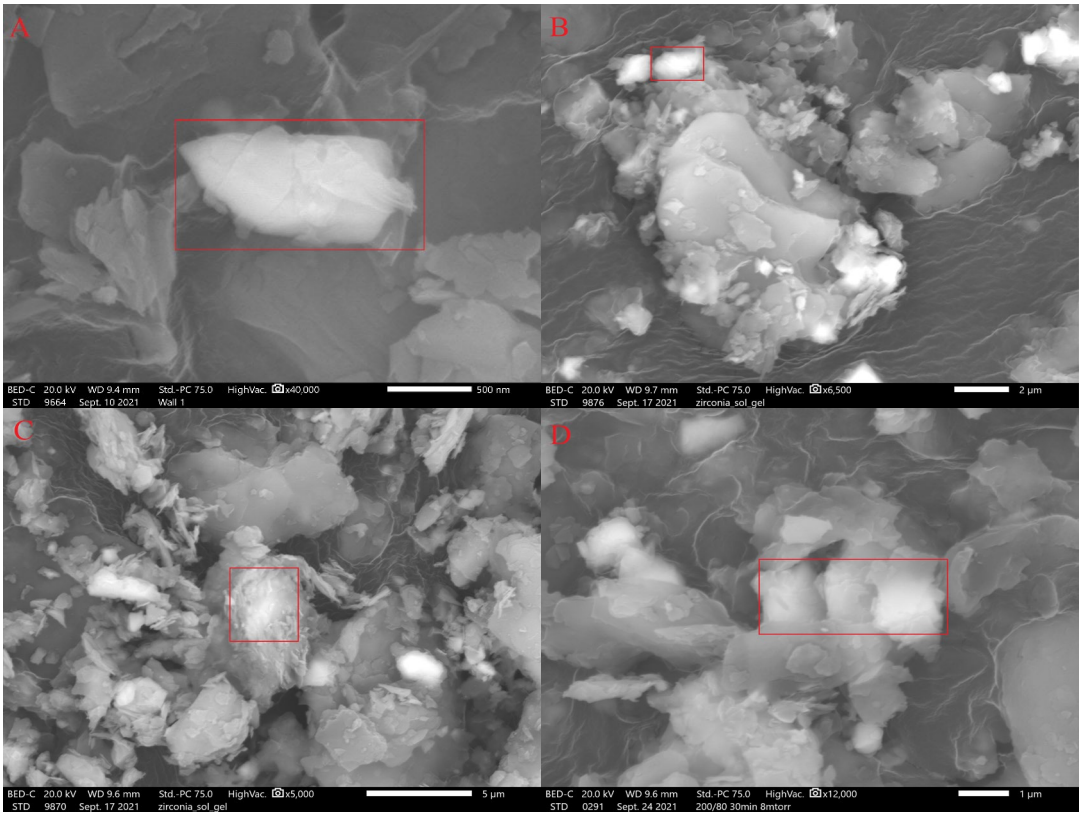

Figure 278. SEM images and their corresponding EDS spectra of rare earth phosphate particles found in the MCMDM sample.

Effect of phosphorous content on the leachability of Coal-based clays

The formation of IACs resulted from the in-situ weathering of REE-enriched host rocks (granitic or igneous) (Moldoveanu *et al.*, 2012). The majority of REEs in IACs are in a physisorbed state, *i.e.,* ion-exchangeable form, which can be readily extracted by ion-exchange leaching. However, there are still minor amounts of REMs that exist (Chi *et al.*, 2005) in IACs. Differing from the IACs, as mentioned before, the REEs in the mineral form (*e.g.,* rare earth phosphates) is the dominant occurrence of REEs in the coal-based clays due to their incomplete weathering. As such, one of the differences between IACs and coal-based clays is the fraction of REEs in mineral form, with much lower fractions of REMs in the former one. Bern *et al.* (2019) investigated the distribution and occurrences of REEs in regolith located in South Carolina, USA. An inverse correlation between the regolith phosphorus (P) content versus the fraction of ion-exchangeable REY in the clay samples. The study reported that the higher the P content in bulk regolith, the less amount of REY in ion-adsorbed form. The HCl leaching results in the study showed that the higher the fraction of HCl-extractable La of the bulk clay, the lower the P amount in bulk regolith (Figure 279). According to this study, P content can be used as an indicator of the fraction of ion-adsorbed REY in a clay sample, which can then be used to evaluate the leachability of a given coal-based clay sample.

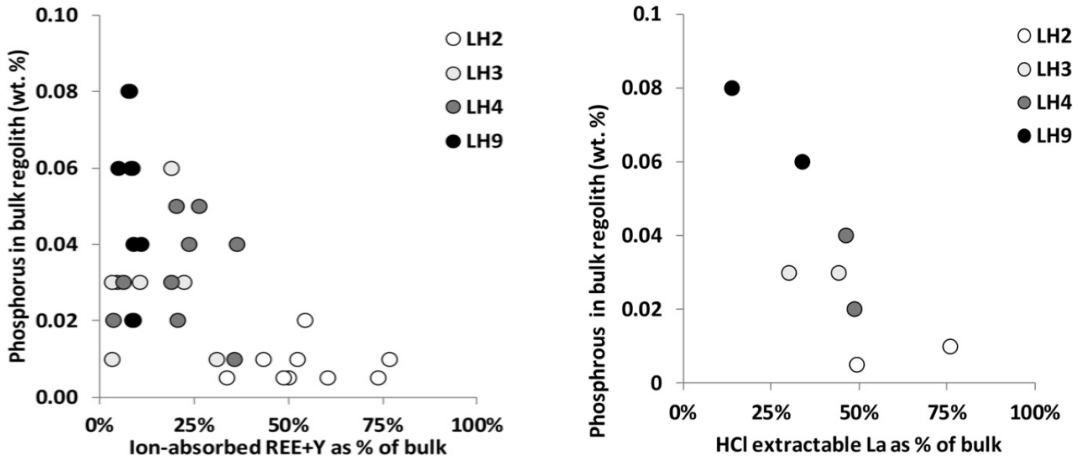

Figure 279. The correlation of the fraction of ion-adsorbed REY versus the phosphorous content in regolith samples (Bern et al. 2017).

Table 59. The samples used for 6 M HCl leaching.

Sample name	TREE/ppm	Phosphorus content/ppm	Fraction of 6M HCl-leachable REEs
MCMDM	278.50	1976.20	44.84
MCMDU	247.80	1403.90	22.81
RB	250.10	1810.80	13.66
Leer	424.34	1619.31	5.48
Underclay	418.85	529.45	13.22
WY	298.87	646.56	12.12

In the current study, the samples tested differ from each other not only in terms of TREE and P contents (Table 59), but also their responses to HCl leaching. The P content in each feed sample versus the fraction of the 6 M HCl-leachable REEs is shown in Figure 280. Generally, except for the MCMDM sample, an inverse correlation was found between the P content and the fraction of HCl-extractable REEs among the rest of the tested samples. Regarding the Leer, WY, and Underclay samples, which had relatively lower fractions of HCl-extractable REEs, the inverse trend is more pronounced. However, for RB and MCMDU samples, their P contents are all over 1.0%, the dependence of the fraction of HCl-extractable REEs on the P content has a smaller slope. Like the MCMDM sample, the high P contents in those two samples are not indicators of the amounts of rare earth phosphates. The existence of minerals such as apatite and crandallite group minerals also contribute to the high P contents. Also, the low crystallinity of rare earth phosphates is another reason for their higher fractions of HCl-leachable REEs. This finding is consistent with the conclusion in Bern's study (2019).

Conclusion

The results of the direct acid leaching of coal-based clay samples showed that difficult-to-leach REEs are the predominant association among the six samples. The elemental distribution of the HCl-leachable REEs display typical MREE-enriched REY patterns. The leaching behaviors of Fe and Mn revealed that a proportion of readily leachable REEs are associated with Fe-Mn, probably passivated by Fe-Mn oxyhydroxide. Except the MCMDM sample, 5 to 20% REEs were extracted by 6 M HCl at room temperature. For the MCMDM sample, the higher fraction (44.81%) of HCl-leachable REEs is likely to be explained by its lower crystallinity of rare earth phosphates. The high fractions of dissolved Ca and P were resulted from apatite and/or crandallite. In general, an inverse correlation between the P content vs. the faction of the HCl-leachable REEs in the tested coal samples. This correlation may be used to evaluate the leachability of REEs in a given coal after knowing its P content.

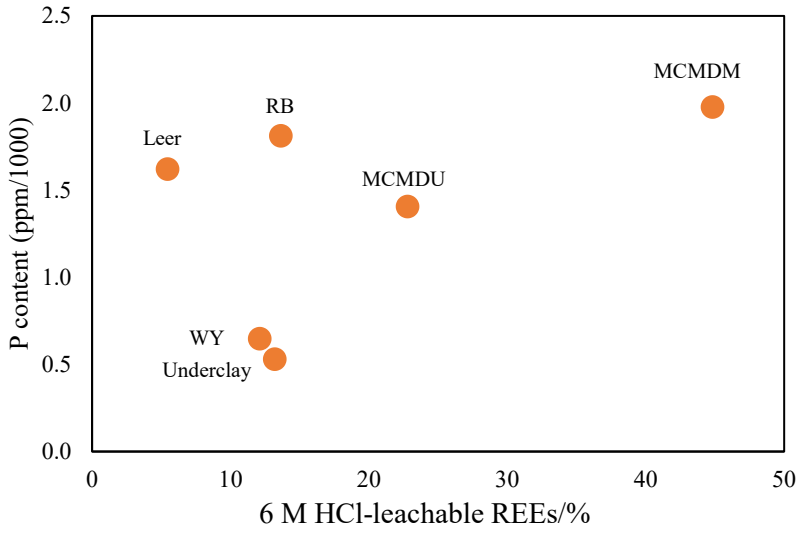

Figure 280. Phosphorous content versus the fraction of HCl-extractable REEs among the tested samples.

Subtask 5.4 – Ion-Exchange Leaching

Introduction

In addition to the REMs in coal of authigenic origin, REEs are also present in the organic matter and clay mineral surfaces. Analysis of the USGS coal quality database show a good correlation between REEs and aluminum (Al) contents in coals, indicating that much of the REEs particularly heavy REEs are associated with coal (Bryan et al., 2015). A part of the ongoing project is to explore the possibility of ion-adsorption clays in coal and finding appropriate ways to extract them.

Although the grades of the ion-adsorption clays are low (500-5,000 ppm), the cost of producing REEs from the ore are low due to their low cost of mining and simplicity of the extraction process. Typically, NH_4^+ ions displace the lanthanide ions (Ln^{3+}) physically adsorbed on clay surface. Tian et al., (2010) proposed the following reaction mechanism,

$$[Al_2Si_2O_5(OH)_4]_a \cdot bLn^{3+}(s) + 3bNH_4^+(aq) = [Al_2Si_2O_5(OH)_4]_a \cdot (NH_4^+)_{3b}(s) + bLn^{3+}(s) \quad [5.4.1]$$

It has been shown, however, that the REE ions adsorbed on clay surface undergo hydrolysis to produce hydroxides (Moldoveano and Papangelakis, 2012),

$$Clay - REE(H_2O)_n^{3+} = clay - REE(OH)_3 + 3H^+ + (n-3)H_2O \quad [5.4.2]$$

that are unleachable by the simple ion exchange reaction. This unleachable form of REEs are referred to being in "colloidal form." It is likely that the U.S. REEs in coal are in this or similar form as the eastern U.S. coals are in limestone bed. It should be noted also that the heavier REEs are more readily hydrolizable.

Exploratory Investigations on Artificial Clay Samples

Background

Approximately 80% of the heavy rare earth elements (HREEs) are produced from ion-adsorption clays (IACs) in south China. They are formed due to adsorption of the REE^{3+} ions on the negatively-charged surfaces of clay minerals. The smaller the ionic radii, the higher the adsorbability, which is the reason for the IACs being the major source of HREEs. Owing to lanthanide contraction, the ionic radii decrease with increasing atomic number.

In general, 60-90% of the REEs in IACs are in the form of free hydrated ions, i.e., $REE(H_2O)n^{3+}$, which can readily be ion-exchanged by a lixiviant such as NH^{4+} ions. At pH > 7, however, they are hydrolyzed to become 'clay-O-REE^{2+}' species that are chemically bound to the surface. Such species known as *colloidal phase* cannot be extracted by an ion-exchange mechanism (Chi and Tian, 2008). On the other hand, the REEs in colloidal phase are readily dissolved in acids albeit at higher costs.

During the current study, artificial ion-adsorption clays were prepared by immersing a kaolinite sample from Sigma-Aldrich in solutions of REE chlorides at different pHs, contact times, and temperatures. The samples were analyzed by ICP/MS and XPS methods. A few samples were subjected to ion-exchange extraction tests using NH_4^+ ions.

Artificial Clay Sample Preparation

A kaolinite sample purchased from Sigma Aldrich was contacted with known concentrations of rare earth chlorides, which included $DyCl_3$, YCl_3, $LaCl_3$, $CeCl_3$, and $NdCl_3$, so that the REE ions adsorb on the negatively charged clay surface. In each experiment, 15 g of the clay sample was placed in a 125 ml Erlenmeyer flask at a 1:5 solid-to-liquid ratio, and the mixture was agitated by means of a magnetic stirrer for a preset time and a desired pH. The concentrations of the REE chloride solutions were determined such that the concentration of individual REE on the artificial clay samples would become 400 ppm after drying. After the agitation, the clay sample was filtered, washed with deionized water repeatedly, and dried in an oven overnight at 60 ºC. The artificial ion-adsorption clays prepared in this manner were analyzed for REEs by means of ICP/MS and XPS.

Figure 281 to Figure 283 show the REE+Y contents of the kaolinite samples contacted with the kaolinite sample by changing the pH at different concentrations. It appears that the adsorption of the REE+Y ions was largely independent of pH and the REE contents did not increase further after one hour of contact time. In general, the kinetics of physical adsorption is faster than those of chemical adsorption. Note that the cerium concentrations were substantially higher than 400 ppm, indicating that the clay samples had ~300 ppm Ce. The clay sample also had approximately 100 ppm La, 80 ppm Dy, and 80 ppm Dy of its own.

Figure 284 to Figure 287 show the effect temperature on the REE+Y contents of the ion-adsorption clay (kaolinite) prepared at pH and contact times. It appears again that the REE+Y adsorption is independent of pH and the adsorption kinetics is fast, which is typical of physical adsorption. These findings are not surprising if the REE^{3+} ions adsorb on the basal surface of the clay mineral, whose surface charge density is independent of pH. The surface chare density, which is of structural origin, should not vary with temperature either, which explains why the adsorption is also independent of temperature.

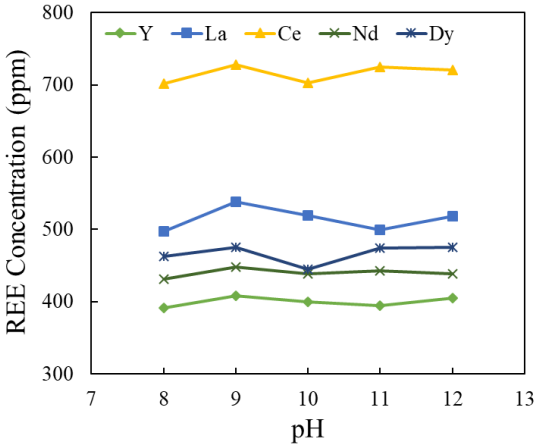

Figure 281. Effect of pH on the REE+Y contents of the artificial ion adsorption clay (kaolinite) prepared at 25˚C and 1 hour contact time.

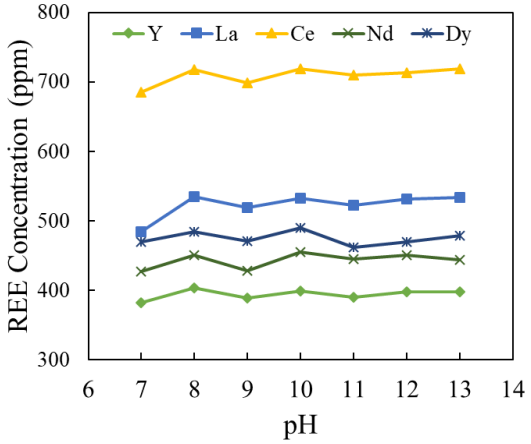

Figure 282. Effect of pH on the REE+Y contents of the artificial ion adsorption clay (kaolinite) prepared at 25˚C and 24 hour contact time.

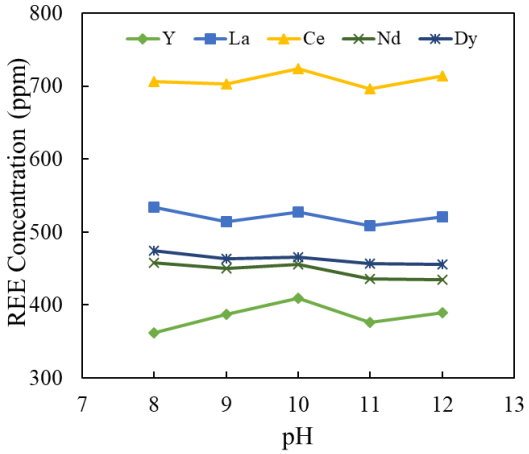

Figure 283. Effect of pH on the REE+Y contents of the artificial ion adsorption clay (kaolinite) prepared at 25˚C and 48 hour contact time.

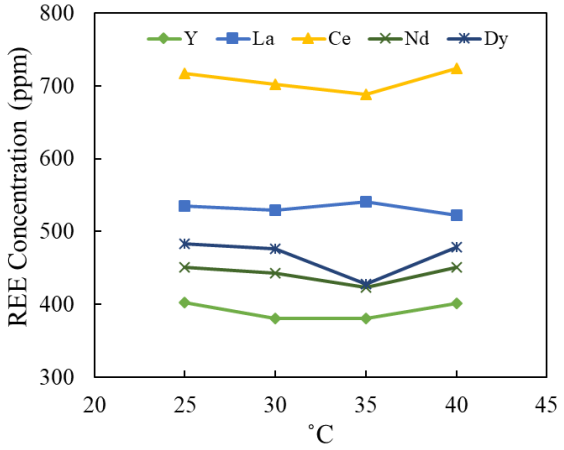

Figure 284. Effect of temperature on the REE+Y contents of the artificial ion-adsorption clay (kaolinite) prepared at pH 8 and 24 hr contact time.

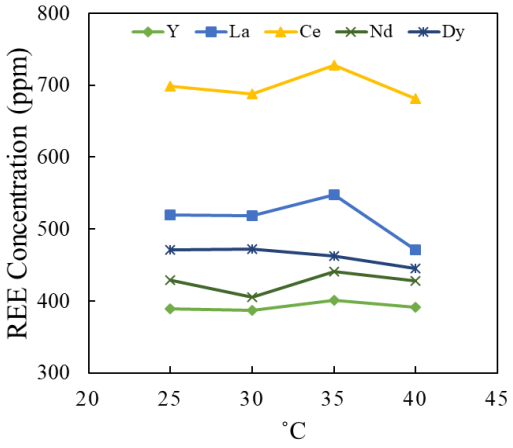

Figure 2850. Effect of temperature on the REE+Y contents of the artificial ion-adsorption clay (kaolinite) prepared at pH 9 and 24 hr contact time.

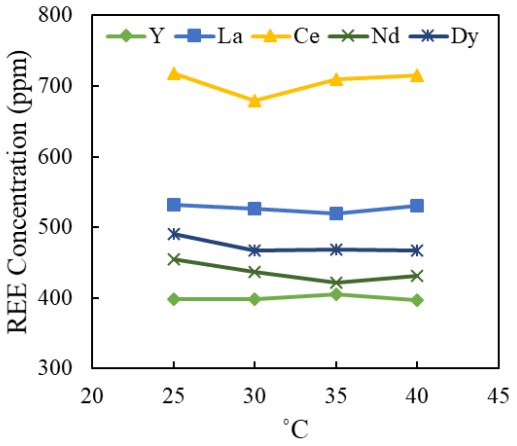

Figure 286. Effect of temperature on the REE+Y contents of the ion-adsorption clay (kaolinite) prepared at pH 10 and 24 hours contact time.

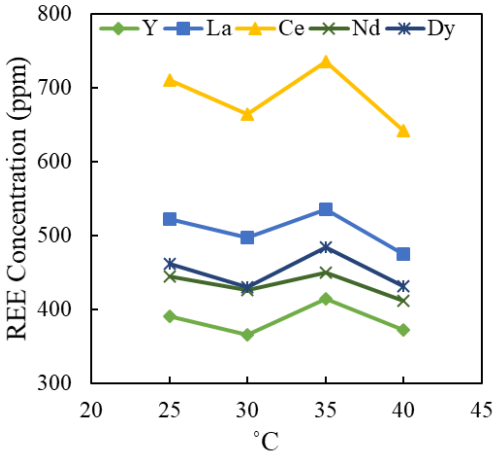

Figure 287. Effect of temperature on the REE+Y contents of the artificial ion-adsorption clay (kaolinite) prepared at pH 11 and 24 hr.

XPS Characterization Artificial Ion Adsorption Clay

Light Rare Earth Elements

Background X-ray photoelectron spectroscopy (XPS) was used to characterize the chemical state of representative light rare earth elements (LEEs) on the surface of artificial clay samples. It is well known that La 3d spectra, the primary La XPS feature, has two peaks ($3d_{5/2}$ and $3d_{3/2}$) resulting from spin-orbit splitting, either of which conveys the same chemical information of the La compound. Furthermore, each spin-orbit peak is split into two components by multiplet splitting, where the lower binding energy component is the primary La $3d_{5/2}$ peak and the higher binding energy component is the satellite peak due to final state effects. In addition to the peak position of the two multiplet-split components, the magnitude of the multiplet splitting and the intensity ratio of each multiplet-split component are also characteristic of different La-containing compounds (Suzuki et al., 1998; Siegmann et al., 1978; Sunding et al., 2011). In this work, an artificial La clay sample and several commercially available La compounds including $La(OH)_3$, La_2O_3 and $LaCl_3$ were measured by XPS. Characteristic La $3d_{5/2}$ features of the artificial La clay sample were compared to those of the high-purity La standards to provide insight into the identification of La species (speciation) on the artificial sample.

Experimental $La(OH)_3$ (Sigma-Aldrich, 99.99%) and $LaCl_3$ (Alfa Aesar, 99.99%) were stored in a desiccator upon arrival and used as received. La_2O_3 (Sigma-Aldrich, 99.99%, hygroscopic) was stored in an Argon-filled glovebox upon arrival and was etched by Argon ion to remove hydrated surface layers prior to XPS measurements. An artificial La clay sample was prepared with 5 REEs (La, Ce, Nd, Dy and Y) on kaolinite clay with REE concentrations > 400 ppm each after contacting REE chloride solutions at pH 10, 25°C for 24 hours.

XPS characterization was performed on a PHI VersaProbe III scanning XPS microscope equipped with a monochromatic Al K-alpha X-ray source (1486.6 eV) with a base pressure of 3×10^{-8} Pa. XPS Spectra were acquired at 10 µm/100 W/20 kV over a 1400×100 µm sample area using 55 eV pass energy, which gives a $Ag3d_{5/2}$ full width at half maximum of 0.65 eV. All binding energies were referenced to C-C peak at 284.8 eV.

Results and Discussion Figure 288 shows the La $3d_{5/2}$ XPS spectra of the standards, $La(OH)_3$, La_2O_3, and $LaCl_3$, along with the artificial ion-adsorption clay sample. Characteristic properties of the La $3d_{5/2}$ feature including the peak position of the two multiplet-split components, the magnitude of the multiplet splitting (ΔE) and the intensity ratio of each multiplet-split component are summarized in Table

Table 60. La $3d_{5/2}$ features for various La compounds.

Compound	La $3d_{5/2}$ BE (eV)	ΔE (eV)	Peak Intensity Ratio
$La(OH)_3$	834.7	3.7	1.00
	838.4		0.71
La_2O_3	834.1	4.5	1.00
	838.6		0.77
$LaCl_3$	835.6	3.5	1.00
	839.1		1.43
Artificial La Clay	835.1	3.6	1.00
	838.7		0.73

60. $La(OH)_3$ shows a La $3d_{5/2}$ peak position of 834.7 eV and a multiplet splitting of 3.7 eV, which are in excellent agreement with previously reported values of 835.1 eV and 3.9 eV respectively [3]. The peak intensity ratio of the satellite peak (838.4 eV) with respect to the La $3d_{5/2}$ peak (834.7 eV) is 0.71, which, to the best of our knowledge, is the first ratio documented for $La(OH)_3$. Compared to $La(OH)_3$, La_2O_3 shows a greater multiplet splitting of 4.5 eV, while $LaCl_3$ has a significantly larger peak intensity ratio of 1.43, These key difference provide evidence that our XPS approach is capable of distinguishing La-containing species from each other.

The artificial La clay sample demonstrates a La $3d_{5/2}$ peak at 835.1 eV, a multiplet splitting of 3.6 eV, and a peak intensity ratio of the satellite peak with respect to the La $3d_{5/2}$ peak of 0.73. All the three values match those of $La(OH)_3$, suggesting that the primary La species on the surface of the artificial clay sample is $La(OH)_3$. A trace amount of F is also shown on the survey spectra of the artificial sample (not shown here), leading to the presence of a F $KL_{23}L_{23}$ Auger peak at 831.4 eV in the La $3d_{5/2}$ region. This observation is not surprising, as F is a common contaminant from solutions and air.

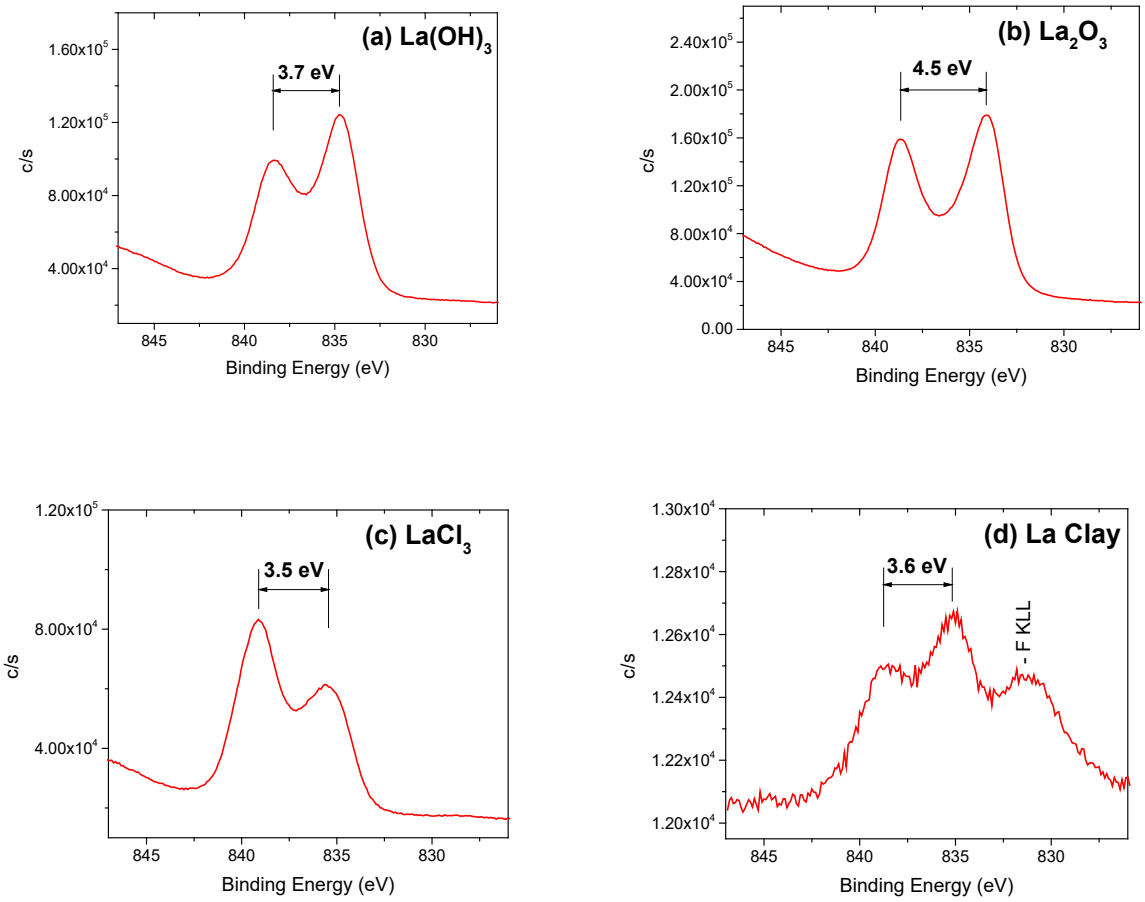

Figure 288. La $3d_{5/2}$ XPS spectra of various La compounds. (a) La(OH)3; (b) La2O3; (c) LaCl3; (d) artificial La clay sample prepared clay (kaolinite) sample contacted with La, Ce, Ne, Dy + Y chlorides for 24 hours at pH 13 and 25oC.

Heavy Rare Earth Elements

Background X-ray photoelectron spectroscopy (XPS) was used to characterize the chemical state of representative heavy rare earth elements (HREEs) on the surface of artificial clay samples. Gd, Tb, Dy, Ho, Er, Tm, Yb and Lu are generally considered as heavy rare earth elements. The binding energies of 3d core electrons of Er, Tm, Yb and Lu are too strong to be excited by the equipped Al X-ray source; therefore, these four elements are impractical for XPS characterization. According to the XPS characterization of La compounds as described in Section (c)-a, the combination of $3d_{5/2}$ peak position, multiplet splitting strength and peak intensity ratio of multiplet-split components provides sufficient evidences to distinguish the chemical form of the rare earth element. Among Gd, Tb, Dy and Ho, Gd is reported to have the most significant multiplet splitting (Mullica et al., 1995), thus making it the best HREE candidate for XPS studies. In this work, an artificial Gd-clay sample and several commercially available Gd compounds including $Gd(OH)_3$, Gd_2O_3 and $GdCl_3$ were measured by XPS. Characteristic Gd $3d_{5/2}$ features of the artificial La-clay sample were compared to those of pure Gd compounds to provide insight into the identification of Gd species on the artificial sample.

Effect of pH

Background X-ray photoelectron spectroscopy (XPS) was used to quantify the relative concentrations of REEs on the surface of artificial ion-adsorption clay (kaolinite) samples prepared at various pH to investigate the effect of pH on the REE surface concentrat ion of artificial clay samples.

Experimental Artificial clay sample was prepared with 5 different REEs (La, Ce, Nd, Dy and Y) adsorbed on kaolinite clays at pH 7 to 13, 25°C, and 24 h contact time. XPS characterization was performed on a PHI VersaProbe III scanning XPS microscope equipped with a monochromatic Al K-alpha X-ray source (1486.6 eV) with a base pressure of 3×10^{-8} Pa. XPS Spectra were acquired at 10 µm/100 W/20 kV over a 1400×100 µm sample area using 55 eV pass energy, which gives a $Ag3d_{5/2}$ full width at half maximum of 0.65 eV. All binding energies were referenced to C-C peak at 284.8 eV. Atomic concentration % of elements were calculated by integrated intensity of primary photoemission features of each element followed by correction with relative atomic sensitivity factors. Two XPS measurements were performed on each sample.

Results and Discussion Figure 289 shows the atomic concentration % of La, Ce and Dy as a function of pH. The values were summarized in Table 61. The atomic concentration % of Nd and Y could not be quantified due to the overlapping of Nd 3d and

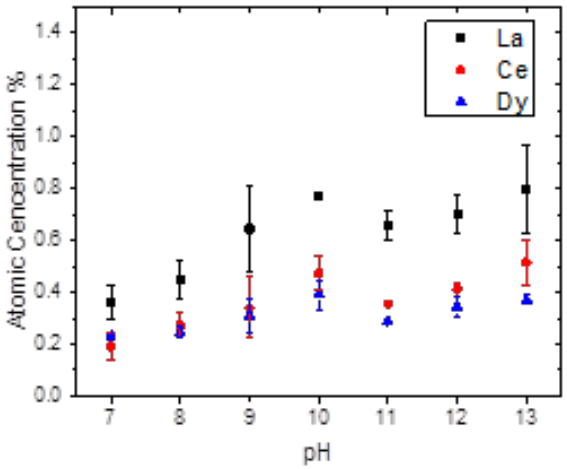

Figure 289. La, Ce and Dy atomic concentration % as a function of pH. La, Ce and Dy atomic concentration % are normalized to 100% of Al.

Table 61. La, Ce and Dy atomic concentration % as a function of pH. La, Ce and Dy atomic concentration % are normalized to 100% of Al.

pH	La	Ce	Dy
7	0.36	0.19	0.23
8	0.45	0.27	0.25
9	0.64	0.34	0.31
10	0.77	0.47	0.39
11	0.65	0.35	0.29
12	0.70	0.41	0.34
13	0.80	0.51	0.37

Y 3d regions with the overwhelming O KLL and Si 2s signals of the kaolinite clay, respectively. The atomic concentration % of La, Ce and Dy all increase with increasing pH from 7 to 10. At pH 11, the atomic concentration % of La, Ce and Dy all decrease compared to those at pH 10, then keep increasing from pH 11 to pH 13. The local maximum of REE concentrations at pH 10 suggests that the ion adsorption of REEs is mostly favored with pH 10 treatment. The drop of REE concentrations from pH 10 to pH 11 could be associated with a phase transformation of REE species on the clay surface.

Note here that the surface analysis data shown in Table 61 and Figure 289 show that the atomic concentrations on the surface of the artificial clay samples vary substantially with pH. Adsorption of the three REEs analyzed, i.e., La, Ce, and Dy, increases with pH, suggesting that hydrolysis products such as $RE(OH)_2^+$ or $RE(OH)_3(s)$ have high propensity for adsorption on clay. The initial peak at pH 10 seems to indicate the adsorption of the former and the one at pH 13 the adsorption of the latter.

Ion-Exchange Leaching Tests

A set of ion-exchange leaching tests were conducted the artificial kaolinite clay sample prepared by contacting La, Ce, Nd, Dy, and Y chlorides at pH 10 for 24 hours. The leaching tests were conducted using $(NH_4)_2SO_4$ as lixiviant at different concentrations at pH 5. The results presented at Figure 290 showed that the REE+Y recoveries increase with the lixiviant dosages. The data presented in Figure 291 shows the residual concentrations.

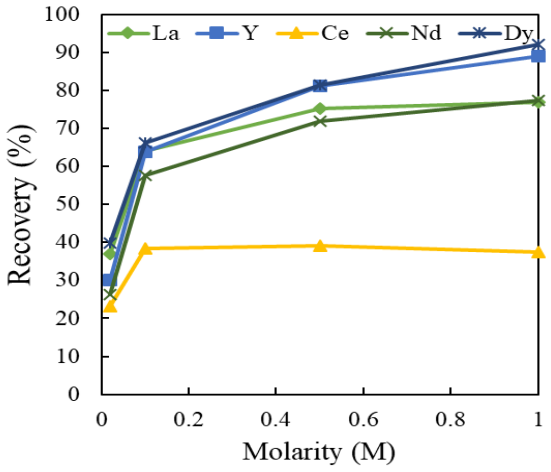

Figure 290. Molarity vs. Recovery at 25 ˚C and 1 hour.

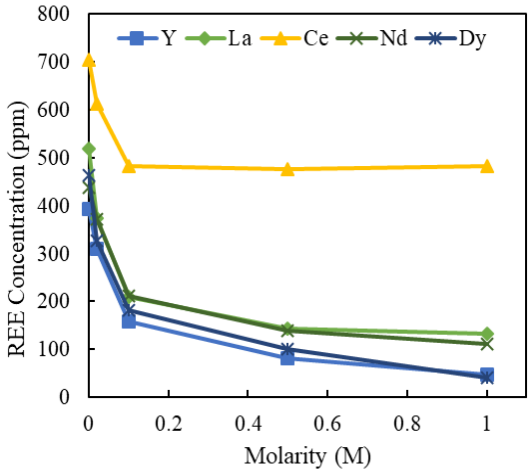

Figure 291. Molarity vs. REE concentration at 25 ˚C and 1 hour.

Detailed Investigations on Artificial Clay Samples (Kaolinite and Montmorillonite)

Background

Approximately 80% of the heavy rare earth elements (HREEs) are produced from ion-adsorption clays (IACs) in south China. They are formed due to adsorption of the REE^{3+} ions on the negatively-charged surfaces of clay minerals. The smaller the ionic radii, the higher the charge density, which is the reason for the IACs being the major source of HREEs.

In general, 60-90% of the REEs in IACs are in the form of free hydrated ions, i.e., $REE(H2O)_n^{3+}$, which can readily be ion-exchanged by a lixiviant such as NH_4^+ ions. At pH > 7, however, they are hydrolyzed to become 'clay-O-REE^{2+}' species that are chemically bound to the surface. Such species known as colloidal phase cannot be extracted by a simple ion-exchange mechanism (Chi and Tian, 2008). On the other hand, the REEs in colloidal form (or phase) can be readily dissolved in acids albeit at higher costs.

In the current study, artificial ion-adsorption clays were prepared by immersing a montmorillonite sample from Sigma-Aldrich in solutions of REE chlorides of known concentration at different pHs, contact times, and temperatures. The samples were subjected to ion-exchange leaching tests. Artificial ion-adsorption clays were also prepared from kaolinite samples for a series ion-exchange extraction tests using a series of novel lixiviants developed in the present work. The results were compared with those obtained using the conventional lixiviant, *i.e.*, NH^{4+} ions.

Preparation of Artificial Ion-Adsorption Clay Samples

The montmorillonite sample purchased from Sigma Aldrich was contacted with known solutions of rare earth elements, so that the REE^{3+} ions could adsorb on the mineral surface. The REE solutions were prepared from the following salts: $DyCl_3$, YCl_3, $LaCl_3$, $CeCl_3$, and $NdCl_3$. In each experiment, a 15 g sample of the clay was placed in a 125 ml Erlenmeyer flask at a 1:5 solid-to-liquid ratio, and the mixture was agitated by means of a magnetic stirrer for a preset time period and pH. The concentrations of the REE chloride solutions were determined in such a way that the resulting ion-adsorption clay would contain 400-600 ppm TREEs after drying. After the agitation, the clay samples were filtered, washed with deionized water repeatedly, and dried in an oven overnight at 60 ˚C. The artificial ion-adsorption clays prepared in this manner were analyzed for REEs contents by means of ICP/MS. Blank tests conducted on the montmorillonite sample purchased from Sigma Aldridge contained 12 ppm La, 25 ppm Ce, 7 ppm Y and 21 ppm Nd of its own, while the Dy content was only 0.92 ppm.

Figure 292 and Figure 293 show the REE+Y contents of the artificial ion-adsorption clays prepared from the montmorillonite sample. The results show that the adsorption of the REE+Y decreases with pH reaching a minimum at pH 11, which is close to the minimum solubility of the rare earth hydroxides, $RE(OH)_3(s)$. At pH above this pH, the adsorption may occur as phase separated hydroxides. Regarding the time effect, the adsorption reaches maxima after one hour of agitation and then decrease. It is difficult to explain why the adsorption decreases after 2 hrs of contact time. Nevertheless, the REE contents of the ion adsorption clays are in the range of typical concentrations of naturally occurring ion-adsorption clays.

Figure 294 shows the effect temperature on the REE+Y contents of the ion-adsorption clay (montmorillonite) prepared at pH 10 and 24 hrs of contact time. As shown, the REE+Y contents decreased at the higher temperature.

According to the data presented above, adsorption of the REE+Y species on montmorillonite is most favored at pH 11, 24 hour of contact time, and 25 ˚C. For kaolinite, the optimal conditions were pH 10, 24 hours of contact time, and 25 ℃ as has been described above.

Ion-Exchange Leaching Tests Using Novel Lixiviants

The ion-adsorption clay samples prepared from the kaolinite and montmorillonite clay samples as described in the foregoing section were used for a series of leaching tests. Table 62 shows the list of nine

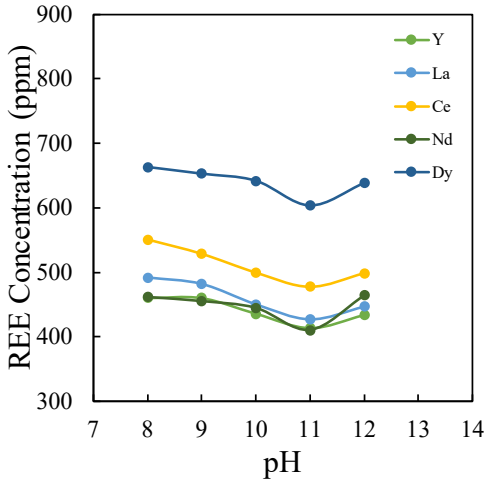

Figure 292. Effect of pH on the REE+Y contents of the artificial ion adsorption clay (montmorillonite) prepared at 25˚C and 24 hour contact time.

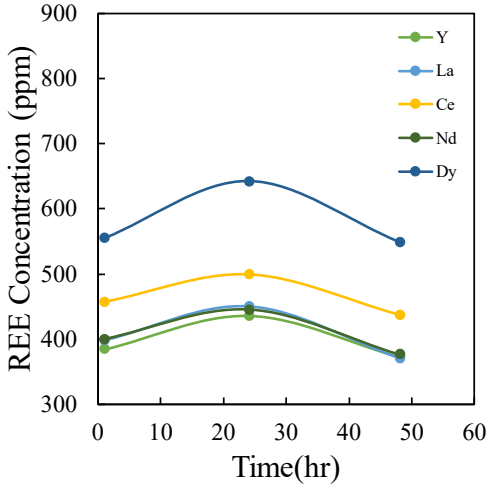

Figure 293. Effect of time on the REE+Y contents of the artificial ion adsorption clay (montmorillonite) prepared at 25˚C and 24 hour contact time.

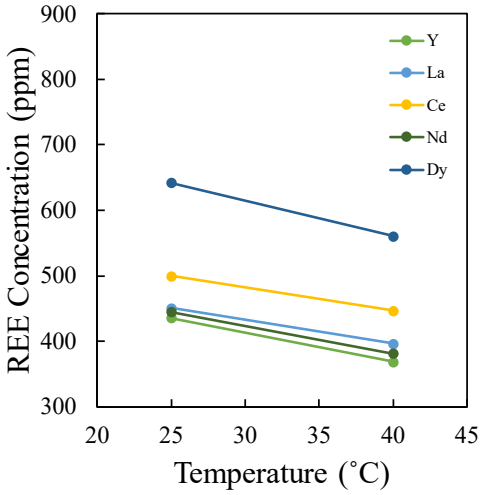

Figure 294. Effect of temperature on the REE+Y contents of the artificial ion-adsorption clay (montmorillonite) prepared at pH 10 and 24 hr contact time.

different novel lixiviants plus the conventional lixiviant that is used commercially in China. All leaching tests were conducted by varying the lixiviant concentrations at pH 5, 25 ˚C, and 1 hour contact time.

Ammonium Sulfate

Figure 295 and Figure 296 show the results obtained using the conventional reagent, i.e., $(NH_4)_2SO_4$, on the kaolinite and montmorillonite samples, respectively. As expected, REE recoveries increased with increasing lixiviant concentration but the recoveries varied with different types of REEs. Most of the REEs responded well reaching maximum recoveries in the range of 75-91%. However, the conventional lixiviant (NH_4^+) was efficient for the extraction of cerium.

Table 62. List of Novel Lixiviants Tested.

Novel Lixiviants Tested	Molecular Formula	Chain Length
Ammonium sulfate (AS)*	$(NH_4)_2SO_4$	-
Tetramethylammonium chloride (TMAC)	$(CH_3)_4N(Cl)$	1
Tetraethylammonium chloride (TEAC)	$(C_2H_5)_4N(Cl)$	2
Aminomethylpropanol (AMP)	$C_4H_{11}NO$	2
Ethylamine Hydrochloride (EAH)	$C_2H_7N.HCl$	2
Butylamine Hydrochloride (BAH)	$C_4H_{11}N.HCl$	4
Hexylamine Hyrdrochloride (HAH)	$C_6H_{15}N.HCl$	6
n-Octylamine Hydrochloride (OAH)	$C_8H_{19}N.HCl$	8
Dodecylamine hydrochloride (DAH)	$C_{12}H_{28}ClN$	12
Hexadecyltrimethyammonium chloride (HTAC)	$C_{16}TACl$	16

*Conventional reagents

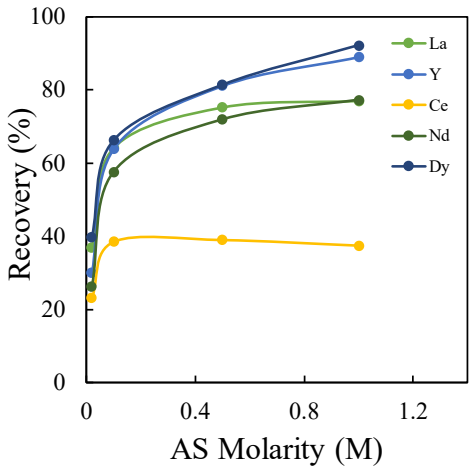

Figure 295. Effect of (NH4)2SO4 concentration on the recovery of REEs from the ion-adsorption clay (kaolinite) at pH 5, 25˚C and 1 hr contact time.

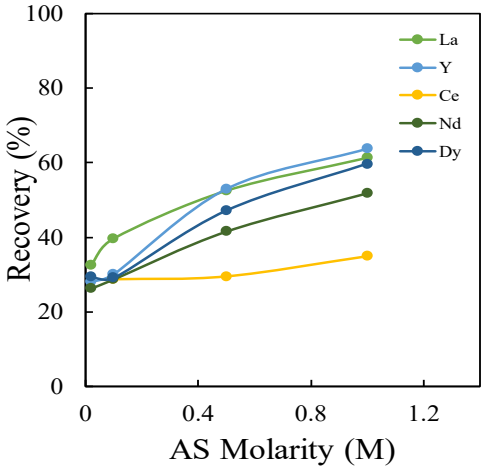

Figure 296. Effect of (NH4)2SO4 concentration on the recovery of REEs from the ion-adsorption clay (montmorillonite) at pH 5, 25˚C and 1 hr of contact time.

The results obtained with the montmorilonite sample were not as good as those obtained with kaolinite. The recoveries were in the range of 50 -65% only, which may be due to the possibility that REE^{3+} ions may be intercalated. As a 2:1 layer structured mineral, some of the REE^{3+} ions may have been adsorbed in between the layers of montmorillonite, which are difficult to be removed by the RNH_4^+ ions.

Dodecylamine Hydrochloride

Figure 297 and Figure 298 show the results of the ion-exchange leaching tests conducted using DAH as lixiviant on the artificial ion-adsorption clays prepared from kaolinite and montmorillonite, respectively. As shown, the recoveries increased with DAH concentration, with the recoveries being the range of 50 to 70% for kaolinite and 25-30% for montmorillonite. These recoveries were lower than obtained using NH_4^+ ions as lixiviant. Note, however, that the DAH concentrations were less than 0.1 M as compared to 1 M for NH_4^+ ions. The maximum solubility of DAH is low because of its long hydrocarbon chain.

Aminomethylpropanol

Figure 299 and Figure 300 show the results of the ion-exchange leaching tests conducted on the kaolinite and montmorillonite samples using 2-amino-2-methylpropanol ($H_2NC(CH_3)_2CH_2OH$). This

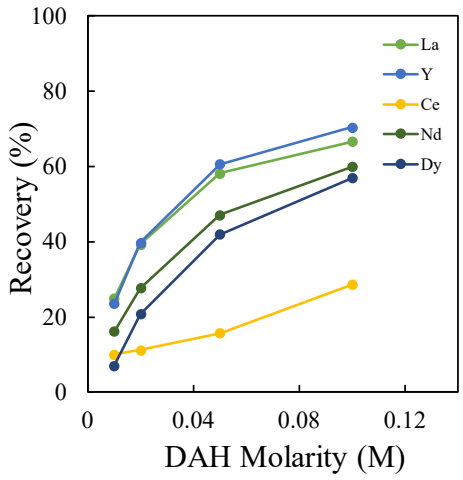

Figure 297. Effect of DAH concentration on the recovery of REEs from an ion-adsorption clay (kaolinite) at pH 5, 25˚C and 1 hr contact time.

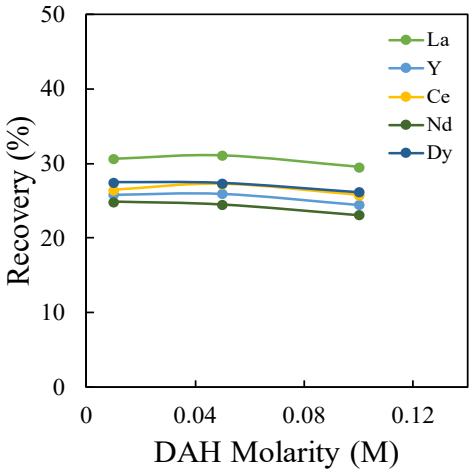

Figure 298. Effect of DAH concentration on the recovery of REEs from an ion-adsorption clay (montmorillonite) at pH 5, 25˚C and 1 hr contact time.

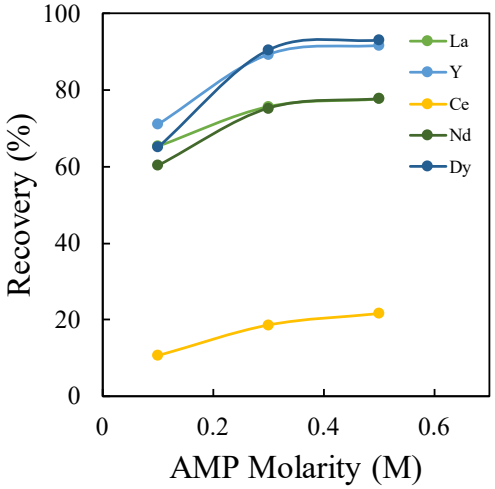

Figure 299. Effect of AMP Concentration vs. REE recovery at pH 5, 25 ˚C and 1 hour on artificial kaolinite.

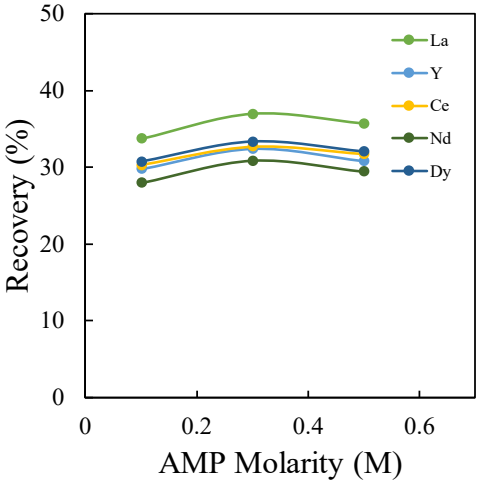

Figure 300. Effect of AMP Concentration vs. REE recovery at pH 5, 25 ˚C and 1 hour on artificial montmorillonite.

reagent was chosen because it has a propanol group which makes it more water soluble than DAH, which in turn made it possible to increase the reagent dosage. Still, the amount of the reagent used was one-half of the amount of the NH^{4+} ions used.

As shown in Figure 299, the reagent was particularly efficient for the extraction of Y and Nd. It was also efficient for the extraction of La and Dy but not for Ce. On the other hand, the reagent was not as efficient as NH_4^+ ions for the extraction of REEs from the montmorillonite sample. It is possible that aminomethylpropanol (AMP) cannot remove the RE^{3+} ions from the interior of the layer-structured mineral.

Tetramethylammonium chloride

Table 63 and Table 64 show the results of the ion-exchange leaching tests obtaining using tetramethylammonium chloride. This reagent was chosen because the heat of hydration of the tetramethylammonium (TMA^+) ions is 185.2 kJ/mole (Nagano et al., J. Phys. Chem. 1988, 92, 5823-5827 5823), which is smaller than the value of 322 kJ/mole for NH_4^+ ions (Moldoveanu and Papangelakis, Hydrometallurgy 117–118 (2012) 71–78). The low value of the heat of hydration suggests that the TMA^+ ions can more readily displace the RE^{3+} ions from clay.

Table 63. Effect of TMAC Concentration vs. REE recovery at pH 5, 25 ˚C and 1 hour on artificial kaolinite.

			Feed		Solid Residue		Recovery (%)
Test#	Lixiviant	Conc. M	REE (ppm)	Wt (g)	REE (ppm)	Wt (%)	
K-La	TMAC	0.5	531.96	5	240.68	93	57.92
K-Y	TMAC	0.5	398.43	5	167.39	93	60.93
K-Ce	TMAC	0.5	718.24	5	660.38	93	14.49
K-Nd	TMAC	0.5	454.71	5	252.75	93	48.31
K-Dy	TMAC	0.5	489.80	5	293.86	93	44.20

Table 64. Effect of TMAC Concentration vs. REE recovery at pH 5, 25 ˚C and 1 hour on artificial montmorillonite.

			Feed		Solid Residue		Recovery (%)
Test#	Lixiviant	Conc. M	REE (ppm)	Wt (g)	REE (ppm)	Wt (%)	
M-La	TMAC	0.5	427.29	5	334.25	82.2	35.70
M-Y	TMAC	0.5	413.33	5	349.95	82.2	30.41
M-Ce	TMAC	0.5	478.13	5	398.94	82.2	31.41
M-Nd	TMAC	0.5	410.42	5	351.43	82.2	29.61
M-Dy	TMAC	0.5	603.75	5	499.68	82.2	31.97

Effect of Concentrations of Different Reagents

Figure 301 and Figure 302 show the results obtained on the kaolinite and montmorillonite samples, respectively, using some of new reagents . For La, the NH_4^+ and AMP^+ ions gave the best recoveries with 77% from the kaolinite sample, followed by DAH^+ and EAH^+ ions with recoveries in the range of 66 to 68%. One distinct advantage of using the AMP^+ ions is that its regent dosage was only 0.3 M AMP rather than 1 M for La. It appears that NH_4^+ ions may be the best option for the ion-adsorption clays prepared from montmorillonite. The reagent gave a 61% recovery for La. The recoveries of using other lixiviants were in the range of 30-40%. The recovery obtained with this reagent may be attributed to the small ionic radius that would be able to displace the RE3+ ions from the interior of the 2:1 layer structured clay mineral.

The results presented in Figure 303 and Figure 304 show recoveries for Y. Again, the NH_4^+ and AMP^+ ions gave the best recoveries in the range of 88- 91% from th e kaolinite sample, followed by the DAH^+ and EAH^+ ions with 70% recoveries. For Y, 0.3 M AMP^+ was sufficient rather than 1 M for NH_4^+ ions.

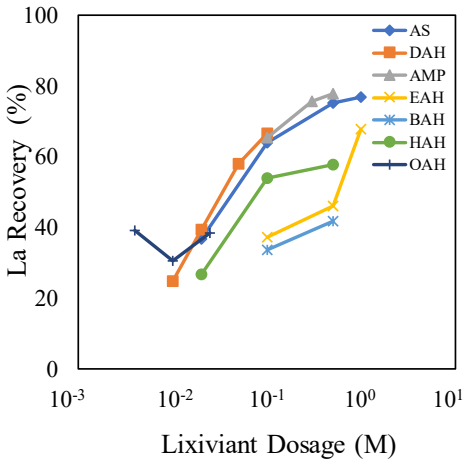

Figure 301. Effect of concentration of different lixiviants on the recovery of La from kaolinite at pH 5, 25˚C and 1 hr contact time.

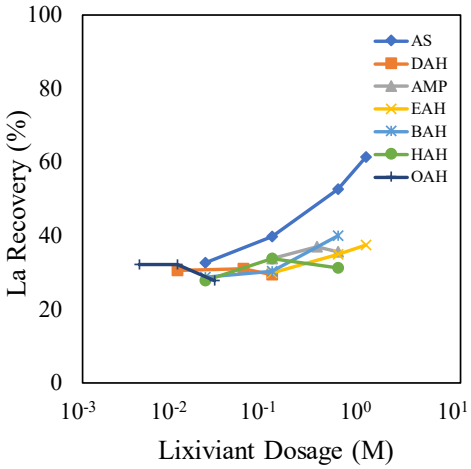

Figure 302. Effect of concentration of different lixiviants on the recovery of La from montmorillonite at pH 5, 25˚C and 1 hr contact time.

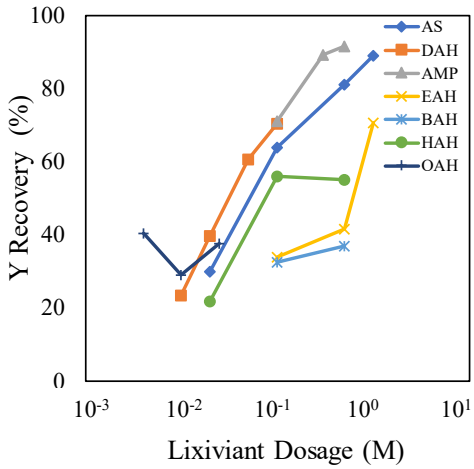

Figure 303. Effect of concentration of different lixiviants on the recovery of Y from kaolinite at pH 5, 25˚C and 1 hr contact time.

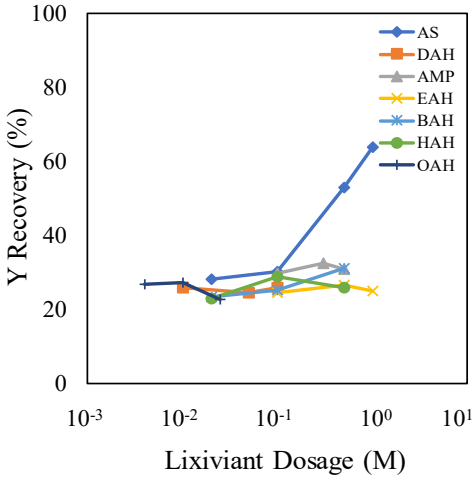

Figure 304. Effect of concentration of different lixiviants on the recovery of Y from montmorillonite at pH 5, 25˚C and 1 hr contact time.

For montmorillonite, NH_4^+ ions gave the best results with a 63% recovery of Y. Other lixiviants have recoveries in the range of 25-30%.

Figure 305 and Figure 306 show that NH_4^+ ions gave the recoveries of 40-45 % on the kaolinite and montmorillonite samples, respectively, for Ce. The novel lixiviants did not give any improvements

Figure 307 and Figure 308 show the results obtained Nd. The NH_4^+ and AMP^+ gave the best recovery at 77% on kaolinite sample. The DAH^+ and EAH^+ ions also gave recoveries of approximately 60 %. The AMP^+ ions gave excellent results for La. For the extraction of Nd from the montmorillonite sample, NH_4^+ gave a 51% recovery, which was better than any other lixiviant tested.

Figure 309 shows the results for Dy. The best reslts were obtained with the NH_4^+ and AMP^+ ions with 91-93% extraction form kaolinite. The DAH^+ and ethanol amine hydrochloride gave recoveries in the range of 57-59 %. At a 0.3 M AMP^+ ions, Dy responded well. It seems from Figure 310 that NH_4^+ gave a 60% recovery for Dy. Other lixiviants gave <30 % recoveries.

To summarize, ammonium sulfate gives the best recovery values for both clay types. However, AMP^+ gave comparable results. The new reagent leached ~91% recoveries for Dy and Y, which is better than achieved with NH_4^+ ions. For kaolinite, La and Nd responded well to AMP^+ and NH_4^+ ions. For montmorillonite, NH_4^+ ions was the best lixiviant.

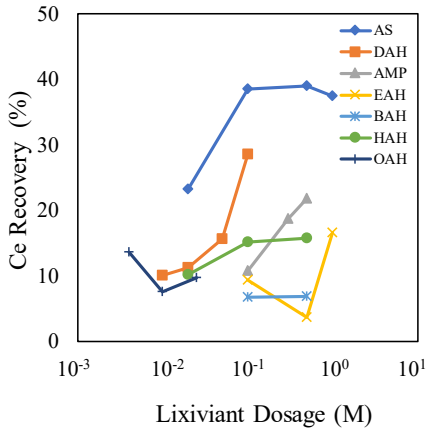

Figure 305. Effect of concentration of different lixiviants on the recovery of Ce from kaolinite at pH 5, 25˚C and 1 hr contact time.

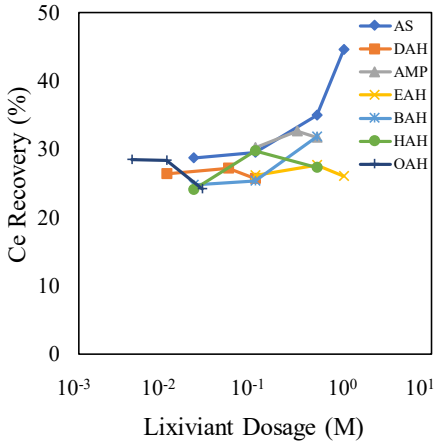

Figure 306. Effect of concentration of different lixiviants on the recovery of Ce from montmorillonite at pH 5, 25˚C and 1 hr contact time.

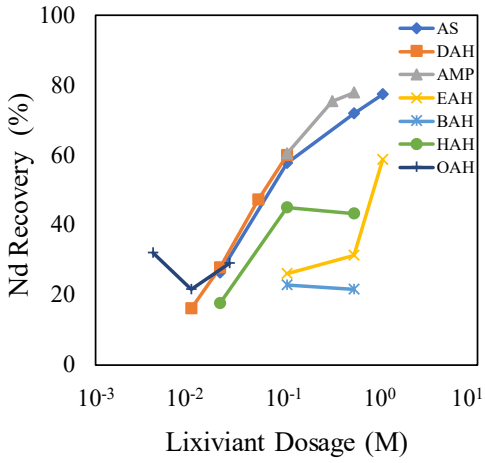

Figure 307. Effect of concentration of different lixiviants on the recovery of Nd from kaolinite at pH 5, 25˚C and 1 hr contact time.

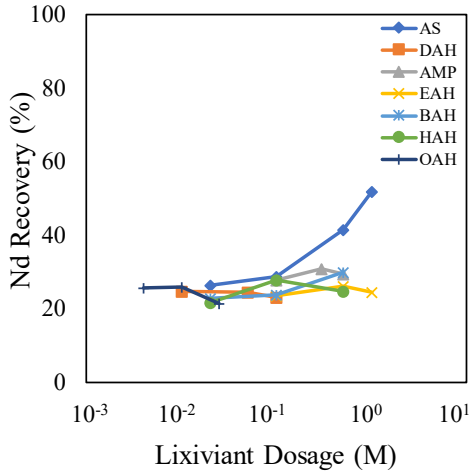

Figure 308. Effect of concentration of different lixiviants on the recovery of Nd from montmorillonite at pH 5, 25˚C and 1 hr contact time.

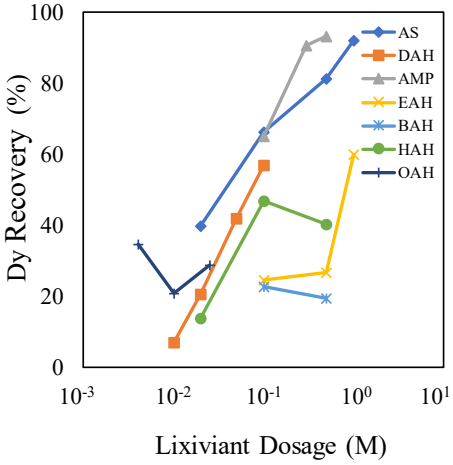

Figure 309. Effect of concentration of different lixiviants on the recovery of Dy from kaolinite at pH 5, 25˚C and 1 hr contact time.

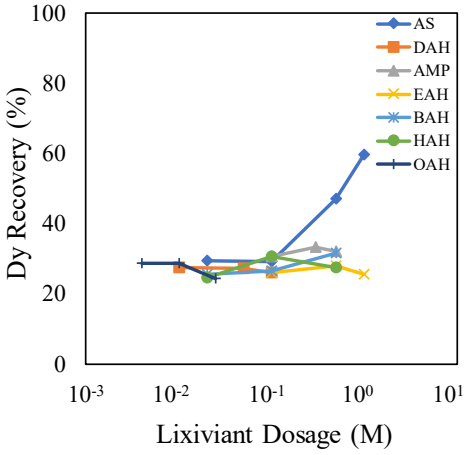

Figure 310. Effect of concentration of different lixiviants on the recovery of Dy from kaolinite at pH 5, 25˚C and 1 hr contact time.

XPS Characterization of LREE (La) Artificial Clay Sample

Introduction

X-ray photoelectron spectroscopy (XPS) was used to characterize the chemical state of representative light rare earth elements on the surface of artificial clay samples. It is well known that La 3d spectra, the primary La XPS feature, has two peaks ($3d_{5/2}$ and $3d_{3/2}$) resulting from spin-orbit splitting, either of which conveys the same chemical information of the La compound. Furthermore, each spin-orbit peak is split into two components by multiplet splitting, where the lower binding energy component is the primary La $3d_{5/2}$ peak and the higher binding energy component is the satellite peak due to final state effects. In addition to the peak position of the two multiplet-split components, the magnitude of the multiplet splitting and the intensity ratio of each multiplet-split component are also characteristic of different La-containing compounds (Suzuki et al., 1998; Siegmann et al., 1978; Sunding et al., 2011). In this work, an artificial La clay sample and several La compounds including $La(OH)_3$, La_2O_3, $LaCl_3$, $LaPO_4$, Monazite and ion-adsorbed La were measured by XPS. Characteristic La $3d_{5/2}$ features of the artificial La clay sample were compared to those of the La standards to provide insight into the identification of La speciation on the artificial sample.

Experimental

$La(OH)_3$ (Sigma-Aldrich, 99.99%), $LaCl_3$ (Alfa Aesar, 99.99%), $LaPO_4$ (Alfa Aesar, 99.99%) and Monazite were stored in a desiccator upon arrival and used as received. La_2O_3 (Sigma-Aldrich, 99.99%, hygroscopic) was stored in an Argon-filled glovebox upon arrival and was etched by Argon ion to remove hydrated surface layers prior to XPS measurements. Ion-adsorbed La was prepared by mixing Amberlite IR-120(H) ion exchange resin (Alfa Aesar) with $LaCl_3$ solution which was then washed by de-ionized water and dried in high vacuum. Artificial La K-clay sample was prepared with 5 REEs (La, Ce, Nd, Dy and Y) on Kaolinite clay (Sigma-Aldrich) with 400ppm each at pH 13, 25°C, 24h. Artificial La G-clay sample was prepared with 5 REEs (La, Ce, Nd, Dy and Y) on Georgia clay with 800ppm each at pH 12, 25°C, 24h. XPS characterization was performed on a PHI VersaProbe III scanning XPS microscope equipped with a monochromatic Al K-alpha X-ray source (1486.6 eV) with a base pressure of 3×10^{-8} Pa. XPS Spectra were acquired at 100 µm/100 W/20 kV over a 1400 µm × 100 µm sample area using 55 eV pass energy, which gives a $Ag3d_{5/2}$ full width at half maximum of 0.65 eV. All binding energies were referenced to C-C peak at 284.8 eV.

Results and Discussion

Figure 311 shows the La $3d_{5/2}$ XPS spectra of the standards, $La(OH)_3$, La_2O_3, $LaCl_3$, $LaPO_4$, Monazite and ion-adsorbed La, along with the artificial La clay sample. Characteristic properties of the La $3d_{5/2}$ feature including the peak position of the two multiplet-split components, the magnitude of the multiplet splitting (ΔE) and the intensity ratio of each multiplet-split component are summarized in Table 65. $La(OH)_3$ shows a La $3d_{5/2}$ peak position of 834.7 eV and a multiplet splitting of 3.7 eV, which are in excellent agreement with previously reported values of 835.1 eV and 3.9 eV respectively [3]. The peak intensity ratio of the satellite peak (838.4 eV) with respect to the La $3d_{5/2}$ peak (834.7 eV) is 0.71, which, to the best of our knowledge, is the first ratio documented for $La(OH)_3$. Compared to $La(OH)_3$, La_2O_3 shows a greater multiplet splitting of 4.5 eV, while $LaCl_3$ has a significantly larger peak intensity ratio of 1.43, These key differences provide evidence that our XPS approach is capable of distinguishing La-containing species from each other.

The artificial La G-clay sample demonstrates a La $3d_{5/2}$ peak at 834.9 eV, a multiplet splitting of 3.7 eV, and a peak intensity ratio of the satellite peak with respect to the La $3d_{5/2}$ peak of 0.68. All the three values match those of $La(OH)_3$, suggesting that the primary La species on the surface of the artificial clay sample is $La(OH)_3$. It is worth noting that the three characteristic values of the artificial La clay sample are also similar to those of $LaPO_4$/Monazite, however P signals were not detected by XPS which does not support the presence of $LaPO_4$/Monazite on the artificial sample surface.

Table 65. La $3d_{5/2}$ features for various La compounds.

Compound	La $3d_{5/2}$ BE (eV)	ΔE (eV)	Peak Intensity Ratio
$La(OH)_3$	834.7	3.7	1.00
	838.4		0.71
La_2O_3	834.1	4.5	1.00
	838.6		0.77
$LaCl_3$	835.6	3.5	1.00
	839.1		1.43
$LaPO_4$	835.3	3.3	1.00
	838.6		0.71
Monazite	835.4	3.3	N/A
	838.7		N/A
La^{3+} ion	836.7	2.8	1.00
	839.5		1.01
artificial La K-clay	834.9	3.7	1.00
	838.6		0.73
artificial La G-clay	835.1	3.6	1.00
	838.7		0.68

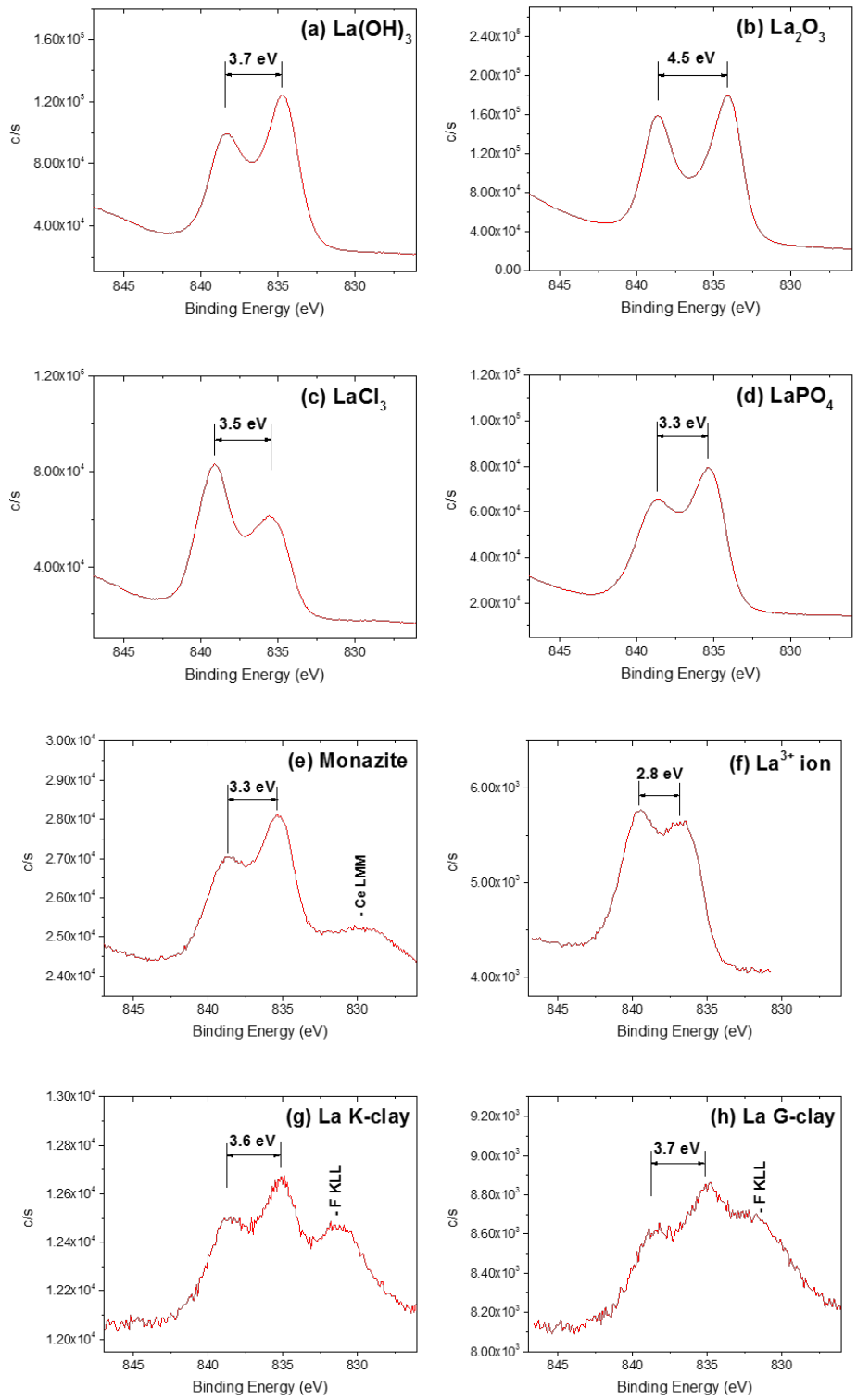

Figure 311. La $3d_{5/2}$ XPS spectra of various La compounds. (a) $La(OH)_3$; (b) La_2O_3; (c) $LaCl_3$; (d) $LaPO_4$; (e) Monazite; (f) La^{3+} ion; (g) artificial La K-clay sample prepared at pH 13, 25°C, 24h; (h) artificial La G-clay sample prepared at pH 12, 25°C, 24h.

XPS Characterization of HREE (Gd) Artificial Clay Sample

Introduction

X-ray photoelectron spectroscopy (XPS) was used to characterize the chemical state of representative heavy rare earth elements on the surface of artificial clay samples. Gd, Tb, Dy, Ho, Er, Tm, Yb and Lu are generally considered as heavy rare earth elements. The binding energies of 3d core electrons of Er, Tm, Yb and Lu are too high to be excited by the equipped Al X-ray source, therefore these four elements are impractical for XPS characterization. According to the XPS characterization of La compounds in *Part D*, the combination of $3d_{5/2}$ peak position, multiplet splitting strength and peak intensity ratio of multiplet-split components provides sufficient evidences to distinguish the chemical form of the rare earth element. Among Gd, Tb, Dy and Ho, Gd is reported to have the most significant multiplet splitting (Mullica et al., 1995), thus making it the best HREE candidate for XPS studies. In this work, an artificial Gd clay sample and several commercially available Gd compounds including $Gd(OH)_3$, Gd_2O_3 and $GdCl_3$ were measured by XPS. Characteristic Gd $3d_{5/2}$ features of the artificial Gd clay sample were compared to those of pure Gd compounds to provide insight into the identification of Gd species on the artificial sample.

Experimental

Gd_2O_3 (99.99%), $Gd(OH)_3$ (99.9%) and $GdCl_3$ (99.99%) were purchased from Alfa Aesar, stored in a desiccator upon arrival and used as received. Artificial Gd clay sample was prepared with 800ppm Gd on Kaolinite clay (Sigma-Aldrich) at pH 13, 25°C, 24h. XPS characterization was performed on a PHI VersaProbe III scanning XPS microscope equipped with a monochromatic Al K-alpha X-ray source (1486.6 eV) with a base pressure of 3×10^{-8} Pa. XPS Spectra were acquired at 100 µm/100 W/20 kV over a 1400 µm × 100 µm sample area using 55 eV pass energy, which gives a $Ag3d_{5/2}$ full width at half maximum of 0.65 eV. All binding energies were referenced to C-C peak at 284.8 eV.

Results and Discussion

Figure 312 shows the Gd $3d_{5/2}$ XPS spectra of the standards, $Gd(OH)_3$, Gd_2O_3, and $GdCl_3$, along with the artificial Gd clay sample. Characteristic properties of the Gd $3d_{5/2}$ feature including the peak position of the two multiplet-split components, the magnitude of the multiplet splitting (ΔE) and the intensity ratio of each multiplet-split component are summarized in Table 66. $Gd(OH)_3$ shows a Gd $3d_{5/2}$ peak position of 1187.8 eV, a multiplet splitting of 9.7 eV, and a peak intensity ratio of the satellite peak (1197.5 eV) with respect to the Gd $3d_{5/2}$ peak (1187.8 eV) of 0.14. Compared to $Gd(OH)_3$, Gd_2O_3 and $GdCl_3$ show similar multiplet splitting and peak intensity ratio, but distinct Gd $3d_{5/2}$ peak position. These key differences provide evidence that our XPS approach is capable of distinguishing Gd-containing species from each other.

The artificial Gd clay sample demonstrates a Gd $3d_{5/2}$ peak at 1187.8 eV, a multiplet splitting of 9.6 eV, and a peak intensity ratio of the satellite peak with respect to the Gd $3d_{5/2}$ peak of 0.19. All the three values match those of $Gd(OH)_3$, suggesting that the primary Gd species on the surface of the artificial clay sample is $Gd(OH)_3$.

Speciation of La on Natural Samples by XPS

It has been demonstrated that our XPS approach is capable of distinguishing both light and heavy REEs on artificial clay samples. However, it is challenging for XPS to probe the speciation of REEs on natural samples due to the naturally low concentration of REEs and signal interference from other elements such as Fe.

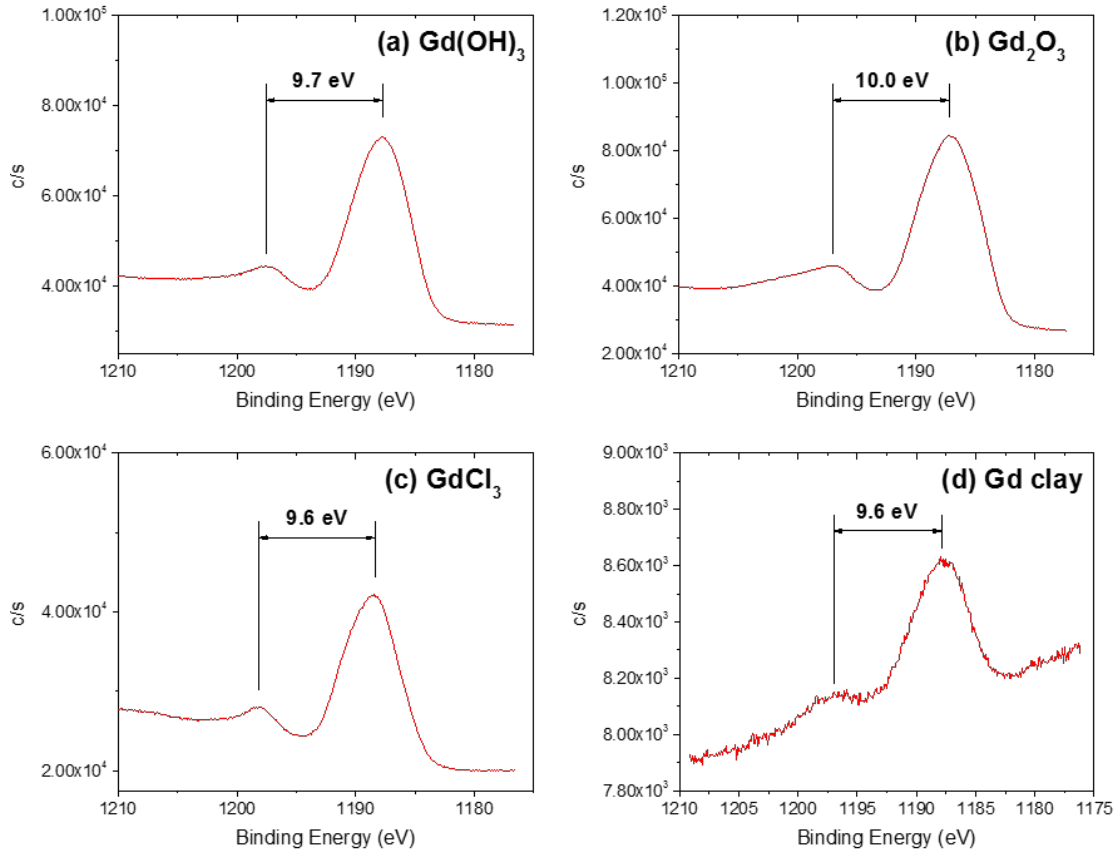

Figure 312. Gd $3d_{5/2}$ XPS spectra of various Gd compounds. (a) $Gd(OH)_3$; (b) Gd_2O_3; (c) $GdCl_3$; (d) artificial Gd K-clay sample prepared at pH 13, 25°C, 24h.

Table 66. Gd 3d5/2 features for various Gd compounds.

Compound	Gd $3d_{5/2}$ BE (eV)	ΔE (eV)	Peak Intensity Ratio
$Gd(OH)_3$	1187.8	9.7	1.00
	1197.5		0.14
Gd_2O_3	1187.1	10.0	1.00
	1197.1		0.19
$GdCl_3$	1188.5	9.6	1.00
	1198.1		0.14
artificial Gd K-clay	1187.8	9.6	1.00
	1197.4		0.19

So far we have investigated a number of natural samples by XPS, including:

1) Coal lump;
2) BHAM ash;
3) BLAM ash;
4) Beckley CR 750°C;
5) Beckley CR 750°C non-magnetic;
6) BHAM oxygen plasma;
7) BLAM oxygen plasma.

La $3d_{5/2}$ signals were not detected by XPS in Sample 1, while significant Fe LMM2 Auger features were present in the La $3d_{5/2}$ binding energy region in sample 2~6, making it impractical for La $3d_{5/2}$ peak deconvolution. It is worth nothing that for the oxygen plasma tr eated BLAM sample (sample 7), a preliminary peak deconvolution gives La $3d_{5/2}$ features with a La $3d_{5/2}$ peak at 835.0 eV, a multiplet splitting of 4.1 eV, and a peak intensity ratio of the satellite peak with respect to the La $3d_{5/2}$ peak of 0.67, which are similar to those of $La(OH)_3$ (see Figure 313). This is the first natural sample in this project of which potential REE features were detected by XPS, and the results are encouraging and worth further investigation.

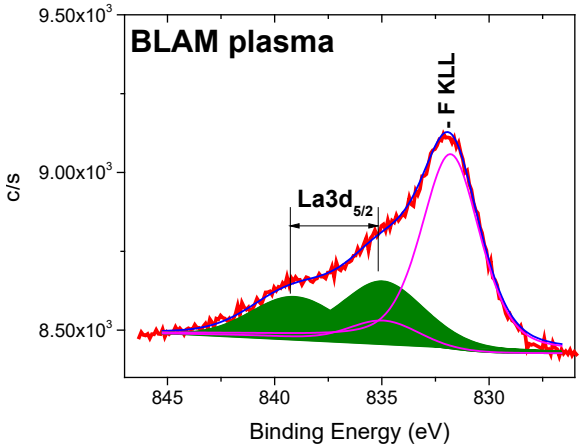

Figure 313. La $3d_{5/2}$ XPS spectra of BLAM oxygen plasma sample. Green areas are La $3d_{5/2}$ peaks from preliminary peak deconvolution.

Speciation of REEs on Natural Samples by XAS

In addition to XPS, we propose a detailed investigation into the speciation of REEs in natural coal samples using X-ray absorption spectroscopy (XAS) at the tender X-ray spectroscopy (TES) beamline in Brookhaven National Laboratory (BNL) to aid in the development of the aforementioned advanced REE recovery processes. XAS is a broadly used method to investigate atomic local structure as well as electronic states which are characteristic features of a chemical compound. This task aims to identify the speciation of representative light and heavy REEs (La and Gd) in natural coal samples by comparing the oxidation states and specific bonding environments to those of REE standard materials. The feasibility of this approach is supported by previous work from the National Energy Technology Laboratory (NETL) (Stuckman et al., 2016), which attempted to characterize both the oxidation state and species of cerium within similar coal combustion byproduct (CCB) samples. Most relevant to our studies is work performed on La (Larson et al., 1991) and Gd (Cao et al., 2015), where X-ray Near Edge Find Structure (XANES) spectra from unknown samples were compared directly with standards of different REE species. As shown in Figure 314, such comparisons can be used to identify the REE species present within the real-world samples.

We propose to pursue a similar strategy to develop an understanding of the speciation of La and Gd in key Appalachian coal samples, selected for their known high REE content (as determined via mass-spectrometric methods of fully digested samples). La and Gd standards and representative artificial and natural samples were submitted to BNL in June 2018 and are currently being analyzed by beamline scientists.

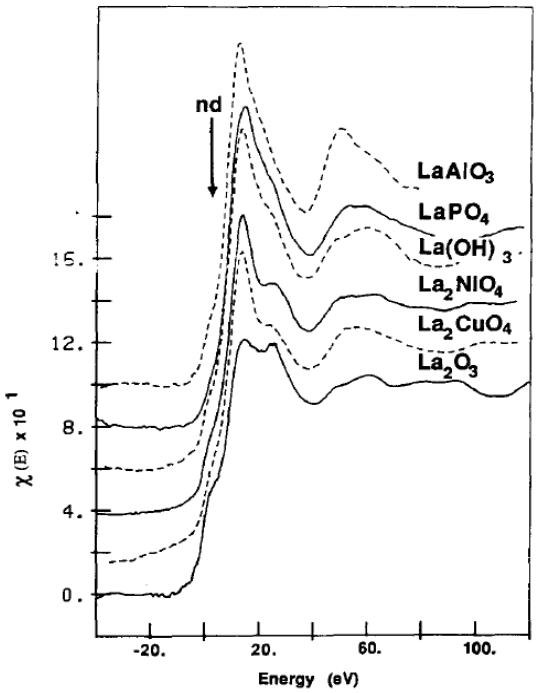

Figure 314. L_1 XANES χ(E) vs. energy (E_b = 6266 eV) spectra for various reference species of La, reproduced from (Larson et al., 1991).

Detailed Investigations on Artificial Clay Samples (Illite and Georgia Kaolinite)

In the current study, artificial ion-adsorption clays were prepared by immersing illite sample from Green Clays company and Georgia Kaolinite sample in solutions of REE chlorides of known concentration at different pHs, contact times, and temperatures. The samples were subjected to ion-exchange leaching tests. Artificial ion-adsorption clays were also prepared from these samples for a series ion-exchange extraction tests using a series of novel lixiviants developed in the present work. The results were compared with those obtained using the conventional lixiviant, *i.e.*, NH_4^+ ions.

Preparation of Artificial Ion-Adsorption Clay Samples

The illite sample purchased from Green Clays company was contacted with known solutions of rare earth elements, so that the REE^{3+} ions could adsorb on the mineral surface. The REE solutions were prepared from the following salts: $DyCl_3$, YCl_3, $LaCl_3$, $CeCl_3$, and $NdCl_3$. In each experiment, a 15 g sample of the clay was placed in a 125 mL Erlenmeyer flask at a 1:5 solid-to-liquid ratio, and the mixture was agitated by means of a magnetic stirrer for a preset time period and pH. The concentrations of the REE chloride solutions were determined in such a way that the resulting ion-adsorption clay would contain 400-600 ppm for each REEs and 2000 ppm TREEs. After the agitation, the clay samples were filtered and directly used for leaching without drying. The artificial ion-adsorption clays prepared in this manner were analyzed for REEs contents by means of ICP/MS. Blank tests conducted on the illite sample purchased from Green Clays Co. contained 26 ppm La, 51 ppm Ce, 22 ppm Y, and 24 ppm Nd of its own, while the Dy content was only 3 ppm. Figure 315 to Figure 317 show the results of artificial illite samples. Depends on the results pH 10, 25 ˚C and 24-hour have chosen as an optimum value to prepare the head sample for ion exchange leaching test.

The Kaolinite sample from Georgia was also used to prepare artificial ion-adsorption clays in the same manner as with illite. The samples were prepared such that the concentrations of the individual REEs were 800 ppm each. Blank tests showed that the run-of-the-mine Georgia Kaolinite sample contained 52 ppm La, 80 ppm Ce, 19 ppm Y and 51 ppm Nd, while the Dy content was only 5 ppm. Previous tests showed that REE adsorption is relatively independent of temperature and contact time but is sensitive to pH. As shown in Figure 318, the adsorption drops off sharply pH 12.

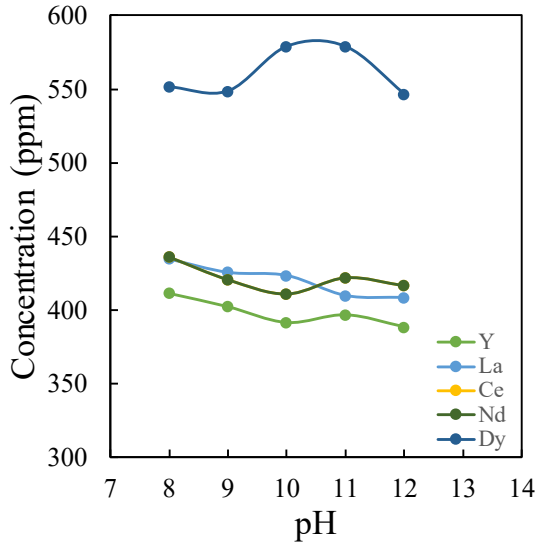

Figure 315. Effect of pH on the REE+Y contents of the artificial ion adsorption clay (illite) prepared at 25˚C and 24-hour contact time.

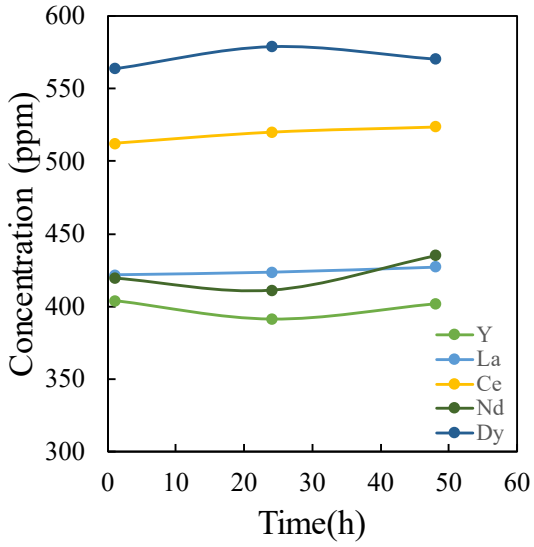

Figure 316. Effect of time on the REE+Y contents of the artificial ion adsorption clay (illite) prepared at 25˚C and pH 10.

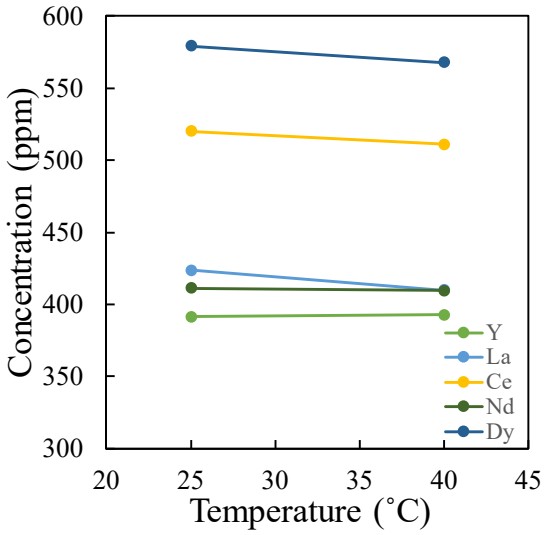

Figure 317. Effect of temperature on the REE+Y contents of the artificial ion adsorption clay (illite) prepared at 24-hour and pH 10.

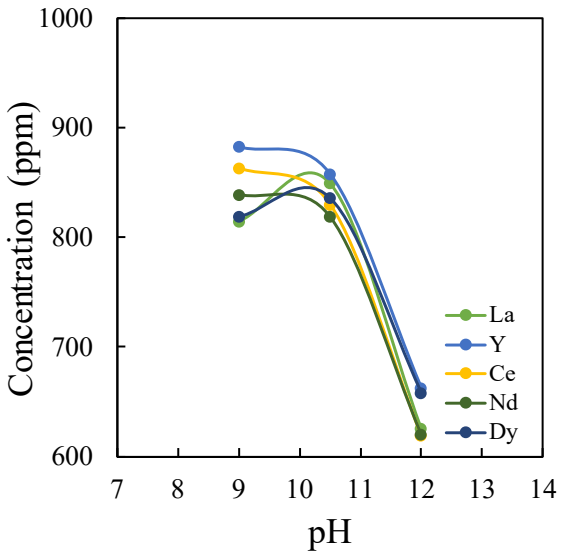

Figure 318. Effect of pH on the REE+Y contents of the artificial ion adsorption clay (Georgia Kaolinite) prepared at 24-hour and 25 ˚C.

Ion-Exchange Leaching Tests Using Novel Lixiviants

The ion-adsorption clay samples prepared from the kaolinite (Sigma Aldrich), Georgia kaolinite, and illite samples as described in the foregoing section were used for a series of leaching tests. All leaching tests were conducted at pH 5 and 25 ˚C by varying the lixiviant concentrations. Encouraging results were obtained by using ammonium sulfate (AS), dodecyl amine hydrochloride (DAH), 2-amino-2-methyl propanol (AMP) and hexadecyltrimethylammonium chloride (HTAC). It was difficult to dissolve DAH ($C_{12}H_{28}ClN$) and HTAC ($C_{16}TACl$) in water due to their long chain lengths. To overcome this problem, these lixiviants were dissolved in ethanol (20 ml) and the lixiviant-in-ethanol solution was mixed with 80 mL deionized water. Appropriate volume of the solution was added to a slurry for ion-exchange leaching tests.

Figure 319 to Figure 321 show the effects of AS on three different clay types. The recoveries of the Georgia Kaolinite and the Kaolinite from Sigma Aldrich obtained at 0.5M AS showed 80-90 % recoveries. The recovery of Ce was 40-50% of other REEs, possibly because Ce adsorbed as $Ce(IV)(OH)_4$. The recoveries obtained with illite sample were only 20-30 % for La, Y, Ce, and Nd, while the Dy recovery was ~50%. The results obtained with the illite sample were not as good as those obtained with kaolinites. Some of the REE^{3+} ions may have been adsorbed in between the layer structures of illite, which are difficult to be removed by the RNH_4^+ ions.

Figure 322 to Figure 324 show the results of the ion-exchange leaching tests conducted using DAH as a lixiviant on the artificial ion-adsorption clays prepared from illite and kaolinites, respectively. As shown, the recoveries increased with DAH concentration, with the recoveries being in the range of 30 to 50% for illite and 60 to 80% for kaolinites.

The results obtained with DAH showed similar trends as those obtained using NH_4^+ ions as lixiviant. Note, however, that the DAH concentrations of 0.05 M was substantially lower than those (0.5-1.0 M) required for NH_4^+ ions. For the illite sample, the recoveries increased sharply above 0.1 M DAH as shown in Figure 322. Had the DAH concentration was increased further by using a solvent such as ethanol,

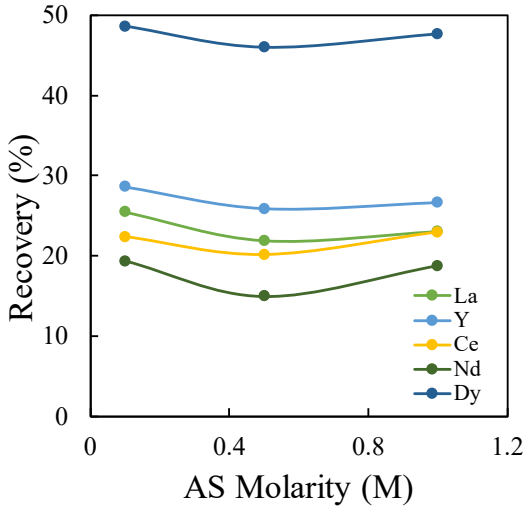

Figure 319. Effect of (NH4)2SO4 concentration on the recovery of REEs from the ion-adsorption clay (illite) at pH 5, 25˚C and 1 hr contact time.

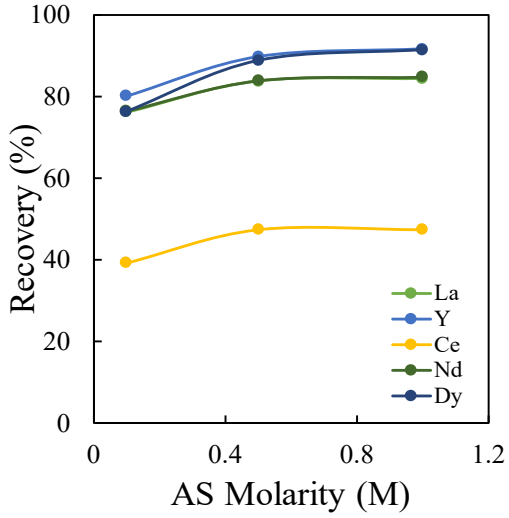

Figure 320. Effect of (NH4)2SO4 concentration on the recovery of REEs from the ion-adsorption clay (Georgia Kaolinite) at pH 5, 25˚C and 1 hr contact time.

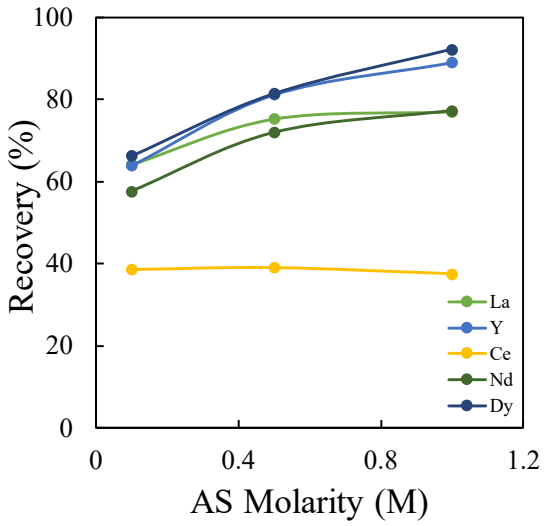

Figure 321. Effect of (NH4)2SO4 concentration on the recovery of REEs from the ion-adsorption clay (Kaolinite-Sigma Aldrich) at pH 5, 25˚C and 1 hr contact time.

the recovery would have been increased further. To sum up, DAH was a more efficient lixiviant than the conventional lixiviant, *i.e.*, AS.

Figure 325 to Figure 327 show the results of the ion-exchange leaching tests conducted on the kaolinite and illite samples using 2-amino-2-methyl-propanol ($H_2NC(CH_3)_2CH_2OH$). This reagent was chosen because it has a propanol group, which makes it more water soluble than DAH, which in turn should make it possible to increase the reagent dosage. AMP was not as efficient as NH_4^+ ions for the extraction of REEs from the illite sample, however. It is possible that 2-amino-2-methyl propanol cannot remove the RE^{3+} ions from the interior of the layer-structured mineral because of the larger molecular size.

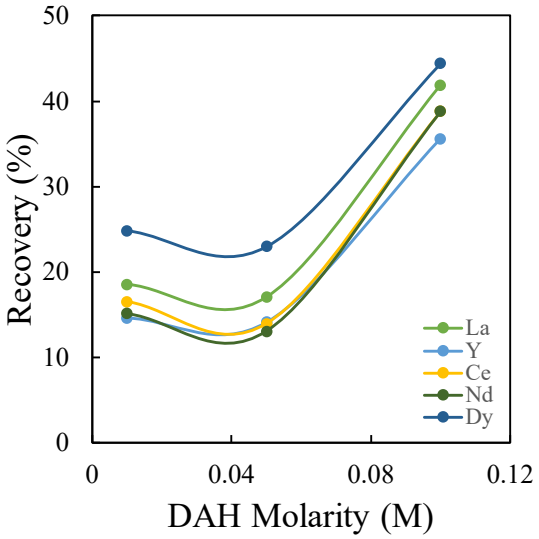

Figure 322. Effect of DAH concentration on the recovery of REEs from an ion-adsorption clay (illite) at pH 5, 25˚C and 1 hr contact time.

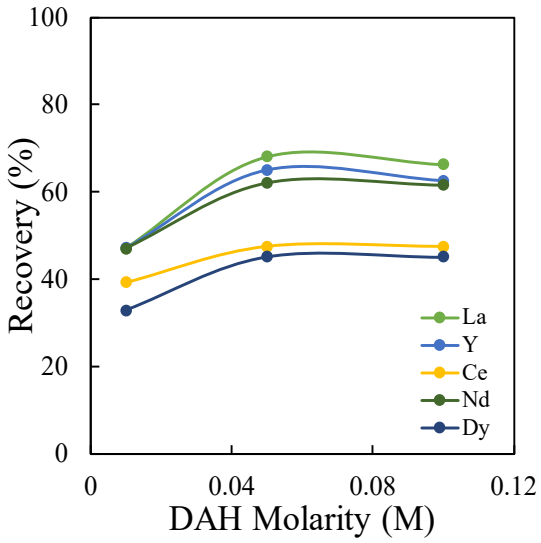

Figure 323. Effect of DAH concentration on the recovery of REEs from an ion-adsorption clay (Georgia Kaolinite) at pH 5, 25˚C and 1 hr contact time.

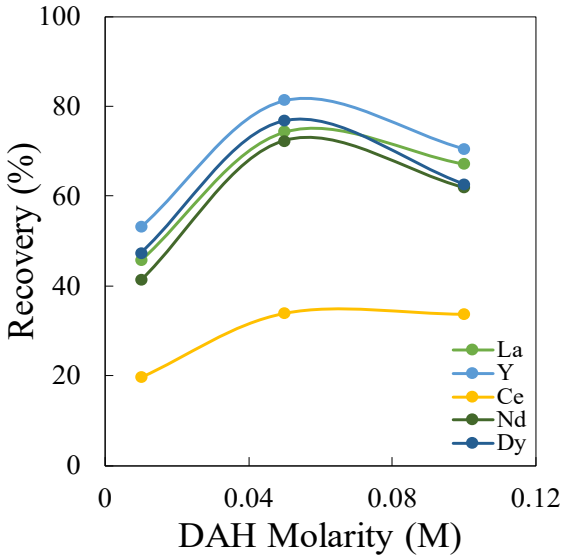

Figure 324. Effect of DAH concentration on the recovery of REEs from an ion-adsorption clay (Kaolinite-Sigma Aldrich) at pH 5, 25˚C and 1 hr contact time.

As shown in Figure 327, the reagent (AMP) was particularly efficient for the extraction of La and Nd from kaolinite. It was also efficient for the extraction of Y and Dy (~90% recovery) but not for Ce. Contrary to other lanthanide elements, which are usually physically adsorbed as trivalent cations, Ce^{3+} ions can be easily oxidized by atmospheric oxygen (O_2) to Ce^{4+}, and precipitates as cerianite, CeO_2, which makes it difficult to be recovered by ion-exchange leaching (Papangelakis and Moldoveanu,2014).

Table 67 to Table 69 show the results obtained on three different artificial clay samples using HTAC as lixiviant. With the Illite sample, recoveries were only in the range of 18-28% at 0.05 M. The

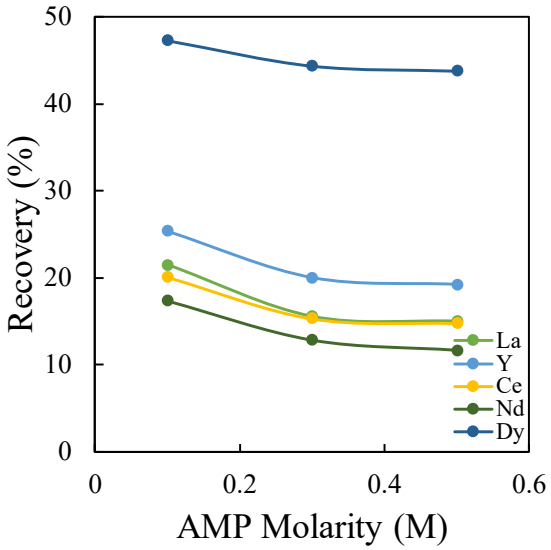

Figure 325. Effect of AMP concentration on the recovery of REEs from an ion-adsorption clay (illite) at pH 5, 25˚C and 1 hr contact time.

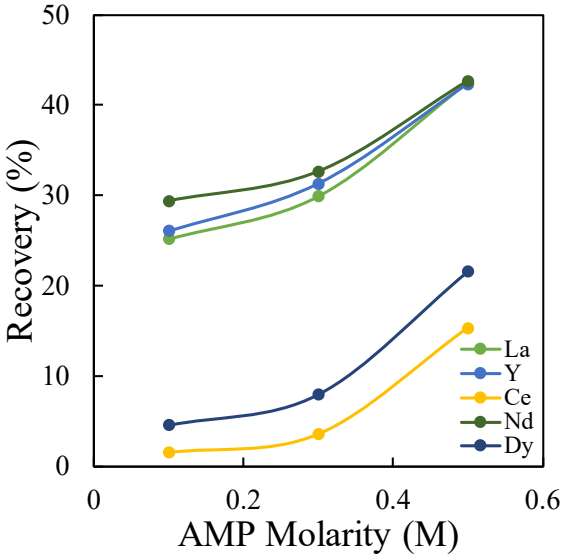

Figure 326. Effect of AMP concentration on the recovery of REEs from an ion-adsorption clay (Georgia Kaolinite) at pH 5, 25˚C and 1 hr contact time.

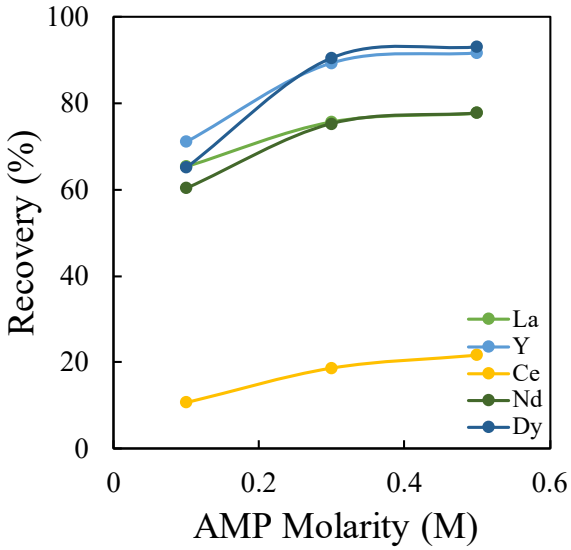

Figure 327. Effect of AMP concentration on the recovery of REEs from an ion-adsorption clay (Kaolinite-Sigma Aldrich) at pH 5, 25˚C and 1 hr contact time.

recoveries obtained using AS and AMP as lixiviants were also low. However, the concentrations of these lixiviants were almost ten times higher than that used for HTAC. The test results obtained with the Georgian kaolinite sample were much higher than those obtained with the illite sample. The results obtained with the kaolinite sample purchased from Sigma Aldridge were in the range of 80-90%. It is surprising indeed that ion-exchange leaching tests conducted on two different sources of kaolinite were so different. Note also that Ce recovery were only one-half of other lanthanides. As has already been noted, Ce adsorbs on clay in colloidal form, which is non-responsive to ion-exchange leaching.

Table 67. Effect of HTAC on the recovery of REEs from an ion-adsorption illite clay

REEs	HTAC Conc. (M)	Feed		Solid Residue		REE Recovery (%)
		REE (ppm)	Wt (g)	REE (ppm)	Wt (%)	
La	0.05	423.63	5	382.51	85.2	23.07
Y	0.05	391.46	5	374.87	85.2	18.41
Ce	0.05	498.31	5	473.17	85.2	19.10
Nd	0.05	411.32	5	394.97	85.2	18.19
Dy	0.05	579.15	5	494.87	85.2	27.20

Table 68. Effect of HTAC on the recovery of REEs from an ion-adsorption Georgia Kaolinite clay

REEs	HTAC Conc. (M)	Feed		Solid Residue		REE Recovery (%)
		REE (ppm)	Wt (g)	REE (ppm)	Wt (%)	
La	0.05	403.00	5	202.63	96.6	51.43
Y	0.05	346.00	5	106.83	96.6	70.17
Ce	0.05	431	5	303.34	96.6	32.01
Nd	0.05	385	5	172.62	96.6	56.69
Dy	0.05	326.6	5	158.32	96.6	53.17

Table 69. Effect of HTAC on the recovery of REEs from an ion-adsorption Kaolinite clay (Sigma Aldrich)

REEs	HTAC Conc. (M)	Feed		Solid Residue		REE Recovery (%)
		REE (ppm)	Wt (g)	REE (ppm)	Wt (%)	
La	0.05	486.13	5	105.44	90	80.48
Y	0.05	391.55	5	42.28	90	90.28
Ce	0.05	711.29	5	429.31	90	45.68
Nd	0.05	417.08	5	90.38	90	80.50
Dy	0.05	465.20	5	55.36	90	89.29

Influence of Preparation pH

Previous tests showed that REE adsorption is relatively independent of temperature and contact time but is sensitive to pH. In the present work, the artificial ion-adsorption clays were prepared at 9, 10 and 12. As shown in Figure 328 and Figure 329, REE adsorption increases with increasing pH. Figure 330 and Figure 331 show the effect of using ammonium sulfate (AS) as a lixiviant at pH 5 and 25 ˚C. The recoveries were in the range of 80-90%.

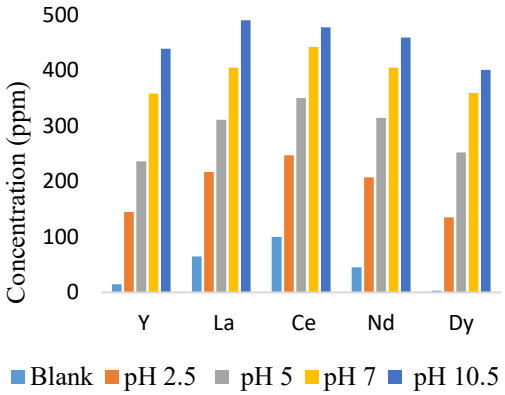

Figure 328. Effect of pH on the REE+Y contents of the artificial ion adsorption clay (Georgia Kaolinite) prepared at 24-hour and 25 ˚C.

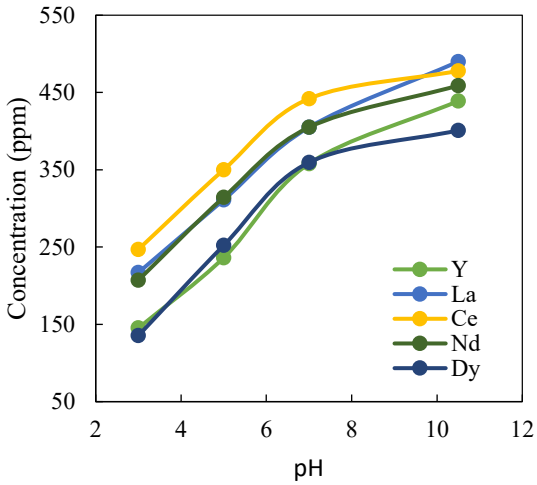

Figure 329. Effect of pH on the REE+Y contents of the artificial ion adsorption clay (Georgia Kaolinite) prepared at 24-hour and 25 ˚C.

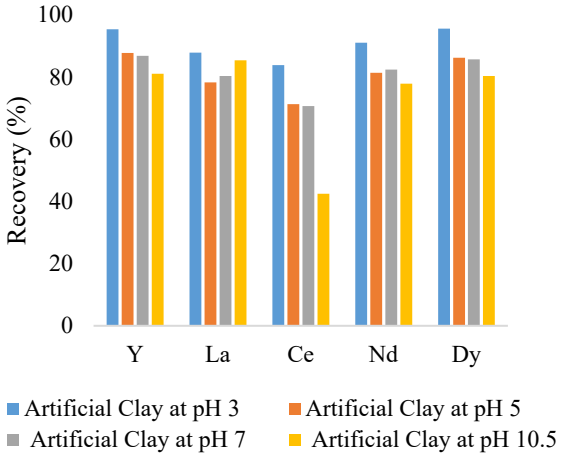

Figure 330. Effect of AS leaching on Georgia Kaolinite clay prepared at different pH values.

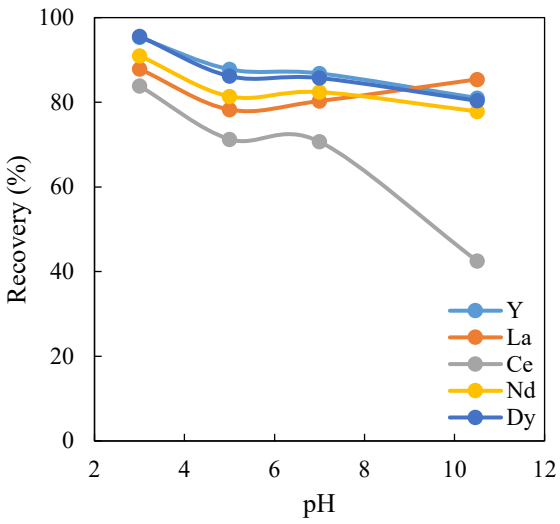

Figure 331. Effect of AS leaching on Georgia Kaolinite clay prepared at different pH values.

Effect of Iron on Ion-Exchange Leaching

The XPS analyses of the coal byproducts taken from operating plants showed that iron (Fe(III)) is omnipresent and often masks the lanthanide peaks. It was, therefore, decided to study the effects of iron on the extraction of REEs from both the artificial and real clay samples. To this end, ion-adsorption clays were prepared artificially by contacting samples of kaolinite from Georgia (Thiele Kaolin Company) in solutions containing both selected lanthanides and Fe^{3+} ions and the artificial ion-adsorption clays for a series of in-exchange leaching tests.

The artificial clays were prepared such that the clay samples would have ~400 ppm each of the La, Y, Ce, Nd, and Dy ions on the surface. Also added to the clay slurry at the same time was $FeCl_3$. The amounts of this reagent added were such that the clay samples would have 4,000, 8,000 and 16,000 ppm Fe on the clay sample. The solution pH was pH 10.5.

The ion-adsorption clay samples prepared in this manner were then subjected to ion-exchange (IX) leaching tests at 0.5 M AS, with the results shown in Figure 332. It is clearly shown that iron is detrimental to the REE recovery by ion-exchange leaching. For the case of Nd, the recovery dropped sharply from 90% to <10% in the presence of iron.

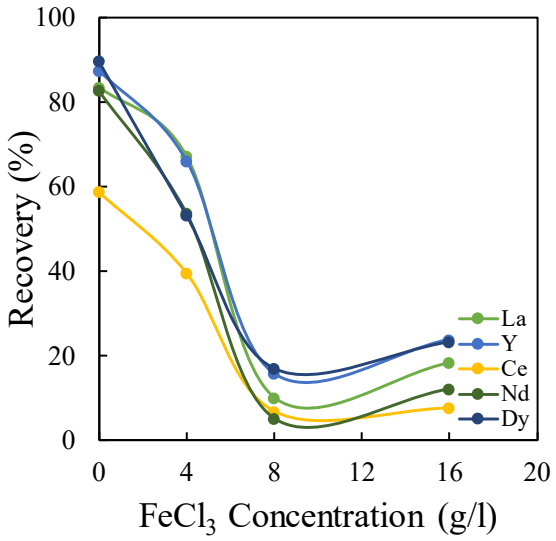

Figure 332. Effect of FeCl3 concentration on the recovery of REEs from an ion-adsorption Georgia Kaolinite clay. The ion-adsorption clay was formed at pH 10.5.

That the efficiency of IX leaching drops precipitously in the presence of iron suggests that REE ions co-precipitate with ion possibly as iron oxides, hydroxide, and/or oxyhydroxide. If this was the case, the only way to extract the REEs would be to dissolve the precipitates in water. One can dissolve them in an acid solution of course, of course. According to the E_h-pH diagram shown in Figure 333, iron oxide at pH ~2. An alternative is to use a reducing agent and dissolve the iron oxide at higher pH. According to the E_h-pH diagram, it is possible to dissolve the oxide at pH as high as 7 (Figure 334). This process, known as reductive leaching, is being used in the kaolin industry in Georgia to remove iron oxide from kaolin clay.

It has recently been known that Ce^{3+} oxidizes to Ce^{4+} and precipitates as $CeO_2/Ce(OH)_4$, which makes it difficult to be recovered by IX leaching (Lai et. al.,2017, Bau 1999 & 2009, Bao and Zhao, 2007). The results obtained in the present work with the artificial ion adsorption clays show indeed that Ce is more difficult to extract than other REEs by IX leaching.

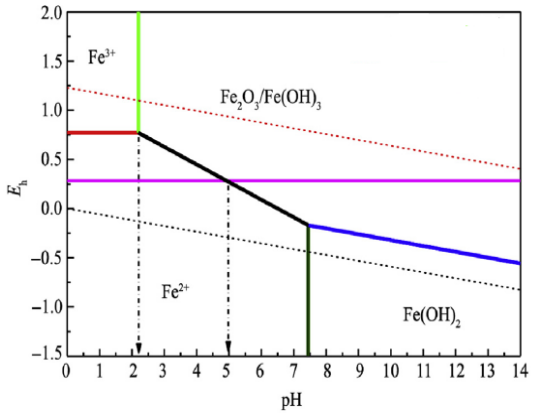

Figure 333. The pH-Eh graph of Fe-H2O. (Lai et al., 2018)

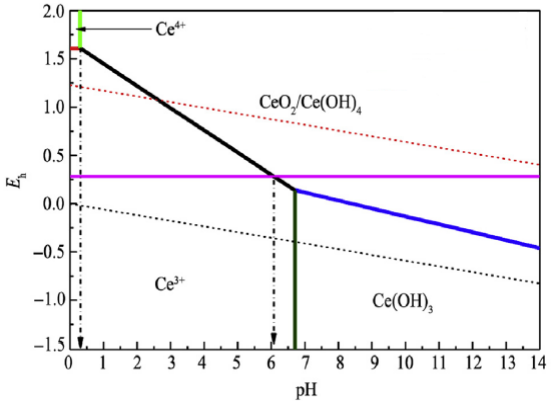

Figure 334. The Eh-pH diagram of Ce-H_2O. (Lai et al., 2018)

Speciation of LREE (La) on Artificial Clay Sample by TOF-SIMS Analysis

Introduction

As shown above, the XPS spectra of the artificial clay sample showed that La exists as $La(OH)_3$. Although the three characteristic bands of La are also similar to those of $LaPO_4$/Monazite, P signals were not detected by XPS, which does not support the presence of $LaPO_4$/Monazite on the artificial sample surface. To complement the XPS results, we utilized another surface analysis technique, *i.e.*, Time-of-Fight Secondary Ion Mass Spectroscopy (TOF-SIMS), to obtain chemical and molecular information of the REEs present on the surface of artificial clay samples. Fragment patterns of the artificial La clay samples were compared to those of the La standards to provide further insights into the identification of La speciation on the artificial sample.

Experimental

$La(OH)_3$ (Sigma-Aldrich, 99.99%) was stored in a desiccator upon arrival and used as received. Artificial La G-clay sample was prepared with 5 REEs (La, Ce, Nd, Dy and Y) on Georgia clay with 400 ppm each at pH 10.5, 25°C, 24 h contact time. Artificial La-mica sample was prepared with 5 REEs (La, Ce, Nd, Dy and Y) adsorbed to a ~2 cm×2 cm mica sheet with 40 ppm each at pH 10.5, 25 °C, 24h contact time. TOF-SIMS characterization was performed on an ION-TOF SIMS 5 Mass Spectrometer in Analytical Instrumentation Facility (AIF) at North Carolina State University.

Results and Discussion

Figure 335 shows the positive ion mass spectra of $La(OH)_3$ standard and the artificial La clay sample. In addition, artificial La mica sample was also prepared and measured as a model supplement of the clay sample, presumably with better signal resolution due to its flat surface. Mica was chosen because its basal surface consists of a layer silica octahedra, which is also found on kaolinite. Two primary

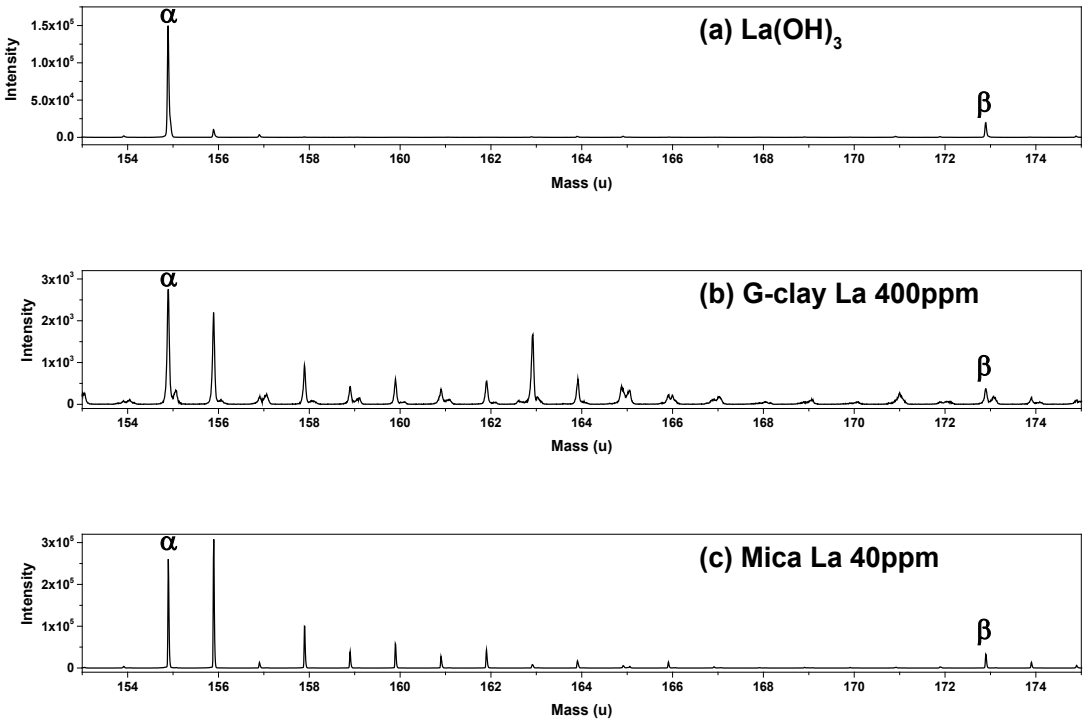

Figure 335. Positive ion mass spectra of various La compounds. (a) La(OH)3; (b) artificial La G-clay sample prepared at pH 10.5, 25°C, 24h; (c) artificial La Mica sample prepared at pH 10.5, 25°C, 24h. α - LaO+; β - LaO2H2+.

fragments of $La(OH)_3$ were detected in the m/z region of 150 to 180 at m/z=154.9 and m/z=172.9, which are attributed to LaO^+ (α) and $LaO_2H_2^+$ (β) respectively, with the peak intensity ratio β/α = 0.13. For the artificial clay and mica samples, LaO^+ (α) and $LaO_2H_2^+$ (β) fragments were also present, with similar peak intensity ratio β/α of 0.15 and 0.14 respectively. These results suggest that the primary La species on artificial clay samples was $La(OH)_3$, which was consistent with the XPS analysis results.

Figure 336 shows the negative ion mapping of the artificial La G-clay sample in a 200 µm × 200 µm area by measuring the primary fragments of clay (SiO_2^-), phosphates (PO_3^-) and those of the five rare earth elements added: $LaO_3H_2^-$, CeO_2^-, NdO_2^-, DyO_2^- and YO^-. All the five rare earth elements demonstrate the same distribution pattern on the clay surface, suggesting that there are no preferred binding sites on the clay surface for individual rare earth species. PO_3^- was not detected, which further confirms that $LaPO_4$/Monazite are not present on the artificial sample surface. Similar but more distinct results were obtained from the negative ion mapping of the artificial La mica sample (Figure 337). All the five rare earth

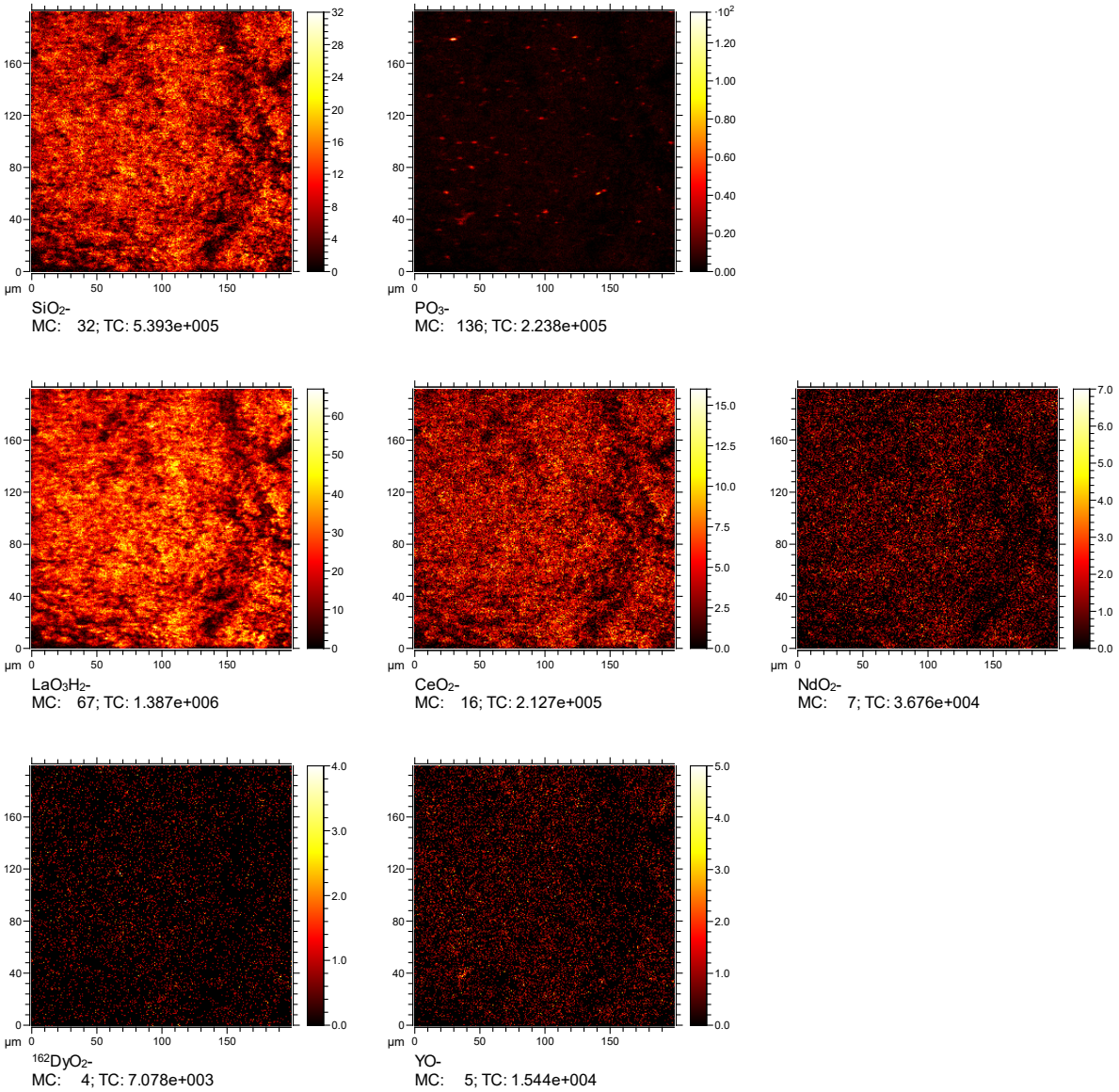

Figure 336. Negative ion mass spectra mapping of the artificial La clay sample in a 200 µm × 200 µm area.

elements form aggregates on the mica surface, excluding the formation of phosphates. The combination of XPS and TOF-SIMS characterizations conclude that the primary rare earth species on the surface of the artificial clay sample in alkaline pH conditions was rare earth hydroxides.

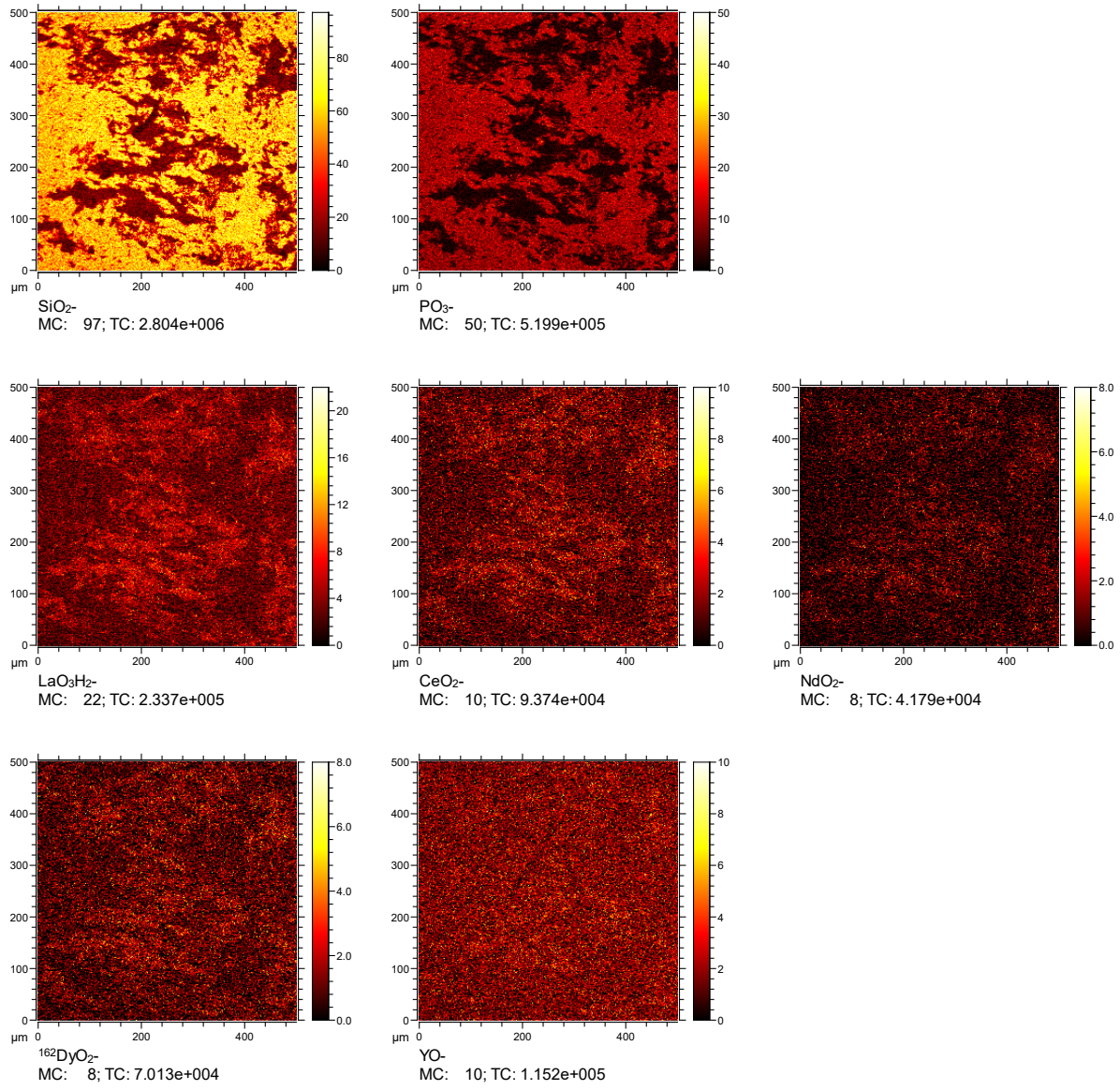

Figure 337. Negative ion mass spectra mapping of the artificial La Mica sample in a 200 µm × 200 µm area.

XPS Characterization of LREE (La) Artificial Clay Sample with addition of Fe

Introduction

We anticipated originally that artificial ion-adsorption clay the primary rare earth species are colloidal forms, e.g. REE hydroxides, on artificial clay sample at alkaline pH. However, we have found that a simple $(NH_4)_2SO_4$ ion-exchange leaching of these artificial clay samples yields surprisingly high REE recovery (> 80%), which is inconsistent with the theory that the colloidal form of REE cannot be efficiently leached by ion-exchange lixiviants. By comparing the elemental composition of artificial and natural clay samples, it is worth nothing that Fe contents are always present in natural samples but negligible in artificial clays. In addition, it has been suggested that rare earth elements are attached to Fe in colloidal form of ion-adsorption REE clay in China (Lai et al., 2018). Therefore, we speculate that the presence of Fe on the clay surface is essential to the formation of colloidal phase of REE in nature, e.g. (REE, Fe)OOH. In this work, X-ray photoelectron spectroscopy (XPS) was used to characterize the chemical state of Fe on the surface of artificial clay samples.

Experimental

Artificial REE G-clay samples with addition of Fe were prepared with 5 REEs (La, Ce, Nd, Dy and Y) on Georgia clay with 400ppm each plus 4000ppm/8000ppm/16000ppm of Fe at pH 10.5, 25°C, 24h. XPS characterization was performed on a PHI VersaProbe III scanning XPS microscope equipped with a monochromatic Al K-alpha X-ray source (1486.6 eV) with a base pressure of 3×10^{-8} Pa. XPS Spectra were acquired at 100 µm/100 W/20 kV over a 1400 µm × 100 µm sample area using 55 eV pass energy, which gives a $Ag3d_{5/2}$ full width at half maximum of 0.65 eV. All binding energies were referenced to C-C peak at 284.8 eV.

Results and Discussion

Figure 332 shows that the recovery of IX leaching decreases with increasing Fe concentration, at which artificial ion-adsorption clays are formed. This finding suggests that the colloidal form of REEs may be a complex oxide, which may be written as (RE, Fe)OOH. Figure 338 shows the $Fe2p_{3/2}$ XPS spectra of the artificial RE-clay samples formed at 0, 4, 8, and 16 g/L $FeCl_3$ concentrations. For the sample prepared without Fe (Figure 338a), no Fe signals were detected as expected. Similar Fe $2p_{3/2}$ features were observed with those formed at higher $FeCl_3$ concentrations as shown in Figure 338b-d. The primary peak at 710.5 eV is broad, suggesting that it consists of multiple Fe chemical states including Fe^{2+} and Fe^{3+}. The characteristics of these Fe features do not match single-valence Fe compounds, such as FeO, Fe_2O_3, FeOOH and $FeCl_3$ (Grosvenor et al., 2004), but are similar to those of Fe_3O_4 (Grosvenor et al., 2004), which further supports the presence of multiple Fe chemical states. More XPS analysis are needed to provide insights into the speciation of Fe and its correlation with rare earth elements on the artificial clay samples.

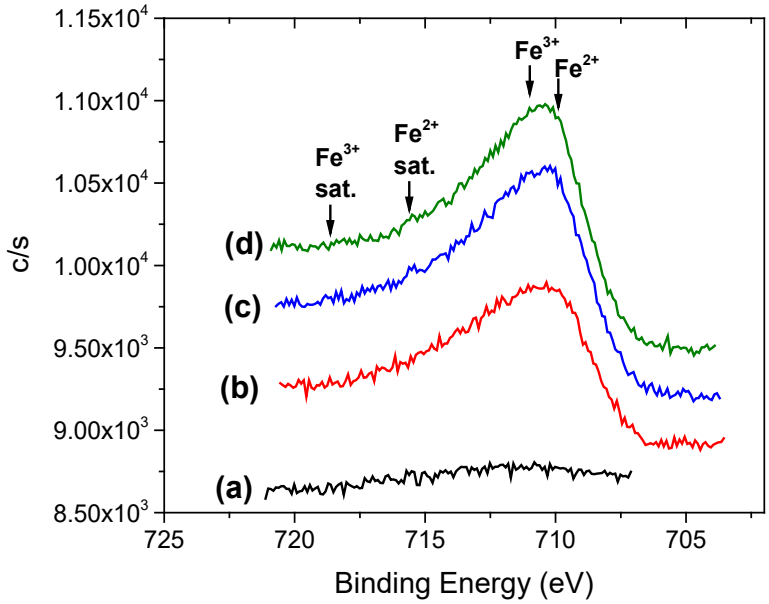

Figure 338. Fe $2p_{3/2}$ XPS spectra of various artificial REE + Fe clay samples. (a) artificial G-clay sample prepared with 400ppm of La, Ce, Nd, Dy and Y at pH 10.5, 25°C, 24h; (b) artificial G-clay sample prepared with 400ppm of La, Ce, Nd, Dy and Y plus 4000ppm of Fe at pH 10.5, 25°C, 24h; (c) artificial G-clay sample prepared with 400ppm of La, Ce, Nd, Dy and Y plus 8000ppm of Fe at pH 10.5, 25°C, 24h; (d) artificial G-clay sample prepared with 400ppm of La, Ce, Nd, Dy and Y plus 16000ppm of Fe at pH 10.5, 25°C, 24h.

Subtask 5.5 – Leaching

Acid Leaching of Coal Refuse (Exploratory Studies)

Introduction

The objective of Subtask 5.5 is to conduct fundamental studies to obtain the information needed for researchers to assess the potential of extracting rare earth elements from coal sources using hydrometallurgical processes. Leaching studies are being conducted on rare earth minerals that may exist in coal sources including monazite, bastnaesite, xenotime and fluorapatite, as well as four well-known coal sources in the U.S., i.e., Illinois No. 6, Fire Clay, Pocahontas No. 3, and Lower Kittanning coals. In this section, the initial leaching studies on Illinois No. 6 and Fire Clay coal sources are described.

The Fire Clay coal is an excellent source for REE extraction due to its high recovery values of REEs. Leaching at a temperature of 75ºC using 1.2 M sulfuric acid resulted in over 75% of the total REEs in the coal being recovered within 2 hours and the recovery of over 85% after 24 hours. The kinetic data obtained from leaching over a range of temperatures suggested that the leaching process follows the shrinking core model with a mixed control mechanism that may be a result of several heterogenous materials leaching simultaneously. The activation energy determined from data obtained over a range of temperatures using 1 M sulfuric acid was 36 kJ/mol for the first 20 minutes of reaction time and 27 kJ/mol for the reaction period of 20 to 120 minutes.

An Illinois No. 6 coal seam source showed very positive leaching characteristics. Scandium recovery was especially elevated relative to other coal sources. Test data indicated that the leaching of the 1.8 x 2.2 specific gravity material achieved the highest total REEs recovery of 62% among all density fractions. The finding agrees with past investigations which indicated that the middling material within coal sources tends to be the most suitable material for REE recovery. Scandium recovery of 87% was achieved when treating the 2.2 SG sink fraction of the 1 x 0.15 mm size class when leaching with 1.2 M sulfuric acid at 75ºC. This fraction typically reports to the spiral reject stream in a coal preparation plant. As such, it is a very accessible material for the recovery of scandium. Scandium was found to be correlated with calcium carbonate among the size by density fractionated samples.

Materials

A representative sample (~200 kg) of the Illinois No. 6 seam coal was collected from Alliance Coal's Hamilton County operation located in southern Illinois. Upon arrival, the coal was processed following a characterization procedure shown in Figure 339. The coal was initially screened at 9.5 mm and 1 mm. The plus 9.5 mm and 9.5 x 1 mm size fractions were subject to density fractionation using an ultrafine magnetite-based media adjust to specific gravity (SG) values of 1.4, 1.8 and 2.2. The material finer than 1 mm was wet screened at 100 mesh (150 microns) on a vibration screen. The 1 x 0.15 mm size material was subjected to density separation at SG value of 2.2 using a heavy liquid lithium metatungstate (LMT). The material finer than 0.15 mm was decarbonized using a three-stage froth flotation (Rougher-Cleaner-Recleaner) process to obtain a low ash clean coal from the froth and a combined tailings material.

A representative sample (~200 kg) of the Fire Clay seam coal was collected from Blackhawk Mining's Blue Diamond Complex located in eastern Kentucky. The material was a prep plant middling sample collected from the product stream of a secondary heavy media vessel. The sample was crushed and ground to a particle size smaller than 1 mm using a laboratory jaw crusher and hammer mill. A representative split was pulverized to a top size of 80 mesh (170 microns) then subjected to further size reduction in an attrition mill for 20 minutes at 200 rpm rotation speed. The solid concentration used in the attrition mill was 40%. The grinding condition was optimized in a previous study performed at the University of Kentucky and funded by DOE. The ground material was subjected to froth flotation to recover clean coal material using diesel fuel No. 2 as the collector and a MIBC solution as the frother. The tailings material collected from the coal recovery process was further treated by a second flotation step using hydroxamic acid at a pH value of 9.5 to remove acid consuming materials. The tailing material was the feed to the current leaching studies. A schematic represents the process is provided in Figure 340.

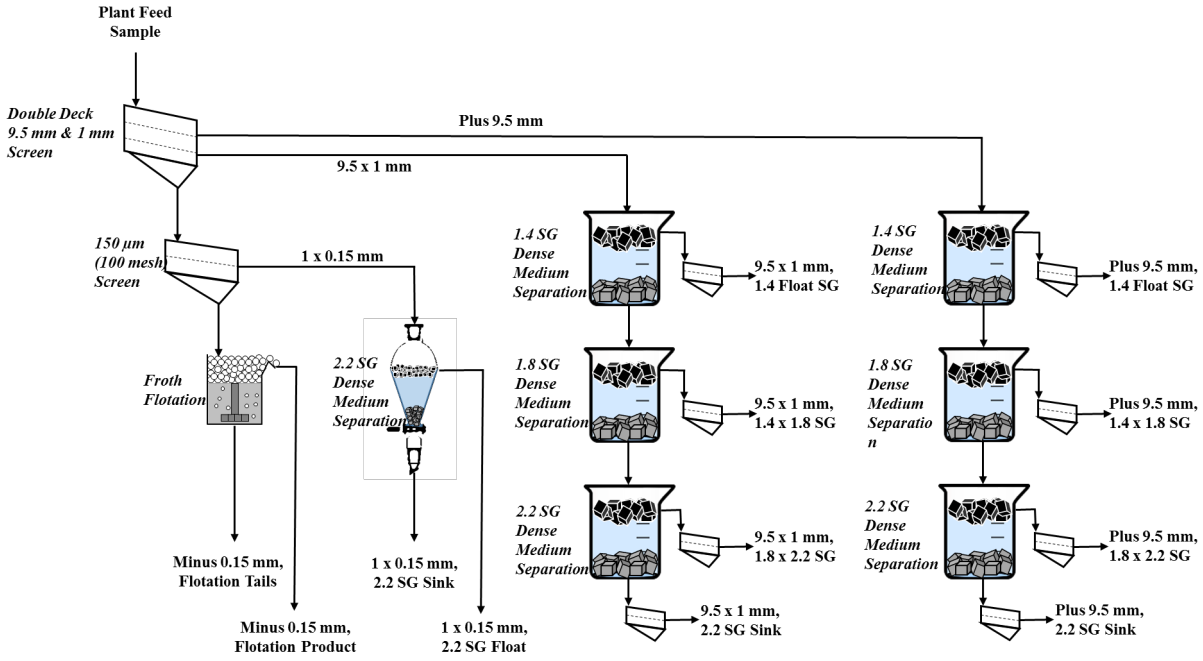

Figure 339. Flowsheet showing the sample preparation process conducted on the Illinois No. 6 coal source.

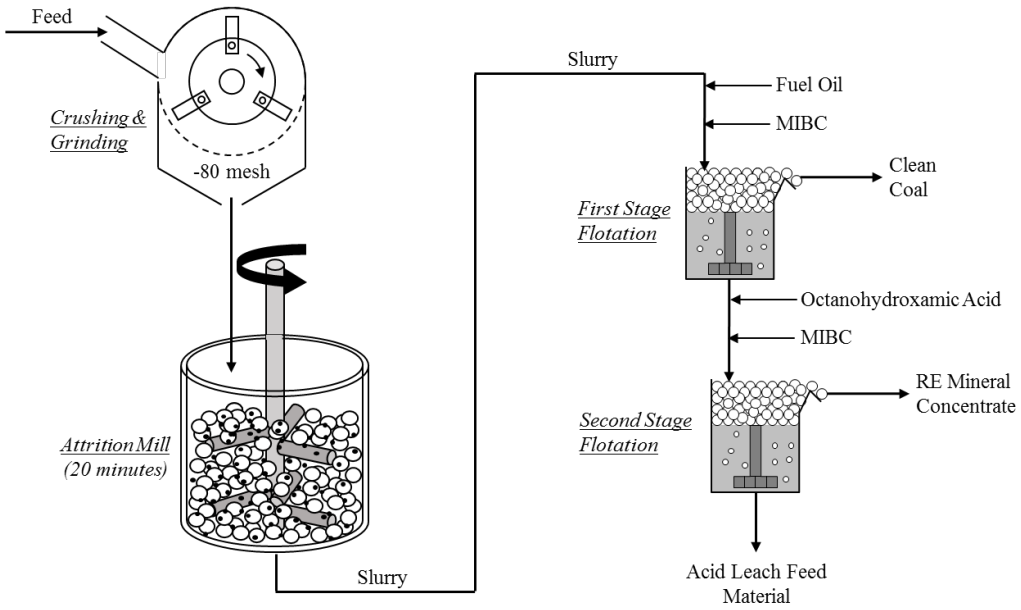

Figure 340. Sample preparation on Fire Clay middling material.

Methods

Leaching experiments were conducted in a triple neck round bottom flask with the middle neck connected to a total reflux condenser. The reactor was placed in a water bath where heating was provided using an immersion heater equipped with a precise temperature control system to maintain the temperature during the test. Agitation was provided using a magnetic stirrer. The leaching experiments were conducted using deionized water and trace metal grade acid (purity>99.99%).

For the Illinois No. 6 basin coal material, a total 12 samples from different size by density fractions were ground to a particle size less than 80 mesh (177 micron). Acid leaching experiments were conducted on each sample using 1.2 mol/L of sulfuric acid with 10 g/L solid concentration at 75 ℃. Sample were collected periodically at 10, 30, 60, 180 and 300 minutes and analyzed for REE content to obtain the leaching kinetic data. The samples were centrifuged to separate the solid and liquid. At the completion of the leaching experiment, the remaining solid residue was filtered using a vacuum flask and thoroughly washed with deionized water.

For the Fire Clay coal source, leaching experiments were conducted to investigate the effect of different acid types (i.e. H_2SO_4, HCl, and HNO_3), acid concentration (i.e. 0.1M, 0.5M, 1M, and 2M etc.), solid-to- liquid ratio (i.e. S/L=1/100, 1/50, 1/10, 1/5 etc.), and various temperatures (i.e. 298K, 313K, 323K, 333K, and 348K). To assess the leaching kinetics, samples were collected at 1 min, 3 min, 5 min, 10 min, 20 min, 30 min, 60 min, 90 min, and 120 min, to obtain a precise kinetic curve. A micro-filter (0.45 microns) was used to separate the leachate from solids within 20 seconds to immediately stop the solid-liquid reaction. The final solid residue was filtered and washed with deionized water.

Both leachate and solid residue samples collected from the tests were subject to ICP analysis for individual REEs concentration and a swipe of other major elements present in sample. The standard solution used in the ICP analysis was the VHG-SM68 multi standard which contains 48 elements. Leaching recovery represents the amount of materials in the test feed source that was solubilized into solution during the leaching process. The value was determined using Eq. [5.5.1]:

$$\text{Leaching recovery (\%)} = \frac{c_L * V_L}{c_L * V_L + c_{SR} * m_{SR}} * 100\% \qquad [5.5.1]$$

where c_L is the elemental concentration in the leachate solution (µg/ml); V_L the volume of the analyzed leachate solution (ml);c_{SR} the elemental concentration in solid residue (µg/g); and m_{SR} the weight of solid residue (g).

X-ray diffraction (XRD) analyses were conducted on all the feed samples using an Advance D8 instrument produced by the Bruker company. The scanning was performed from 10° to 70° with a stepwise increase of 0.02° and a scanning speed of 0.5°/min. The XRD spectra were analyzed to estimate concentrations of major mineral components using the EVA software developed by the Bruker company.

Results and discussions – Fire Clay Coal

The decarbonized Fire Clay middling material contains 607 ±18 ppm of total REEs of which Ce content accounted for 42% of the total REEs (Figure 341a). The Fire Clay material is rich in light REEs as indicated by a content of 534 ppm or 88.0% of the total. Yttrium is the most abundant heavy REE with a concentration of 47 ppm. The major minerals present in the sample are quartz, kaolinite, illite, and muscovite as shown in the XRD plot in Figure 341b. A previous study found that REEs in the Fire Clay coal were strongly associated with micro-dispersed kaolinite that can be liberated and released through size reduction (Zhang et al., 2018).

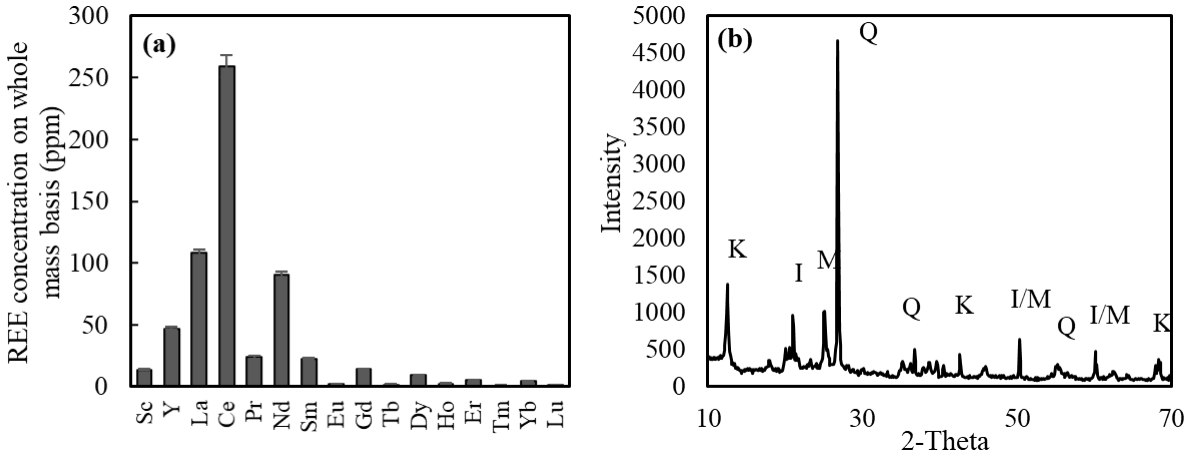

Figure 341. (a) Rare earth content on whole mass basis in decarbonized Fire Clay middlings and (b) X-ray Diffraction analysis of the material. (Q-quartz, K-kaolinite, I-illite, M-muscovite.)

Effect of acid type

Leaching experiments were conducted using different inorganic acids using an acid concentration of 1M, solid/liquid ratio of 10 g/L and a temperature of 348 K. Sulfuric acid (H_2SO_4), hydrochloric acid (HCl), and nitric acid (HNO_3) were used to study the leaching process. Figure 342 compares the REE leaching recovery and reaction rate between the different lixiviants. The total REE (TREEs) recovery values of 80%, 76%, and 74% were achieved after 3 hours of leaching using HCl, HNO_3, and H_2SO_4 solution, respectively. The pH of the leachate solutions at the end of the tests were 0.105, 0.113, and 0.112, respectively.

Hydrochloric acid provided the fastest leaching rate which achieved 73% recovery after the first 5 minutes of leaching, and slowly reached equilibrium after 3 hours. Nitric acid also provided fast leaching rate at the first 30 minutes. Sulfuric acid was the least effective under the leaching conditions and provided the slowest leaching rate. The finding is likely due to the fact that sulfate ions have a higher coordination ability with rare earths than chloride ions even in high monovalent concentration solutions (Xiao et al., 2016).

The coal-based leachate contains high concentrations of trivalent ions that may coordinate with sulfate ions resulting in depression of the rare earth-sulfate coordination. In addition, sulfuric acid requires two steps of dissociation reaction to release H^+ into solution whereas hydrochloric acid and nitric acid dissociates more rapidly into solution. Viscosity of the sulfuric acid solution is another factor that could have resulted in the slower reaction rate as the wetting rate of the solid particle surfaces is reduced

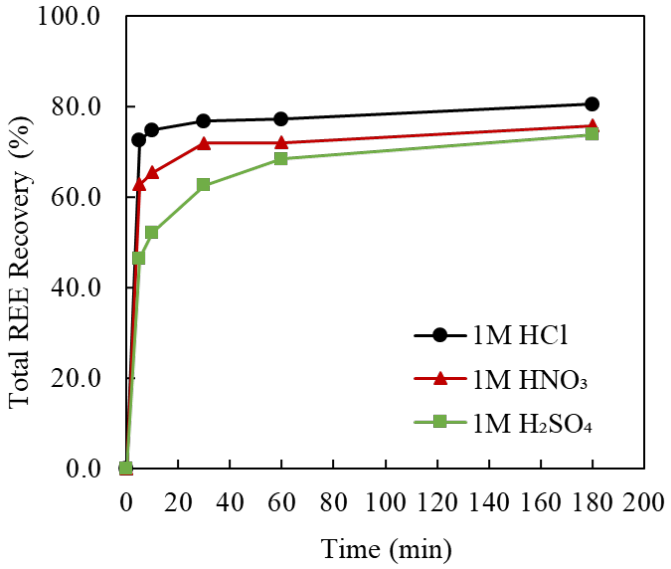

Figure 342. Effect of acid type on the leaching recovery of total rare earth elements contained in the Fire Clay coal middlings (348 K, 530 rpm, S/L=10g/L, d_{80}=8.7 micron).

when the solution viscosity is high. Despite the negative aspects of sulfuric acid, the lixiviant is still considered a viable lixiviate due to its relatively low cost and the negative aspects of the other lixiviants including the volatility of hydrochloric acid and the decomposability of nitric acid under 348 K (Yu et al., 2013).

Effect of stirring speed

The stirring speed affects the film thickness around the film layer of a solid particle suspended in the lixiviate solution. High stirring speed creates a high shear rate in solution which reduces the film layer thickness thereby increasing the mass transfer rate through the film diffusion layer (Makanyire et al., 2016). The effect of stirring speed was evaluated at 300 rpm, 530 rpm, 760 rpm, and 900 rpm as shown in Figure 343. The leaching condition included a 1M sulfuric acid solution and a solid/liquid ratio of 10 g/L at 348 K. The test results indicate a stirring speed of 300 rpm had a negative effect on leaching kinetics while stirring speeds of 530 rpm to 900 rpm provided nearly equal kinetics. The recovery at a 900 rpm stirring speed was slightly lower than that obtained at 760 rpm. A stirring speed of 530 rpm was established as an adequate value for the standard test conditions.

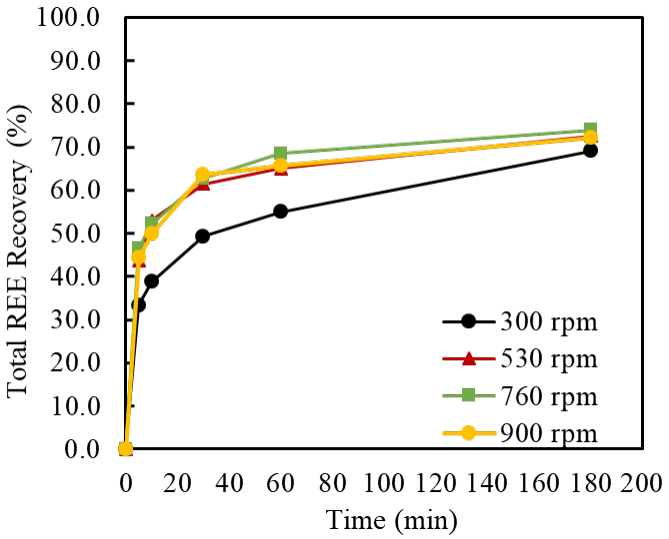

Figure 343. Effect of stirring speed on the leaching recovery of total rare earth elements contained in the Fire Clay coal middlings (348 K, 1 M H_2SO_4, 530 rpm, D_{80}=8.7 micron)

Effect of solid-to-liquid ratio

The effect of solids-to-liquid ratio on rare earth leaching recovery was investigated in the range of 10g/1L to 200g/1L while keeping the other parameters constant at 348 K, 1 M H_2SO_4, 530 rpm. The association between reactants decreased with an increase in the solid/liquid ratio which resulted in a decrease in the extraction rate as shown in Figure 344. Leach recovery was reduced from 74% to 40% after increasing the solid-to-liquid ratio from 10g/L to 200 g/L. The magnitude of the recovery reduction is not commonly observed in other metal leaching operations. In the metallic copper leaching process, the leaching reaction was more effective when the Cu^{2+} concentration in solution was higher because the Cu^{2+} reacted with metallic Cu to Cu^{+} (Wang et al., 2016). This type of reaction mechanism does not occur in a REE solution since the REEs exist mostly

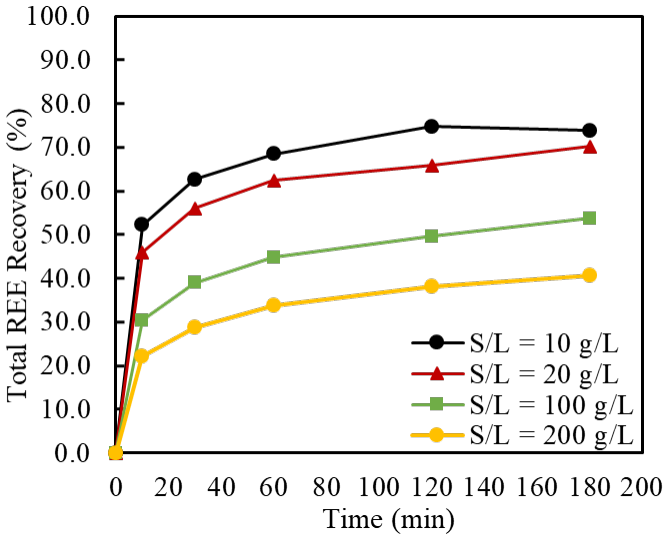

Figure 344. Effect of solid to liquid ratio on the leaching recovery of total rare earth elements contained in the Fire Clay coal middlings (348 K, 1 M H_2SO_4, 530 rpm, D_{80}=8.7 micron)

as a compound. Niobium leaching from titanium oxide residues did not show any effect of solid-to-liquid ratio on leaching recovery (Makanyire et al., 2016) However, Li et. al. (2013) reported on a study on rare earth concentrate leaching that found the solid/liquid ratio to have a negative effect when the ratio was higher than 100 g/L. Therefore, the solid/liquid ratio effect varies from source to source in different leaching environments. Future test work will involve measuring the change in surface area and pore volume as a function of leach time over a range of solid-to-liquid ratios. These tests will evaluate the hypothesis that the leaching rate and recovery reductions are a result of pore plugging resulting from high ionic concentrations and localized pH increases in the pores where alkaline earth minerals may be present.

Effect of acid concentration

The effect of sulfuric acid concentration on leaching recovery was studied using 0.1 M, 0.5 M, 1 M, and 2 M acid concentrations and the standard conditions for temperature, stirring speed, and solid- to-liquid ratio. The initial acid concentration of 0.1 M, 0.5 M, 1 M, and 2 M resulted in ending pH values of 1.04, 0.38, 0.11, and -0.25, respectively, after 3 hours of leaching. As shown in Figure 345, the total REE recovery increased substantially from 40% to 74% by increasing acid concentration from 0.1 to 1 M. However, from 1 M to 2 M, recovery only increased by 2.5%. The optimal acid concentration was selected to be 1 M since higher concentrations of acid does not provide a significant increase in recovery of REEs and adds significantly to the contaminant concentration.

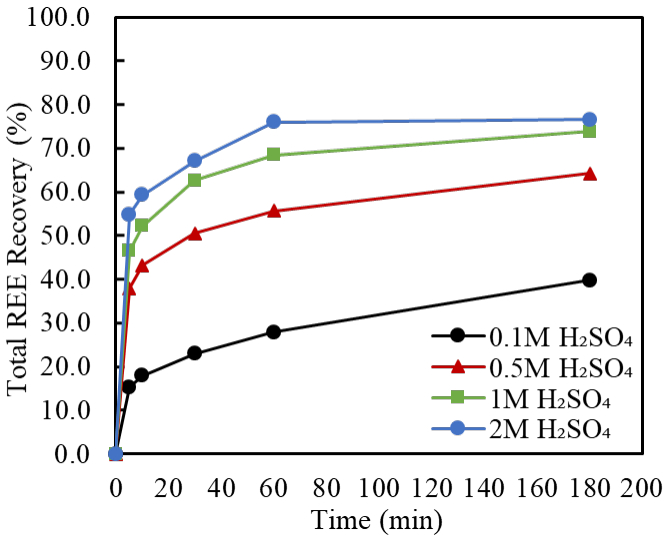

Figure 345. Effect of sulfuric acid solution concentration on the leaching recovery of total rare earth elements contained in the Fire Clay coal middlings (348 K, 530 rpm, S/L=10g/L, D_{80}=8.7 micron).

Effect of temperature

The effect of temperature on REE leaching using 1 M H_2SO_4 was investigated with stirring speed of 530 rpm and the S/L of 10 g/L for 2 hours. Samples were taken over shorter time increments due to the relatively fast kinetics over the first 20-30 minutes. Figure 346 demonstrates that the REE leaching recovery increased with an elevation in leaching temperature. When the temperature was increased from 298 K (25℃) to 348 K (75℃), leaching recovery increased from 35% to 75% after 2 hours of leaching. The data suggests the existence of a relatively fast leaching process during the first 20 minutes followed by a slow process. As such, two or more reaction mechanisms may be occurring when leaching the coal source.

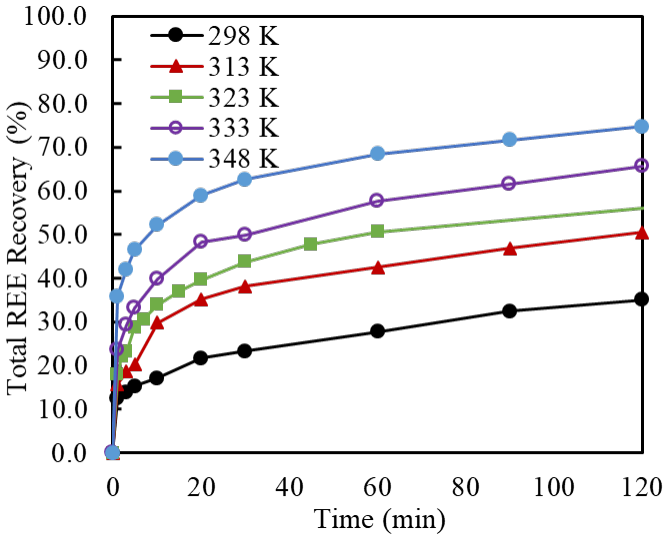

Figure 346. Effect of leaching reaction temperature on the leaching recovery of total rare earth elements contained in the Fire Clay coal middlings (1 M H_2SO_4, 530 rpm, S/L=10g/L,

The effect of temperature on individual REEs is shown in Figure 347. Most of the light REEs (i.e. La, Ce, Pr, Nd, Sm) appeared to be very sensitive to temperature which indicated that the leaching mechanism of light REEs was mostly chemical reaction controlled. The recovery of Ce, Pr, and Nd increased from 36%, 39%, and 36% to 79%, 84%, and 80%, respectively, by increasing the temperature from 298 K to 348 K. The heavy REEs and scandium recovery improved with higher temperature but the increase was not as significant. Scandium recovery rose from 29% to 36%. For the recovery of elements that were relatively insensitive to temperature, the activation energy is generally low and more likely to be a result of a diffusion controlled process (Free, 2013).

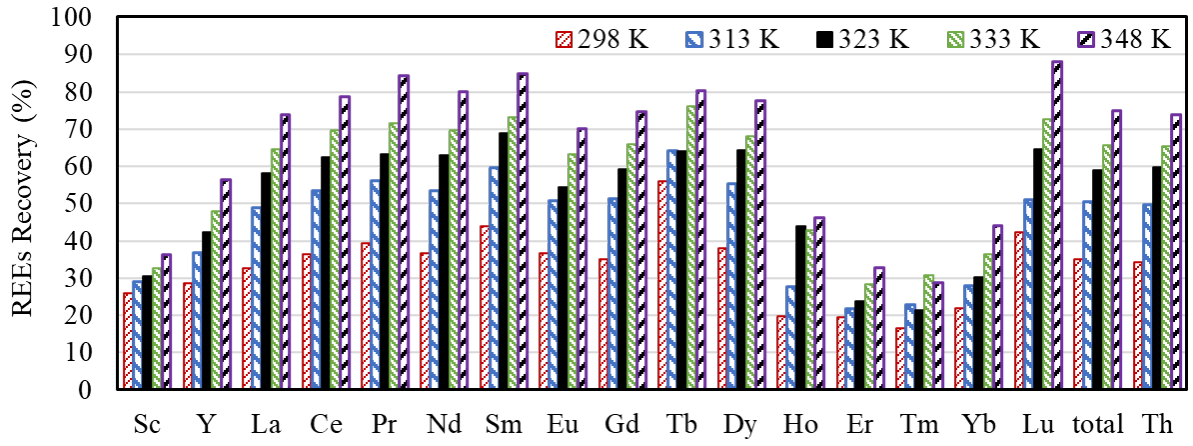

Figure 347. Effect of leaching reaction temperature on the leaching recovery of individual rare earth element. (1 M H_2SO_4, 530 rpm, S/L=10g/L, D_{80}=8.7-micron, retention time of 120 minutes)

Kinetic analysis

The leaching process is classified as fluid-particle heterogeneous reaction in which a liquid reacts with a solid by contacting and transforms the solid into a product (Levenspiel, 1999). A solid particle that reacts with a liquid and shrinks in size during the reaction which can be described by a shrinking core model. The reaction is a five-step process, i.e.,: 1) diffusion through the film layer, 2) diffusion through the product layer, 3) chemical reaction on the surface, 4) product diffusion through the product layer and 5) product diffusion through the film layer to the solution (Xiao et al., 2015). The slowest step is known as the rate determining process. In most of the cases, the latter two diffusion processes are not the major controls. The model equations used to describe the rate constant of either process are as shown in Eq. [5.5.2] for diffusion and Eq. [5.5.3] for chemical reaction (Gharabaghi et al., 2009; Levenspiel, 1999):

$$\left[1-\frac{2}{3}\alpha-(1-\alpha)^{\frac{2}{3}}\right]=\frac{2M_B D C_A}{\rho_B a r_0}t=k_d t \qquad [5.5.2]$$

$$\left[1-(1-\alpha)^{\frac{1}{3}}\right]=\frac{kM_B C_A}{\rho_B a r_0}t=k_r t \qquad [5.5.3]$$

where α is the fraction that reacted; k the kinetic constant; M_B the solid molecular weight; C_A the acid concentration; a the stoichiometric coefficient of the component in reaction; r_0 the initial radius of the particle; t the reaction time; and D the diffusion coefficient in the porous product layer.

For a kinetic analysis of the rare earth leaching reaction from coal, the shrinking core models with surface chemical reaction and diffusion through the product layer were evaluated by plotting the real leaching time versus $[1-(1-\alpha)^{1/3}]$ and $[(1-2\alpha/3)+(1-\alpha)^{2/3}]$. The later plot showed a straight line among all the temperatures using the experimental data for the first 20 minutes of leaching and 20-120 minutes reaction, as shown in Figure 348. The correlation coefficient values (R^2) and the corresponding

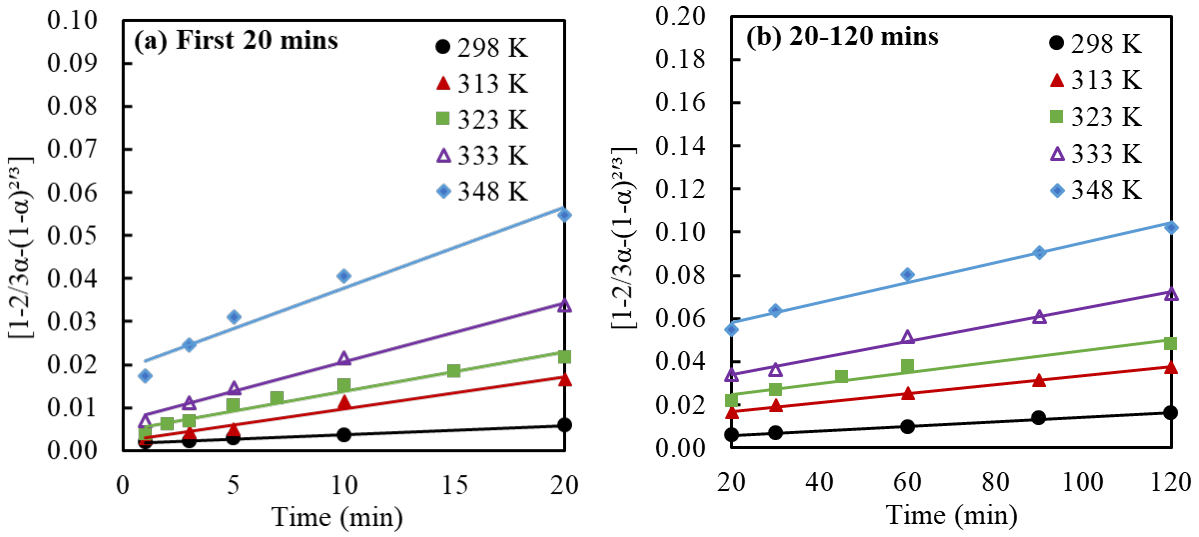

Figure 348. Kinetic modelling of total REEs recovery during the (a) first 20 minutes, and (b) 20-120 minutes of leaching at various temperatures for the Fire Clay middlings (1 M H_2SO_4, 530 rpm, S/L=10g/L, D_{80}=8.7-micron, retention time of 120 minutes).

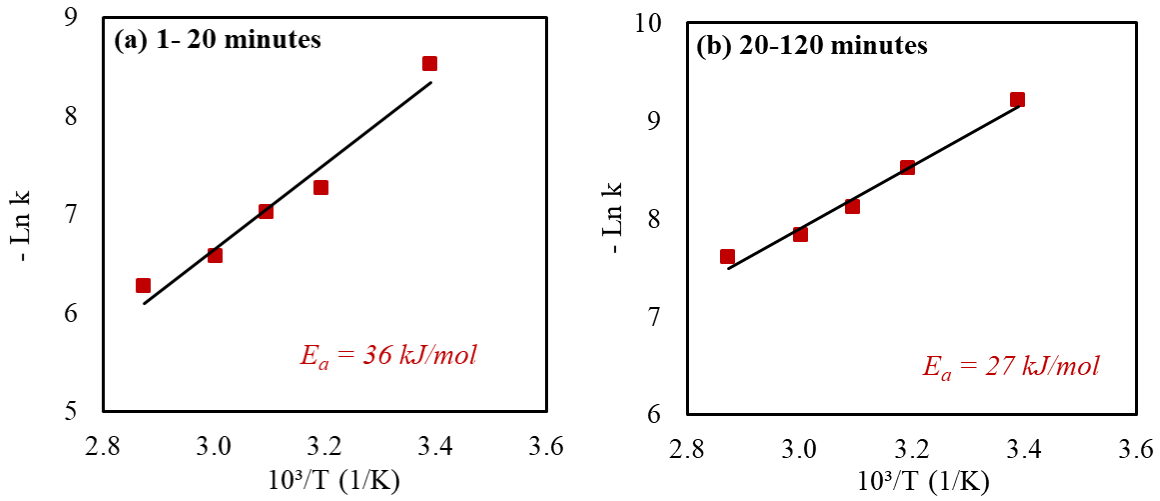

Figure 349. Arrhenius plot for the total REEs leached from the Fire Clay coal middlings during the (a) first 20 minutes, and (b) 20-120 minutes of leaching (1 M H_2SO_4, 530 rpm, S/L=10g/L, d_{80}=8.7-micron).

slopes (k) of the plots are listed in Table 70. Rate constants were calculated and the Arrhenius plots of ln(k) versus 1/K are as shown in Figure 349 for the two leaching stages. The activation energy determined for the first 20 minutes was 36 kJ/mol and 27 kJ/mol for the following 20-120 minutes of leaching. The activation energy values for both leaching periods were close to the energy barrier between the diffusion and chemical reaction processes which is around 20 kJ/mol (Free, 2013). The interfacial transfer of product through the porous structure of the solid particles requires high activation energies as reported by Li et.al. (2010 and 2013) which is about 40 kJ/mol (Li et al., 2013, 2010). It is believed that the heterogenous characteristics of the coal tailings material created a mixed controlled process during the leaching reaction.

The morphology of the Fire Clay coal middling particles before and after sulfuric acid leaching was studied using SEM. As shown in Figure 350a, the feed material consists of heterogenous particles comprised of mostly quartz and clay (Figure 341b). After 2 hours of leaching at 323 K, the particles were found to have a porous structure on the surface with a micropore structure as shown in Figure 350b. After 2 hours of leaching at 348 K, the porous structure on some of the particle surfaces appeared larger size as shown in Figure 350c. The images showed no reaction product layer or any coating product on the surface. Therefore, the diffusion process in this reaction may be contributed by the interfacial transfer of the products and the reagent diffusion through the porous structure of solid particles.

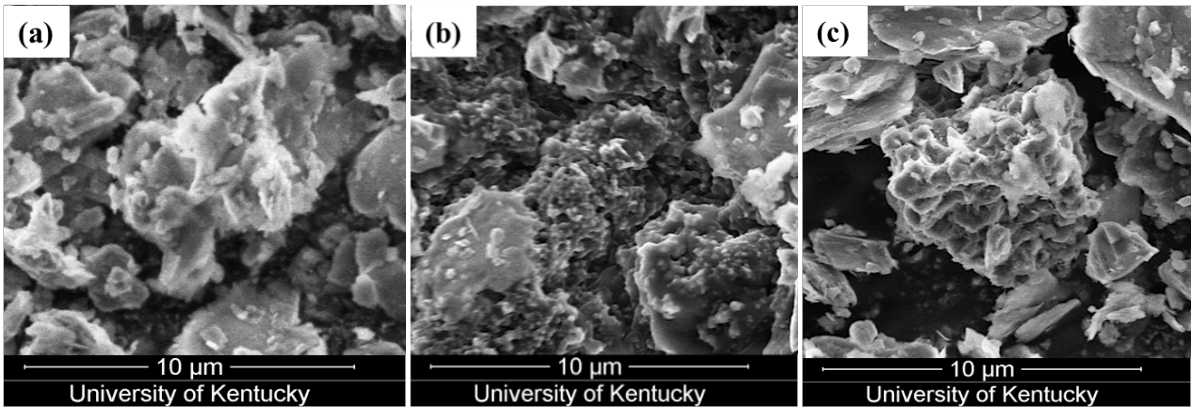

Figure 350. SEM images of particles found in (a) leaching feed material; (b) solid residue after 2 hours leaching at 323 K; (c) solid residue after 2 hours leaching at 348 K. (1 M H_2SO_4, 530 rpm, S/L=10g/L, d_{80}=8.7-micron)

The leaching process involved several simultaneous reactions due to the complication of the mineralogy and the variety of REEs association. Based on a past study, water soluble or ion exchangeable portion of REEs in the current feed source is less than 5%. The REEs were found to exist in crystalized structures (mostly silicates and phosphate compounds) which usually require decomposition to be extracted under the current leaching condition. Therefore, the REEs are mostly present as RE ion substitution in clays and as RE containing minerals. Based on the experimental data, light REEs in this coal source were mostly mineral association, whereas the heavy REEs were ion-adsorbed or ion substitution in clay minerals.

Table 70. Correlation coefficients of inner layer diffusion-controlled kinetics models at different temperatures.

T, K	Diffusion 1-20 mins			Diffusion 20-120 mins		
	k	a	R^2	k	a	R^2
298	0.0002	0.0017	0.9949	0.0001	0.0036	0.996
313	0.0007	0.0022	0.9648	0.0002	0.0129	0.9977
323	0.0009	0.0046	0.9616	0.0003	0.0196	0.9402
333	0.0014	0.0068	0.9919	0.0004	0.0262	0.9934
348	0.0019	0.0189	0.9627	0.0005	0.0487	0.9796

Results and Discussion – Illinois #6 Coal

Characterization

The representative coal sample collected from an Illinois No. 6 coal source was density fractionated and screened to obtain particle size by density fractions for rare earth analysis and leaching studies. The distribution of weight, ash content and total rare earth concentration in each fraction are shown in Table 71. The total REEs concentration of the collected material was 229 ppm on a dry ash basis and 81 ppm on a whole mass basis. The overall ash content was 35% on a dry whole mass basis. The ash content versus REEs content followed the same trend that was observed in a past study of 20 coal plants located in the central and northern Appalachia coalfields (Honaker et al., 2015). The total REEs of the whole feed were distributed mostly in the 2.2 sink fractions of the various particle size classes, i.e., 18.7% in the +9.5 mm class and 29% in the 9.5 x 1 mm class.

The correlation of existence between any two elements including REEs and other selective elements was evaluated. La and Ce concentration had greater than 95% correlation as shown in Figure 351a which was commonly seen in other sources. Surprisingly, the correlations between La and Nd or the other light REEs were not very strong (<50%). Moreover, Th concentration had a significant correlation (>91%) with Na as shown in Figure 351b. This finding indicates a potential mineral coexistence of sodium and thorium. The top three major elements that had the highest concentration in the overall sample was titanium, aluminum, and iron, which were 24%, 9%, and 8%, respectively. Potassium and calcium were the fourth and fifth highest which counted for about 2% and 1.5%, respectively.

Table 71. Characterization of REE content in IL No.6 seam coal after size and density fractionated.

Size Fraction	Density Fraction	Weight (%)	Ash (%)	TREE (ppm)		Distribution (%)
				Ash Basis	Coal Basis	
Plus 9.5 mm	s.g. 1.4 Float	23.7	7.2	368.1	26.6	7.8
	s.g. 1.4 - 1.8	10.3	16.6	321.6	53.5	6.8
	s.g. 1.8 - 2.2	2.0	50.8	354.2	179.9	4.5
	s.g. 2.2 Sink	8.1	81.5	230.9	188.2	18.7
9.5 mm x 1 mm	s.g. 1.4 Float	19.1	6.4	356.3	22.8	5.4
	s.g. 1.4 - 1.8	6.0	13.9	322.5	44.9	3.3
	s.g. 1.8 - 2.2	3.3	67.0	285.2	191.0	7.9
	s.g. 2.2 Sink	11.1	83.4	255.0	212.7	29.1
1 mm x 0.15 mm	s.g. 2.2 Float	8.0	11.2	310.7	34.6	3.4
	s.g. 2.2 Sink	0.8	90.2	196.8	177.5	1.7
Minus 0.15 mm	Coal	4.0	7.1	410.5	29.3	1.5
	Tailing (3)	3.6	87.9	257.2	226.0	9.9
Total		100.00	35.4	229.2	81.0	100.0

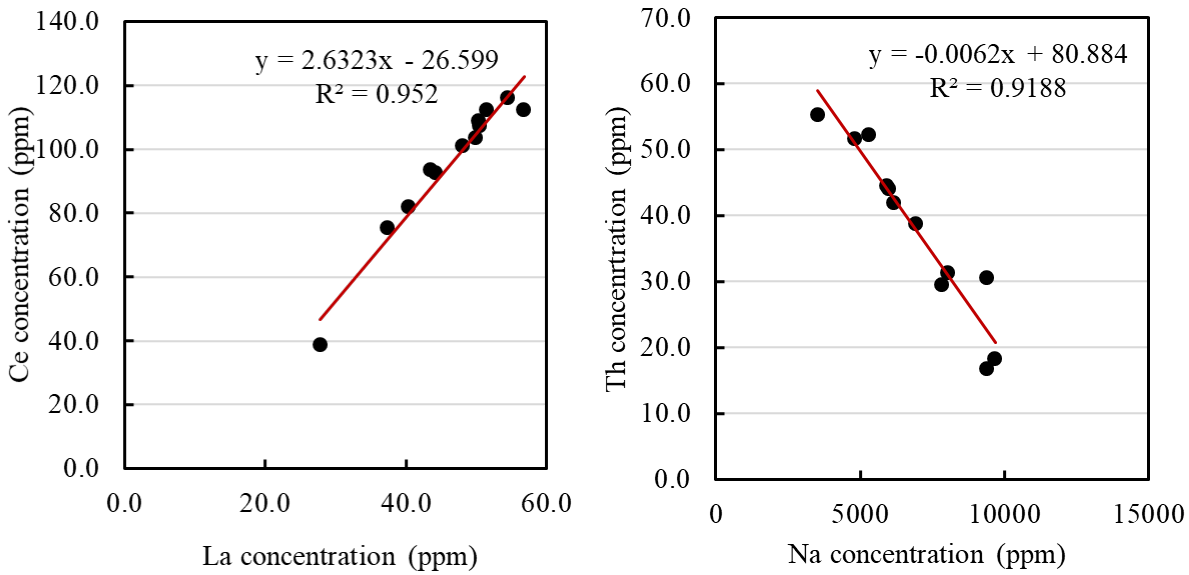

Figure 351. Correlation of concentration in each size by density fraction between (s) La and Ce on a dry ash basis and (b) Na and Th on a dry ash basis.

Mineralogy

XRD analyses were performed on the high ash samples (ash content >50%) as shown in Figure 352. Major mineral components in the Illinois No. 6 coal seam were quartz, kaolinite, illite, muscovite, pyrite and calcite. The compositions of each fraction were very similar but the intensity of each composition varies from sample to sample. The most prominent change on intensity among all samples was the calcite composition in the fine fractions (1 x 0.15 mm and -0.15 mm). The estimated content of the major mineral components is listed in Table 72. Quartz counts for almost half of the weight percentage in each fraction. The total clay material (kaolinite, illite, and muscovite) represents about 30% by weight of the material in each fraction. The estimated calcite contents were 38.7% and 17.7% in the 1 x 0.15 mm 2.2 sink fraction and the -0.15 mm flotation tailing material, respectively. From cross checking the mineral contents and the elemental concentration, a correlation was detected between scandium concentration and the calcite content as shown in Figure 353. Additional investigations are required to produce sufficient data leading to a solid conclusion.

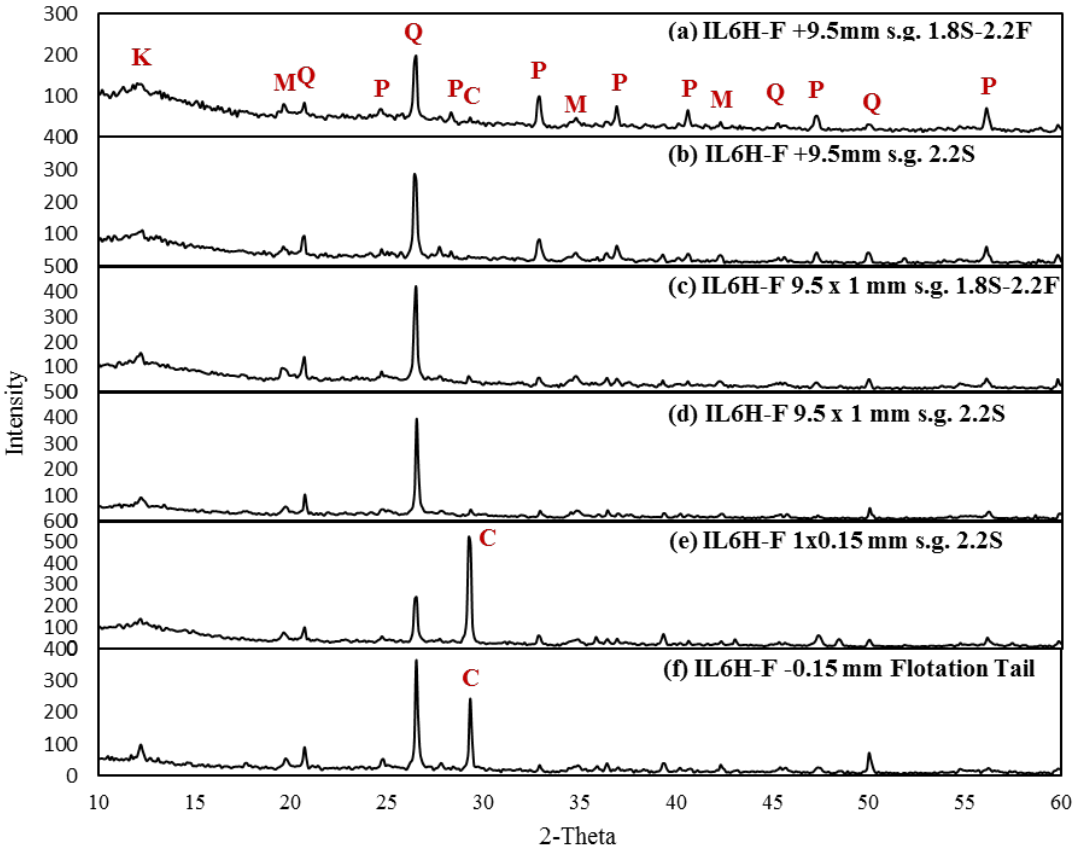

Figure 352. XRD analysis of the high ash (ash content >50%) fractions in Illinois No. 6 coal; P = pyrite, M = muscovite, Q = quartz and C = calcite.

Table 72. Minerology of the high ash (ash content >50%) fractions in IL No. 6 coal.

IL No. 6 Hamilton Feed	Quartz (%)	Calcite (%)	Kaolinite (%)	Illite (%)	Pyrite (%)	Muscovite (%)
+9.5 mm s.g. 1.8S-2.2F	42.9	2.3	16.8	0.8	27.6	9.6
+9.5 mm s.g. 2.2S	55.1	3.2	10.6	0	20.4	10.7
9.5 x 1 mm s.g. 1.8S-2.2F	51.7	3.9	11.2	2.6	9.3	21.3
9.5 x 1 mm s.g. 2.2S	54.8	3.3	10.2	1.8	7.4	22.4
1 x 0.15 mm s.g. 2.2S	27.3	38.7	11.6	1.5	8.7	12.2
-0.15 mm Tail	47.7	17.7	7.5	0	5	22.2

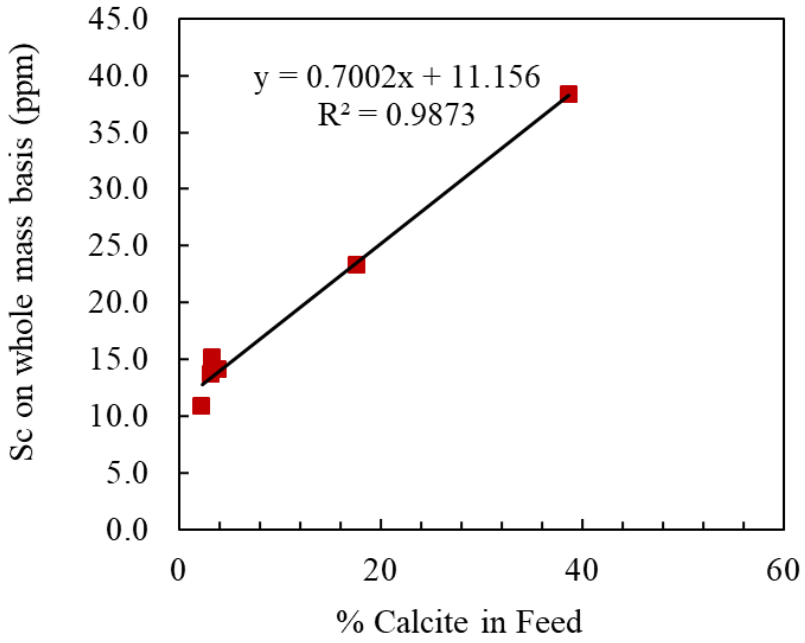

Figure 353. Correlation between calcite content and scandium concentration in high ash (ash content >50%) fractions in IL No. 6 coal.

Leaching characteristics

The leaching characteristics of each fraction was examined using 1.2M sulfuric acid using a stirring speed of 530 rpm and S/L ratio of 10 g/L at a temperature of 348 K. The results of the total REE leaching recovery are shown in Figure 354. Figure 355 shows the individual REE recovery values and the recovery of Al, Ca, Fe, K, Na, and P. In general, the lower density coal fractions tend to have slower leaching rates at the beginning of the tests because of the hydrophobicity of the particle surface and the low wetting rate. The low ash fractions achieved lower recovery values regardless of the size. The initial leaching rates of the high density, high ash material (specific gravity > 1.8, ash content > 80%) were relatively high and reached equilibrium within one hour.

The highest total REE recovery achieved after 5 hours of leaching was 62% on the +9.5 mm 1.8 to 2.2 density material. The recovery of Y and Nd was 81% and 84%, respectively, from the size fraction. Both Y and Nd are critical REEs and account for more than 80% of the total CREEs. Scandium recovery was significantly high (over 60%) after 5 hours of leaching. This finding is important given that the recovery value is much higher than other coal sources including the Fire Clay coal. This fraction represents the coarse middling fraction produced in a coal preparation plant. The leaching success on the 1. 8 x 2.2 SG fraction agrees with the findings of a past study performed on the West Kentucky No. 13 and the Fire Clay seam coals which found that the middling material provided highest leaching recovery of REEs.

Scandium recovery was generally high in the Illinois No. 6 coal source. Recovery values of 87% was achieved on the 1 x 0.15 mm 2.2 sink material. The same density fraction in the material coarser than 9.5 mm material and flotation tailings sample also achieved over 60% Sc recovery. This observation aligned well with findings on REEs leaching of the West Kentucky No. 13 coal material. Considering the correlation of Sc and calcite content, it is possible that the portion of Sc that is extractable is associated with calcite minerals. However, the observation requires a further investigation to verify the hypothesis.

Ti, Al, and Fe are the three elements that have the highest concentration in the feed. However, the leaching recovery values for the three elements in each fraction were not very high. The Ti recovery was less than 1% in all the fractions. Aluminum recovery was in a range of 4~7% among all fractions. The recovery of Fe was in a range of 10~12% among all fractions with the exception of the fraction smaller than 0.15 mm in the flotation tailings for which the Fe recovery was 27%. However, due to their high concentrations in the feed material, the resulting concentrations in the leachate solution were still significant despite their low recovery values.

Among all fractions, the Ca and P recovery values were prominent relative to the other elements. The recovery value for Ca were over 90% for most of the fractions except for the two low density materials (s.g. <1.4). As calcite was detected in the XRD analysis, it was likely the primary source of Ca. However, P showed a similar trend which led to a hypothesis that the apatite mineral may present in the material in a trace amount and thus not detectable by XRD. A more precise analysis will be performed to verify.

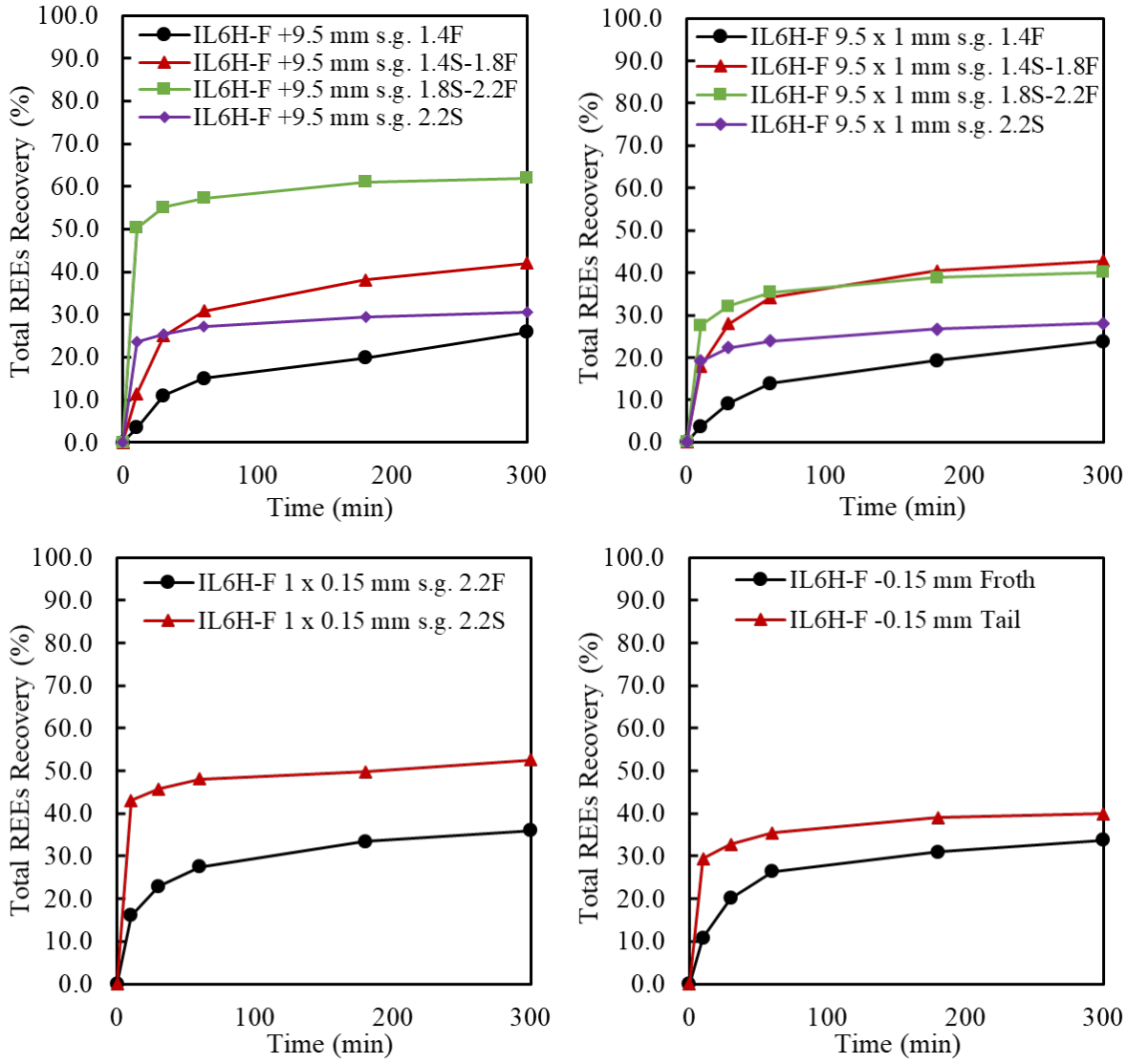

Figure 354. Leaching recovery of total REEs in each size by density fraction of IL No. 6 seam coal (1.2M sulfuric acid, 530 rpm, S/L of 10 g/L, 348 K)

(a) IL6H-F +9.6 mm s.g. 1.4F

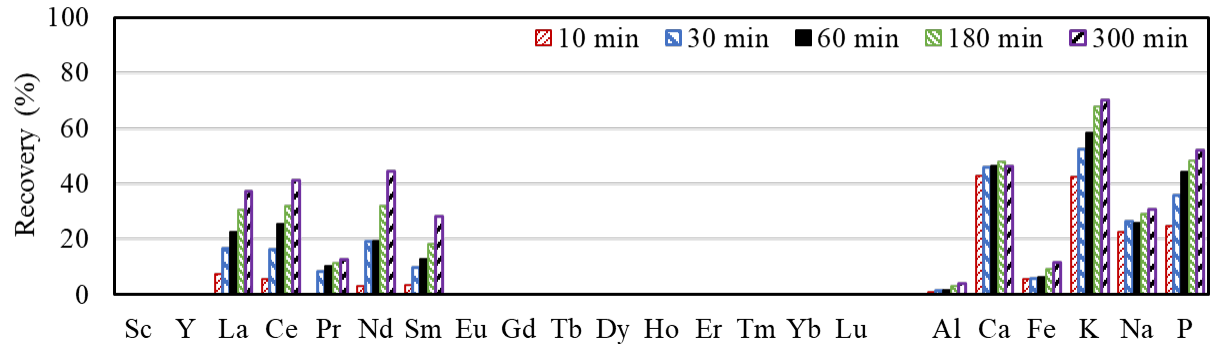

(b) IL6H-F +9.6 mm s.g. 1.4S-1.8F

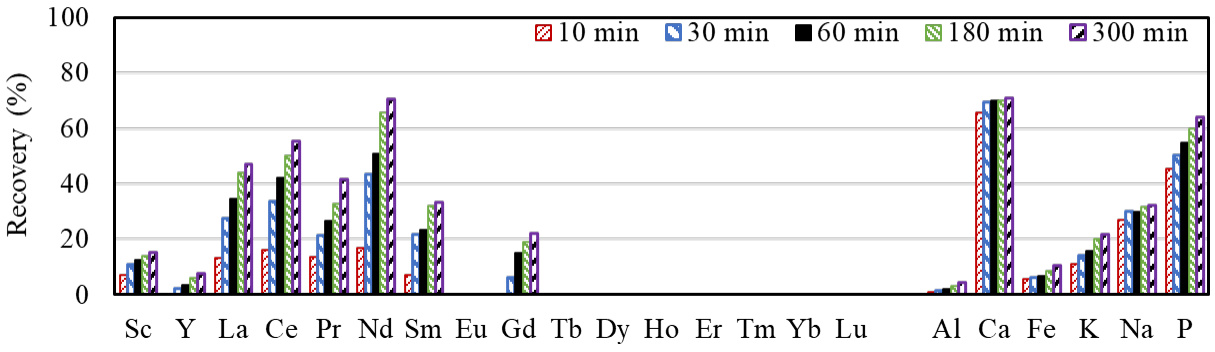

(c) IL6H-F +9.6 mm s.g. 1.8S-2.2F

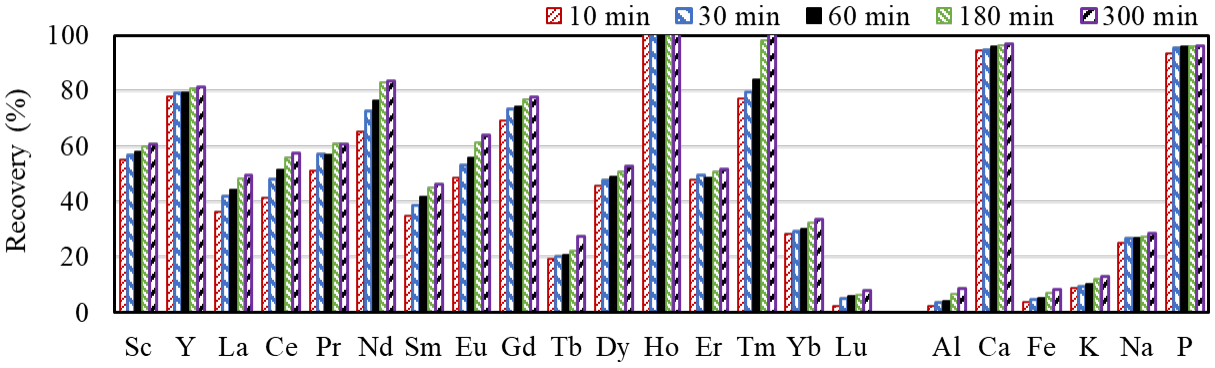

(d) IL6H-F +9.6 mm s.g. 2.2S

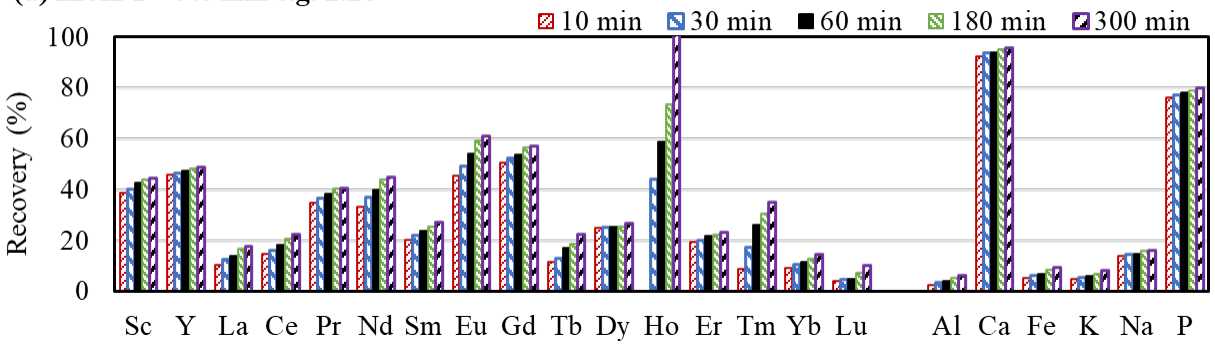

(e) IL6H-F 9.6x1 mm s.g. 1.4F

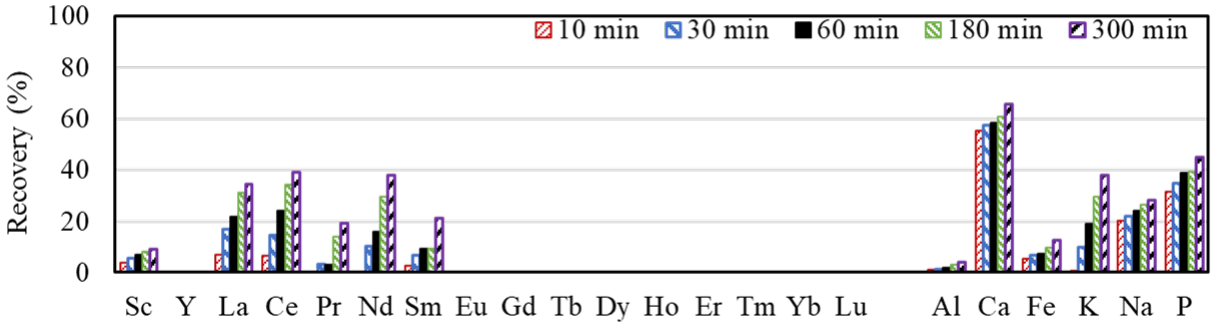

(f) IL6H-F 9.6x1 mm s.g. 1.4S-1.8F

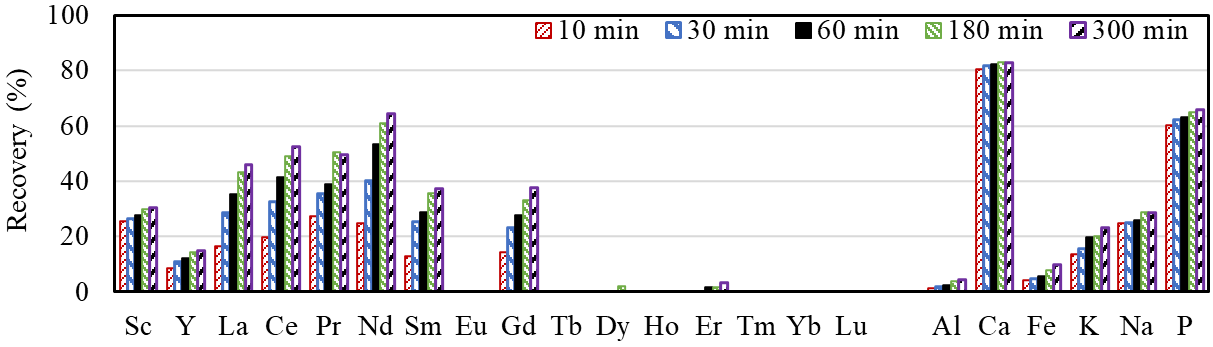

(g) IL6H-F 9.6x1 mm s.g. 1.8S-2.2F

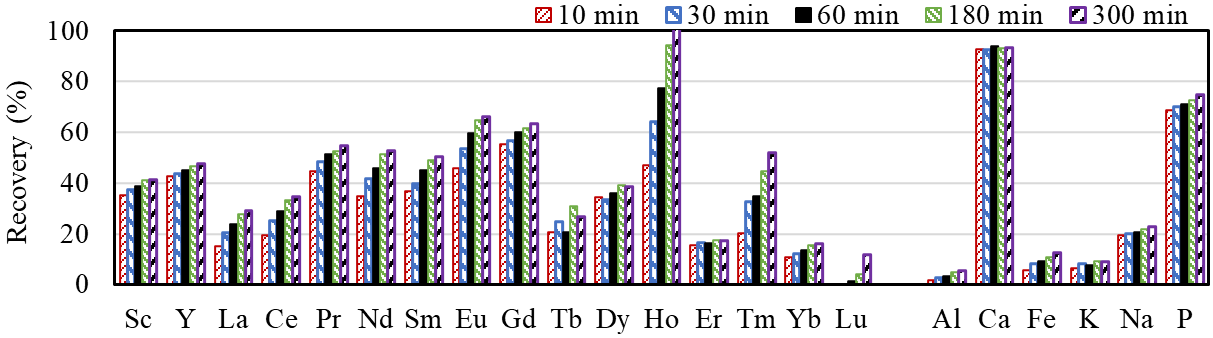

(h) IL6H-F 9.6x1 mm s.g. 2.2S

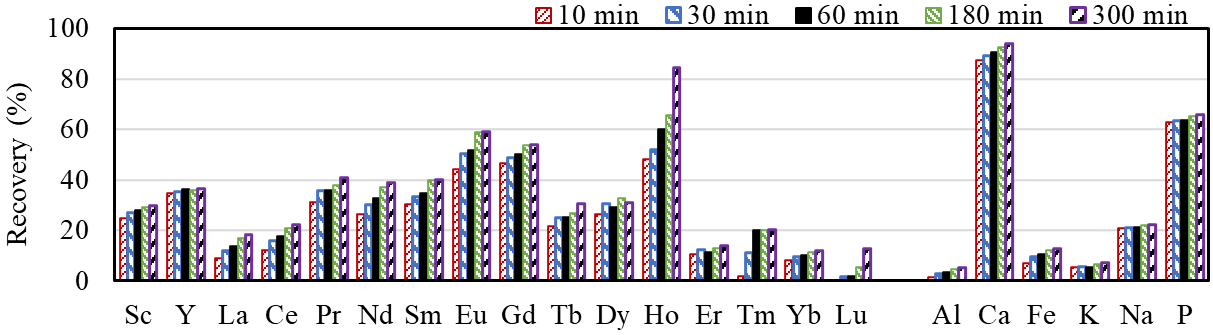

(i) IL6H-F 1x0.15 mm s.g. 2.2F

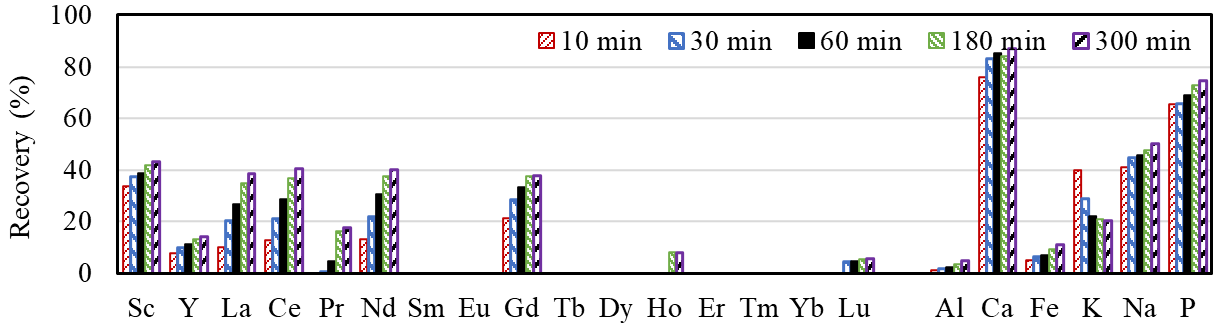

(j) IL6H-F 1x0.15 mm s.g. 2.2S

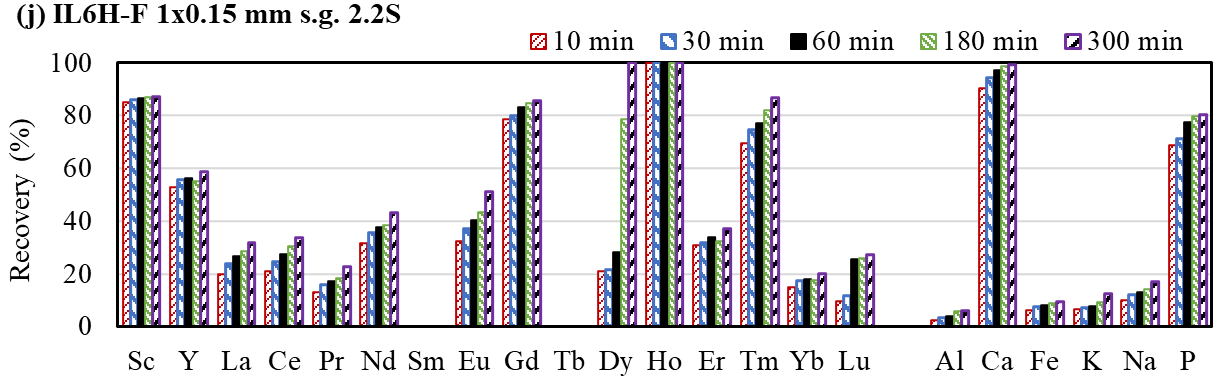

(k) IL6H-F -0.15 mm Coal

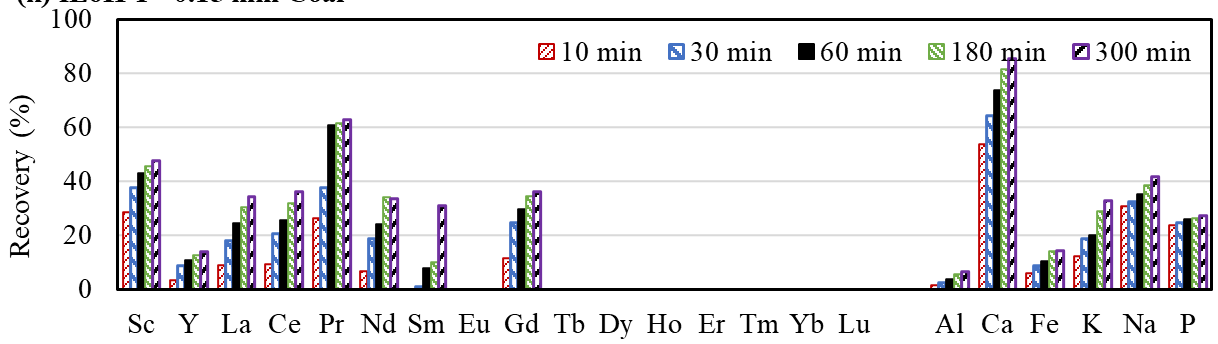

(l) IL6H-F -0.15 mm Tailing

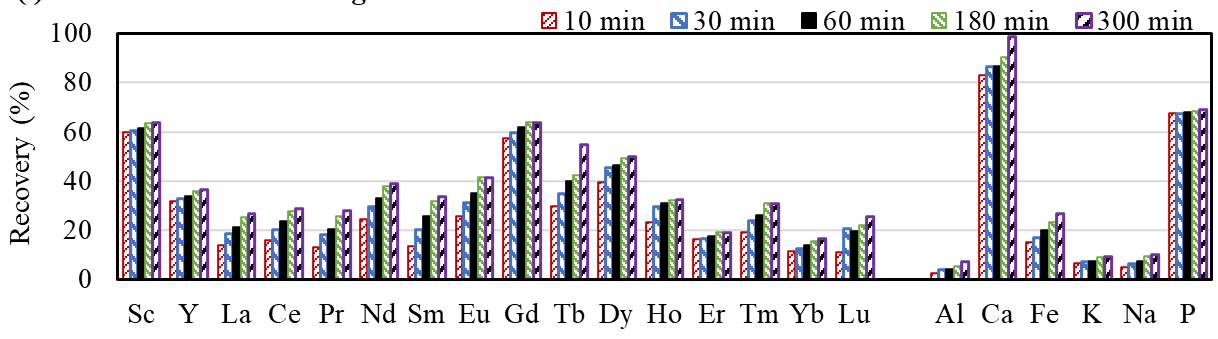

Figure 355. Leaching recovery of individual rare earth element and major contamination elements in each size by density fraction of IL No. 6 seam coal (1.2M sulfuric acid, 530 rpm, S/L of 10 g/L, 348 K)

Acid Leaching of Coal Refuse (Detailed Studies)

Introduction

The chemical extraction studies conducted in this section focused on assessing leaching kinetic characteristics and developing extraction curves that define the separation achieved by solvent extraction between rare earth and contaminant elements in the presence of a phase modifier. A detailed leaching study was performed on a fraction of an Illinois No. 6 coal source that has attractive characteristics. A majority of the rare earth elements in the fraction coarser than 9 mm and having a specific gravity between 1.8 and 2.2 was recovered within one minute from the start of the leaching process using 0.5 M H_2SO_4. Evaluations performed as a function of temperature and leaching time revealed that the leaching process was diffusion controlled within the first ten minutes with an activation energy of 14.6 kJ/mol. After ten minutes, the leaching rate considerably slowed as the process was chemical reaction controlled with an activation energy of 35.9 kJ/mol. Tests were conducted using different lixiviates and acid concentrations from which the results indicated limited recovery gains between acid concentrations of 0.5M and 2.0M. A similar study was initiated on particle size and density fractions of a representative sample collected from the Fire Clay coal seam. Experiments were also performed to develop a process scheme involving solvent extraction that will allow scandium to be recovered as a separate concentrate from the other rare earth elements using alkaline stripping and the addition of phase modifiers. Extraction curves were developed which fine the separation between the rare earth and associated contaminant ions.

The leaching kinetics of REEs in the 1.8 x 2.2 specific gravity fraction of the Illinois No. 6 coal seam was further investigated due to its excellent leachability characteristics to assess the effect of leaching acid concentration, solids concentration, lixiviate type, leaching time and temperature. The leaching process of this material can be defined by two distinct stages that occur during different leaching time periods. The first 10 minutes of leaching was characterized by fast leaching rates whereas the leaching process from 10 to 120 minutes slowed considerably and reached equilibrium. The kinetic data was fitted with both the diffusion and chemical reaction models. The activation energy determined for the first 10 minutes was 14.6 kJ/mol using the diffusion-controlled model and 12.9 kJ/mol using the reaction-controlled model. For the 10-120 minutes leaching stage, the activation energy was 31.6 kJ/mol as determined using the diffusion model and 35.9 kJ/mol calculated using the reaction model. The results indicated that the first 10 minutes of leaching was controlled by a diffusion process whereas the later stage of the leaching process was controlled by chemical reaction.

A study to quantify the leaching characteristics of the Fire Clay seam coal was conducted. A barrel of Leatherwood plant feed material was processed into 12 individual size-by-density fractions. The leaching recovery of REEs in all the high ash content fractions were very similar. The REE recovery from the "middling" material was 40% after 5 hours leaching, whereas the recovery of the mechanically liberated and decarbonized middling material was about 75% under the same leaching conditions.

Illinois #6 Coal Testing

Material

The leaching results presented in this section for the Illinois No. 6 coal source focuses on the fraction of the coal coarser than 9.5 mm and having a specific gravity between 1.8 and 2.2. This fraction was found to have exceptional leaching characteristics with over 50% recovery achieved within the first two minutes of leaching as reported above. The total REE recovery was 62% after 5 hours using 1.2M sulfuric acid at a solids content of 10 g/L solid concentration and a temperature of 75℃. This fraction, which contained 52.8% ash, corresponds to the coarse middling fraction produced in a coal preparation plant.

To release the REEs present in the micro-dispersed mineral matter contained within the 1.8 x 2.2 SG fraction, particle size reduction and decarbonization were applied. A representative sample was pulverized to a top size of 80 mesh (170 microns) followed by 20 minutes grinding in an attrition mill at 200 rpm rotation speed. The solid concentration used in the attrition mill was 40%. The ground material was

subjected to three stages of froth flotation using a Rougher-Cleaner-Recleaner approach to recover clean coal material and create a decarbonized tailings material. Diesel fuel No. 2 was used as the collector and MIBC solution as the frother. The tailing collecting from the three flotation stages were combined. The overall ash content of the combined flotation tailing material was 82%. The individual REE content on a whole mass basis is provided in Figure 356. After coal removal, the REE content in tailing material was upgraded from 180 ppm to about 280 ppm.

Fe, Al, Ca were the three elements with the highest contents in the sample followed by potassium (1.7%) and phosphors (0.4%). XRD analyses were performed on the selected sample to understand the sources of the major components both before and after coal flotation. The mineralogy composition is showed and compared in Table 73. Pyrite was one of the major mineral components in the 1.8 x 2.2 SG fraction. The pyrite content increased from 28% to about 60% on a whole sample basis as a result of removing the coal from the sample by flotation. From the XRD results, the major sources of Fe, Al, and Ca in this material were pyrite, clays, and calcite, respectively. After coal removal, the Fe, Al, and Ca concentration on a whole mass basis increased from 8.3%, 4.9%, and 1.3% to about 16.2%, 6.6%, and 1.7%, respectively.

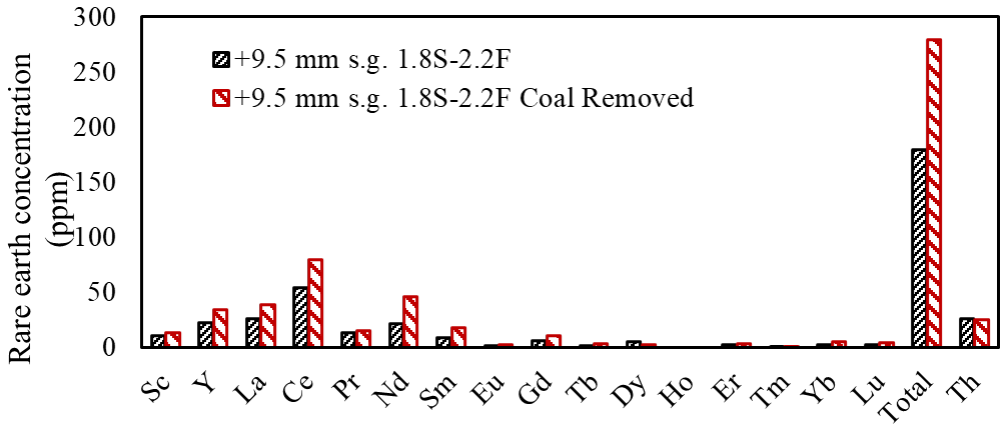

Figure 356. Rare earths contents in the Illinois No. 6 fraction coarser than 9.5 mm with a specific gravity between 1.8 and 2.2 on a whole sample basis before and after coal flotation.

Table 73. Mineralogy of the plus 9mm, 1.8 x 2.2 SG fraction of the Illinois No. 6 coal before and after coal flotation as determined by XRD analysis.

IL No. 6 Hamilton Feed	Quartz (%)	Calcite (%)	Kaolinite (%)	Illite (%)	Pyrite (%)	Muscovite (%)
+9.5 mm s.g. 1.8S-2.2F	42.9	2.3	16.8	0.8	27.6	9.6
+9.5 mm s.g. 1.8S-2.2F Coal Removed	23.4	4.9	6.4	2.4	59.2	3.6

Experiments

Leaching experiments were conducted in a 1 liter leaching reactor equipped with a total reflux condenser. Heat was provided by a water bath with precise temperature control. Agitation was provided using a magnetic stir. A detailed leaching experimental procedure was provided above. Tests were carried out to investigate the effects of different lixiviate types (i.e. H_2SO_4, HCl, and HNO_3), acid concentrations (i.e. 0.1M, 0.5M, 1M, and 2M etc.), solid-to-liquid ratio (i.e. S/L=1/100, 1/10, 1/5 etc.), and leaching temperature (i.e. 25℃, 40℃, 50℃, 60℃, and 75℃). Leachate samples were collected at 1 min, 3 min, 5 min, 10 min, 20 min, 30 min, 60 min, 90 min, and 120 min to obtain precise kinetic leaching data. A micro-filter (0.45 microns) plug was used to separate the leachate from solids to immediately stop the solid-liquid reaction. The final solid residue was filtered and washed with deionized water. Both the leachate and solid residue from each experiment were analyzed for rare earth and other metal concentration by ICP-OES. Leaching recovery values were calculated using the amount of rare earth in the leachate divided by the total amount of rare earth in both leachate and solid residue.

Results and discussions

Effect of acid type

Leaching experiments were conducted using different inorganic acids at concentration of 1M, solid/liquid ratio of 10 g/L, and temperature of 75 ℃. Sulfuric acid (H_2SO_4), hydrochloric acid (HCl), and nitric acid (HNO_3) were used to study the leaching process. Figure 357 shows the leaching recovery and reaction rate of TREEs, Al, Fe, and Ca using the different lixiviates. The total REE (TREE) recovery values of 75%, 73%, and 71% were achieved after 2 hours of leaching using HCl, HNO_3, and H_2SO_4 solution, respectively. The hydrochloric acid solution provided the highest leaching recovery; however, nitric acid achieved the fastest leaching rate which resulted in 60% leaching recovery in one minute.

The ending pH values for each lixiviate were 0.14, 0.21, and 0.13 using HCl, HNO_3, and H_2SO_4 solutions, respectively, after 2 hours. The major increase in pH while leaching using HNO_3 was due to the high dissolution rate of pyrite in HNO_3. Fe recovery was 95% in 1M HNO_3, whereas only about 25% Fe was recovered using 1M H_2SO_4 and 1M HCl under the same leaching conditions. Among all three types of inorganic acids, nitric acid has a strong oxidation feature due to its +5-valence state of N and its completely disassociation in water. The pyrite reaction with nitric acid can be very complicated and sensitive to temperature and concentrations. At 70℃ temperature leaching system, the dominant reaction between pyrite and nitric acid is (Kadoğlu, Karaca, and Bayrakçeken 1995):

$$6FeS_2 + 30HNO_3 \rightarrow 3Fe_2(SO_4)_3 + 3H_2SO_4 + 30NO + 12H_2O \quad [5.1]$$

Figure 358 shows the XRD analyses on the samples before and after leaching using the different lixiviates. The pyrite peak completely disappeared using nitric acid leaching. The estimated mineral composition showed that the pyrite content was zero after nitric acid leaching, whereas the remaining pyrite content was 43% and 47% after leaching using sulfuric acid and hydrochloric acid, respectively. The leaching behavior of pyrite in this material indicated that very limited REEs are associated with pyrite minerals in coal. Calcium recovery increased rapidly within the first one minute of leaching which was due to solubility of calcite. XRD results indicate the calcite is the major source for Ca in this material.

Aluminum recovery was not very high in any of the three acids system which indicated that the dissolution of clays was not a major contribution to the REEs recovery. The 1M HCl and H_2SO_4 both achieved about 7.4% of Al after 2 hours of leaching whereas Al recovery with 1M HNO_3 was 5.8%. The slightly lower recover using HNO_3 was mostly due to the higher ending pH value of the nitric acid system.

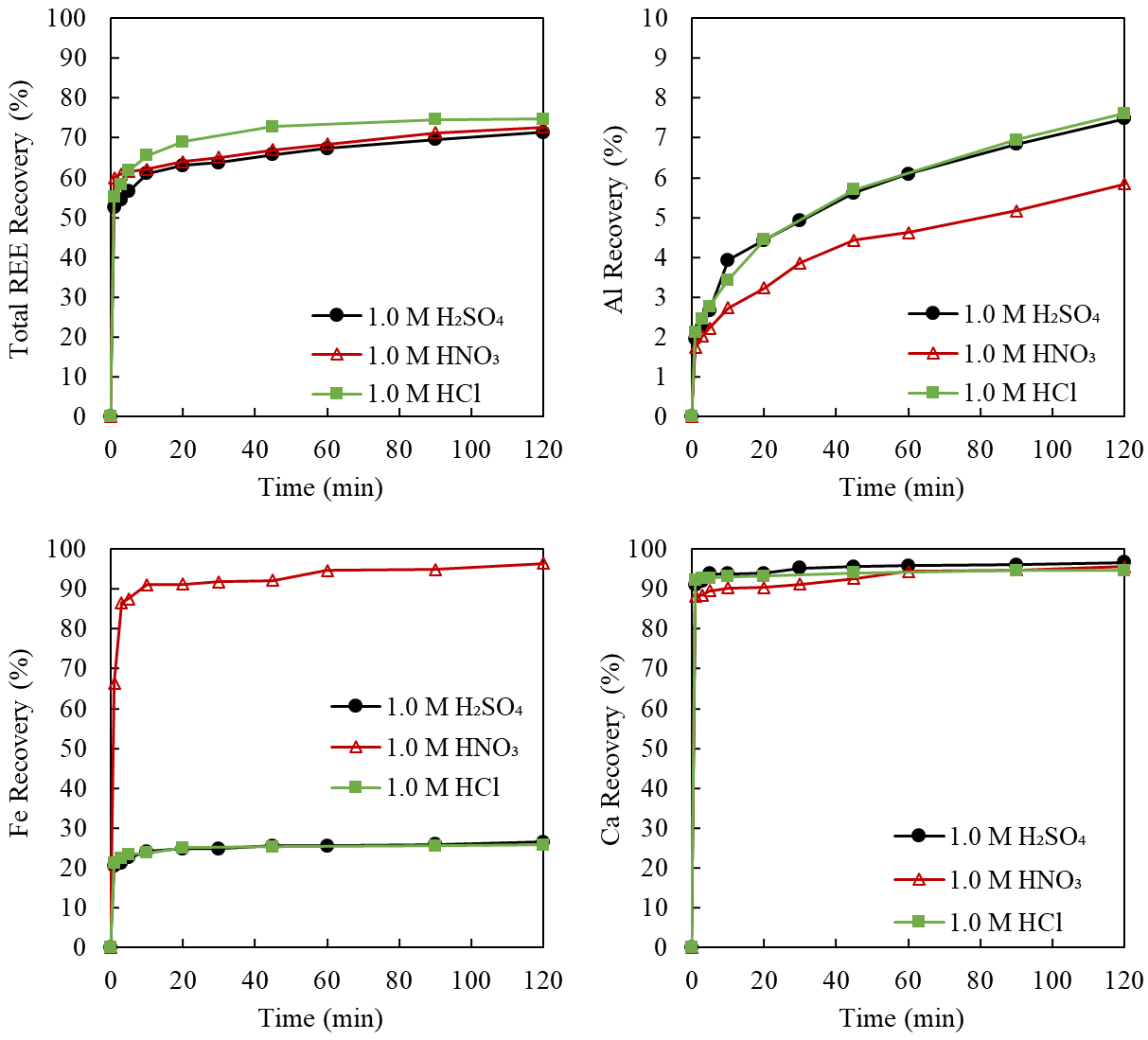

Figure 357. Effect of acid type on the leaching recovery of total rare earths from the plus 9 mm, 1.8 x 2.2 SG fraction in an Illinois No. 6 coal source; test condition: 348 K, 530 rpm, S/L=10g/L.

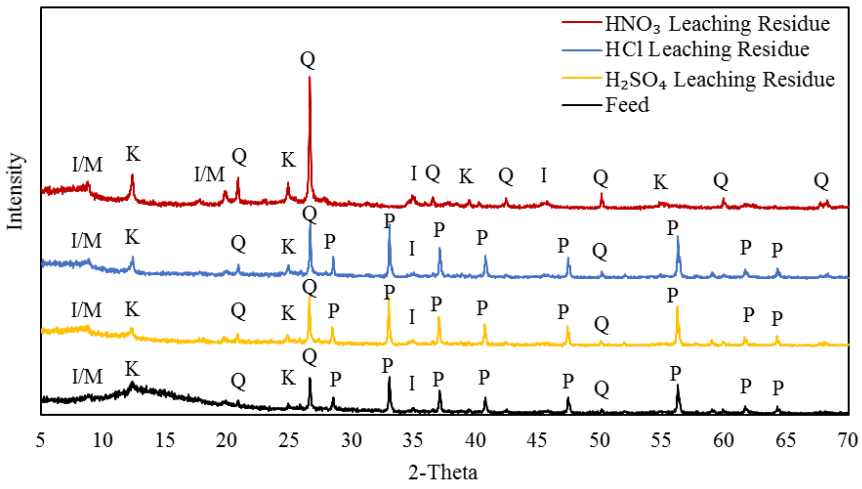

Figure 358. X-ray Diffraction analysis of the feed and solid residues after leaching of the plus 9 mm, 1.8 x 2.2 SG fraction in an Illinois No. 6 coal source using three different lixiviates; P = pyrite, Q = quartz, K = kaolinite, I = illite and M= muscovite.

Effect of solid-to-liquid ratio

Previous studies conducted on other feed sources found that an increase in solid concentration has a significant negative effect on REE recovery. The same trend was observed with this material while varying the solid-to-liquid ratio using values of 10 g/L, 100 g/L, and 200 g/L. As shown in Figure 359, REE recovery in 10 g/L, 100 g/L, and 200 g/L system were 71%, 59%, and 48%, respectively, after 2 hours of leaching. An explanation for the negative effect on recovery is the decrease between reactants with an elevation in the solid/liquid ratio which reduces the reaction rate. However, the recovery reduction was not observed for Al and Fe. Calcium recovery in 10 g/l and 100 g/L system was above 90%, however, in the highest solid concentration system, Ca recovery only reached 80% and slightly declined with time which was likely due to the high concentrations of Ca and other anions in the leachate solution. The precipitation of Ca in acid leaching system has been commonly reported in other leaching systems (Bandara and Senanayake 2015 ; Seferinoglu et al. 2003; Wang et al. 2010).

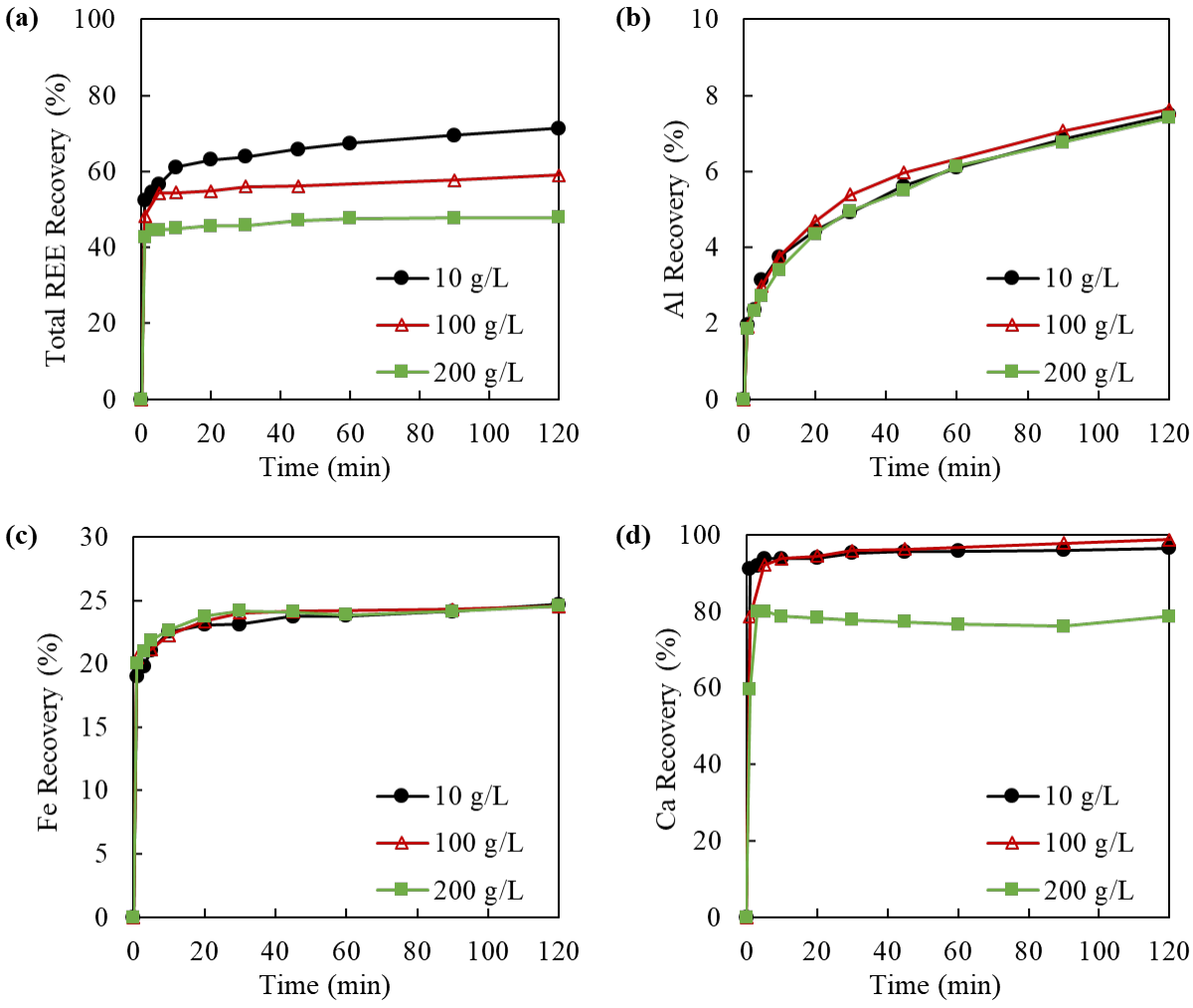

Figure 359. Effect of solid-to-liquid ratio on the leaching recovery of (a) Total rare earths, (b) Aluminum, (c) Iron, and (d) Calcium from the plus 9mm, 1.8 x 2.2 SG fraction of an Illinois No. 6 coal source; test conditions: 348 K, 1 M H_2SO_4 and 530 rpm.

Effect of acid concentration

The effect of sulfuric acid concentration on REE recovery was studied using 0.1 M, 0.5 M, 1 M, and 2 M of initial acid concentration while maintaining the values of the other parameters at their standard values. The initial acid concentration of 0.1 M, 0.5 M, 1 M, and 2 M resulted in ending pH values of 1.13, 0.45, 0.14, and -0.23, respectively, after 2 hours of leaching. As shown in Figure 360, REE recovery values of 56%, 69%, 71%, and 74% were achieved after 2 hours leaching using 0.1 M, 0.5 M, 1 M, and 2 M of sulfuric acid, respectively. The concentration of acid did not play an important role on REEs leaching recovery when the pH value was lower than 0.5. The Fe and Ca recovery values insensitive to acid concentration since calcite dissolution can be completed at pH 4-5 and pyrite reaction with acid occurs at a pH value around 2 (Tessier, Campbell, and Bisson 1979). Aluminum recovery doubled over the acid concentration range but remained below 10% which may be indicative of some association with the REEs.

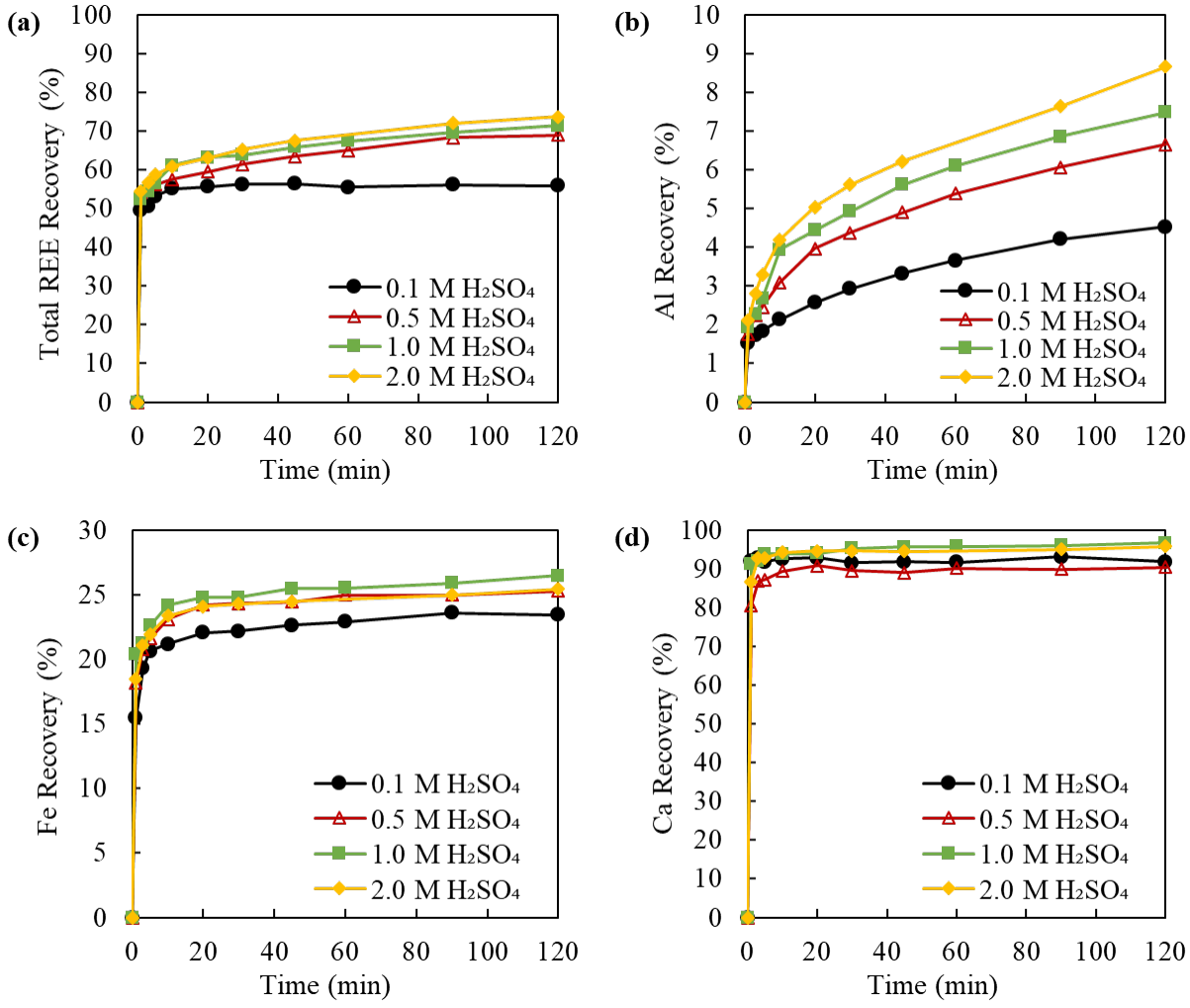

Figure 360. Effect of sulfuric acid solution concentration on the leaching recovery of (a) Total rare earths, (b) Aluminum, (c) Iron, and (d) Calcium from the plus 9mm, 1.8 x 2.2 SG fraction of an Illinois No. 6 coal source; test conditions: 75 ℃, 530 rpm and S/L=10g/L.

Effect of temperature

The effect of temperature on REE leaching using 1 M H_2SO_4 was investigated using standard conditions for 2 hours. As shown in Figure 361, the leaching recovery of REEs increased dramatically within the first one minute of the reaction. After 10 minutes, the temperature had almost no effect on the recovery of total REEs, reaching values in the range of 56% to 71% when increasing temperature from 25°C to 75°C. For the elements that were not very dependable on temperature, the activation energy is generally low and their leaching is more likely diffusion controlled (Free 2013). Aluminum leaching appeared to be sensitive to temperature during the entire leaching time. Iron recovery remained relatively fast within the first minute but reached higher values with an increase in temperature after 10 minutes of leaching. Calcium recovery was reaching 100% regardless of the temperature.

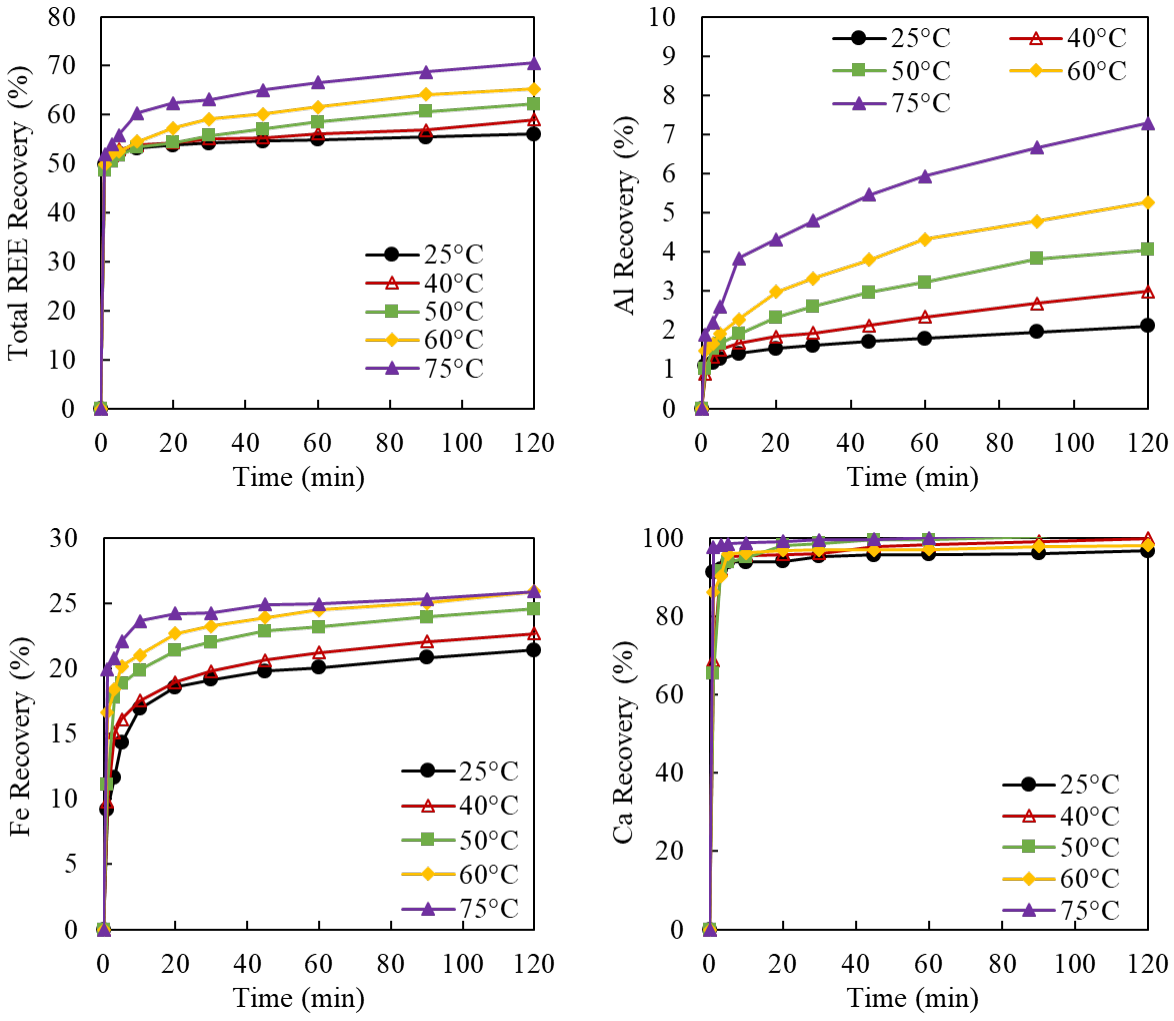

Figure 361. Effect of leaching reaction temperature on the leaching recovery of (a) Total rare earths, (b) Aluminum, (c) Iron, and (d) Calcium from the plus 9mm, 1.8 x 2.2 SG fraction of an Illinois No. 6 coal source; test conditions: 1 M H_2SO_4, 530 rpm and S/L=10g/L.

The temperature effect on the element-by-element recovery values after 2 hours of leaching is shown in Figure 362. The leaching recovery of yttrium and most of the heavy REEs were not dependent on leaching temperatures. Recovery values greater than 90% were achieved for Y, Dy and Tb at all temperature values tested. However, the leaching recovery values of La, Ce, Pr, and Nd were significantly impact by temperature which may be indicative of their existence in a mineral form whose dissolution is controlled by chemical reaction. This observation aligned very well with previous findings obtained from the treatment of Fire Clay decarbonized middlings material.

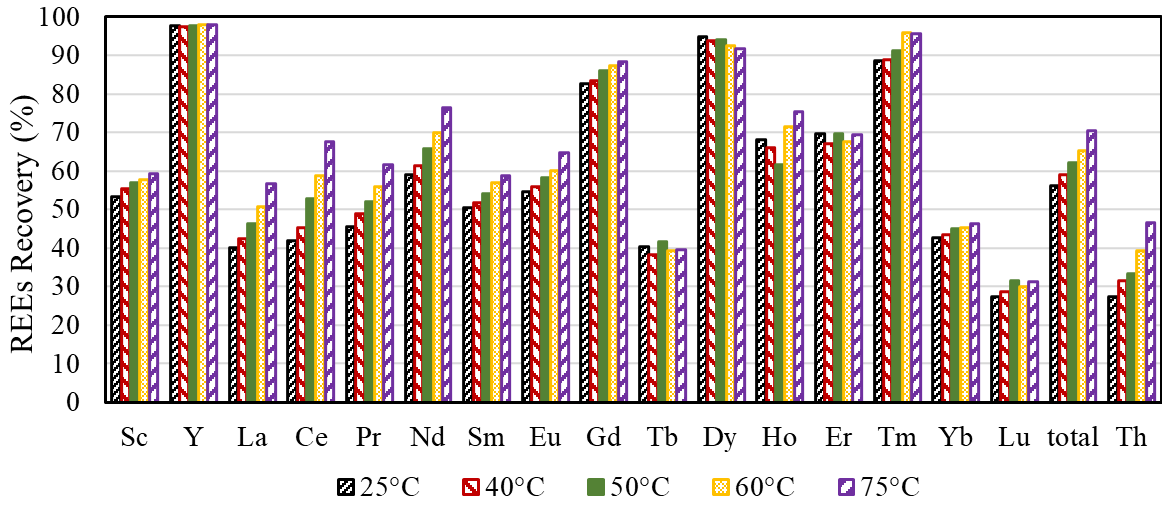

Figure 362. Elemental recovery as a function of temperature when leaching the plus 9mm, 1.8 x 2.2 SG fraction of an Illinois No. 6 coal source; test conditions: 1 M H_2SO_4, 530 rpm, S/L=10g/L and leaching time of 120 minutes).

Kinetic analysis

The leaching process for the extraction of REEs from coal-based material can be described by the shrinking core model based on previous investigations. Based on the shrinking core model, the reaction can be divided into a five-step process: diffusion through the film layer, diffusion through the product layer, chemical reaction on the surface, product diffusion through the product layer and product diffusion through the film layer to the solution (Xiao et al. 2015). Among the processes, the slowest is typically referred to as the controlling process that ultimately determines leaching rate. In most cases, the latter two diffusion processes are not the major controls. For the leaching kinetic analysis associated with the extraction of REEs from coal, the shrinking core model including surface chemical reaction and diffusion through the product layer were evaluated by plotting the real leaching time versus $[1-(1-\alpha)^{1/3}]$ and $[(1-2\alpha/3)+(1-\alpha)^{2/3}]$ (Gharabaghi, Noaparast, and Irannajad 2009; Levenspiel 1999).

Since the leaching reaction rate appeared to be different for REE recovery values before and after 10 minutes of leaching, the kinetic analyses were conducted separately. Using the data presented in the previous section, the rate process plots were generated for the first 10 minutes and 10-120 minutes reaction using both diffusion model and chemical reaction model as shown in Figure 363 and Figure 364, respectively. Both plots showed a straight line among all the temperatures using the experimental data for the 2 stages of the leaching process. The correlation coefficient values (R^2) and the corresponding slopes (k) are listed in Table 74 and Table 75. Rate constants were calculated and the Arrhenius plots of ln(k) versus 1/K are as shown in Figure 365 for the two leaching stages.

The activation energy determined for the first 10 minutes of leaching was 14.6 kJ/mol using the diffusion-controlled model and 12.9 kJ/mol using the reaction-controlled model. For the 10-120-minute period of leaching, the activation energy was 31. 6 kJ/mol as calculated using the diffusion model, and 35.9 kJ/mol calculated using the reaction model. The results indicated that the first 10 minutes of leaching was controlled by the diffusion process whereas the later stage of leaching was controlled by chemical reaction.

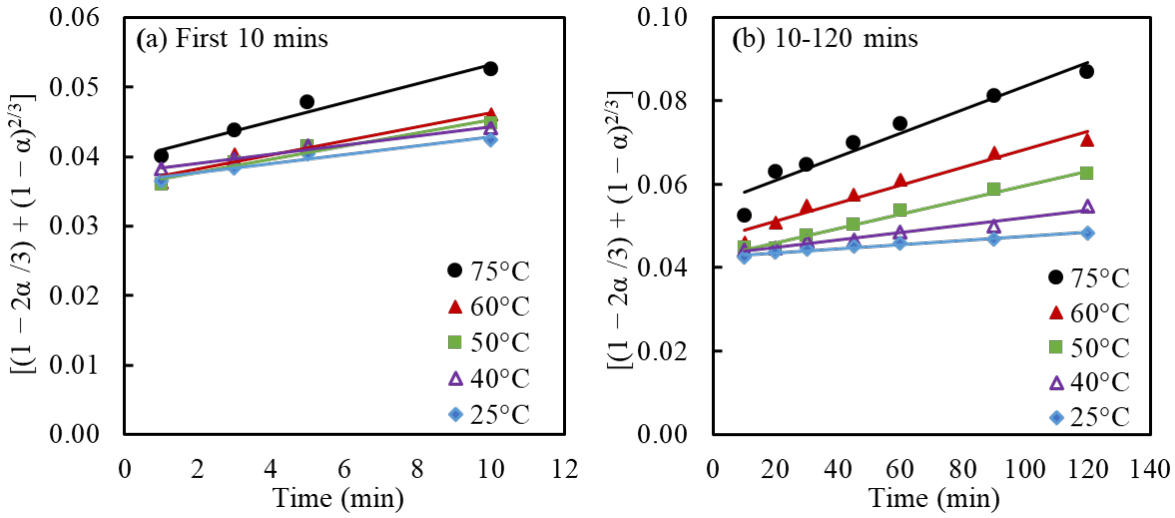

Figure 363. Diffusion through inner layer controlled kinetic model of total REEs recovery at (a) first 10 minutes, and (b) 10-120 minutes of leaching at various temperatures for the plus 9mm, 1.8 x 2.2 SG fraction of an Illinois No. 6 coal source; test conditions: 1 M H_2SO_4, 530 rpm, S/L=10g/L and leaching time of 120 minutes).

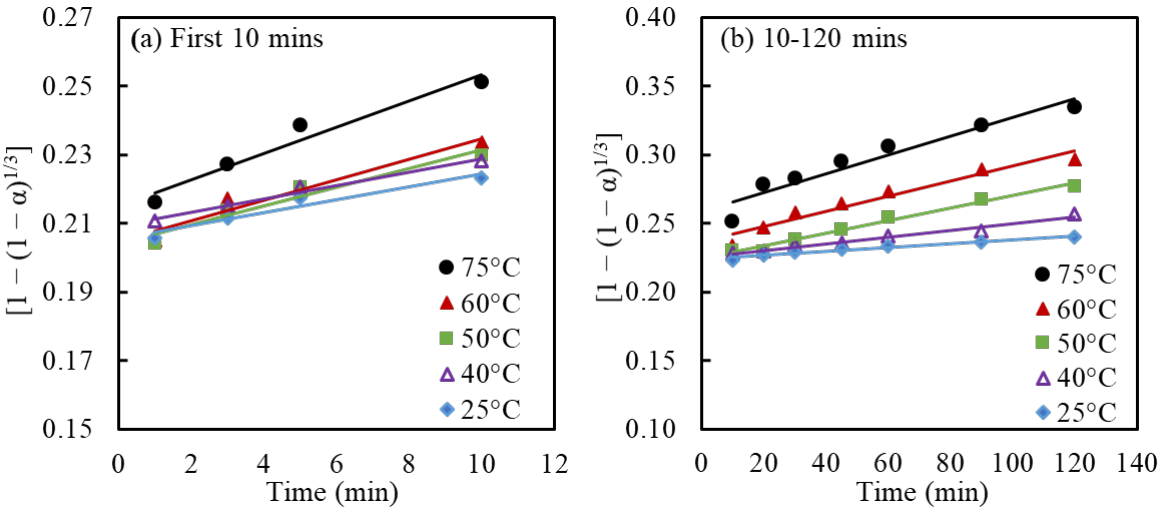

Figure 364. Chemical reaction controlled kinetic model of total REEs recovery at (a) first 10 minutes, and (b) 10-120 minutes of leaching at various temperatures for the plus 9mm, 1.8 x 2.2 SG fraction of an Illinois No. 6 coal source; test conditions:1 M H_2SO_4, S/L=10g/L and leaching time of 120 minutes).

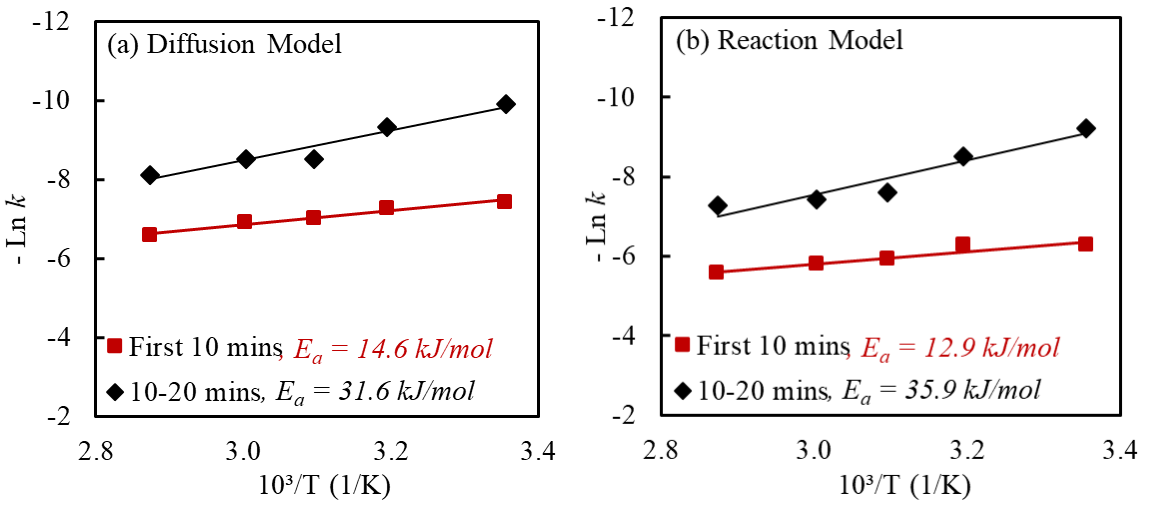

Figure 365. Arrhenius plot for the leaching of REEs from the plus 9mm, 1.8 x 2.2 SG fraction of an Illinois No. 6 coal using the (a) diffusion model, and (b) chemical reaction model; test conditions: 1 M H_2SO_4, 530 rpm and S/L=10g/L.

Table 74. Correlation coefficients of inner layer diffusion-controlled kinetic models at different temperatures for the plus 9mm, 1.8 x 2.2 SG fraction of an Illinois No. 6 coal source.

T, K	Diffusion First 10 mins			Diffusion 10-120 mins		
	k	a	R^2	k	a	R^2
298	0.0006	0.0364	0.9462	0.00005	0.0426	0.9619
313	0.0007	0.0377	0.9818	0.00009	0.043	0.9709
323	0.0009	0.0359	0.9526	0.0002	0.0425	0.9866
333	0.001	0.0361	0.9566	0.0002	0.0467	0.958
348	0.0014	0.0395	0.9588	0.0003	0.0551	0.9385

Table 75. Correlation coefficients of chemical reaction controlled kinetic models at different temperatures from the plus 9mm, 1.8 x 2.2 SG fraction of an Illinois No. 6 coal source.

T, K	Reaction First 10 mins			Reaction 10-120 mins		
	k	a	R^2	k	a	R^2
298	0.0019	0.2054	0.9425	0.0001	0.2239	0.9591
313	0.0019	0.2094	0.9798	0.0002	0.2252	0.9732
323	0.0027	0.204	0.9467	0.0005	0.2241	0.9837
333	0.003	0.2047	0.9512	0.0006	0.2362	0.949
348	0.0038	0.2151	0.9529	0.0007	0.2589	0.9249

Fire Clay Coal Testing

Characterization

A representative sample (~200 kg) of the Fire Clay seam coal was collected from the Leatherwood operation of Blackhawk Mining located in eastern Kentucky. The coal was air dried and screened at 9.5 mm and 1 mm. The plus 9.5 mm and 9.5 x 1 mm size fractions were density fractionated using media adjusted to specific gravity (SG) values of 1.4, 1.8 and 2.2. The medium was created using ultrafine magnetite that was suspended in tap water. The material finer than 1 mm was wet screened at 100 mesh (150 microns) on a vibration screen. The 1 x 0.15 mm size material was density fractionated using a medium having an SG value of 2.2. The medium was a heavy liquid Lithium Metatungstate (LMT). The minus 0.15 mm material was decarbonized using three stages of froth flotation in a manner described as a Rougher-Cleaner-Recleaner to obtain a low ash clean coal product and three flotation tailing products that were combined to form a decarbonized feedstock for REE leaching studies. The REE contents in each size by density fraction are provided in Table 76. The individual REE contents along with the contents of other major elements are listed in Table 77 and Table 78.

The REE concentrations in the Fire Clay coal is well known as one of the most concentrated REE sources among all the coal seams worldwide (Hower, Ruppert, and Eble 1999). The total REEs in the low ash content fractions on an ash basis was over 2000 ppm. Most of the REEs in this coal source was distributed into the high ash and density fraction which represent the coarse refuse stream in the coal preparation plant. The REEs contained in the +9.5 mm 2.2 SG sink fraction material account for over 50% of the total REEs in the coal source.

Table 76. Characterization of the REE content in Fire Clay seam coal after size and density fractionated.

Size Fraction	Density Fraction	Weight (%)	Ash (%)	TREE (ppm)		REE Distribution (%)
				Ash Basis	Coal Basis	
Plus 9.5 mm	s.g. 1.4 Float	21.4	6.4	2002	127.3	11.7
	s.g. 1.4 - 1.8	3.2	32.8	1030	337.8	4.6
	s.g. 1.8 - 2.2	4.3	74.9	605	453.4	8.5
	s.g. 2.2 Sink	40.1	88.1	330	291.0	50.1
9.5 mm x 1 mm	s.g. 1.4 Float	15.6	6.8	1454	98.9	6.6
	s.g. 1.4 - 1.8	5.1	56.9	526	299.2	6.6
	s.g. 1.8 - 2.2	5.3	88.9	335	297.7	6.8
	s.g. 2.2 Sink	0.6	92.0	293	269.9	0.7
1 mm x 0.15 mm	s.g. 2.2 Float	0.7	10.2	1124	114.6	0.3
	s.g. 2.2 Sink	0.3	91.1	333	303.6	0.3
Minus 0.15 mm	Coal	1.2	7.8	1399	109.7	0.6
	Tailing (3)	2.1	93.2	383	357.3	3.2
Total		100.00	55.4	421	233.1	100

Table 77. Rare earth element concentration on a dry ash basis in each size by density fraction of the Fire Clay Coal.

Size Fraction	Density Fraction	Weight (%)	REE Concentration as dry ash basis (ppm)																	
			Sc	Y	La	Ce	Pr	Nd	Sm	Eu	Gd	Tb	Dy	Ho	Er	Tm	Yb	Lu	Total	Th
Plus 9.5 mm	s.g. 1.4 Float	21.4	55	288	283	726	74	312	66	6	55	3	65	11	21	10	24	4	2002	96
	s.g. 1.4 - 1.8	3.2	36	88	154	383	42	163	35	4	27	1	13	5	11	3	9	1	977	61
	s.g. 1.8 - 2.2	4.3	22	43	98	247	26	102	22	2	16	0	11	3	6	2	4	0	605	38
	s.g. 2.2 Sink	40.1	14	28	56	119	14	59	13	1	10	0	6	1	4	1	3	0	330	22
9.5 mm x 1 mm	s.g. 1.4 Float	15.6	45	208	204	519	54	234	48	4	40	2	46	8	14	7	18	3	1454	75
	s.g. 1.4 - 1.8	5.1	21	45	86	202	21	90	19	2	15	0	11	3	7	2	4	0	526	41
	s.g. 1.8 - 2.2	5.3	15	28	55	125	14	59	13	1	10	0	6	1	4	1	3	0	335	24
	s.g. 2.2 Sink	0.6	16	27	51	92	15	55	13	1	9	1	4	0	4	1	3	1	293	21
1mm x 0.15 mm	s.g. 2.2 Float	0.7	37	140	179	405	42	206	0	3	31	0	16	12	18	5	15	15	1124	115
	s.g. 2.2 Sink	0.3	16	24	59	127	15	61	2	2	10	0	1	3	5	1	4	5	333	38
-0.15 mm	Coal	1.2	47	180	208	465	49	249	46	5	37	3	48	10	23	6	19	3	1399	137
	Tailing (3)	2.1	16	30	63	141	15	67	14	2	11	1	9	3	6	1	4	1	383	39
Total		100.00	17	40	68	155	18	73	16	1	12	0	9	2	5	1	4	0	420	28

Table 78. Other major element contents on a dry ash basis present in each size by density fractions in the Fire Clay coal.

Size Fraction	Density Fraction	Weight (%)	Major Elements Concentration as dry ash basis (ppm)																	
			Al	B	Ba	Ca	Co	Cu	Fe	K	Li	Mg	Mn	Na	Ni	P	Pb	Sr	V	Zn
Plus 9.5 mm	s.g. 1.4 Float	21.4	128930	256	896	7649	79	172	44220	7784	166	2877	208	3806	105	687	155	1141	241	131
	s.g. 1.4 - 1.8	3.2	124287	109	462	3003	19	33	25290	22840	159	6364	195	3296	28	382	114	183	113	82
	s.g. 1.8 - 2.2	4.3	126899	109	545	1679	20	43	21435	20700	212	5759	137	3414	37	553	120	293	141	79
	s.g. 2.2 Sink	40.1	107761	99	537	2133	18	21	39752	26605	98	7831	427	4712	27	438	88	154	100	105
9.5 mm x 1 mm	s.g. 1.4 Float	15.6	127707	222	832	8963	69	131	46821	11908	161	4000	214	4141	95	602	153	998	254	135
	s.g. 1.4 - 1.8	5.1	123583	98	472	3152	20	33	26964	23526	158	6623	218	3419	30	390	106	188	116	89
	s.g. 1.8 - 2.2	5.3	115863	105	507	2386	19	26	31169	26475	139	7757	271	4019	28	394	96	151	109	131
	s.g. 2.2 Sink	0.6	106397	108	512	4684	20	22	62772	27292	110	8482	774	4092	27	468	94	151	109	112
1mm x 0.15 mm	s.g. 2.2 Float	0.7	139464	162	750	8497	17	121	34812	15925	913	4770	170	3839	84	462	150	824	260	87
	s.g. 2.2 Sink	0.3	119158	55	497	5205	5	25	45011	26976	628	7786	293	4145	26	326	83	142	105	91
-0.15 mm	Coal	1.2	133220	197	1448	17390	82	252	51796	16606	173	6304	227	3494	135	735	206	1033	325	211
	Tailing (3)	2.1	114894	69	1415	6572	21	30	32903	33072	114	9564	216	5536	31	436	96	275	110	108
Total		100.00	106524	100	550	2585	20	29	35239	24123	115	7079	345	4227	30	425	91	204	107	100

Results and Discussion

Acid leaching experiments were carried out on each size by density fractionated sample using 1.2 M sulfuric acid and solids concentration of 10 g/L at 75 ℃. Intermediate samples were collected at 10, 30, 60, 180 and 300 minutes to obtain leaching kinetic data. The intermediate samples were centrifuged to separate the solid and liquid. At the completion of the leaching experiment, the remaining solid residue was filtered using a vacuum flask and thoroughly washed with deionized water. Both leachate and solid residue from each experiment were analyzed for elemental content using ICP-OES. Rare earth leaching recovery was calculated using the amount of rare earth in leachate divided by the total amount of rare earth in both leachate and solid residue.

The leaching recovery of TREEs from each fraction are plotted in Figure 366. The results of the individual REE recovery and the recovery of Al, Ca, Fe, and P are listed in Figure 367 (a)-(j). By comparing

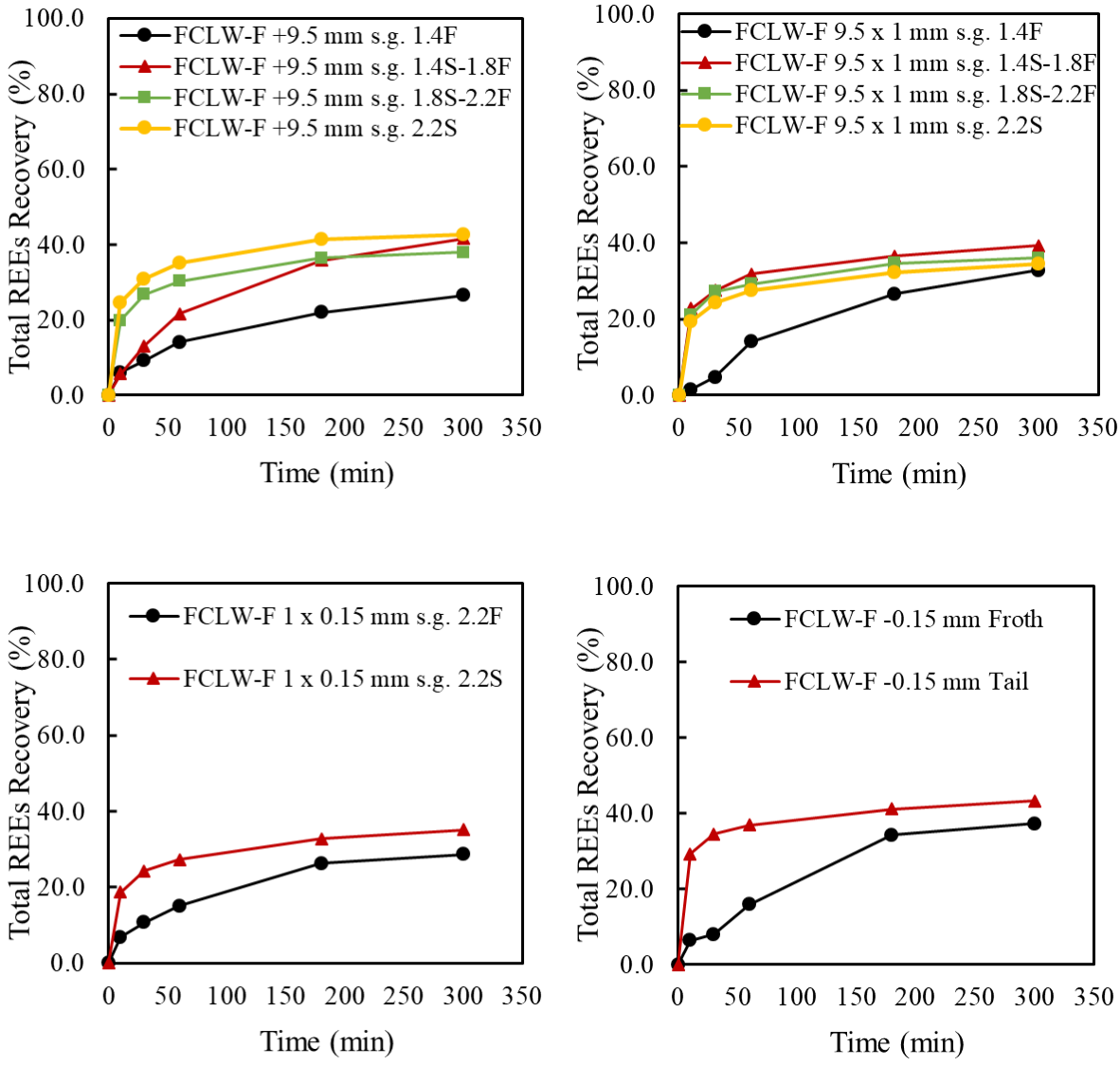

Figure 366. Leaching recovery of total REEs in each size by density fraction of the Fire Clay seam coal; test condition: 1.2M sulfuric acid, 530 rpm, S/L of 10 g/L and 75 ℃.

the leaching recovery of individual and total REEs among each sample, an interesting pattern was observed in that leaching recovery values of individual REE were similar for all the high ash content fractions. As shown in Figure 367 (c), (d), (f), (g), (h), (j), and (l), the recovery values of Sc were close to 20%, the recoveries of La, Ce, Nd were around 40%, and the values for Pr, Sm, Eu were around 50%. This observation indicates that the origin of REEs in Fire Clay coal seam were originally from same source.

The previous study conducted on the leaching kinetics of Fire Clay middling material indicated that after grinding and decarbonization, 75% of the total REEs was able to be extracted under the standard leaching conditions. The middling material represented the material coarser than 9.5 mm with a specific gravity between 1.4 and 1.8. The REEs leaching recovery of the abovementioned fraction was 40% after 5 hours leaching. Therefore, without mechanical liberation, the portion of REEs that was associated with the micro-dispersed mineral matter in coal was not effectively accessed by the lixiviate solution due to restrictions created by pores that are extremely hydrophobic. However, in the Illinois #6 material, the REEs leaching recovery of the 1.8-2.2 density fraction was 60% and 70% before and after mechanical liberation and decarbonization. The difference is likely due to coal rank between these two coal sources. The higher rank coal (Fire Clay) has a tight bond structure, whereas the lower rank coal is more porous. This hypothesis requires further investigation.

(a) FCLW-F +9.6 mm s.g. 1.4Float

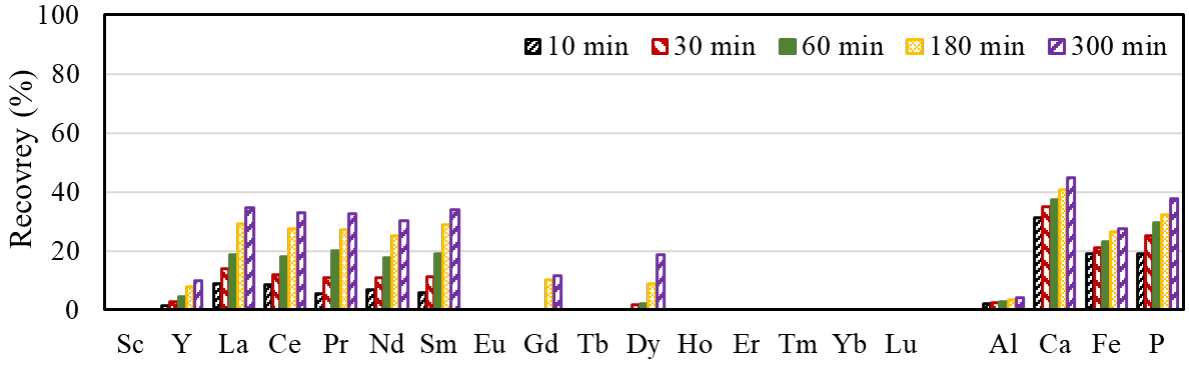

(b) FCLW-F +9.6 mm s.g. 1.4-1.8

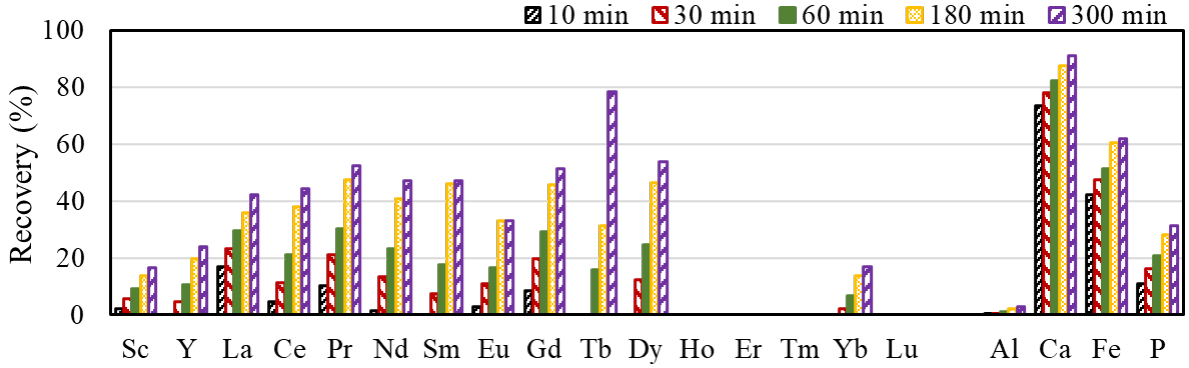

(c) FCLW-F +9.6 mm s.g. 1.8-2.2

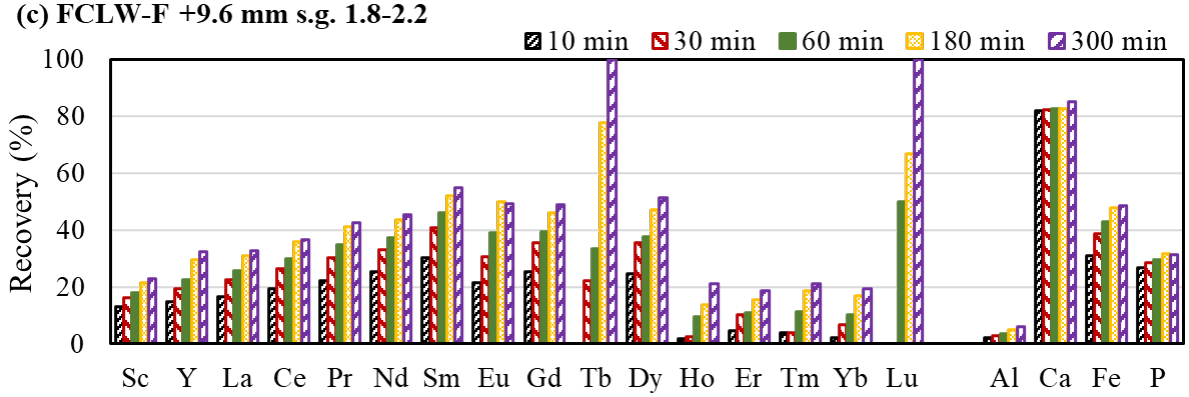

(d) FCLW-F +9.6 mm s.g. 2.2Sink

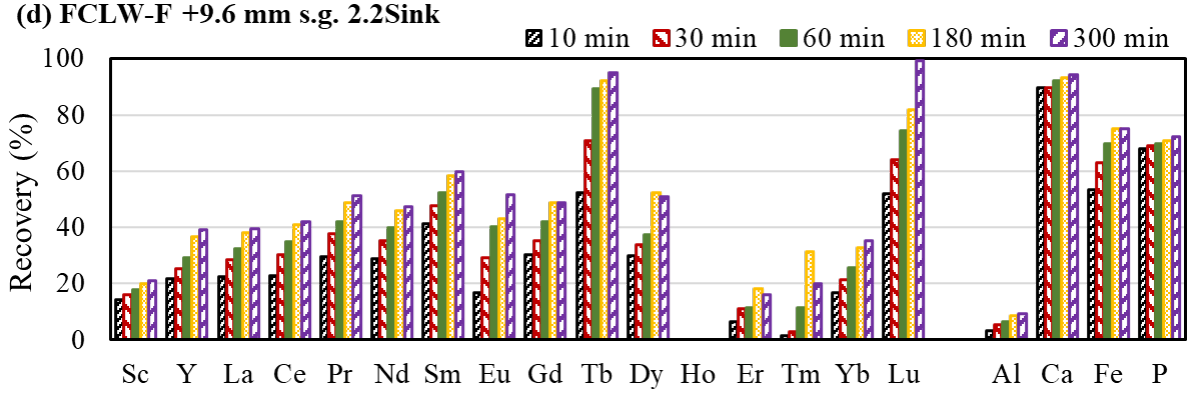

(e) FCLW-F -9.6 x1 mm s.g. 1.4Float

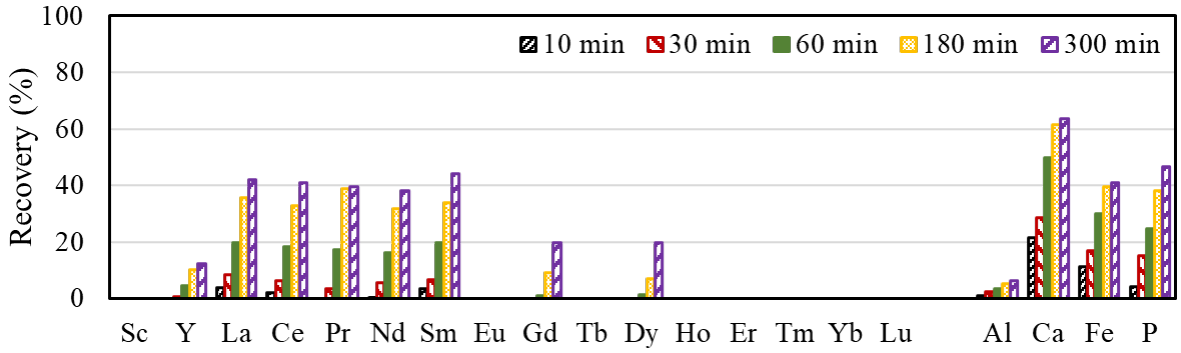

(f) FCLW-F -9.6 x1 mm s.g. 1.4-1.8

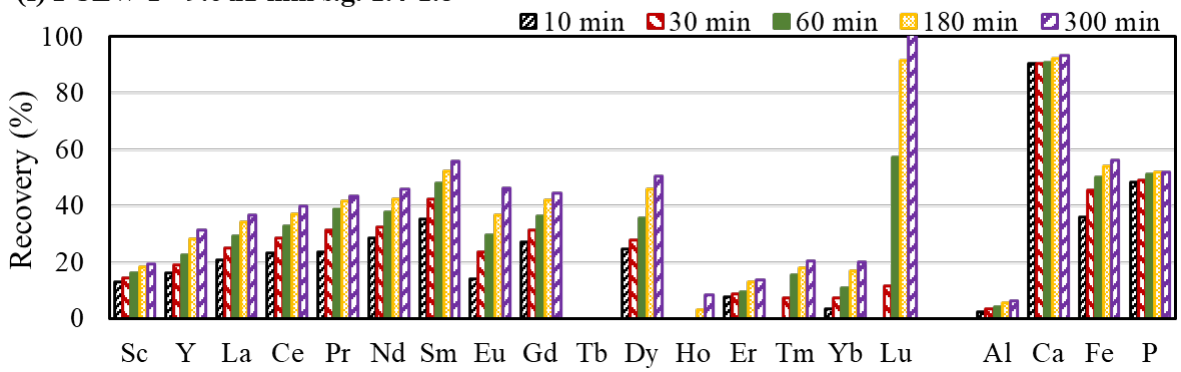

(g) FCLW-F -9.6 x1 mm s.g. 1.8-2.2

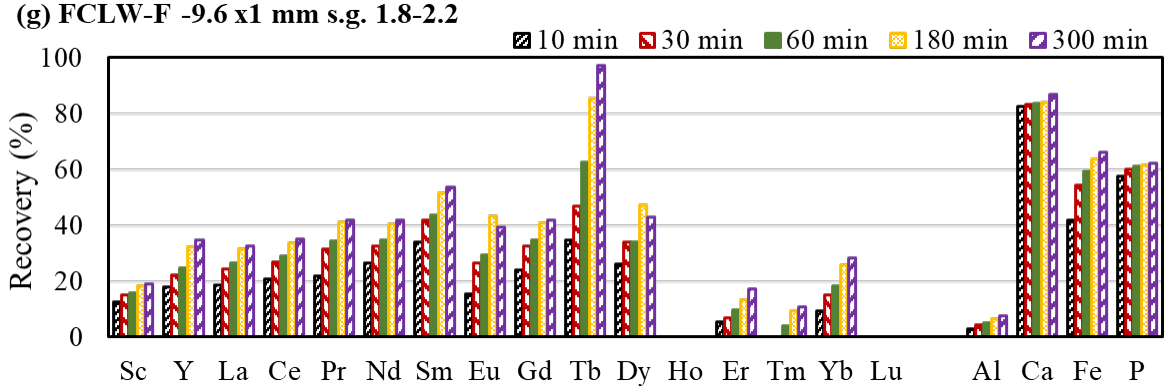

(h) FCLW-F -9.6 x1 mm s.g. 2.2Sink

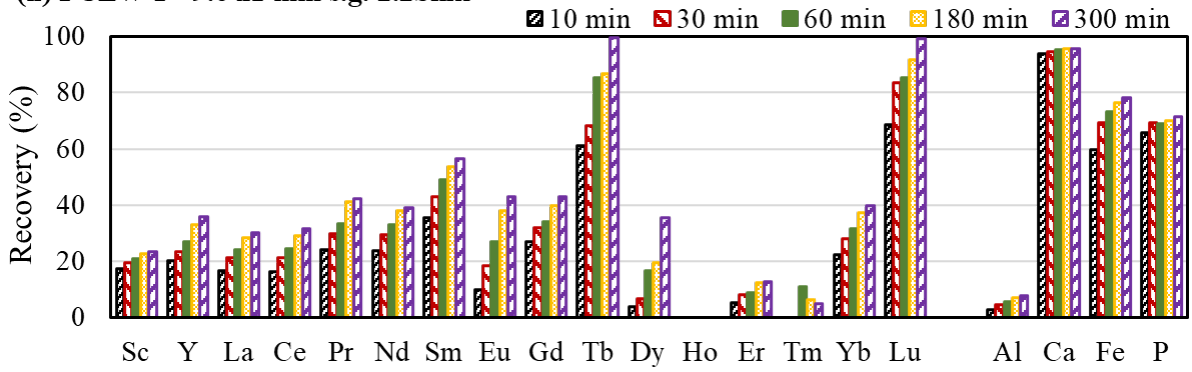

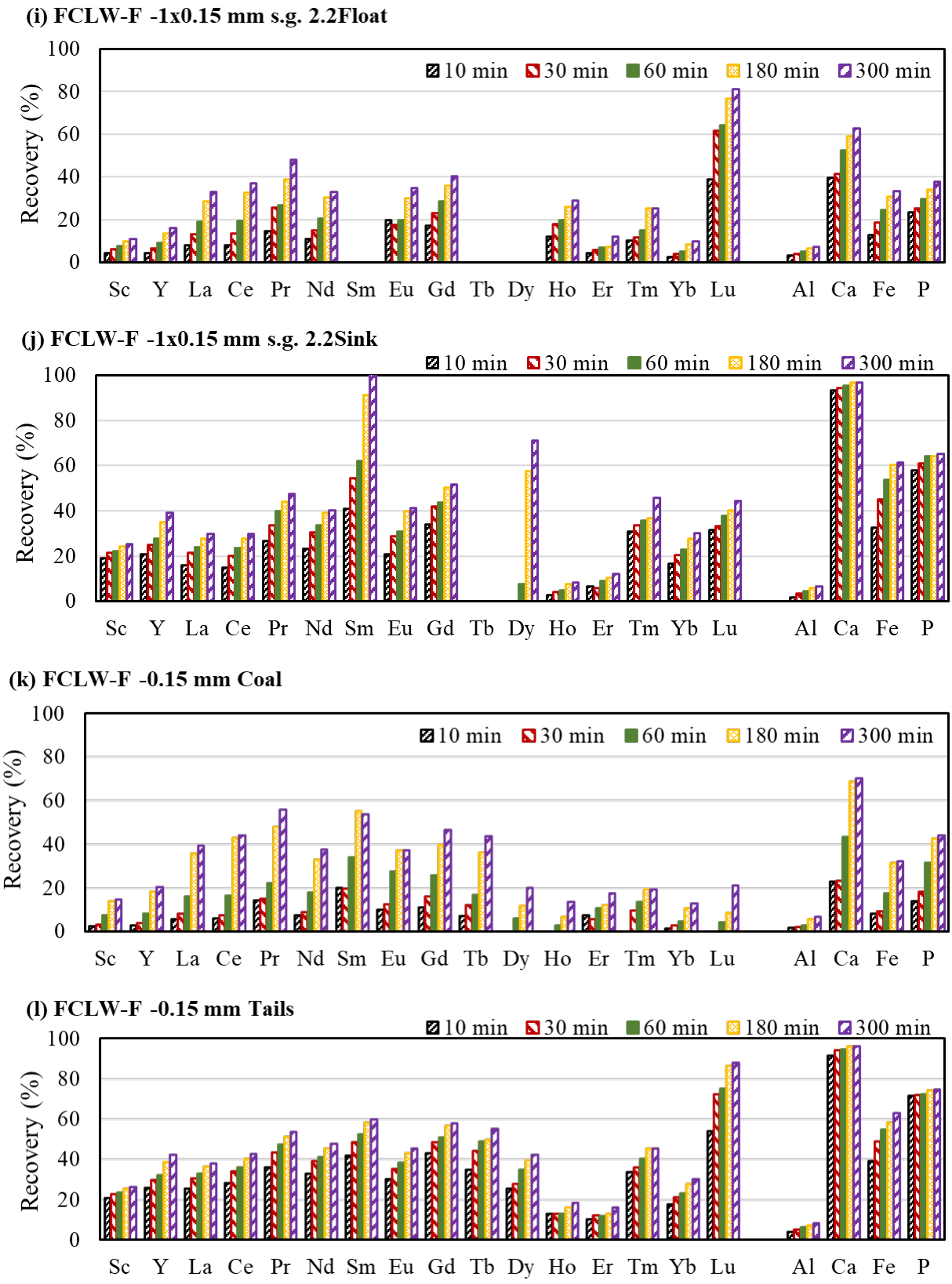

Figure 367. Leaching recovery of individual rare earth element and major contamination elements in each size by density fraction of the Fire Clay seam coal (1.2M sulfuric acid, 530 rpm, S/L of 10 g/L, 75°C).

Investigations of Leaching Mechanism

Introduction

Past studies have shown that leaching of REEs from coal sources were mostly controlled by product layer diffusion. In this section, the investigation focused on the surface characteristic change during leaching under different conditions on various materials. The elemental analyses showed that Fe and Ca are major contaminations in the leachate solution which have potential to form precipitates due to the local pH and Eh variations on the particle surface during leaching reaction. The hypothesis was that the precipitates formed on the particle surface caused blockage of pores as well as a barrier between the reactants and bulk solution.

A shrinking core model describes a leaching process where the initial solid particle shrinks in size and forms flaking ash layer and/or gaseous products with leaching time. The reaction occurs on the particle surface where the reactants and products transport between the solid particle surface and the bulk solution. The rate of the leaching process is relevant to either the reaction rate on the solid surface or the rate of transport (diffusion) whichever is the slowest. The diffusion rate depends on different mass transfer mechanisms in a solid-liquid reaction, such as film diffusion, pore diffusion, and product layer diffusion. Film diffusion usually occurs on a nonporous particle where surface reaction is fast. Pore diffusion is reaction controlling when the particle is porous and usually limits the reaction rate internally. Product layer diffusion occurs when there are flaking ash (precipitates) or metal oxides/hydroxides formation on the surface of the particles that limits the reaction.

In the coal tailing material, clays and quartz are the major minerals with minor minerals such as calcite, pyrite, and a minimal amount of micron-size RE minerals (phosphates). Previous investigations showed that the leaching process was mostly diffusion controlled which required approximately 20-40 kJ/mol of activation energy. In the current leaching system, the reacted particles are mostly porous, and the concentrations of Fe and Ca are generally dominating in the leachate solution. Thus, the pore diffusion and product layer diffusion mechanisms are taking place and controlling the leach rate. A series of surface characterization analyses were performed to investigate the phenomenon.

Surface Area and Pore Distribution Analysis

Materials

The sample used in this series of tests was the coarse reject sample collected from a coal preparation plant that treats the west Kentucky No. 13 seam coal. The sample was ground to a top size of 80 mesh (170 micron) and processed through column flotation to remove coal and alkali metal minerals. The processed material contained 90% ash-bearing material and about 350 ppm of total REEs on a whole sample basis. The material was wet screened using a sieve series to determine the particle size distribution. The major portion of the material was clays which accounted for over 62% of the weight which had a particle size finer than 500 mesh (<25 micron). X-ray diffraction analyses showed that the material contained typical mineral compositions that exist in most coal wastes: quartz (30%~35%), kaolinite (20%~30%), illite/muscovite (20%~30%), pyrite (4%~7%), and calcite (5%~13%) among all the size fractions. Therefore, the major source of Al, Fe, and Ca are clays, pyrite, and calcite, respectively. (see Table 79)

Past studies showed that the total REE leaching recovery reduced while increasing the leaching solid concentration. The association between reactants decreased with increasing the solid/liquid ratio which resulted in a decrease in the extraction rate. To eliminate the effect of reactant association, the acid consumption of this material was first tested with initial sulfuric acid concentration of 1.2 M and solid concentration of 200 g/L at 75℃. The test indicated that, with additional 0.4 M of sulfuric acid, the pH was maintained at the same initial condition. Therefore, the acid consumption was determined to be 0.2 g of sulfuric acid per gram of solid sample. Accordingly, four different solid concentrations (i.e. 20 g/L, 50 g/L, 100 g/L, and 200 g/L) were selected with 1.2 M, 1.3 M, 1.4 M, and 1.6 M sulfuric acid, respectively. Samples were collected at different time intervals during each test to analyze the change on surface characteristics as a function of time.

Table 79. Particle size distribution and REEs, Al, Fe, Ca concentration in each fraction.

Size Fraction	Ash (%)	Wt. (%)	Dry mass ash basis (ppm)					
			TREE	HREE	LREE	Al	Ca	Fe
+100 mesh	87.6	2.38	493	64	429	157543	8320	31848
-100x200 mesh	89.5	17.84	467	61	406	152116	5360	31401
-200x325 mesh	89.9	7.57	472	62	410	153805	4830	33783
-325x400 mesh	90.1	4.55	460	61	400	153519	4688	32961
-400x500 mesh	90.4	5.55	440	61	380	152175	4604	33643
-500 mesh	91.2	62.11	377	56	321	151087	3579	29767

Methodology

The BET surface area and pore size distribution analyses were conducted at the Center for Applied Energy Research (CAER) lab affiliated with the University of Kentucky. The instrument used for surface analysis is shown in Figure 368. The test started with measuring an accurate mass of solid sample after low temperature drying followed by immersion in nitrogen for adsorption of nitrogen onto the particle surfaces. Next, heat and vacuum were applied to desorb the nitrogen from sample. The amount of nitrogen adsorbed and desorbed at the sample surface under different relative chamber pressures was plotted as the isotherm sorption curve which was used to calculate the surface area and pore distribution of the solid sample using different models.

Figure 368. Instrumentation used for surface area analysis.

The isotherm sorption curve obtained for the solid sample follows multi-layer adsorption with capillary condensation. The isotherm curve was type IV with a type IV hysteresis. The surface area of each sample was calculated using the Brunauer–Emmett–Teller (BET) method where the single point total volume is equal to the volume of nitrogen that is dosed in the system at a specific P/Po. Since the sample does not appear to have cylindrical pore geometry, the average pore diameter was calculated using the Barrett-Joyner-Halenda (BHJ) method. BHJ method assumes capillary condensation of the liquid nitrogen within the pores. The desorption branch was used to plot the pore size distribution because it considers the meniscus which is not formed during the adsorption.

Results and Discussion

Leaching results showed that, with higher solid concentrations, leaching efficiency reduces even with an excessive amount of lixiviant as shown in Table 80. At a low solid concentration of 20 g/L, leaching recovery reached 16.3% after 5 hours. However, with 200 g/L solid concentration, the leaching recovery was 11.5% after 5 hours leaching. The BET analyses were performed to confirm the pore access change during leaching.

The results from surface area and pore distribution analyses on the leached samples under varying conditions are plotted in Figure 369 and summarized in Figure 370. The pore size of minerals are usually classified into three categories: micropores (< 2 nm), mesopores (2nm~50 nm), and macropores (>50 nm) (Zdravkov et al. 2007). Figure 369(a) shows that the pore size of the feed material was mainly 50 nm and above; thus, the pores can be classified as mostly mesopores and macropores. The surface area of the particles increased from about 21 m^2/g to an average of about 32 m^2/g after 5 hours of leaching at a solids concentration of 10 g/L (Figure 369b). The surface area increased rapidly at the beginning then stabilized throughout the test which indicated that the reaction was rapid at the beginning and gradually slowed thereafter which was similar to the leaching kinetics. The leaching efficiency results in Table 80 indicate 11% of the TREEs were leached during the first 30 minutes then slowly increased to 16% after 5 hours. These findings implied that the accessible surface area played an important role in the initial stage. However, at the end of the test, the surface area did not vary significantly among tests with different solid concentrations.

The increased surface area also created more adsorption capabilities that should have positively impacted the leaching process and potentially allow selective adsorption of anions from the bulk solution onto the particle surface. In many applications, acid-activated clays were generally used as a bleach (adsorbent) to decolorize waste water in dying process (Komadel and Madejová 2013; San Cristóbal et al. 2009). The swelling type of clay has more potential of being activated such as smectite and bentonite, whereas kaolinite can only be slightly activated by acid treatment. The acid-activated sample has higher capacity for cation exchange on the clay surface due to the change in Al coordination (San Cristóbal et al. 2009).

Table 80. Leaching efficiency of total REEs with different solid concentrations.

Test #	Time (min)	Solid Concentration	Lixiviate	Ending pH	TREEs Recovery (%)
1	30	200 g/L	1.6M H_2SO_4	0.03	7.71
	180				10.28
	300				11.50
2	30	100 g/L	1.4M H_2SO_4	0.04	8.32
	180				11.17
	300				13.21
3	30	50 g/L	1.3M H_2SO_4	0.02	9.70
	180				13.09
	300				14.45
4	30	20 g/L	1.2M H_2SO_4	0.08	10.84
	180				15.13
	300				16.33

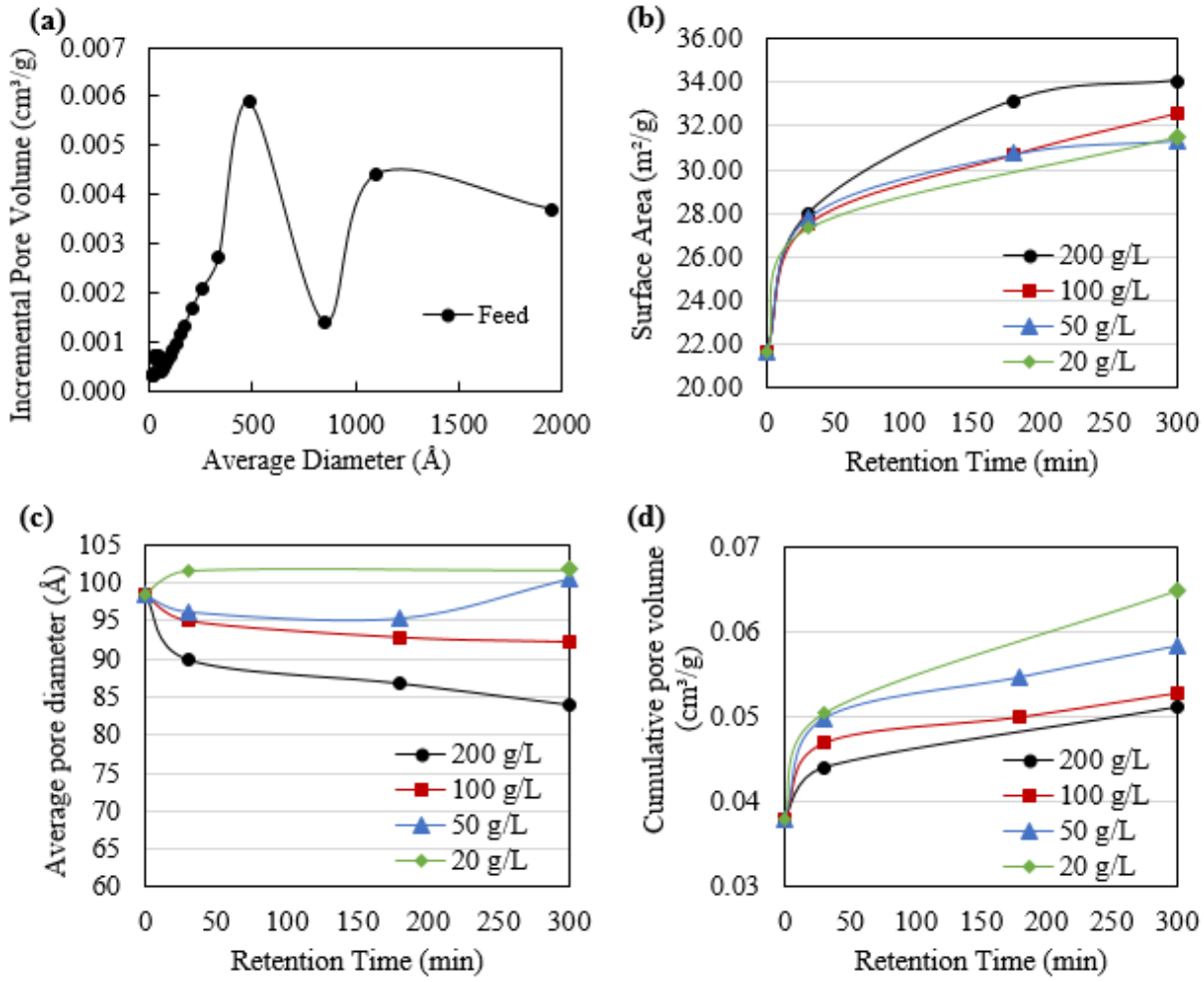

Figure 369. (a) Pore types in feed. (b) Surface area change during leaching; (c) Pore size change during leaching; (d) Pore volume change during leaching.

The cumulative pore volume increased with retention time which indicated that the material porosity increased as shown in Figure 369(d). Leaching with low solid concentration resulted in higher porosity compared to the that of the high solid concentration leaching on a per sample mass basis. While leaching with 20g/L of solids, the pore volume increased from about 0.04 cm^3/g to about 0.065 cm^3/g after 5 hours, which was more than a 50% increase. However, while leaching with 200 g/L solids, the pore volume only increased to 0.05 cm^3/g. When leaching with 200 g/L of solid, there were 1400 ppm of Fe, 700 ppm of Ca, and 1000 ppm of Al in the leachate solution at the end of 5 hours leaching. A possible explanation is that, at the particle surface and in the inner pores, localized areas of high pH values can occur due to the dissolution of micro dispersed minerals such as calcite which consumes hydrogen ions. The dissolved Fe and Ca ions form precipitates which block the pore access and create a boundary to prevent further reactions with the lixiviants. This hypothesis may explain why the average pore size changed differently with leaching time for the solid concentrations evaluated. At low solid concentrations, the pore size increased with leaching time as shown in Figure 369(c) due to the lower bulk concentrations of the metal ions and the pH shift to higher values was minimal. When treating high solid concentration solutions, the average pore size decreased with leaching time and the solution pH increase with time was significant. At a solids concentration of 200 g/L, pore size decreased slightly from 98 Å (9.8 nm) to about 83 Å (8.3 nm). Figure 371 shows the pore distribution shifts after leaching at varies solid concentrations which

indicated that more macropores were generated during leaching, but the effect of pore blockage became more severe with an increase in solid concentration.

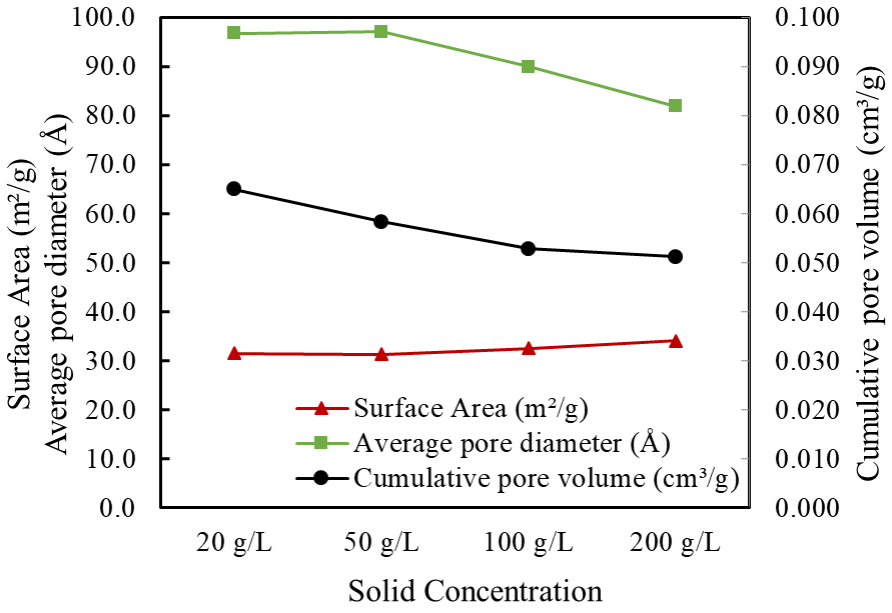

Figure 370. The effect of solid concentration on particle surface area, average pore size, and cumulative pore volume after 5 hours of leaching.

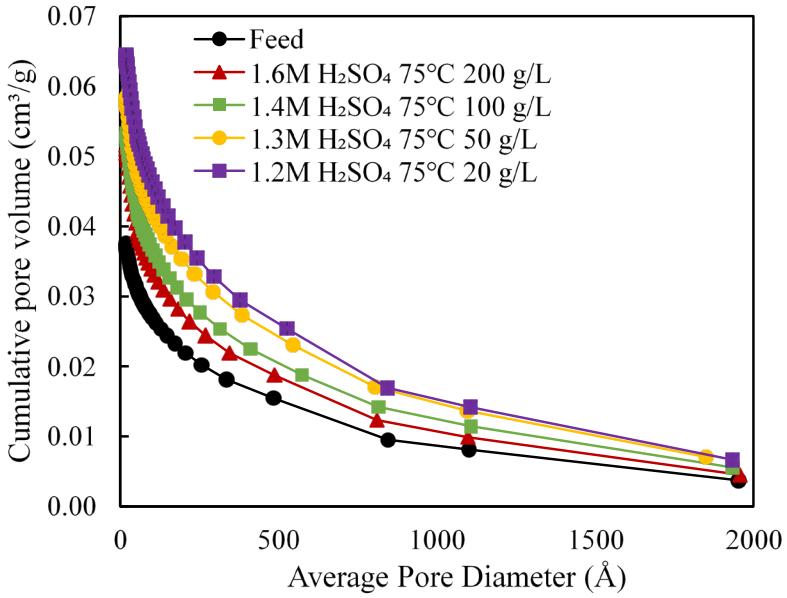

Figure 371. Pore size distribution before and after five hours leaching over a range of solids concentrations.

Investigation on Product Layer Formation

Material

The material used in this analysis was collected from the Hamilton mine preparation plant which processes coal originating from the Illinois No. 6 seam located in southern Illinois. The sample was fractionated into four different particle sizes (+9.5 mm, 9.5x1 mm, 1 mm x0.15 mm, and minus 0.15 mm), followed by density fractionation into four density categories (S.G. 1.4 float, S.G. 1.4x1.8, S.G. 1.8x2.2, and S.G. 2.2 sink). In the previous study, the size fraction that achieved the highest REE recovery value was the material coarser than 9.5 mm having a specific gravity (SG) in the range of 1.8 SG to 2.2 SG. This fraction contains 50.8% ash and 180 ppm of total REEs on a whole mass basis. The total REEs content of this material was upgraded to about 280 ppm on whole mass basis after coal removal using froth flotation. The leaching kinetics achieved using 1.2 M sulfuric acid at a solids concentration of 10 g/L indicated that the leaching process of this material was controlled by diffusion. The activation energy within the first 10 minutes was about 14.6 kJ/mol and around 31.6 kJ/mol during the 10- to 120-minute leaching period.

Methodology

To investigate the product layer diffusion in the leaching process, a set of tests were performed on the prepared material and analyzed for surface characteristic changes before and after leaching. Leaching tests were conducted in a heated water bath that was maintaining a 75 °C temperature. The test lasted for five hours and the final solid sample was filtered on a vacuum filter and washed thoroughly with deionized water. The solid residue sample was dried at a low temperature in an oven. The solid and leachate sample was subjected to elemental analysis using ICP-OES by the Kentucky Geological Survey located at the University of Kentucky. As shown in Table 81, leaching conditions were varied to examine the effect of solid concentration and inorganic acid types. The feed sample and the solid residue samples were submitted for XPS analysis to obtain the knowledge of the state change in the elements at the solid surface.

The X-ray photoelectron spectroscopy (XPS) analysis measures the elemental composition, chemical state, and electronic state of elements on a material surface by irradiating the surface with a beam of X-ray and collecting the emitted electron energy, intensity and direction. The XPS characterization was performed on a PHI Versa Probe III scanning XPS microscope using monochromatic Al K-alpha X-ray source (1486.6 eV) in the Surface Analysis Laboratory at Virginia Tech. Spectra were acquired with 100 µm/100 W/20 kV X-ray and dual-beam charge neutralization over a 1400 µm × 100 µm area. All binding energies were referenced to C-C at 284.8 eV. Peak deconvolution and chemical state of elements were assigned based on the PHI and NIST XPS.

Table 81. Leaching conditions and corresponding leaching recoveries of REEs and major metal elements.

Test #	Acid Type	Acid Concentration	Solid Concentration	Solid Loss (%)	Ending pH	Leaching Recovery at 5 hours (%)			
						TREE	Al	Ca	Fe
1	H_2SO_4	1 M	10 g/L	20.8	0.15	71.4	7.5	96.6	24.7
2	H_2SO_4	1 M	100 g/L	20.0	0.26	59.0	7.2	98.6	24.5
3	H_2SO_4	1 M	200 g/L	18.1	0.28	47.8	7.4	78.7	24.6
4	HCl	1 M	10 g/L	21.9	0.18	74.7	7.6	94.9	25.8
5	HNO_3	1 M	10 g/L	43.1	0.21	72.6	5.8	95.6	96.4

Results and Discussion

The XPS full spectra detected the presence of the following elements as shown in Figure 372: Mg, C, O, Fe, F, Ca, N, K, S, and Al. The O1s was overwhelmed by lattice oxygen in the clay, so oxygen in possible metal hydroxides or oxides could not be observed. There was a noticeable chemical state change of iron as shown in Figure 373, where Fe2p3/2 peak at 707eV binding energy is Fe metal and the peak at 712eV could be multiple compounds such as FeOOH, $FeSO_4$, and Fe_2O_3. To provide further distinction, solution chemistry analyses were performed. Calcium (Ca) was mostly absent in the solid residue after leaching with the exception of the residues from the high solid concentration (200 g/L) test as shown in Figure 374. This finding indicated that calcium precipitates may be forming during the leaching process when treating elevated solid concentrations (e.g., gypsum). It should be noted that gypsum is relatively insoluble in a sulfuric acid solution.

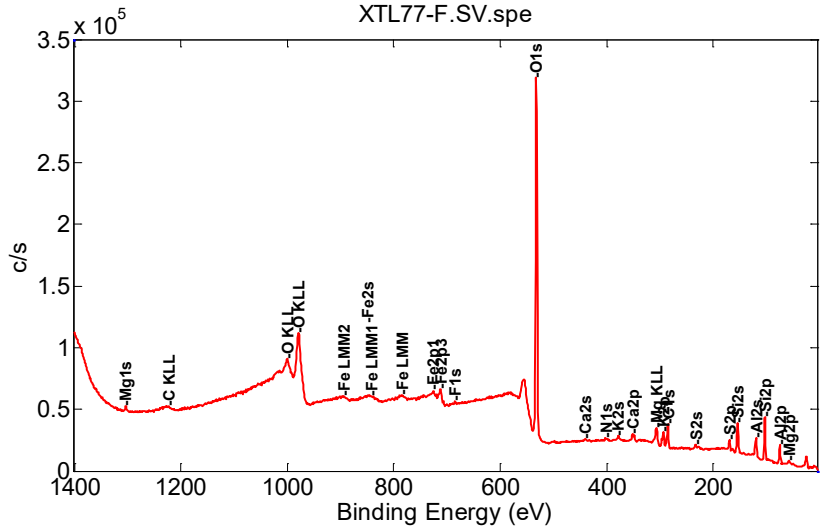

Figure 372. Full XPS spectra of the feed sample indicating major elements on the solid surface.

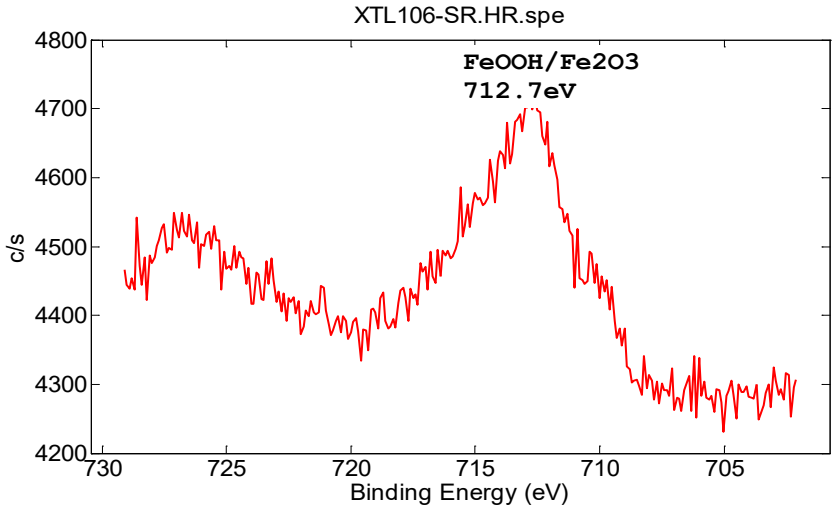

Figure 373. Fe state change on the particle surface after 5 hours leaching (1M HNO_3, 10 g/L solids, 75 ℃).

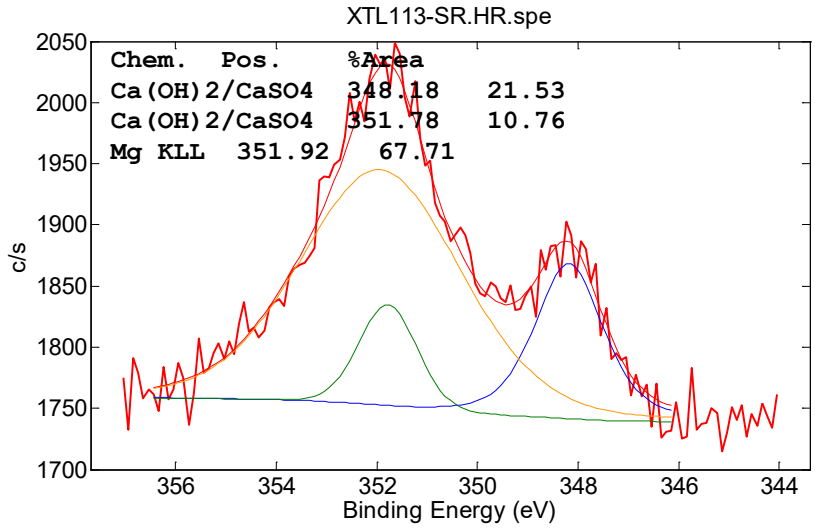

Figure 374. Ca state change on the particle surface after 5 hours leaching (1M H_2SO_4, 200 g/L solids, 75 ℃).

The reason for the difference in the Fe state in the sulfuric and nitric acid systems may be the varying levels of pyrite oxidation. The leaching reaction of pyrite with nitric acid in an aqueous environment can be described as:

$$FeS_2 + 5HNO_3 + 4H^+ = Fe^{3+} + 2{SO_4}^{2-} + 5NO(g) + 2H_2O. \qquad [5.1]$$

This reaction shows a natural production of the ferric (Fe^{3+}) ions in solution when using nitric acid. However, the reaction associated with pyrite in a sulfuric acid solution favors the generation of ferrous (Fe^{2+}) ions in solution. It should be noted that solutions that are aerated by mixing or other means will result in a reducing environment where Fe^{2+} is converted to Fe^{3+}.

In the nitric acid system, while increasing the solution pH, ferric ion hydrolysis will occur to form iron oxyhydroxide coatings on the particle surfaces. The coating acts as a product ash layer that reduces the exposure of the particle surface to the bulk solution. According to Huminicki and Rimstidt (2009), the formation of this product layer occurs in two stages: 1) The hydrolysis of Fe^{3+} forms iron hydroxide colloidal particles in the leachate solution which initiates the formation of a thin, porous layer (ash layer) on the solid surfaces; and 2) With the colloidal particle built up on the particle surfaces, the layer becomes thicker and less porous. A more structurally stable form of iron hydroxide such goethite (FeOOH) forms due to the presence of Fe^{3+} in solution.

However, pyrite reaction with sulfuric acid is less effective than that of nitric acid due to the generation of SO_4^{2-} in the solution. Considering that the redox potential change involved in ferric and ferrous systems, the Eh-pH diagram was generated for both nitric acid and sulfuric acid leaching systems with the actual concentrations of major elements in the coal-derived leachate solutions using a commercial software known as HSC Chemistry developed by Outotec. The input parameters and information are listed in Table 82. As shown in Figure 375 and Figure 376, the form of iron products in the sulfuric leaching system is more complicated than that of the nitric acid leaching system. At a pH value of 0.15 and redox potential of 300~600 mV, the Eh-pH diagram when using a H_2SO_4 solution indicates the existence of $(H_3O)Fe(SO_4)_2(H_2O)_3$, which is a solid phase material that forms around the pyrite particles. This finding may explain why the Fe recovery was only about 25% in the sulfuric leaching system.

Table 82. The input elemental concentration in HSC Chemistry software (Temperature of 75 ℃).

Test #	Acid Type	Acid Concentration	Solid Concentration	Ending pH	Concentration (µL/L)		
					Fe	Al	Ca
1	H_2SO_4	1 M	10 g/L	0.15	7.14E-06	1.73E-06	4.10E-06
5	HNO_3	1 M	10 g/L	0.21	2.50E-05	1.36E-06	4.03E-06

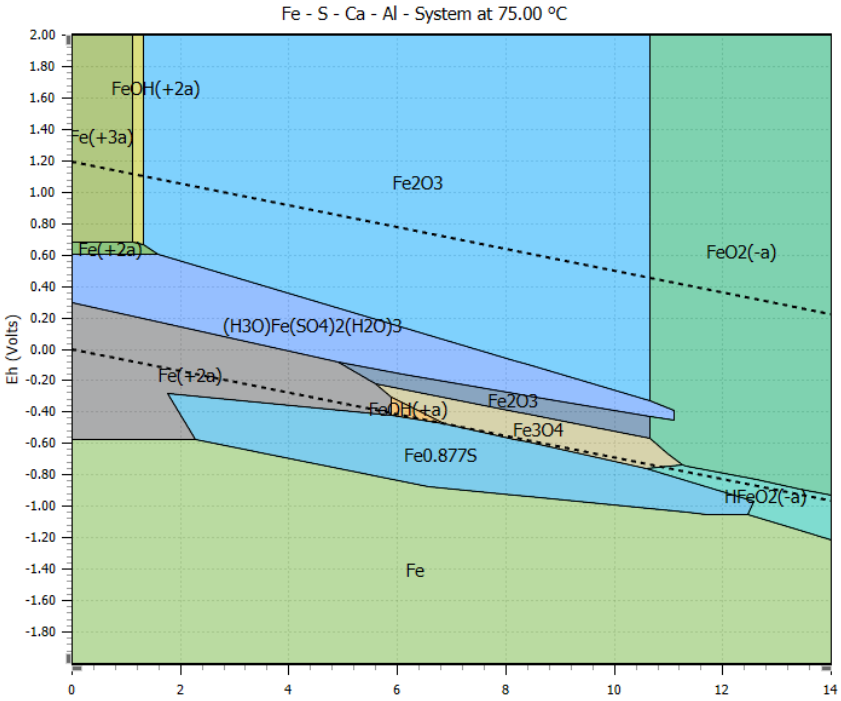

Figure 375. Eh-pH diagram of Fe in the system leaching with 1M H_2SO_4 and 10 g/L solid concentration at 75 ℃.

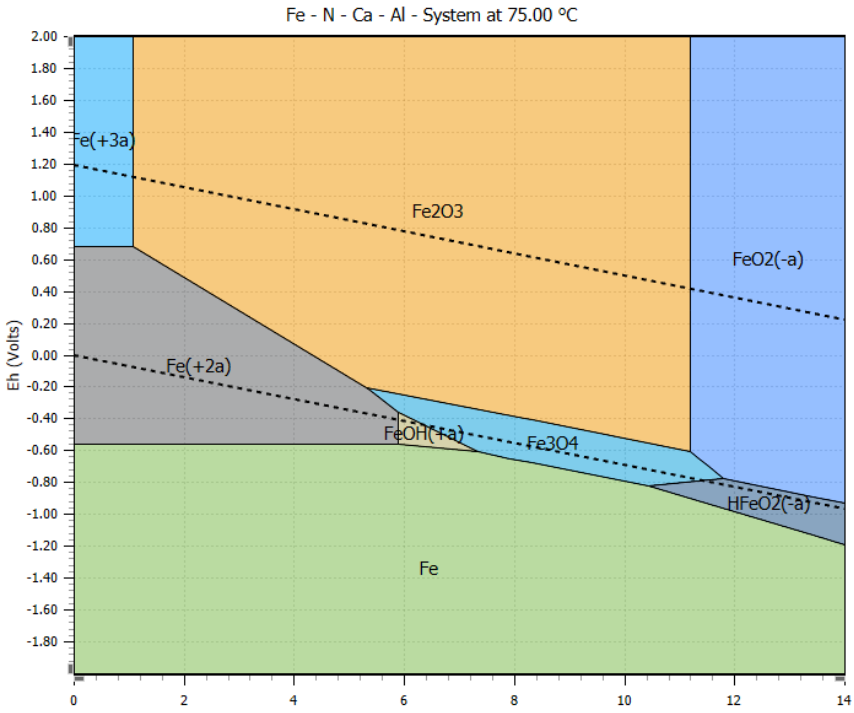

Figure 376. Eh-pH diagram of Fe in the system leaching with 1M HNO_3 and 10 g/L solid concentration at 75 °C.

REEs are known to co-precipitate with the gypsum formation during the leaching process due to their similarity to the Ca ionic radii (Bandara and Senanayake 2015; Brahim et al. 2008; Dutrizac 2017; Wang et al. 2010). In the current leaching system, the major Ca source was from calcite minerals that easily dissolve during leaching with 1M sulfuric acid. When leaching using a lower solid concentration, Ca recovery was close to 100% which indicated that no Ca was remaining in the solid. However, when the solid concentration increased to 200 g/L, the Ca recovery reached 99% at the beginning and then dropped to about 78%. The hypothesis is that the localized pH increases occurred at the particle surface and the inner pores during the leaching process which resulted in gypsum formation.

The rare earth ions are structurally incorporated in gypsum by replacing three Ca^{2+} ions with two trivalent rare earth ions and leaving a Ca^{2+} lattice. The findings of a study reported by Dutrizac (2017) indicate that the light REEs were more likely to co-precipitate with $CaSO_4$ compared to heavy REEs which was also observed in the current leaching system. From our experiments, the heavy REE recovery values at solid concentrations of 10 g/L, 100 g/L, and 200 g/L were 79%, 79%, and 76%, respectively, whereas the light REE recovery for 10 g/L, 100 g/L, and 200 g/L solid concentration were 68%, 53%, and 39%, respectively.

The XPS results showed a formation of either $Ca(OH)_2$ or $CaSO_4$, or a combination of both. The solution chemistry was further studied to identify the precipitation species using the software MINTEQ. The input information and parameters are listed in Table 83, where the major elements in solution were calculated based on the real leachate solution analysis. The concentration of SO_4^{2-} was assumed to be 1 M since it was the initial concentration of acid and the molarity is much higher compare to other species.

Table 83. IInput values and parameters in MINTEQ to estimate species and corresponding activities in the real leachate solution.

Input information	Value
pH	0.28
Temperature	75 ℃
Ca^{2+}	7.00E-05 M
Fe^{2+}	0.0001 M
Al^{3+}	3.60E-05 M
SO_4^{2-}	1 M

The major species of the real leachate system and their corresponding concentration/activities are listed in Table 84. The ionic strength calculated for this system is 0.82 M which is acceptable to validate the calculations. The major form of existence of Al, Ca, and Fe in the leachate solution was $Al(SO_4)_2^-$, Ca^{2+}, and Fe^{2+}, respectively. The formation of insoluble $Ca(OH)_2$ or $CaSO_4$ precipitation can be described as: (Kim et al. 2016)

$$Ca^{2+} + 2OH^- = Ca(OH)_2\,, K_{s1} \qquad [5.5.4]$$

$$Ca^{2+} + SO_4^{2-} = CaSO_{4(s)}\,, K_{s2} \qquad [5.5.5]$$

Using the calculated activities listed in Table 84, the solubility coefficients can be calculated for $Ca(OH)_2$ or $CaSO_4$ as shown below:

$$K_{s1} = [Ca^{2+}][OH^-]^2 = 3.8 \times 10^{-30} \qquad [5.5.6]$$

$$K_{s2} = [Ca^{2+}][SO_4^{2-}] = 5.6 \times 10^{-8}. \qquad [5.5.7]$$

These solubility coefficient values indicate that a relatively insoluble $CaSO_4$ precipitate can be easily formed when using a sulfuric acid solution as the lixiviant. However, in a nitric acid solution, the sulfate groups are mostly combined with hydrogen ions which limits the formation of relatively insoluble gypsum.

Table 84. Estimation of species in leachate solution leaching with 1M sulfuric acid at 200 g/L, 75 ℃. (Calculated by MINTEQ). Ionic strength = 0.82.

Species	Concentration (M)	Activity (M)	Log activity
$Al(OH)_2^+$	8.3E-14	6.2E-14	-1.3E+01
$Al(OH)_{3\ (aq)}$	8.5E-19	1.0E-18	-1.8E+01
$Al(OH)_4^-$	1.9E-24	1.4E-24	-2.4E+01
$Al(SO_4)_2^-$	1.8E-05	1.4E-05	-4.9E+00
Al^{3+}	3.9E-06	2.9E-07	-6.5E+00
$Al_2(OH)_2^{4+}$	4.6E-17	4.5E-19	-1.8E+01
$Al_3(OH)_4^{5+}$	1.8E-26	1.3E-29	-2.9E+01
$AlOH^{2+}$	2.8E-10	8.8E-11	-1.0E+01
$AlSO^{4+}$	1.4E-05	1.0E-05	-5.0E+00
Ca^{2+}	5.4E-05	1.7E-05	-4.8E+00
$CaOH^+$	3.5E-16	2.6E-16	-1.6E+01
$CaSO_{4\ (aq)}$	1.6E-05	1.9E-05	-4.7E+00
$Fe(OH)_{2\ (aq)}$	2.2E-22	2.7E-22	-2.2E+01
$Fe(OH)_3^-$	3.1E-32	2.4E-32	-3.2E+01
Fe^{2+}	7.5E-05	2.4E-05	-4.6E+00
$FeOH^+$	6.0E-13	4.5E-13	-1.2E+01
$FeSO_{4\ (aq)}$	2.5E-05	3.0E-05	-4.5E+00
H^+	7.0E-01	5.2E-01	-2.8E-01
HSO_4^-	9.9E-01	7.4E-01	-1.3E-01
OH^-	6.3E-13	4.7E-13	-1.2E+01
SO_4^{2-}	1.0E-02	3.2E-03	-2.5E+00

Sequential Extraction Tests

Introduction

Recent research has found that pretreating bituminous coal sources prior to leaching in a lower temperature, oxidizing environment at around 600ºC provides improved leaching characteristics that results in a higher recovery of the REEs with lower chemical consumption. This environment does not convert the associated mineral matter into a glassy matrix. In this study, the 1.4 specific gravity (SG) float fractions of three different bituminous seam coal sources, i.e., Fire Clay, West Kentucky No.13, and Illinois No.6, were treated at 600℃ for 2 hours prior to leaching using a sequential extraction procedure. Both the untreated and treated coal samples were characterized to identify the mineralogical changes after the high temperature treatment. Sequential extraction tests were performed on the roasted material to quantify the modes of occurrence of the REEs. Leaching tests using different solution pH and ammonium sulfate dosages were also conducted to assess the possibility to economically recover the REEs.

Experimental

Materials

Representative samples of three coal seam sources were collected from three coal preparation plants located in Kentucky, USA. The plants processed coals originating from the Fire Clay, West Kentucky No.13, and Illinois No.6 seams, respectively. The samples were air dried and the plus 1 cm fraction obtained by dry sieving. The oversize fraction was density fractionated using a magnetite media adjusted to a 1.4 specific gravity (SG). The 1.4 SG float fractions were collected, rinsed, and air dried. The dry ash contents of the three coal samples were 6.51%, 6.71%, and 7.13%, respectively.

Trace metal grade acids, including hydrochloric acid (HCl), nitric acid (HNO_3), hydrofluoric acid (HF), and acetic acid (CH_3COOH), were purchased from Fisher Scientific and used for sequential extraction and leaching tests as well as solid sample digestion. Magnesium chloride ($MgCl_2$), sodium acetate (CH_3COONa), and hydroxylammonium chloride ($NH_2OH\cdot HCl$) of more than 99% purity was used for the sequential extraction tests. Ammonium sulfate of 99.95% purity was purchased from Alfa Aesar and used for the ion exchange tests. All the tests were performed using deionized water with a resistivity of 18.2 MΩ·cm at 25℃.

High Temperature Pretreatment

The 1.4 SG float samples obtained from the three coal seams were divided 5 gram increments and poured into ceramic crucibles (5 g per crucible). The samples and crucibles were placed in an oven manufactured by Thermo Scientific. The samples were calcined at the predetermined temperature (e.g., 600℃) for 120 min, which was achieved by heating from room temperature with an elevation rate of 4.2℃/min. After the treatment, the temperature in the oven cooled automatically. The roasted material in the crucibles was collected and used for the experiments in this study.

Sequential Extraction Tests

Sequential extraction tests have been widely used to determine the modes of occurrence of metallic elements in solid materials, including coal, coal ash, soils, etc. (Chou et al., 2009; Finkelman et al., 2018; Huggins, 2002; Lin et al., 2018; Mittermüller, et al., 2016; Pan et al., 2019). In these tests, the samples were sequentially reacted with different reagents that have specific affinities for certain mineral forms. The fractions of ion-exchangeable forms of metallic elements are usually quantified by using cations with low hydration energies, such as NH_4^+, Ca^{2+}, and Mg^{2+}. Acids of low concentrations (e.g., dilute HCl and acetic acid) have been used to selectively dissolve the carbonates. Chou et al. (2009) and Pan et al. (2019) used 0.04 M hydroxylammonium chloride ($NH_2OH\cdot HCl$) in 25% acetic acid to extract Pb, Cu, Cd, and rare earth elements (REEs) from coal fly ash. Lin et al. (2018) quantified the fractions of REEs in fly ash associated with amorphous and crystalline iron oxides using combinations of ammonium oxalate, oxalic acid, and ascorbic acid. Sulfides in coal are usually leached using nitric acid (e.g., 2M at 25℃) and elements associated with silicates have been extracted using HF with and without aqua regia (HNO_3/HCl=1/3). To

determine the amount of elements combined with organics, oxidants such as concentrate HNO_3 and H_2O_2 have been used to destroy the organic matrix.

A sequential extraction procedure was designed for the roasted samples obtained by oxidizing the coal samples at 600℃ for 2 hours. The occurrence of rare earth elements was classified into five types: 1) exchangeable, 2) carbonates, 3) metal oxides, 4) acid soluble, and 5) insoluble, which were quantified by leaching the solids using different reagents (Table 85) and test conditions. For each sequential extraction test, two grams of solids were mixed with the extractants using a magnetic stirring. After each step, both the residual solid and leachate were collected by a centrifuge at 3000 rpm. The residual solid was dried and used as a feed for the following extraction step. The REE concentration in the leachate was analyzed using an ICP-OES. In the last step, the solid was completely digested using a mixed acid of hydrofluoric acid and aqua regia. The digestion solution was also analyzed using the ICP-OES. The REE content in the feed solid was back-calculated using the REE concentration and the volume of the leachates. The deviations between the back-calculated and the directly measured REE contents of the feeds were less than 5%. The fraction of the REEs was calculated using the amount of REEs existed in the leachate divided by the total amount of REEs in the solid.

Table 85. Sequential extraction procedure

Fraction	Extraction Reagent	Reaction Condition	
		Time(h)	Temperature(℃)
Exchangeable	$MgCl_2$ Solution (1M, 40ml)	1	25
Carbonate	CH_3COONa Solution (1M, 40ml)	5	25
Metal Oxides	0.04M $NH_2OH\cdot$ HCl in 25% Acetic Acid (100ml)	3	95
Acid Soluble	Nitric Acid Solution (2M, 40ml)	18	25
Insoluble/Silicates	Digestion (aqua regia+HF)	8	120

Leaching Tests

A systematic study was performed to evaluate the effects of pH (4 and 5) and ion-exchange lixiviant (0, 0.1, and 1 M ammonium sulfate) on the leaching recovery and kinetics of rare earth elements from the coal ash samples obtained by calcination. The leaching tests were performed in a round bottom flask and the leaching temperature was maintained at 75°C, which was achieved by using a water bath. For each test, 10 gram solids were mixed with 1 liter deionized water in the flask by using a magnetic stirrer. If required, certain amounts of ammonium sulfate were added into the solution prior to the solid addition. The suspension pH was maintained at a constant value (5 or 4) by using diluted HNO_3 and NaOH. Represent samples were taken from the flask at different time intervals (5min, 15min, 30min, 45min, 60min, 90min, 2h, 3h, 4h, and 5h) of the leaching process, which was lasted for a total period of 5 hours. The solid and liquid were separated by filtration and the REE concentration in the liquid was analyzed using an ICP-OES. The residual slurry after leaching was also filtered and the solid was dried and digested for elemental analysis. Elemental contents (E_f, ppm) in the feed solids were back calculated using the following equations:

$$E_f = 100 \times (C_s \times m_s + C_l \times V_l) \times m_i / (m_i - m_m) \quad [5.5.8]$$

where C_s and C_l represent the elemental concentrations (ppm) in the solid residual and final leachate; m_s (kg) weight of the leaching solid residual; V_l (liter) volume of the residual leachate; m_i (kg) weight of the total leaching slurry; m_m (kg) weight of all the representative samples collected during the leaching process. The difference between the back-calculated contents and the values measured directly using ICP was within ±5%, indicating minor experimental errors. Leaching recovery (R_i, %) was calculated using the following equation:

$$R_i = 100\% \times C_i \times V / (E_f \times 0.01). \quad [5.5.9]$$

where C_i (ppm) represents elemental concentrations in the filtrates collected during the leaching process, V volume of the feed solution (1 liter), and E_f (ppm) the back-calculated elemental contents in the feed solids. All the REE contents in solids are based on a dry whole sample basis.

Sample Characterization

Digestion of the solid samples followed the ASTM D6357-11 standard, which utilized hydrofluoric, nitric, and hydrochloric acids of trace metal basis at an elevated temperature. The ICP-OES, used for measuring element concentration in solution, was manufactured by Thermo Scientific. X-ray diffraction (XRD) characterization was performed using a Bruker-AXS D8 DISCOVER diffractometer which was configured in a parallel beam geometry with Cu-Kα radiation. XRD patterns were recorded over a 2θ range of 5°-70° with a step size of 0.02°. XRD patterns were analyzed using DIFFRAC, a commercial software developed by Bruker Corporation.

Results and Discussion

Sample Characterization

The rare earth element contents in the three roasted coal samples are shown in Table 86. The Fire Clay roasted coal material contained a significantly higher amount of rare earth elements (REEs) relative to the other two resources, i.e., West Kentucky No.13 and Illinois No.6. The extremely high contents of REEs in Fire Clay coals have been reported previously by Hower et al. (1999), which was ascribed to the existence of a Tonstein layer in the coal seam. The West Kentucky No.13 coal ash contained relatively higher amounts of heavy REEs (HREEs) as indicated by the highest heavy-to-light REE (H/L) ratio (0.51).

Table 86. REE contents in the roasted coal samples (TREE: total REE; HREE: heavy REE; LREE: light REE; H/L: heavy to light REE ratio)

Sample	TREE	HREE	LREE	H/L	Sc	Y	La	Ce	Pr	Nd
FC	1852	459	1393	0.33	54.8	266.2	264.1	682.5	66.6	268.7
WK13	489.5	164.7	325.0	0.51	49.4	83.4	51.1	110.2	18.9	70.3
IL6	396.6	107.1	289.5	0.37	30.1	52.5	51.4	115.5	18.1	57.6
Sample	Sm	Eu	Gd	Tb	Dy	Ho	Er	Tm	Yb	Lu
FC	56.6	5.0	48.6	3.5	58.1	10.5	29.4	8.4	24.7	4.3
WK13	25.0	4.9	19.8	7.1	17.1	0.3	10.3	3.1	12.4	6.4
IL6	16.9	2.9	14.1	3.4	14.9	0.3	6.1	1.9	7.2	3.7

Table 87. Semi-quantification of the minerals in the samples using the XRD analysis (FC-Fire Clay, WK13-West Kentucky No.13, IL6-Illinois No.6)

Sample	Quartz	Kaolinite	Illite	Pyrite	Hematite	Calcite	Anatase
FC-Coal	32.2	55.0	8.0	0	0	0	4.8
FC-Roasted	87.6	0	8.9	0	0	0	3.5
WK13-Coal	31.5	36.0	7.7	12.4	0	5.5	6.9
WK13-Roasted	44.0	0	8.8	0	41.0	5.2	0.9
IL6-Coal	27.5	31.7	25.1	11.8	0	3.9	0
IL6-Roasted	58.4	0	20.3	0	17.5	2.4	1.3

Mineralogical compositions of both the untreated and treated (roasted) coal samples were analyzed using X-ray diffraction (XRD). The patterns and semi-quantification results are shown in Figure 377 and Table 87, respectively. For the West Kentucky No.13 and Illinois No.6 coals, quartz, kaolinite, illite, and pyrite were the dominant minerals, while for the Fire Clay coal, pyrite was not detected. The Fire Clay coal was also characterized by elevated kaolinite and anatase contents, which may originate from the volcanic ash fall during the coalification stage (Hower et al., 2018). The diffraction peaks of both the kaolinite and the pyrite disappeared after roasting, which can be explained by the dehydration of kaolinite interlayer structure (Cao et al., 2016) and thermal decomposition of pyrite into hematite (Music et al., 1992), respectively. The hematite content in the West Kentucky No.13 coal ash was extremely high (41.0%) which likely affects the REE leaching characteristics.

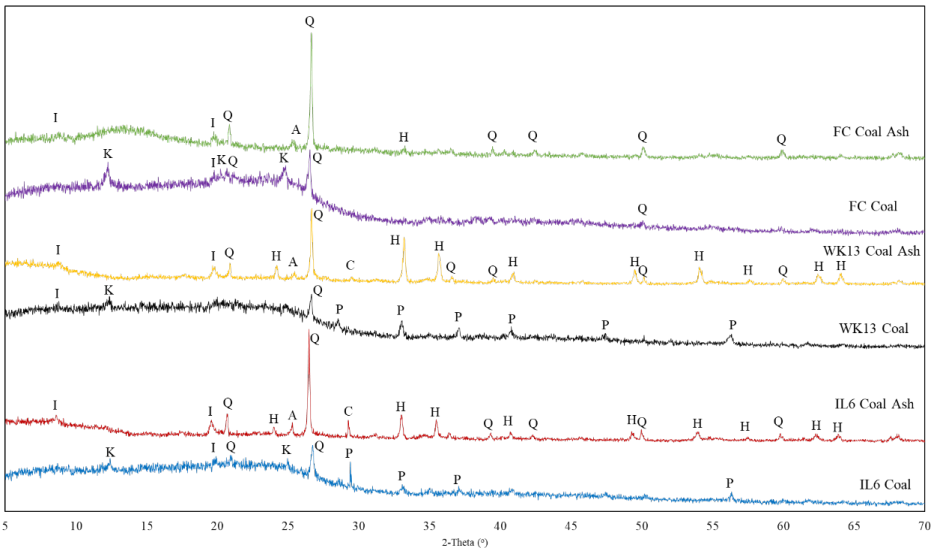

Figure 377. XRD patterns of the Fire Clay (FC), West Kentucky No.13 (WK13), and Illinois No.6 (IL6) coal and roasted samples (A-anatase, C-calcite, H-hematite, I-illite, K-kaolinite, P-pyrite, Q-quartz).

Sequential Extraction

The occurrence of REEs in the three roasted coal samples obtained by calcining the coals at 600℃ was studied using the sequential extraction procedure (Table 85). As shown in Figure 378, very minor fractions (less than 2%) of REEs existed as ion-exchangeable and carbonate forms, indicating the inefficiency of using solely ion-exchange lixiviants (e.g., Na^+, NH_4^+, and Cs^+) to recover the REEs. Significant amounts of REEs in the coal ash were associated with oxides, especially for West Kentucky No.13 and Illinois No.6 seams (54% and 38%, respectively). For the Fire Clay ash sample, the majority of REEs occurred as acid soluble forms.

Sequential extraction studies have been performed on several fly ash samples by researchers and the findings indicated that the majority of REEs (about 80%) were associated with insoluble silicate (Table 88). However, in the roasted coal material obtained by calcination, less than 40% of REEs occurred in this form. This finding may be due to the complicated mineralogy changes caused by the extremely high combustion temperature in a pulverized coal boiler (normally in excess of 1200℃). Finkleman et al. (2018) performed sequential extraction on several bituminous coals and reported that the REEs mainly occurred in the acid soluble (2 M HNO_3 dissolved) form. As such, the coal ash obtained by calcination at 600℃ was different from both the untreated, raw coal and the fly ash samples.

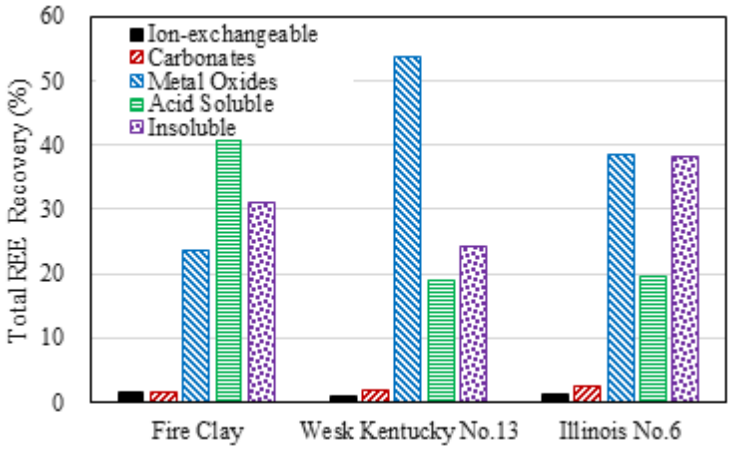

Figure 378. Fractions of the REEs determined using the sequential extraction.

Table 88. The fraction of REEs occurred as insoluble/silicate forms in fly ash reported in literature.

Ref	Sample	Plant Name	Location	Insoluble/Silicate Fraction (%)
Pan et al., 2019	Fly Ash	Panbei	Guangzhou, China	75.75%
Pan et al., 2019	Fly Ash	Faer	Guangzhou, China	77.90%
Wang et al., 2019	Fly Ash	Luzhou	Sichuan, China	About 90%
Lin et al., 2018	Fly Ash	NA	Ohio, USA	86.1%
Pan et al., 2019	Fly Ash	Nayong	NA	65.22%
Present Study	Roasted	NA	NA	<40%

Several changes during the oxidization process may increase the fraction of REE oxides, e.g.,: 1) the REEs originally that existed as free elements in the organic matrix may transform into oxides after coal combustion; 2) the REEs originally associated with the associated minerals in coal such as clays and pyrite may be converted to oxides; 3) the insoluble REEs minerals may be thermally decomposed into oxides. It has been reported that volcanic ash fall contributed to the enrichment of REEs in the Fire Clay coal and REEs mostly occurred as phosphates (Hower et al., 2018, 1999; Zhang et al., 2018). Rare earth phosphates are normally less soluble than oxides, which may explain the relatively smaller fraction of REE oxides in the Fire Clay coal ash. XRD characterization showed that the West Kentucky No.13 coal ash contained a significant amount of hematite. This agrees with the high fraction of REEs occurring as metal oxides. Many studies have reported that some REEs are associated with pyrites in coals (Dai et al., 2014; Hower et al., 2015; Pan et al., 2018). After thermal oxidization, these REEs may be associated with the iron oxides in an ion-substitution form.

The small fractions of insoluble/silicate REEs in the roasted coal material indicated a higher economic feasibility of the recovery using relatively mild leaching conditions. In addition, the ratios of HREEs-to-LREEs (H/L) in the leachate obtained from the first three steps (i.e., ion-exchangeable, carbonates, and oxides) of the sequential extraction process were higher than the last two steps (Figure 379). This finding indicates that solution containing relatively higher amounts of HREEs can be obtained by using a mild leaching condition.

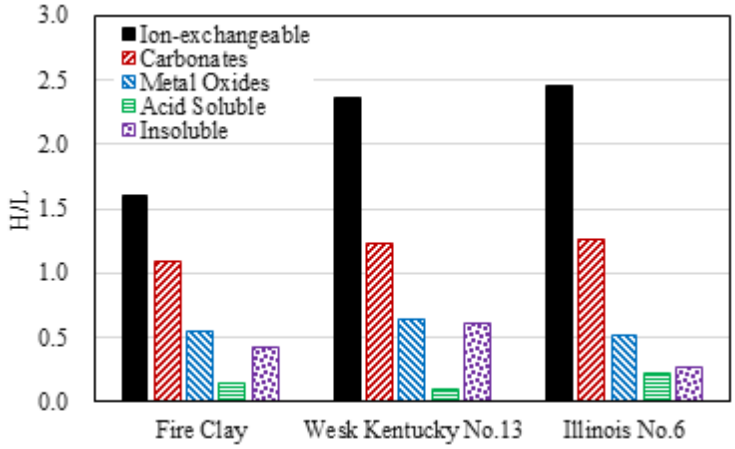

Figure 379. H/L ratios of the REEs associated with different modes of occurrence.

Leaching Tests

Leaching tests were performed on the roasted coal samples obtained by calcination under mild leaching conditions. As shown in Figure 380 (a-c), less than 5% of the REEs were leached by solely maintaining the slurry pH at 5.0. However, when the pH was decreased from 5 to 4, a significant increase in REE recovery occurred, especially for the West Kentucky No.13 coal ash sample (from 3.6% to 23.9%). This can be explained by the dissolution of rare earth oxides under the more acidic condition. The addition of ion-exchange lixiviant, i.e., ammonium sulfate, also significantly enhanced the REE recovery. At pH 5, an increase in REE recovery of 11, 20, and 20 absolute percentage point was obtained for the Fire Clay, West Kentucky No.13, and Illinois No.6 coal ash samples, respectively. The sequential extraction results showed that a very minor amount of REEs occurred as ion-exchangeable forms, which seems to be in conflict with the leaching results. The roasted samples contained a significant amount of clays (e.g., kaolinite, Figure 377). When the REE oxides were dissolved, the REE cations in solution were likely adsorbed by the clays which impaired the recovery. However, this can be prevented by introducing

ammonium ions into the solution due to the lower hydration energy which creates a higher affinity for the clay surfaces and interlayers.

The changes in H/L ratios in the leachate as a function of time are shown in Figure 380 (d-e). A gradual decrease in the H/L ratio was observed for all the tests which indicates a preferential release of HREEs in the early stage of the leaching process. It has been reported that HREEs have higher hydration energies compared to LREEs, and thus the former is less likely adsorbed and more likely desorbed from clays (Moldoveanu and Papangelakis, 2012). In coal geological studies, it also has been reported that

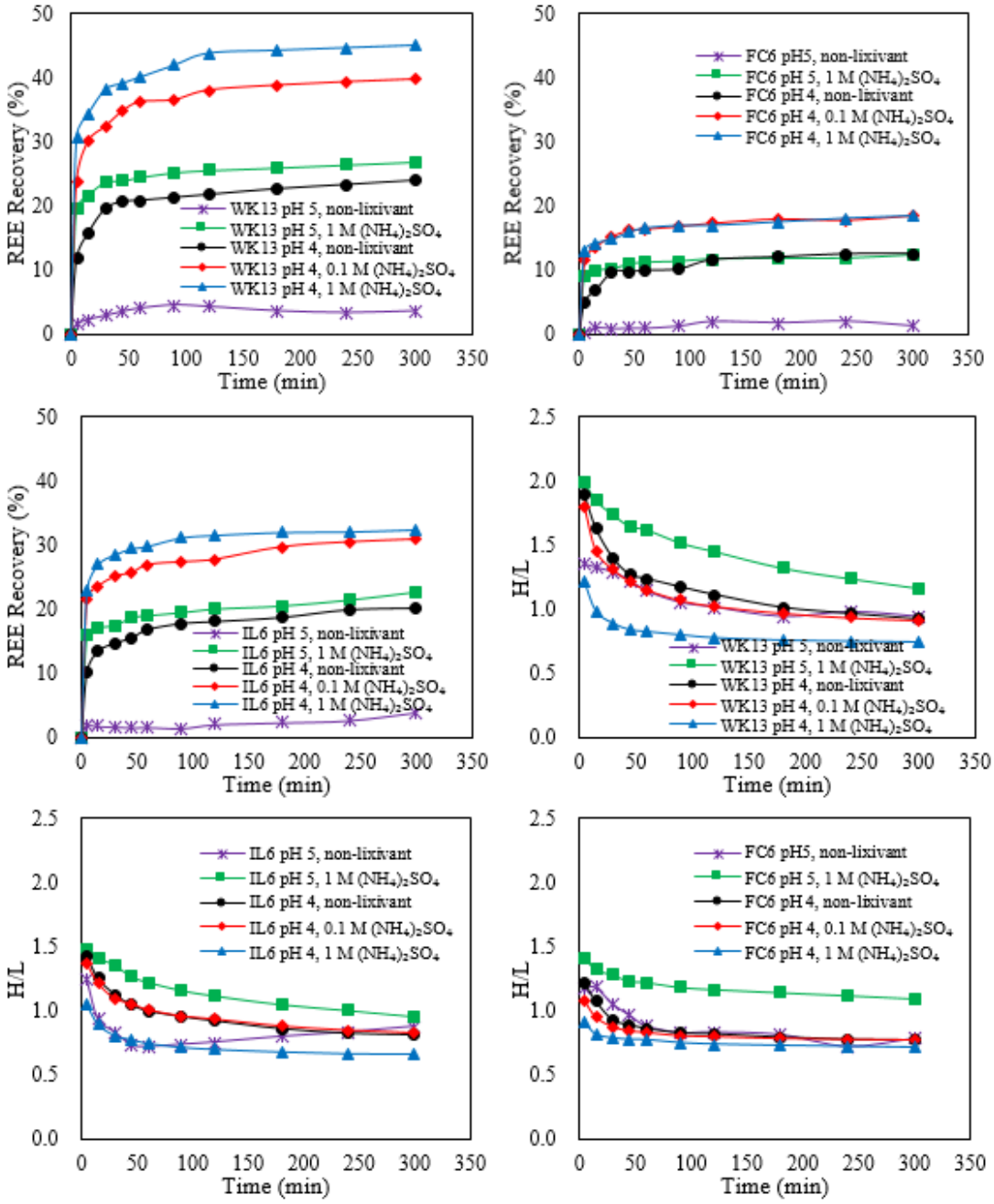

Figure 380. REE recovery from the three coal ash samples (a-c) and H/L ratios in the leachate (b-d) as a function

LREEs are more likely associated with clays relative to HREEs (Eskenazy, 1987; Seredin, 1996). The final leachate obtained after five hours of reaction still contains relatively more HREEs than the coal ash samples. As such, a higher amount of HREEs were recovered using relatively mild leaching condition. For example, about 64% of HREEs were leached from the West Kentucky No.13 coal ash with an overall REE recovery of 45%.

Subtask 5.6 – Speciation of Leach Liquor

Evaluation of Acid Leaching

Theory

Calculation Method

When ions are put into solution, a series of reaction such as protonation and de-protonation will occur. In equilibrium, all the possible species of the ion may co-exist in the system, which is controlled by reaction free energy, solution pH, initial concentration, etc. For example, when a metal ion (Mn^{+}) was put into solution, hydrolysis will occur, which can be expressed as follows:

$$M^{n+} + H_2O \rightarrow M(OH)^{(n-1)+} + H^{+} \quad [5.6.1]$$

The reaction free energy can be expressed as:

$$\Delta G = -RT\ln K, \quad [5.6.2]$$

where K is the reaction constant and expressed as:

$$K = \frac{a_{(M(OH)^{(n-1)+})} a_{H^+}}{a_{M^{n+}}}. \quad [5.6.3]$$

where a is the activity, which can be calculated using activity coefficient (γ) and molar concentration (m):

$$a_i = \gamma_i \times m_i. \quad [5.6.4]$$

For solution equilibrium calculations, the initial concentration of M^{n+} (m_I) is usually given. Assuming at equilibrium, the concentration of M^{n+} is m_{I-m}, and thus the molar concentration of the product is m. Activities of the different species are:

$$a_{(M(OH)^{(n-1)+})} = \gamma_{(M(OH)^{(n-1)+})} \times (m_I - m), \quad [5.6.5]$$

$$a_{M^{n+}} = \gamma_{(M^{n+})} \times m. \quad [5.6.6]$$

As such, the reaction constant can be expressed as:

$$K = \frac{\gamma_{(M(OH)^{(n-1)+})} \times a_{H^+} \times (m_I - m)}{\gamma_{(M^{n+})} \times m}. \quad [5.6.7]$$

The K value can be calculated using the known Gibbs free energy value. The activity coefficient needs to be given to calculate m using Eq. [5.6.7]. Significant studies have been performed to obtain appropriate models for specific solutions, which is critical for the accurate speciation calculations. If the ionic strength is less than 0.00001, the solution can be assumed to be ideal and the activity coefficient, γ_i,

can be assumed to be unity. If the ionic strength is larger than 0.00001, the activity coefficient can no longer be assumed to be unity.

Activity Coefficient Models

The most common method of calculating the individual species activity coefficient for solutions with ionic strengths between 0.00001 and 0.1 is the Debye-Hückel model, which can be expressed as:

$$\log\gamma_i = -\frac{A\sqrt{I}}{1+Ba_i\sqrt{I}} + \dot{B}_i I, \qquad [5.6.8]$$

Here, A and B are Debye-H ückel constants and a_i and B_i are parameters specific to a particular ion. The activity coefficient is defined by the equation $a_i = \gamma_i m_i$, where a_i is the activity of species i and m_i is the molar concentration. I is ionic strength, which is defined as:

$$\mathrm{I} = \frac{1}{2}\sum_i^n m_i z_i^2, \qquad [5.6.9]$$

where m_i is molarity (moles per 1000 g of water) of species i, and z_i means charge of species i. For ionic strength values larger than 0.1 M, other models are required for the solution equilibrium calculation. Almost all of these models are an extension of the early work on ionic solutions by Debye-Hückel (1932). Some of the most commonly used models are listed in Table 89.

One of the earliest and most successful attempts made for mixed electrolyte solutions was the Bronsted-Guggenheim specific interaction model. The specific interaction theory (SIT) was first proposed by Bronsted and was further developed by Guggenheim. Scatchard extended the theory to allow the interaction coefficients to vary with ionic strength. The equations for activity coefficients are

$$\ln\gamma_{M'X'} = -\frac{A_\gamma|z_M z_X|I^{0.5}}{1+I^{0.5}} + \frac{2\nu_+}{\nu_+ + \nu_-}\sum_X \beta_{M'X} m_X + \frac{2\nu_-}{\nu_+ + \nu_-}\sum_M B_{MX'} m_M, \qquad [5.6.10]$$

$$A_\gamma = \left(\frac{2\pi N_0 d_W}{1000}\right)^{0.5} l^{1.5}, \qquad [5.6.11]$$

Table 89. Some of the most commonly used activity coefficient models.

Name	Equation	Applicability
Limiting Law	$\log\gamma_i = -Az_i^2\sqrt{I}$	I < 0.01 M
Extended Debye-Hückel	$\log\gamma_i = \frac{-Az_i^2\sqrt{I}}{1+Ba_i\sqrt{I}}$	I < 0.1 M
Davies Equation	$\log\gamma_i = \frac{-Az_i^2\sqrt{I}}{1+\sqrt{I}} + 0.3Az_i^2 I$	I < 0.5 M
Truesdell-Jones Equation	$\log\gamma_i = -Az_i^2\left(\frac{\sqrt{I}}{1+Ba_i^0\sqrt{I}}\right) + b_i I$	I < 1 M
Güntelberg equation	$\log\gamma_i = \frac{-Az_i^2\sqrt{I}}{1+\sqrt{I}}$	I < 0.1 M

$$l = e^2/DkT\ . \qquad [5.6.12]$$

Here, the sums over M and X cover all positive and negative ions, respectively; A_γ is the usual Debye-Hückel coeffieicnt with N_0 Avogadro's number and d_W the density of the solvent; and l is a parameter which expresses the distance at which the electrostatic energy for singly charged ions in the dielectric equals thermal energy. The Guggenheim-Scatchard model has proven to be applicable for electrolyte solutions with less than 0.1 M ionic strength.

The activity models described above are limited to solutions of less than 1 M ionic strength. However, acids of more than 1 M are usually utilized to leach REEs from coal and coal refuse samples, and the final leachates often have higher ionic strengths (> 1 M). As such, other activity models are required for solution chemistry calculations of some leachates generated from the REEs leaching tests.

Pitzer developed a system of equations on the basis of theoretical insights from an expanded analysis of the Debye-Hückel model. An ionic strength dependence of the effect of short-range forces in binary interactions was recognized. By modifying the usual second virial coefficients to include this feature, a system of equations was generated that produced results that were in agreement with experimental solutions having ionic concentrations of several molar. The pertinent equations for a single electrolyte for the excess Gibbs energy G^{ex}, the osmotic coefficient φ, and the activity coefficient γ are as follows:

$$\ln \gamma_{MX} = |z_M z_X| f^\gamma + m\left(\frac{2\upsilon_M \upsilon_X}{\upsilon}\right) B_{MX} + m^2 \frac{2(\nu_M \upsilon_X)^{3/2}}{\upsilon} C_{MX}, \qquad [5.\ 6.13]$$

where υ_M and υ_X are the numbers of M and X ions in the formula and z_M and z_X give their respective charges in electronic unit; also $\upsilon = \nu_M + \nu_X$. f^γ is the Debye-Hückel limiting law slope given by:

$$f^\gamma = -A_\varphi\left[\frac{I^{0.5}}{1+bI^{0.5}} + \frac{2}{b}\ln(1 + bI^{0.5})\right], \qquad [5.\ 6.14]$$

$$B_{MX} = 2\beta^0_{MX} + \frac{2\beta^{(1)}_{MX}}{\alpha^2 I}\left[1 - e^{-\alpha I^{0.5}}\left(1 + \alpha I^{0.5} - \left(\frac{1}{2}\right)\alpha^2 I\right)\right]. \qquad [5.\ 6.15]$$

The third or higher virial coefficients can be included in Pitzer equations for the accurate predictions of thermodynamic properties above ionic strengths of 4 M.

Mean Salt Method

The most popular way of dividing mean activity coefficients into ionic components is to extend the Macinnes convention. This convention assumes that $\gamma_K = \gamma_{Cl} = \gamma\pm(KCl)$ at the ionic strength of the solution.

$$\gamma \pm (\mathrm{KCl}) = \sqrt{\gamma_K \gamma_{Cl}} \qquad [5.\ 6.16]$$

The value of γ_M for cations can be estimated from chloride salts:

$$\gamma_M = \left[\gamma \pm \left(MCl_{\nu_{Cl}}\right)\right]^{\nu} / [\gamma \pm (\mathrm{KCl})]^{\nu_{Cl}} \quad [5.6.17]$$

and the value of γ_X for the anions can be estimated from potassium salts

$$\gamma_X = \left[\gamma \pm \left(K_{\nu_K} X\right)\right]^{\nu} / [\gamma \pm (\mathrm{KCl})]^{\nu_K}. \quad [5.6.18]$$

Since K^+ and Cl^- salts do not normally form strong ion pairs, this method gives reasonable estimates for the activity coefficients of free ions. The activity coefficients of anions can also be estimated from sodium salts, i.e.:

$$\gamma_X = \left[\gamma \pm \left(Na_{\nu_{Na}} X\right)\right]^{\nu} / [\gamma \pm (\mathrm{NaCl})]^{\nu_{Na}}. \quad [5.6.19]$$

For an ionic media like $NaClO_4$, it is possible to estimate the activity coefficient of cations from ClO_4^- salts:

$$\gamma_M = \left[\gamma \pm \left(MClO_{4_{\nu_{ClO_4}}}\right)\right]^{\nu} / [\gamma \pm (\mathrm{NaClO_4})]^{\nu_{ClO_4}}. \quad [5.6.20]$$

By combining the Pitzer equations and the Macinnes convention, it is possible to get the following equations:

$$\ln \gamma_i = z_i^2 f^{\gamma} + B_i^0 I + B_i^1 f^1 + C_i I^2 \quad [5.6.21]$$

$$f^1 = [1 - \exp(-2I^{0.5})(1 + 2I^{0.5} - 2I). \quad [5.6.22]$$

The coefficients for this equation can be determined from the Pitzer parameters (β^0, β^1, and C^{ϕ}) for Na^+ and ClO_4^- salts. For mono- and divalent anions the values are given by:

$$B_X^0 = 4\beta_{NaX}^0 - B_{Na}^0 = (8/3)\,\beta_{Na2X}^0 - 2B_{Na}^0 \quad [5.6.23]$$

$$B_X^1 = \beta_{NaX}^1 - B_{Na}^1 = (2/3)\,\beta_{Na2X}^1 - 2B_{Na}^1 \quad [5.6.24]$$

$$C_X = 3C_{NaX}^{\phi} - C_{Na} = \left(\frac{2^{3/2}}{3}\right) C_{Na2X}^{\phi} - 2C_{Na} \quad [5.6.25]$$

and for trivalent cations by:

$$B_M^0 = 2\beta_{M(ClO_4)_3}^0 - 3B_{ClO_4}^0 \quad [5.6.26]$$

$$B_M^1 = (1/2)\beta_{M(ClO_4)_3}^1 - 3B_{ClO_4}^1 \quad [5.6.27]$$

$$C_M = (3^{1/2}/4)C_{M(ClO_4)_3}^{\phi} - 3C_{ClO_4} \quad [5.6.28]$$

where B^0_{Na} = 0.2093, B^1_{Na} = 0.1603, and C_{Na} = 0.00507, and $B^0_{ClO_4}$ = 0.0123, $3B^1_{ClO_4}$ = 0.1152, and C_{ClO_4} = -0.00861.

Activity Coefficient of Ion Pairs

The formation of an ion pair between a rare earth metal (M) and a ligand (X) can be characterized by:

$$\mathrm{M}^{3+} + X^n \rightarrow MX^{3-n}\,. \qquad [5.6.29]$$

The stoichiometric stability constant, K^*_{MX}, for the formation of this ion pair is given by:

$$K^*_{MX} = K_{MX}\gamma_M\gamma_X/\gamma_{MX} \qquad [5.6.30]$$

where K_{MX} is the thermodynamic constant in pure water and the values of γ_i are the activity coefficients of the ions and the ion pair. Existing data have been used to estimate the activity coefficients of the lanthanide ion pairs γ_{MX} and the infinite dilution thermodynamic stability constant:

$$\ln\gamma_{MX} = \ln K_{MX} - \ln K^*_{MX} + \ln\gamma_M + \ln\gamma_X \qquad [5.6.31]$$

If the ion pair is charged its concentration dependence would be of the form:

$$\ln\gamma_{MX} = \ln\gamma_{ELECT} + 2m_{ClO4}B_{MX} \qquad [5.6.32]$$

where B_{MX} is the Pitzer parameter for the ion pair. The electrical contribution is given by:

$$\ln\gamma_{ELECT} = 4\,f + 4\,m_{Na}m_{ClO4}B'_{ClO4} + 2m_{Na}m_{ClO4}C_{ClO4}. \qquad [5.6.33]$$

Combination of the above equations gives:

$$\ln K^*_{MX} - \ln\gamma_M - \ln\gamma_X - \ln\gamma_{ELECT} = \ln K_{MX} - 2B_{MX}m_{ClO4}. \qquad [5.6.34]$$

This equation has been utilized to determine the infinite dilution thermodynamic stability constant (K_{MX}) and the Pitzer parameter for the rare earth ion pairs.

Sample Characterization & Calculation Method Description

In this study, full spectrum analyses were performed on four real leachates obtained from different feedstocks including Fire Clay coarse refuse, Fire Clay middlings, Fire Clay spiral refuse, and Dotiki coarse refuse. Leachates were generated by leaching the solid samples using 1.5 M sulfuric acid in three-neck round bottom flasks. Metal ions concentration in the leachate were measured using ICP-OES. Based on the fact that elements with very low concentration will impose minor effects on speciation in solution, in

addition to REEs, only the elements with concentrations larger than 1 x 10-4 M were considered in the study. Table 90 shows the concentrations of various metal ions utilized for solution chemistry calculation.

The major ions in the leachates are Fe^{3+}, Al^{3+}, Ca^{2+}, Mg^{2+}, K^{+} and Na^{+}, which have a concentration range of about 0.13-0.26 M, 0.10-0.15 M, 0.014-0.023 M, 0.015-0.032 M, 0.011-0.013 M, 0.0028-0.0095 M, respectively. The purpose of solution chemistry calculation is to study the effects of different cations and anions in solution on the speciation of REEs. As such, the calculation should be able to predict all the

Table 90. Full spectrum analyses of leachates generated from different feed stocks.

Metal Ions	Fire Clay Coarse Refuse	Fire Clay Middlings	Fire Clay Spiral Refuse	Dotiki Coarse Refuse
Fe^{3+}	0.1253	0.2568	0.1769	0.1825
Al^{3+}	0.0919	0.1470	0.1371	0.1108
Ca^{2+}	0.0232	0.0205	0.0143	0.0199
Mg^{2+}	0.0153	0.0321	0.0314	0.0216
K^{+}	0.0128	0.0111	0.0110	0.0122
Na^{+}	0.00278	0.0095	0.0054	0.0058
Mn^{2+}	0.0026	0.0037	0.0034	0.0027
Ni^{2+}	0.0010	0.0010	0.0010	0.0011
Cr^{3+}	0.0003	0.0004	0.0003	0.0007
Cu^{2+}	0.0002	0.0003	0.0002	0.0002
Sr^{2+}	0.0001	0.0002	0.0001	0.0001
Sc^{3+}	1.78×10^{-6}	1.11×10^{-6}	1.33×10^{-6}	6.67×10^{-7}
Y^{3+}	1.69×10^{-6}	2.59×10^{-6}	1.57×10^{-6}	1.69×10^{-6}
La^{3+}	5.04×10^{-7}	4.39×10^{-6}	1.30×10^{-6}	5.04×10^{-7}
Ce^{3+}	1.28×10^{-6}	1.14×10^{-5}	3.50×10^{-6}	1.28×10^{-6}
Pr^{3+}	4.26×10^{-7}	1.35×10^{-6}	7.01×10^{-7}	4.26×10^{-7}
Nd^{3+}	6.24×10^{-7}	4.58×10^{-6}	1.59×10^{-6}	6.24×10^{-7}
Sm^{3+}	3.33×10^{-7}	1.06×10^{-6}	6.00×10^{-7}	3.33×10^{-7}
Eu^{3+}	6.58×10^{-8}	6.58×10^{-8}	6.58×10^{-8}	6.58×10^{-8}
Gd^{3+}	2.54×10^{-7}	6.36×10^{-7}	3.18×10^{-7}	2.54×10^{-7}
Tb^{3+}	6.29×10^{-8}	6.29×10^{-8}	1.26×10^{-7}	6.29×10^{-8}
Dy^{3+}	2.46×10^{-7}	3.69×10^{-7}	2.46×10^{-7}	2.46×10^{-7}
Ho^{3+}	0	6.06×10^{-8}	0	0
Er^{3+}	5.98×10^{-7}	0	0	5.98×10^{-8}
Tm^{3+}	0	5.92×10^{-8}	0	0
Yb^{3+}	1.16×10^{-7}	1.16×10^{-7}	1.16×10^{-7}	1.16×10^{-7}
Lu^{3+}	5.72×10^{-8}	5.72×10^{-8}	1.14×10^{-7}	5.72×10^{-8}

real leachates instead of a specific sample. In this case, the mean concentration of the above major ions was utilized for the calculation. When study the effect of a specific ion, its concentration will be varied, while concentration of the other metal ions will be fixed.

Figure 381. The main operation interface of the Visual MINTEQ software.

Total REE concentration in the leachates is in the range of $6x10^{-6}$ to $3x10^{-5}$ M with La and Ce as the dominant components. The solution chemistry calculation was first performed with only Ce to simply the problem. After investigating the effects of solution components on the speciation of Ce, calculation will be performed by considering the overall REEs. The selection of REEs concentration is similar to that of the major ions, i.e., the mean value will be utilized for initial calculation.

Solution chemistry calculation was performed using the Visual MINTEQ software, which is a free software and maintained by Jon Petter Gustafsson at KTH, Sweden, since 2000. The software can be utilized for the calculation of metal speciation, solubility equilibria, sorption etc. for natural waters. Figure 381 shows the main operation interface of the software. The unit of concentration was selected as molar per liter (M).

Calculation Results & Discussion

Cerium Speciation

Solution chemistry calculations were first performed on a solution containing the major elements (i.e., Fe^{3+}, Al^{3+}, Ca^{2+}, Mg^{2+}, K^{+} and Na^{+}) and Ce^{3+}. The sulfate (SO_4^{2-}) concentration was 1.5 M, which was selected based on the sulfuric acid concentration (1.5 M) utilized for the leaching test. The other anionic species such as Cl^{-} and NO^{3-} were ignored. The input information is shown in Table 91. The pH value and solution temperature were fixed at 0 and 25°C, respectively. The activity coefficient used for the calculations was calculated using the Davies model.

Table 92 shows the percentage distribution of various species in the solution. The majority of the sulfate existed as HSO_4^{-}, $FeSO_4^{+}$, $AlSO_4^{+}$, and $Al(SO_4)^{2-}$. Instead of existing as free cations, Fe^{3+} and Al^{3+} mostly existed as metal sulfates. However, for the lower valence metal ions, such as K^{+} and Na^{+}, the sulfate

Table 91. Leachate components and molar concentrations used for the solution chemistry calculations.

Elements	Fe^{3+}	Al^{3+}	Ca^{2+}	Mg^{2+}	K^{+}	Na^{+}	Sc^{3+}	Y^{3+}	La^{3+}
M	0.20	0.13	0.018	0.023	0.012	0.0062	$1.2x10^{-6}$	$2.1x10^{-6}$	$2.4x10^{-6}$
Elements	Ce^{3+}	Pr^{3+}	Nd^{3+}	Sm^{3+}	Eu^{3+}	Gd^{3+}	Tb^{3+}	Dy^{3+}	Ho^{3+}
M	$6.4x10^{-6}$	$8.9x10^{-7}$	$2.6x10^{-6}$	$7.0x10^{-7}$	$6.6x10^{-8}$	$4.5x10^{-7}$	$9.4x10^{-8}$	$3.1x10^{-7}$	$3.0x10^{-8}$
Elements	Er^{3+}	Tm^{3+}	Yb^{3+}	Lu^{3+}					
M	$3.0x10^{-8}$	$3.0x10^{-8}$	$1.0x10^{-7}$	$5.7x10^{-8}$					

complexes only accounted for a minor fraction. Due to large stability constants of the cerium sulfates species, about 94% of cerium in the solution were existed as $CeSO_4^+$ and $Ce(SO_4)^{2-}$. Saturation indexes of all the possible mineral phases that are included in the software are shown in Table 93. Gypsum and anhydrite ($CaSO_4$) has positive saturation indexes indicating that the solution is oversaturated and the likely occurrence of precipitation. As such, in the leachate produced from REE leaching, calcium sulfate precipitate will form, while cerium hydroxide precipitate will not likely form. It should be noted that the software does not include the REEs double sulfates in its database.

Table 92. Percentage distribution of different species.

Component	% of Total Concentration	Species Name		Component	% of Total Concentration	Species Name
SO_4^{-2}	1.13	SO4-2		Ca^{+2}	52.919	Ca+2
	0.021	NaSO4-			47.081	CaSO4 (aq)
	0.051	KSO4-		Mg^{+2}	58.592	Mg+2
	71.699	HSO4-			41.408	MgSO4 (aq)
	5.514	AlSO4+		K^{+1}	93.68	K+1
	5.776	Al(SO4)2-			6.32	KSO4-
	11.621	FeSO4+		Na^{+1}	95.023	Na+1
	2.988	Fe(SO4)2-			4.977	NaSO4-
	0.635	MgSO4 (aq)		Ce^{+3}	5.628	Ce+3
	0.565	CaSO4 (aq)			20.346	Ce(SO4)2-
Fe^{+3}	1.627	Fe+3			74.026	CeSO4+
	87.161	FeSO4+				
	11.205	Fe(SO4)2-				
Al^{+3}	3.052	Al+3				
	63.626	AlSO4+				
	33.322	Al(SO4)2-				

Table 93. Saturation indexes of mineral phases possibly occurred in the solution.

Mineral	log IAP	Sat. index		Mineral	log IAP	Sat. index
Al(OH)3 (am)	-3.027	-13.827		Goethite	-3.093	-3.584
Al(OH)3 (Soil)	-3.027	-11.317		Gypsum	-4.334	0.276
Al2O3(s)	-5.992	-25.644		Hematite	-6.164	-4.746
Al4(OH)10SO4(s)	-14.089	-36.789		H-Jarosite	-13.341	-7.951
AlOHSO4(s)	-5.006	-1.776		K-Alum	-9.271	-4.101
Alunite	-15.072	-13.672		K-Jarosite	-15.331	-4.331
Anhydrite	-4.292	0.068		Lepidocrocite	-3.093	-4.464
Boehmite	-3.006	-11.584		Lime	-2.292	-34.992
Brucite	-2.163	-19.263		Maghemite	-6.164	-12.55
Ce(OH)3(s)	-7.069	-26.959		Magnesioferrite	-8.306	-25.165
Diaspore	-3.006	-9.879		Mg(OH)2 (active)	-2.163	-20.957
Epsomite	-4.289	-2.163		Mirabilite	-6.817	-5.703
Ettringite	-26.421	-83.271		Na-Jarosite	-15.612	-10.292
Fe2(SO4)3(s)	-12.163	-8.429		Periclase	-2.142	-23.726
Ferrihydrite	-3.114	-6.314		Portlandite	-2.313	-25.017
Ferrihydrite (aged)	-3.114	-5.804		Spinel	-8.133	-44.981
Gibbsite (C)	-3.027	-10.767		Thenardite	-6.605	-6.927

The effects of Fe^{3+} and Al^{3+} concentration on the speciation of cerium in solution are shown in Figure 382. With increases in Fe^{3+} and Al^{3+} concentration from 0 to 0.5 M, the Ce^{3+} distribution increased slightly from 4.6% to about 7.5% and 8.4%, respectively. As such, the major metal ions in solution has minor effects on the speciation of REEs. Saturation index calculation for the studied Fe^{3+} and Al^{3+} concentration ranges showed that precipitates of iron and aluminum species were not likely occur, while calcium sulfate precipitate was always formed. The effects of calcium concentration on the saturation indexes of two possible solid phases (i.e., anhydrite and gypsum) were also investigated. As shown in Figure 383, with the increases in calcium concentration, the saturation indexes of both phases were increased and precipitates were likely formed at 0.01 M concentration. As such, for the real leachate samples of pH 0, calcium sulfate will be precipitated out from solution and attention needs to be paid regarding its effects on REEs fractionation.

Acid leaching tests sometimes will be operated using elevated temperatures to enhance leaching performance. As such, temperature should be considered as a variable in the solution chemistry calculation, which will reflect the real leaching conditions. As shown in Figure 384, the percentage of cerium existing as free metal ions slightly increased from 5.6% to 9.1% with the increase in temperature from 25°C to 75°C.

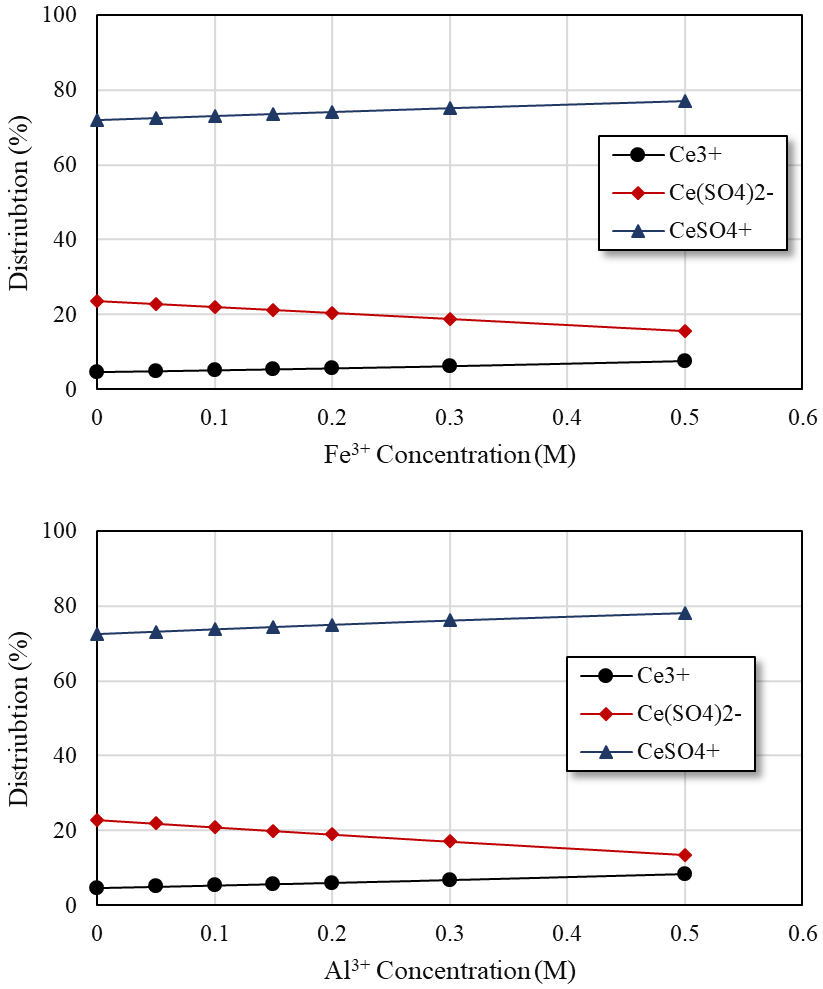

Figure 382. Effects of (a) Fe^{3+} and (b) Al^{3+} concentration on the speciation of cerium in the solution.

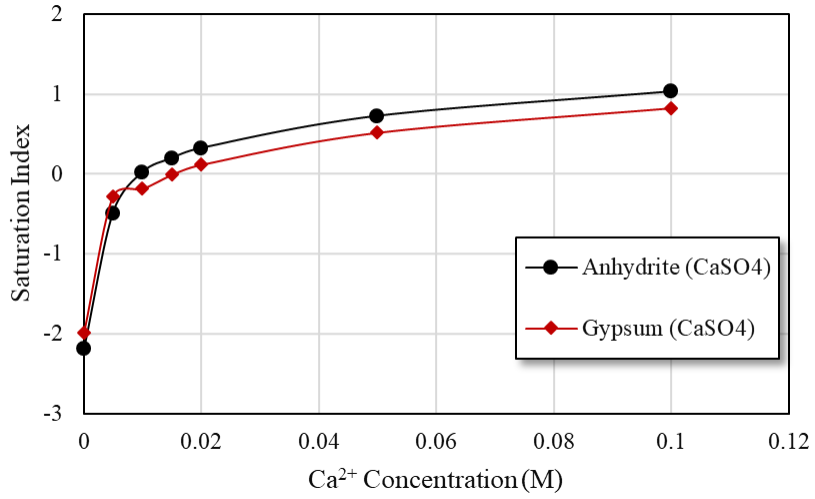

Figure 383. Effects of Ca^{2+} concentration on the saturation indexes of anhydrite and gypsum.

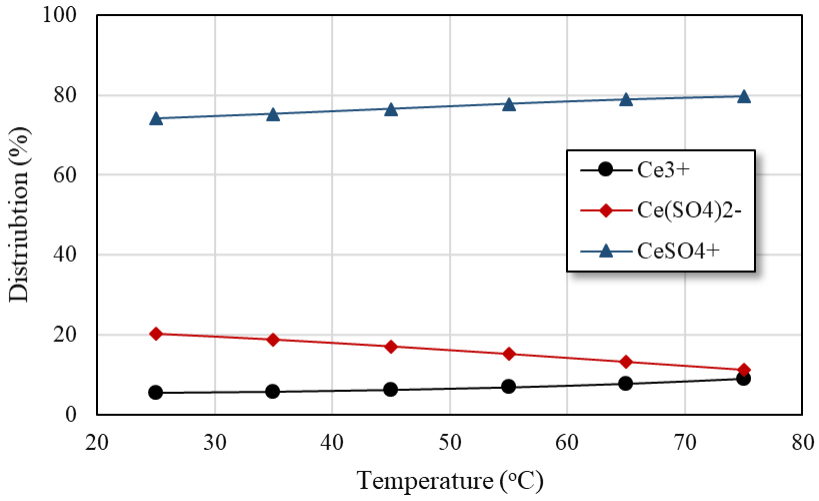

Figure 384. Effects of temperature on the speciation of cerium in the solution.

Sulfate species distribution indicated that the percentage of HSO_4^- increases with the elevation in temperature, which explained the increases in free metal species. Furthermore, temperature enhancement also make calcium sulfate less likely to be formed. Figure 385 shows that at 75°C, calcium sulfate solid phases only occurred when the calcium concentration exceeds about 0.03 M, which is higher than that of 25°C (0.01 M). The maximum concentration of the four real leachate samples is 0.023 M, thus no precipitates were expected to be formed for acid leaching test at 75°C using 1.5 M sulfuric acid. However, if the leaching system is cooled down to room temperature, precipitation will occur.

A significant number of studies have reported that, in an acidic environment, iron is likely precipitated in the form of jarosite, which can be expressed as $AFe_3(SO_4)_2(OH)_6$, where A is H^+, Na^+, K^+, NH_4^+, Ag^+, Rb^+, Tl^+, $0.5Ca^{2+}$ or $0.5Pb^{2+}$. Co-precipitation and/or adsorption of REEs may occur when jarosite is formed which is especially problematic due to its high surface area. As such, it is critical to investigate the precipitation behavior of iron in the solution. The saturation indexes of three jarosite minerals are shown in Figure 386. The jarosite minerals were more likely formed at higher pH values, as

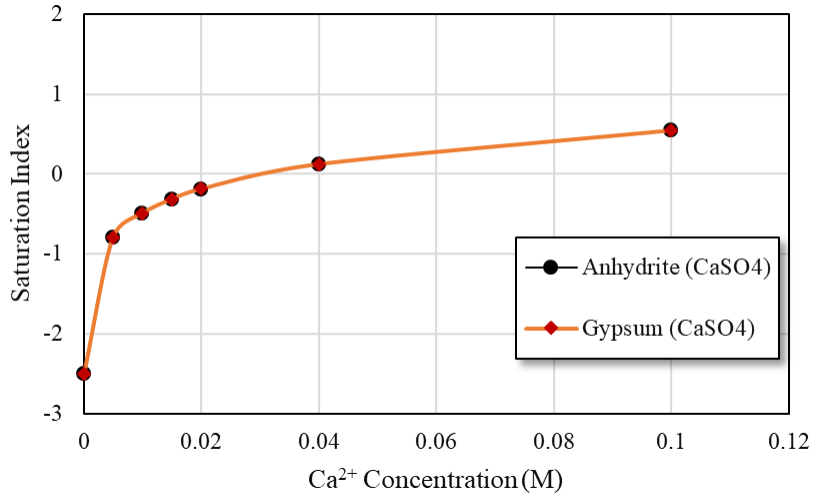

Figure 385. Effect of Ca^{2+} concentration on the saturation indexes of anhydrite and gypsum at 75°C.

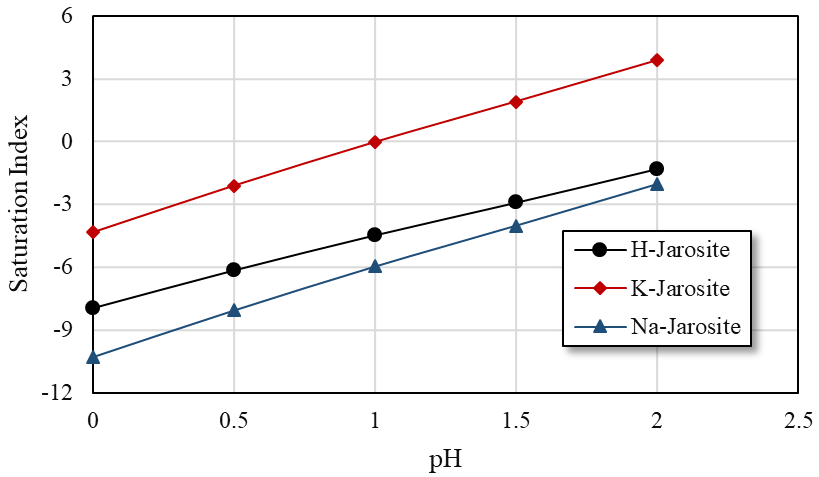

Figure 386. Effects of solution pH on the saturation indexes of jarosite minerals in the solution.

indicated by the increases in saturation indexes with the elevation in solution pH. For the solution described in Table 93 at 25°C, precipitation of K-jarosite will occur at pH 1.0, while the other two possible jarosites (H-jarosite and Na-jarosite) will be at higher pH values. As such, acid leaching at 25°C using 1.5 M sulfuric acid does not result in the generation of jarosite and thus its negative effects on REE fractionation can be ignored.

Previous investigations assumed that sulfate (SO_4^{2-}) was the only anionic species existing in the real leachates. However, other species such as Cl^- and NO^{3-} also appears in the solution based on the investigation of acid mine leachate samples collected from coal preparation plants. These anionic species compete with sulfate in complexing with metal ions. As such, solution chemistry calculations were performed at 1.5 M SO_4^{2-} and different concentrations of Cl^- and NO^{3-} Figure 387 shows the distribution of various cerium species as a function of Cl^- concentration. The dominant cerium chloride specie is $CeCl_2^+$. Its distribution increased slightly with an increase in Cl^- concentration and reached 3.4% when 0.5 M Cl^- existed in the system. As such, Cl^- has a much smaller complexing ability with Ce^{3+} compared with sulfate. NO_3^- showed a similar effect as Cl^- (Figure 387). Based on the fact that concentration of Cl^- and NO_3^- is smaller than that of sulfate in real leachates, their effects on the speciation of Ce^{3+} are negligible.

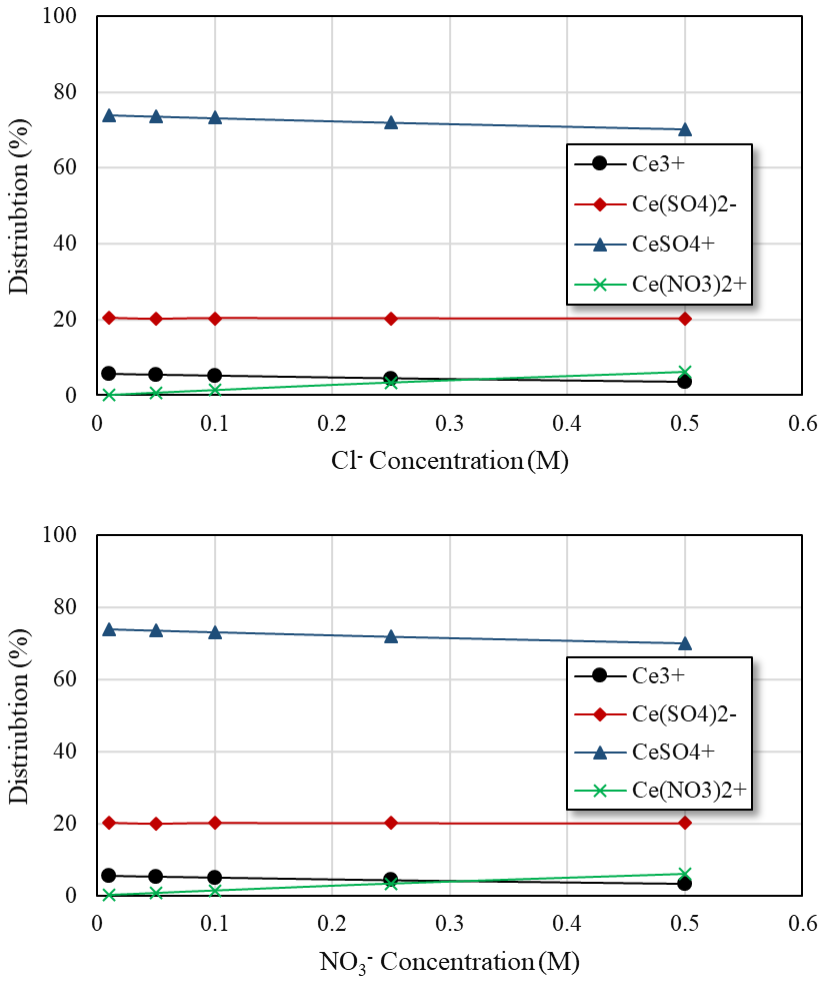

Figure 387. Effects of (a) Cl^- and (b) NO_3^- on the speciation of cerium in solution.

It has to be notified that iron in solution can exist as both Fe^{2+} and Fe^{3+}. The mean value (0.2 M) used for the above calculation is the total concentration of the two species. As such, the effects of the ratio of Fe^{2+}/Fe^{3+} need to be investigated. In the study, the total concentration of iron was fixed at 0.2 M, while the concentration of Fe^{2+} was varied. Figure 388 shows the distribution of different cerium species as a function of Fe^{2+}. The fraction of cerium free ions decreased slightly with an elevation in concentration, which means more cerium was combined with sulfate anions. This can be explained by the lower complexing ability of Fe^{2+} with sulfate compared with Fe^{3+}. As such, for the tank leaching tests, the Fe^{2+} concentration relative to the total amount of iron in the leachates does not significantly affect the speciation of cerium in solution.

The above studies focused on the solution speciation of cerium in a leachate containing the major cationic and anionic species. The results indicated that the majority of cerium (>90%) existed as sulfate species in solution. The appearance of anionic species such as Cl^- and NO_3^- did not change the cerium speciation significantly. Furthermore, an increase in Fe^{2+}/Fe^{3+} ratio with a constant concentration of iron in the real leachate slightly reduced the fraction of free cerium metal ions. Saturation index calculations showed that calcium sulfate (gypsum and anhydrite) was likely formed in the real leachates, while jarosite (including H-jarosite, Na-jarosite and K-jarosite) did not appear. The fractionation of REEs to the calcium sulfate precipitates should be investigated in future studies.

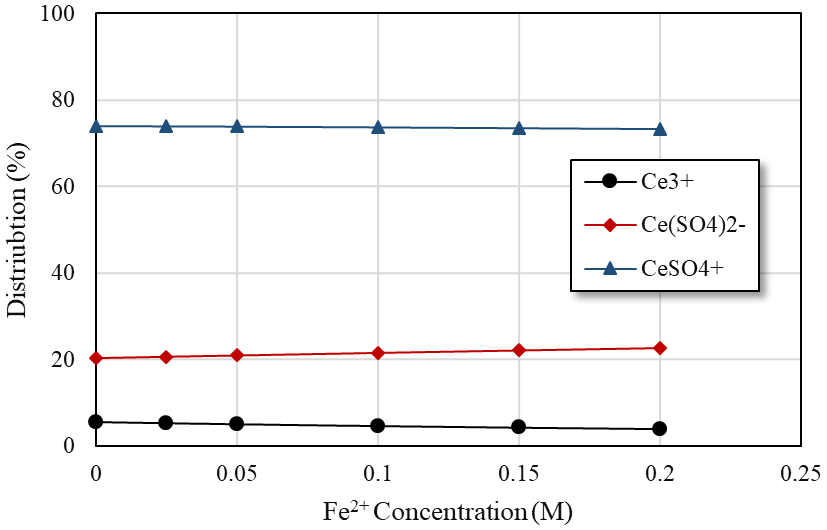

Figure 388. Effects of Fe^{2+} on the speciation of cerium in solution.

Speciation of REEs

In addition to cerium, speciation of all the REEs was calculated in this section. The data shown in Table 91 was used as the real leachate composition. Table 94 shows the input information for the calculation. The sulfate concentration was assumed to be 1.5 M based on the fact that 1.5 M sulfuric acid was used for the leaching test. Cl^- and NO_3^- were ignored in the calculation, which was proven to be reasonable in the cerium speciation study. The solution pH and temperature were fixed at 0 and 25°C, respectively. Davies acidity coefficient model with a b value of 0.3 was used for the calculation. Concentration unit used in the calculation was molar per liter (M).

Table 94. Input information for REEs speciation study.

Component name	Total concentration* Molal
H+1	0
Fe+3	0.2
Al+3	0.13
Ca+2	0.018
Mg+2	0.023
K+1	0.012
Na+1	0.0062
Sc+3	0.0000012
Y+3	0.0000021
La+3	0.0000024
Ce+3	0.0000064
Pr+3	0.00000089
Nd+3	0.0000026
Sm+3	0.0000007
Eu+3	0.000000066
Gd+3	0.00000045
Tb+3	0.000000094
Dy+3	0.00000031
Ho+3	0.00000003
Er+3	0.00000003
Tm+3	0.00000003
Yb+3	0.0000001
Lu+3	0.000000057
SO4-2	1.5

The percentages of different species in the total concentration are shown in Table 95. A comparison between Table 92 and Table 95 indicate that the addition of REEs in the calculation did not change the speciation of the other species, including both the major cations and anions as well as cerium. This can be explained by the fact that the REE concentrations were much smaller than the other species. Almost all the REEs showed a similar distribution pattern, i.e., only a small fraction (5-6%) exists as free metal ions and the majority is associated with sulfate anions. However, it is noted that only 1.7% of the scandium is in free metal form, which is about three times lower than the other REEs.

Effects of Activity Coefficient Models

Three activity coefficient models including Debye-Hückel, Davies, and specific ion interaction (SIT) were built in the Visual MINTEQ software. All the previous calculations were performed using the Davies model, which is suitable for relatively high ionic strengths (< 0.5 M). To better understanding effects of activity coefficient models, calculations were conducted using the three models, which will contribute to the selection and/or development of more efficient models for the leachates. The input information was the same as the cerium speciation study (Table 91).

Species distribution of cerium is shown in Table 96. The activity coefficient models had significant impact on the results. Davies and Debye-Hückel models generated similar results, i.e., the majority (about 95%) of cerium was combined with sulfate. However, the SIT gave opposite results, which may seem unreasonable due to the fact that sulfate is able to form relatively strong complexes with rare earth metal ions. As such, the activity coefficient models play significant role in speciation study, and their selection and/or development are determined by the solutions. In the further study, ap propriate models will be provided for leachates generated from coal related solids in different conditions.

Table 95. Species distribution in the leachate solution.

Component	% of total concentration	Species	Component	% of total concentration	Species
SO4-2	1.13	SO4-2	Pr+3	6.085	Pr+3
	71.698	HSO4-		13.879	Pr(SO4)2-
	5.514	AlSO4+		80.035	PrSO4+
	5.776	Al(SO4)2-	Nd+3	5.439	Nd+3
	11.621	FeSO4+		19.66	Nd(SO4)2-
	2.988	Fe(SO4)2-		74.901	NdSO4+
	0.635	MgSO4 (aq)	Sm+3	5.345	Sm+3
	0.565	CaSO4 (aq)		19.323	Sm(SO4)2-
	0.021	NaSO4-		75.332	SmSO4+
	0.051	KSO4-	Eu+3	4.483	Eu+3
Fe+3	1.627	Fe+3		32.336	Eu(SO4)2-
	87.161	FeSO4+		63.181	EuSO4+
	11.205	Fe(SO4)2-	Gd+3	5.175	Gd+3
Al+3	3.052	Al+3		23.551	Gd(SO4)2-
	63.626	AlSO4+		71.273	GdSO4+
	33.322	Al(SO4)2-	Tb+3	5.628	Tb+3
Ca+2	52.919	Ca+2		20.346	Tb(SO4)2-
	47.081	CaSO4 (aq)		74.026	TbSO4+
Mg+2	58.592	Mg+2	Dy+3	6.629	Dy+3
	41.408	MgSO4 (aq)		12.009	Dy(SO4)2-
K+1	93.68	K+1		81.362	DySO4+
	6.32	KSO4-	Ho+3	6.666	Ho+3
Na+1	95.024	Na+1		15.203	Ho(SO4)2-
	4.976	NaSO4-		78.132	HoSO4+
Sc+3	1.723	Sc+3	Er+3	6.121	Er+3
	19.697	Sc(SO4)2-		22.127	Er(SO4)2-
	78.58	ScSO4+		71.752	ErSO4+
Y+3	6.826	Y+3	Tm+3	6.121	Tm+3
	62.11	YSO4+		22.127	Tm(SO4)2-
	31.064	Y(SO4)2-		71.752	TmSO4+
La+3	5.03	La+3	Yb+3	6.157	Yb+3
	28.817	La(SO4)2-		28.02	Yb(SO4)2-
	66.153	LaSO4+		65.823	YbSO4+
Ce+3	5.628	Ce+3	Lu+3	6.44	Lu+3
	20.346	Ce(SO4)2-		29.308	Lu(SO4)2-
	74.026	CeSO4+		64.252	LuSO4+

Conclusions

A detailed review of solution chemistry calculations was performed in the study. The major challenge for the solution chemistry study of REE leachates produced from coal byproducts using acids of high concentration (>1 M) was the selection and/or development of appropriate activity coefficient models. Full spectrum ICP-OES analyses of four leachates, which were generated from different coal refuse samples using 1.5 M sulfuric acid solution, were conducted and the results were used for the solution chemistry calculations. Preliminary calculations of the leachates were performed using Visual MINT EQ software. Despite the fact that the activity coefficient models that built in the software are not accurate enough for the leachates, many meaningful findings were obtained. The major elements including Fe^{3+} and Al^{3+} in the leachates were existed as metal sulfates. More than 90% of the REEs in the leachate were in forms of $REE(SO_4)^+$ and $REE(SO_4)^2$, while only a small fraction occurred as free metal ions. Cl- and NO3- in the leachates had minor effects on the speciation of REEs in the leachates obtained using relatively concentrated sulfuric acid solution. Jarosite minerals were not likely formed in the leachates, while calcium sulfate precipitates (gypsum and anhydrite) were formed based on saturation index calculations. Calcium sulfate precipitates were more likely formed at low temperatures, which explained the occurrence of suspended particles in the leachates when they were cooled down. The redox state of iron in leachates had minor effects on the speciation of REEs in the leachates, and the fraction of REEs existed as sulfate complexes increased slightly as the Fe^{2+}/Fe^{3+} ratio increased in the leachates.

Table 96. Speciation of cerium based on different activity coefficient models.

Model	Ce^{+3}	$Ce(SO_4)^{2-}$	$CeSO_4^+$
Davies	5.628	20.346	74.026
Debye-Hückel	4.319	15.158	80.524
SIT	67.994	5.493	26.512

Thermodynamics of EDTA Leaching

Thermodynamic calculations were conducted in the Medusa program (Puigdomenech et al., 2013) to understand the role of EDTA during the NaOH pretreatment stage. Data shown in other report sections indicates that when used in the pretreatment stage, EDTA has the potential to increase the sample leachability and reduce the amount of NaOH needed.

In the simulation work, La, Nd, and Y were selected as representatives REEs. The amounts of those three REEs and phosphate were set as 10^{-5} M, which was the approximate concentrations in the NaOH pretreatment step as determined in the experimental triasl (25 g/L). Two fraction diagrams as a function of pH were initially constructed to simulate the dissolution of $LaPO_4$(s) in the absence and presence of 0.1 M EDTA at 25 °C. Additionally, the predominance diagrams for the La-, Nd-, Y-PO_4-EDTA-H_2O systems ($[La^{3+}] = [PO_4^{3-}] = 10^{-5}$ M) were also created to study the effects of both EDTA concentration and pH on the dissoluton of $REPO_4$(s). The stability constants used for the similation work were from the intenral Medusa database, and no new data were added during simulation process.

In the absense of EDTA, $LaPO_4$(s) is the predominant species from pH 2 to pH 12, as indicated in the fractional speciation diagram shown in the top panel of Figure 389. Below pH 2, $LaPO_4$(s) dissolves and produces soluble La^{3+} ions, while above pH 12, $La(OH)_3$(s) is the prominent speies. The wide region of stability for $LaPO_4$(s) suggests that the mineral is stable and diffucult to dissolve under weakly acidic and basic pH conditions. Alternatively, the bottom panel of the figure shows that EDTA greatly increases the solubility of $LaPO_4$(s) at all pH points. The data indicates that EDTA can complex with La^{3+} ions and causes decomposition of $LaPO_4$(s).

At approximately pH 13.5, both the La-$EDTA^-$ and $La(OH)_3$(s) species exist in equilibtrium. The thermodynamic data shows that this pH is a critical point for the conversion of La-$EDTA^-$ to $La(OH)_3$(s) since the fraction of La-$EDTA^-$ sharply decreases and the formation of $La(OH)_3$(s) starts and is dramastically enhanced thereafter. Comparison of the two plots shows that EDTA has the potential to promote $LaPO_4$(s) decomposition at lower pHs than that of NaOH alone.

To compare the differences of the dissolution among different REEs, the predominance diagrams for La, Nd, and Y-PO_4^3-$EDTA^{4-}$-H_2O system were also created at different EDTA concentrations (Log[$EDTA^{4-}$]) and pH. As shown in Figure 390, $LaPO_4$(s) is prominant between pH 2 and 13. When the pH is between 2 and 8, the minimium EDTA concentration needed for the dissolution of $LaPO_4$(s) is approximate $10^{-3.5}$ M, and lower concentraitons of EDTA are required at basic pH values since OH^- ions can also facilitate the decomposition of $LaPO_4$(s). In the system of Nd, $NdPO_4$(s) begins to dissolve when the EDTA concentration is larger than ~$10^{-4.0}$ M between pH 2 and 10. The region of $Nd(OH)_3$(s) expands with the decrease of EDTA concentration between pH 12 and 14. As for the Y system, the minimium EDTA concentration required for the solubilization of YPO_4(s) further decerases to 10^{-5} M between pH 2 and 12, suggesting that YPO_4(s) is more readily leachable than La and Nd. It can be found that the minimium EDTA concentration required decreases from La to Nd, and to Y. it may result from an increasingly stronger affinity with EDTA from La to Nd, and to Y, which correlates to increasing Log K values for these elements.

Another issue during NaOH pretreatment is the dissolution of gangue minerals such as clays caused by NaOH. Dissolution of these elements can also consume EDTA and lead to higher reagent consumption. To evaluate this effect, the thermodynamic simulations were revaluated in the presence of Al^{3+}. AS shown in Figure 391, 0.1 M Al^{3+}, increases the minimium EDTA concentration required to solubilize $LnPO_4$(s) from $10^{-3.5}$ to 10^{-1} M when pH is between 2 and 7. At higher pH values, no no noticeble change was found at alkaline pH. The pH-dependent influence of Al^{3+} ions on the dissolution of $LnPO_4$(s) may be ascribed to the decreased complexing ability of Ln^{3+} and EDTA, which results from the higher degree of protonation of EDTA at acidic pH (see Figure 392). As shown, at basic pH, EDTA can be more easily deprotonated, and thus more $EDTA^{4-}$ ligands are avaliable for the dephosphrization. A similar shrinking region of the soluble Nd-$EDTA^-$ species at acidic pH is shown for the system of Nd, as the minimium EDTA concentration increases from $10^{-4.2}$ to $10^{-1.5}$ M between pH 3 and 7. Though the introduction of Al^{3+} ions

leads to minor variation of the stability diagram for the Y system, a general trend is that the contaminating ions negatively inflence the dissolution of $REPO_4$(s) especially under acidic conditions; however, the influence is less prevalent at the basic conditions where NaOH pretreatment has been conducted.

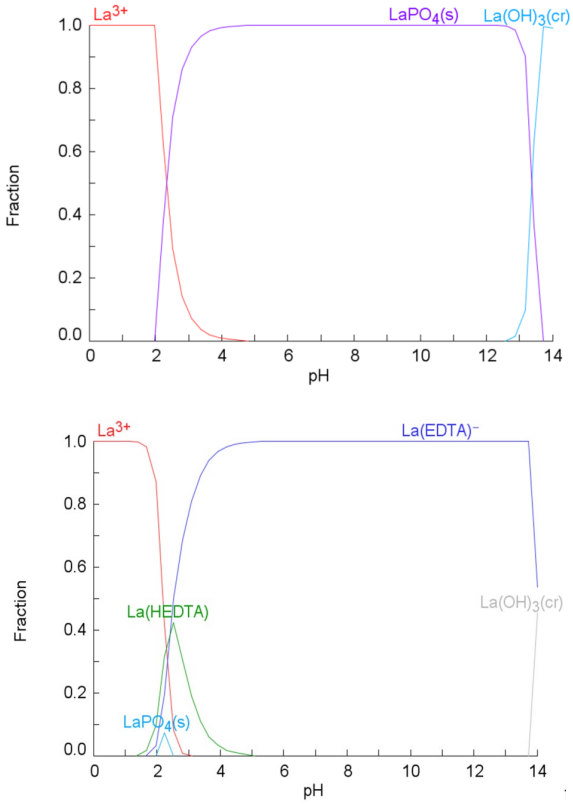

Figure 389. Fraction diagrams of La in the systems of La^{3+}-PO_4^{3-}-H_2O (top) and La^{3+}-PO_4^{3-}-EDTA-H_2O (bottom) at 25 °C, conditions: $[La^{3+}] = [PO_4^{3-}] = 10^{-5}$ M, [EDTA] = 0.1 M.

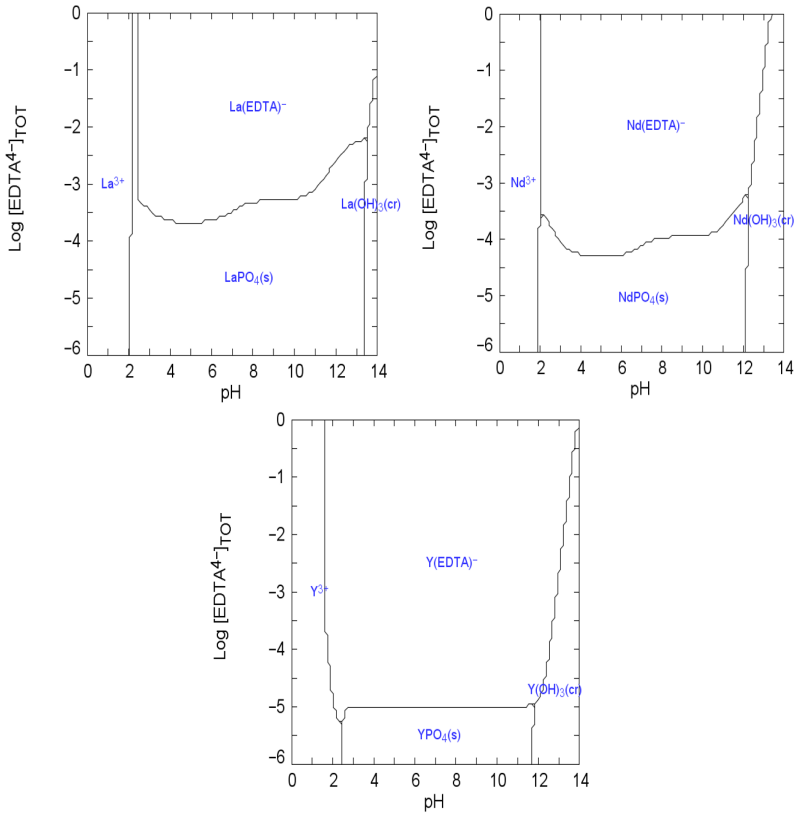

Figure 390. Species diagrams of La (a), Nd (b), and Y (c) in the system of REE^{3+}-PO_4^{3-}-$EDTA^{4-}$-H_2O, conditions: $[REE^{3+}] = [PO_4^{3-}] = 10^{-5}$ M, [EDTA] = 0.1 M.

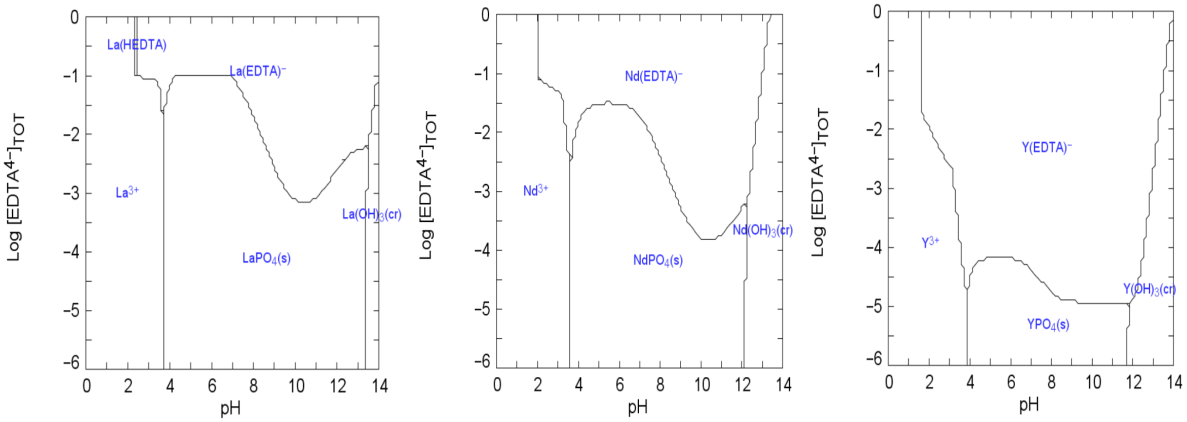

Figure 391. Species diagrams of La (a), Nd (b), and Y (c) in the systems of REE^{3+}-PO_4^{3-}-$EDTA^{4-}$-Al^{3+}-H_2O, conditions: $[REE^{3+}] = [PO_4^{3-}] = 10^{-5}$ M, $[Al^{3+}] = 0.1$ M.

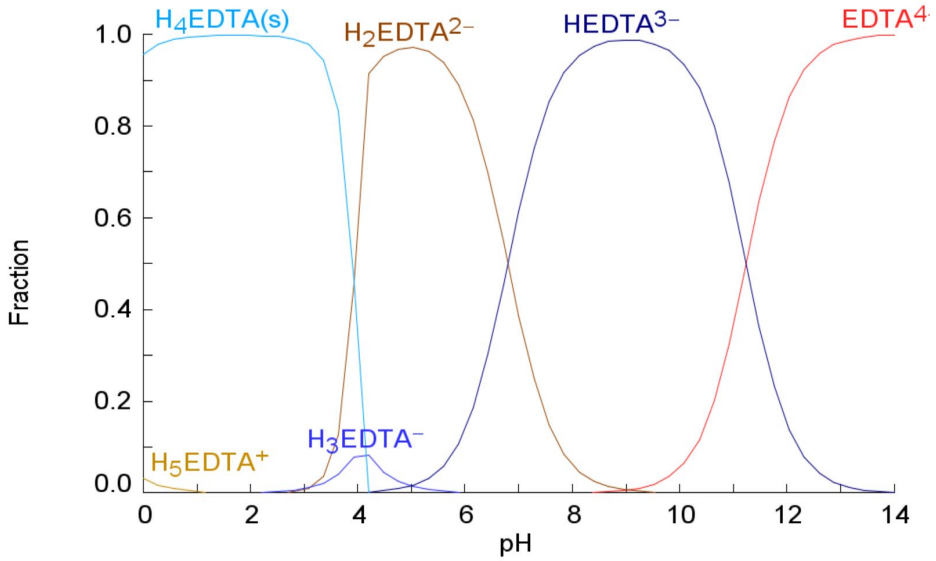

Figure 392. Fraction diagram of 0.1 M EDTA as a function of pH at 25 °C (created by Medusa software).

PRODUCTS

1. Feng, X., Onel, O., Council-Troche, M., Noble, A., Yoon, R. H., & Morris, J. R. (2021). A study of rare earth ion-adsorption clays: The speciation of rare earth elements on kaolinite at basic pH. *Applied Clay Science*, *201*, 105920.
2. Honaker, R. Q., Zhang, W., & Werner, J. (2019). Acid leaching of rare earth elements from coal and coal ash: implications for using fluidized bed combustion to assist in the recovery of critical materials. *Energy & Fuels*, *33*(7), 5971-5980.
3. Huang, K., & Yoon, R. H. (2019). Effect of ζ-Potentials on Bubble-Particle Interactions. *Mining, Metallurgy & Exploration*, *36*(1), 21-34.
4. Huang, K., & Yoon, R. H. (2019). Surface forces in the thin liquid films (TLFs) of water confined between n-alkane drops and hydrophobic gold surfaces. *Langmuir*, *35*(48), 15681-15691.
5. Huang, K., & Yoon, R. H. (2020). Control of bubble ζ-potentials to improve the kinetics of bubble-particle interactions. *Minerals Engineering*, *151*, 106295.
6. Huang, K., Keles, S., Sherrell, I., Noble, A., & Yoon, R. H. (2022). Development of a flotation simulator that can predict grade vs. Recovery curves from mineral liberation data. *Minerals Engineering*, *181*, 107510.
7. Yang, X., & Honaker, R. Q. (2020). Leaching kinetics of rare earth elements from fire clay seam coal. *Minerals*, *10*(6), 491.
8. Zhang, W., & Honaker, R. (2019). Enhanced leachability of rare earth elements from calcined products of bituminous coals. *Minerals Engineering*, *142*, 105935.

REFERENCES

1. Abreu, R. D., & Morais, C. A. (2010). Purification of rare earth elements from monazite sulphuric acid leach liquor and the production of high-purity ceric oxide. Minerals Engineering, 23(6), 536-540.
2. Ali, A., & Waqar, F. (2015). Synergistic extraction of Eu (III) with mixture of picrolonic acid and neutral organophosphorous extractants. Journal of Radioanalytical and Nuclear Chemistry, 303(1), 139-145.
3. Arbuzov, S. I., Maslov, S. G., & Il'enok, S. S. (2015). Modes of occurrence of scandium in coals and peats (A review). Solid Fuel Chemistry, 49(3), 167-182.
4. Arbuzov, S. I., Volostnov, A. V., Mezhibor, A. M., Rybalko, V. I., & Ilenok, S. S. (2014). Scandium (Sc) geochemistry in coals (Siberia, Russian Far East, Mongolia, Kazakhstan, and Iran). International Journal of Coal Geology, 125, 22-35.
5. Aveyard, R., Binks, B. P., & Clint, J. H. (2003). Emulsions stabilised solely by colloidal particles. Advances in Colloid and Interface Science, 100, 503-546.
6. Bandara, A. M. T. S., & Senanayake, G. (2015). Leachability of rare-earth, calcium and minor metal ions from natural Fluorapatite in perchloric, hydrochloric, nitric and phosphoric acid solutions: Effect of proton activity and anion participation. Hydrometallurgy, 153, 179-189.
7. Bao, Z., & Zhao, Z. (2008). Geochemistry of mineralization with exchangeable REY in the weathering crusts of granitic rocks in South China. Ore Geology Reviews, 33(3-4), 519-535.
8. Bau, M. (1999). Scavenging of dissolved yttrium and rare earths by precipitating iron oxyhydroxide: experimental evidence for Ce oxidation, Y-Ho fractionation, and lanthanide tetrad effect. Geochimica et Cosmochimica Acta, 63(1), 67-77.
9. Bau, M., & Koschinsky, A. (2009). Oxidative scavenging of cerium on hydrous Fe oxide: evidence from the distribution of rare earth elements and yttrium between Fe oxides and Mn oxides in hydrogenetic ferromanganese crusts. Geochemical Journal, 43(1), 37-47.
10. Bauer, D. J. (1966). Extraction and separation of selected lanthanides with a tertiary amine (Vol. 6809). US Department of the Interior, Bureau of Mines.
11. Bern, C. R., Yesavage, T., & Foley, N. K. (2017). Ion-adsorption REEs in regolith of the Liberty Hill pluton, South Carolina, USA: An effect of hydrothermal alteration. Journal of Geochemical Exploration, 172, 29-40.
12. Bingen, B., Demaiffe, D., & Hertogen, J. (1996). Redistribution of rare earth elements, thorium, and uranium over accessory minerals in the course of amphibolite to granulite facies metamorphism: the role of apatite and monazite in orthogneisses from southwestern Norway. Geochimica et Cosmochimica Acta, 60(8), 1341-1354.
13. Borst, A. M., Smith, M. P., Finch, A. A., Estrade, G., Villanova-de-Benavent, C., Nason, P., ... & Geraki, K. (2020). Adsorption of rare earth elements in regolith-hosted clay deposits. Nature communications, 11(1), 1-15.
14. Brenner, H. (1961). The slow motion of a sphere through a viscous fluid towards a plane surface. Chemical engineering science, 16(3-4), 242-251.
15. Butt, H. J. (1991). Measuring electrostatic, van der Waals, and hydration forces in electrolyte solutions with an atomic force microscope. Biophysical Journal, 60(6), 1438-1444.
16. Cao, M., Wang, P., Kou, Y., Wang, J., Liu, J., Li, Y., ... & Chen, C. (2015). Gadolinium (III)-chelated silica nanospheres integrating chemotherapy and photothermal therapy for cancer treatment and magnetic resonance imaging. ACS applied materials & interfaces, 7(45), 25014-25023.
17. Cao, Z., Cao, Y., Dong, H., Zhang, J., & Sun, C. (2016). Effect of calcination condition on the microstructure and pozzolanic activity of calcined coal gangue. International Journal of Mineral Processing, 146, 23-28.
18. Chen, J. (2013). Column Flotation of Subbituminous Coal Using the Blend of Trimethyl Pentanediol Derivatives and Pico-Nano Bubbles. West Virginia University.

19. Chi, R., & Tian, J. (2008). Weathered crust elution-deposited rare earth ores. Nova Science Publishers.
20. Chin, P. K. F., & Mills, G. L. (1991). Kinetics and mechanisms of kaolinite dissolution: effects of organic ligands. Chemical Geology, 90(3-4), 307-317.
21. Chou, J. D., Wey, M. Y., & Chang, S. H. (2009). Evaluation of the distribution patterns of Pb, Cu and Cd from MSWI fly ash during thermal treatment by sequential extraction procedure. Journal of hazardous materials, 162(2-3), 1000-1006.
22. Churaev, N. V. (1995). Contact angles and surface forces. Advances in Colloid and Interface Science, 58(2-3), 87-118.
23. Dai, S., Zhao, L., Hower, J. C., Johnston, M. N., Song, W., Wang, P., & Zhang, S. (2014). Petrology, mineralogy, and chemistry of size-fractioned fly ash from the Jungar power plant, Inner Mongolia, China, with emphasis on the distribution of rare earth elements. Energy & Fuels, 28(2), 1502-1514.
24. Debye, P., & Hückel, E. (1923). Physik Z. 24, 185 (1923). Google Scholar CAS.
25. Derjaguin, B. (1940). On the repulsive forces between charged colloid particles and on the theory of slow coagulation and stability of lyophobe sols. Transactions of the Faraday Society, 35, 203-215.
26. Djerdjev, A. M., & Beattie, J. K. (2008). Electroacoustic and ultrasonic attenuation measurements of droplet size and ζ-potential of alkane-in-water emulsions: effects of oil solubility and composition. Physical Chemistry Chemical Physics, 10(32), 4843-4852.
27. Dong, H., Kukkadapu, R. K., Fredrickson, J. K., Zachara, J. M., Kennedy, D. W., & Kostandarithes, H. M. (2003). Microbial reduction of structural Fe (III) in illite and goethite. Environmental Science & Technology, 37(7), 1268-1276.
28. Dutrizac, J. E. (2017). The behaviour of the rare earth elements during gypsum ($CaSO4 \cdot 2H2O$) precipitation. Hydrometallurgy, 174, 38-46.
29. Eick, M. J., Peak, J. D., & Brady, W. D. (1999). The effect of oxyanions on the oxalate-promoted dissolution of goethite. Soil Science Society of America Journal, 63(5), 1133-1141.
30. Eskenazy, G. M. (1987). Rare earth elements in a sampled coal from the Pirin deposit, Bulgaria. International Journal of Coal Geology, 7(3), 301-314.
31. Exerowa, D., & Kruglyakov, P. M. (1997). Foam and foam films: theory, experiment, application (Vol. 5). Elsevier.
32. Fang, L., Shi, Q., Nguyen, J., Wu, B., Wang, Z., & Lo, I. M. (2017). Removal mechanisms of phosphate by lanthanum hydroxide nanorods: investigations using EXAFS, ATR-FTIR, DFT, and surface complexation modeling approaches. Environmental Science & Technology, 51(21), 12377-12384.
33. Feng, J., Zhou, F., Chi, R., Liu, X., Xu, Y., & Liu, Q. (2018). Effect of a novel compound on leaching process of weathered crust elution-deposited rare earth ore. Minerals engineering, 129, 63-70.
34. Finch, J. A., & Smith, G. W. (1973). Dynamic surface tension of alkaline dodecylamine solutions. Journal of Colloid and Interface Science, 45(1), 81-91.
35. Finkelman, R. B., Palmer, C. A., & Wang, P. (2018). Quantification of the modes of occurrence of 42 elements in coal. International Journal of Coal Geology, 185, 138-160.
36. Fontes, M. P. F. (1992). Iron oxide-clay mineral association in Brazilian Oxisols: A magnetic separation study. Clays and Clay Minerals, 40(2), 175-179.
37. Free, M. L. (2021). Hydrometallurgy: fundamentals and applications. Springer Nature.
38. Frumkin, A. N. (1938). On the wetting phenomena and attachment of bubbles. Zhur. Fiz. Khim.(J. Phys. Chem.), 12(4), 337-345.
39. Fuerstenau, D. W. (1957). Correlation of contact angles, adsorption density, zeta potentials, and flotation rate. Trans. AIME, 208, 1365-1367.
40. Fuguo, L., Guohua, G., Li, H., Yanfei, X., Run, Y., & Kaizhong, L. (2018). Compound leaching of rare earth from the ion-adsorption type rare earth ore with magnesium sulfate and ascorbic acid. Hydrometallurgy, 179, 25-35.

41. Gado, M. A., Atia, B. M., & Fathy, W. M. (2020). Selective recovery of the main metal values from Rosetta monazite mineral concentrate. International Journal of Environmental Analytical Chemistry, 100(3), 254-267.
42. Gasparatos, D. (2013). Sequestration of heavy metals from soil with Fe–Mn concretions and nodules. Environmental Chemistry Letters, 11(1), 1-9.
43. Gharabaghi, M., Noaparast, M., & Irannajad, M. (2009). Selective leaching kinetics of low-grade calcareous phosphate ore in acetic acid. Hydrometallurgy, 95(3-4), 341-345.
44. Gougazeh, M., & Buhl, J. C. (2014). Conversion of Natural Jordanian Kaolin into Zeolite A without Thermal Pre-activation. Zeitschrift für anorganische und allgemeine Chemie, 640(8-9), 1675-1679.
45. Grosvenor, A. P., Kobe, B. A., Biesinger, M. C., & McIntyre, N. S. (2004). Investigation of multiplet splitting of Fe 2p XPS spectra and bonding in iron compounds. Surface and Interface Analysis: An International Journal devoted to the development and application of techniques for the analysis of surfaces, interfaces and thin films, 36(12), 1564-1574.
46. Gupta, N., Li, B., Luttrell, G., Yoon, R. H., Bratton, R., & Reyher, J. (2016, February). Hydrophobic-hydrophilic separation (HHS) process for the recovery and dewatering of ultrafine coal. In Proceedings of the 2016 SME Annual Conference and Expo, Phoenix, AZ, USA (pp. 21-24).
47. Hernández, L. G., Rueda, L. I., Díaz, A. R., & Antón, C. C. (1986). Preparation of amorphous silica by acid dissolution of sepiolite: kinetic and textural study. Journal of Colloid and Interface Science, 109(1), 150-160.
48. Hogg, R. T. W. D. W., Healy, T. W., & Fuerstenau, D. W. (1966). Mutual coagulation of colloidal dispersions. Transactions of the Faraday Society, 62, 1638-1651.
49. Honaker, R. Q., Groppo, J., Yoon, R. H., Luttrell, G. H., Noble, A., & Herbst, J. (2017). Process evaluation and flowsheet development for the recovery of rare earth elements from coal and associated byproducts. Minerals & Metallurgical Processing, 34(3), 107-115.
50. Honaker, R., Hower, J., Eble, C., Weisenfluh, J., Groppo, J., Rezaee, M., ... & Kiser, M. (2014). Laboratory and bench-scale testing for rare earth elements. Cell, 724, 554-3652.
51. Hower, J. C., Berti, D., Hochella Jr, M. F., & Mardon, S. M. (2018). Rare earth minerals in a “no tonstein” section of the Dean (Fire Clay) coal, Knox County, Kentucky. International Journal of Coal Geology, 193, 73-86.
52. Hower, J. C., Groppo, J. G., Henke, K. R., Hood, M. M., Eble, C. F., Honaker, R. Q., ... & Qian, D. (2015). Notes on the potential for the concentration of rare earth elements and yttrium in coal combustion fly ash. Minerals, 5(2), 356-366.
53. Hower, J. C., Ruppert, L. F., & Eble, C. F. (1999). Lanthanide, yttrium, and zirconium anomalies in the Fire Clay coal bed, Eastern Kentucky. International Journal of Coal Geology, 39(1-3), 141-153.
54. Huang, Kaiwu, Lei Pan, and Roe-Hoan Yoon. "A capillary flow model for filtration." Minerals Engineering 115 (2018): 88-96.
55. Huggins, F. E. (2002). Overview of analytical methods for inorganic constituents in coal. International Journal of Coal Geology, 50(1-4), 169-214.
56. Huminicki, D. M., & Rimstidt, J. D. (2009). Iron oxyhydroxide coating of pyrite for acid mine drainage control. Applied Geochemistry, 24(9), 1626-1634.
57. Husin, H., Leong, Y. K., & Liu, J. S. (2013). Surface force arising from adsorbed diethylenetriaminepentacetic acid (DTPA) and related compounds and their metal ions complexes in alumina suspensions. Colloids and Surfaces A: Physicochemical and Engineering Aspects, 422, 172-180.
58. Israelachvili, J. N. (1972, November). The calculation of van der Waals dispersion forces between macroscopic bodies. In Proc. R. Soc. Lond. A (Vol. 331, No. 1584, pp. 39-55). The Royal Society.
59. Israelachvili, J. N. (2011). Intermolecular and surface forces. Academic press.
60. Ji, B., Li, Q., & Zhang, W. (2022). Rare earth elements (REEs) recovery from coal waste of the Western Kentucky No. 13 and Fire Clay Seams. Part I: Mineralogical characterization using SEM-EDS and TEM-EDS. Fuel, 307, 121854.

61. Johannesson, K. H., & Zhou, X. (1999). Origin of middle rare earth element enrichments in acid waters of a Canadian High Arctic lake. Geochimica et Cosmochimica Acta, 63(1), 153-165.
62. Jun, T., Jingqun, Y., Ruan, C., Guohua, R., Mintao, J., & Kexian, O. (2010). Kinetics on leaching rare earth from the weathered crust elution-deposited rare earth ores with ammonium sulfate solution. Hydrometallurgy, 101(3-4), 166-170.
63. Kadıoğlu, Y. Y., Karaca, S., & Bayrakceken, S. (1995). Kinetics of pyrite oxidation in aqueous suspension by nitric acid. Fuel Processing Technology, 41(3), 273-287.
64. Khamaiuml; s, B., Kaiuml; s, A., Ismaiuml; l, K., & Mohamed, J. (2008). Effect of temperature on the attack of fluorapatite by a phosphoric acid solution. Scientific Research and Essays, 3(1), 035-039.
65. Kim, C. J., Yoon, H. S., Chung, K. W., Lee, J. Y., Kim, S. D., Shin, S. M., ... & Kim, S. H. (2014). Leaching kinetics of lanthanum in sulfuric acid from rare earth element (REE) slag. Hydrometallurgy, 146, 133-137.
66. Kim, E. Y., Lee, J. C., Kim, B. S., Kim, M. S., & Jeong, J. (2007). Leaching behavior of nickel from waste multi-layer ceramic capacitors. Hydrometallurgy, 86(1-2), 89-95.
67. Kim, E., & Osseo-Asare, K. (2012). Aqueous stability of thorium and rare earth metals in monazite hydrometallurgy: Eh–pH diagrams for the systems Th–, Ce–, La–, Nd–(PO4)–(SO4)–H2O at 25 C. Hydrometallurgy, 113, 67-78.
68. Kim, R., Cho, H., Han, K., Kim, K., & Mun, M. (2016). Optimization of Acid Leaching of Rare-Earth Elements from Mongolian Apatite-Based Ore. Minerals, 6(3), 63.
69. Komadel, P., & Madejová, J. (2013). Acid activation of clay minerals. In Developments in clay science (Vol. 5, pp. 385-409). Elsevier.
70. Kumari et al. Process development to recover rare earth metals from monazite mineral: A review. Minerals Engineering 79 (2015) 102–115.
71. Kumari, A., Jha, M. K., Yoo, K., Panda, R., Lee, J. Y., Kumar, J. R., & Pathak, D. D. (2019). Advanced process to dephosphorize monazite for effective leaching of rare earth metals (REMs). Hydrometallurgy, 187, 203-211.
72. Kydros, K. A., Angelidis, T. N., & Matis, K. A. (1993). Selective flotation of an auriferous bulk pyrite-arsenopyrite concentrate in presence of sodium sulphoxy-salts. Minerals engineering, 6(12), 1257-1264.
73. Lai, F., Huang, L., Gao, G., Yang, R., & Xiao, Y. (2018). Recovery of rare earths from ion-absorbed rare earths ore with MgSO4-ascorbic acid compound leaching agent. Journal of Rare Earths, 36(5), 521-527.
74. Langmuir, D. (2004). Issue paper on the environmental chemistry of metals. US Environmental Protection Agency.
75. Lapidus, G. T., & Doyle, F. M. (2015). Selective thorium and uranium extraction from monazite: I. Single-stage oxalate leaching. Hydrometallurgy, 154, 102-110.
76. Larson, E. M., Ellison, A. J. G., Lytle, F. W., Navrotsky, A., Greegor, R. B., & Wong, J. (1991). XAS study of lanthanum coordination environments in glasses of the system K2O□ SiO2□ La2O3. Journal of non-crystalline solids, 130(3), 260-272.
77. Laudal, D. A., Benson, S. A., Addleman, R. S., & Palo, D. (2018). Leaching behavior of rare earth elements in Fort Union lignite coals of North America. International Journal of Coal Geology, 191, 112-124.
78. Lazo, D. E., Dyer, L. G., Alorro, R. D., & Browner, R. (2018). Treatment of monazite by organic acids II: Rare earth dissolution and recovery. Hydrometallurgy, 179, 94-99.
79. Levenspiel, O. (1998). Chemical reaction engineering. John wiley & sons.
80. Li, K., Chen, J., Zou, D., Liu, T., & Li, D. (2019). Kinetics of nitric acid leaching of cerium from oxidation roasted Baotou mixed rare earth concentrate. Journal of Rare Earths, 37(2), 198-204.
81. Li, M., Wei, C., Qiu, S., Zhou, X., Li, C., & Deng, Z. (2010). Kinetics of vanadium dissolution from black shale in pressure acid leaching. Hydrometallurgy, 104(2), 193-200.

82. Li, M., Zhang, D., Yan, Y., Gao, K., Liu, X., & Li, J. (2017). Effect of oxidation behavior of cerium during the roasting process on the leaching of mixed rare earth concentrate. Hydrometallurgy, 174, 156-166.
83. Li, M., Zhang, X., Liu, Z., Hu, Y., Wang, M., Liu, J., & Yang, J. (2013). Kinetics of leaching fluoride from mixed rare earth concentrate with hydrochloric acid and aluminum chloride. Hydrometallurgy, 140, 71-76.
84. Lin, P., Yang, X., Werner, J. M., & Honaker, R. Q. (2021). Application of Eh-pH Diagrams on Acid Leaching Systems for the Recovery of REEs from Bastnaesite, Monazite and Xenotime. Metals, 11(5), 734.
85. Lin, R., Howard, B. H., Roth, E. A., Bank, T. L., Granite, E. J., & Soong, Y. (2017). Enrichment of rare earth elements from coal and coal by-products by physical separations. Fuel, 200, 506-520.
86. Lin, R., Stuckman, M., Howard, B. H., Bank, T. L., Roth, E. A., Macala, M. K., ... & Granite, E. J. (2018). Application of sequential extraction and hydrothermal treatment for characterization and enrichment of rare earth elements from coal fly ash. Fuel, 232, 124-133.
87. Long, P., Wang, G., Zhang, C., Yang, Y., Cao, X., & Shi, Z. (2020). Kinetics model for leaching of ion-adsorption type rare earth ores. Journal of Rare Earths, 38(12), 1354-1360.
88. Makanyire, T., Jha, A., & Sutcliffe, S. (2016). Kinetics of hydrochloric acid leaching of niobium from TiO2 residues. International Journal of Mineral Processing, 157, 1-6.
89. Martín-García, J. M., Sánchez-Marañón, M., Calero, J., Aranda, V., Delgado, G., & Delgado, R. (2016). Iron oxides and rare earth elements in the clay fractions of a soil chronosequence in southern S pain. European Journal of Soil Science, 67(6), 749-762.
90. Matsumoto, M., Otono, T., & Kondo, K. (2001). Synergistic extraction of organic acids with tri-n-octylamine and tri-n-butylphosphate. Separation and Purification Technology, 24(1-2), 337-342.
91. Metal Chelates-Dojindo EU GmbH (2012). <https://www.dojindo.eu.com/images/ Product%20Photo/ Chelate_Table_of_Stability_Constants.pdf>
92. Mittermüller, M., Saatz, J., & Daus, B. (2016). A sequential extraction procedure to evaluate the mobilization behavior of rare earth elements in soils and tailings materials. Chemosphere, 147, 155-162.
93. Moldoveanu, G. A., & Papangelakis, V. G. (2012). Recovery of rare earth elements adsorbed on clay minerals: I. Desorption mechanism. Hydrometallurgy, 117, 71-78.
94. Moldoveanu, G., & Papangelakis, V. (2021). Chelation-assisted ion-exchange leaching of rare earths from clay minerals. Metals, 11(8), 1265.
95. Mongruel, A., Lamriben, C., Yahiaoui, S., & Feuillebois, F. (2010). The approach of a sphere to a wall at finite Reynolds number. Journal of Fluid Mechanics, 661, 229-238.
96. Montross, S. N., Yang, J., Britton, J., McKoy, M., & Verba, C. (2020). Leaching of rare earth elements from Central Appalachian coal seam underclays. Minerals, 10(6), 577.
97. Mullica, D. F., Lok, C. K. C., Perkins, H. O., Benesh, G. A., & Young, V. (1995). The X-ray photoemission spectra of Nd (OH) 3, Sm (OH) 3, Eu (OH) 3 and Gd (OH) 3. Journal of Electron Spectroscopy and Related Phenomena, 71(1), 1-20.
98. Music, S., Popović, S., & Ristić, M. (1992). Thermal decomposition of pyrite. Journal of radioanalytical and nuclear chemistry, 162(2), 217-226.
99. Nagaiyar, K., & Gupta, C. K. (2016). Extractive Metallurgy of Rare Earth. Second Edi.
100. Nagano, Y., Sakiyama, M., Fujiwara, T., & Kondo, Y. (1988). Thermochemical study of tetramethyl-and tetraethylammonium halides: nonionic cohesive energies in the crystals and hydration enthalpies of the cations. The Journal of Physical Chemistry, 92(20), 5823-5827.
101. Nowack, B. and Sigg, L., 1996. Adsorption of EDTA and metal–EDTA complexes onto goethite. Journal of Colloid and Interface Science, 177(1), pp.106-121.
102. Ohta, A., & Kawabe, I. (2000). Rare earth element partitioning between Fe oxyhydroxide precipitates and aqueous NaCl solutions doped with NaHCO3: Determinations of rare earth element complexation constants with carbonate ions. Geochemical Journal, 34(6), 439-454.

103. Pan, J., Zhou, C., Liu, C., Tang, M., Cao, S., Hu, T., ... & Zhang, N. (2018). Modes of Occurrence of Rare Earth Elements in Coal Fly Ash: A Case Study. Energy & Fuels, 32(9), 9738-9743.
104. Pan, J., Zhou, C., Tang, M., Cao, S., Liu, C., Zhang, N. & Ji, W. (2019). Study on the modes of occurrence of rare earth elements in coal fly ash by statistics and a sequential chemical extraction procedure. Fuel, 237, 555-565.
105. Pan, L., & Yoon, R. H. (2016). Measurement of hydrophobic forces in thin liquid films of water between bubbles and xanthate-treated gold surfaces. Minerals Engineering, 98, 240-250.
106. Pan, L., & Yoon, R. H. (2018). Effects of elctrolytes on the stability of wetting films: Implications on seawater flotation. Minerals Engineering, 122, 1-9.
107. Pan, L., Jung, S., & Yoon, R. H. (2011, March). Stability of the wetting films formed on hydrophilic and hydrophobic gold surfaces. In ABSTRACTS OF PAPERS OF THE AMERICAN CHEMICAL SOCIETY (Vol. 241). 1155 16TH ST, NW, WASHINGTON, DC 20036 USA: AMER CHEMICAL SOC.
108. Panda, R., Kumari, A., Jha, M. K., Hait, J., Kumar, V., Kumar, J. R., & Lee, J. Y. (2014). Leaching of rare earth metals (REMs) from Korean monazite concentrate. Journal of Industrial and Engineering Chemistry, 20(4), 2035-2042.
109. Papangelakis, V. G., & Moldoveanu, G. (2014, September). Recovery of rare earth elements from clay minerals. In Proceedings of the 1st Rare Earth Resources Conference, Milos (Vol. 191, p. 202).
110. Park, S., Kim, M., Lim, Y., Yu, J., Chen, S., Woo, S. W., ... & Kim, H. S. (2021). Characterization of rare earth elements present in coal ash by sequential extraction. Journal of Hazardous Materials, 402, 123760.
111. Paschalidou, P., & Pashalidis, I. (2019). Recovery of uranium from phosphate rock with EDTA-mediated dissolution and cation exchange. Hydrometallurgy, 189, 105118.
112. Paspaliaris, Y., & Tsolakis, Y. (1987). Reaction kinetics for the leaching of iron oxides in diasporic bauxite from the parnassus-giona zone (Greece) by hydrochloric acid. Hydrometallurgy, 19(2), 259-266.
113. Pickering, S. U. (1907). CXCVI.—emulsions. Journal of the Chemical Society, Transactions, 91, 2001-2021.
114. Puigdomenech, I. (2013). Make equilibrium diagrams using sophisticated algorithms (Medusa). In: Inorganic Chemistry. Royal Institute of Technology, Stockholm, Sweden.
115. Qi, D. (2018). Hydrometallurgy of rare earths: extraction and separation. Elsevier.
116. Qi, D. (2018). Hydrometallurgy of rare earths: extraction and separation. Elsevier.
117. Reddy, M. L. P., Bharathi, J. B., Peter, S., & Ramamohan, T. R. (1999). Synergistic extraction of rare earths with bis (2, 4, 4-trimethyl pentyl) dithiophosphinic acid and trialkyl phosphine oxide. Talanta, 50(1), 79-85.
118. San Cristóbal, A. G., Castelló, R., Luengo, M. A. M., & Vizcayno, C. (2009). Acid activation of mechanically and thermally modified kaolins. Materials Research Bulletin, 44(11), 2103-2111.
119. Sastri, V. S., Perumareddi, J. R., Rao, V. R., Rayudu, G. V. S., & Bunzli, J. C. (2003). Modern aspects of rare earths and their complexes. Elsevier.
120. Seferinoğlu, M., Paul, M., Sandström, Å., Köker, A., Toprak, S., & Paul, J. (2003). Acid leaching of coal and coal-ashes☆. Fuel, 82(14), 1721-1734.
121. Seredin, V. V. (1996). Rare earth element-bearing coals from the Russian Far East deposits. International Journal of Coal Geology, 30(1-2), 101-129.
122. Seredin, V. V., & Dai, S. (2012). Coal deposits as potential alternative sources for lanthanides and yttrium. International Journal of Coal Geology, 94, 67-93.
123. Sheludko, A. (1962). Certain peculiarities of foam lamellas, Parts I− III. In Proc. Koninkl. Ned. Akad. Wetenschap. B (Vol. 65, pp. 76-108).
124. Shelyug, A., Mesbah, A., Szenknect, S., Clavier, N., Dacheux, N., & Navrotsky, A. (2018). Thermodynamics and stability of rhabdophanes, hydrated rare earth phosphates REPO4· n H2O. Frontiers in chemistry, 6, 604.

125. Siegmann, H. C., Schlapbach, L., & Brundle, C. R. (1978). Self-Restoring of the Active Surface in the Hydrogen Sponge La Ni 5. Physical Review Letters, 40(14), 972.
126. Sinkankas, J. (1972). Gemstone and mineral data book; A compilation of data, recipes, formulas, and instructions for the mineralogist, gemologist, lapidary, jeweler, craftsman and collector.
127. Siracusa, P. A., & Somasundaran, P. (1987). The role of mineral dissolution in the adsorption of dodecylbenzenesulfonate on kaolinite and alumina. Colloids and surfaces, 26, 55-77.
128. Slobodník, M., Dillingerová, V., Blaženková, M., Huraiová, M., & Hurai, V. (2020). Trace Elements in Apatite as Genetic Indicators of the Evate Apatite-Magnetite Deposit, NE Mozambique. Minerals, 10(12), 1125.
129. Somasundaran, P., & Ananthapadmanabhan, K. P. (1979). Solution chemistry of surfactants and the role of it in adsorption and froth flotation in mineral-water systems. Solution chemistry of surfactants, 2, 777.
130. Stachurski, J., & MichaŁek, M. (1996). The effect of the ζ potential on the stability of a non-polar oil-in-water emulsion. Journal of colloid and interface science, 184(2), 433-436.
131. Stuckman, M., Lopano, C., Dixon, E., & Granite, E. (2016, September). Distribution and Speciation of Rare Earth Elements in Coal Combustion Byproducts. In Proceedings of the 18th International Conference on Heavy Metals in the Environment.
132. Su, S., Liu, Q., Liu, J., Zhang, H., Li, R., Jing, X., & Wang, J. (2017). Enhancing adsorption of U (VI) onto EDTA modified L. cylindrica using epichlorohydrin and ethylenediamine as a bridge. Scientific reports, 7(1), 1-9.
133. Sun, C., Wu, X., Meng, H., Xu, X., Xu, J., & Zhang, X. (2014). Surface modification with EDTA molecule: a feasible method to enhance the adsorption property of ZnO. Journal of Physics and Chemistry of Solids, 75(6), 726-731.
134. Sun, H. Q., Jing, S. O. N. G., Shuai, S. U. N., Qu, J. K., Wei, L. Ü., & Tao, Q. I. (2019). Decomposition kinetics of zircon sand in NaOH sub-molten salt solution. Transactions of Nonferrous Metals Society of China, 29(9), 1948-1955.
135. Sun, X., Wang, J., Li, D., & Li, H. (2006). Synergistic extraction of rare earths by mixture of bis (2, 4, 4-trimethylpentyl) phosphinic acid and Sec-nonylphenoxy acetic acid. Separation and purification technology, 50(1), 30-34.
136. Sunding, M. F., Hadidi, K., Diplas, S., Løvvik, O. M., Norby, T. E., & Gunnæs, A. E. (2011). XPS characterisation of in situ treated lanthanum oxide and hydroxide using tailored charge referencing and peak fitting procedures. Journal of Electron Spectroscopy and Related Phenomena, 184(7), 399-409.
137. Suzuki, C., Mukoyama, T., Kawai, J., & Adachi, H. (1998). Calculation for the charge-transfer effect of La compounds in the 3 d− 1 core-hole state. Physical Review B, 57(16), 9507.
138. Tang, J., Qiao, J., Xue, Q., Liu, F., Chen, H., & Zhang, G. (2018). Leach of the weathering crust elution-deposited rare earth ore for low environmental pollution with a combination of (NH4) 2SO4 and EDTA. Chemosphere, 199, 160-167.
139. Tessier, A., Campbell, P. G., & Bisson, M. (1979). Sequential extraction procedure for the speciation of particulate trace metals. Analytical chemistry, 51(7), 844-851.
140. Tuncuk, A., & Akcil, A. (2014). Removal of iron from quartz ore using different acids: A laboratory-scale reactor study. Mineral Processing and Extractive Metallurgy Review, 35(4), 217-228.
141. Van Oss, C. J. (2006). Interfacial forces in aqueous media. CRC press.
142. Vanderah, T., Karen, V., Linstrom, P., & Burgess, D. (2012). NIST Databases for Materials Research.
143. Wang, H., Feng, Q., & Liu, K. (2016). The dissolution behavior and mechanism of kaolinite in alkali-acid leaching process. Applied Clay Science, 132, 273-280.
144. Wang, L., Liao, C., Yang, Y., Xu, H., Xiao, Y., & Yan, C. (2017). Effects of organic acids on the leaching process of ion-adsorption type rare earth ore. Journal of Rare Earths, 35(12), 1233-1238.

145. Wang, L., Long, Z., Huang, X., Yu, Y., Cui, D., & Zhang, G. (2010). Recovery of rare earths from wet-process phosphoric acid. Hydrometallurgy, 101(1-2), 41-47.
146. Wang, L., Long, Z., Huang, X., Yu, Y., Cui, D., & Zhang, G. (2010). Recovery of rare earths from wet-process phosphoric acid. Hydrometallurgy, 101(1-2), 41-47.
147. Wang, Y., Noble, A., Vass, C., & Ziemkiewicz, P. (2021). Speciation of rare earth elements in acid mine drainage precipitates by sequential extraction. Minerals Engineering, 168, 106827.
148. Wang, Z., Guo, S., & Ye, C. (2016). Leaching of copper from metal powders mechanically separated from waste printed circuit boards in chloride media using hydrogen peroxide as oxidant. Procedia Environmental Sciences, 31, 917-924.
149. Xue, B., Jianli, C., Zhihua, Z., Shaohua, Y. I. N., Yao, L. U. O., ZHANG, F., & Wenyuan, W. U. (2010). Kinetics of mixed rare earths minerals decomposed by CaO with NaCl-CaCl2 melting salt. Journal of Rare Earths, 28, 86-90.
150. Yanfei, X., Zongyu, F., Guhua, H., Huang, L., Huang, X., Yingying, C., & Zhiqi, L. (2016). Reduction leaching of rare earth from ion-adsorption type rare earths ore with ferrous sulfate. Journal of Rare Earths, 34(9), 917-923.
151. Yanfei, X., Zongyu, F., Xiaowei, H., Li, H., Yingying, C., Liangshi, W., & Zhiqi, L. (2015). Recovery of rare earths from weathered crust elution-deposited rare earth ore without ammonia-nitrogen pollution: I. leaching with magnesium sulfate. Hydrometallurgy, 153, 58-65.
152. Yanfei, X., Zongyu, F., Xiaowei, H., Li, H., Yingying, C., Liangshi, W., & Zhiqi, L. (2015). Recovery of rare earths from weathered crust elution-deposited rare earth ore without ammonia-nitrogen pollution: I. Leaching with magnesium sulfate. Hydrometallurgy, 153, 58-65.
153. Yanfei, X., Zongyu, F., Xiaowei, H., Li, H., Yingying, C., Xiangsheng, L., ... & Zhiqi, L. (2016). Recovery of rare earth from the ion-adsorption type rare earths ore: II. Compound leaching. Hydrometallurgy, 163, 83-90.
154. Yang, L., Li, C., Wang, D., Li, F., Liu, Y., Zhou, X., ... & Li, Y. (2019). Leaching ion adsorption rare earth by aluminum sulfate for increasing efficiency and lowering the environmental impact. Journal of Rare Earths, 37(4), 429-436.
155. Yang, X., & Honaker, R. Q. (2020). Leaching kinetics of rare earth elements from fire clay seam coal. Minerals, 10(6), 491.
156. Yang, X., Rozelle, P. L., & Pisupati, S. V. (2021). The effect of caustic soda treatment to recover rare earth elements from secondary feedstocks with low concentrations. Minerals Engineering, 173, 107184.
157. Yang, X., Werner, J., & Honaker, R. Q. (2019). Leaching of rare Earth elements from an Illinois basin coal source. Journal of Rare Earths, 37(3), 312-321.
158. Yoon, R. H. (2016). U.S. Patent No. 9,518,241. Washington, DC: U.S. Patent and Trademark Office.
159. Yoon, R. H., & Yordan, J. L. (1986). Zeta-potential measurements on microbubbles generated using various surfactants. Journal of Colloid and Interface Science, 113(2), 430-438.
160. Yoon, R. H., & Yordan, J. L. (1986). Zeta-potential measurements on microbubbles generated using various surfactants. Journal of Colloid and Interface Science, 113(2), 430-438.
161. Yoon, R. H., Salman, T., & Donnay, G. (1979). Predicting points of zero charge of oxides and hydroxides. Journal of colloid and interface science, 70(3), 483-493.
162. Yu, J., Guo, Z., & Tang, H. (2013). Dephosphorization treatment of high phosphorus oolitic iron ore by hydrometallurgical process and leaching kinetics. ISIJ international, 53(12), 2056-2064.
163. Zdravkov, B., Čermák, J., Šefara, M., & Janků, J. (2007). Pore classification in the characterization of porous materials: A perspective. Open Chemistry, 5(2), 385-395.
164. Zhang, J. P., & Lincoln, F. J. (1994). The decomposition of monazite by mechanical milling with calcium oxide and calcium chloride. Journal of alloys and compounds, 205(1-2), 69-75.
165. Zhang, J., Zhao, B., & Schreiner, B. (2016). Separation hydrometallurgy of rare earth elements.

166. Zhang, P., Han, Z., Jia, J., Wei, C., Liu, Q., Wang, X., ... & Miao, S. (2019). Occurrence and distribution of gallium, scandium, and rare earth elements in coal gangue collected from Junggar Basin, China. International Journal of Coal Preparation and Utilization, 39(7), 389-402.
167. Zhang, Q., & Saito, F. (1998). Non-thermal process for extracting rare earths from bastnaesite by means of mechanochemical treatment. Hydrometallurgy, 47(2-3), 231-241.
168. Zhang, W., & Honaker, R. (2019). Calcination pretreatment effects on acid leaching characteristics of rare earth elements from middlings and coarse refuse material associated with a bituminous coal source. Fuel, 249, 130-145.
169. Zhang, W., & Honaker, R. (2019). Enhanced leachability of rare earth elements from calcined products of bituminous coals. Minerals Engineering, 142, 105935.
170. Zhang, W., Noble, A., Yang, X., & Honaker, R. (2020). A comprehensive review of rare earth elements recovery from coal-related materials. Minerals, 10(5), 451.
171. Zhang, W., Yang, X., & Honaker, R. Q. (2018). Association characteristic study and preliminary recovery investigation of rare earth elements from Fire Clay seam coal middlings. Fuel, 215, 551-560.
172. Zhou, C., Liang, Y., Gong, Y., Zhou, Q., Chen, Y., Qiu, X., ... & Yan, C. (2014). Modes of occurrence of Fe in kaolin from Yunnan China. Ceramics International, 40(9), 14579-14587.